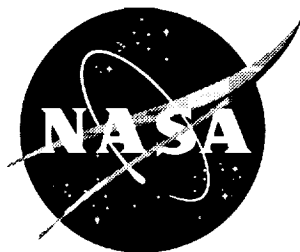# 1997 NASA High-Speed Research Program Aerodynamic Performance Workshop

Volume II—High Lift

Edited by
Daniel G. Baize
Langley Research Center, Hampton, Virginia

December 1999

The NASA STI Program Office . . . in Profile

Since its founding, NASA has been dedicated to the advancement of aeronautics and space science. The NASA Scientific and Technical Information (STI) Program Office plays a key part in helping NASA maintain this important role.

The NASA STI Program Office is operated by Langley Research Center, the lead center for NASA's scientific and technical information. The NASA STI Program Office provides access to the NASA STI Database, the largest collection of aeronautical and space science STI in the world. The Program Office is also NASA's institutional mechanism for disseminating the results of its research and development activities. These results are published by NASA in the NASA STI Report Series, which includes the following report types:

- TECHNICAL PUBLICATION. Reports of completed research or a major significant phase of research that present the results of NASA programs and include extensive data or theoretical analysis. Includes compilations of significant scientific and technical data and information deemed to be of continuing reference value. NASA counterpart of peer-reviewed formal professional papers, but having less stringent limitations on manuscript length and extent of graphic presentations.

- TECHNICAL MEMORANDUM. Scientific and technical findings that are preliminary or of specialized interest, e.g., quick release reports, working papers, and bibliographies that contain minimal annotation. Does not contain extensive analysis.

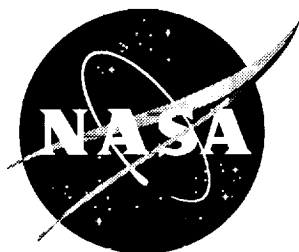- CONTRACTOR REPORT. Scientific and technical findings by NASA-sponsored contractors and grantees.

- CONFERENCE PUBLICATION. Collected papers from scientific and technical conferences, symposia, seminars, or other meetings sponsored or co-sponsored by NASA.

- SPECIAL PUBLICATION. Scientific, technical, or historical information from NASA programs, projects, and missions, often concerned with subjects having substantial public interest.

- TECHNICAL TRANSLATION. English-language translations of foreign scientific and technical material pertinent to NASA's mission.

Specialized services that complement the STI Program Office's diverse offerings include creating custom thesauri, building customized databases, organizing and publishing research results . . . even providing videos.

For more information about the NASA STI Program Office, see the following:

- Access the NASA STI Program Home Page at *http://www.sti.nasa.gov*

- Email your question via the Internet to help@sti.nasa.gov

- Fax your question to the NASA STI Help Desk at (301) 621-0134

- Telephone the NASA STI Help Desk at (301) 621-0390

- Write to:
  NASA STI Help Desk
  NASA Center for AeroSpace Information
  7121 Standard Drive
  Hanover, MD 21076-1320

1997 NASA High-Speed Research Program Aerodynamic Performance Workshop

Volume II—High Lift

Edited by
Daniel G. Baize
Langley Research Center, Hampton, Virginia

December 1999

PREFACE

The High-Speed Research Program and NASA Langley Research Center sponsored the NASA High-Speed Research Program Aerodynamic Performance Workshop on February 25–28, 1997. The workshop was designed to bring together NASA and industry High-Speed Civil Transport (HSCT) Aerodynamic Performance technology development participants in areas of: Configuration Aerodynamics (transonic and supersonic cruise drag prediction and minimization), High-Lift, Flight Controls, Supersonic Laminar Flow Control, and Sonic Boom Prediction. The workshop objectives were to: (1) report the progress and status of HSCT aerodynamic performance technology development; (2) disseminate this technology within the appropriate technical communities; and (3) promote synergy among the scientist and engineers working HSCT aerodynamics. In particular, single- and multi-point optimized HSCT configurations and HSCT high-lift system performance predictions were presented along with executive summarizes for all the Aerodynamic Performance technology areas.

The workshop was organized in three sessions as follows:

Session I	Plenary Session
Session II	Independent Session
Session III	Executive Summaries

The proceedings are published in two volumes:

Volume I, Parts 1 and 2	Configuration Aerodynamics
Volume II	High Lift

Conference Chairmen: Daniel G. Baize and Robert L. Calloway
NASA Langley Research Center

CONTENTS

Volume I, Part 2—Configuration Aerodynamics

Adams, Jr.
William M.
NASA Langley Research Center
Mail Stop 489
Hampton VA 23681-0001
Ph. 757-864-4013
fax 757-864-7795
eMail: w.m.adams@larc.nasa.gov

Agrawal
Shreekant
McDonnell Douglas Aerospace Co.
Mail Code 71-35
2401 E. Wardlow Road
Long Beach CA 90807-5309
Ph. 562-593-3436
fax 562-593-7593
eMail: agrawal@mdta.mdc.com

Allen
Jerry M.
NASA Langley Research Center
Mail Stop 499
Hampton VA 23681-0001
Ph. 757-864-5592
fax 757-864-4869
eMail: j.m.allen@larc.nasa.gov

Anders
Scott G.
NASA Langley Research Center
Mail Stop 170
Hampton VA 23681-0001
Ph. 757-864-8044
fax 757-864-8801
eMail: s.g.anders@larc.nasa.gov

Anderson
W. Kyle
NASA Langley Research Center
Mail Stop 128
Hampton VA 23681-0001
Ph. 757-864-2164
fax 757-864-8816
eMail: w.k.anderson@larc.nasa.gov

Antani
Tony
McDonnell Douglas Aerospace Co.
Mail Code 71-35
2401 E Wardlow Road
Long Beach CA 90807-5309
Ph. 562-593-3920
fax 562-593-7593
eMail: C362247@mdcpo05.lb.mdc.com

Applin
Zac
NASA Langley Research Center
Mail Stop 286
Hampton VA 23681-0001
Ph. 757-864-5062
fax 757-864-8192
eMail: z.t.applin@larc.nasa.gov

Arslan
Alan
McDonnell Douglas Aerospace Co.
Mail Code 71-35
2401 E. Wardlow Road
Long Beach CA 90807-5309
Ph. 562-593-8535
fax 562-593-7593
eMail: aea@indigo1.mdc.com

Bailey
F. Alan
The Boeing Company
Mail Stop 6H-FK
P.O. Box 3707
Seattle WA 98124-2207
Ph. 206-965-2699
fax 206-234-4543
eMail: frazier.a.bailey@boeing.com

Bailey
Mel
Lockheed Engineering & Sciences Co
NASA Langley Research Center
Mail Stop 389
Hampton VA 23681-0001
Ph. 757-864-4030
fax 757-864-7795
email: m.l.bailey@larc.nasa.gov

Bailey
Randall
Calspan Advanced Tech Center
P.O. Box 400
4455 Genesee Street
Buffalo NY 14225-0400
Ph. 716-631-6939
fax 716-631-6990
eMail: bailey@calspan.com

Baize
Dan
NASA Langley Research Center
Mail stop 119
Hampton VA 23681-0001
Ph. 757-864-1071
fax 757-864-8852
eMail: d.g.baize@larc.nasa.gov

Ball
Doug
The Boeing Company
Mail Stop 6H-FK
P.O. Box 3707
Seattle WA 98124-2207
Ph. 206-965-2151
fax 206-234-4543
eMail: baldnb00@ccmail.ca.boeing.com

Barrett
Mike
Honeywell Inc.
MS: MN65-2810
3660 Technology Drive
Minneapolis MN 55418
Ph. 612-951-7286
fax 612-951-7438
eMail: mike_barrett@htc.honeywell.com

Belcastro
Christine
NASA Langley Research Center
Mail Stop 161
Hampton VA 23681-0001
Ph. 757-864-4035
fax 757-864-7795
eMail:christine.m.belcastro@larc.nasa.go

Bencze
Dan
NASA Ames Research Center
Mail Stop 227-6
Moffett Field CA 94035-1000
Ph. 415-604-6618
fax 415-604-0737
eMail: dbencze@mail.arc.nasa.gov

Bengston
Robert
Pratt & Whitney
Mail Stop 165-21
400 Main St.
East Eartford CT 06108
Ph. 860-565-2080
fax 860-565-0123
eMail: bengtsrj@pweh.com

Bharadvaj
Bala
McDonnell Douglas Aerospace Co.
Mail Code 71-35
2401 E Wardlow Road
Long Beach CA 90807-5309
Ph. 562-593-3514
fax 562-982-7787
eMail: c336381@mail.mdc.com

Borland
Chris
The Boeing Company
Mail Stop 6H-FK
P.O. Box 3707
Seattle WA 98124-2207
Ph. 206-965-0336
fax 206-234-4543
eMail: christopher.j.borland@boeing.com

Bunin
Bruce
McDonnell Douglas Aerospace Co.
Mail Code 71-30
2401 E. Wardlow Road
Long Beach CA 90807-5309
Ph. 562-593-0629
fax 562-982-7383
eMail: bunin@mdta.mdc.com

Buning
Pieter G.
NASA Langley Research Center
Mail Stop 280
Hampton VA 23681-0001
Ph. 757-864-3093
fax 757-864-8195
eMail: p.g.buning@larc.nasa.gov

Burner
Alpheus W.
NASA Langley Research Center
Mail Stop 236
Hampton VA 23681-0001
Ph. 757-864-4635
fax 757-864-7607
eMail: a.w.burner@larc.nasa.gov

Buttrill
Carey
NASA Langley Research Center
Mail Stop 132
Hampton VA 23681-0001
Ph. 757-864-4016
fax 757-864-7795
eMail: c.s.buttrill@larc.nasa.gov

Calloway
Robert
NASA Langley Research Center
Mail Stop 119
Hampton VA 23681-0001
Ph. 757-864-2960
fax 757-864-8852
eMail: r.l.calloway@larc.nasa.gov

Camache
Peter
McDonnell Douglas Aerospace Co.
Mail Code 71-30
2401 E. Wardlow Road
Long Beach CA 90807-5309
Ph. 562-593-7012
fax 562-982-7787
eMail: camacho@mdta.mdc.com

Campbell
Brian A.
NASA Langley Research Center
Mail Stop 286
Hampton VA 23681-0001
Ph. 757-864-5069
fax 757-864-8192
eMail: b.a.campbell@larc.nasa.gov

Campbell
James F.
NASA Langley Research Center
Mail Stop 499
Hampton VA 23681-0001
Ph. 757-864-2866
fax 757-864-8469
eMail: j.f.campbell@larc.nasa.gov

Campbell
Richard L.
NASA Langley Research Center
Mail Stop 499
Hampton VA 23681-0001
Ph. 757-864-2872
fax 757-864-8469
eMail: r.l.campbell@larc.nasa.gov

Capone
Fran J.
NASA Langley Research Center
Mail Stop 280
Hampton VA 23681-0001
Ph. 757-864-3004
fax 757-864-8195
eMail: f.j.capone@larc.nasa.gov

Cappuccio
Mina
NASA Ames Research Center
Mail Stop 227-6
Moffett Field CA 94035-1000
Ph. 415-604-1313
fax 415-604-0737
eMail: mcappuccio@mail.arc.nasa.gov

Chaney
Steve R.
The Boeing Company
Mail Stop 6H-FK
P.O. Box 3707
Seattle WA 98124-2207
Ph. 206-237-2878
fax 206-234-4543
eMail:

Chang
Bor-Chin
Drexel University
Dept. Mechanical Engineering
Philadelphia PA 19104
Ph. 215-895-1790
fax 215-895-1478
eMail: bchang@coe.drexel.edu

Chen
Allen W.
The Boeing Company
Mail Stop 6H-FK
P.O. Box 3707
Seattle WA 98124-2207
Ph. 206-965-3490
fax 206-234-4543
eMail: awc@hsctaero.ca.boeing.com

Cheung
Samson
McDonnell Douglas Aerospace Co.
Mail Code 71-35
2401 E. Wardlow Road
Long Beach CA 90807-5309
Ph. 562-593-9025
fax 562-593-7593
eMail: shc@indigo1.mdc.com

Christhilf
David M.
Lockheed Engineering & Sciences Co.
NASA Langley Research Center
Mail Stop 389
Hampton VA 23681-00
Ph. 757-864-4029
fax 757-864-8838
eMail: d.m.christhilf@larc.nasa.gov

Chu
Julio
NASA Langley Research Center
Mail Stop 248
Hampton VA 23681-0001
Ph. 757-864-5136
fax 757-864-3553
eMail: j.chu@larc.nasa.gov

Clark
Roger
McDonnell Douglas Aerospace Co.
Mail Code 71-35
2401 E Wardlow Road
Long Beach CA 90807-5309
Ph. 562-982-5334
fax 562-593-7593
eMail: c08375@mdcpo17.lb.mdc.com

Cliff
Susan
NASA Ames Research Center
Mail Stop 227-6
Moffett Field A 94035-1000
Ph. 415-604-3907
fax 415-604-0737
eMail: cliff@ra-iris.arc.nasa.gov

Coen
Peter
NASA Langley Research Center
Mail Stop 248
Hampton VA 23681-0001
Ph. 757-864-5991
fax 757-864-3553
eMail: p.g.coen@larc.nasa.gov

Conner
Roy S.
The Boeing Company
Mail Stop 6H-FK
P.O. Box 3707
Seattle WA 98124-2207
Ph. 206-965-3774
fax 206-234-4543
eMail: rsc7463@hsctaero.ca.boeing.com

Cuthbertson
R. D.
The Boeing Company
Mail Stop 6H-FR
P.O. Box 3707
Seattle WA 98124-2207
Ph. 206-237-7594
fax 206-234-4543
eMail: robert.d.cuthbertson@boeing.com

Darden
Christine
NASA Langley Research Center
Mail Stop 119
Hampton VA 23681-0001
Ph. 757-864-5258
fax 757-864-8852
eMail: c.m.darden@larc.nasa.gov

Deere
Karen A.
NASA Langley Research Center
Mail Stop 280
Hampton VA 23681-0001
Ph. 757-864-8986
fax 757-864-8195
eMail: k.a.deere@larc.nasa.gov

DeLoach
Richard
NASA Langley Research Center
Mail Stop 236
Hampton VA 23681-0001
Ph. 757-864-4657
fax 757-864-7607
eMail: r.deloach@larc.nasa.gov

Derry
Steve
NASA Langley Research Center
Mail Stop 125B
Hampton VA 23681-0001
Ph. 757-864-7412
fax 757-864-8837
eMail: s.d.derry@larc.nasa.gov

Domack
Christopher S.
Lockheed Engineering & Sciences Co.
NASA Langley Research Center
Mail Stop 248
Hampton VA 23681-0001
Ph. 757-864-6504
fax 757-864-3553
eMail: domack@avd00.larc.nasa.gov

Duffy
Keith S.
The Boeing Company
Mail Stop 6H-FA
P.O. Box 3707
Seattle WA 98124-2207
Ph. 206-965-0116
fax 206-234-4543
eMail: keith@brazil.ca.boeing.com

Ebner
N. Keith
The Boeing Company
Mail Stop 6H-FK
P.O. Box 3707
Seattle WA 98124-2207
Ph. 206-965-0198
fax 206-234-4543
eMail: keith.ebner@boeing.com

Elgersma
Mike
Honeywell Inc.
MS: MN 65-2810
3660 Technology Drive
Minneapolis MN 55418
Ph. 612-951-7208
fax 612-951-7438
eMail: mike_elgersma@htc.honeywell.com

Erickson
Gary E.
NASA Langley Research Center
Mail Stop 413
Hampton VA 23681-0001
Ph. 757-864-2886
fax 757-864-8095
eMail: g.e.erickson@larc.nasa.gov

Fan
Xuetong
ASE Technologies Inc.
Suite 203
4015 Exeuctive Park Drive
Cincinnati OH 45241
Ph. 513-563-8855
fax 513-563-8865
eMail: fan@mars.asetach.com

Feifel
Winfried M.
The Boeing Company
Mail Stop 6H-FK
P.O. Box 3707
Seattle WA 98124-2207
Ph. 206-965-0561
fax 206-234-4543
eMail:

Fenbert
James W.
NASA Langley Research Center
Mail Stop 248
Hampton VA 23681-0001
Ph. 864-5973
fax
eMail: j.w.fenbert@larc.nasa.gov

Funk
Joan G.
NASA Langley Research Center
Mail Stop 119
Hampton VA 23681-0001
Ph. 757-864-3092
fax 757-864-8852
eMail: j.g.funk@larc.nasa.gov

Garg
Sanjay
NASA Lewis Research Center
Mail Stop 77-1
21000 Brookpark Road
Cleveland OH 44135
Ph. 216-433-2685
fax 216-433-8643
eMail: sanjay.garg@lerc.nasa.gov

Ghaffari
F.
NASA Langley Research Center
Mail Stop 499
Hampton VA 23681-0001
Ph. 757-864-2856
fax 757-864-8469
eMail: f.ghaffari@larc.nasa.gov

Giesy
Dan
Lockheed Engineering & Sciences Co.
NASA Langley Research Center
Mail Stop 389
Hampton VA 23681-0001
Ph. 757-864-4006
fax 757-864-8838
eMail: d.p.giesy@larc.nasa.gov

Gilbert
Bill
NASA Langley Research Center
Mail Stop 119
Hampton VA 23681-0001
Ph. 757-864-6392
fax 757-864-8852
eMail: w.p.gilbert@larc.nasa.gov

Glaab
Louis
Lockheed Engineering & Sciences Co.
NASA Langley Research Center
Mail Stop 343
Hampton VA 23681-0001
Ph. 757-864-1159
fax 757-864-7722
eMail: l.j.glaab@larc.nasa.gov

Goldberg
Perry
McDonnell Douglas Aerospace Co.
Mail Code 71-35
2401 E. Wardlow Road
Long Beach CA 90807-5309
Ph. 562-982-2126
fax 562-593-7593
eMail: goldbet@citm.mdc.com

Gracey
Chris
NASA Langley Research Center
Mail Stop 161
Hampton VA 23681-0001
Ph. 757-864-4019
fax 757-864-7795
eMail: c.gracey@larc.nasa.gov

Gregory
Irene
NASA Langley Research Center
Mail Stop 132
Hampton VA 23681-0001
Ph. 757-864-4075
fax 757-864-7795
eMail: i.m.gregory@larc.nasa.gov

Griffiths
Robert C.
The Boeing Company
Mail Stop 6H-FK
P.O. Box 3707
Seattle WA 98124-2207
Ph. 206-965-3465
fax 206-234-4543
eMail: robert.c.griffiths@boeing.com

Hager
James
McDonnell Douglas Aerospace Co.
Mail Code 71-35
2401 E. Wardlow Road
Long Beach CA 90807-5309
Ph. 562-982-9217
fax 562-593-7593
eMail: joh@indigo1.mdc.com

Halberg
Eric N.
Naval Postgraduate School
Mail Code 31
Halligan Hall
Monterey CA 93940
Ph. 408-656-5040
fax 408-656-2313
eMail: hallberg@aa.nps.navy.mil

Green
Lawrence L.
NASA Langley Research Center
Mail Stop 159
Hampton VA 23681-0002
Ph. 757-864-2228
fax 757-864-9713
eMail: l.l.green@larc.nasa.gov

Greiner
Glenn P.
George Washington University
NASA Langley Research Center
Mail Stop 132
Hampton VA 23681-0001
Ph. 757-864-4086
fax 757-864-7795
eMail: g.p.greiner@larc.nasa.gov

Gumbert
Clyde R.
NASA Langley Research Center
Mail Stop 159
Hampton VA 23681-0001
Ph. 757-864-2221
fax 757-864-9713
eMail: c.r.gumbert@larc.nasa.gov

Hahne
Dave
NASA Langley Research Center
Mail Stop 153
Hampton VA 23681-0001
Ph. 757-864-1162
fax 757-864-7722
eMail: d.e.hahne@larc.nasa.gov

Hamner
Marvine P.
McDonnell Douglas Aerospace Co.
Mail Code S1022272
P.O. Box 516
St Louis MO 63166-0516
Ph. 314-233-1600
fax 314-777-2984
eMail: mph@indigo1.mdc.com

Hartwich
Peter M.
McDonnell Douglas Aerospace Co.
Mail Code 71-35
2401 E. Wardlow Road
Long Beach CA 90807-4418
Ph. 562-593-2965
fax 562-593-7593
eMail: pmh@indigo1.mdc.com

Henderson
Dennis K.
McDonnell Douglas Aerospace Co.
Mail Code 71-35
2401 E Wardlow Road
Long Beach CA 90807-5309
Ph. 562-982-9269
fax 562-593-7593
eMail: dhenderson@c17m.mdc.com

Hickey
Paul K.
ASE Technologies, Inc.
Suite 203
4015 Executive Park Drive
Cincinnati OH 45241
Ph. 513-563-8855
fax 513-563-8865
eMail: phickey@asetech.com

Hines
Dick
Pratt & Whitney
Mail Stop 165-22
400 Main St.
East Hartford CT 06108
Ph. 860-565-7239
fax 860-565-0168
eMail: hinesrw@pwfl.com

Jackson
Bruce
NASA Langley Research Center
Mail Stop 132
Hampton VA 23681-0001
Ph. 757-864-4060
fax 757-864-7795
eMail: e.b.jackson@larc.nasa.gov

Jackson
Mike
Honeywell Inc.
MS: MN 65-2810
3660 Technology Drive
Minneapolis MN 55418
Ph. 612-951-7748
fax 612-951-7438
eMail: mike_jackson@htc.honeywell.com

Jager
Merle L.
McDonnell Douglas Aerospace Co.
Mail Code 71-30
2401 E. Wardlow Road
Long Beach CA 90807-5309
Ph. 562-593-4003
fax 562-982-7787
eMail: C391818@mdcpo10.lb.mdc.com

Joshi
Suresh
NASA Langley Research Center
Mail Stop 132
Hampton VA 23681-0001
Ph. 757-964-6608
fax 757-864-7795
eMail: s.m.joshi@larc.nasa.gov

Joslin
Ron
NASA Langley Research Center
Mail Stop 170
Hampton VA 23681-0001
Ph. 757-864-2234
fax 757-864-8801
eMail: r.d.joslin@larc.nasa.gov

Kaminer
Issac I.
Naval Postgraduate School
Mail Code AA/KA
Monterey CA 93943
Ph. 408-656-5040
fax 408-656-2313
eMail: kaminer@aa.nps.navy.mil

Kandula
Max
Dynacs Engineering Co., Inc.
Building 3, Suite B
258 S.W. 43rd
Renton WA 98055
Ph. 206-251-8692
fax 206-251-9564
eMail: kandula@vm.nas.gov

Kennelly
Robert A.
NASA Ames Research Center
Mail Stop 227-6
Moffett Field CA 94035-1000
Ph. 415-604-5860
fax 415-604-0737
eMail: rakennelly@mail.arc.nasa.gov

Klopter
Goetz H.
MCAT, Inc.
NASA Ames Research Center
Mail Stop 258-1
Moffett Field CA 94035-1000
Ph. 415-604-3993
fax 415-604-2238
eMail: klopter@nas.nasa.gov

Krause
Fred
General Electric
Mail Drop T34
1 Neumann Way
Cincinnati OH 45215-1988
Ph. 513-552-4279
fax 513-552-4350
eMail: fred.h.krause@ae.ge.com

Kubiatko
Paul
McDonnell Douglas Aerospace Co.
Mail Code 71-35
2401 E. Wardlow Road
Long Beach CA 90807-5309
Ph. 562-982-7850
fax 562-593-7593
eMail: kubiatko@mdta.mdc.com

Kemmerly
Guy T.
NASA Langley Research Centr
Mail Stop 286
Hampton VA 23681-0001
Ph. 757-864-5070
fax 757-864-8192
eMail: g.t.kemmerly@larc.nasa.gov

Kinard
Tom A.
Lockheed Martin
86 South Cobb Drive
Mail Code 0685
Marietta GA 30063-0685
Ph. 770-494-8588
fax 770-494-3055
eMail: kinard@mar.lmco.com

Kobayashi
Takahisa
NASA Lewis Research Center
Mail Stop 77-1
21000 Brookpark Road
Cleveland OH 44135-3191
Ph. 216-433-3739
fax 216-433-8643
eMail: tak@lerc.nasa.gov

Krist
Steven E.
NASA Langley Research Center
Mail Stop 280
Hampton VA 23681-0001
Ph. 757-864-3046
fax
eMail: s.e.krist@larc.nasa.gov

Kulfan
Bob
The Boeing Company
Mail Stop 6H-FK
P.O. Box 3707
Seattle WA 98124-2207
Ph. 206-965-3779
fax 206-234-4543
eMail: robert.m.kulfan@boeing.com

Kwatny
Harry
Drexel University
Dept Mechanical Engineering
Philadelphia PA 19104
Ph. 215-895-2356
fax 215-895-1478
eMail: hkawtny@coe.drexel.edu

Lawrence
Scott
NASA Ames Research Center
Mail Stop T27-B-2
Moffett Field CA 94035-1000
Ph. 415-604-4050
fax 415-604-1095
eMail: lawrence@nas.nasa.gov

Leavitt
Larry
NASA Langley Research Center
Mail Stop 280
Hampton VA 23681-0001
Ph. 757-864-3017
fax 757-864-8195
eMail: l.d.leavitt@larc.nasa.gov

Lessard
Victor R.
VIGYAN
30 Research Drive
Hampton VA 23666-1325
Ph. 757-864-5072
eMail: v.r.lessard@larc.nasa.gov.

Lessard
Wendy
NASA Langley Research Center
Mail Stop 286
Hampton VA 23681-0001
Ph. 757-864-1165
fax 757-864-8192
eMail: w.b.lessard@larc.nasa.gov

Light
Bruce A.
The Boeing Company
Mail Stop 6H-FP
P.O. Box 3707
Seattle WA 98124-2207
Ph. 206-965-1934
fax 206-234-4543
eMail:

Lin
Kyong
NASA Langley Research Center
Mail Stop 161
Hampton VA 23681-0001
Ph. 757-864-4342
fax 757-864-7797
eMail: k.b.lim@larc.nasa.gov

Liu
Tianshu
High Technology Corporation
28 Research Drive
Hampton VA 23666
Ph. 757-865-6766
eMail: tianshu@htc.tech.com

Ludas
Kevin
McDonnell Douglas Aerospace Co.
Mail Code 71-30
2401 E Wardlow Road
Long Beach CA 90807-5309
Ph. 562-593-2889
fax 562-982-7383
eMail: ludas@mdta.mdc.com

Lund
David W.
The Boeing Company
Mail Stop 6H-FK
P.O. Box 3707
Seattle WA 98124-2207
Ph. 206-965-2151
fax 206-234-4543
eMail: david.w.lund@boeing.com

MacKinnon
Malcolm I.K.
The Boeing Company
Mail Stop 6H-FM
P.O. Box 3707
Seattle WA 98124-2207
Ph. 206-237-0339
fax 206-234-4543
eMail: malcolm.i.mackinnon@boeing.com

Maddalon
Dal V.
NASA Langley Research Center
Mail Stop 170
Hampton VA   23681-0001
Ph. 757-864-1909
fax 757-864-8801
eMail: d.v.maddalon@larc.nasa.gov

McMillin
S. Naomi
NASA Langley Research Center
Mail Stop 499
Hampton VA 23681-0001
Ph. 757-864-5581
fax 757-864-8469
eMail: s.n.mcmillin@larc.nasa.gov

Mejia
Kevin K.
The Boeing Company
Mail Stop 6H-FK
P.O. Box 3707
Seattle WA 98124-2207
Ph. 206-965-3773
fax 206-234-4543
eMail: devin.m.mejia@boeing.com

Morgenstern
John
McDonnell Douglas Aerospace Co.
Mail Code 71-30
2401 E Wardlow Road
Long Beach CA 90807-5309
Ph. 562-982-9276
fax 562-982-7787
eMail: morgenstern@mdta.mdc.com

MacWilkinson
Derek G.
McDonnell Douglas Aerospace Co.
Mail Code 71-30
2401 E. Wardlow Road
Long Beach CA 90807-5309
Ph. 562-496-8723
fax 562-982-7383
eMail: dmacw@mdta.mdc.com

Martin
Grant L.
McDonnell Douglas Aerospace Co.
Mail Code 71-35
2401 E. Wardlow Road
Long Beach CA 90807-5309
Ph. 562-593-0040
fax 562-593-7593
eMail: glm@indigo1.mdc.com

McMinn
Dana
NASA Langley Research Center
Mail Stop 132
Hampton VA 23681-0001
Ph. 757-864-4069
fax 757-864-7795
eMail: j.d.mcminn@larc.nasa.gov

Meredith
Paul T.
The Boeing Company
Mail Stop 6H-FK
P.O. Box 3707
Seattle WA 98124
Ph. 206-965-3468
fax 206-234-4543
eMail: paul.t.meredith@ca.boeing.com

Morris
Martin J.
McDonnell Douglas Aerospace Co.
Mail Code 106-7126
P.O. Box 516
St. Louis MO 63166-0516
Ph. 314-232-6939
fax 314-777-1328
eMail: mmorris@mdc.com

Mortlock
Alan
McDonnell Douglas Aerospace Co.
Mail Code 71-30
2401 E Wardlow Road
Long Beach CA 90807-5309
Ph. 562-593-3937
fax 562-982-7787
eMail: mortlock@mdta.mdc.com

Narducci
Robert
McDonnell Douglas Aerospace Co.
Mail Code 71-35
2401 E. Wardlow Road
Long Beach CA 90807-5309
Ph. 562-593-0171
fax 562-593-7593
eMail: rpn@indigo1.mdc.com

Nelms, Jr.
Pres
NASA Ames Research Center
Mail Stop 237-2
Moffett Field CA 94035-1000
Ph. 415-604-6093
fax 415-604-6990
eMail: p_nelms@qmgate.arc.nasa.gov

Nelson
Chester P.
The Boeing Company
Mail Stop 6H-FK
P.O. Box 3707
Seattle WA 98124-2207
Ph. 206-965-5514
fax 206-234-4543
eMail: chester.p.nelson@boeing.com

Newman
Brett
Old Dominion University
Ph. 757-683-3720
fax 757-683-3200

Owens
Lewis
NASA Langley Research Center
Mail Stop 286
Hampton VA 23681-0001
Ph. 757-864-5127
fax 757-864-8192
eMail: l.r.owens@larc.nasa.gov

Ozoroski
L. P.
NASA Langley Research Center
Mail Stop 248
Hampton VA 23681-0001
Ph. 757-864-5992
fax 757-864-3553
eMail: l.p.ozoroski@larc.nasa.gov

Pao
S. Paul
NASA Langley Research Center
Mail Stop 280
Hampton VA 23681-0001
Ph. 757-864-3044
fax 757-864-8195
eMail: s.p.pao@larc.nasa.gov

Patton
Robert E.
The Boeing Company
Mail Stop 6H-FK
P.O. Box 3707
Seattle WA 98124-2207
Ph. 206-965-1425
fax 206-234-4543
eMail: robert.e.patton@boeing.com

Peavey
Charles C.
Northrop Grumman Corp.
Mail Code 9B52/GK
8900 E. Washington Blvd.
Pico Rivera CA 90660
Ph. 562-948-8937
fax 562-948-8068
eMail: cpeavey@world.northgrum.com

Pittman
James L.
NASA Langley Research Center
Mail Stop 395
Hampton VA 23681-0001
Ph. 757-864-1361
fax 757-864-8193
eMail:

Popernack, Jr.
Thomas G.
NASA Langley Research Center
Mail Stop 267
Hampton VA 23681-0001
Ph. 757-864-5163
fax
eMail: t.g.popernack.jr@larc.nasa.gov

Powell
Art
McDonnell Douglas Aerospace Co.
Mail Code 71-35
2401 E. Wardlow Road
Long Beach CA 90807-5309
Ph. 562-593-3225
fax 562-593-7593
eMail: C306624@mdcpo11.lb.md.com

Radeztsky
Ronald
High Technology Corporation
28 Research Drive
Hampton VA 23666
Ph. 757-865-0818
fax 757-865-6766
eMail: ron@htc.tech.com

Ray
James K.
The Boeing Company
Mail Stop 6H-FA
P.O. Box 3707
Seattle WA 98124-2207
Ph. 206-965-1997
fax 206-234-4543
eMail: james.k.ray@.boeing.com

Polito
Ryan C.
McDonnell Douglas Aerospace Co.
Mail Code 71-35
2401 E. Wardlow Road
Long Beach CA 90807-5309
Ph. 562-593-0048
fax 562-593-7593
eMail: rp@indigo1.mdc.com

Pototzky
Anthony S.
NASA Langley Research Center
Mail Stop 389
Hampton VA 23681-0001
Ph. 757-864-2827
fax 757-864-8838
eMail: a.s.pototzky@larc.nasa.gov

Proffitt
Melissa
Lockheed Engineering and Sciences Co.
NASA Langley Research Center
Mail Stop 389
Hampton VA 23681-0001
Ph. 757-864-4024
fax 757-864-7795
eMail: m.s.proffitt@larc.nasa.gov

Raney
David
NASA Langley Research Center
Mail Stop 489
Hampton VA 23681-0001
Ph. 757-864-4033
fax 757-864-7795
eMail: d.l.raney@larc.nasa.gov

Reuther
James
RIACS
NASA Ames Research Center
Mail Stop 227-6
Moffett Field CA 94035-1000
Ph. 415-604-1516
fax 415-604-0737
eMail: reuther@ra.iris-arc.nasa.gov

Ricketts
Rodney H.
NASA Langley Research Center
Mail Stop 119
Hampton VA 23681-0001
Ph. 757-864-1209
fax 757-864-8852
eMail: r.h.ricketts@larc.nasa.gov

Rimlinger
Mark J.
Sterling Software, Inc.
NASA Ames Research Center
Mail Stop 227-6
Moffett Field CA 94035-1000
Ph. 757-864=5944
fax 757-864-0737
eMail: rimlinge@ra-iris.arc.nasa.gov

Rivers
Melissa B.
NASA Langley Research Center
Mail Stop 499
Hampton VA 23681-0001
Ph. 757-864-5161
fax 757-864-7892
eMail: m.b.rivers@larc.nasa.gov

Rivers
Rob
NASA Langley Research Center
Mail Stop 132
Hampton VA 23681-0001
Ph. 757-864-3917
fax 757-864-8549
eMail: r.a.rivers@larc.nasa.gov

Roberts
Thomas W.
NASA Langley Research Center
Mail Stop 128
Hampton VA 23681-0001
Ph. 757-864-6804
fax 757-864-8166
eMail: t.w.roberts@larc.nasa.gov

Rossitto
Ken
McDonnell Douglas Aerospace Co.
Mail Code 36-41
2401 E Wardlow Road
Long Beach CA 90807-5309
Ph. 562-593-3870
fax 562-593-7593
eMail: rossitto@mdta.mdc.com

Saladino
Anthony J. ·
Dynacs Engineering Co., Inc.
Building 3, Suite B
258 S.W. 43rd Street
Renton WA 98055
Ph. 206-251-8692
fax 206-251-9564
eMail: saladino@indyl.dynacsgen.com

Sawyer
Wallace C.
NASA Langley Research Center
Mail Stop 119
Hampton VA 23681-0001
Ph 757-864-2267
fax 757-864-8852
Email: w.c.sawyer@larc.nasa.gov

Scott
Michael
NASA Langley Research Center
Mail Stop 132
Hampton VA 23681-0001
Ph. 757-864-6618
fax 757-864-7795
eMail: michael.allen.scott@larc.nasa.gov

Shaw
Joe
NASA Lewis Research Center
Mail Stop 60-2
21000 Brookpark Road
Cleveland OH 44135-3191
Ph. 216-977-7135
fax 216-977-7133
eMail: robert.j.shaw@lerc.nasa.gov

Shields
Bill
Lockheed Engineering & Sciences Co.
NASA Langley Research Center
Mail Stop 248
Hampton VA 23681-0001
Ph. 757-864-5958
fax 757-864-5958
eMail: c.w.shields@larc.nasa.gov

Siclari
Michael J.
Northrop Grumman Corp.
Mail Stop KO8-14
South Oyster Bay Road
Bethpage NY 11714
Ph. 516-575-8067
fax 516-346-2937
eMail: siclari@gateway.grumman.com

Smith
Brian
NASA Ames Research Center
Mail Stop 247-2
Moffett Field CA 94035-3191
Ph. 415-604-6669
fax 415-604-3489
eMail: bsmith@mail.arc.nasa.gov

Snyder
Phil
NASA Ames Research Center
Mail Stop 237-2
Moffett Field CA 94035-1000
Ph. 415-604-4592
fax 415-604-6990
eMail: p.t.snyder@mail.arc.gov

Sundaram
Pichuraman
McDonnell Douglas Aerospace Co.
Mail Code 71-35
2401 E. Wardlow Road
Long Beach CA 90807-5309
Ph. 562-496-9787
fax 562-593-7593
ps@indigo1.mdc.com

Tamrat
Befecadu
Boeing North American Inc.
Mail Code Sk12
2600 Westminster Blvd.
Seal Beach CA 90740
Ph. 310-797-4948
fax 310-797-4854
eMail: bftamrat@naa.boeing.com

Thomas
James L.
NASA Langley Research Center
Mail Stop 128
Hampton VA 23681-0001
Ph. 757-864-2163
fax 757-864-8816
eMail: j.l.thomas@larc.nasa.gov

Thomas
Scott D.
Sterling Software, Inc.
NASA Ames Research Center
Mail Stop 237-2
Moffett Field CA 94035-1000
Ph. 415-604-6387
fax 415-604-6990
eMail: thomas@nas.nasa.gov.

Troha
William A.
NASA Lewis Research Center
Mail Stop 86-1
21000 Brookpark Road
Cleveland OH 44135-3191
Ph. 216-433-3195
fax 216-433-6624
eMail: william.a.troha@lerc.nasa.gov

Unger
Eric R.
McDonnell Douglas Aerospace Co.
Mail Code 71-35
2401 E. Wardlow Road
Long Beach CA 90807-5309
Ph. 562-593-3037
fax 562-593-7593
eMail: c386821@hc1038.mdc.com

Vasquez
Moises
George Washington University
NASA Langley Research Center
Mail Stop 286
Hampton VA 23681-0001
Ph.
Fax
eMail: vasquez@ab80.larc.nasa.gov

Vatsa
Veer N.
NASA Langley Research Center
Mail Stop 128
Hampton VA 23681-0001
Ph. 757-864-2236
fax 757-864-8816
eMail: v.n.vatsa@larc.nasa.gov

Viars
Philip
General Electric
Mail Drop T34
1 Neumann Way
Cincinnati OH 45215-1988
Ph. 513-552-4132
fax 513-552-4350
eMail: Philip.Viars@ae.ge.com

Wahls
Richard A.
NASA Langley Research Center
Mail Stop 499
Hampton VA 23681-0001
Ph. 757-864-5108
fax 757-864-8469
eMail: r.awahls@larc.nasa.gov

Wallace
Hoyt
McDonnell Douglas Aerospace Co.
Mail Code S270-2370
P.O. Box 516
St Louis MO 53166-0516
Ph. 314-233-7712
fax 314-234-7210
eMail: hwallace@mdc.com

Walsh
Michael J.
NASA Langley Research Center
Mail Stop 170
Hampton VA 23681-0001
Ph. 757-864-5542
fax 757-864-7897
eMail: m.j.walsh@larc.nasa.gov

Wechsler
Jim
McDonnell Douglas Aerospace Co.
Mail Code 71-35
2401 E. Wardlow Road
Long Beach CA 90807-5309
Ph. 562-496-7627
fax 562-982-7787
eMail: jwex@mdta.mdc.com

Westra
Bryan W.
Northrop Grumman Corp.
Mail Code 9B52/GK
8900 E. Washington Blvd.
Pico Rivera CA 90660
Ph. 562-948-7560
fax 562-948-8068
eMail: bwestra@world.northgrum.com

Whitehead
Allen H. Jr.
NASA Langley Research Center
Mail Stop 119
Hampton VA 23681-0001
Ph. 757-864-7800
fax 757-864-8852
eMail: allen.h.whitehead@larc.nasa.gov

Wilhite
Alan W.
NASA Langley Research Center
Mail Stop 119
Hampton VA 23681-0001
Ph. 757-864-2982
fax 757-864-8852
eMail: a.w.wilhite@larc.nasa.gov

Williams
Todd
McDonnell Douglas Aerospace Co.
Mail Code 71-12
2401 E. Wardlow Road
Long Beach CA 90807-5309
Ph. 562-496-8795
fax 562-496-9244
eMail: twilliams@mdta.mdc.com

Wittenberg
K. Robyn
The Boeing Company
Mail Stop 6H-FK
P.O. Box 3707
Seattle WA 98124-2207
Ph. 206-965-1091
fax 206-234-4543
eMail:

Wood
Rick
NASA Langley Research Center
Mail Stop 499
Hampton VA 23681-0001
Ph. 757-864-6174
fax 757-864-8469
eMail:

Yaghmaee
Sasan S.
The Boeing Company
Mail Stop 6H-FK
P.O. Box 3707
Seattle WA 98124-2207
Ph. 206-965-3777
fax 206-234-4543
eMail: sasan.yagmaee@boeing.com

Yeh
David T.
McDonnell Douglas Aerospace Co.
Mail Code 71-35
2401 E. Wardlow Road
Long Beach CA 90807-5309
Ph. 562-496-9113
fax 562-593-7593
eMail: dty@indigo1.mdc.com

Wilson
Doug
The Boeing Company
Mail Stop 6H-FK
P.O. Box 3707
Seattle WA 98124-2207
Ph. 206-965-3458
fax 206-234-4543
eMail: douglas.l.wilson@boeing.com

Woan
Chung-Jin
Boeing North American, Inc.
Mail Code SK07
P.O. Box 3644
Seal Beach CA 90740-7644
Ph.
fax
eMail

Wyatt
Greg
The Boeing Company
Mail Stop 6H-FK
P.O. Box 3707
Seattle WA 98124-2207
Ph. 206-965-3466
fax 206-234-4543
eMail: douglas.l.wilson@boeing.com

Yaros
Steven
NASA Langley Research Center
Mail Stop 286
Hampton VA 23681-0001
Ph. 757-864-3050
fax 757-864-8192
eMail: s.f.yaros@larc.nasa.gov

Zuniga
Fanny
NASA Ames Research Center
Mail Stop 247-2
Moffett Field CA 94035-1000
Ph. 415-604-2017
fax 415-604-3489
eMail: fzuniga@mail.arc.nasa.gov
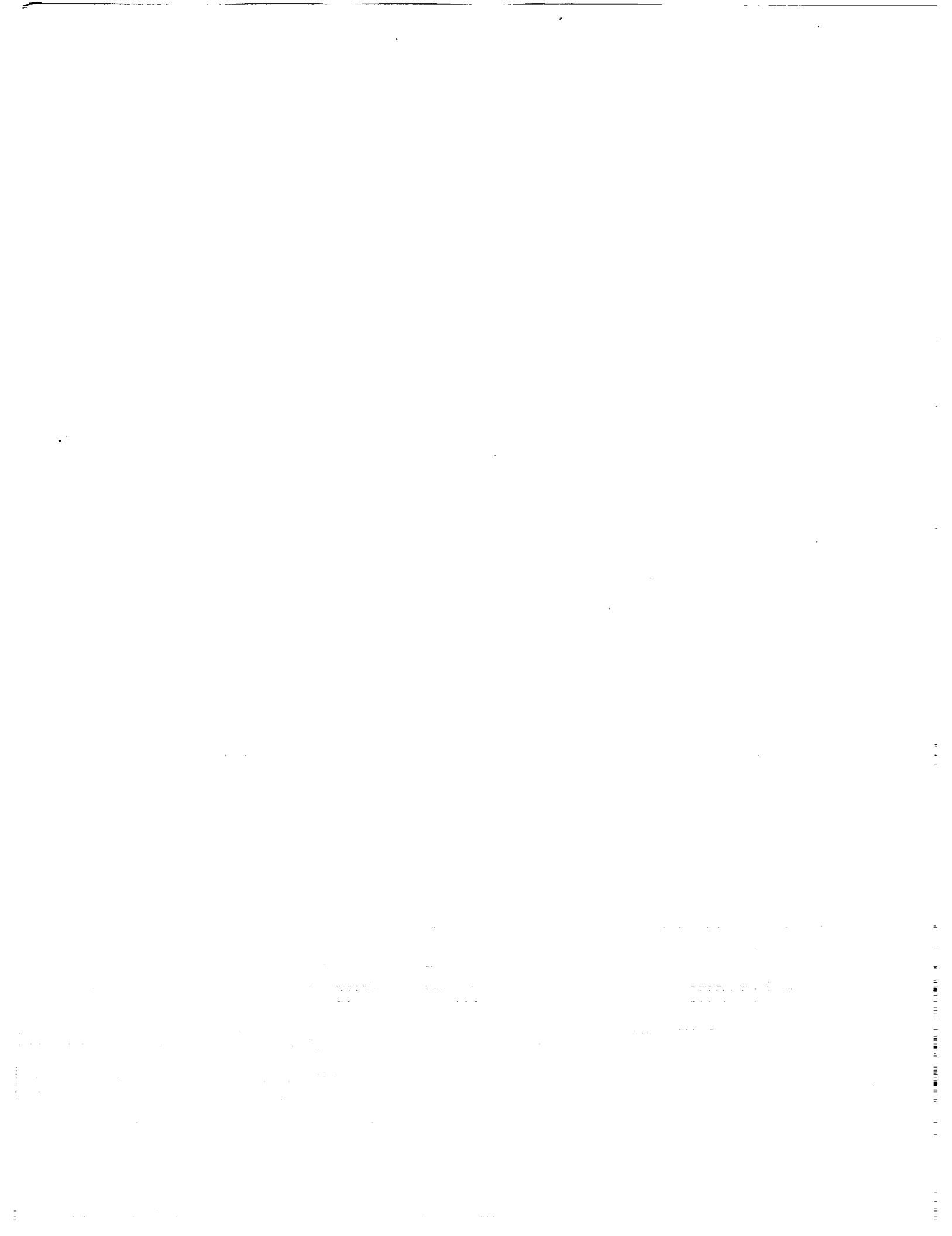
4.3.2 HSR High Lift Program and PCD2 Update

High Lift ITD Team

Guy T. Kemmerly, Langley   Roger Clark, McDonnell Douglas

Peter Coen, Langley   Dave Hahne, Langley

Paul Meredith, Boeing   Brian Smith, Ames

February 25, 1997

Aero Performance Workshop

As a representative of the High Lift Integrated Technology Development team I am here to "kick-off" the high lift independent sessions with an overview - where we have been, where we are, and where we are headed.

I'll also describe some of the interfaces we have so everyone can see how we connect with the rest of the program.

High Lift Mission

4.3.2

The mission of High-Lift Technology is to develop technology allowing the design of practical high lift concepts for the High-Speed Civil Transport (HSCT) in order to:

- **operate safely and efficiently**
- **reduce terminal control area and community noise.**

In fulfilling this mission, close and continuous coordination will be maintained with other High-Speed Research (HSR) technology elements in order to support optimization of the overall airplane (rather than just the high lift system).

4.3.2 High Lift Technology

This is the mission of the high lift team.

We will develop technologies for safe and quiet low-speed operations of a High Speed Civil Transport. That includes both high lift and stability-and-control technologies.

And, we will do so as an integrated part of the larger program.

The work is broken into four overlapping subelements.

Technology Concept Assessment

4.3.2.1

Develop an efficient high-lift system for the Technology Concept airplane (TCA) and provide an assessment of the low speed aerodynamic performance and stability and control characteristics.

- TCA
  - 5% model for 14 X 22 and 12-Ft
  - AERO2S
  - CFL3D and TetrUSS
- Modified Ref H
  - 2.2% model for NTF
  - CFL3D modeling

4.3.2 High Lift Technology

First subelement: TCA Assessment for both high lift and S&C

As with the Ref H, low Re parametric studies will be conducted in the 14 X 22. Linear codes have been used to predict optimum flap settings and both structured and unstructured viscous codes have modeled the configuration in an attempt to define the limitations of those codes on this type of configuration. Status reports will be presented on the CFD efforts which, of course, have the ultimate goal of reducing risk and the design cycle time for high performance aircraft. In the 14 X 22, the low speed model will also be used to define powered ground effects on the aft body this summer.

Early in FY'98, that model will be tested in the 12-Ft Pressure Tunnel over a moderate Re range. That will be an unpowered test.

High Re estimates will be made from Re trends seen on the Ref H adjusted for planform and leading edge radius effects as measured in our most recent test in the NTF. Because of constraints created by a long, scheduled facility shut-down, the NTF testing was conducted on a heavily modified Ref H model. Viscous codes are being validated using that data and will hopefully give us an understanding of the Re effects and help "push" the data out to higher Re. I encourage you to attend the presentations on the results of that test.

High Lift System Concept Design

4.3.2.2

Design and evaluate refinements to the TCA high-lift system in order to identify and develop potential improvements required to meet performance targets established for the HSR Phase II High-Lift Technology program.

- Arrow Wing
  - 4% model in 12-Ft
- Ref H
  - 6% model in 14 X 22
- Modified Ref H
  - 2.2% model in NTF
- Non-Linear CFD

4.3.2 High Lift Technology

Work is continuing in the more general category of high lift system development. This work will be used to refine the TCA high lift system at the end of this FY.

Again, the experimental work is being conducted in the same three facilities and is being accompanied at all levels of complexity computationally.

Propulsion/Airframe Integration

4.3.2.3

Evaluate the installation effects of the propulsion system on the low speed aerodynamic performance and stability and control characteristics both in and out of the influence of the ground.

- Isolated Nozzle
- HEAT 1A
- TCA 2

4.3.2 High Lift Technology

A great deal of work has been conducted in the ARC 40X80 to define the powered effects and the nacelle installation effects on this type of vehicle. The test referred to as HEAT 1 (High-Lift/ Engine and Aeroacoustic Test 1) studied, among other things, the effects of a powered inboard nacelle on the configuration. A semispan model was used so ground-effect and sideslip testing were impractical or impossible.

A follow-on test will look at the effect of a powered outboard nacelle and both nacelles powered on the same semi-span model. A wind-on, isolated nozzle calibration will be performed first leading to that test which is refereed to as the HEAT 1A test. It will look at the effect of:

 - the high lift leading edge flap configuration on the inlet flowfield

 - the nacelle installation on the high lift system

 - high lift wing on the performance of the nozzle.

Also, as stated earlier, the 5% TCA model will be used to define some of the powered ground effects on TCA.

Tools and Methods Development

4.3.2.4

Develop the tools and methods required for:
– accurate assessment full scale aerodynamic performance of HSCT configurations
– aerodynamic design of the HSCT high lift systems.

- CFD Development and Validation
  - AERO2S, A502, DACVINE, ...
  - CFL3D and TetrUSS
- Support System Interference
- Re Scaling and Transition Detection
- Ground Effect Modeling
- "Real Airplane" Effects
- Ice Accretion

4.3.2 High Lift Technology

This subelement contains a number of different activities all aimed at successfully making the jump from model to full scale.

It is true that CFD is being used in our test planning, but our test results are also being used to build confidence in our CFD tools. Linear codes are still being widely used and CFL3D is still the most commonly used viscous code by those working in this area, but several exciting new CFD packages are now being evaluated which could dramatically reduce the time required to get a viscous solution. We are involved in some technique development work and in validation efforts on an unstructured NS package and in some rapid structured grid development efforts.

There are experimental and computational efforts ongoing to remove the support system interference effects from the wind tunnel data sets.

Much of our Re scaling and boundary-layer-transition detection work is for this subelement, as well.

Another modeling issue being addressed involves the prediction of the ground effects that the vehicle will encounter. To date, the ground effects have been predicted based on testing that didn't model the sink rate that the aircraft will actually have on approach. Some work is being done in this element, both computationally and experimentally, to see if we think that modeling is giving us good predictions.

Also, a "piggy-back" activity is being considered for the HEAT 1A test which would look at the effect on high lift system performance of the messy aspects of real airplanes. These are the things that we experimentalists work hard to eliminate from our models like that gaps between leading edge flap segments and less-than-smooth hingelines.

Finally, we are using the LeRC Icing Research Tunnel to grow some representative ice shapes for testing.

Now lets look at the planned flow of the work in each of these subelements.

Logic Network

Inputs From TI

Output To FC HL03FC

Output To FC HL04FC

Output To TI HL08TI

Output To TI HL09TI

Output To TI HL10TI

4.3.2.1 Tech Concept Assess.

Tech Concept High-Lift Geometry Def. | 2 | 8

Tech Concept Preliminary Assessment | 3 | 10

Tech Concept Final Assessment | 7 | 11

Define S&C Aerodynamic Requirements | 9

Output To FC HL02FC

4.3.2.2 High-Lift System Concept Design

Assess. High-Lift System Refinements | 12

High-Lift System Update | 4 | 13

High-Lift Wind Tunnel Evaluation | L2

Inputs From EI & Prop. PR01HL

4.3.2.3 Prop/Airframe Integration

HEAT 1 Aeroacoustic Assessment | 14

HEAT 1A Defined | 1

HEAT 1A Aerodynamic Assessment | 15

HL/PAI Aerodynamic Assessment | 6

4.3.2.4 Tools & Method Development

Support/Wall Interference | 17

BL Transition Technique Recommendation | 18

Full-Scale Prediction Methodology | 21

Tools & Methods Assessment | 5

TU-144 Flight Test TU00HL

Viscous USG Tech. Concept Assessment | 20

Ground Effects Methodology Assessment | 19

Note: Number at upper corner is Level 3 milestone number.
Number at lower corner is Level 4 milestone number.
Shaded items are completed.
* Interfaces with other program elements described in sections 3.14-15.

This is a sketch of the flow of the work and of the interfaces with the outside world. The shaded activities are done.

In the TCA assessment you see that, based on TCA definition from Technology Integration and based on what we learned from Ref H, we have designed a TCA high lift system. We also have a set of S&C requirements for the vehicle which we will use to evaluate the performance measurements we will get from our testing. Our test results will be given to the Flight Controls element for simulator development. After a few tests of the TCA, a preliminary assessment will be done and forwarded to TI. Following some refinements and another year of testing, a final assessment will be done and again, the results will go to TI.

Interface HL02FC was the hand-off of ground effects data on the Ref H in high lift configuration to Flight Controls. The plan is to take what we have learned from the recent NTF test and the Arrow Wing test currently in the 12-Ft and develop a refined high lift system for the TCA. That will be evaluated on the TCA models and the results will impact the high lift system for the Technology Configuration.

As I said earlier, HEAT 1 is complete. That was a test with data for acoustics and propulsion as well as high lift. They made suggestions for the follow-on test, HEAT 1A, and the test has been defined. Following the test, the aerodynamic data will be studied and then combined with other HL/PAI data and CFD results to develop a generalized HL/PAI assessment of this type of aircraft.

As you saw on my last slide, this subelement contains a number of different activities. Following the first test of the TCA in 14 X 22, existing unstructured NS solutions will be compared to the data and that new code will be assessed. A number of wind tunnel testing methods are also being developed. These include removing support system and wall interference effects, detecting boundary layer transition at all Re, and measuring ground effects accurately. Data from the TU-144 flight test will help in the ground effects assessment. These will all roll up into a methodology for predicting full scale performance from sub-scale testing.

That's the work; here's how it lays out in time.

Level III & IV Milestones

4.3 AERODYNAMIC PERFORMANCE
4.3.2 High-Lift Technology

TASKS	FY 1996	1997	1998	1999
Program Milestones	▲ Technology Concept			Technology Configuration △
Level II Milestones	▲ High-Lift Concept Selection			High-Lift Wind Tunnel Evaluation △
	HEAT 1A Defined	High-Lift System Update	Tools and Methods Assess.	Tech. Concpt Final Assess.
Level III Milestones	▲▲	△ △	△	△△
4.3.2.1 Technology Concept Assessment	Tech. Concpt HL Geom. Defined △	Tech. Concpt HL Geom. Defined ... Def. S&C Aero. Requirements ▶△△ ... Tech. Concpt Prelim. Assess. △ ... Tech. Concpt Prelim. Assess. △	HL/PAI Aerodynamic Assess. ... Tech. Concpt Final Assess. △	
4.3.2.2 High-Lift System Concept Design		Assess. High-Lift System Refinements ▶△ ... High-Lift System Update △		
4.3.2.3 Propulsion/Airframe Integration	HEAT 1 Aeroacoustic Assess. △	Large-Scale Feasibility Study Decision ▲ ... Large-Scale Test Req. Defined △	HEAT 1A Aerodynamic Assess. △	
4.3.2.4 High-Lift Tools and Methods Development		Support/Wall Interference ▶△△ ... BL Trans. Technique Recom.	Ground Effects Methodology Assess. △△ ... Viscous USG Tech. Concpt Assess.	Full-Scale Prediction Methodology △
4.3.2.99 Task Coordination and Planning				

Shaded items are completed * Added 2/97

4.3.2 High Lift Technology

These are the milestones as they were defined at the start of PCD 2. Slips are indicated.

The definition of S&C requirements for TCA arrived later than planned, but still early enough to be used during the wind tunnel tests of the configuration.

Because the Arrow Wing entry in the ARC 12-Ft was delayed, refinements to the TCA high lift system will be defined a couple of months later than predicted, but this won't affect any downstream milestones.

Odd-looking data from our last test in the 14 X 22 has delayed our definition support-system interference effects in the data acquired in that facility, however it does appears that the CFD estimates are accurate.

And, the dynamic ground effects test in the 14 X 22 was pushed back to the end of this FY and we have added the evaluation of a time-marching Euler code to that milestone so we slid it into 1998. Again, the change has little impact on the larger program.

You can look at the other dates on your own.

1996 Major Technical Accomplishments

- ◆ All milestones, deliverables, and interfaces completed on schedule and within cost.
- ◆ Demonstrated viability of temperature sensitive paint technique for boundary layer state measurements at high Reynolds number conditions.
- ◆ Demonstrated 2% increase in suction parameter (15 counts drag reduction) on 6% Ref. H due to sealed slat concept on outboard leading edge.
- ◆ All wind tunnel test activities on schedule.
- ◆ Development of viscous unstructured grid capability progressing slowly, but initial results show promise.
- ◆ Supported initial assessment of "Earned Value" procedure within HSR.

4.3.2 High Lift Technology

Here are some of our accomplishments from last year. This slide was prepared for an end-of-the-year report to Wally Sawyer.

We are on schedule and resources were fine last year.

Check out the TSP talk and see the results of the transition detection tests at cryogenic temperatures. It is very promising.

A new outboard l.e. slat has nudged us a little higher in our principal metric, suction parameter.

Our program's high priority within NASA has allowed the tests to be scheduled such that we get what we need when we need it.

Exciting progress has also been made in the area of unstructured NS codes. Catch that talk, too.

And finally, we supported the tracking of a new metric for management called "Earned Value."

Technology Performance Metrics

Trimmed Suction Parameter @ Cutback

(C_L = 0.50 on gross wing area)
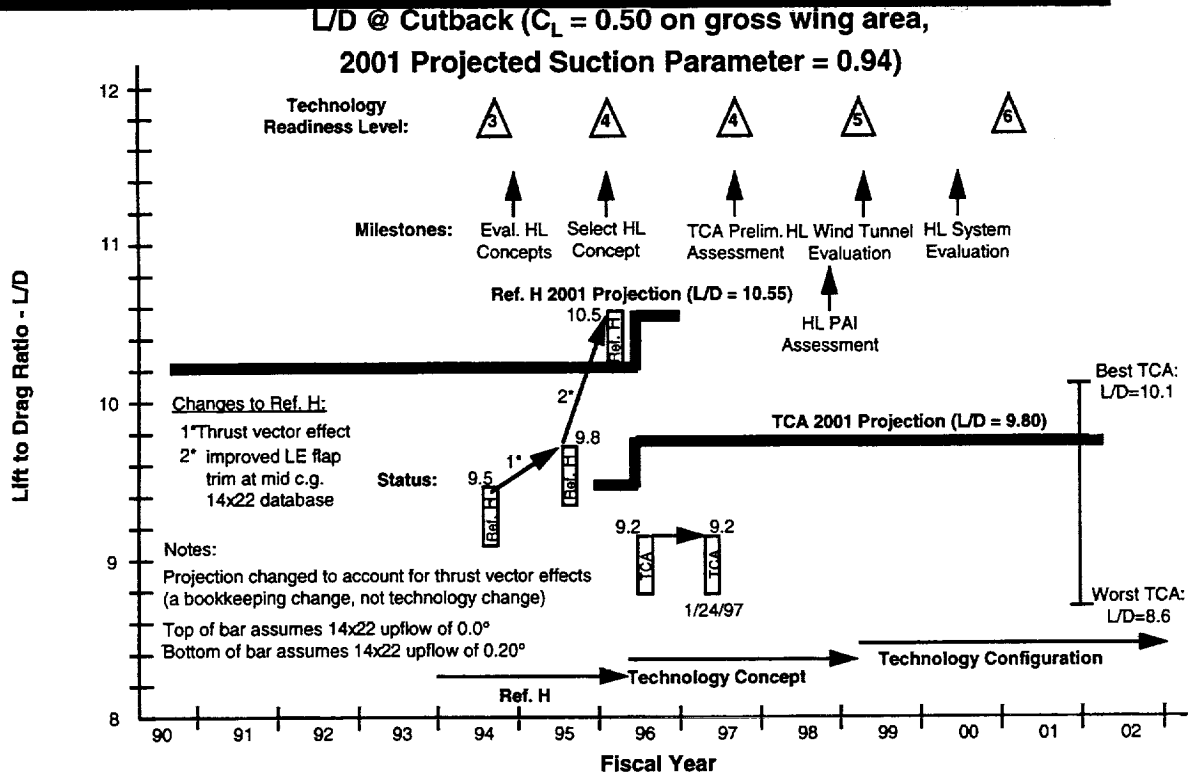

4.3.2 High Lift Technology
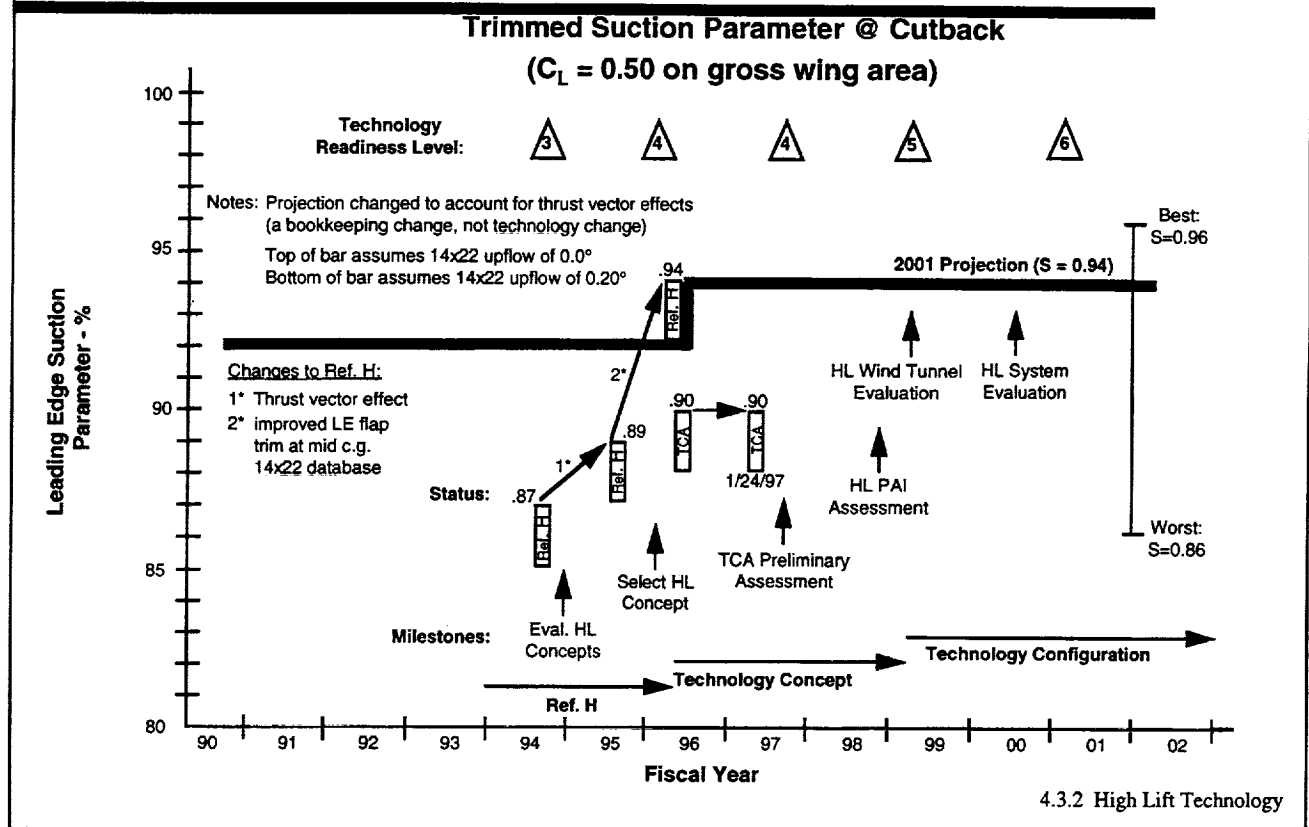
As I said earlier, Suction Parameter is our principal metric. Here's how we're doing.

Our goal is 94% and we were getting there with the Ref H. The length of the bar indicates the difference 0.2 degrees of flow angularity could mean to the conclusions drawn from he wind tunnel data.

Changing to the TCA we moved back some, but should be able to get back to 94%.

Technology Performance Metrics (cont)

L/D @ Cutback (C_L = 0.50 on gross wing area, 2001 Projected Suction Parameter = 0.94)

4.3.2 High Lift Technology

This is a similar slide for L/D.

As you can see, L/D is sensitive to the change in planform that happened between Ref H and TCA. As a result, the final projection is lower. That's the result of the lower aspect ratio.

Issues, etc.

◆ Large uncertainty with schedule and availability of NASA wind tunnels.

◆ 14- X 22-FST upwash data uncertain.

There are some issues that could cause problems in the future if we don't address them.

The uncertain availability of the ARC tunnels and the backlog of tests at the 14 X 22 create a big unknown.

As I have said before, the data from the last 14 X 22 test looks funny. Without it, not only is the flow angularity in the facility unknown, but, if the cause is not identified, the data from upcoming tests will be questionable.

Conclusions

- ◆ Excellent progress
- ◆ Future looks bright
  - – Funding is solid
  - – Support is strong

- ◆ Still challenges

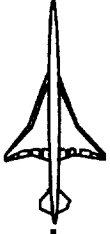For the most part, though, the High Lift element is making excellent progress.

The support is still strong for HSCT at NASA HQ and in congress. Resources are good.

But, there are still some issues and plenty of technical hurdles to keep us all challenged.

This page intentionally left blank.

High Lift Aero/ptm/02/19/97

Prediction of TCA Full Scale High Lift Characteristics

**HSR Aero-Performance Workshop
NASA Langley Research Center
February 25, 1997**

**Paul T. Meredith
Boeing Commercial Airplane Group
HSCT High Lift Aerodynamics**

Introduction

BOEING

HSCT Aerodynamics

This page is intentionally blank

Introduction

BOEING

HSCT Aerodynamics

- **Objectives for HSCT High Lift System**

- **TCA Full Scale Predictions**

- **Potential L/D Improvements**

- **Airplane Design Process (ADP)**
  Common High Lift Prediction Process
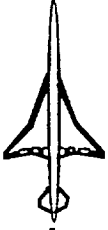
- **Summary**

BOEING

HSCT High Lift System Objectives & Characteristics
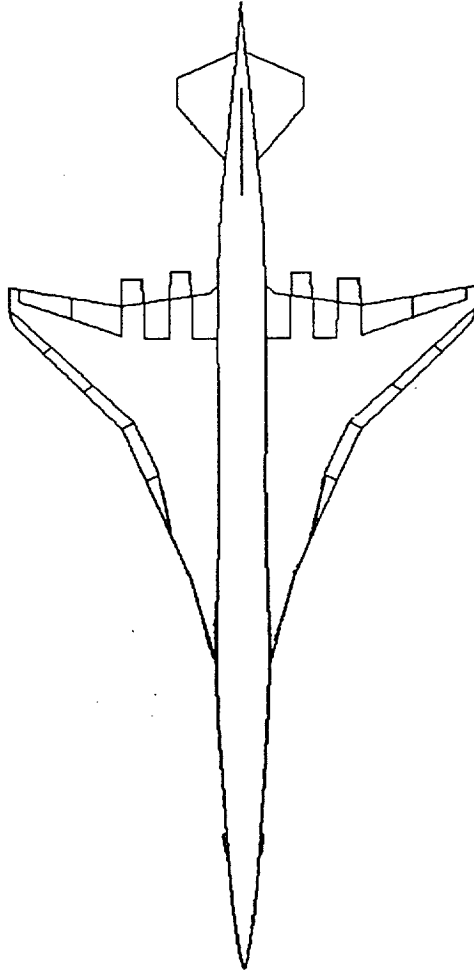
HSCT Aerodynamics

This page is intentionally blank

HSCT High Lift System Objectives & Characteristics

Objectives:
Noise ≤ Stage III minus 3 to 5 db
Approach Speed ≤ 155 knots
Takeoff Field Length ≤ 10800 ft

Leading Edge Flaps:
Simply hinged
Maintain attached flow
Increase L/D

Trailing Edge Flaps:
Simply hinged
Increase L/D
Decrease touchdown attitude
Decrease takeoff field length

L.E. & T.E. Flaps are Programmable
Deflection = f(flight condition)
Optimize L/D subsonic & transonic
Minimize attitude at touchdown

High Lift Aero/ptm/12/06/96

1711

Sensitivty of MTOW to L/D and Cutback Noise Requirement

BOEING

HSCT Aerodynamics

This Figure shows the change in TCA MTOW as a function of percent change in climbout L/D for three different cutback noise levels (Stage III - 3db, - 4db, and - 5db). The TCA was sized for Stage III - 3db.

A 10% reduction in L/D results in a 40,000lb increase in MTOW for the TCA sized to III - 3db.

Sizing to III - 5db at the same L/D results in a 70,000lb increase in MTOW and a 10% reduction in L/D adds another 60,000lbs.

There are two main reasons that MTOW increases as L/D decreases. First, as L/D decreases, thrust must be increased to maintain the required minimum climb gradient after cutback. Second, for a given thrust a reduction in L/D results in a lower altitude at cutback, since the cutback point is defined as 6500 meters from the brake release point. A larger engine is therefore required to compensate for reduced L/D and MTOW increases as a result.

The message is that MTOW is sensitive to climbout L/D because of noise requirements and the more stringent the noise requirement becomes, the greater the sensitivity of MTOW to L/D.

1712

Noise Sensitivity to Climbout L/D for 1080-1459te9_3770_60fcn_overflowed

Changes in SIZED Airplane MTOW

Relative to Nominal Airplane
Sized to Stage III -1 dB at Sideline and Stage III-3dB at Cutback

Change in -XdB sized MTOW (lbs)

Percent Change in Climbout L/D

-5 dB

-4 dB

-3 dB
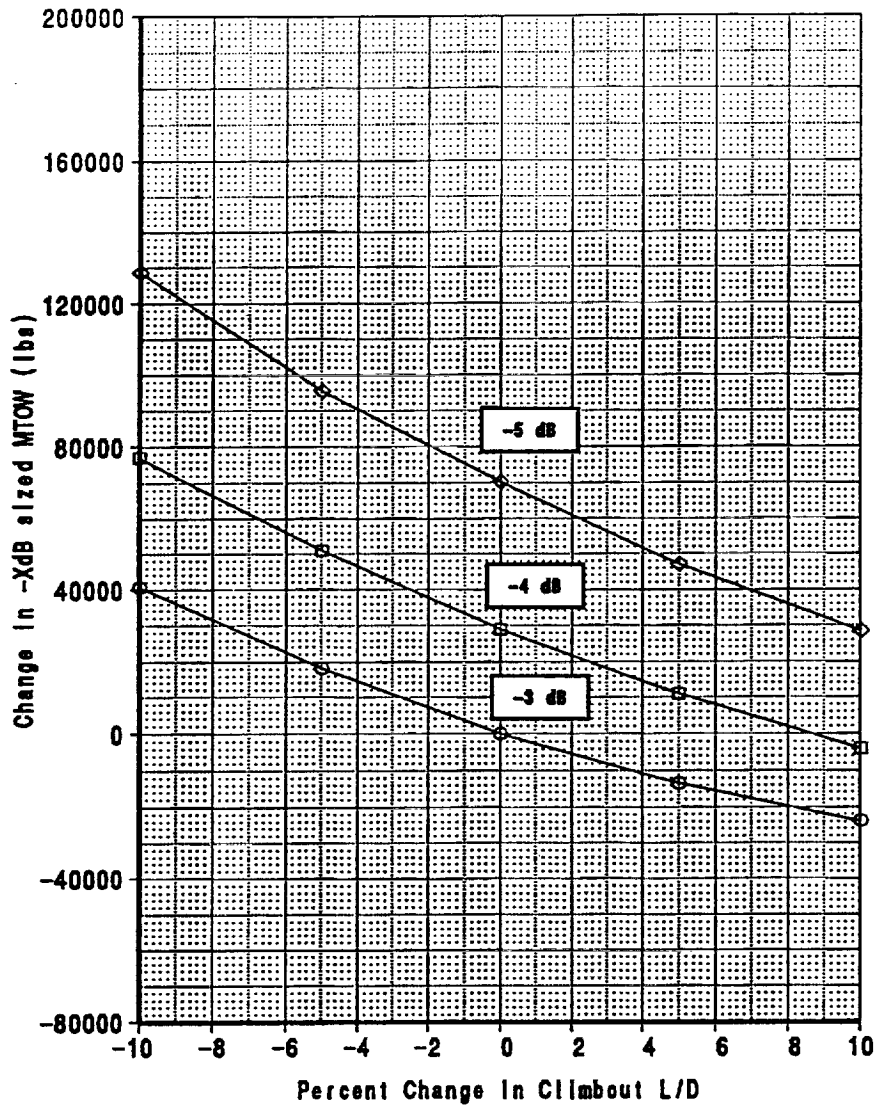
CALC	JB Coffey	6Dec96	REVISED	DATE	Sensitivity to CLimbout L/D	
CHECK					Based on 1080-1459te9_3770_60fcn_overflowed	
APPD.						
APPD.					BOEING	PAGE

BOEING

HSCT Aerodynamics

TCA FULL SCALE HIGH LIFT CHARACTERISTICS

This page is intentionally blank

1714

TCA FULL SCALE HIGH LIFT CHARACTERISTICS

BOEING

HSCT Aerodynamics

- **Drag Build-ups & Technology Projection**

  current BCAG process, different than what was used for TCA sizing, ADP common process will give similar results

  uncertainties due to upflow and support interference will likely increase drag by 10 to 30 counts

- **Takeoff Lift Curve**

- **Touchdown Lift Curve**

1715

Build-Up Process

Flight lift and drag estimates for the TCA are obtained by adding configuration increments from AERO2S (TCA minus Ref. H) to Ref. H flight estimates.

Ref. H flight estimates are based on 14x22 wind tunnel data, adjusted to flight Reynolds number using NTF and analytical corrections, and with excrescence drag estimates applied.
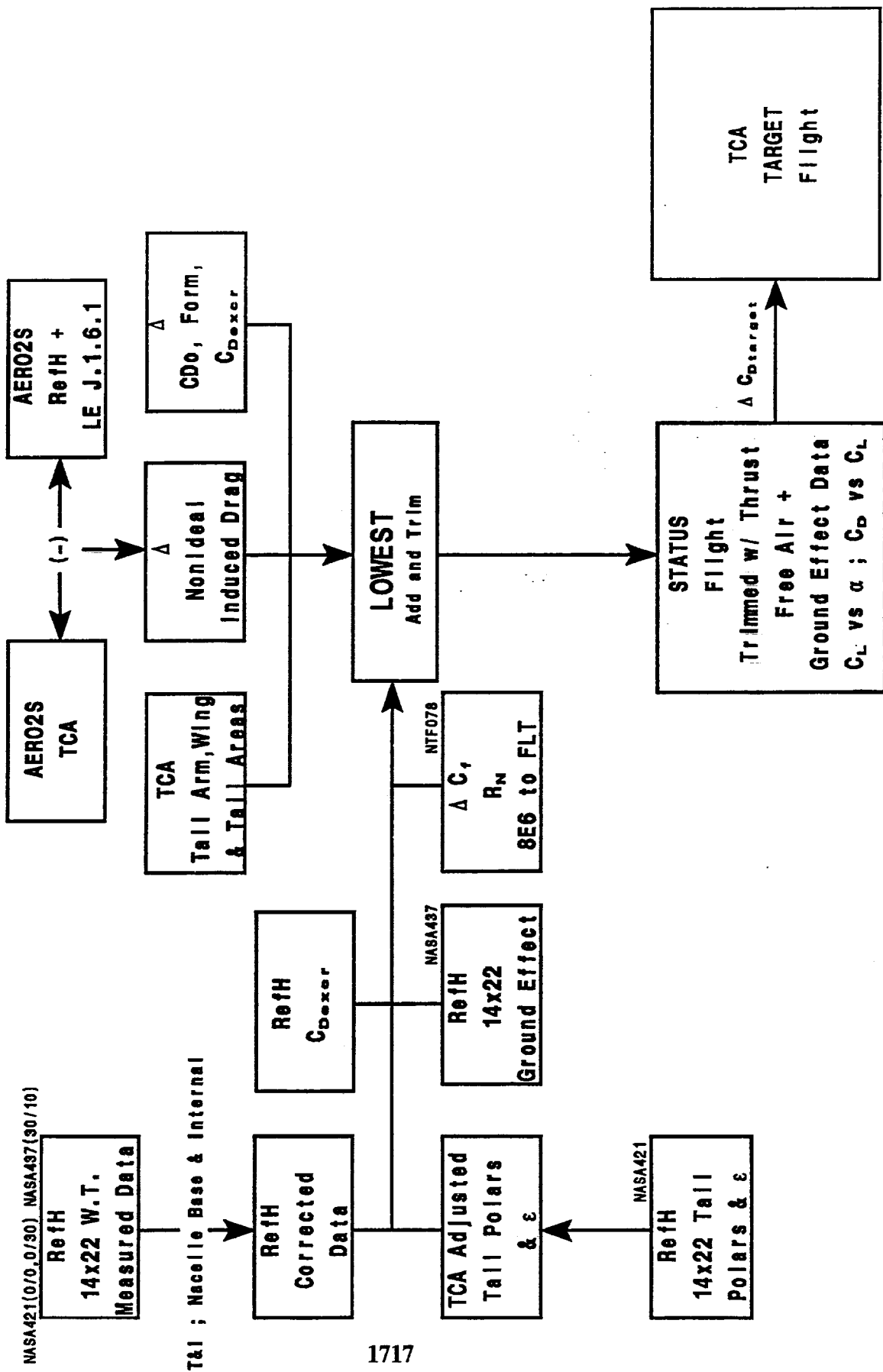
Ref. H tail polars and downwash are obtained from 14x22 wind tunnel data and adjusted for configuration differences to derive TCA tail polars and downwash.

For BCAG use, the orientation of the gross thrust and ram drag vectors is bookkept in lift and drag. This is called "with thrust" data while the strictly aerodynamic data is termed "no thrust".

For climb-out, programmable flaps are assumed with both leading and trailing edge flaps deflected for minimum drag as a function of CL.

A technology projection is applied to the TCA estimated flight drag (the TCA status polars) to obtain the projected or target polars. The technology projection results in a suction parameter of 94.3% with thrust vector bookkeeping (L/D = 9.8) or 92% without thrust vector bookkeeping (L/D = 9.4) at CL = 0.50

1716

Build-Up Process

NASA421(0/0,0/30) NASA437(30/10)

```
RefH
14x22 W.T.
Measured Data
```

T&I ; Nacelle Base & Internal

```
RefH
Corrected
Data
```

```
AERO2S
TCA
```

```
AERO2S
RefH +
LE J.1.6.1
```

(−)

```
Δ
CDo, Form,
C_Dexor
```

```
Δ
NonIdeal
Induced Drag
```

```
TCA
Tail Arm,Wing
& Tail Areas
```

```
RefH
C_Dexor
```

```
NASA437
RefH
14x22
Ground Effect
```

```
NTF078
Δ C_f
R_N
8E6 to FLT
```

```
LOWEST
Add and Trim
```

```
STATUS
FlIght
Trimmed w/ Thrust
Free Air +
Ground Effect Data
C_L vs α ; C_D vs C_L
```

Δ C_Dtarget

```
TCA
TARGET
FlIght
```

```
TCA Adjusted
Tail Polars
& ε
```

```
NASA421
RefH
14x22 Tail
Polars & ε
```

1717

TCA Climb-Out Drag Build-Up

The build-up is done using the Boeing (Wimpress) reference areas. CL = 0.524 corresponds to CL = 0.50 on gross area.

Start with the horiz.-off, 30/10 flaps, fully corrected Ref. H 14x22 wind tunnel data.

Remove Ref. H ideal induced drag and add TCA ideal induced drag. Add the Ref. H-to-TCA drag increments from AERO2S (excluding Δ ideal induced drag) and from estimated skin friction drags (ΔCDo).

Scale to flight Reynolds number (NTF and estimated CDo changes) and add estimated excrescence drag.

Add the horizontal tail and trim the wing-body pitching moment (cg @ 51.5% of m.a.c.)

Adjust drag for gross thrust and ram drag vector orientation. Lift is also adjusted. This is done only for bookkeeping as the BCAG performance program assumes that net thrust equals drag in level flight.

Use AERO2S to determine lift and drag changes relative to 30/10 for a variety of leading and trailing edge flaps. Use the above process to estimate flight polars for this large number of flap deflections and define the optimum L/D envelope as a function of CL.

Apply a technology projection to achieve 92% suction parameter without the thrust vector bookkeeping. Suction parameter with thrust is 94.3%. The projection is equivalent to a -33.4 count drag reduction at this CL.

1718

TCA Climb-Out Drag Build-Up

$S_{ref} = 8109.$ ft^2
C.G. = 51.5 %

C_D @
$C_L = 0.524$
(Counts)

0.05329

Δ =
-0.00094

Δ =
+0.04118

TCA
Ideal
Induced
Drag
AR=2.125

Δ =
+0.00497

Δ =
-0.00320

Δ =
+0.00088

Δ =
+0.00057

Δ =
-0.00288

Δ =
-0.00088
C_D =
0.05601
L/D =
9.22

Δ =
-0.00334
C_D =
0.05347
L/D =
9.80

RefH with
J1.6.1 LE
Fully
Corrected
WT
Data
30/10
Tail-Off

RefH
Ideal
Induced
Drag
AR=2.366
Tail-Off

C_{Do},
nonideal
Induced
drag,
AERO2S
TCA - RefH

NTF+
Flat
Plate
8E6 to
Flight R.

C_{Doex}

C_{Dtrim}
+
Tail

Thrust

Programmed
Flaps

Target

1719

Alternate TCA Climb-Out Drag Build-Up

This build-up provides a sanity check. As before, it is done on Boeing reference area at a CL of 0.524.

CDo is estimated at flight Reynolds number and includes an allowance for form drag and excrescence drag.

Ideal induced drag is added along with non-ideal induced drag as determined from potential flow analysis of the 30/10 configuration.

Trim drag and thrust vector bookkeeping adjustments are added as before.

The resulting drag is 0.04968. The target drag is 0.05347. The status drag from the wind tunnel based build-up is 0.05681.

Since the alternate build-up doesn't account for any increase in viscous drag beyond CDo nor loss of leading edge suction, it is nearly the best drag possible deviating from the optimum only in that non-elliptic spanloading and trimming are accounted for.

That the target CD is about 38 counts higher implies that the target is certainly attainable, though the difficulty in attaining it is not addressed.

The status drag is 33.4 counts higher than the target, so, coincidentally, the target is about halfway between the current status and the near-optimum drag.

Alternate TCA Climbout Drag Build-Up

S_{ref} =8109. ft^2

C.G. = 51.5 %

- - TCA Target C_D = 0.05347

C_D @
C_L =0.524
(Counts)

600
500
400
300
200
100
0

Δ =
+0.00579

0.04988

Δ =
-0.00258

Δ =
+0.00057

Δ =
+0.00310

Δ =
+0.04118

C_{Do} =
0.00746

Excrescence	Ideal	nonideal	Δ Trim	Δ Thrust	Drag
= 0.00056	Induced	Induced			Budget
Form	Drag	drag			Loss of
= 0.00020					Suction,
Skin Friction					Viscous
= 0.00670					Polar Shape
					etc.

1721

TCA L/D Comparisons

The plot shows L/D, with thrust, versus CL based on gross wing area for the status TCA flaps 30/10, status programmed flaps, and target programmed flaps. An ideal curve is also shown.

The ideal L/D is defined as the ratio of CL to an optimum drag consisting of only CDo and ideal induced drag.

At low CL's, the target curve intersects the ideal curve, which should not happen. This is because of the way the technology projection is added as a function of CL. The problem will be corrected in the near future.

The CL of interest for cutback noise is about 0.50.

TCA L/D Comparisons
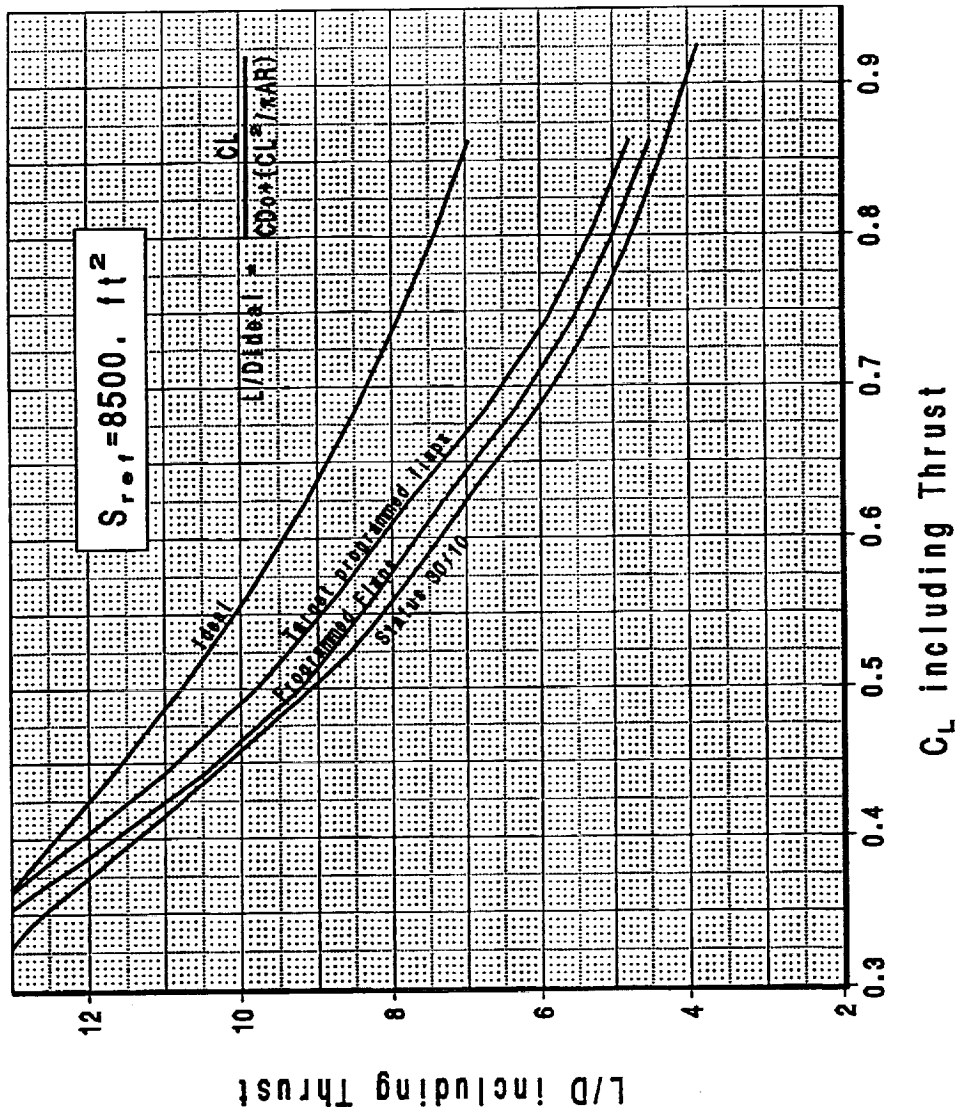
TCA vs Ref. H L/D Comparisons

HSCT High Lift Aerodynamics

This plot shows L/D versus CL (on gross area) curves for the Ref. H and TCA. The curves represent ideal L/D, target programmed flap L/D with thrust, and target programmed flap L/D without thrust for both the Ref. H and TCA.

1724

TCA vs RefH L/D Comparisons

$$L/D[ideal] = \frac{C_L}{CD_0 + [C_L^2/\pi AR]}$$

TCA S_{ref}=8500. ft^2
RefH S_{ref}=7590. ft^2

C_L

L/D
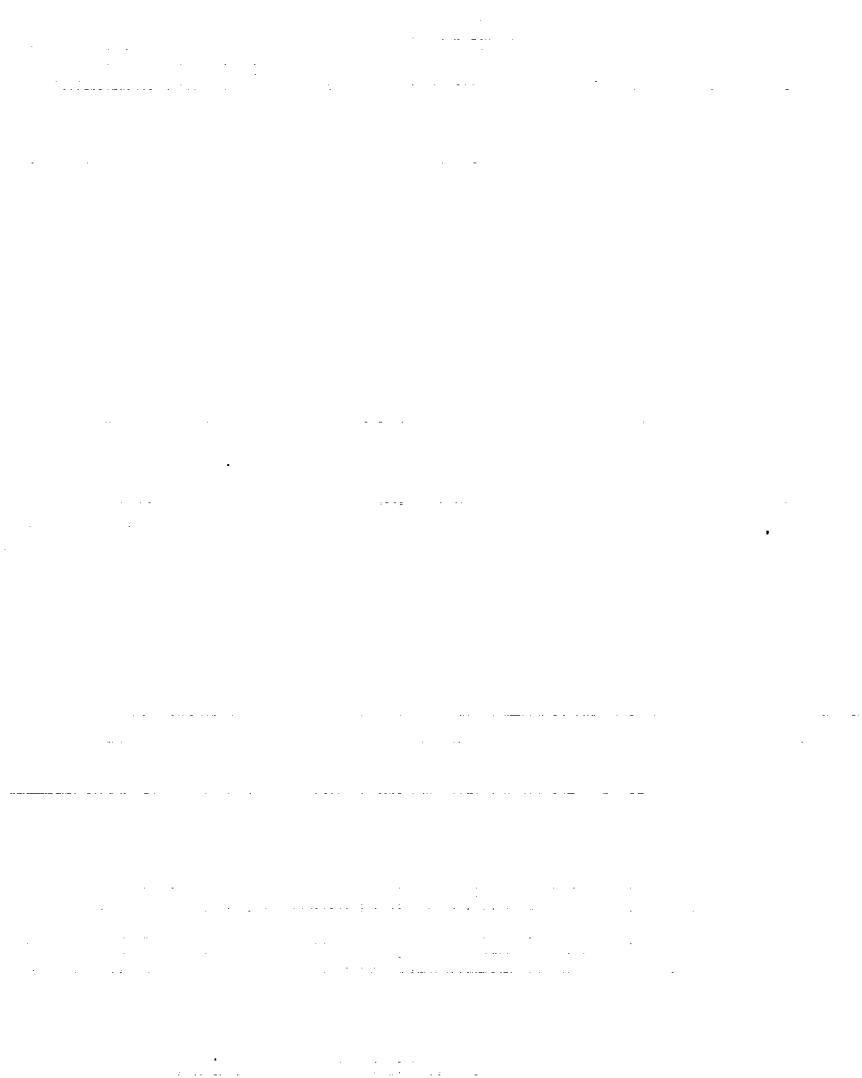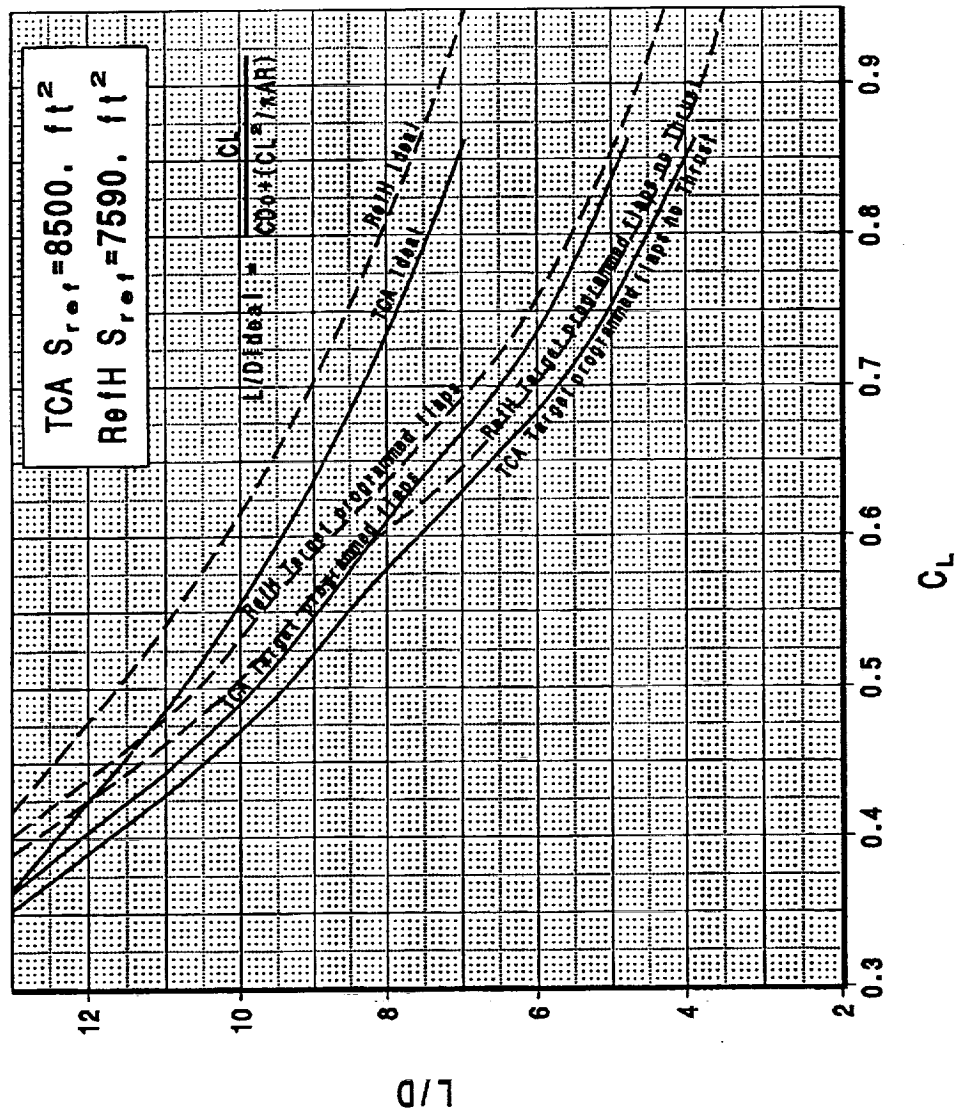
Impact of the Type of Leading Edge Flow on Drag

The sketch shows different types of leading edge flow and the expected drag polar characteristics.

The worst flow in terms of drag is that of a fully separated leading edge flow (zero leading edge suction) which does not reattach. Drag is given by $CD = CL\tan\alpha$.

The next worst type of flow is where the flow separates but reattaches as a stable leading edge vortex. Drag is still given by $CD = CL\tan\alpha$ but CL at a given α is increased due to the vortex so L/D is improved.

An improvement can be made with a vortex flap where the normal force produced by the leading edge vortex is pointed forward as well as up thus reducing drag while increasing lift.

The best possible flow is obtained for a fully attached leading edge where the drag is given by the ideal induced drag $CD = CL^2/pi/AR$.

For a sharp leading edge and a fixed leading edge flap deflection, the flow will be attached over a small angle of attack range. Outside of that range, the flow will be like that of the vortex flap, assuming a stable vortex is formed. With programmable leading edge flaps, the wing is able to operate along the ideal polar (or close to it) over a broad angle of attack range by changing the flap deflection as a function of angle off attack.

The suction parameter is seen to be the ratio of the difference between the zero suction polar and the actual polar to the difference of the zero suction polar and the ideal polar.

IMPACT OF TYPE OF L.E. FLOW ON DRAG

WORST

VERY BAD

c_s

BAD

c_s

BEST

c_s

c_s

Vortex Flap

$\dfrac{c_L^2}{\pi AR}$

Polhamus
Flat Plate
$c_L \tan \alpha$

Flat Plate
no suction
$c_L \tan \alpha$

$$S = \dfrac{a}{b}$$

a

b

C_L

$C_D - C_{D_o}$

BOEING
PTH 2/3/96

1727
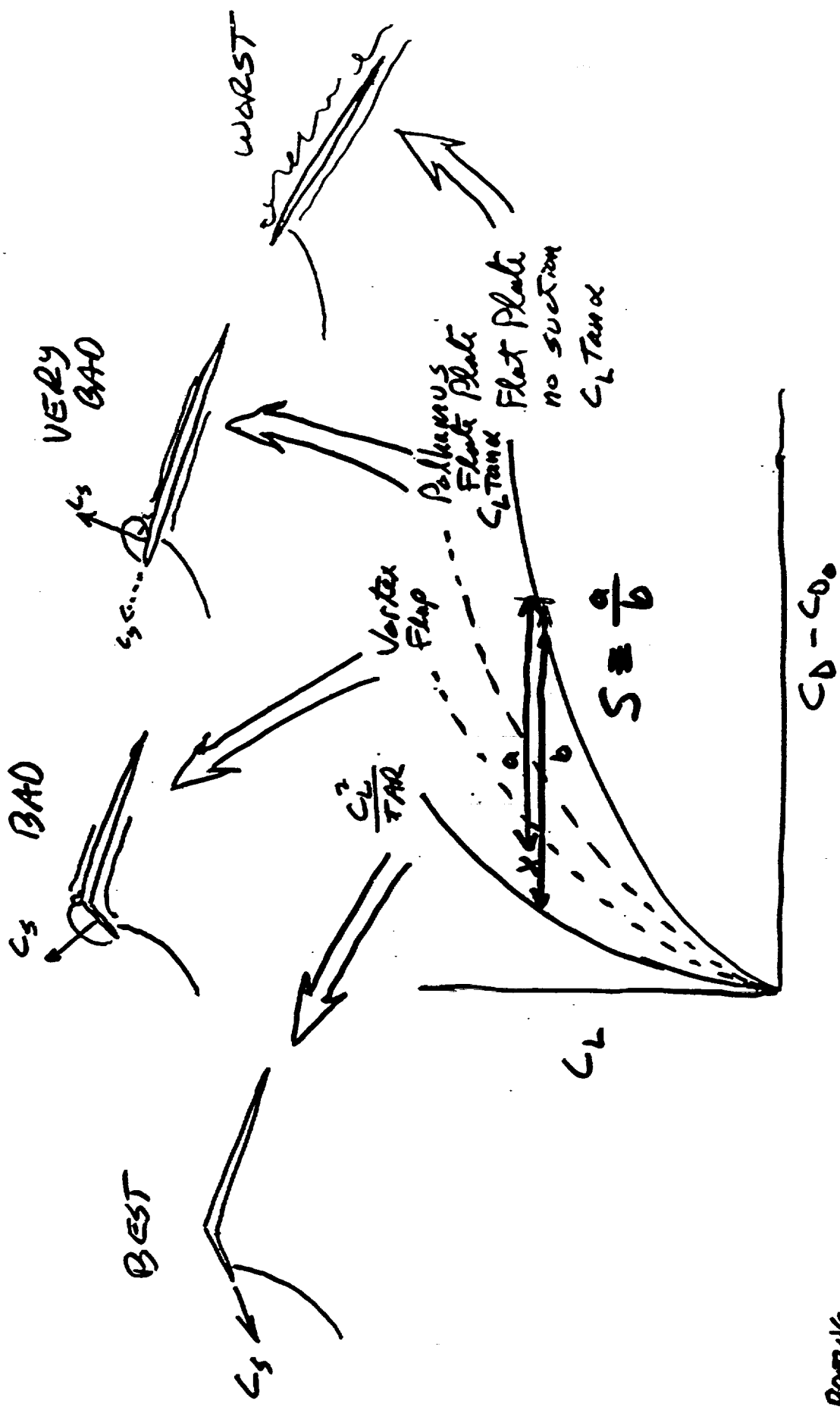
TCA Suction Parameter & L/D Metrics

The left hand graph show suction parameter (S) versus CL. The right hand graph shows the L/D metric η versus CL. Curves are presented for status and target TCA polars, with and without thrust vector accounting.

The characteristics of the the S curves and η curves are similar. The suction parameter S is the metric currently tracked, though it has been computed differently by Boeing and McDonnell Douglas. One could argue for the adoption of η as a better airplane metric but it is not clear if it is worth the trouble to make such a change. If S is retained, a common definition must be agreed to.
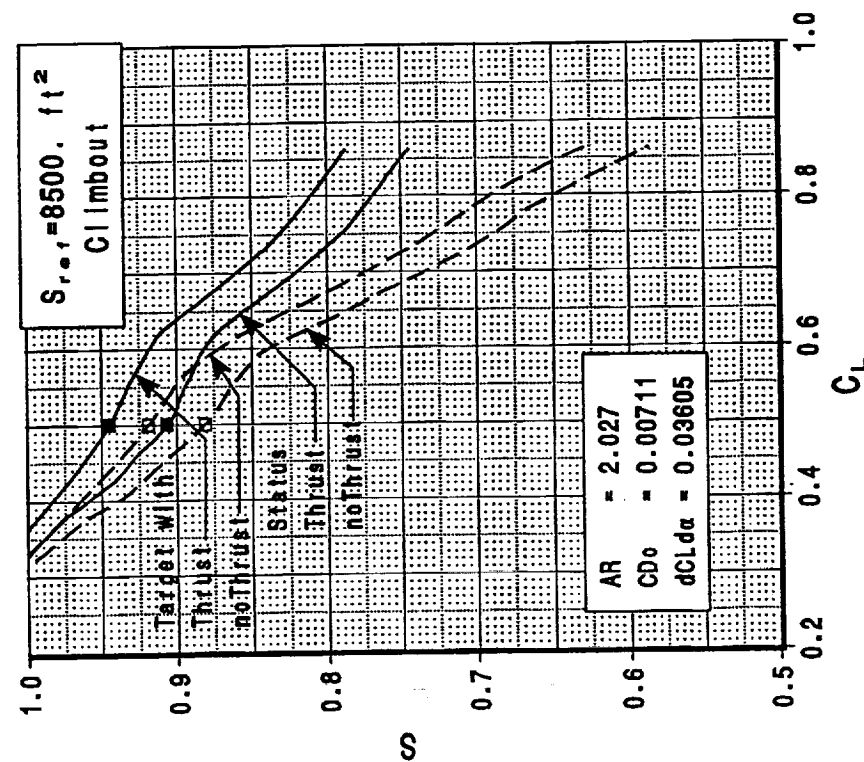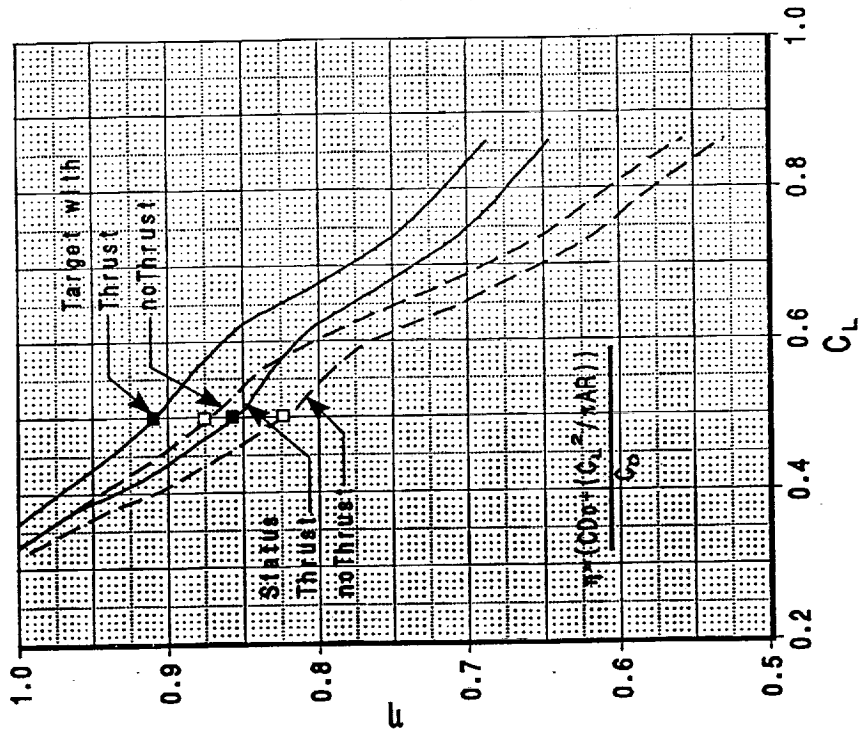
1728

TCA Suction Parameter & L/D Metrics

1729

COMPARISON OF TCA STATUS, PROJECTION, & IDEAL DRAG

BOEING

HSCT Aerodynamics

The chart shows four drag levels for the TCA (status, target or projected, alternate build-up, and ideal) at a CL of 0.50, with no thrust vector accounting included.

A 32 count drag reduction is required to go from the status drag level to the target drag level which is an increase in η (CDideal/CD) from 0.82 to 0.87. An η of 0.87 is equivalent to a suction parameter (S) of 0.92 (no thrust). The target drag level in relation to the ideal (η of 0.87) is similar to that achieved by subsonic transports in the cruise configuration at low Mach numbers.

The alternate bottoms-up build-up is 36 counts less than the target level and has η of 0.93. The ideal drag level is 35 counts less than the alternate build-up result and has η of 1.0 and S of 1.0. The alternate build-up differs from the ideal by including allowances for non-elliptic induced drag (span efficiency of 0.93 rather than 1.0) and trimming.

COMPARISON OF TCA STATUS, PROJECTION, & IDEAL DRAG

BOEING

HSCT Aerodynamics

CL = 0.50, S = 8500 sqft
programmed flaps
no thrust vector accounting
$\eta = (CD/CDideal)^{-1}$

Drag Coefficient - CD

0.058
0.056
0.054
0.052
0.05
0.048
0.046
0.044
0.042
0.04

Status Drag
0.0567
$\eta = .82$

Target Drag
0.0535
$\eta = .87$
-0.0032

Alternate Build-up
0.0499
$\eta = .93$
-0.0036
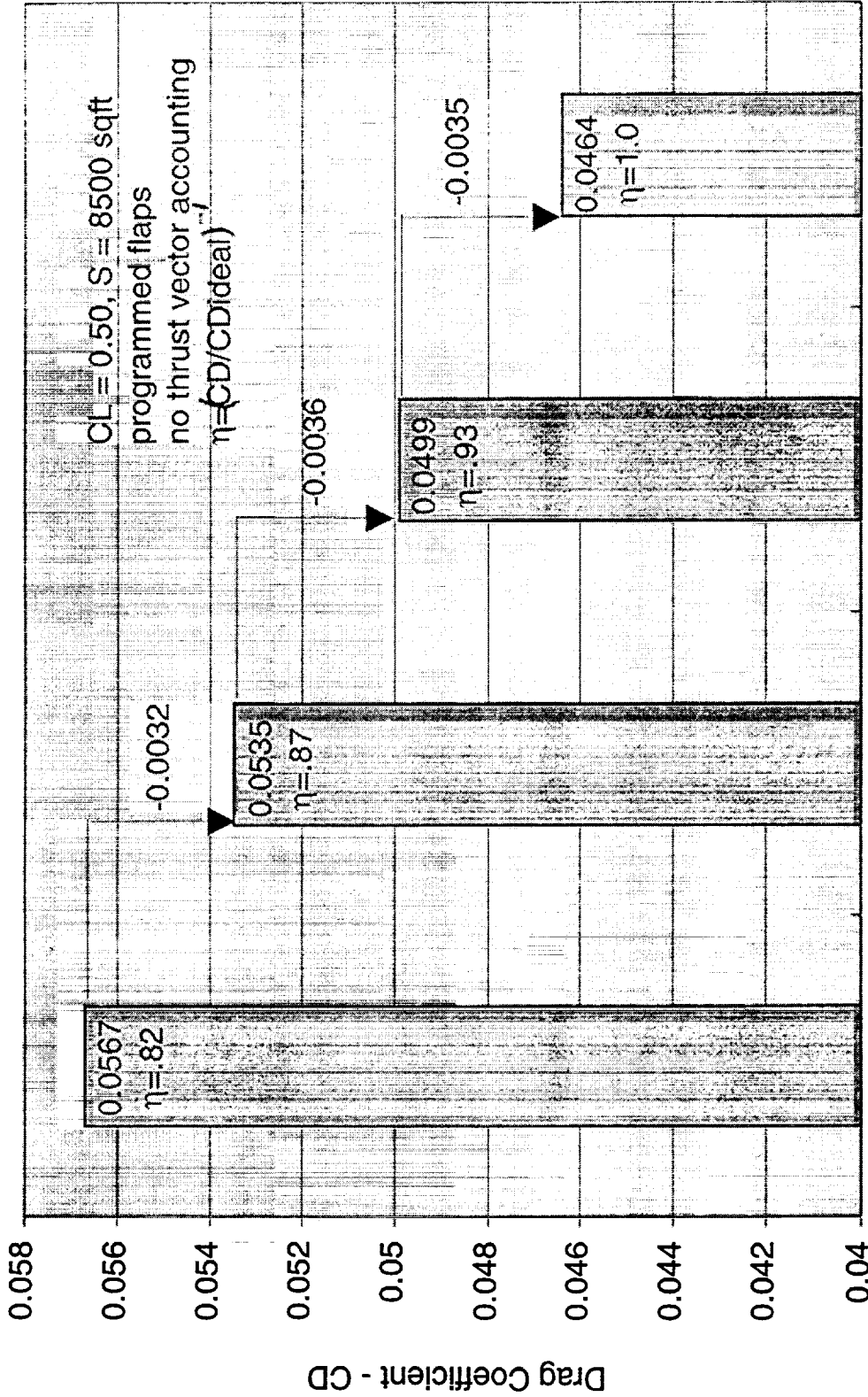
Ideal = CDo + CL*CL/pi/AR
0.0464
$\eta = 1.0$
-0.0035

High Lift Aero/ptm/02/21/97

1731

Lift-Off CL and CLref

The chart shows a plot of CL versus α and Vlof/Vref versus T/W (a speed schedule).

The left plot shows lift curves for 30/10 flaps gear down, in free air and in ground effect. The McDonnell Douglas lift-off lift curve is shown for comparison.

The angle of attack at which the airplane strikes the ground is 11.5° (oleos extended). To preclude frequent strikes, we require a 2° margin to contact. This determines the maximum lift-off angle of attack (9.5°) and lift-off CL of 0.558 without thrust vector accounting or 0.580 with thrust (Boeing lift curve in ground effect). The McDonnell Douglas lift curve is very similar at this angle of attack.

The right plot shows lift-off speed schedules for all engines and engine-out. These and other speed and flare time schedules are used along with the limiting CLlift-off to determine the Vref used for take-off performance calculations.

Lift-Off C_L , $C_{L\ ref}$

Calculate variety of $C_{L\ ref}$, $C_{L\ ref} = C_{L\ LOF}(V_{LOF}/V_{ref})^2 = f(t/w,$ all engine, engine out)
Then pick lowest, $C_{L\ ref} = 0.690$ engine out, $t/w = 0.2$

1733

Touch Down Attitude

The plot shows CL (Boeing reference area) versus α. Lift curves are shown for the free air case, the in ground effect case, and from the McDonnell Douglas build-up in ground effect for comparison.

The angle of attack at which the airplane strikes the ground is 9.4° (oleos compressed). To preclude frequent strikes, we require a 3° margin to contact. This determines the maximum touchdown angle of attack (6.4°) and touchdown CL of 0.626 (Boeing lift curve in ground effect). The approach speed may be calculated given the wing loading and the approach CL, CLappr = CLTD*(0.97)^2. This accounts for a 3% speed bleed off during the flare.

With a 3° margin to contact, using the Boeing touchdown lift curve, the TCA approach speed is 162.6 knots. Using a 2.5° contact margin, as agreed to for purposes of sizing the TCA, yields a 160.2 knot approach speed. The McDonnell Douglas lift curve, which is not based on wind tunnel data, yields an approach speed of about 155 knots using a 2.5° contact margin.

The ground effect used is representative of an airplane with zero sink rate. Literature indicates that for slender wings, the favorable ground effect may be halved for flight path angles typical on approach (3°). Potentially, the TCA has a serious approach speed problem due to touchdown attitude limitations. However, changes in noise assessments which increase wing area of the noise sized airplane may offset the attitude problem. Further study of unsteady ground effect and investigation of sizing constraints with Technology Integration Team is required to determine the extent of the approach speed problem.
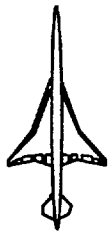
Touch-Down Attitude
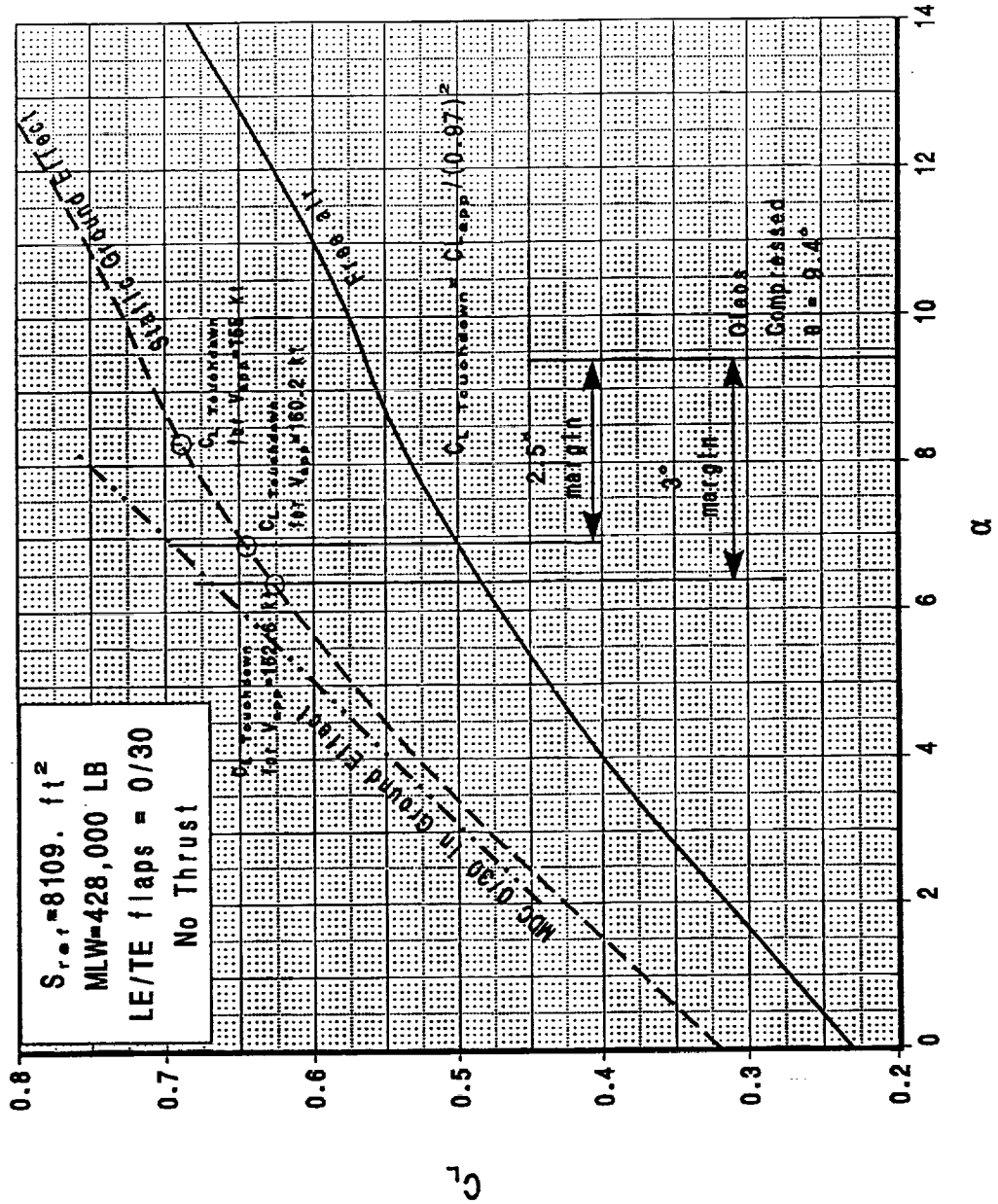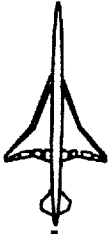
BOEING

HSCT Aerodynamics

POTENTIAL L/D IMPROVEMENTS

This page is intentionally blank

BOEING

HSCT Aerodynamics

POTENTIAL L/D IMPROVEMENTS

- **Induced and Trim Drag Optimization**

- **Leading Edge Flap Improvements**

  Outboard flaps

  Inboard flaps

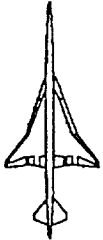- **Status versus Projected L/D Impact on Sizing**

Improved Leading Edge Devices

The plot shows change in drag versus CL relative to the previous best Ref. H leading edge configuration. Coefficients are referenced to Boeing reference area.

The data are from the 14x22 test #437. The attached flow flap was designed with a very generous leading edge radius and smooth transition to the upper wing surface. This provided a 20 count drag reduction at CL of 0.53.

The sealed slat is similar to the baseline leading edge flap except for some fowler motion and reduced curvature at the flap hingeline. This device provided about the same drag reductions as the attached flow flap indicated that it is the hingeline which matters most in terms of L/D i.e., leading edge separations are prevented by suitable flap deflection even with very sharp leading edges.

The leading edge tab, mislabeled as a vortex tab, provides about a 10 count improvement at a CL of 0.53. It also seems to work by improving the flow across the hingeline by reducing the pressure gradient on the flap so that the boundary layer is less affected by the pressure gradients caused by the large curvature at the hingeline. It is therefore thought that the effects of the tab and the sealed slat are not additive though that configuration was not tested.

Delta Drag counts vs. CL
Deltas are from baseline plain flaps
with best inboard flap span coverage →

L.E. tab

Sealed Slat

Attached Flow

ΔDrag
counts

20

0

-20

-40

-60

0.4

0.5

0.6

0.7

C_L

1739
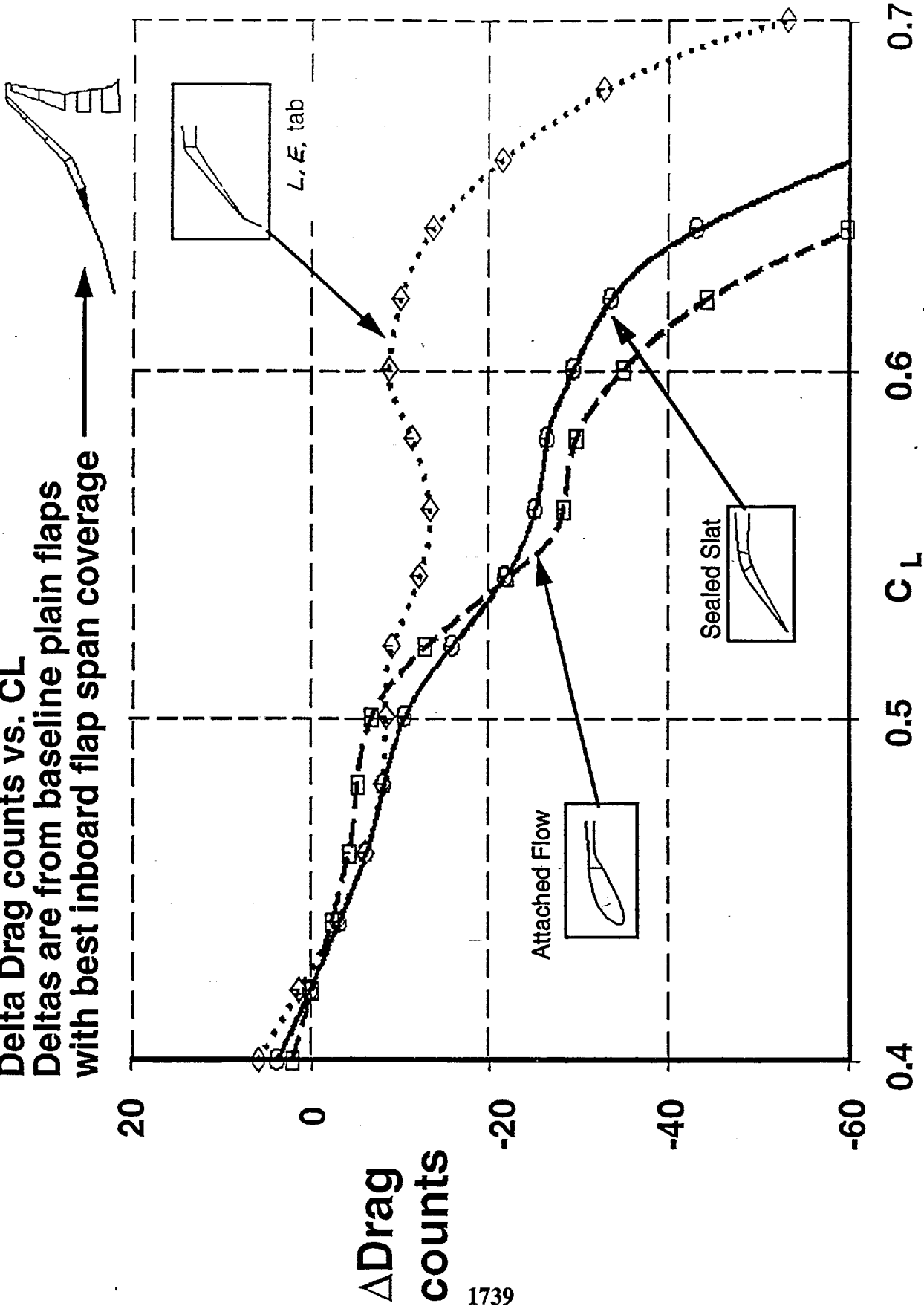
BOEING

HSCT Aerodynamics

STATUS vs PROJECTED L/D IMPACT ON MTOW

The TCA and other configurations are sized using projected characteristics. Therefore, improvements in L/D at cutback are not manifested as MTOW reductions but as a movement of the status L/D towards the projected L/D.

As the status approaches the projection, risk and uncertainty are diminished and technology readiness level (TRL) is increased. These are tracked as part of the Technology Integration (Task 20) metrics task.

If we are unsuccessful in achieving the projected L/D, then, for the TCA, the MTOW will increase at a rate of about 4000lb for each 1% shortfall in L/D.

Some configuration changes such as canards may result in an adjustment of the projected L/D. Also, the technology projection can be adjusted as we progress in the program and learn more about what is and is not possible.

1740

STATUS vs PROJECTED L/D IMPACT on MTOW

TCA, CL =0.50, S = 8500 sqft, no thrust
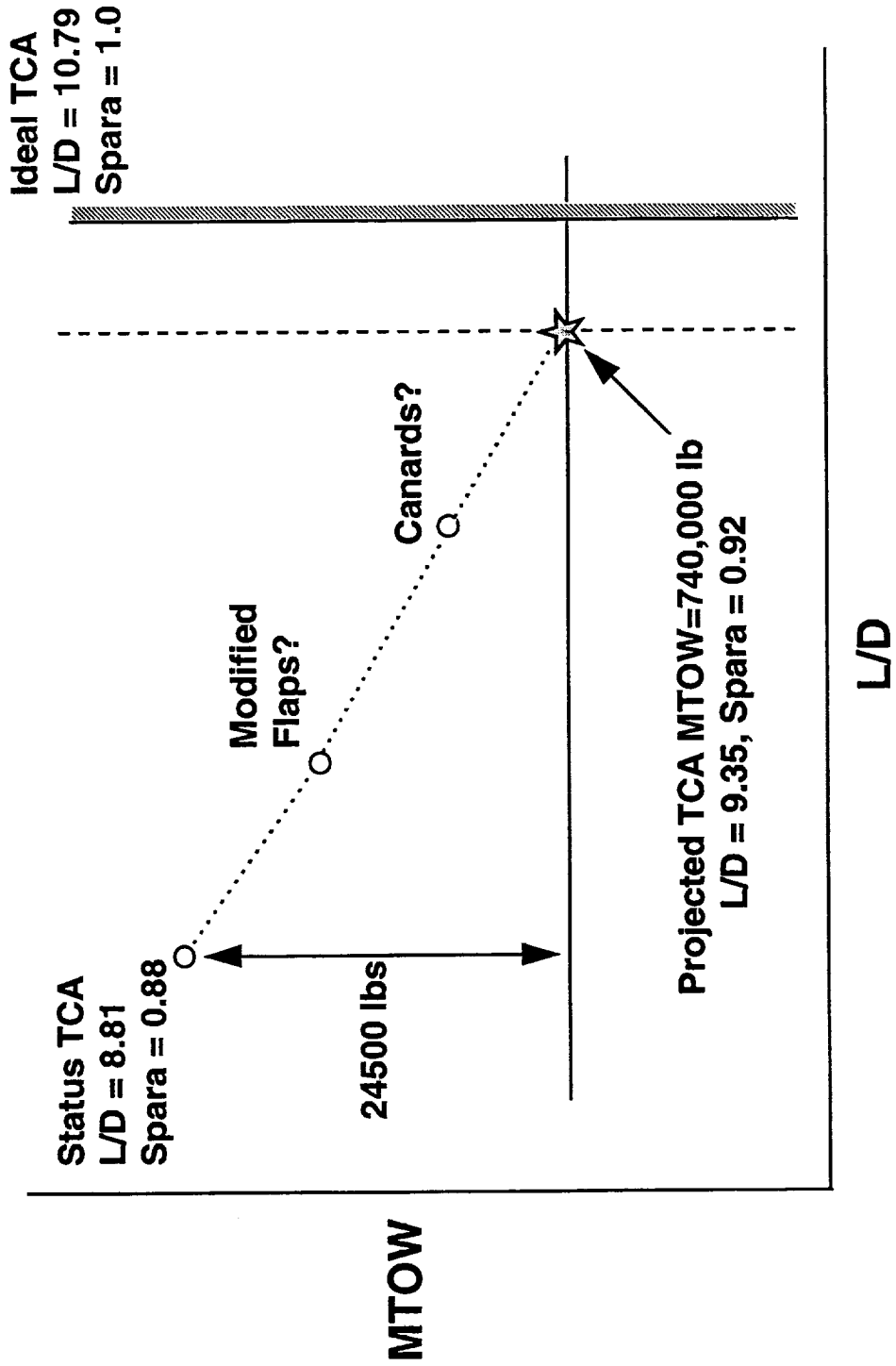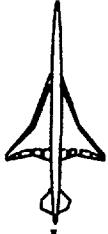
BOEING

HSCT Aerodynamics

Ideal TCA
L/D = 10.79
Spara = 1.0

Canards?

Modified
Flaps?

Status TCA
L/D = 8.81
Spara = 0.88

24500 lbs

Projected TCA MTOW=740,000 lb
L/D = 9.35, Spara = 0.92

MTOW

L/D

COMMON HIGH LIFT PD PROCESS

HSCT Aerodynamics

This page is intentionally blank

BOEING

HSCT Aerodynamics

COMMON HIGH LIFT PD PROCESS

- **Part of Technology Integration (TI) Aircraft Design Process (ADP)**

- **Process Flow Chart**

- **1997 Task Schedule & Progress**

1743

COMMON HIGH LIFT PD PROCESS FLOW DIAGRAM

HSCT Aerodynamics

Wind tunnel data for a reference configuration (currently Ref. H) is used to provide basic tail-off and tail-on data for a variety of flap settings, landing gear up and down, stabilizer angles, etc. 14'x22' data provides the bulk of the needed information with NTF data used to account for Reynolds number effects between 8 million (14'x22' Rn) and 90 million (NTF max Rn).

AERO2S is used to compute configuration increments (changes in CL, CD, and CM) between the new configuration and the reference configuration.

These differences are added to the wind tunnel based reference configuration data. Essentially, AERO2S is used to adjust the wind tunnl data for configuration differences. CDo is further adjusted to account for skin friction drag reduction between 90 million and 180 million (flight) Reynolds numbers.

Finally, the data are trimmed, flap angles are optimized, and a technology projection is added to bring the status suction parameter up to the projected level (94% accounting for thrust vector in CL and CD, 92% without).

1744

HSR AERODYNAMICS HIGH LIFT PROCESSES

Process : High Lift Parameters Prediction

Process Mission: Predict Configuration High Lift Aerodynamic Parameters

Process Owner(s):
NASA, Boeing, & MDC

Inputs:
- Configuration Memo
- Requirements & Objectives
- Schedules
- Resources
- Weight & CG Location
- Configuration Lofts
- Wind Tunnel Data

Suppliers:
- Tech Integration Group
- Propulsion Group
- Research Orginations
- Wind Tunnel
- Management
- Library

Outputs:
- Tables, Files, Memos, & Charts as required (C_L vs. α, C_D vs. C_L, C_{Lref}, C_{Ltd}, C_{Lap}, α_{td}, α_{lof}, C_{Deo} Ground Roll, Yaw Drag, Element Loads, Pressures, and Slat & Flap Schedules, Flap Placard Speeds, etc.).

Customers:
- Tech Integration group
- Research Orginations
- Project groups
- Wind Tunnel
- Management

Measurements:
- Flow Time
- Cost
- Accuracy

1745

BOEING

HSCT Aerodynamics

COMMON HIGH LIFT PD PROCESS SCHEDULE

This page is intentionally blank

High Lift Common Process

ID	Task Name
1	Plan & Schedule Method
2	Define Method
3	Consensus Geometry
4	Consensus Tools
5	Consensus Data
6	Establish Ground Rules
7	Test Case #1
8	Test Case #2
9	Status Report
10	ABRO2S Automation 1997
11	ABRO2S Calibration 1997
12	TCA Update 1997
13	Flap Deflection Optimization
14	Dynamic Effects
15	Common Process Update 1997
16	Status Report
17	AERO23 vs. WT Data
18	TCA Update 1998
19	Common Process Update 1998
20	Final Report

Timeline columns: 1996 (Qtr 2, Qtr 3), Qtr 4, 1997 (Qtr 1, Qtr 2, Qtr 3), Qtr 4, 1998 (Qtr 1, Qtr 2, Qtr 3), Qtr 4

Milestones: 11/27, 11/25, 11/2

Legend:
Task
Progress
Milestone
Summary
Rolled Up Task
Rolled Up Milestone
Rolled Up Progress

Page 1

SUMMARY

This page is intentionally blank

SUMMARY

BOEING

HSCT Aerodynamics

(1) Projected TCA L/D reasonable but risky

(2) TCA does not meet touchdown attitude requirements for a 155kt approach speed

(3) L/D improvements may not show up as MTOW reductions since the TCA is sized with projected L/D.

The status will approach the projection, risk & uncertainty will decrease, and the technology readiness level (TRL) will increase

(4) Common High lift Process is mostly defined but not implemented

High Lift Aero/ptm/02/20/97

1749

THIS PAGE IS INTENTIONALLY LEFT BLANK

Use of Boundary Layer Transition Detection to Validate Full-Scale Flight Performance Predictions

Marvine Hamner, Senior Project Engineer, McDonnell Douglas Aerospace
L.R. Owens, Jr., Aerospace Engineer, NASA Langley Research Center
R.A. Wahls, Aerospace Engineer, NASA Langley Research Center
David Yeh, Principal Engineer, McDonnell Douglas Aerospace

Full-scale flight performance predictions can be made using CFD or a combination of CFD and analytical skin-friction predictions. However, no matter what method is used to obtain full-scale flight performance predictions knowledge of the boundary layer state is critical. The implementation of CFD codes solving the Navier-Stokes equations to obtain these predictions is still a time consuming, expensive process. In addition, to ultimately obtain accurate performance predictions the transition location must be fixed in the CFD model. An example, using the M2.4-7A geometry, of the change in Navier-Stokes solution with changes in transition and in turbulence model will be shown. Oil flow visualization using the M2.4-7A 4.0% scale model in the 14'x22' wind tunnel shows that fixing transition at 10% x/c in the CFD model best captures the flow physics of the wing flow field.

A less costly method of obtaining full-scale performance predictions is the use of non-linear Euler codes or linear CFD codes, such as panel methods, combined with analytical skin-friction predictions. Again, knowledge of the boundary layer state is critical to the accurate determination of full-scale flight performance. Boundary layer transition detection has been performed at 0.3 and 0.9 Mach numbers over an extensive Reynolds number range using the 2.2% scale Reference H model in the NTF. A temperature sensitive paint system was used to determine the boundary layer state for these conditions. Data was obtained for three configurations: the baseline, undeflected flaps configuration; the transonic cruise configuration; and, the high-lift configuration. It was determined that at low Reynolds number conditions, in the 8 to 10 million Reynolds number range, the baseline configuration has extensive regions of laminar flow, in fact significantly more than analytical skin-friction methods predict. This configuration is fully turbulent at about 30 million Reynolds number for both 0.3 and 0.9 Mach numbers. Both the transonic cruise and the high-lift configurations were fully turbulent aft of the leading-edge flap hingeline at all Reynolds numbers.

Use of Boundary Layer Transition Detection to Validate Full-Scale Flight Performance Predictions

Marvine Hamner, Senior Project Engineer, McDonnell Douglas Aerospace
L. R. Owens, Jr., Aerospace Engineer, NASA Langley Research Center
R. A. Wahls, Aerospace Engineer, NASA Langley Research Center
David Yeh, Principal Engineer, McDonnell Douglas Aerospace

This presentation is again the successful result of the collaboration of NASA, McDonnell Douglas, and Boeing researchers in planning and testing an HSCT-class configuration under a wide variety of conditions. It focuses on the affect the boundary-layer state has on our ability to predict full-scale flight performance.

Acknowledgments

- ## LaRC TSP Team:
    - **Team Leader:** T.G. Popernack, Jr.
    - **NASA LaRC:** M. Mitchell, B.T. Upchurch, M.A. Scott, C.G. Burkett, Jr., B.S. Sealey, B.D. Leighty, W.P. Chambers, W.K. Goad, W.C. Alexander, L.R. Owens, Jr., R.A. Wahls, T.E. Deans, Jr., J.L. Hester, R. Shaiken, K. Stacy
    - **McDonnell Douglas Aerospace:** M. Hamner
    - **The Boeing Company:** W. Burggraf
    - **Vigyan, Inc.:** A. Jalali
    - **Calspan Corp.:** G. Walkup, A. Kilgore
    - **Lockheed Engineering and Sciences Corp.:** D. Neuhart
    - **Purdue University:** J. Sullivan
    - **University of Florida:** K. Schanze
    - **Old Dominion University:** D.M. Oglesby

This paper represents more than just a wind tunnel test or a CFD study. It is the combined effort of a huge number of researchers. Of particular interest is the LaRC Temperature Sensitive Paint Team who put together the transition detection technique that will ultimately enhance full-scale flight performance predictions from low Reynolds number wind tunnel data. This team brings an immense body of knowledge to bear on the problem of transition detection. It is composed of engineers and scientists from NASA, industry, and academia.

Acknowledgments

- **NTF TSP Staff:**
  - Thomas E. Deans, Jr., Jerry B. Adcock, Ronald Shaiken, Joshua L. Hester, W. Allen Kilgore, Robert J. Done, P. Anthony Guthrie, Pat Quander Jones, Bruce Raiford, John F. Bledsoe, Greg F. Walkup, Arbria L. Wright, Dave Butler, John L. Stobierski, J. Russel McHatton, William G. Johnson, Jr., W. Chris Alexander, David Coleman, John W. Meador
- **McDonnell Douglas Staff:**
  - Marty Morris, Mike Benne, Tom Kihlken, John Donovan

More than just the TSP Team, the people who made the initial tests using this transition detection technique work should be recognized. Without the extraordinary effort and dedication of the NTF TSP Staff we would not have the success story told in this presentation. The NTF TSP Staff put in the extra effort, often repeating conditions, and pushing tunnel operations beyond perceived limits that allowed us to acquire the wide range of transition data we now have.

Presentation Outline

- **Effect of Fixing Transition on CFD Solutions**
- **Transition Effects in Analytical Skin-friction Predictions**
- **Transition Detection using Temperature Sensitive Paints**
- **Summary**
- **The Next Steps**

Overall Wind Tunnel Test Objectives

- **Obtain free and fixed transition data on three configurations: baseline, high-lift, and transonic**
    - Use data to design/validate a transition fixing methodology for HSCT-class configurations
    - Incorporate data in full-scale flight performance prediction methodology
- **Obtain data for CFD validation**

Goal

- **Be able to predict full-scale flight performance using low Reynolds number wind tunnel test data *with confidence***

Last year I said that, "To develop full-scale performance predictions an understanding of Reynolds number effects on HSCT-class configurations is essential." Today we still have the same overriding premise in our wind tunnel test objectives. Our ultimate goal is to be able to predict full-scale flight performance using the data we acquire during configurations development, at low Reynolds number. When I say, "with confidence," I mean that we should be able to say what the level of confidence is in our predictions.

MCDONNELL DOUGLAS ═══════════════ HIGH-SPEED CIVIL TRANSPORT

Model/Configurations Definition
Used for Transition Tests

2.2% Model used for testing in the NTF

Wing: Reference H wing
  Flap deflections available:

	LE	TE
Baseline	0/0	0/0
Transonic	0/10	0/3
High Lift	30/30	10/10

Body: Fuselage truncated at station 60.8150

Nacelles: Axisymmetric

The 2.2% scale Reference H model used for transition testing at the NTF includes:

- wing - with various flap deflections representing high-speed and high-lift configurations
- fuselage
- axisymmetric nacelles

The truncated fuselage is run on the straight sting. Trips normally applied include the forebody ring and nacelle internals. A "conventional" wing tripping scheme based on Braslow criteria was used to obtain the fixed transition data.

Model/Configurations Definition

4.0% model used for testing in the 14'x22'

Wing: M2.4-7A Arrow wing
                   Flap deflections available: various

Body: Complete fuselage

Nacelles: Axisymmetric

The 4.0% scale M2.4-7A Arrow wing model used at the 14'x22' includes:

- wing with various leading- and trailing-edge flap deflections
- complete fuselage and tails
- axisymmetric nacelles

The model is run on a post mount.

Spanwise Pressure Comparison Locations
for the M2.4–7A Configuration

MCDONNELL DOUGLAS   HIGH-SPEED CIVIL TRANSPORT   HSCT

FS = Fuselage Stations (in inches)

FS 1792.48   FS 2227.78   FS 2671.35

FS 1546.40   FS 2009.75   FS 2445.80   FS 2879.00
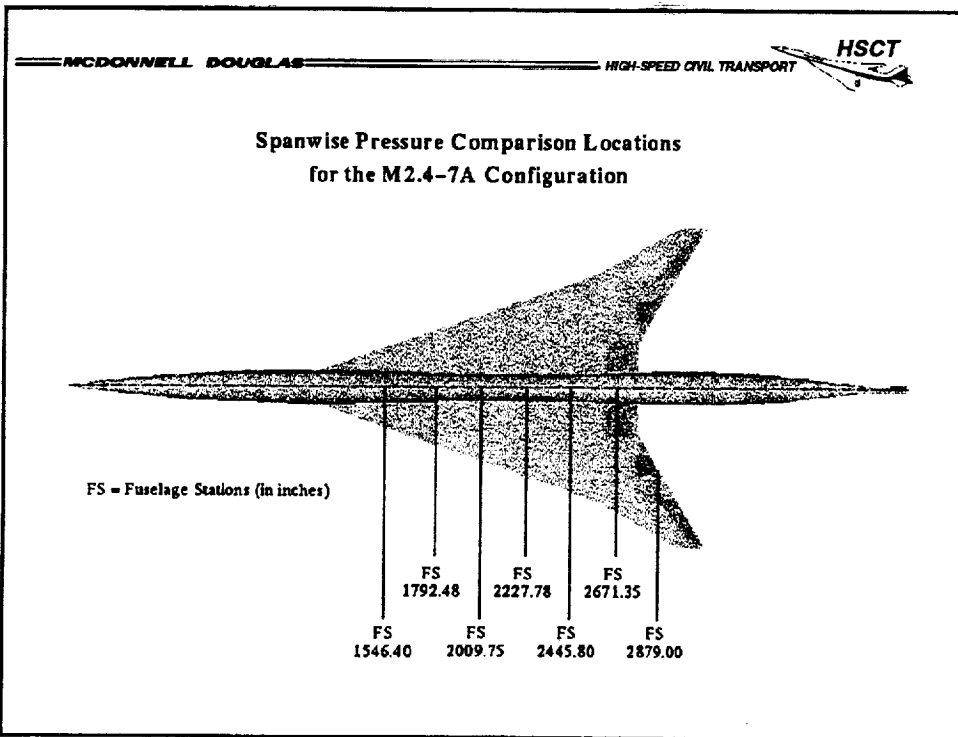
The spanwise pressure distribution at various stations can be used to illustrate the effect of describing the boundary layer state on the CFD solution. This figure shows which stations are used.

Spanwise Pressure Comparison for the M2.4-7A Configuration
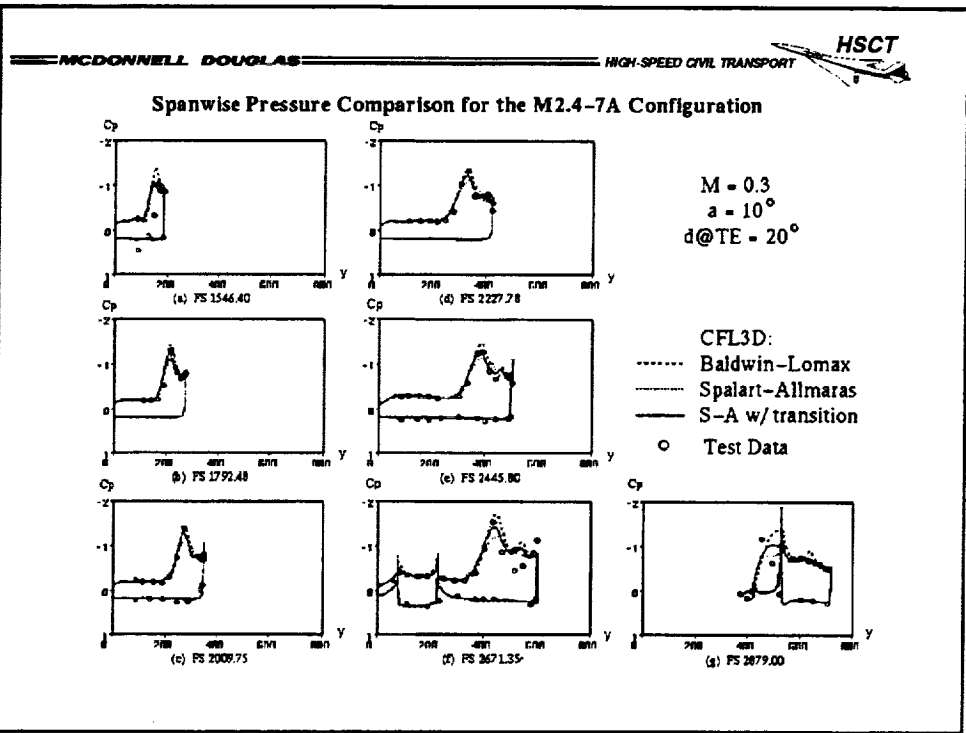
CFD solutions using two different turbulence models were obtained as well as the solution fixing transition at 10% x/c. This slide illustrates the difference in the solutions obtained for these cases. In addition to determining which turbulence model to use, describing the boundary-layer state plays an important role in obtaining CFD solutions that best model wing flow field.

Comparison of Wind Tunnel Oil Flow and CFD Solutions
Near the Trailing–Edge for the M2.4–7A Configuration
Trailing–Edge Flap Deflection = 20°
Alpha = 10 Degrees
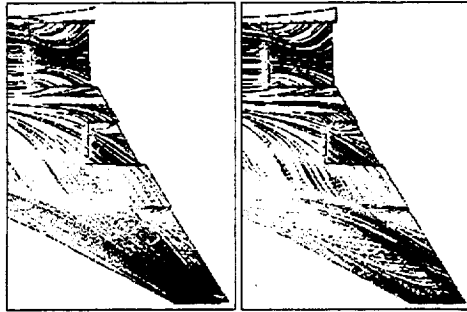
As shown in this figure, fixing transition at 10% x/c in obtaining the CFD solution better models vortex formation.

Skin Friction Values Based on Flat Plate Wind Tunnel Data
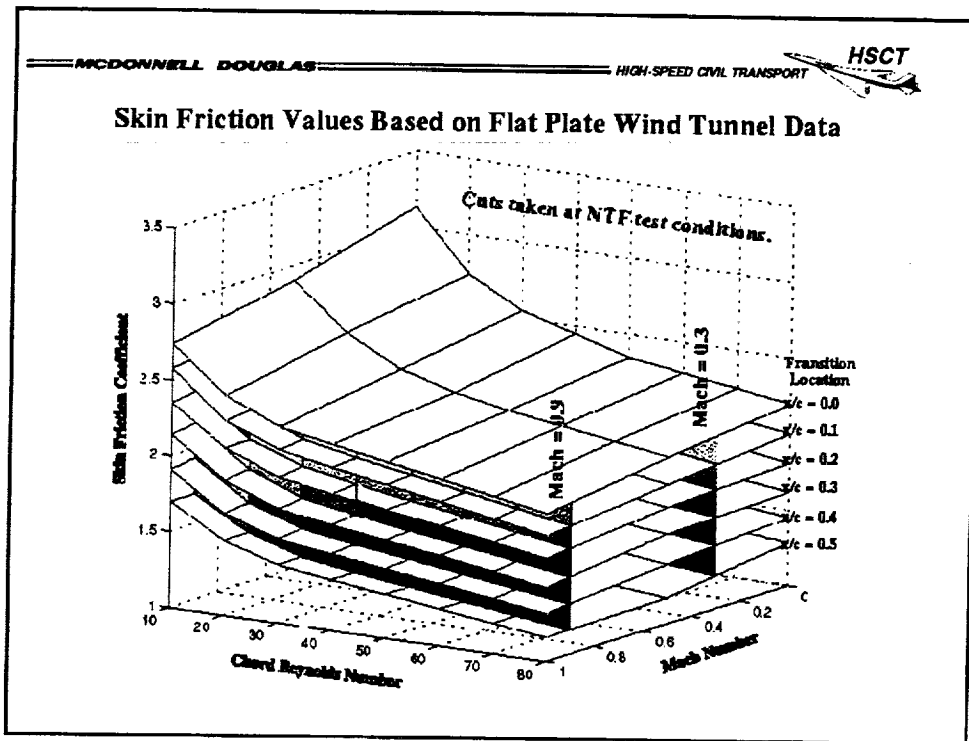
This slide illustrates the variation of flat plate skin friction coefficient with Reynolds number and Mach number for various transition locations. A cut taken at an NTF test condition yields a family of curves representing the flat plate skin friction coefficient as a function of Reynolds number at various transition locations. This cut represents a linar interpolation between original data at Mach 0.0, 0.5, and 1.0. This data was obtained from the "Clutter charts," Douglas Aircraft Company, Inc., Report Number ES 29074. They represent a smooth, insulated flat plate.

Analytical Skin-friction Calculations

Skin-friction drag = Contribution from wing +
                      Contribution from fuselage

$$= \Delta C_{DWing} + \Delta C_{DFuselage}$$

Each contribution = Form Factor * (S_{wet}/S_{ref}) * C_f

Form Factor, S_{wet} and S_{ref} based on physical geometry
C_f based on previous analytical and experimental work

The flat plate skin friction coefficient is scaled by the form factor, the wetted area, and the reference area. These factors are based on physical geometry. The TI group provided the values of these factors. Because of the presence of the forebody trip ring, the fuselage can be considered fully turbulent. Thus the contribution from the fuselage becomes constant based on Reynolds number while overall skin-friction drag varies as a function of transition location on the wing.
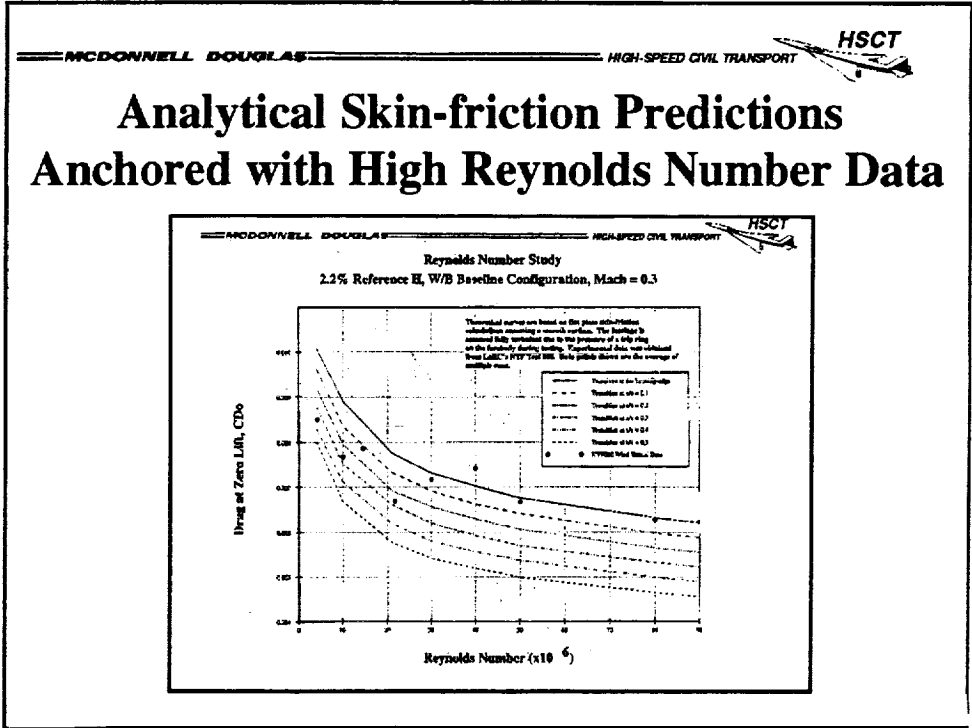
The chart in this slide was presented last year. It represents the scaled flat plate skin friction coefficient for various transition locations, anchored at the minimum drag level for the high Reynolds number condition. This particular slide includes data for the Mach 0.3 case. The 40 million Reynolds number data shown in this chart has since been determined to be bad.

This chart illustrates the variation in transition location as a function of Reynolds number.

Analytical Skin-friction Predictions
Anchored with High Reynolds Number Data
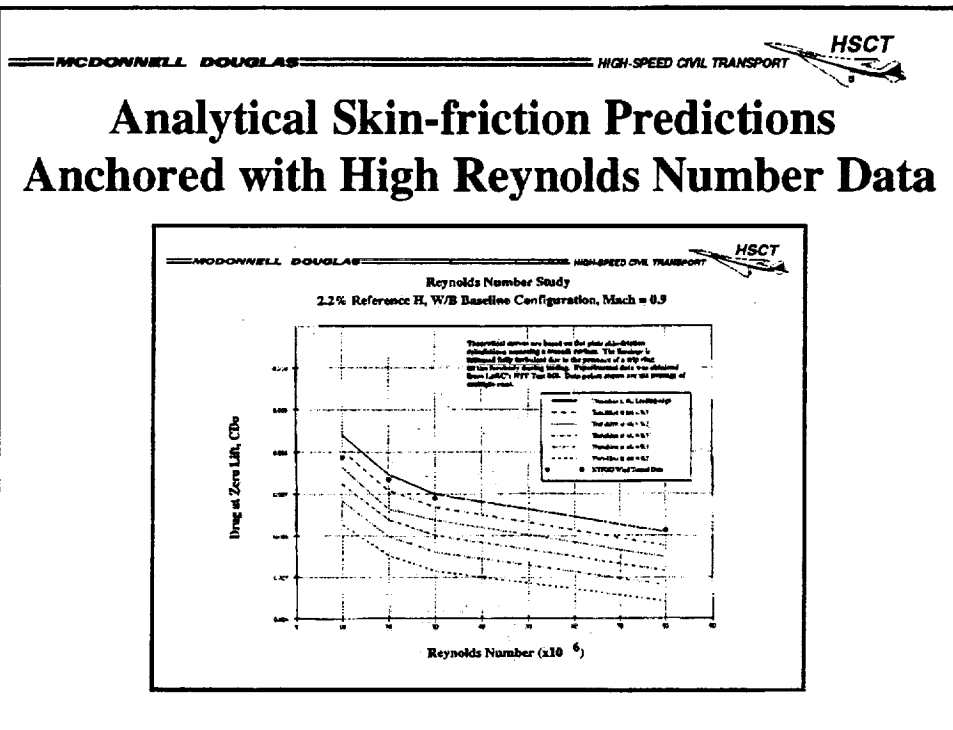
The chart in this slide was also presented last year. It represents the scaled flat plate skin friction coefficient for various transition locations, anchored at the minimum drag level for the high Reynolds number condition. This particular slide includes data for the Mach 0.9 case.

This chart also illustrates the variation in transition location as a function of Reynolds number.

Mapped TSP Image Data

Surface grid

TSP image

Laminar region

Planar cuts through grid
to determine surface area
of laminar region
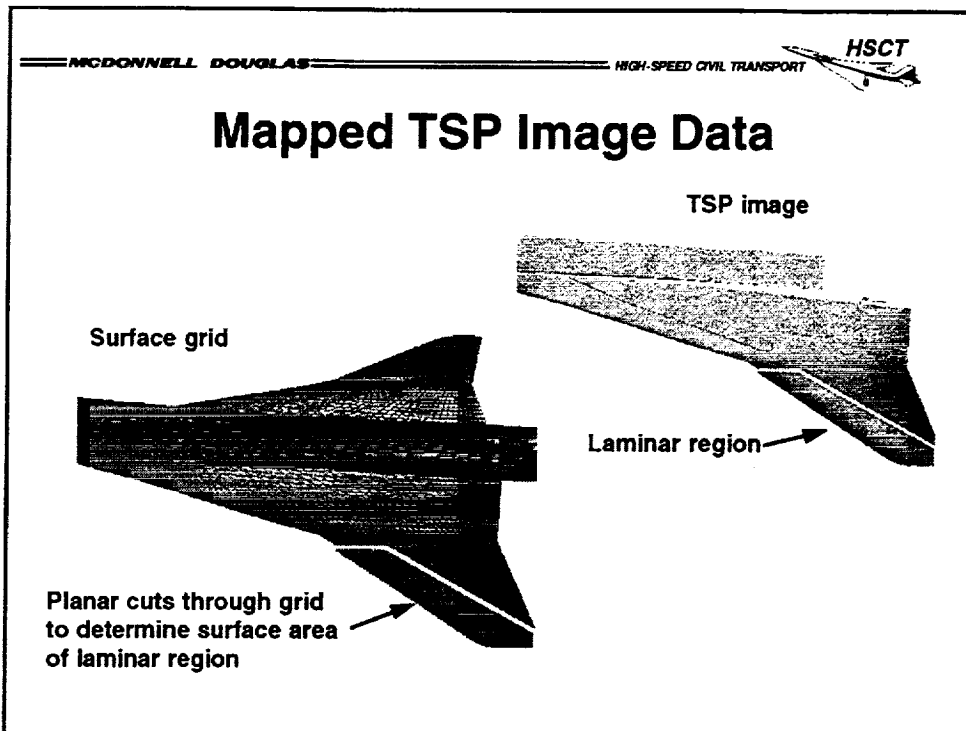
The capability of directly determining the boundary layer state, that is laminar versus turbulent, allows us to reconsider the analytical skin friction predictions. To determine the square inches of laminar boundary layer present the 2-D TSP image acquired during two NTF tests last year was mapped to a 3-D grid. Because the extent of the laminar boundary layer is not symmetric, this grid was split into upper and lower surfaces. These surfaces were cut with planes determined by two points at the edge of the laminar boundary layer nearest the side-of-body and two points at the edge of the laminar boundary layer nearest the trailing-edge. This technique disallows turbulent wedges issuing from areas of damaged paint. However, for conditions where a larger transitional region occurs it may overstate the extent of the laminar boundary layer. The surface area representing this "laminar region" was then computed.

Percent Laminar Surface Area

Mach Number	Chord Reynolds Number	Laminar Area (in²)	Percent Laminar Area Based on Wimpress Area	Percent Laminar Area Based on Gross Area
0.3	8.5	109.9	44.5	39.6
	14.4	65.4	26.4	23.5
	21.6	54.6	22.1	19.7
	34.0	-32.8	13.3	11.8
0.9	10.2	93.8	37.9	33.7
	20.0	50.9	20.6	18.3
	30.0	35.3	14.3	12.7

This table in this slide shows the computed "laminar region" for various test conditions. Because no lower surface data was obtained for the Mach 0.3, 34.0 million Reynolds number condition, the upper surface laminar area was doubled to obtain the value shown. Specific values for upper and lower surface areas are available on request.

To obtain this table the following assumption was made.

1) It was assumed that the flat plate skin coefficient data was obtained at zero degrees angle of attack. Since the twist on the outboard panel (where most of the laminar boundary layer exists) is about one and one-half degrees, this table was computed for data obtained at one degree angle of attack.
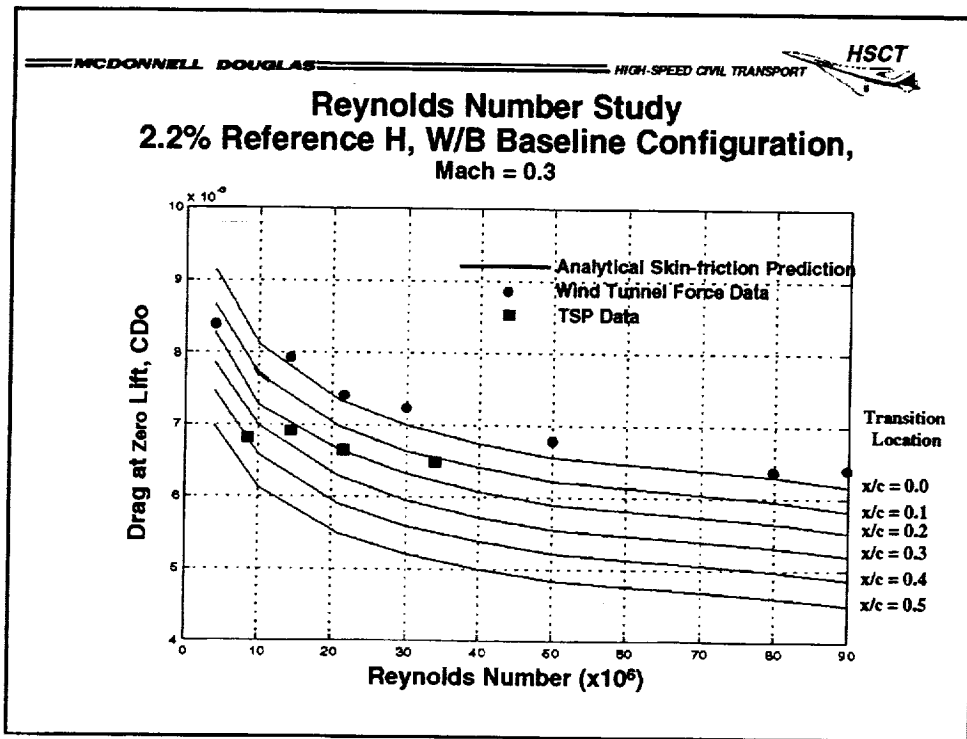
Reynolds Number Study
2.2% Reference H, W/B Baseline Configuration,
Mach = 0.3

This slide illustrates the analytical skin friction predictions for various transition locations, the wind tunnel force data previously acquired, and the computed laminar surface areas at Mach 0.3. Previously, anchoring the analytical skin friction curves using high Reynolds number data moved the curves such that there appeared to be more laminar flow at low Reynolds numbers than analysis alone predicts. Direct determination of the laminar surface area bears this out. However, there still appears to be a discrepancy at low Reynolds numbers. This may be due to the presence of other phenomena such as separation. It may be also be due to data quality.

Reynolds Number Study
2.2% Reference H, W/B Baseline Configuration,
Mach = 0.9
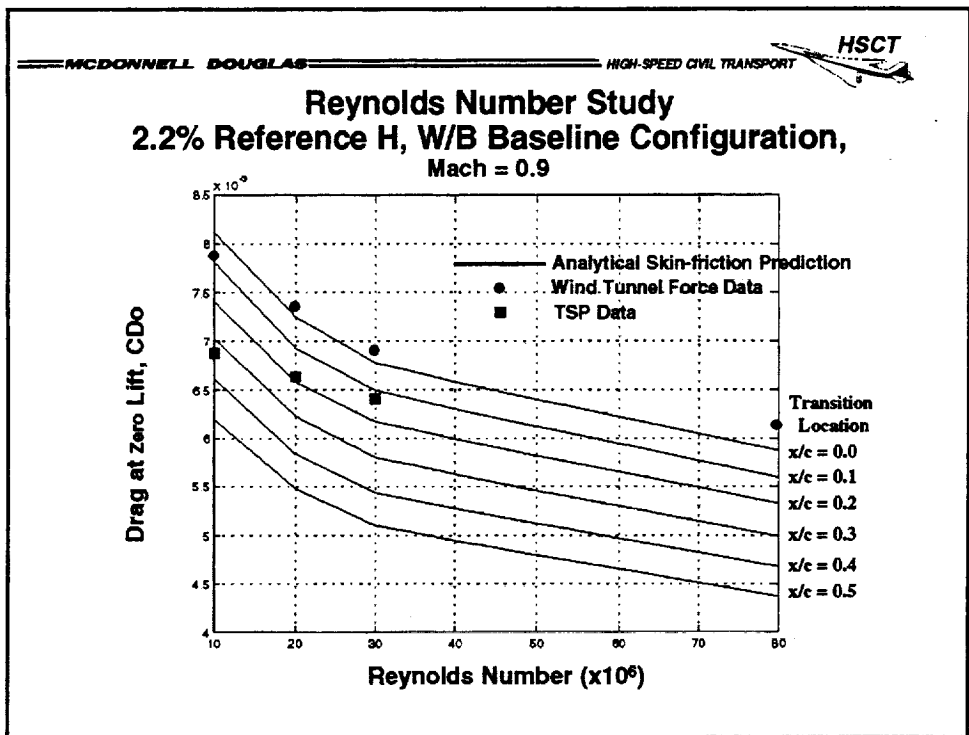
This slide illustrates the analytical skin friction predictions for various transition locations, the wind tunnel force data previously acquired, and the computed laminar surface areas at Mach 0.9. As in the previous slide, when the analytical skin friction curves were anchored using high Reynolds number data the curves moved such that there appeared to be more laminar flow at low Reynolds numbers than analysis alone predicted. Again, direct determination of the laminar surface area bears this out. And again, there still appears to be a discrepancy at low Reynolds numbers. This may be due to the presence of other phenomena such as separation. It may be also be due to data quality. However, because the Mach 0.9 data is acquired at higher dynamic pressures data quality issues in coefficients generally become less observable.

Boundary Layer Transition Detection Reduces Risk in Full–Scale Flight Performance Predictions
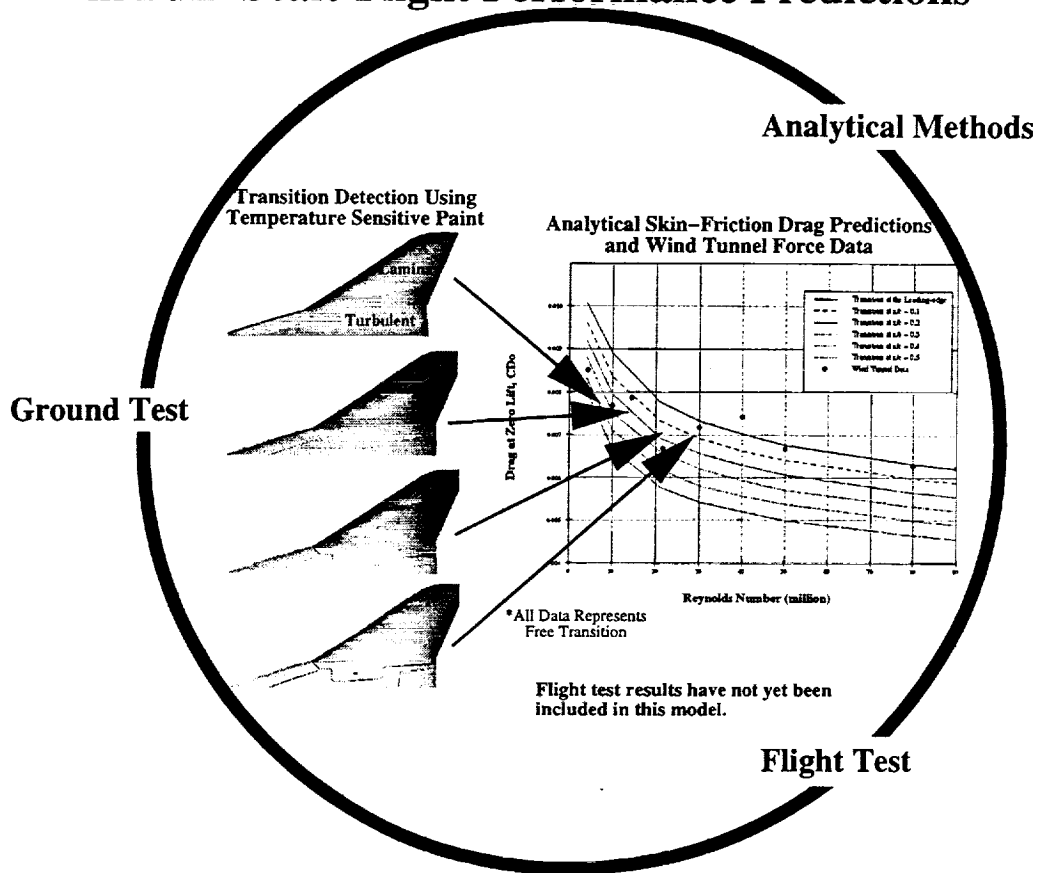
Summary illustrating scaled skin–friction curves anchored using high Reynolds Number data, NTF wind tunnel data, and NTF TSP data. This figure illustrates the consistency in trends and levels between the three data sources. It also depicts the interdependency between over all design techniques, that is, between ground test, flight test, and analytical methods.

Summary

- **Fixing transition has a significant effect on CFD solutions.**

- **Measured drag levels at low Reynolds numbers are somewhat different than changes in boundary-layer state show indicating the presence of other phenomena, for example separation.**

- **Knowledge of the boundary-layer state allows anchoring analytical skin friction predictions with low Reynolds number data.**

- **An assessment of the confidence level can be made.**

As shown in this presentation, fixing transition has a significant effect on CFD solutions. This can be seen in both the resulting pressure distributions and in surface streamlines illustrating vortex formation.

Measure drag levels indicate the presence of phenomena other than boundary layer transition. Trends across Mach numbers between force data and transition data are consistent.

Once the boundary layer state has been determined analytical skin friction predictions can be anchored and full-scale flight performance predictions completed. An assessment of the confidence level of the full-scale flight performance prediction can be made by determining upper and lower bounds on the extent of laminar surface area and force data quality.

The Next Steps

- **Acquisition of low Reynolds number transition data on additional models to support methodology development.**

- **Continued transition detection development.**

- **Adaptation of methodology to configurations and conditions of interest.**
  - The high-lift configuration appears to be fully turbulent at angles of attack of interest.
  - The outboard leading-edge flap is laminar at angles of attack of interest for the transonic configuration.
  - The cruise configuration maintains some laminar flow outboard at the cruise angle of attack.

- **Incorporation of stability code predictions.**

Continued effort to determine the extent of the laminar boundary layer including acquisition of data on models at low Reynolds numbers will be key in fully developing a methodology for full-scale flight performance predictions. This includes continuing to develop transition detection techniques and understanding how to apply this methodology to additional configurations at a variety of conditions. Incorporation of stability code results will play a major role in developing computational techniques that completely model the flow physics present.

Assessment of Computational Methods Applied to HSCT High-Lift Configurations with Multiple Flap Surfaces

David T. Yeh
Roger W. Clark

February 25-28, 1997
HSR Workshop
at
LaRC, Hampton, VA

Outline

This report starts with the description of the objective for the HSCT high-lift aerodynamics, followed by the numerical approach. The automated flap deflection procedures used for high-lift applications will be briefly described. The numerical results for the high-lift configurations will be presented including code validation, predicted flow physics as well as the discussion of the numerical issues that affect the flow solutions. This report concludes with a summary and future plans.

OUTLINE

- Objectives - HSCT High-Lift Aerodynamics

- Approach

- Automated Flap Deflection Procedures

- Numerical Simulations & Code Validation

  1. M2.4-7A Opt2A - Code validation

  2. M2.4-7A Mod3 - On-going test

     - Effects of LE deflections (30/10, 40/10)

     - Effects of LE blowing(40/10)

  3. TCA - Pretest Analysis

     - Effects of turbulence models

     - Effects of LE deflections (0/0, 30/0)

     - Preliminary comparison with Modified Ref-H data

- Summary & Future Plans
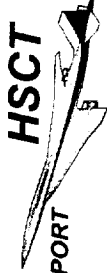
Objective

The objective of the HSCT high-lift effort is to analyze and optimize the aerodynamic performance. To achieve the objective, it is necessary to develop and validate the numerical methods required for analysis of the high-lift systems.

The computational emphases are focused in the following areas:

1. Conduct Numerical simulations of the high-lift configurations for
   wind-tunnel support;

2. Assess the numerical capability in capturing the flow physics under
   high-lift, low-speed conditions;

3. Complement wind-tunnel results in deriving optimal high-lift systems
   through parametric studies.

OBJECTIVE – HSCT High–Lift Aerodynamics

Maximize L/D (minimize noise)

  – LE Flaps : Promote Attached Flow

  – TE Flaps : Optimize Span Loading

Computationally,

  ● Develop/Validate Numerical Methods

  ● Provide Wind–Tunnel Support

  ● Flap Optimization
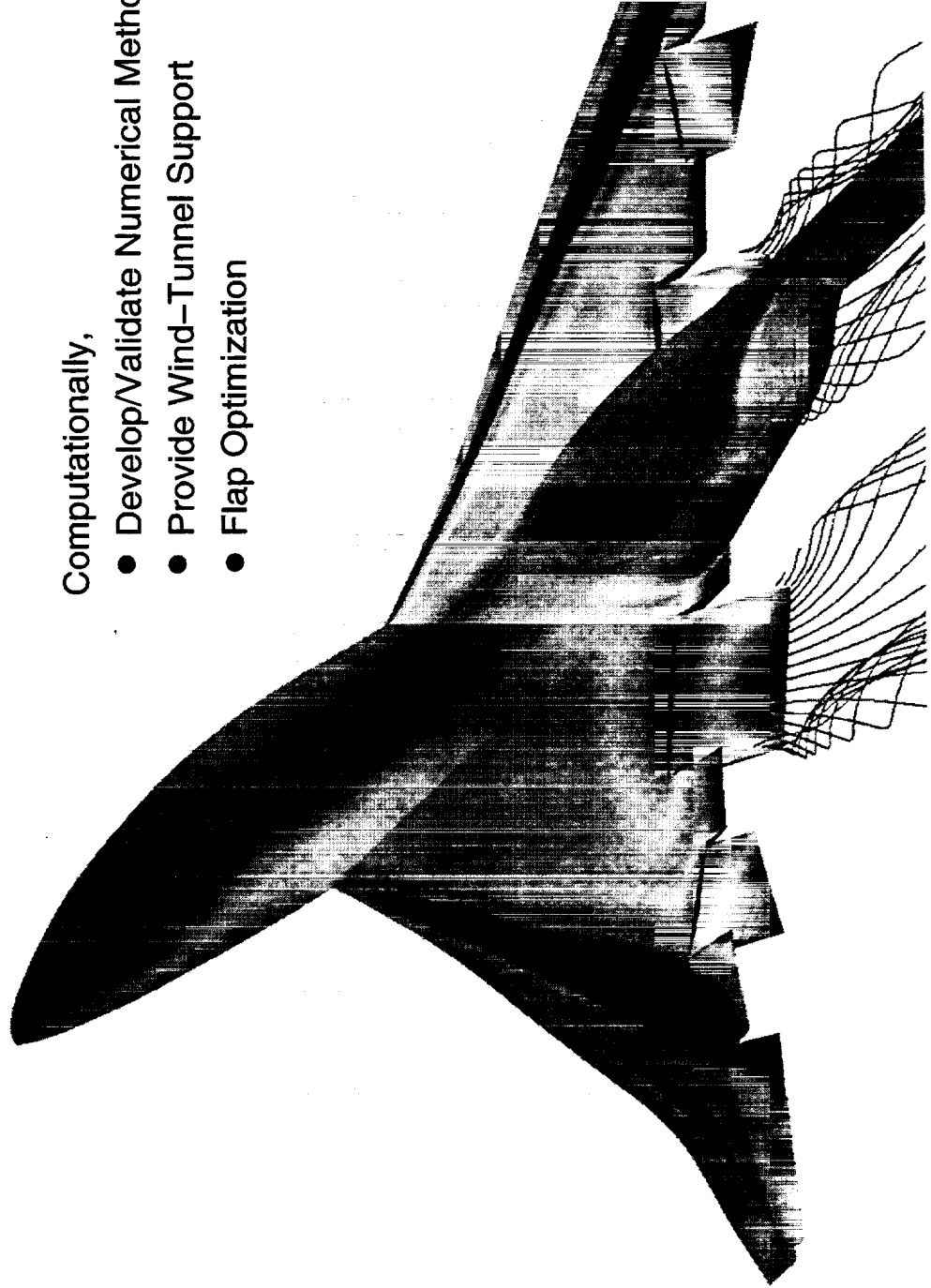
Approach

The approach is to utilize the recent development of the automated flap deflection procedures at MDC and the CFL3D code developed at NASA LaRC for high-lift flow simulation. The numerical results are compared with available test data for code validation and evaluation including the influence of the numerical parameters on the flow solutions. Parametric studies of flap planforsm and angular deflections will be performed to support wind-tunnel tests in deriving an optimal configuration.
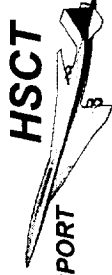
Approach

- Develop Automated Flap Deflection Procedures
  - Reduce turn-around time

- Utilize CFL3D Flow solver for simulation of High-Lift Configurations

- Assess numerical accuracy through direct comparison with test data

- Perform sensitivity studies on the numerical issues

- Conduct parametric studies (δ, flap chord/extent) for wind-tunnel test support
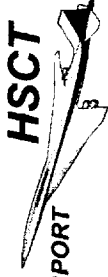
Numerical Applications

Advanced computational methods such as the current CFD codes and automated flap deflection procedures provide excellent tools for the analysis and optimization of high-lift configurations. The numerical results can provide valuable informations about the flow physics; pre-test analysis and post-test verification. Geometric perturbations can be easily incorporated in the computational model for optimization analysis.

Numerical Applications to HSCT High–Lift Aerodynamics

- Flow Visualization

- W–T Support

- Automated LE/TE Flap Deflections
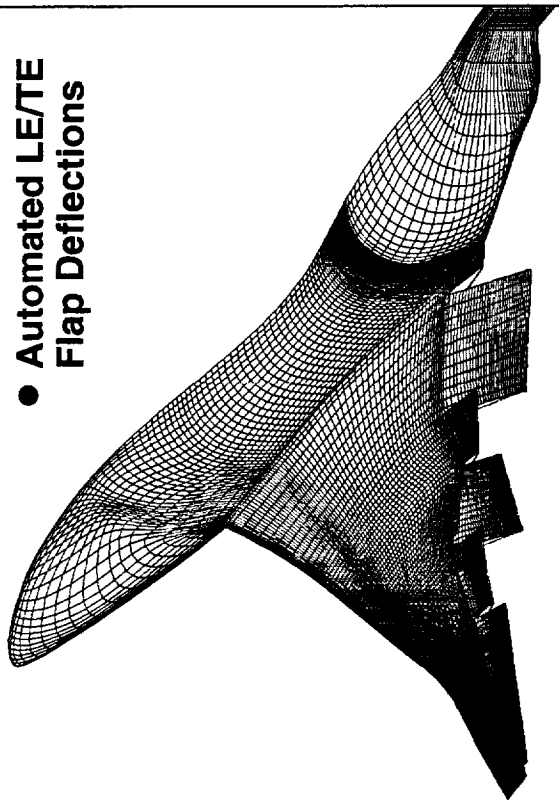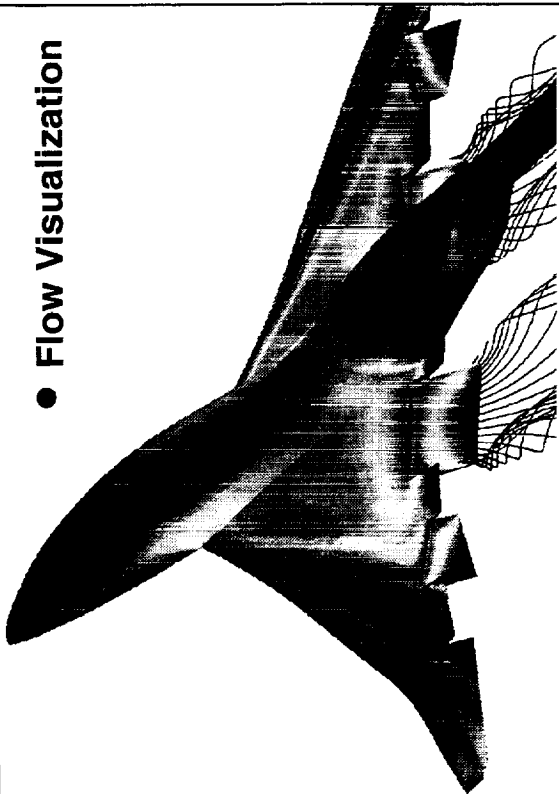
- Parametric/Optimization Studies
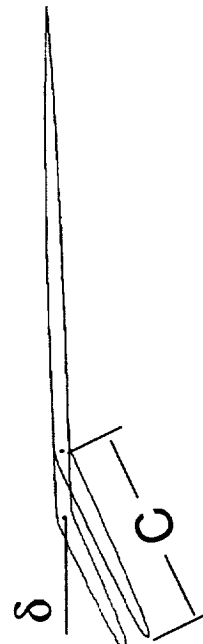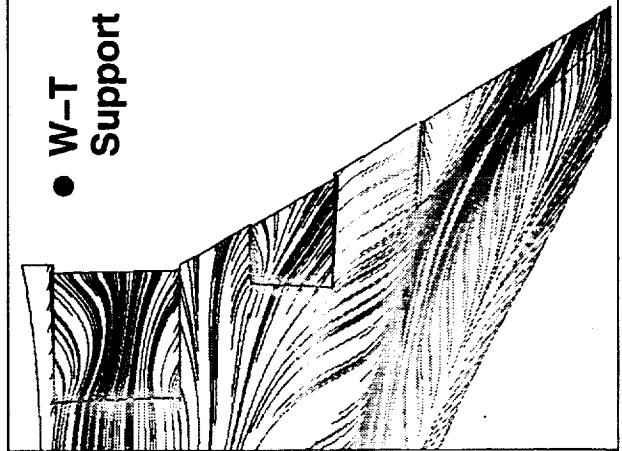
Automatic Flap Deflection

Design and optimization of HSCT high-lift configurations require the modeling of the LE and TE flaps with a wide range of planforms and angular deflections. Automated flap deflection procedures have been implemented to efficiently modify the baseline grid to account for variable flap deflections. These procedures have been implemented in such a way that only flap deflection angles are required to generate a modified grid for CFD analysis. In doing so, the regridding process for different flap deflections is eliminated.

Automated Flap Deflection Procedures Reduce Turn–Around Cycle for Performance Analysis and Flap Optimization

Start with a Clean Grid (No Flaps)

1 Specify Flap Deflections
(LEI, LEO, TEI, TEM, TEO)

2 Run Flap Deflection Procedures

3 Obtain a Modified Volume Grid

TEI

TEM

LEI

TEO

LEO

Flap Deflection Flow Chart

The automated flap deflection procedures consist of 3 procedures: a pre-processor, LE flap and TE Flap deflection procedures. For the cases where only the LE flap deflection is required, the pre-processor is bypassed and the process goes directly to the LE flap deflection procedure. The pre-processor is only used to line up the grid lines with TE flap edges whenever the TE flap modeling is needed. The running process for using these procedures has been automated for a number of HSCT High-Lift Configurations.

Flap Deflection Flow Chart

LE only → LE Flap Deflection Procedure

TE → Pre-Processor

Pre-Processor

Align grid lines with TE flap edges

LE Flap Deflection Procedure

TE Flap Deflection Procedure

LE Flaps Only

LE & TE Flaps

TE Flaps Only

LE Flap Deflection Procedure

The LE flap deflection procedure consists of a series of mapping, grid modification and smoothing techniques that modifies a baseline grid to account for LE flap deflections. The basic idea is to isolate the LE flap geometry so that the flap geometry can be rotated about the hinge axis of an arbitrary orientation, or can easily be modified in the design process. Once a desirable flap rotation/geometry is determined, the surface grid points upstream of the hinge line are mapped onto the new flap surface. The corresponding volume grid is then generated for the CFD analysis, or is used in the TE flap deflection procedure for simultaneous LE/TE deflections.

Automated Grid Modification Procedure for Modeling Leading–Edge Flap Segments

4. Hinge–Line Surface Smoothing

Spline

Interpolation

δ_f

5. Mapping

Relaxed to the original grid

TE

Distribution for TE Flaps

Deflected LE

6. Grid Modification & Clustering

1. Identify Flap Segments

TCA Configuration

2. Generate Flap Geometries

Inboard

Additional cuts for better accuracy

Tip

3. Rotate about Hinge Lines

Hingewise Rigid Body Rotation

TE Flap Deflection Procedure

A grid modification procedure for modeling the TE flap deflections has been developed. This chart illustrates the overview of the regridding process. This procedure consists of 6 computer codes that are used sequentially to modify a baseline volume grid through grid revision techniques. These techniques consist of blocking and regional regridding near the flap region; spanwise wing/flap gap modeling; rigid-body-rotation about user specified axes; grid perturbation; upper surface smoothing and lower surface interpolation near the hinge line; and grid clustering for viscous calculations.

Automated Grid Modification Process for TE Flap Deflections

3. Flap Rotate

$V_3 = V_1 \times V_2$

$V_2 = V_1 \times Z$

$V_1 =$ hinge axis

4. Grid modification

S_n

S_1

$S_n = S_1 \cdot fac$

δ

2. Gap modeling

① Wing

Wing/flap

Flap

② Wing

Gap

Flap

5. Surface smoothing

J-2 J-1 J+1 J+2

Cubic Spline

Interpolation

Original
Fitted

1. Blocking / Regridding
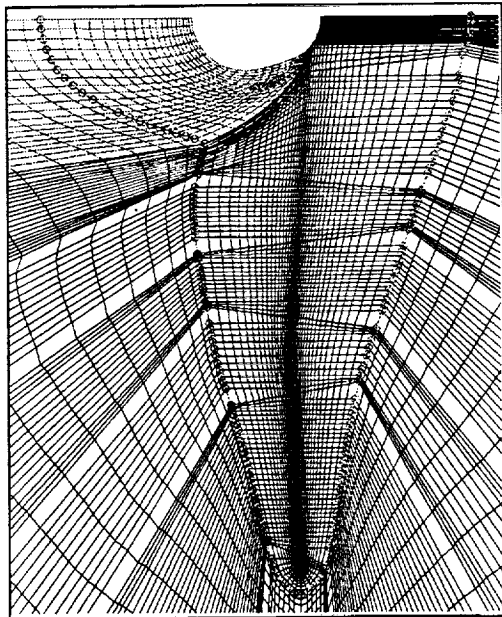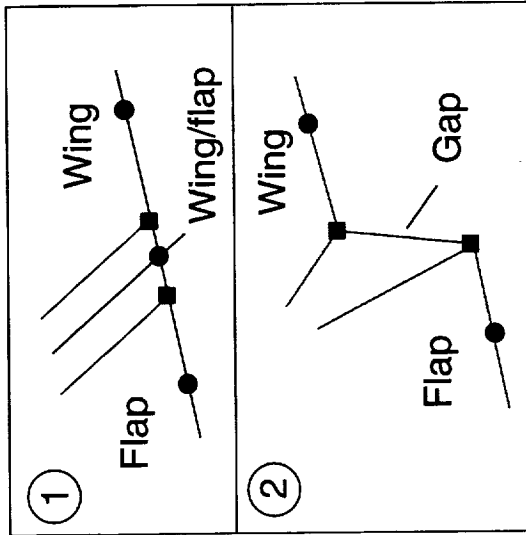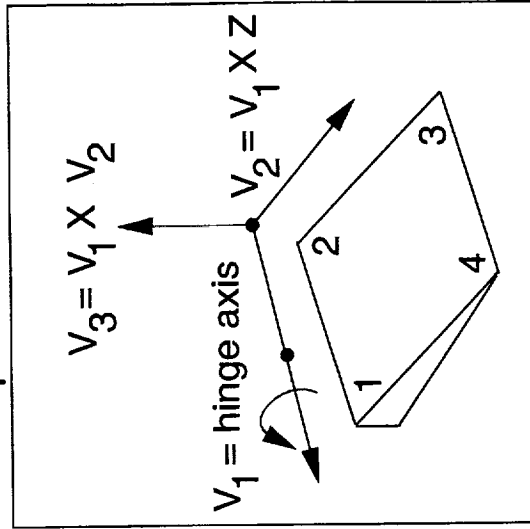
6. Grid Clustering
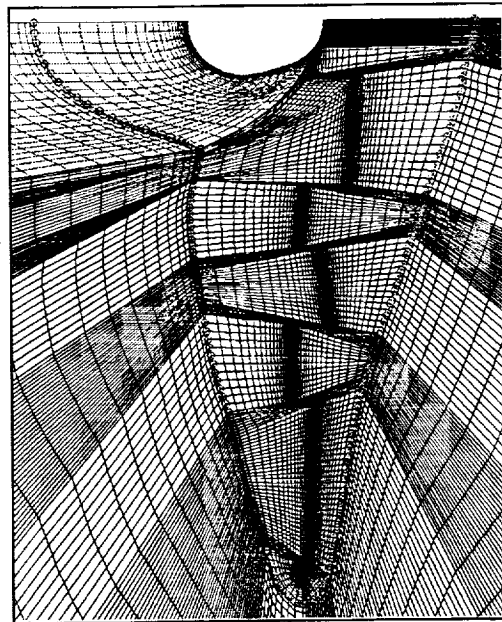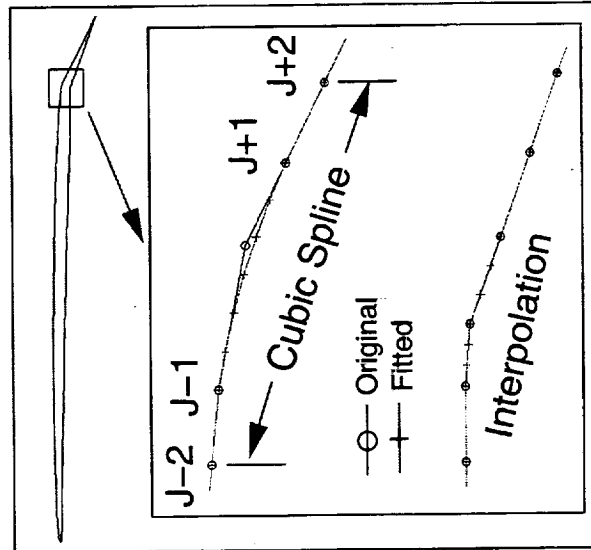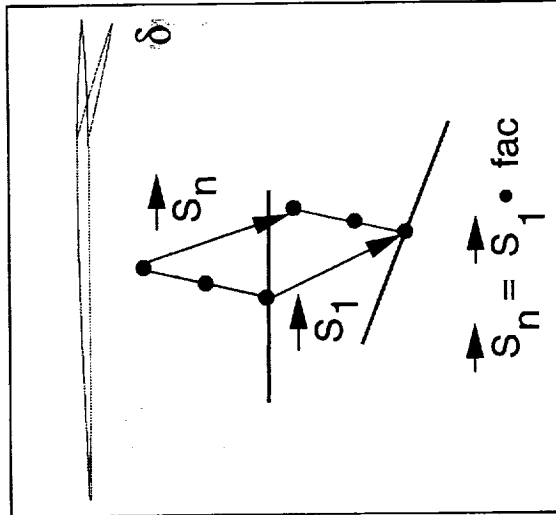
Typical Computational Model

A typical grid consists of a single-zone with approximately 3.3 million grid points for a half-body model. Spanwise gaps across the wing and TE flap surfaces are modeled through 'web grids' where flow interface is imposed. The number of grid points in each direction and subregion are arranged such that 3-level of multigrid option can be specified to improve convergence.

Typical HSCT High–Lift Computational Model

- Single Zone Consists of 3.3 Million Grid Points for the Half–Body (305X65X169) : (Chordwise X Radial X Spanwise)

- C–O Grid Topology (C : Chordwise; O–Spanwise)

- Spanwise Gaps are Modeled through 'Web Grid' for Flow Interface

- Grids are Generated for 3–Level of Multigrid Calculation for Each Sub–Region (Fuselage, Wing, Flap, Gaps etc.)
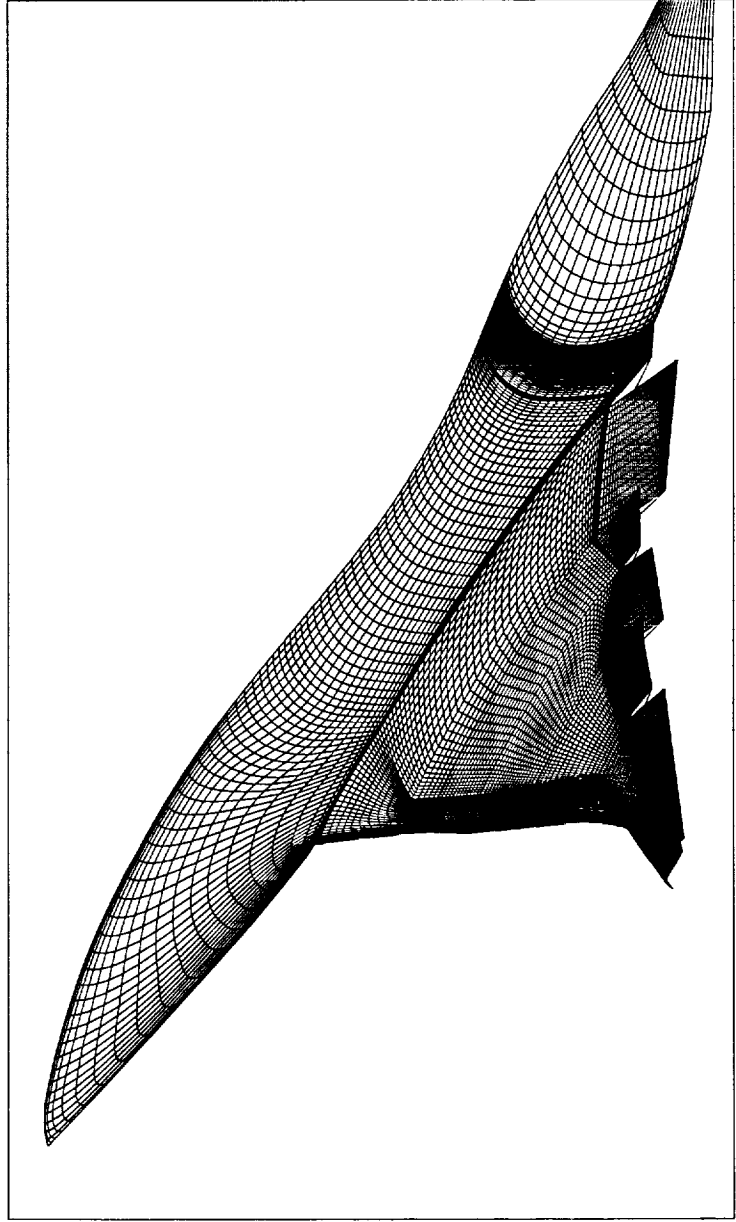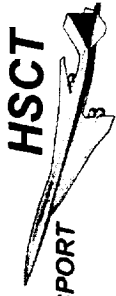
Numerical Solutions

Pre-test and post-test analyses for 3 high-lift configurations are presented. Some of the numerical results have been compared with the existing test data for code validation and evaluation. Additional comparisons will be performed once the test data becomes available.

MCDONNELL DOUGLAS

HSCT

HIGH-SPEED CIVIL TRANSPORT

Numerical Solutions and Code Validation
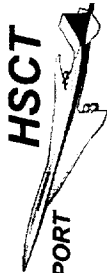
M2.4-7A Opt2A-Effects of TE Flaps-Upper Surface

This chart shows the upper surface pressure of the M2.4-7A Opt2A configuration at M=0.3, alpha=10 for 2 TE flap deflections (10, 20 deg). These solutions were obtained using the CFL3D and the Baldwin-Lomax turbulence model with Degani-Schiff modification.

Similar vortex induced low pressure regions and corresponding locations are observed for both cases at a constant angle-of- attack. A lower pressure near the hinge line is clearly visible at a higher flap deflection angle (δ=20) case. As the percentage of the flap-to-wing chord increases near wing tip, the influence of the TE flap deflection on the upstream increases as indicated by the lower pressure near the outboard LE.

Predicted Surface Pressure for the M2.4–7A Opt2A Configuration at M = 0.3, α = 10 degrees, Re=8 million

CFL3D and Baldwin–Lomax Turbulence Model with Degani–Schiff Modification

(a) $\delta_{flap} = 0^{\circ}/10^{\circ}$

(b) $\delta_{flap} = 0^{\circ}/20^{\circ}$

M2.4-7A Opt2A-Effects of TE Flaps-Lower Surface

Using the same flow solutions shown in the previous chart, this chart shows the lower surface pressure of the M2.4-7A Opt2A configuration at M=0.3, alpha=10 for 2 TE flap deflections (10, 20 deg).

Similar pressure patterns can be seen for both cases except near the hinge lines where a higher pressure is observed for the higher flap deflection case (20 deg). It also shows a stronger flap influence on the lower surface of the wing near the flap regions.

Predicted Surface Pressure for the M2.4–7A Opt2A Configuration at M = 0.3, α = 10 degrees, Re=8 million

CFL3D and Baldwin–Lomax Turbulence Model with Degani–Schiff Modification

Cp

≥0.50

0.00

≤−0.50

(a) $\delta_{flap} = 0^{\circ}/10^{\circ}$

(b) $\delta_{flap} = 0^{\circ}/20^{\circ}$
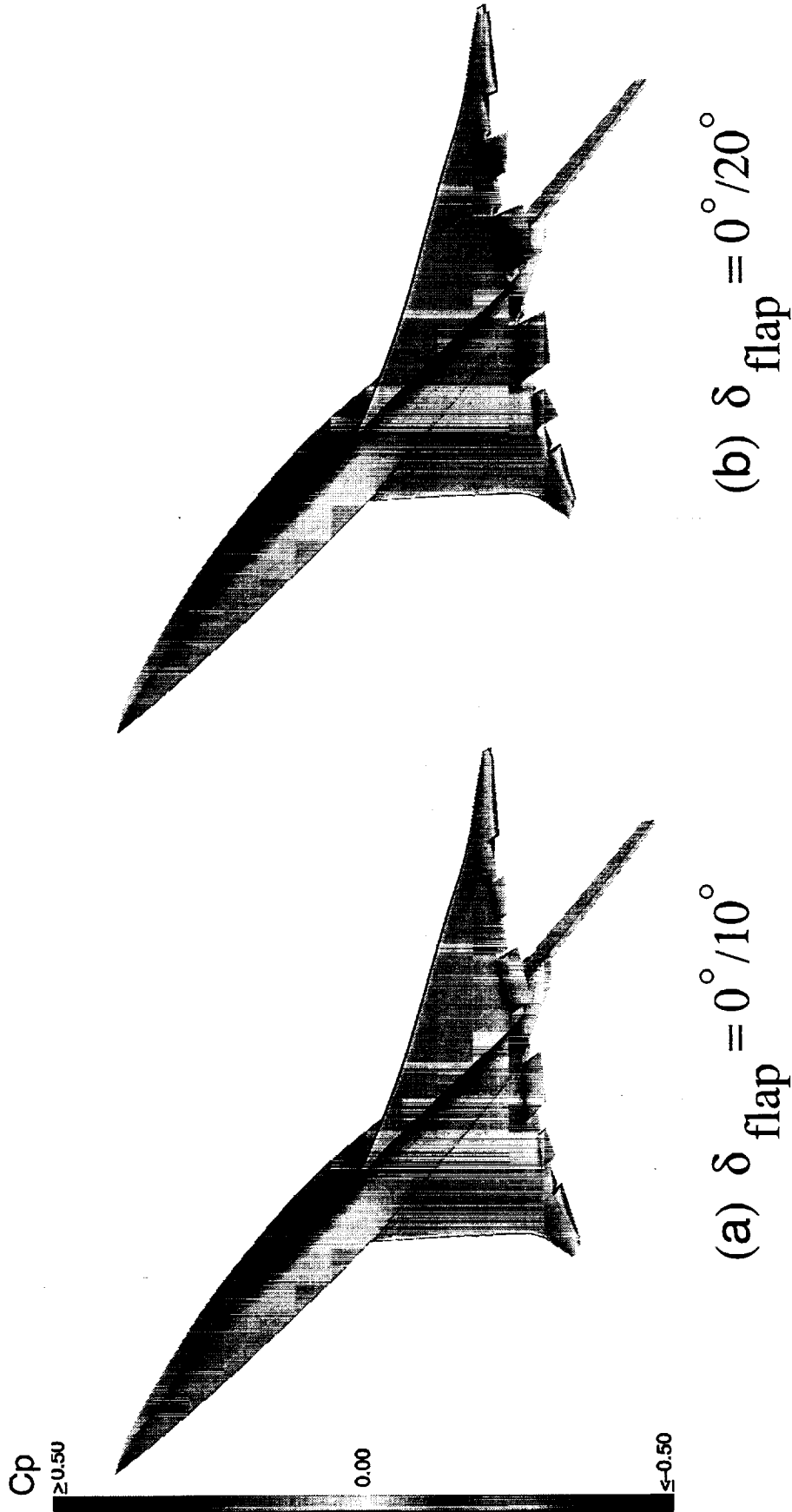
M2.4-7A Opt2A- α-Sweep

This figure shows the upper surface flow pattern for the M2.4-A Opt2A configuration at various angle-of-attack(α). It shows the magnitude and extent of the the LE vortex induced low pressure increase as α increases. The vortex formation is also seen to move forward as α increases.

Surface Pressure for the M2.4–7A Opt2A Configuration
at M = 0.3, δ= 0/20 deg., Re=8 million

α = 10°

α = 14°

α = 0°

α = 4°

Cp

≥0.00
−0.20
−0.40
−0.60
−0.80
−1.00
≤−1.20
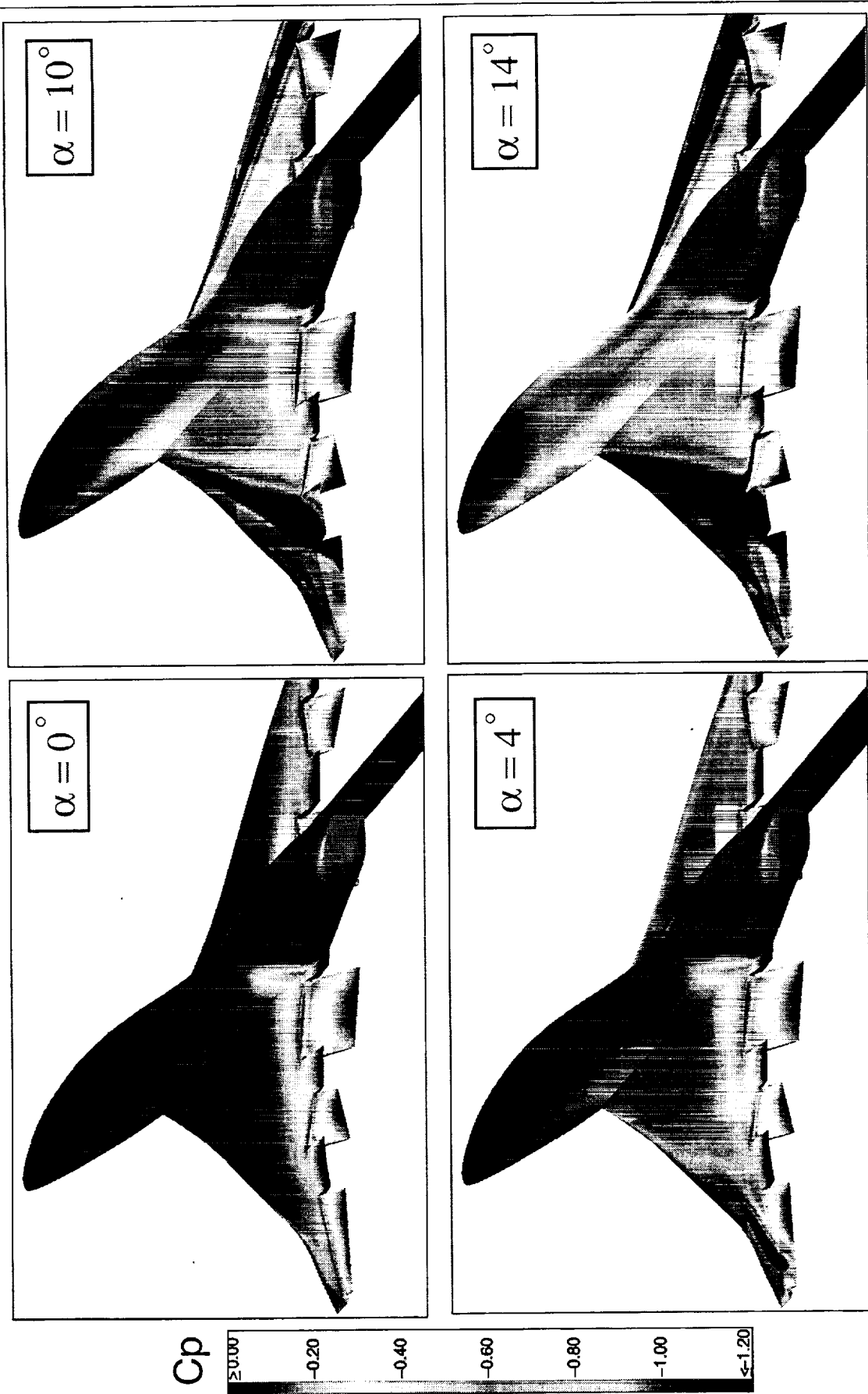
M2.4-7A Opt2A-Force Comparison (δ=10)

The predicted forces for the M2.4-7A Opt2A with TE flap deflection of 10 deg are compared with the test data. The comparison consist of the lift variation as a function of angle-of-attack and the drag polar. The comparison shows a good agreement both in the linear as well as the nonlinear regions.

Comparison of Test Data and CFD Results

LaRC 428 and CFL3D N-S Solution

M2.4-7A Opt2A, δ (TE)=10

Lift Coefficient, C_L

Drag Coefficient, C_D

LaRC 428 Run 134 WB 0/10
CFL3D 0/10 (Baldwin-Lomax)

Lift Coefficient, C_L

Angle of Attack, α (deg)

LaRC 428 Run 134 WB 0/10
CFL3D 0/10 (Baldwin-Lomax)
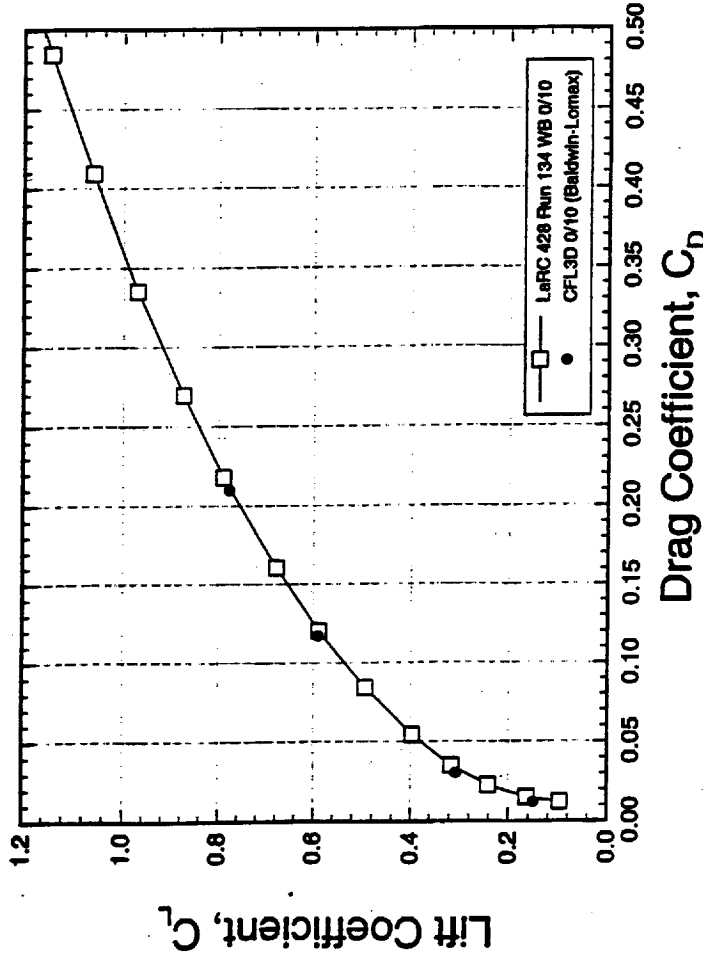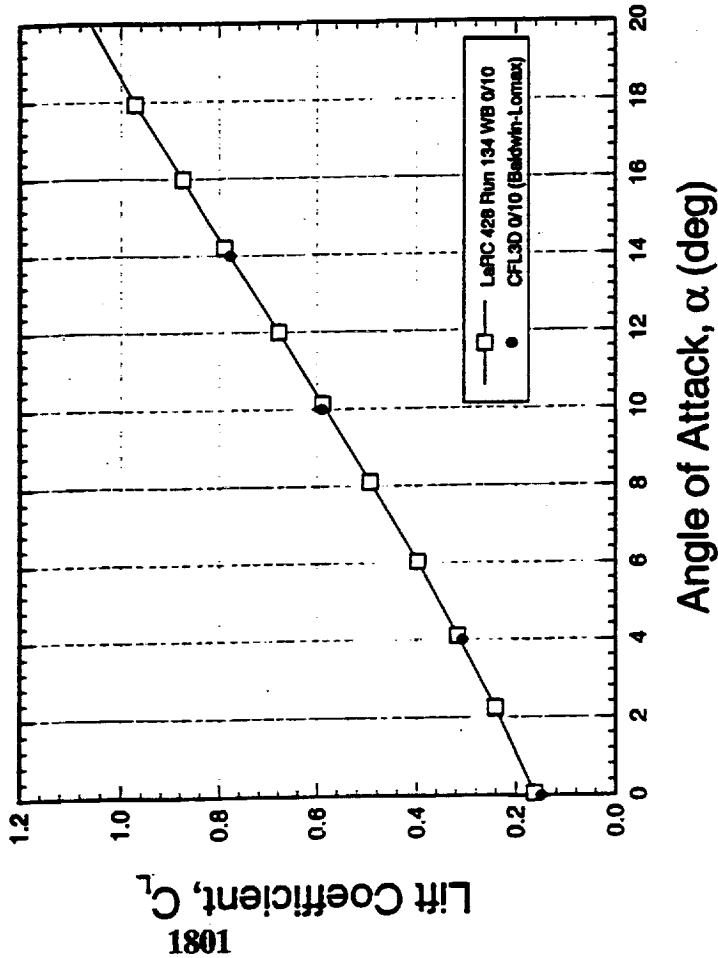
M2.4-7A Opt2A-Force Comparison (δ=20)

A similar comparison is also made for the M2.4-7A Opt2A with TE flap deflection of 20 deg. A favorable agreement is also obtained at the higher TE flap deflection.

MCDONNELL DOUGLAS

Comparison of Test Data and CFD Results

LaRC 428 and CFL3D N-S Solution

M2.4-7A Opt2A, δ (TE)=20
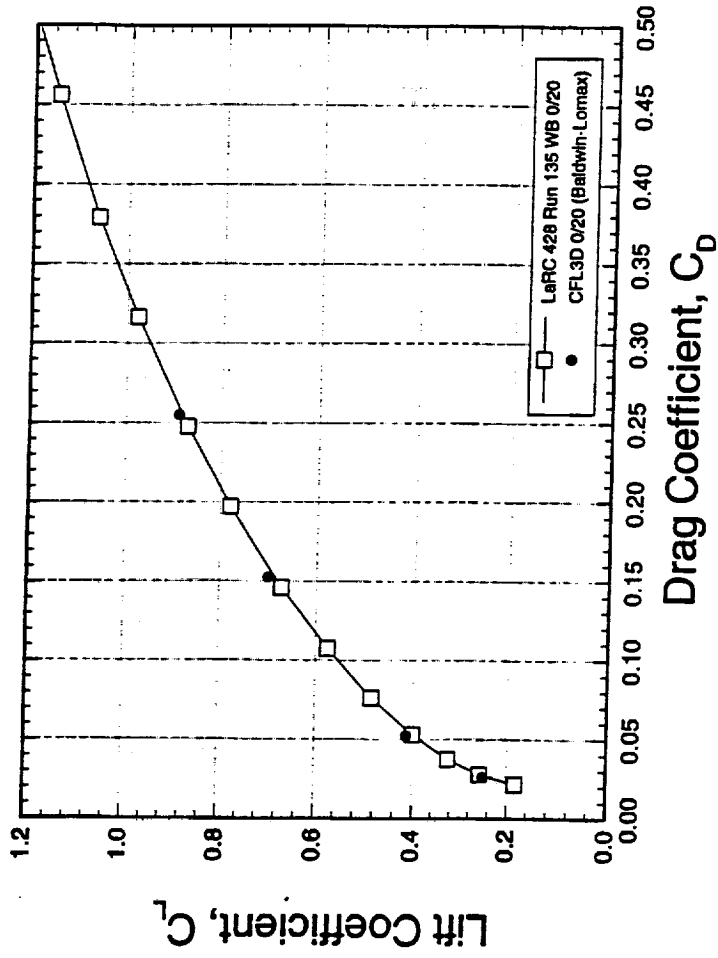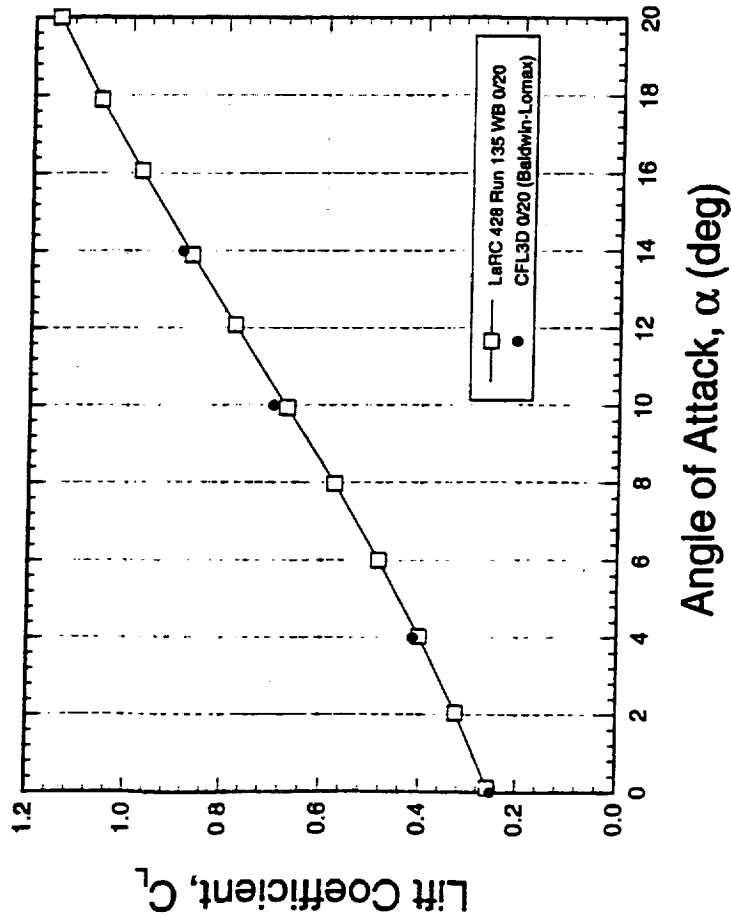
M2.4-7A Opt2A-Convergence

This chart shows a typical convergence history for the lift, drag, pitching moment and the residual of the physical equations. The solutions clearly show the convergence after 1200 iterations with the overall residual being monotonically decreasing to more than 3 orders of magnitude.

The CPU requirement for a converged solution is about 15 Cray C-90 hours using the Baldwin-Lomax turbulence model while 19 Cray C-90 hours are required using the Spalart-Almaras turbulence model. The memory requirements are 145 MW and 153 MW for using Baldwin-Lomax and Spalart-Almaras turbulence models respectively.

Typical Convergence and Computational Resources Requirements

Variable Time Steps and 3 Multigrid Levels

● Convergence
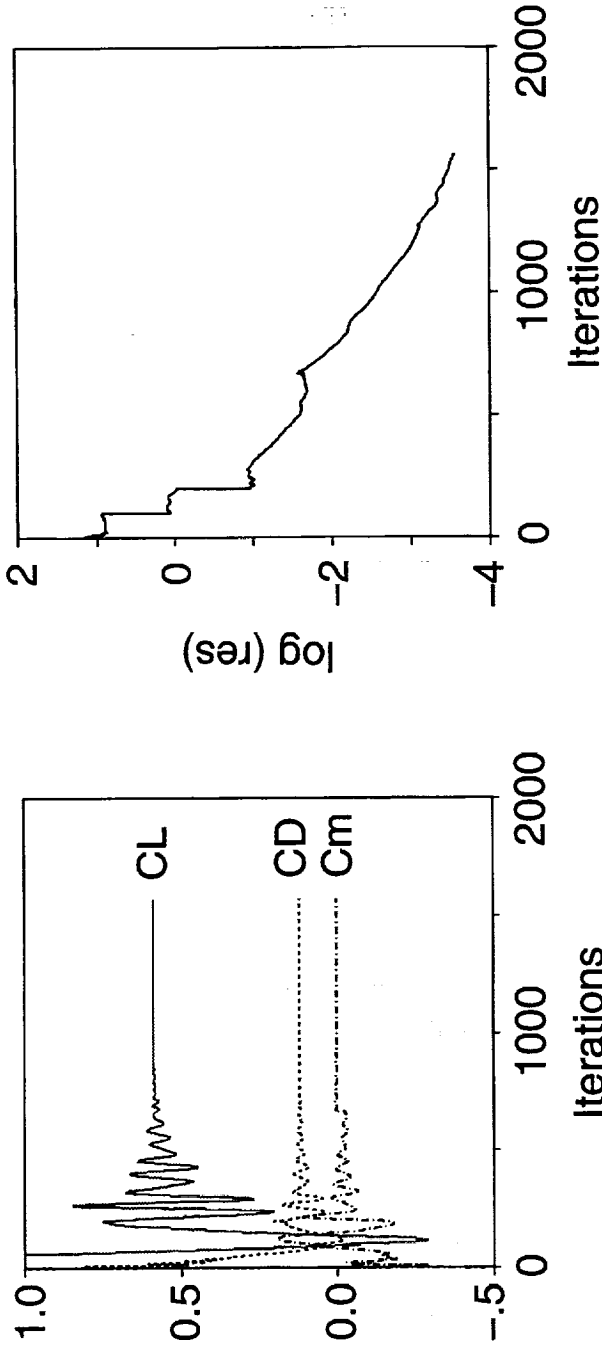
● Resources Requirements

Turbulence Models	CPU/iteration Seconds	Memory Required MW (Megawords)
BL/DS	43.9	145
SA	51.0	153
SA/Trans	51.0	153

BL/DS = Baldwin–Lomax (0–Eq) turbulence model with the Degani–Schiff modification

SA = Spalart–Allmaras (1–Eq) turbulence model

SA/Trans = Spalart–Allmaras model with the transition at the 10% local chord from the LE

1805
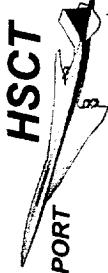
M2.4-7A Mod3-Introduction

The Second configuration in the study is a modified Arrow Wing (M2.4-7A Mod3) with a larger inboard LE radius. Creating a more rounded LE is intended to promote attached flow to maximize L/D at the high-lift conditions. This configuration is currently being tested in the 12-ft tunnel at NASA ARC.

The numerical solutions have been generated which are primarily used for flow visualization prior to the test. The current simulation objective is focused on the effects of LE flap deflections on the vortex flow characteristics. In addition, the numerical capability to model LE blowing on a deflected LE flap surface is also demonstrated in the study to further enhance the high-lift performance.

Predicted Surface Pressure for the M–2.4–7A Mod–3 Configuration
M=0.3, α=10°, δ (LE/TE)=40°/10°

1807

M2.4-7A Mod3-LE Flap - Flow Pattern

The effects of the LE flap deflections are illustrated for the M2.4-7A Mod3 with flap deflections (LE/TE) of 40/10 and 30/10 deg. The upper surface flow patterns for the 40/10 and 30/10 cases are shown in this figure. The low pressure region induced by the LE vortex is shown to be further outboard for the 30/10 case. The primary separation line (converging) near the leading-edge is seen for both cases. For the 40/10 case, the flow reattachment line (diverging) and separation line near the hinge line are observed throughout the LE flap. On the other hand, the reattachment line for the 30/10 case, disappears at approximately 40% of the root chord downstream.

Effects of LE Flap Deflection on the Upper Surface Flow Pattern for the M2.4–7A Configuration

M=0.3, α=10, Re=8 Million

δ (LE/TE) = 30 / 10

Surface Pressure

Limiting Streamlines

δ (LE/TE) = 40 / 10

Surface Pressure

Limiting Streamlines
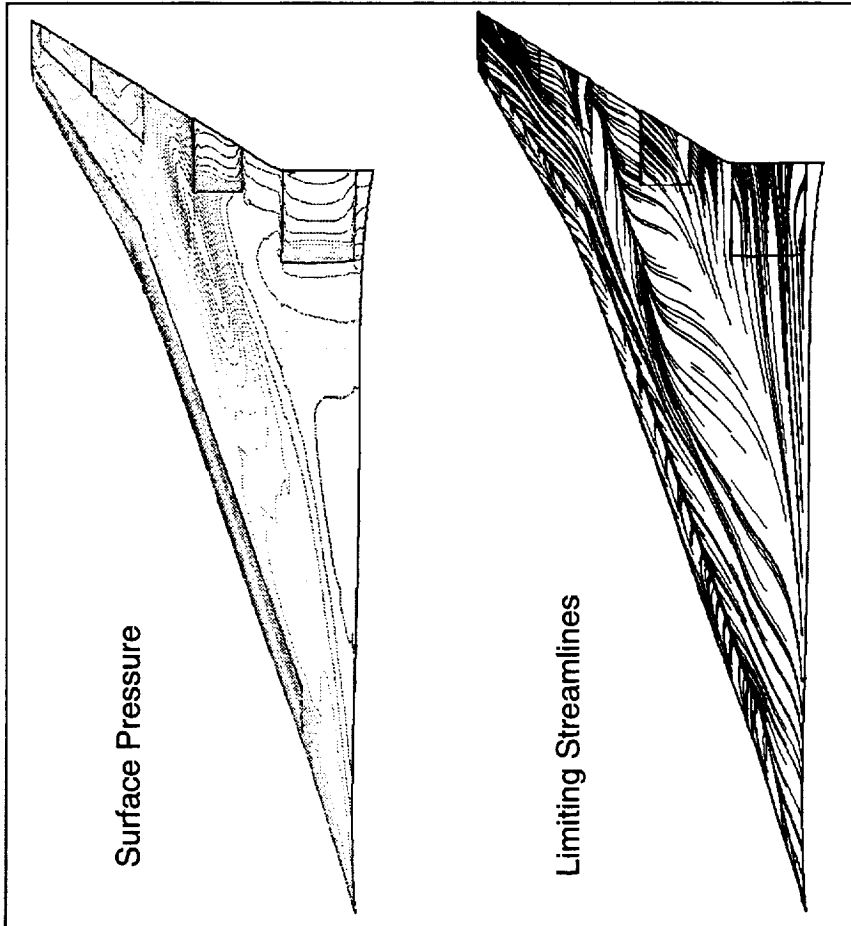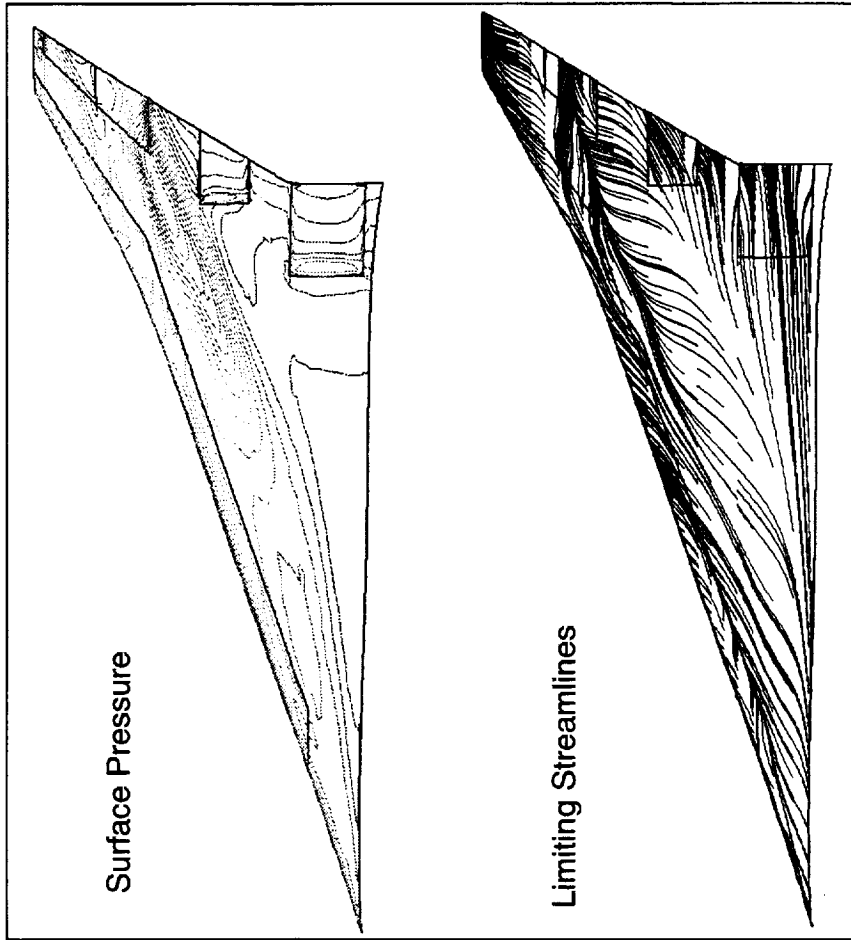
M2.4-7A Mod3-LE Flap - Total Pressure

This figure shows the normalized total pressure contours for the 40/10 and 30/10 cases. The extend of the boundary layer and shear layers are clearly visible in the figure as indicated by the total pressure loss in the field. A thicker mixing layer in the flap region for the 30/10 case indicates that the flap may be underdeflected. On the other hand, the flap is seen to be more aligned with the local flow at 40-deg flap deflection.

Effects of Leading–Edge Flap Deflection on the Cross–Flow Total Pressure
for the M2.4–7A Mod3 Configuration

M=0.3, α=10 deg, X=FS 2227.78

δ(LE/TE)= 30 /10

δ(LE/TE)= 40 /10

1811
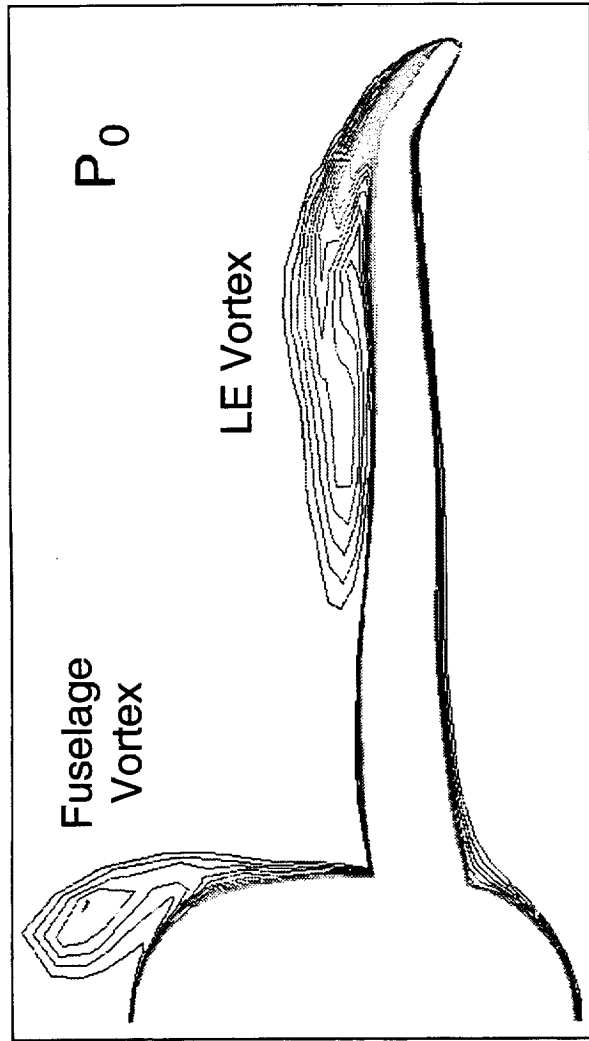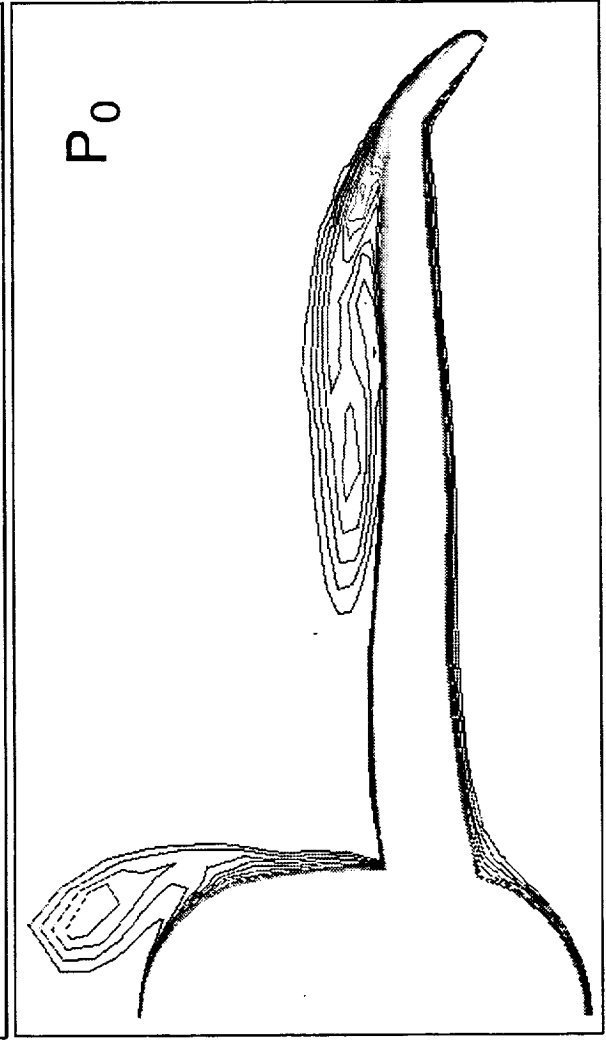
M2.4-7A Mod3-LE Flap - Pressure

The effects of the LE flap deflections are further illustrated through spanwise surface pressure. In both cases, flow acceleration around the LE is visible through the suck peaks at the LE. On the other hand, a stronger suction peak associated with the LE vortex is shown for the 30/10 case and its location is further outboard.

Effects of LE Flap Deflection on the Spanwise Pressure

M2.4-7A Mod3 Configuration

M=0.3, AOA=10, Re=8 million

FS 2445.80

Legend:
- 40-10
- 30-10
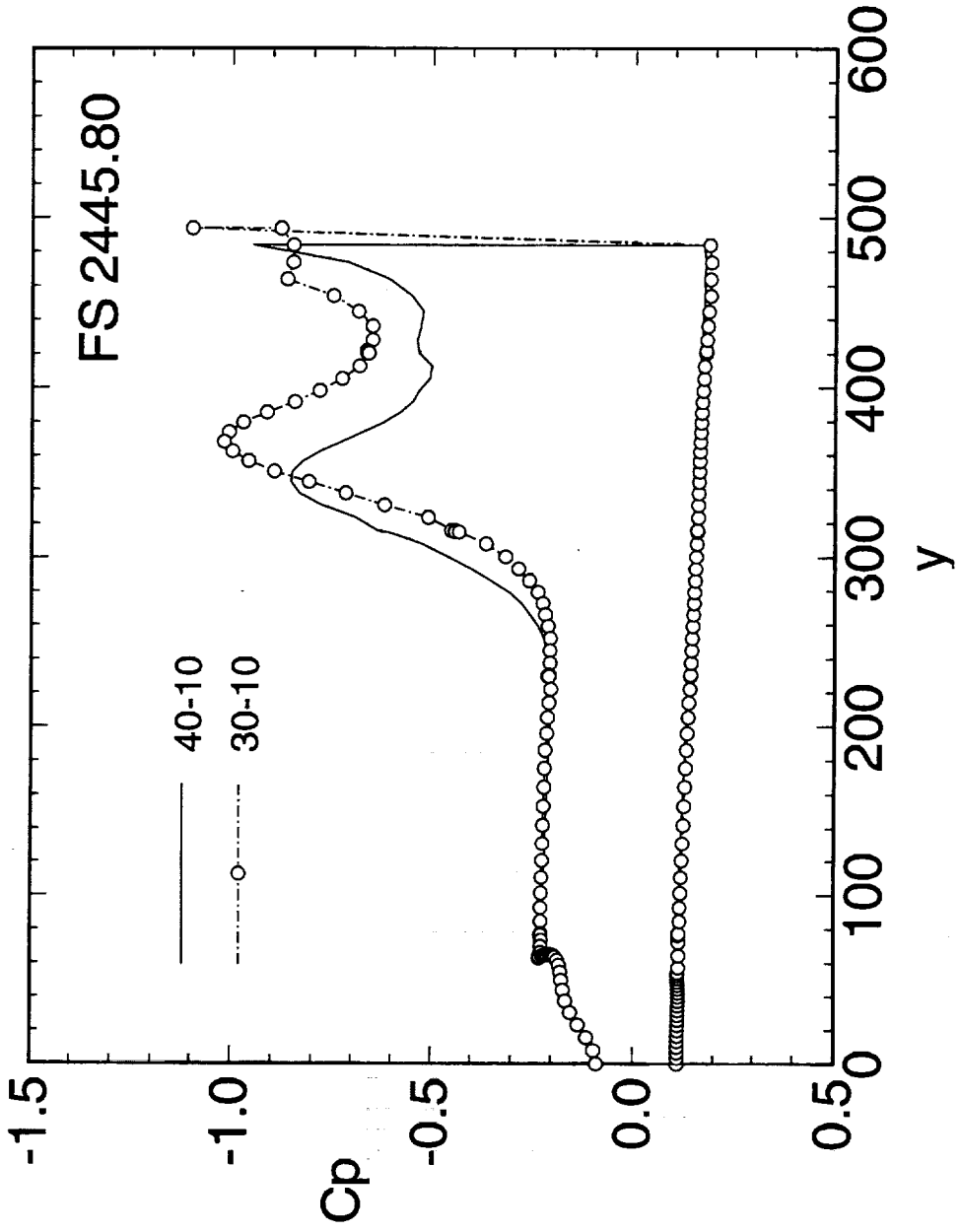
M2.4-7A Mod3-LE Blowing - Geometry

In an effort to further enhance the high-lift performance, a leading-edge slot blowing mechanism has been implemented into the CFD study. A preliminary study was performed with an arbitrary chosen slot height and its extend for demonstration. This figure shows the slot geometric location at the flap deflections of (LE/TE) 40/10 degrees. The pressure ratio (Pt/Ps_infinity) at the slot exit plane was specified to be 1.4 and the kinematic variables were computed through the method of characteristics.

Leading–Edge Blowing Slot Modeling for High–Lift Performance Study

M2.4–7A Mod3 Configuration with $\delta(LE/TE)=40/10$

Slot extent

A

A

A

A
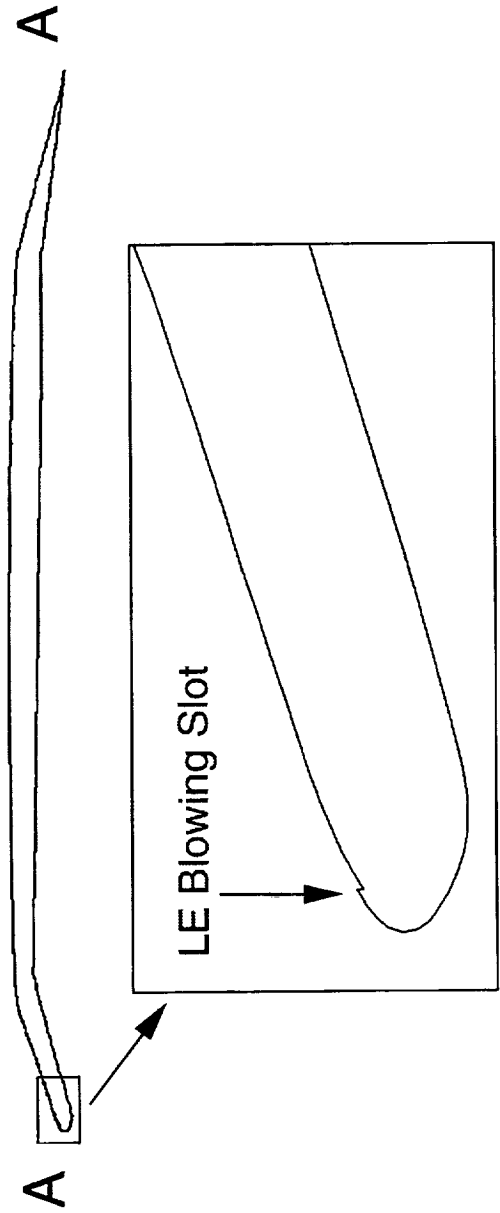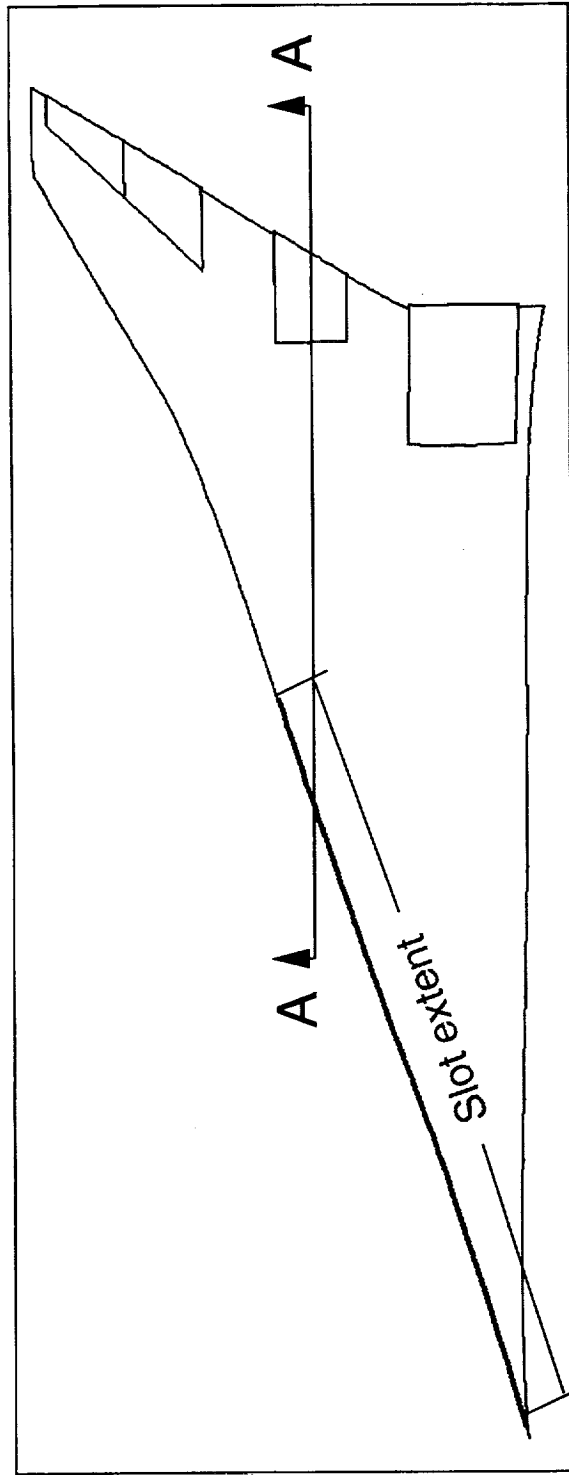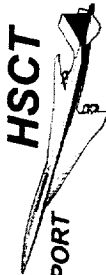
LE Blowing Slot

M2.4-7A Mod3-LE Blowing - Solutions

This figure shows the upper surface flow pattern with and without blowing. The use of blowing shows a significant influence on the LE vortex by energizing the boundary layer and thus delays the flow separation. As a result, the total lift decreases due to the lower vortex induced nonlinear lift while the lift-to-drag ratio increases.

Effects of LE Blowing on the Upper Surface Flow Pattern for the M2.4–7A Mod3 Configuration

M=0.3, α=10, Re=8 Million, δ(LE/TE)=40 / 10

Cμ = 0

Cμ = 0.0012

Surface Pressure

Surface Pressure

Limiting Streamlines

Limiting Streamlines

Leading-Edge Blowing Slot
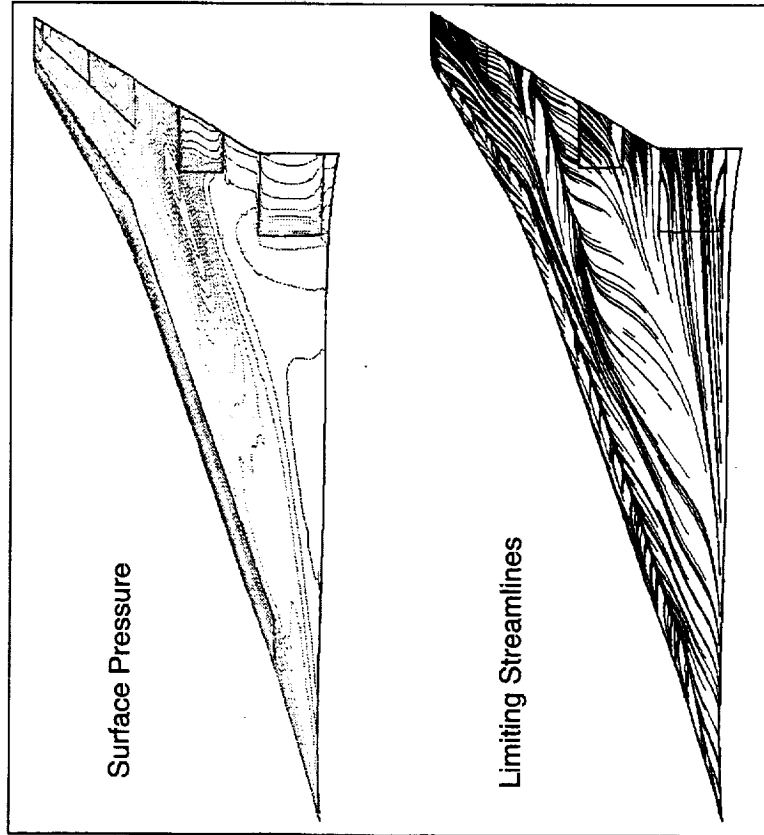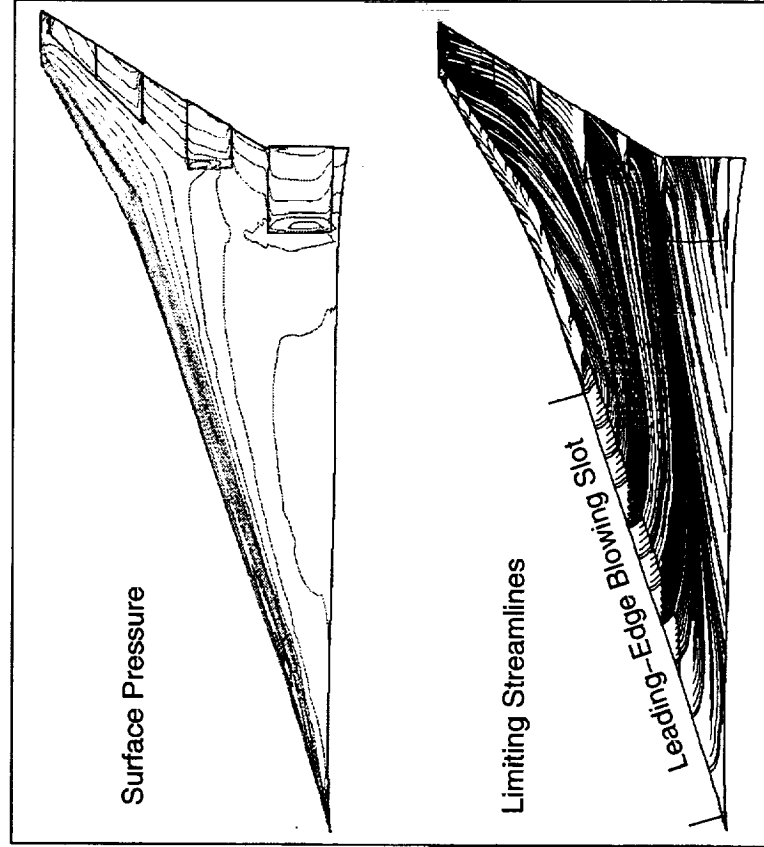
Clean TCA Configuration - α-Sweep

The technology concept airplane (TCA) model is the current baseline configuration which is the primary focus of the numerical studies. The numerical simulations start with the clean configuration at various angle-of-attack using CFL3D code and Baldwin-Lomax turbulence model with Degani-Schiff modification. This figure shows the plan view of the free particle traces released along the LE. The LE vortex starts from the outboard region at a lower angle-of-attack(α), and progressively moves forward as alpha increases.

Predicted Partical Traces for the Baseline TCA Configuration

CFL3D with Baldwin-Lomax Turbulence Model with D-S Modification

M=0.3, Re=8 Million

$\alpha = 4^{\circ}$

$\alpha = 8^{\circ}$

$\alpha = 10^{\circ}$

$\alpha = 14^{\circ}$
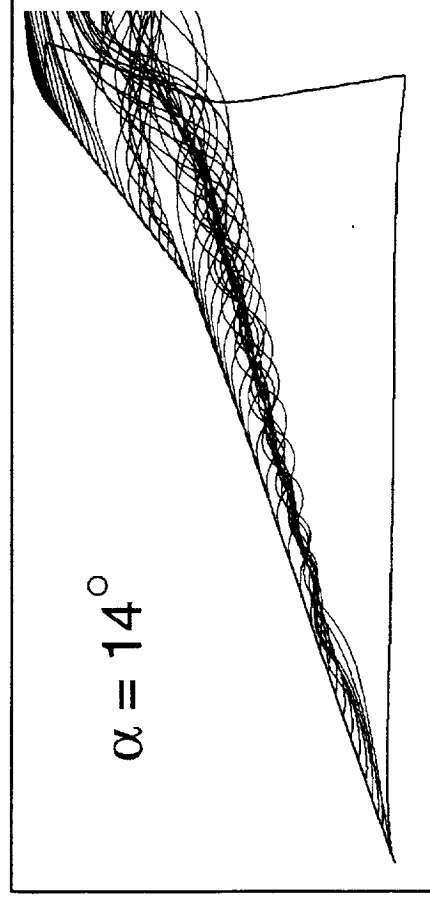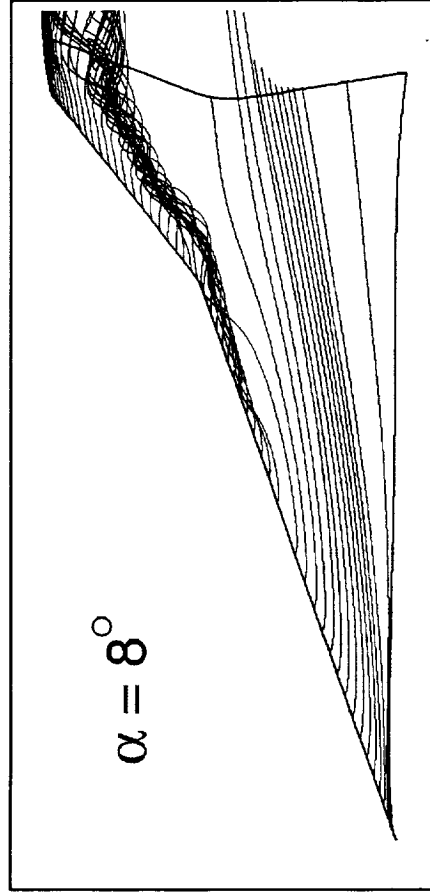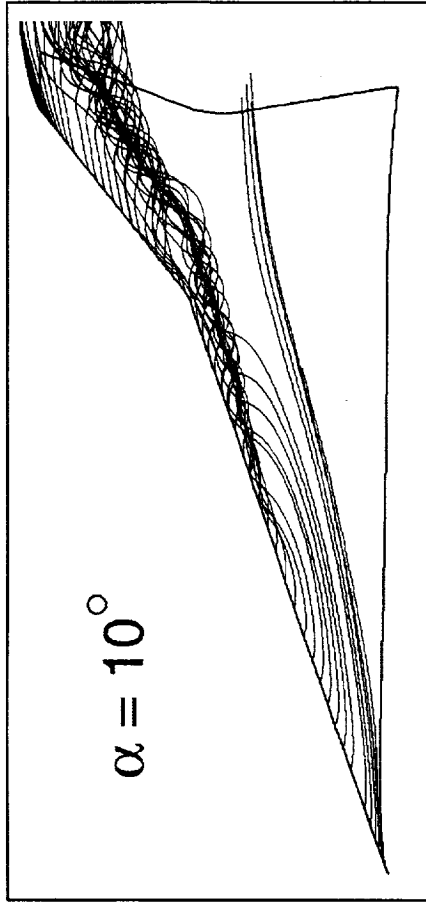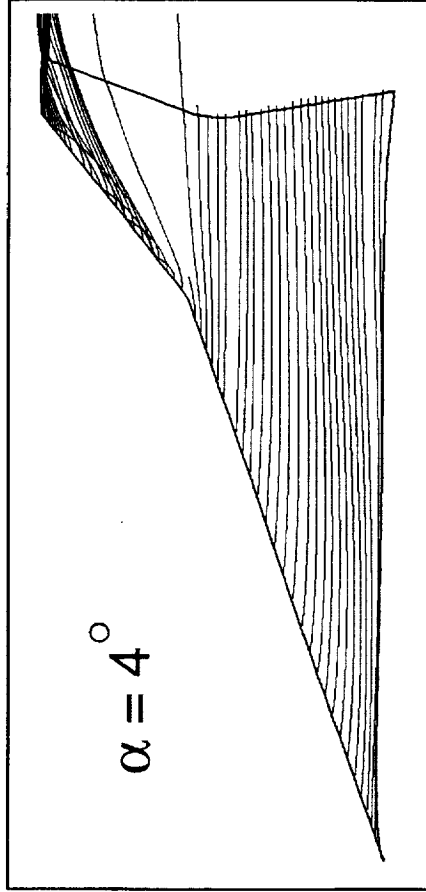
Clean TCA Configuration - Turbulence Model

The effects of turbulence models on the flow solutions have been studied. The test cases were conducted under the free stream conditions of M=0.3, Re=8 Million at 10-degree angle-of-attack.

This figures shows the plan view of the LE particle traces obtained from the CFL3D code using 3 different turbulence modelings. A strong vortex interaction between the inboard and outboard wing panels is observed when the Baldwin-Lomax turbulence model with Degani-Schiff modification was utilized. On the other hand, a weak interaction were revealed using the Spalart-Almaras turbulence model. Based on a preliminary low-speed test measurement obtained from the 16-ft tunnel at NASA LaRC, as shown in the next figure , the solution obtained using the Spalart-Almaras turbulence model gives a better agreement with the test data in terms of lift force.

The Degani-Schiff modification within the CFL3D code is provided to restrict the search of the first extremum (90% criterion) of the F function (F~length*vorticity) and exclude the global maximum which may lie inside of the vortical field. However, the cutoff distance sometimes can be difficult to define if the shear layer is located close to the boundary layer. Therefore, modifications have been made to the Baldwin-Lomax turbulence model routine to further limit the searching within a specified grid location near the LE region. The numerical solution obtained from the modified Baldwin-Lomax shows a similar result as that of using the Spalart-Almaras turbulence model in terms of the vortex flow characteristics as shown in the figure.

Effects of Turbulence Modelings on the Vortex Flow Characteristics
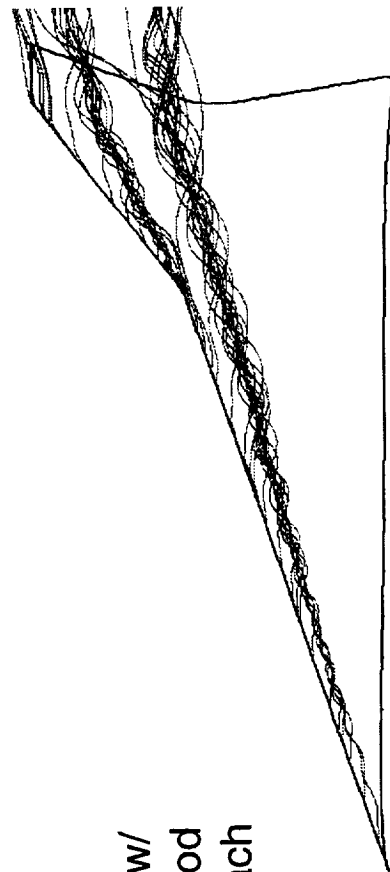
Clean TCA Configuration, M=0.3, a=10, Re=8 million
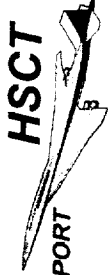

- Baldwin–Lomax w/ Degani–Schiff Mod
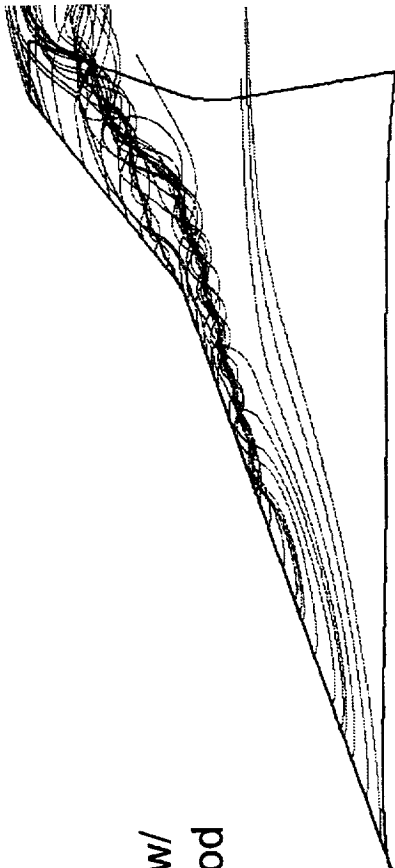
- Spalart–Almaras
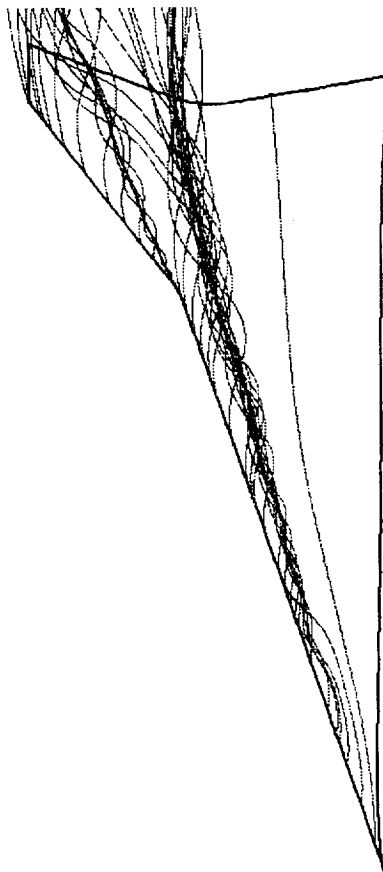
- Baldwin–Lomax w/ Degani–Schiff Mod & Restricted Seach

Clean TCA Configuration - Force Comparison

This figure shows the comparison of the lift as a function of angle-of-attack between the CFL3D solutions and the test results. The solutions obtained using the Spalart-Almaras and the modified Baldwin-Lomax turbulence models show a better agreement at alpha=10.

TCA Clean W/B Configuration
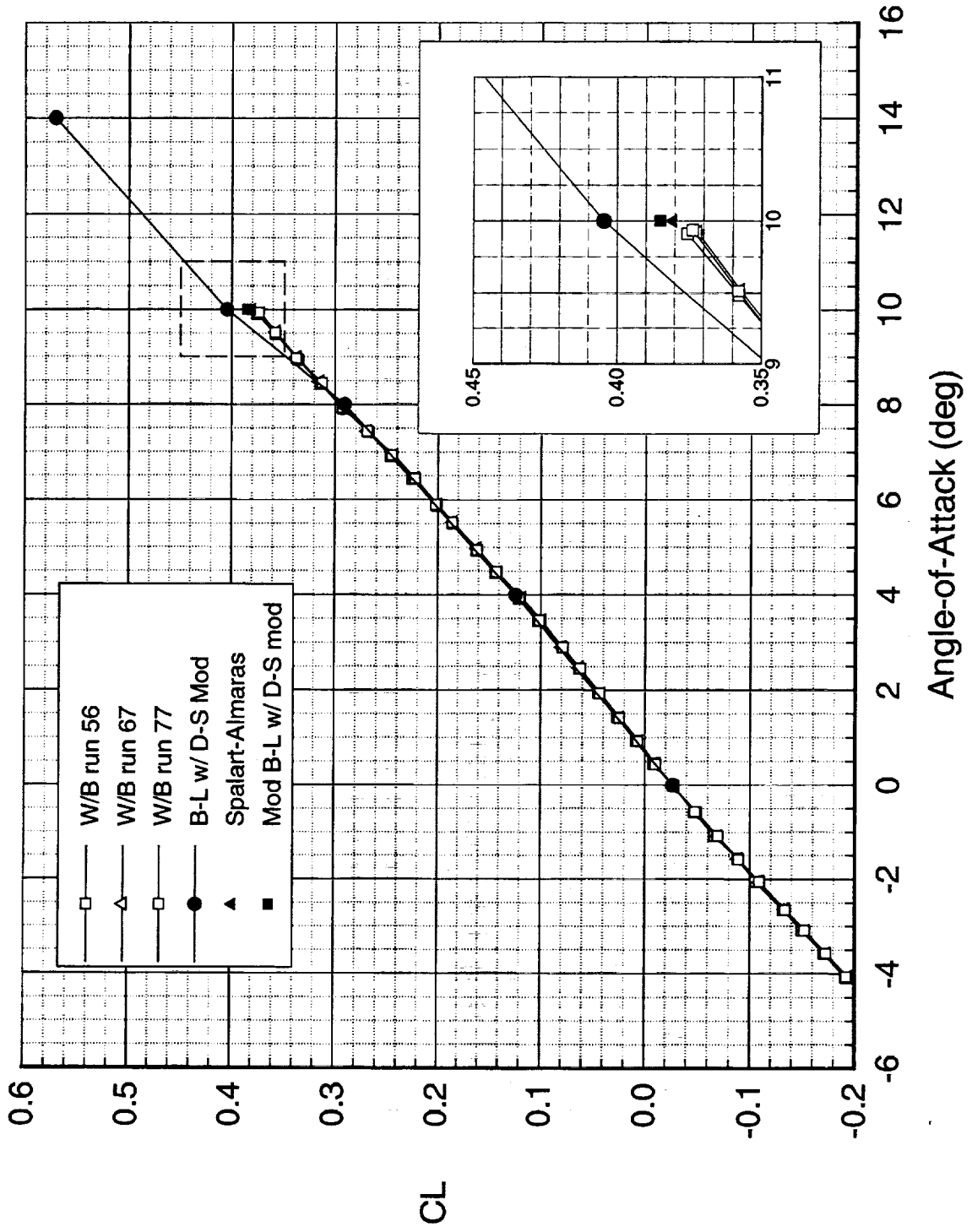
TCA LE Effects

The effects of LE flap deflection on the flow field for the TCA configuration is studied. This figure shows the upper flow pattern for the 0/0 (no flaps) and 30/0 cases. A predominately vortical flow phenomenon is observed in the 0/0 case, while the flow is seen to reattach on the deflected flap surfaces. As a result, only a weak vortex is formed near the wing and the inboard triangular flap element. For the 30/0 case, it is also interesting to note the formation of the flap vortex along the LE of the outboard flaps where the free particle traces are 'trapped' along the LE.

Effects of LE Flap Deflection on the Flow Field for the TCA Configuration

M=0.3, α=10°, Re=8 Million

δ (LE/TE) = 0/0 deg

δ (LE/TE) = 30/0 deg

Pressure

LE particle traces

Limiting streamlines

1825
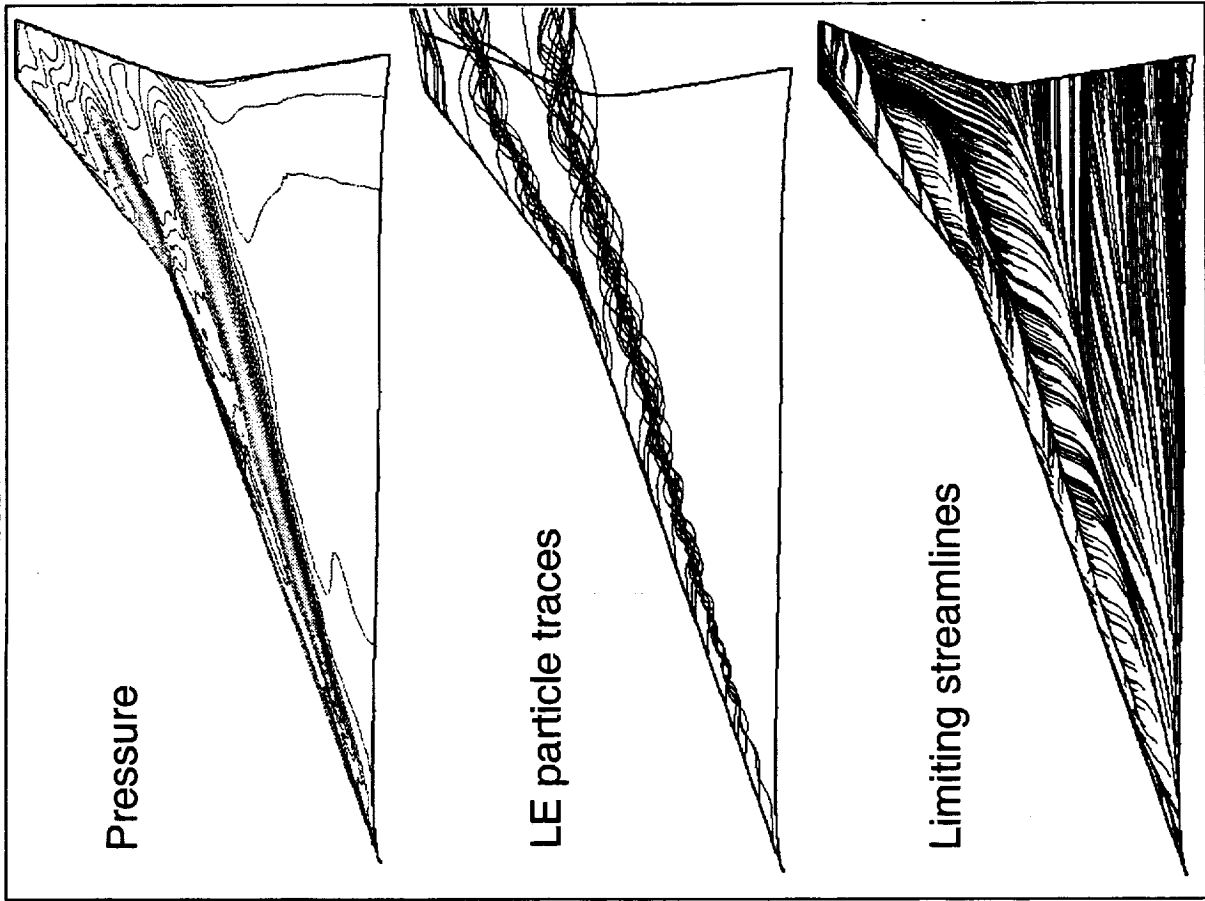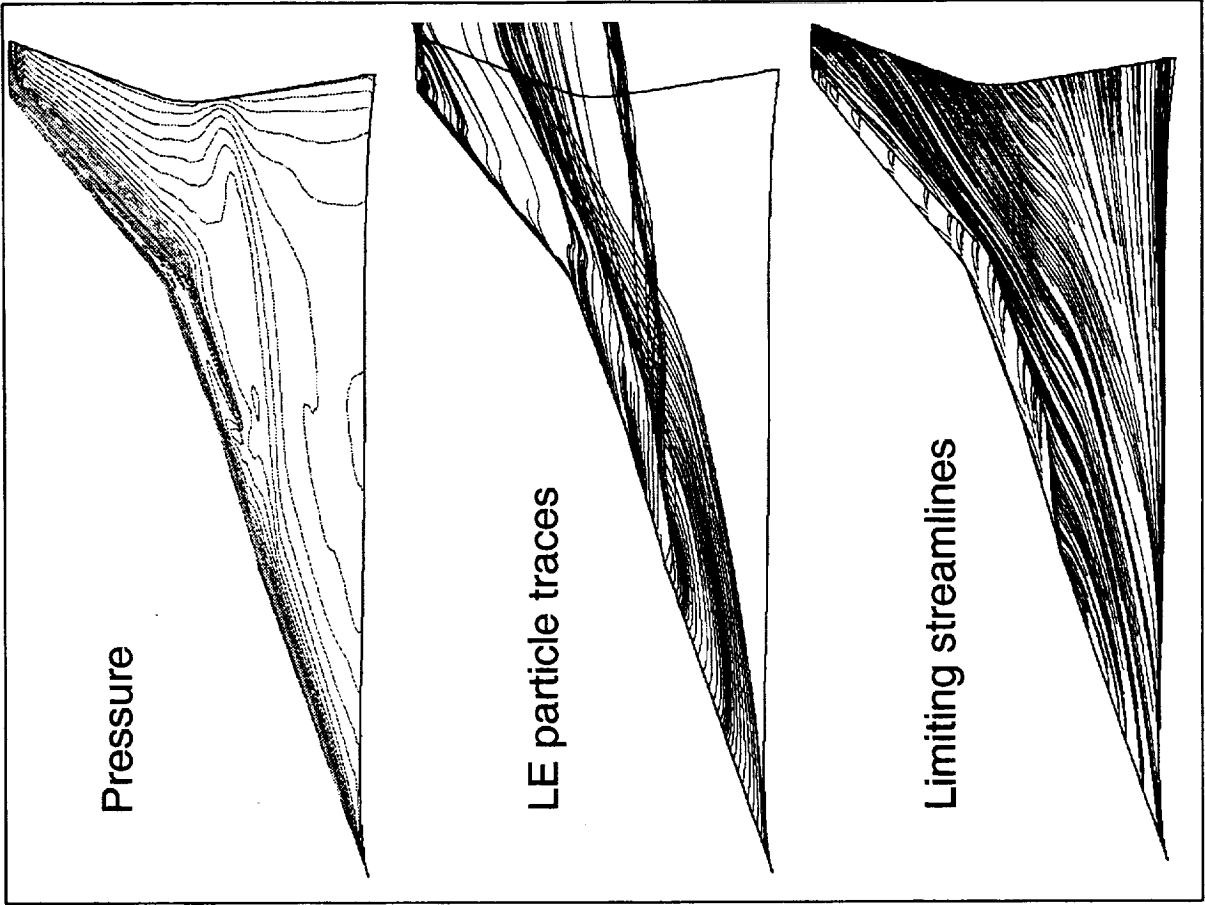
TCA Flap Vortex

This figure shows the predicted surface pressure and the free particle traces released near the LE for the TCA 30/0 configuration. The formation of the inboard vortex (just inboard of the LE flap), the outboard flap vortex and the tip vortex are clearly visible. The low pressure regions along the LE as well as near the outboard upper hinge line are also seen in the figure.

TCA W/B Configuration with δ(LE/TE)=30/0 at AoA=10
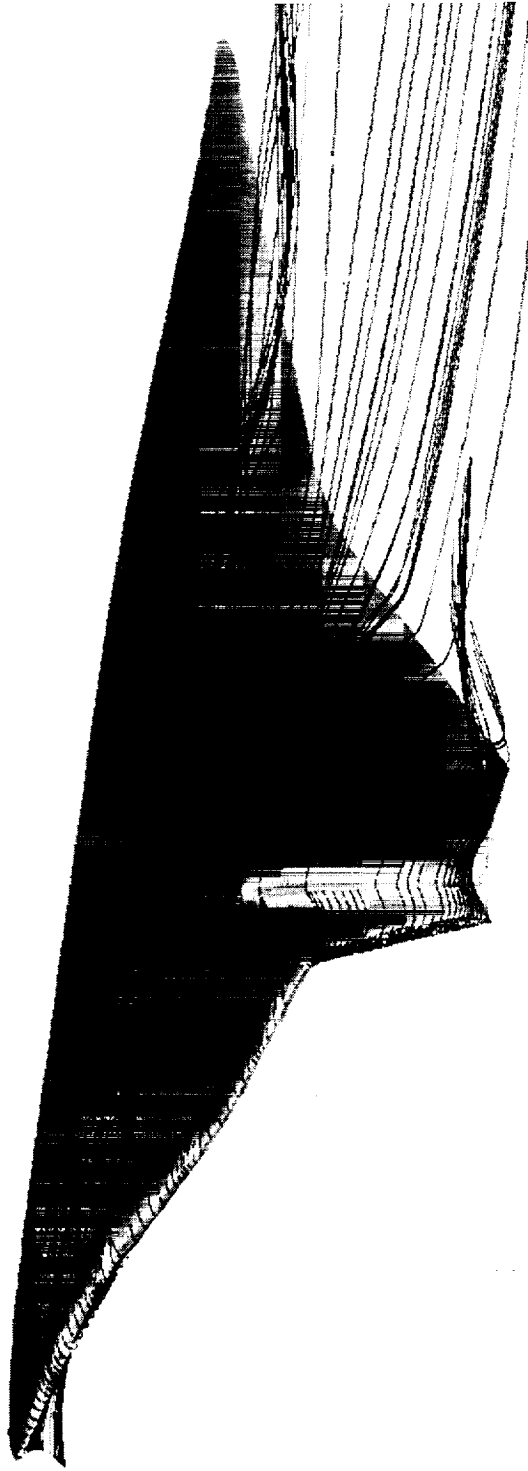
Pressure Coefficient

-2.7   -2.1   -1.5   -0.9   -0.3   0.3

TCA 30/10 Solution

The numerical solution for the TCA 30/10 configuration has been obtained. The upper surface flow pattern is illustrated in this figure. Similar flow patterns are observed between the 30/0 and 30/10 configurations, except a predominate spanwise flow is shown on the deflected outboard TE flap surfaces. The 3-D edge effect is also visible on the inboard and middle TE flap surfaces.
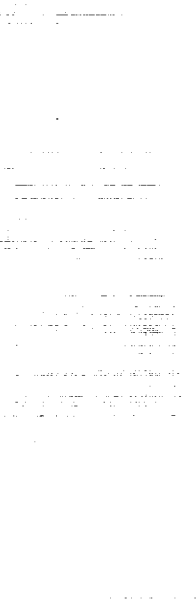
Upper Surface Flow Pattern for the TCA 30/10 Configuration
M=0.3, α=10, Re=8 million

Pressure
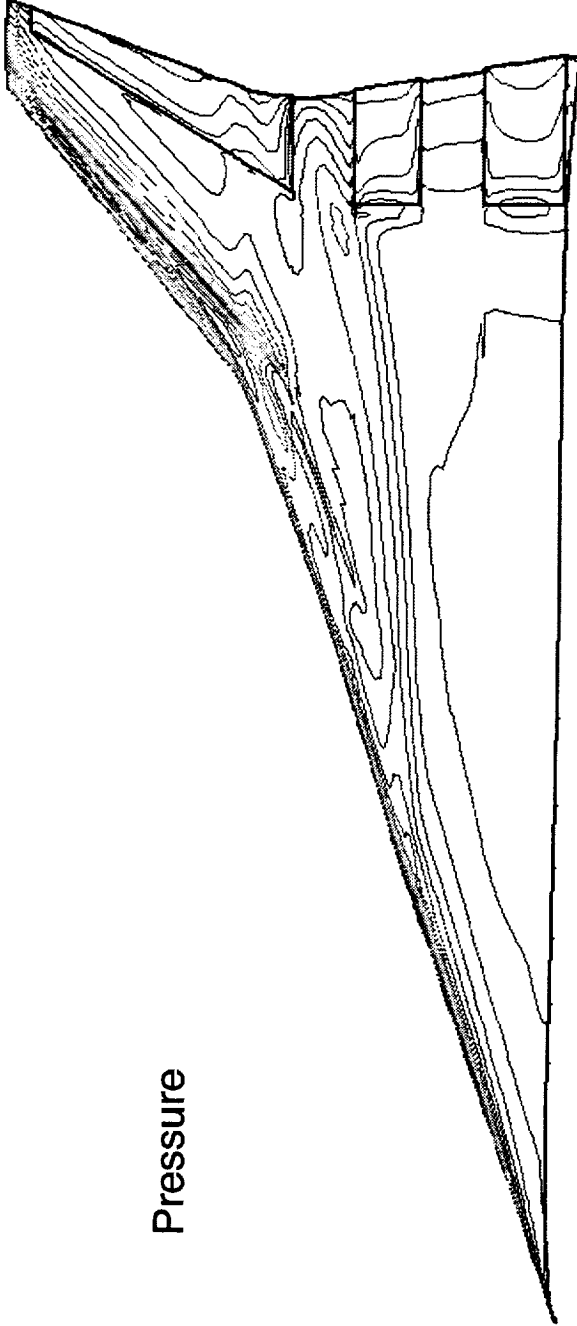
Limiting streamlines
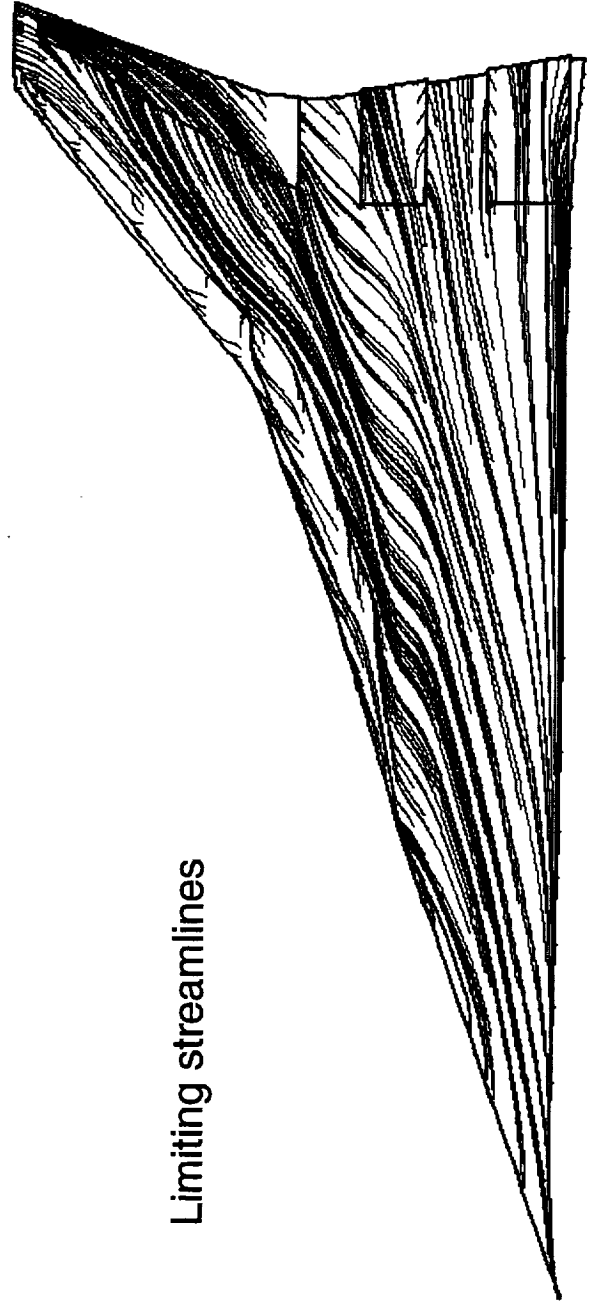
TCA 30/10 Surface Pressure

This figure shows the upper surface pressure contours for the TCA 30/10 configuration. The low pressure regions near the LE and TE hinge lines are clearly visible as a result of flow acceleration around the curved surfaces. The effects of the TE spanwise gaps are also seen from the flap pressure contours.

Predicted Surface Pressure for the TCA Configuration (Part Span)

$\delta(LE/TE)=30^\circ/10^\circ$, M=0.3, $\alpha=10^\circ$, Re=8 million
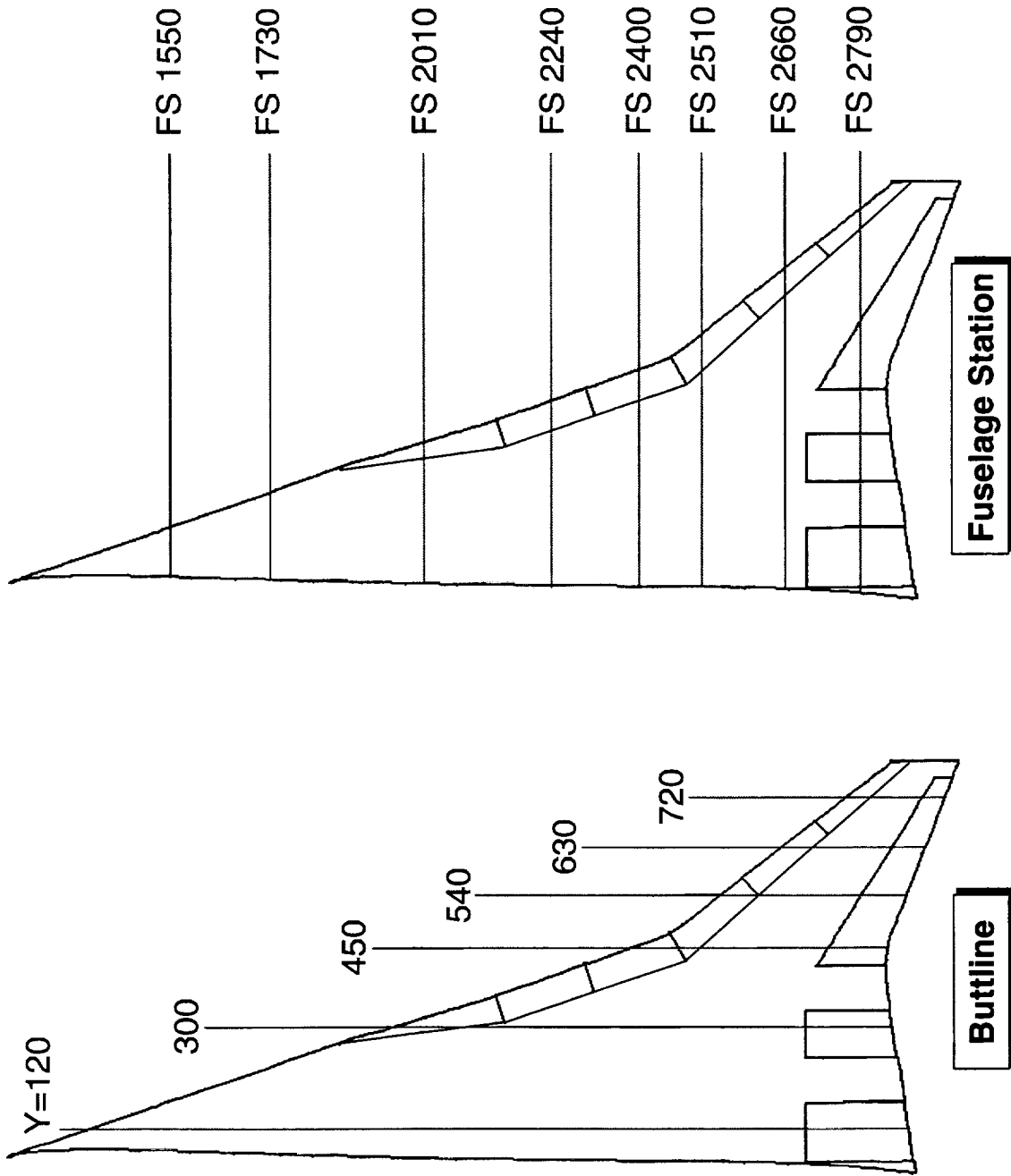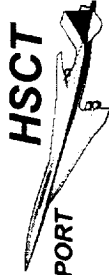
Cp

0.50

−0.35

−1.20
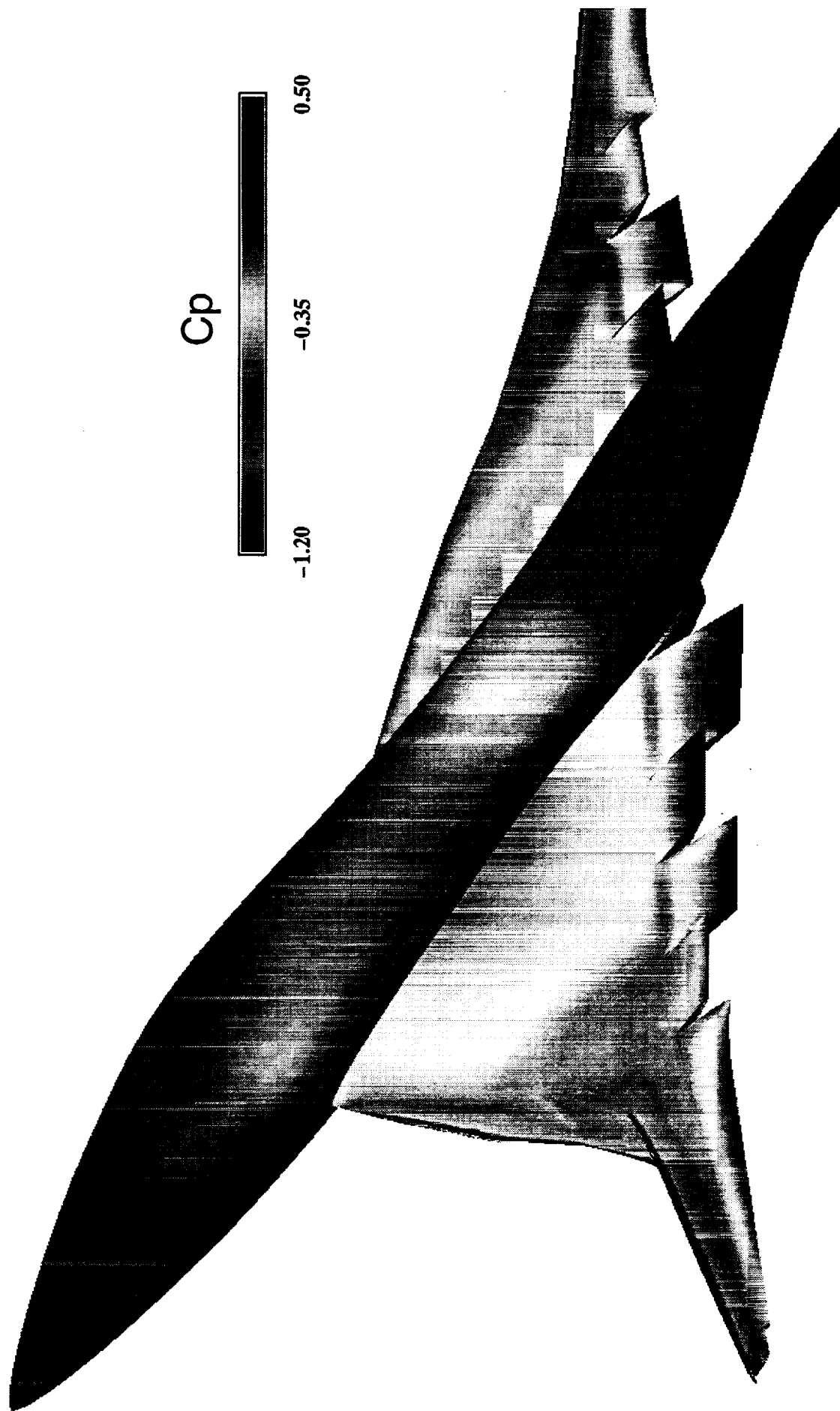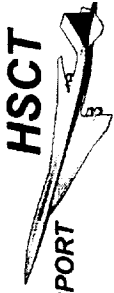
TCA Pressure Tap Locations

The solution for the TCA 30/10 configuration at AoA=10 has been postprocessed to get the spanwise and chordwise pressure distributions. The pressure locations were chosen at the pressure tap locations corresponding to the 5% TCA model as shown in figure.

Pressure Tap Locations for the TCA Configuration

FS 1550
FS 1730
FS 2010
FS 2240
FS 2400
FS 2510
FS 2660
FS 2790

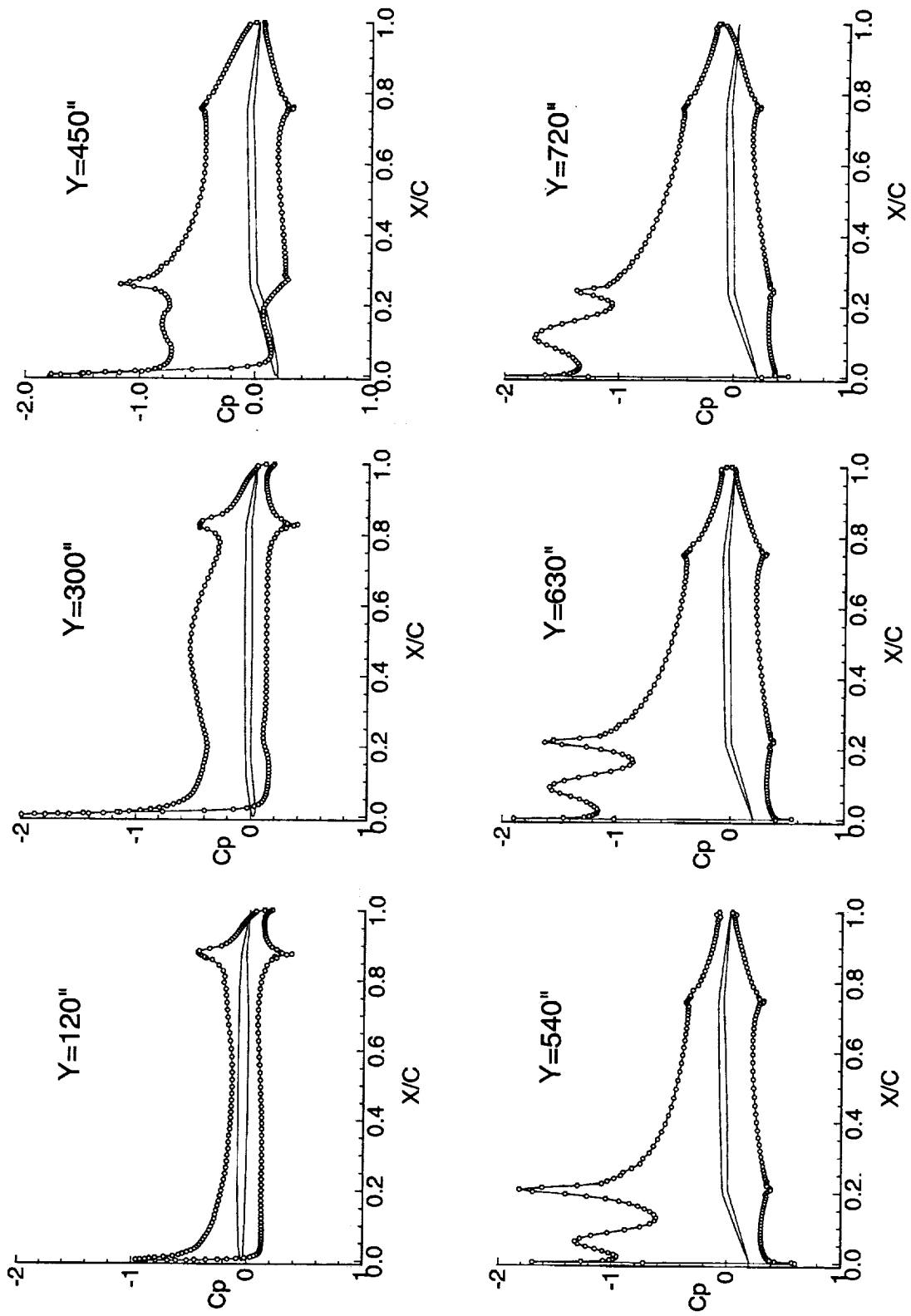Fuselage Station

Y=120
300
450
540
630
720

Buttline

1833

TCA 30/10 Chordwise Pressure

The predicted chordwise pressure at the tap locations for TCA 30/10 configuration are plotted in the figure. Flow acceleration around the LE and the upper hinge lines are clearly visible as indicated by the local low pressure regions. It is interesting to note that the flow undergoes a double deflection flap surfaces at Y=450", which is a direct result of the transition between the flap elements with different hinge-line sweep angles.

Chordwise Pressure for TCA 30/10 Configuration (Part Span)

M=0.3, alpha=10 deg, Re=8 million

TCA 30/10 Spanwise Pressure

The predicted spanwise pressure at the tap locations for TCA 30/10 configuration are plotted in the figure. Only 4 fuselage stations are shown in the figure for clarity. Vortex formation and propagation along the hinge line of the inboard triangular flap element is visible in the spanwise pressure distributions starting from the X=2010" station. Higher pressure differences between the upper and lower surfaces in the TE flap regions are seen in the figure which translates into a higher lift due to the TE flap deflections.

Two directional interpolation has been incorporated in the spanwise pressure calculations so that an adequate resolution near the tip region can be resolved.

1836

Spanwise Pressure for TCA 30/10 Configuration (Part Span)

M=0.3, alpha=10 deg, Re=8 million

1837
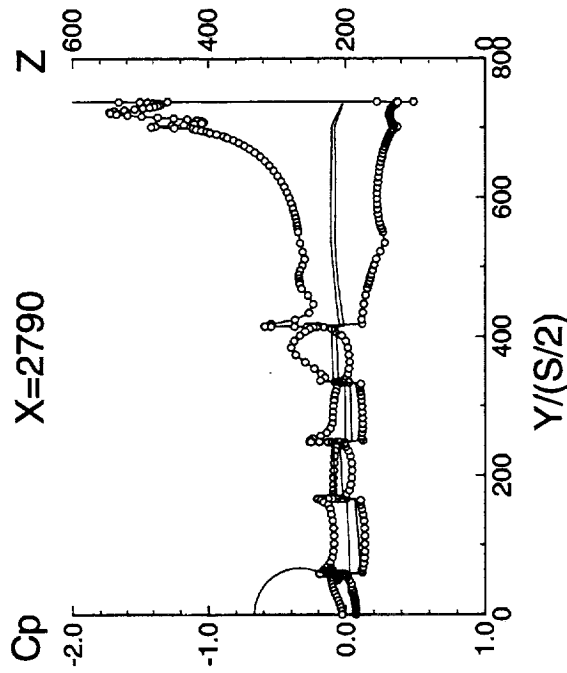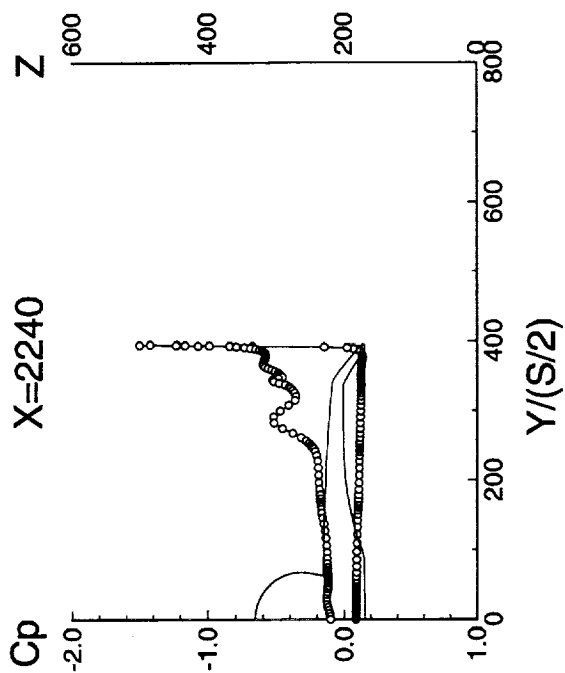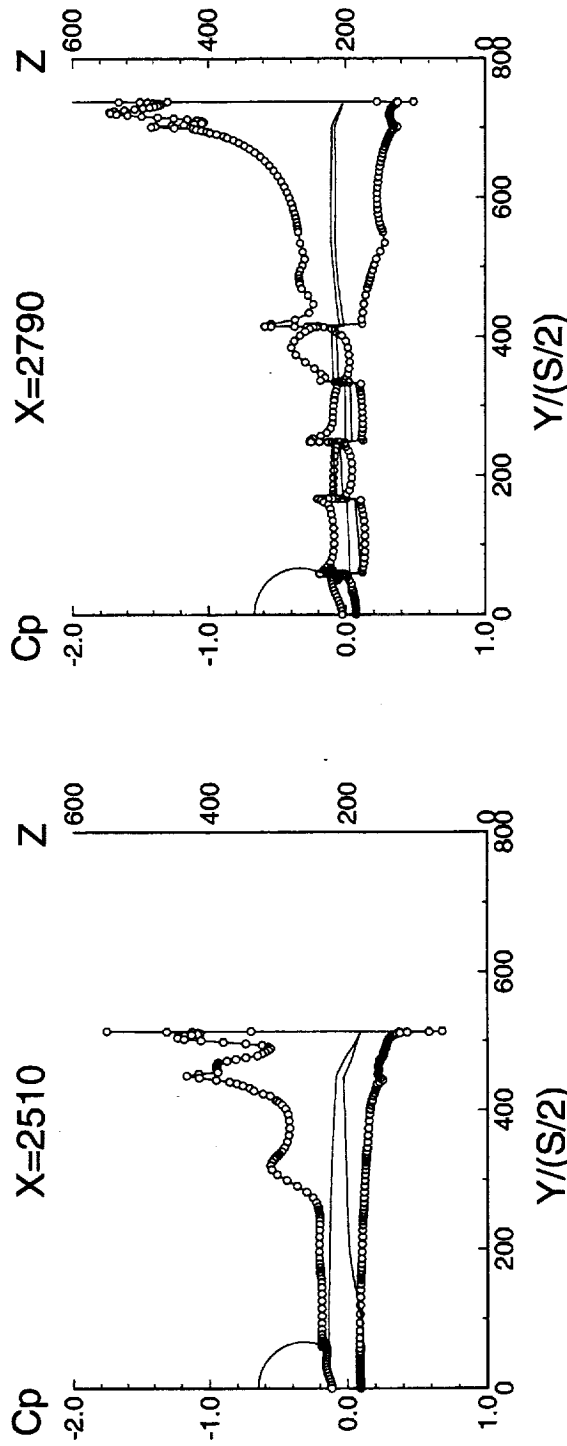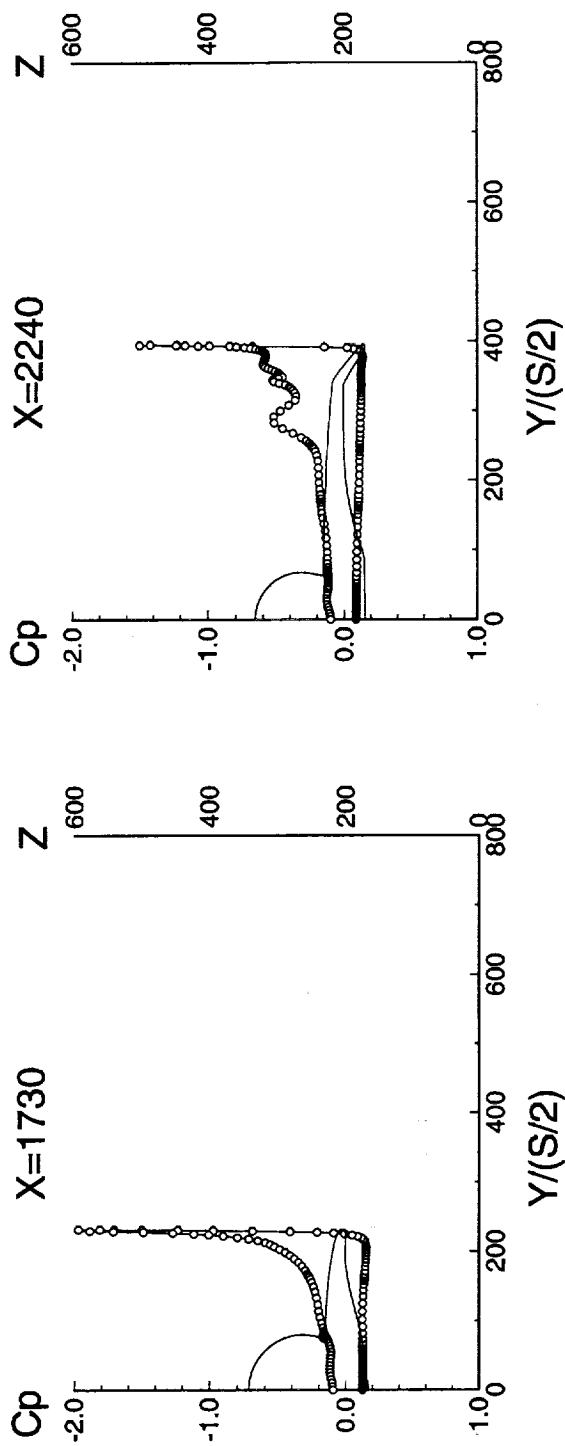
TCA 30/10 Preliminary Comparison

An additional solution is obtained for the TCA 30/10 configuration at alpha= 12 degrees. The angle-of-attack was derived to get CL=0.5 based on the existing solution of alpha=10. A preliminary comparison of the TCA CFD solutions and the modified Ref-H data has been made to qualitatively assess the aerodynamic trends. It should be mentioned that the modified Ref-H model has the same wing/flap planform as that of the TCA configuration. A good correlation is seen between the CFD solutions and the test data including a dramatic change in pitching characteristics in the region of interest. On the other hand, the test data for the full span LE flap model shows a better stability characteristics in the CL=0.5 region.

Preliminary Comparison - TCA CFD Sol'n & Mod Ref-H Data
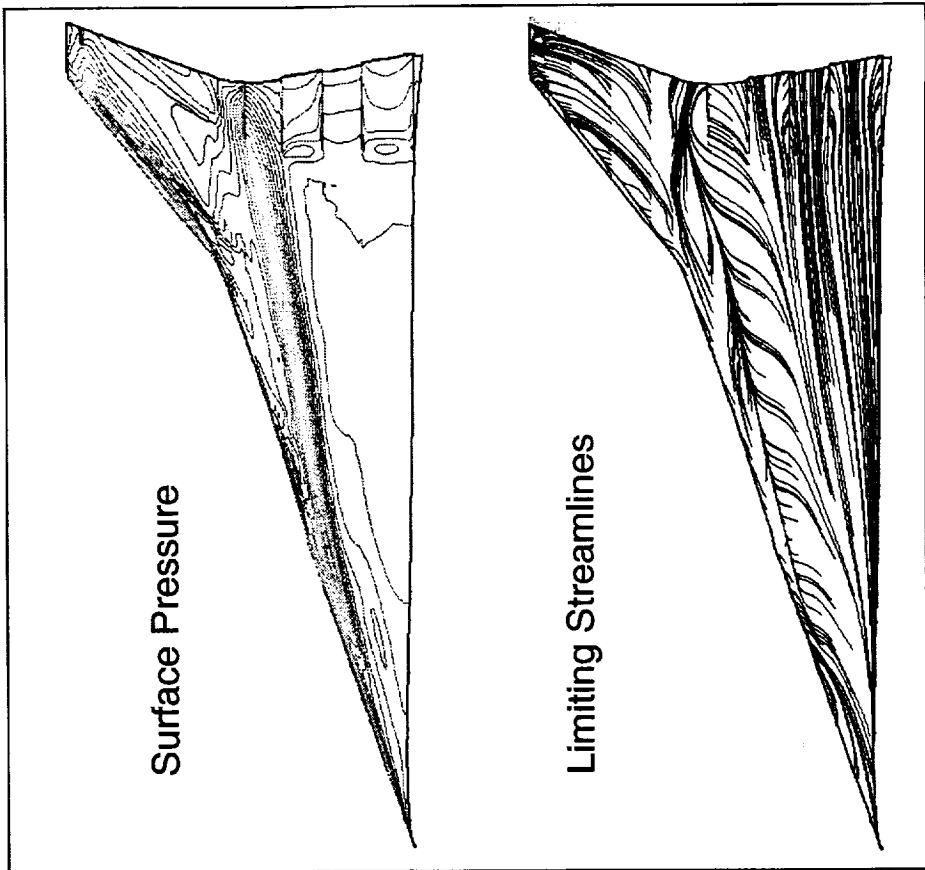
W/B with 30/10 Flaps
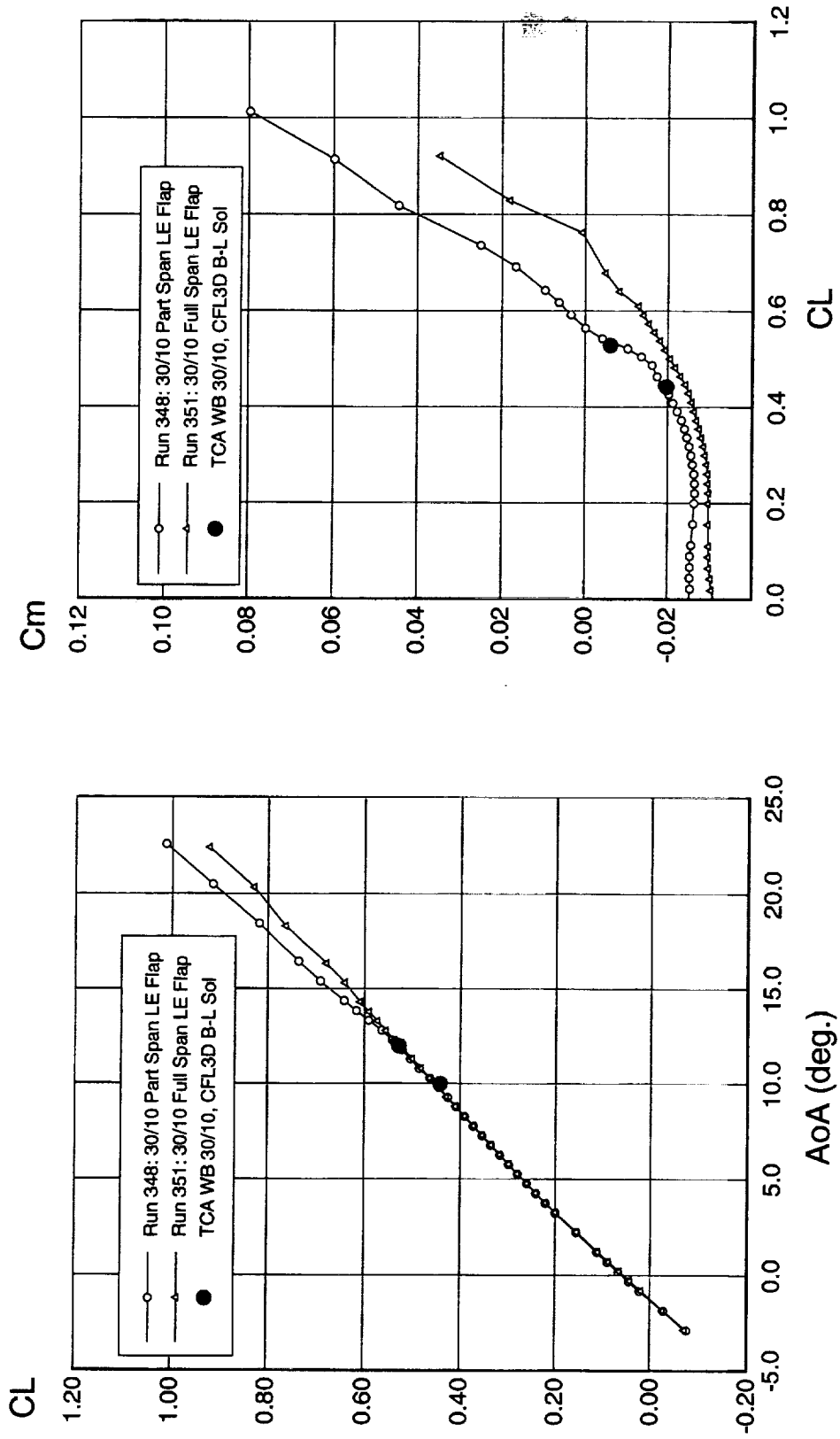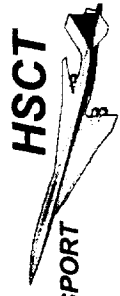
TCA 30/10 - α-Sweep

This figure shows the predicted upper surface flow patterns for TCA 30/10 configuration at alpha=10 and 12 deg. The appearance of the vortical flow emanating from the inboard of the LE flap is clearly visible. As a result, the center of pressure moves forward and changes the longitudinal stability characteristics.

Predicted Upper Surface Flow Pattern for the TCA Configuration (Part Span)

M=0.3, Re=8 Million, δ(LE/TE)=30/10

α=10°

Surface Pressure

Limiting Streamlines

α=12°

Surface Pressure

Limiting Streamlines

1841
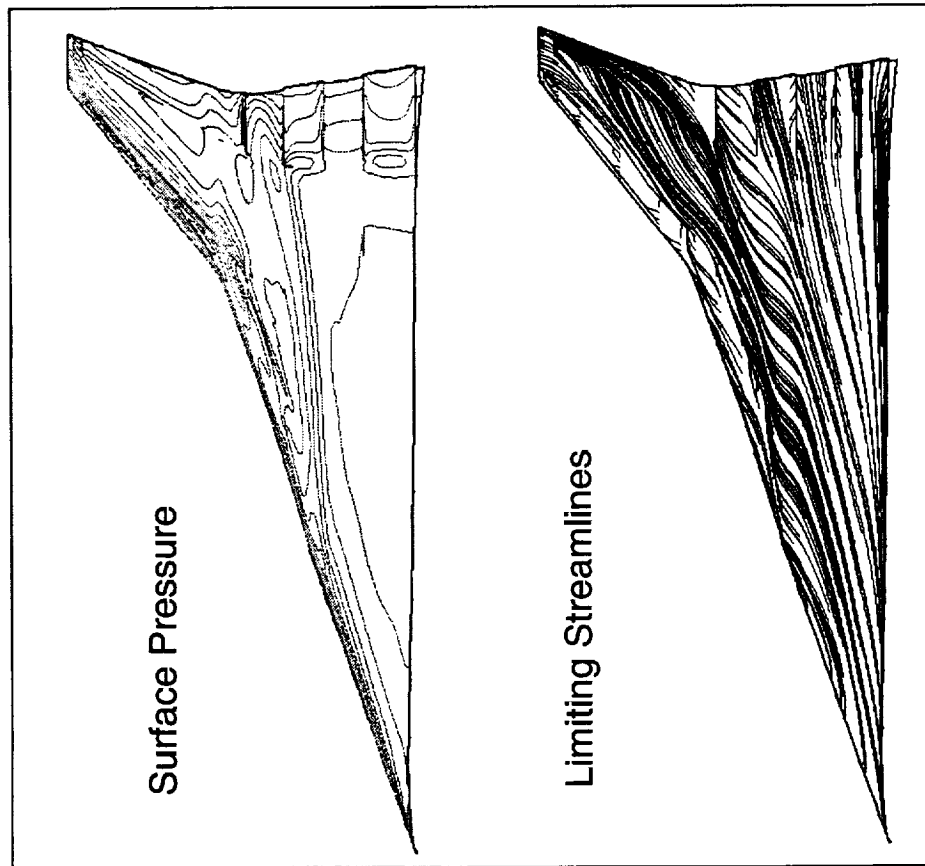
TCA 30/10 - Full Span LE Flap

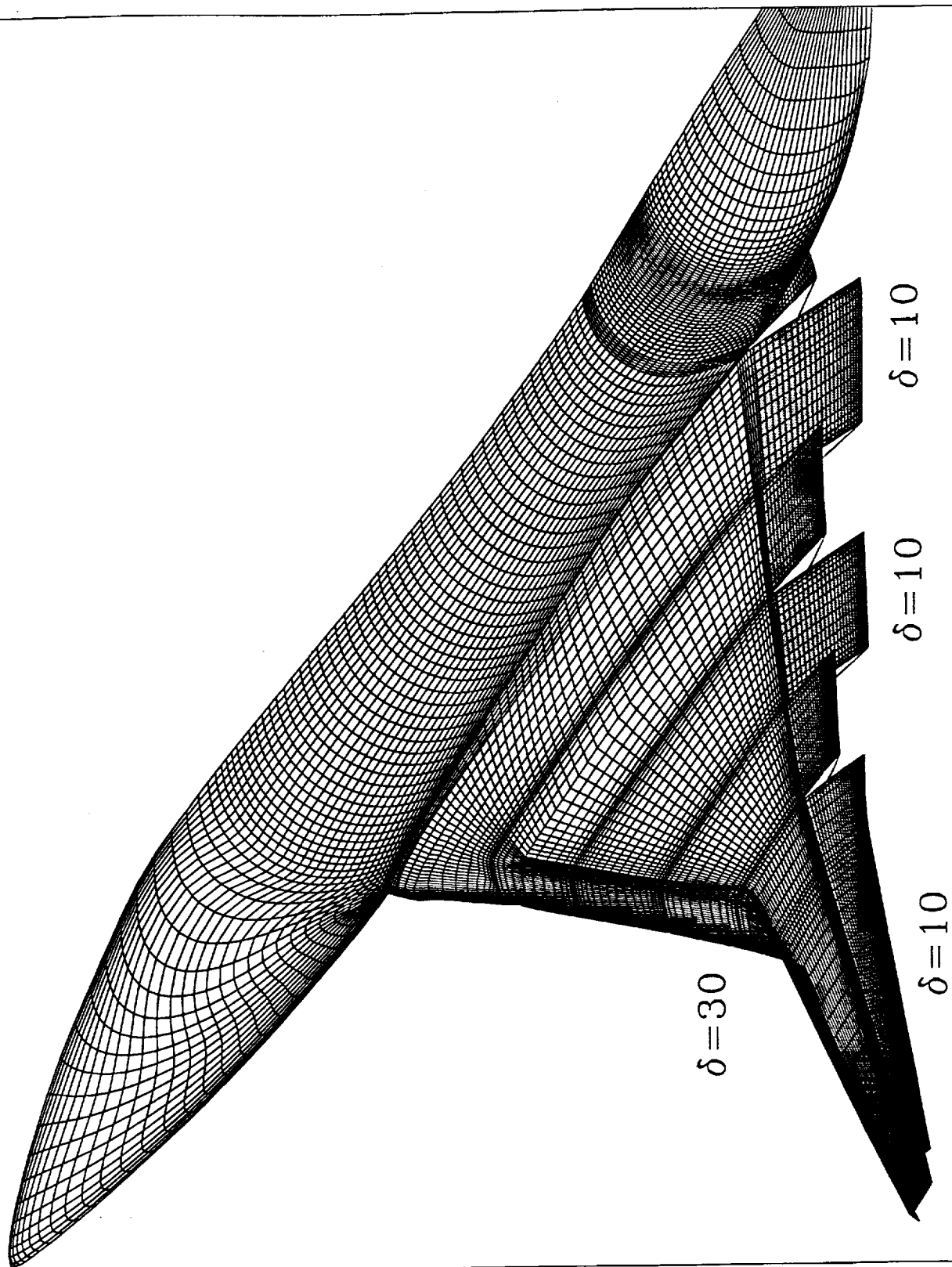Work is currently under way to simulate the TCA 30/10 configuration with a full span LE flap. The suppression of the inboard vortex through full span LE flap deflection is expected to have a favorable impact on the performance and longitudinal stability at high-lift conditions.

TCA 30/10 Configuration with Full-Span LE Flap

$\delta=30$

$\delta=10$

$\delta=10$

$\delta=10$

$\delta=10$

Summary

The automated flap deflection procedures have been successfully applied to a number of high-lift configurations. The ability of these procedures to model variable flap deflections reduces the turn around time for the analysis of the high-lift systems.

CFL3D solutions, in general, have shown to compare favorably with test data and resolve the necessary flow physics for high-lift applications.

Additional enhancements to the flap modeling procedures have been made to include the options of modeling variable LE flap chord, differential inboard/outboard LE flap deflections and grid-based hinge lines. These options will be utilized in the parametric studies to support the wind-tunnel testing in deriving the optimal flap planform and deflection schedule.
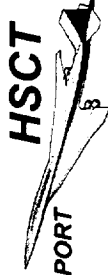
Summary

- Automated flap deflection procedures have been developed to reduce the turn-around time for design and analysis

- CFL3D solutions, in general, have shown to compare favorably with test data and associated flow physics

- Numerical modeling capabilities for parametric studies (δ, flap chord/extent) have been implemented to support wind-tunnel tests in deriving the optimal flap planform and angular deflections
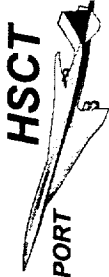
Current and Future Plans

Computational effort will be continued to support high-lift wind-tunnel testing and perform code validation as test data becomes available. Parametric studies will be conducted for flap optimization.

HSCT High-Lift CFD Activities

Current Activities:

- Support the ongoing M2.4-7A Mod3 wind-tunnel tests
- Conduct pre-test analysis for the TCA configuration
  - Partial-span LE flap model
  - Full-span LE flap model
- Enhance grid generation tools as needed

Planned Activities:

- Continue wind-tunnel support for High-Lift Configurations
- Perform code validation as test data becomes available
- Conduct parametric studies for performance optimization
  - Flap schedule
  - LE flap chord length/extent

This page intentionally left blank.

ASE Technologies, Inc.

APPLICATION OF CFL3D TO AERODYNAMIC ANALYSIS
OF HSCT HIGH LIFT WING/BODY/NACELLE CONFIGURATIONS

Xuetong Fan
Paul Hickey
ASE Technologies, Inc.

Objectives

- Develop effective modeling procedure for CFD analysis of HSCT High Lift Wing/Body/Nacelle (WBN) configurations

    - Develop multi-zone grid structure to include nacelle installation with and without deflected trailing edge flaps

    - Apply CFL3D to these complex wing/body/nacelle configurations using RONNIE preprocessor for block interfacing

- Evaluate the effect of nacelle installation on the aerodynamic performance of HSCT High Lift configurations

    - Identify and analyze important flow characteristics due to nacelle installation to support Propulsion Airframe Integration (PAI)

    - Provide flow and performance data to supplement wind tunnel test

Outline

1. MDA M2.4-7A Arrow Wing Configuration

A) Clean Wing :

- Grid structure
- Convergence history
- Comparison with test data
- Flow visualization

B) Deflected Trailing Edge :

- Grid structure
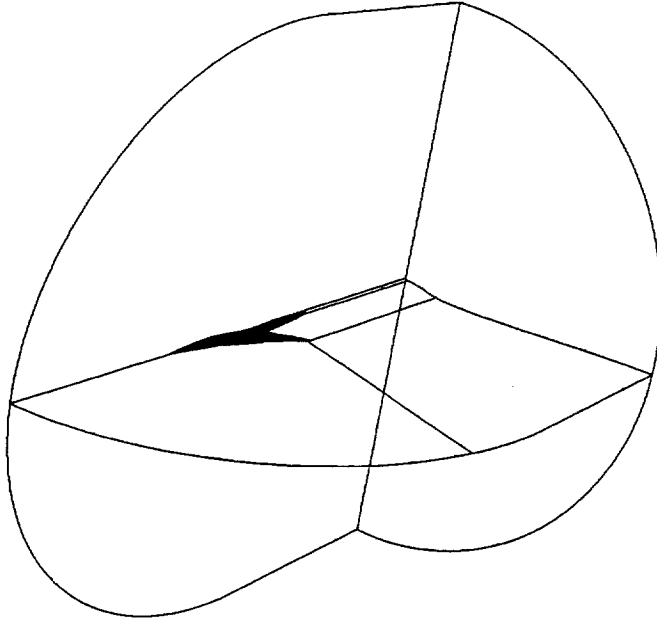- Diagnosis and lessons learned

2. HSCT TCA Configuration

A) Clean Wing :

- Grid structure
- Convergence history
- Results
- Flow visualization

B) Deflected Leading Edge and Trailing Edge :

- Proposed new grid structure

3. Summary and Future Plan

ASE *Technologies, Inc.*

M2.4-7A Clean Wing Wing/Body N-S Grid

- Single Block

- C-O Topology

- 297x65x117

We first present our work in the case of MDA M2.4-7A clean wing with nacelle installation. The WBN model is based on the wing/body (WB) grid provided by MDA. The WB grid is a single block grid using a C-O topology, with i in the streamwise direction, j in the direction normal to the wing/body surface, and k in the spanwise direction. In this case, the WB grid has a dimension of 297x65x117 with about 2.3 million grid points.

M2.4–7A Clean Wing N–S Grid Cut

- To make room for nacelles and diverters
- Under Wing:

    i=1–113; j=1–41; k=33–85
- Above Wing:

    i=257–297; j=1–29; k=33–85
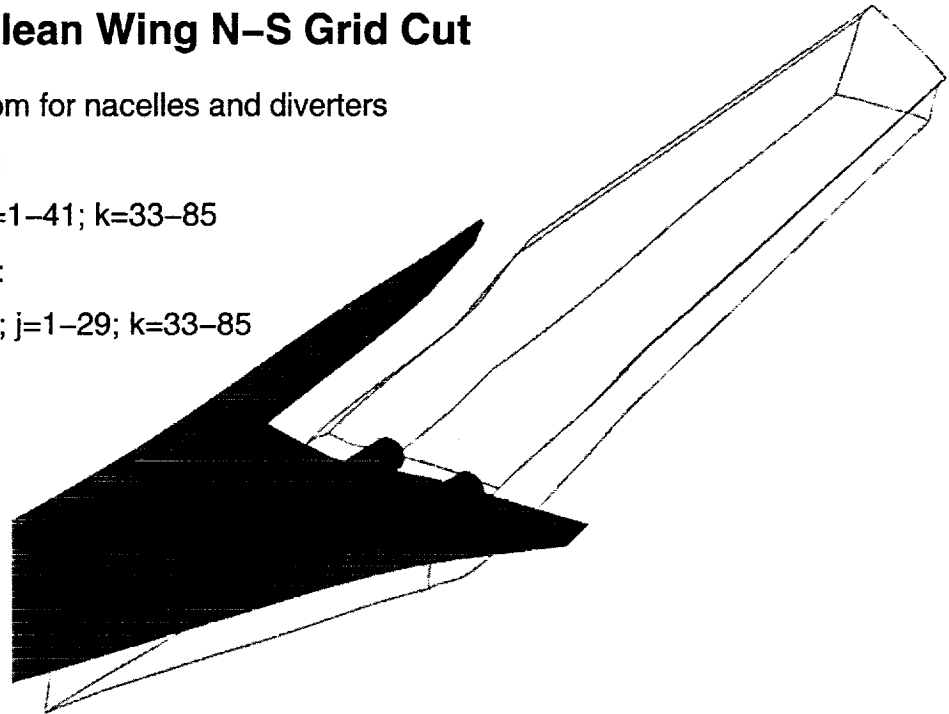
In WBN model, we split the single block WB grid at appropriate locations to obtain a few smaller blocks. We then remove two blocks, one underneath the wing and one above the wing, to make room for the nacelles and diverters. In this case, the two blocks removed are i=1–113, j=1–41, and k=33–85 from under the wing, and i=257–297, j=1–29, and k=33–85 from above the wing in the original WB grid.

ASE *Technologies, Inc.*

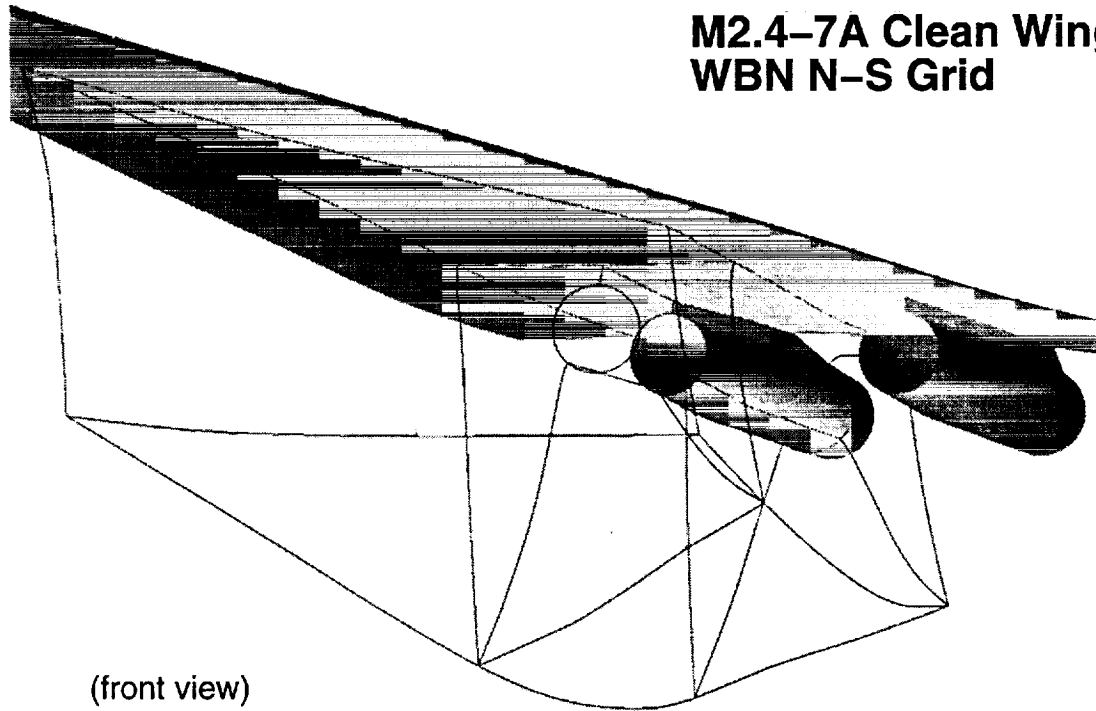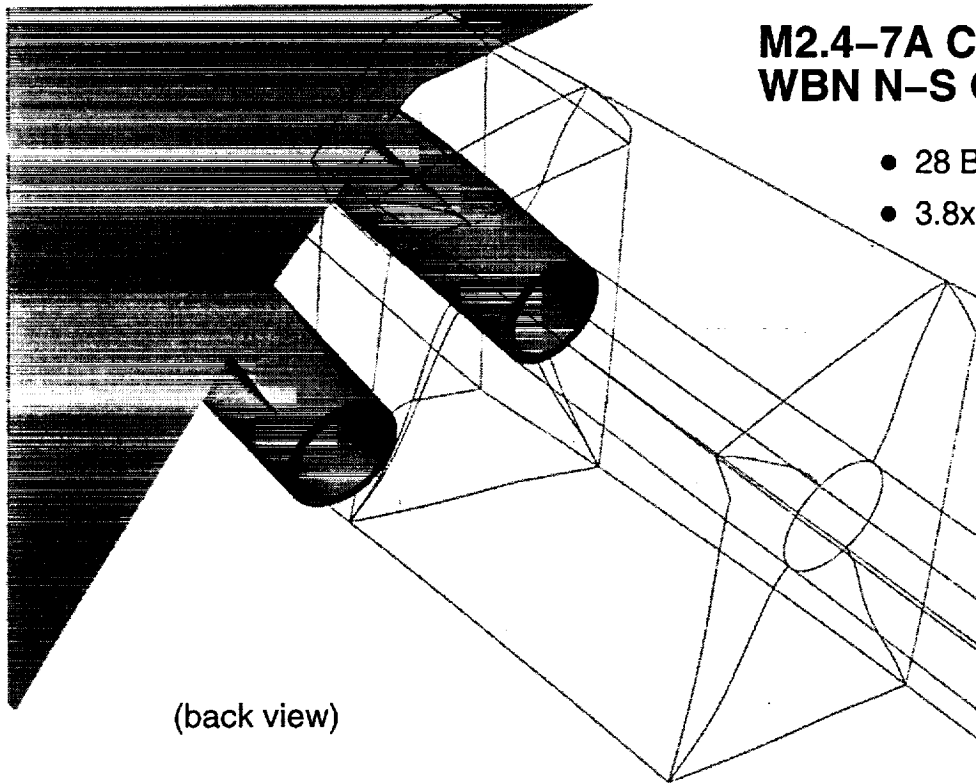**M2.4-7A Clean Wing WBN N-S Grid**

(front view)

We then incorporate the axisymmetric nacelles and diverters geometry into the remaining WB grid and generate new grid blocks around the nacelles and diverters (ND). This picture shows the front view of the ND grid around the forward portion of the inboard nacelles. Basically we use a C-grid around the ND outer surface and an O-grid for nacelle interior. The C-grid and the O-grid extend upstream of the nacelle leading edge and interface with an H-grid which fill the space between the C & O grids and the highly swept existing WB grid around the wing leading edge. Similar blocks are used for the outboard nacelle. Due to the limitation of CFL3D Version 4 which does not allow viscous surfaces at both ends of any one grid direction (I, J, or K), the C grid in this region has to be divided into three blocks.

M2.4–7A Clean Wing WBN N–S Grid

- 28 Blocks
- 3.8×10^6 grid points

(back view)

In the aft portion of the nacelles downstream of the wing trailing edge, O-grid topology is used for both inside and outside of the nacelles. The outside O-grid is broken into pieces for better control of grid quality. As a result, a total of 28 blocks with about 3.8 million grid points are used for the entire M2.4-7A clean wing WBN model. Both 1-1 grid point match and surface patching are used for the block interfaces. Block interface patching is done using CFL3D's preprocessor RONNIE.

ASE Technologies, Inc.

M2.4–7A Clean Wing WBN N–S Solution

Free stream conditions: Mach = 0.3; Re = $8x10^6$

Turbulence Model: Baldwin–Lomax with Degani–Schiff option

Convergence History

AOA= 0
AOA= 4
AOA=10
AOA=15
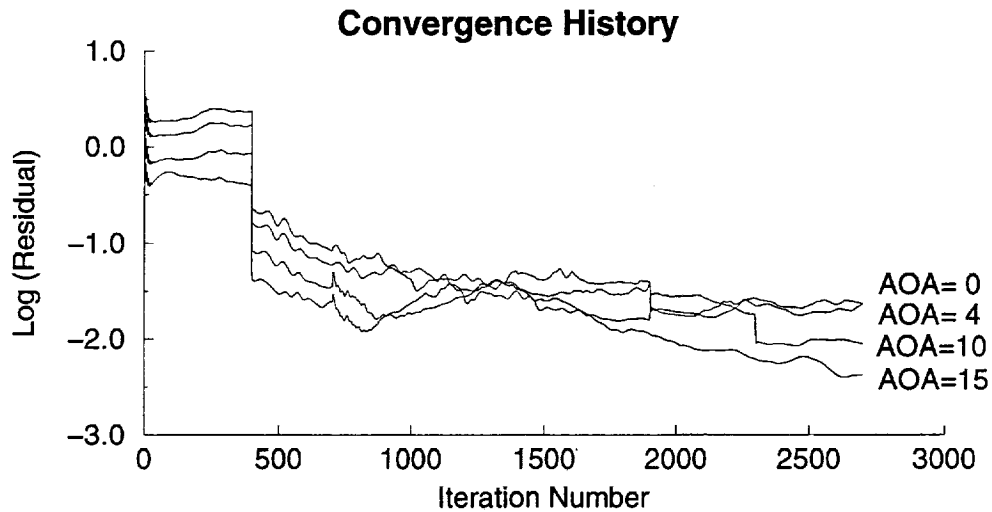
The M2.4-7A clean wing WBN model is run using CFL3D V.4 for low speed free stream conditions (M=0.3) at four different angles of attack (AOA=0, 4, 10, and 15 degrees). The free stream Reynolds number is 8 million based on the reference chord. Baldwin-Lomax turbulence model with Degani-Schiff option is used. Two-level grid sequencing and multi-grid cycles are used for faster convergence. In all four cases, converged steady state solutions are obtained. This figure shows the Log-scale residual history.

M2.4-7A Clean Wing WBN N-S Solution

Free stream conditions: Mach = 0.3; Re = $8x10^6$
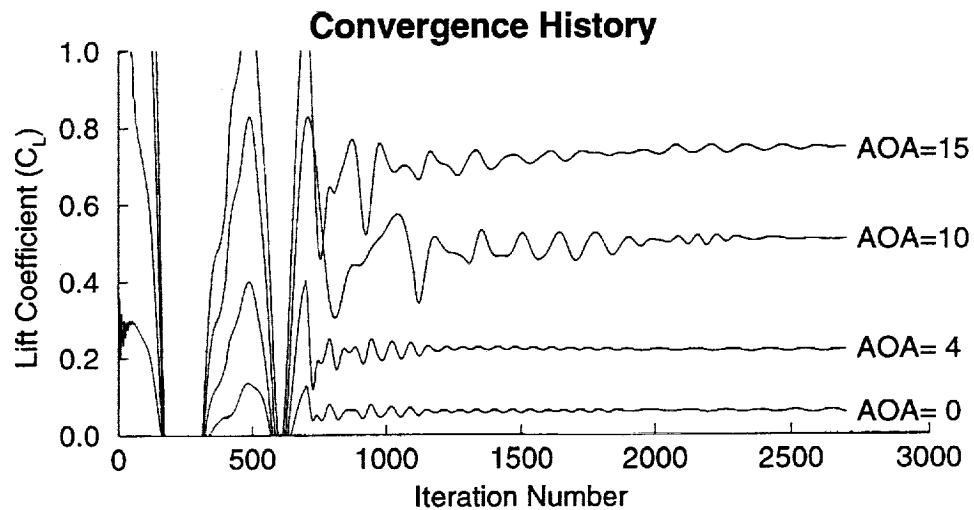
Turbulence Model: Baldwin-Lomax with Degani-Schiff option

Convergence History

Even though the total residual did not decrease to a more satisfactory level, the integrated lift coefficients (and the drag coefficients) have converged to a constant steady state level with very small variations. At this point, we concluded that additional iterations would not further improve the results, as seen in the trend of the residual history.

ASE Technologies, Inc.

M2.4-7A Opt2a High-Lift System Performance

Legend:
- × Navier-Stokes 0/0 WB
- ● Navier-Stokes 0/0 WBN
- LaRC 428 Run 140 0/0 WB
- LaRC 428 Run 122 0/0 WBN

Y-axis: Lift Coefficient, C_L

X-axis: Angle of Attack, α (deg)
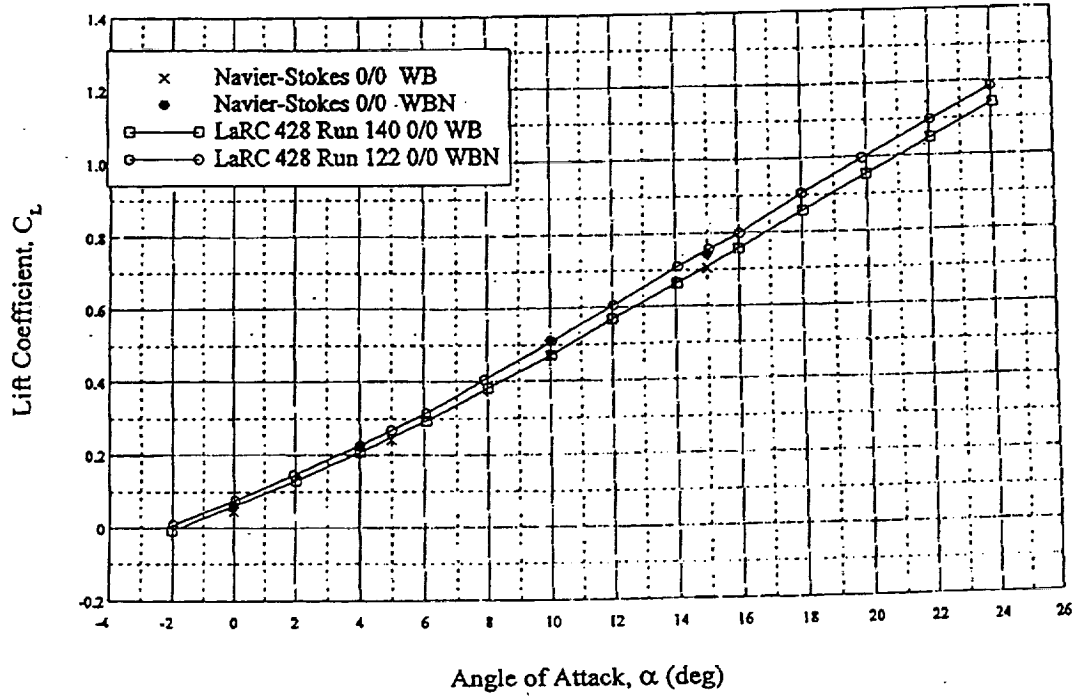
Comparing with the wind tunnel test results for the same M2.4-7A WBN configuration, the predicted lift coefficients agree well with the test data for all four angles of attack.

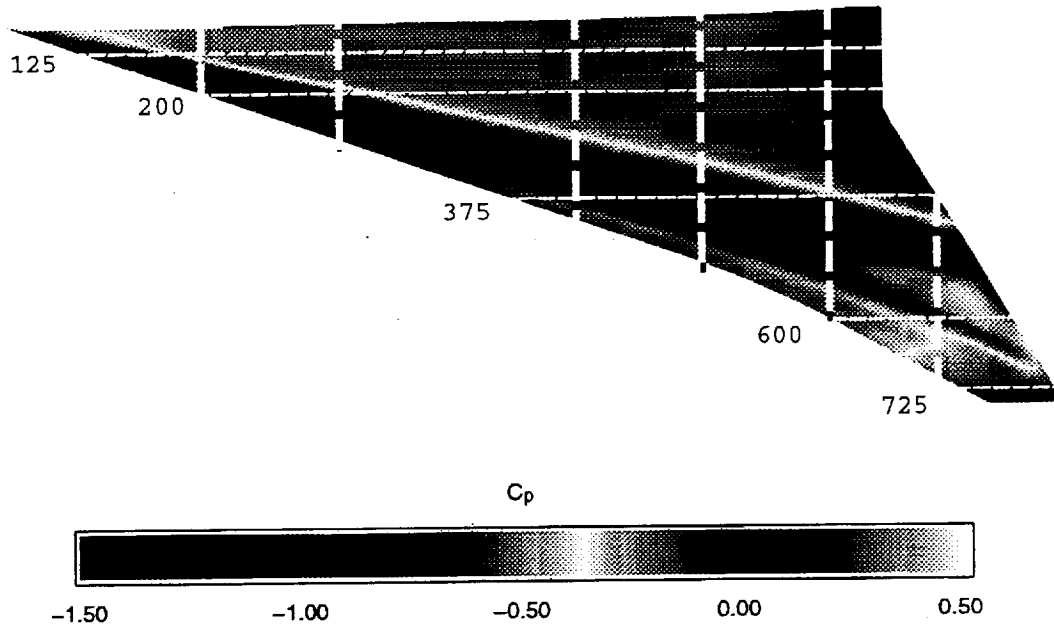# M2.4-7A Opt2a High-Lift System Performance
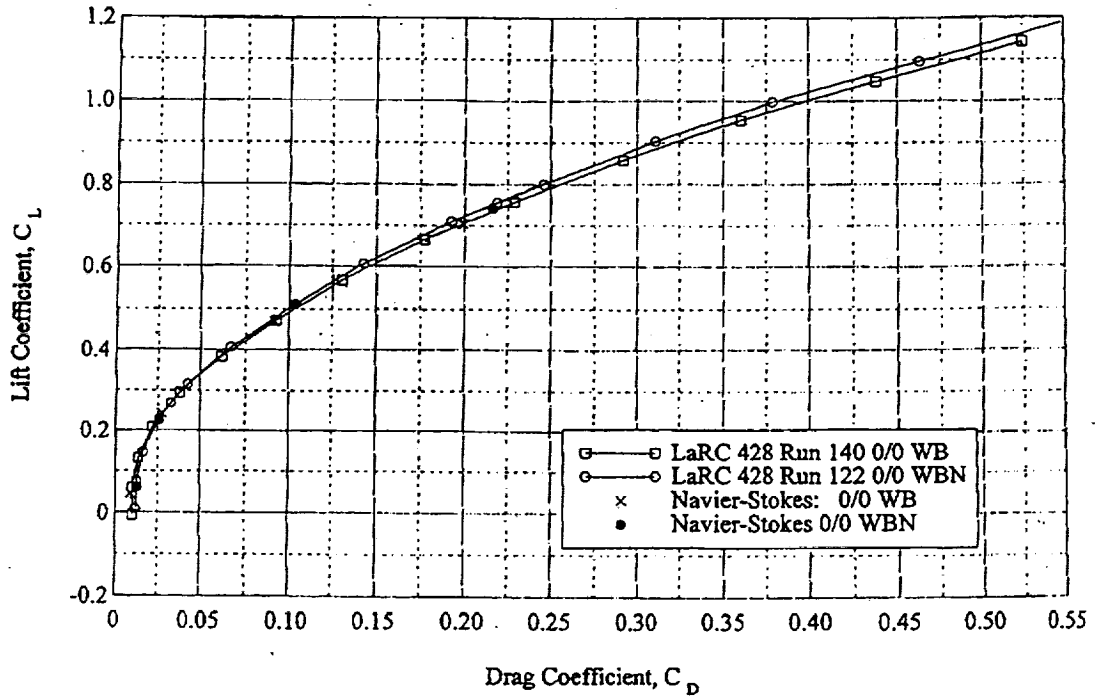
Predicted lift and drag increments also agree well with the wind tunnel test data, as seen in the drag polar plot.

M2.4–7A Clean Wing WBN N–S Solution

Wing Upper Surface Pressure Distribution at AOA=10 deg

This picture shows the pressure distribution at AOA=10 degrees on the wing upper surface. Similar distribution is seen in the WB CFD solution completed by MDA. The CFD solution captured the primary and secondary leading edge vortices above the wing. Though not shown in this picture, it is noted that, at AOA=10 degree, the leading edge vortex strikes directly on the aft portion of the outboard nacelle, which may have some impact on the performance of outboard engine when operating in suppressed mode.

The white horizontal and vertical lines in this picture illustrate the chordwise and spanwise locations where pressure data are taken in the wind tunnel tests.

M2.4-7A Clean Wing WBN N-S Solution

Wing Lower Surface Pressure Distribution at AOA=10 deg

C_p
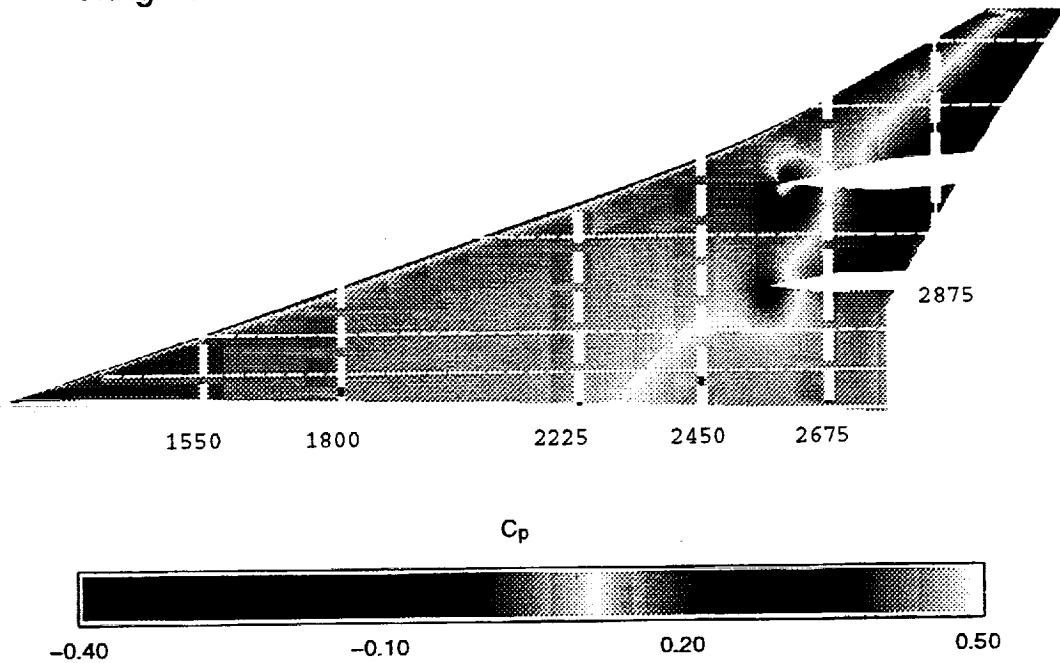
This picture shows the pressure distribution at AOA=10 degrees on the wing lower surface. The low pressure region around the leading edge of the outboard diverter indicates a relatively strong cross flow component in that area.

Again, the white lines shows the pressure tap locations in the wind tunnel tests.

M2.4-7A Clean Wing
WBN N-S Solution

Spanwise Pressure Distribution

AOA=10 deg

sla=2450 inches

sta=2675 inches

slot=2875 inches
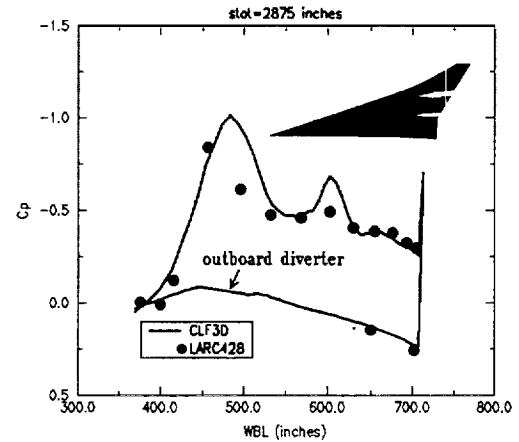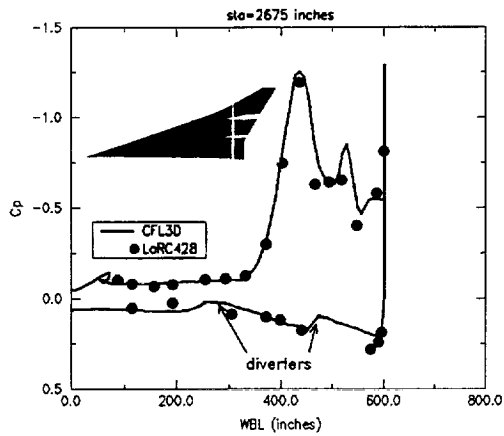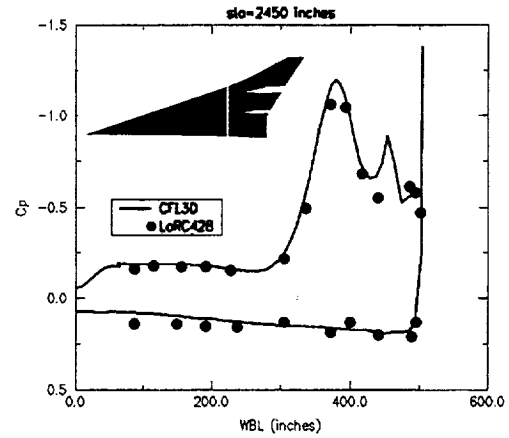
The following plots show the comparison of CFD results with wind tunnel test data in terms of spanwise pressure distribution near the nacelles. We can conclude in general that the CFD results agree well with the test data.

M2.4-7A Clean Wing
WBN N-S Solution

Chordwise Pressure Distribution
AOA=10 deg

WBL = 200 inches

WBL = 375 inches

WBL = 600 inches
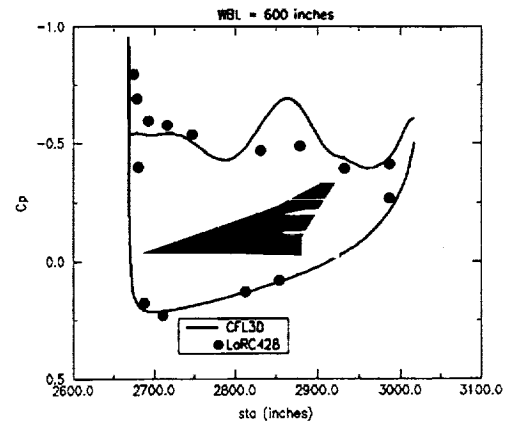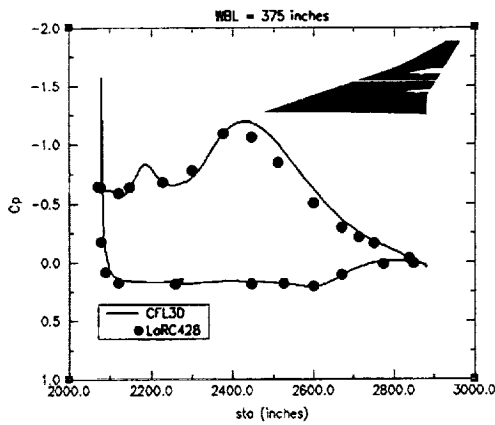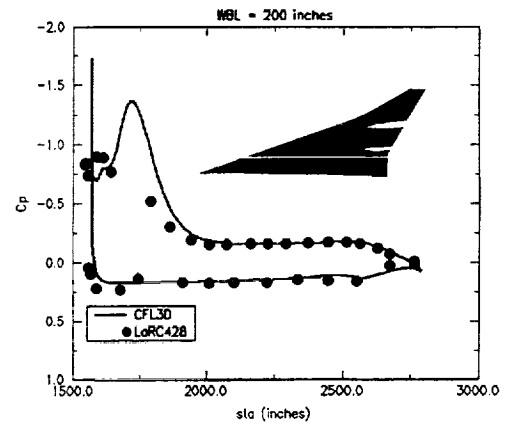
Good agreement is also seen in these chordwise pressure distributions.

M2.4-7A Clean Wing WBN N-S Solution

Limiting streamlines around nacelles and nacelle inlets for AOA=10 deg.
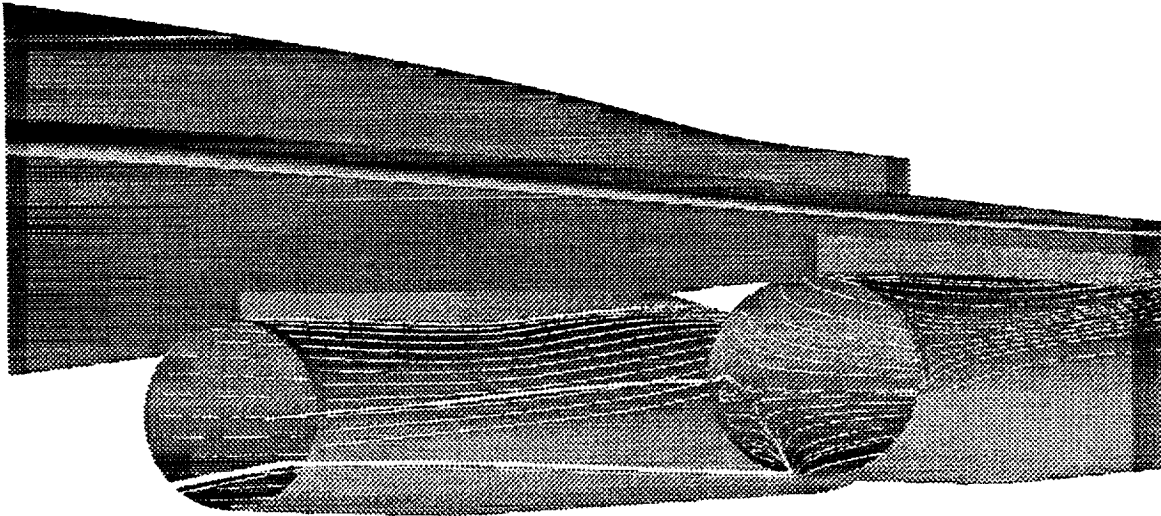
One of the objectives of this work is to provide support by predicting important flow characteristics around the nacelle inlet. This streamline plot shows that, at AOA=10 degrees, a region of flow separation exists downstream of the outboard nacelle leading edge. This separation will result in flow distortion at the outboard engine inlet.

M2.4-7A Clean Wing WBN N-S Solution

Nacelle Inlets Cross Sectional Static Pressure

AOA=10 deg

Inboard   Outboard

| 0.920 | 0.945 | 0.970 | 0.995 | 1.020 | 1.045 |
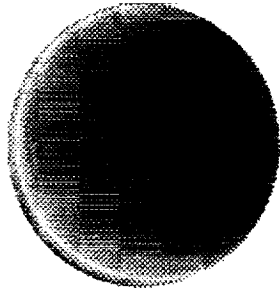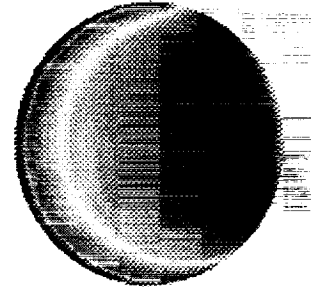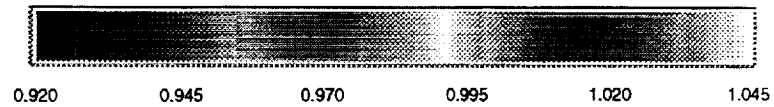
The aforementioned outboard engine inlet flow distortion at AOA=10 degrees can also be seen from the cross-sectional static and total pressure distribution at the outboard nacelle entrance plane.

ASE *Technologies, Inc.*

M2.4-7A Clean Wing WBN N-S Solution

Nacelle Inlets Cross Sectional Total Pressure

AOA=10 deg

Inboard   Outboard

```
0.86        0.89        0.92        0.95        0.98        1.01
```

A SE *Technologies, Inc.*
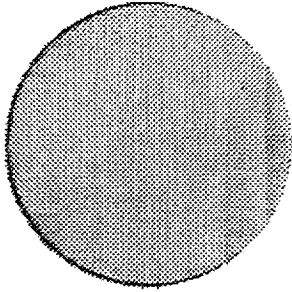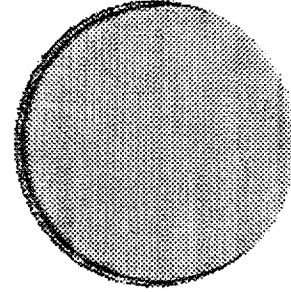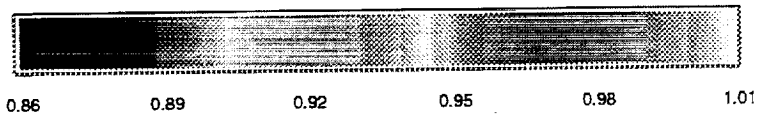
Summary: M2.4-7A Clean Wing WBN N-S Simulation

- Obtained converged solutions for four angles of attack

- Integrated aerodynamic performance agrees well with test data

- Predicted lift and drag increment due to nacelle installion agrees well with wind tunnel test data

- Surface pressure distribution agrees well with test data

- Captured significant flow characteristics

- Predicted flow distortion at nacelle inlets

ASE Technologies, Inc.
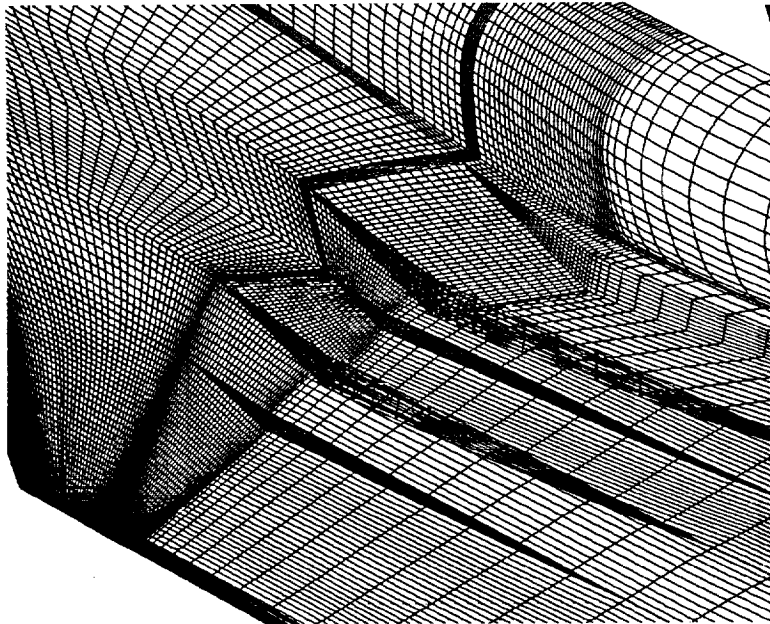
M2.4-7A Flaps 0/10 Wing/Body Grid

- Single Block

- C-O Topology

- 305x65x169

- 1-1 match between webs in wing upper and lower surfaces

Upper surface web

Lower surface web
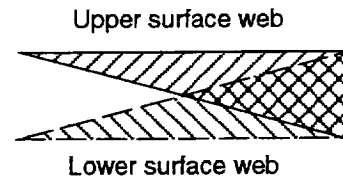
Our next task was to model the MDA arrow wing WBN configuration with 10 degrees deflected trailing edge flap. Again, our model is based on the single block WB grid provided by MDA. In the WB upper surface grid, "webs" are used to connect the undeflected wing upper surface to the deflected flap upper surface. Similar "webs' are used to connect the undeflected wing lower surface to the deflected flap lower surface. In the WB CFD model, a 1-to-1 grid point match was enforced between the upper surface web grid and the lower surface web grid. In our attempt to model this complicated configuration, we tried to follow the same approach in the deflected TE region.

1867

A S E **Technologies, Inc.**

M2.4–7A Flaps 0/10
WBN N–S Grid

● Large variation in hinge line sweep

● Close proximity of flap TE to nacelles

● "Web" regions difficult to interface
  with existing W/B upper surface grid
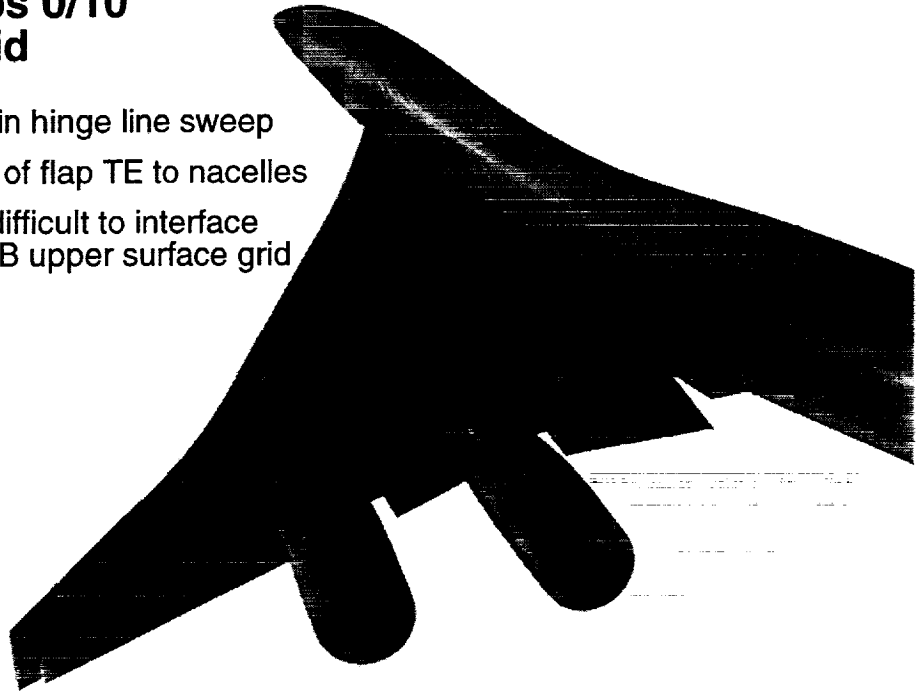
The actual layout of the deflected flaps and the nacelles further complicated the problem. There exists a large variation in the flap hinge line sweep. Because the grid line has to follow the hinge lines and the wing/flap trailing edges, highly skewed grid results. In addition, the trailing edge corners of the deflected flaps are very close to the nacelle surface, which further complicates grid generation in those regions. Finally, trying to use the same approach to handle the communication between webs, we made the decision to maintain the existing WB upper surface grid and to make the new nacelle/diverter grid to match it.
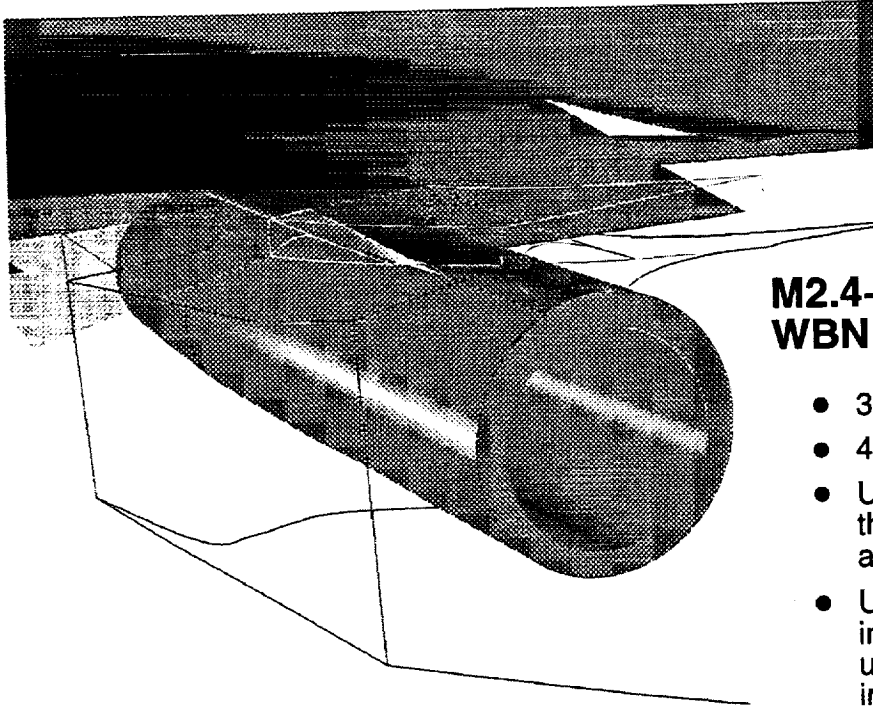
M2.4–7A Flaps 0/10 WBN N–S Grid

- 35 Blocks
- 4.8 Million Grid Points
- Used wedges to match the existing W/B grid at wing upper surface
- Unable to obtain good interface between wing upper and lower surfaces in web regions

As a result, we had to use many wedges to fill the highly skewed geometric space between the nacelles and the trailing edge wing/flaps. The final WBN grid has 35 blocks with a total of 4.8 million grid points. However, we were unable to obtain good interface between the wing upper surface (existing WB grid) and the wing lower surface (new ND grid) in those web regions.

ASE *Technologies, Inc.*

Summary: M2.4–7A Flaps 0/10 WBN N–S Simulation

Status and Lessons Learned:

- Obtained converged laminar solution

- Unsuccessful running with turbulence model

- Modifying existing grid unlikely to solve the problem

- Concluded that "web" interface is the cause of failure

- New grid topology is conceived to properly handle the geometry

Action:

- Focus was shifted to TCA configuration

- Will apply experience gained to better model TCA WBN configuration with leading edge and trailing edge flap deflections
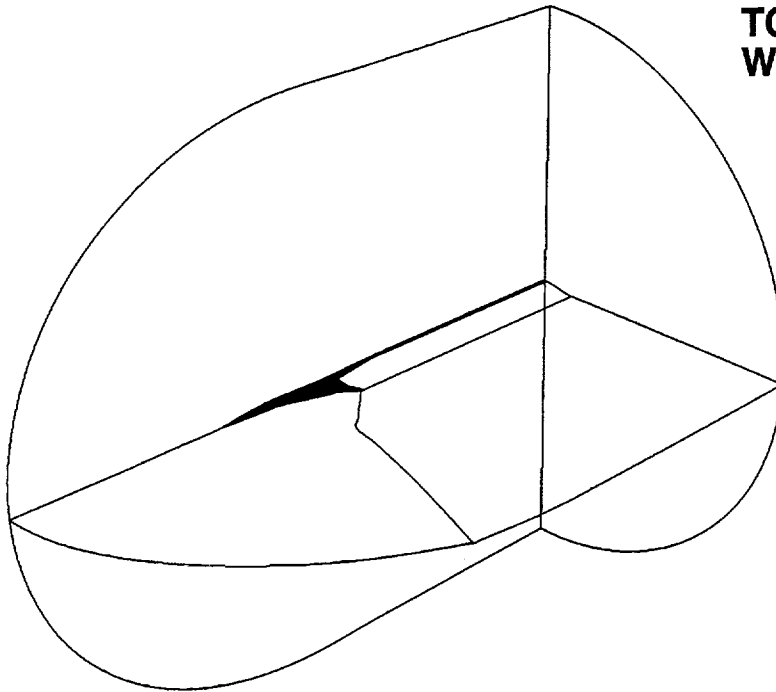
TCA Clean Wing
Wing/Body Grid

- Single Block

- C–O Topology

- 281x69x133

- Min Viscous Spacing
  $2x10^{-3}$ in. (y^+=0.2)

- Constant grid spacing
  for the 1st 2–3 cells
  off solid surfaces

As before, our work on TCA WBN configurations started with a clean wing model. Again, our WBN grid is based on the single block WB grid provided by MDA. In the MDA WB grid, minimum viscous grid spacing of 0.002 inches is used which yields a minimum y^+=0.2 for low speed simulation. (M=0.3, Re=$8x10^6$) In addition, experience at MDA indicates that maintaining the same grid spacing for the first two to three cells off solid surfaces helps to predict a more accurate drag coefficient. We followed the same guidelines in our WBN model.

TCA Clean Wing N–S Grid Cut

- Under Wing:

    i=1–105; j=1–41; k=33–113

- Above Wing:

    i=233–281; j=1–37; k=33–113
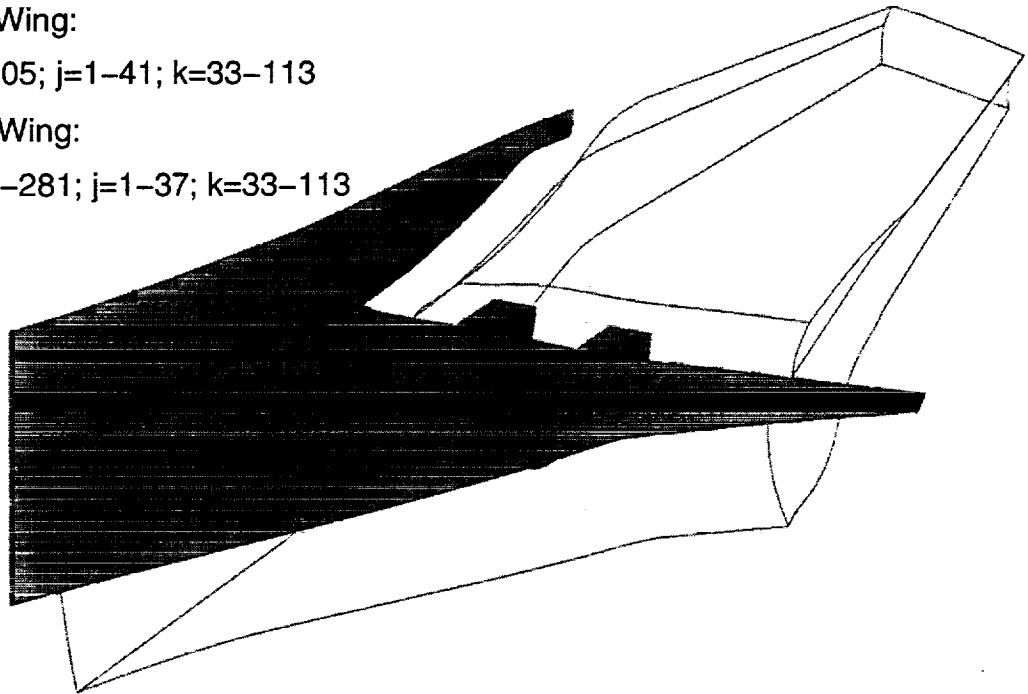
Once again, the WB grid is divided into several sub-blocks and a region is removed to make room for the nacelles and diverters. In this case, the two blocks removed are i=1–105, j=1–41, and k=33–113 from under the wing, and i=233–281, j=1–37, and k=33–113 from above the wing in the original WB grid.
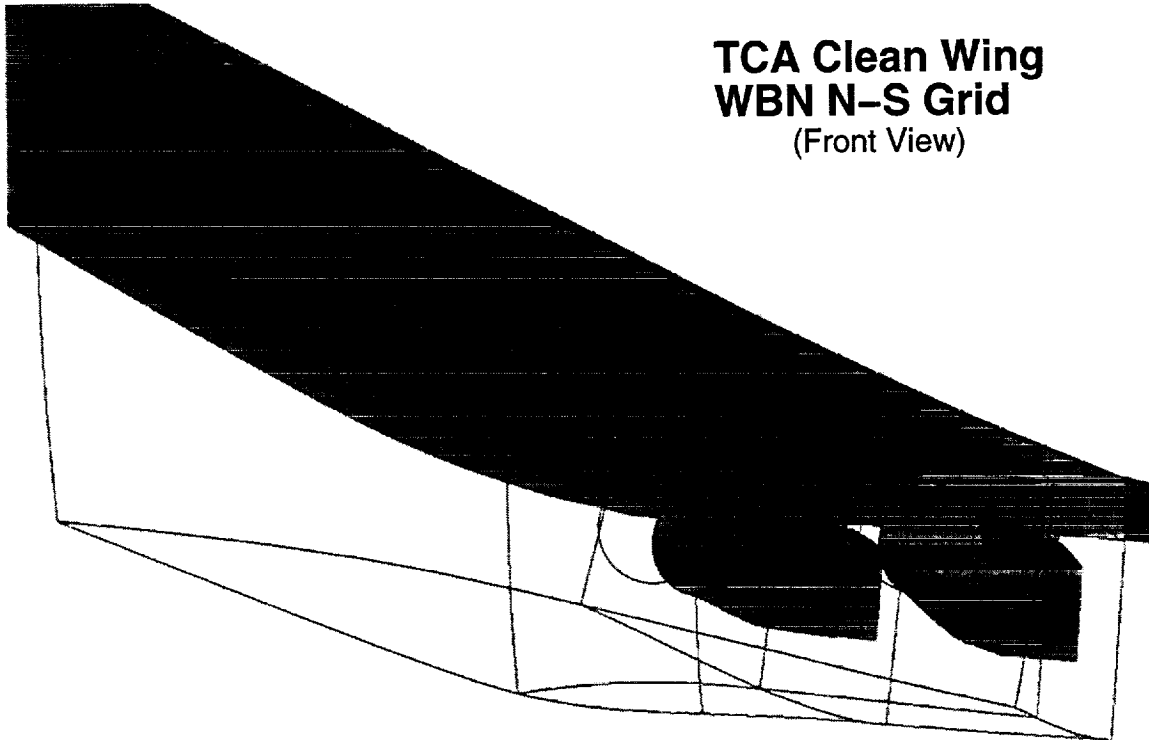
**TCA Clean Wing
WBN N–S Grid**
(Front View)

We used the same grid topology for the forward portion of the nacelles as in the MDA arrow wing case. Since CFL3D Version 5 allows viscous surface specifications at both ends of any grid direction, we don't need to break the C-grid into pieces. This reduced the total number of blocks in the model.

A S E *Technologies, Inc.*
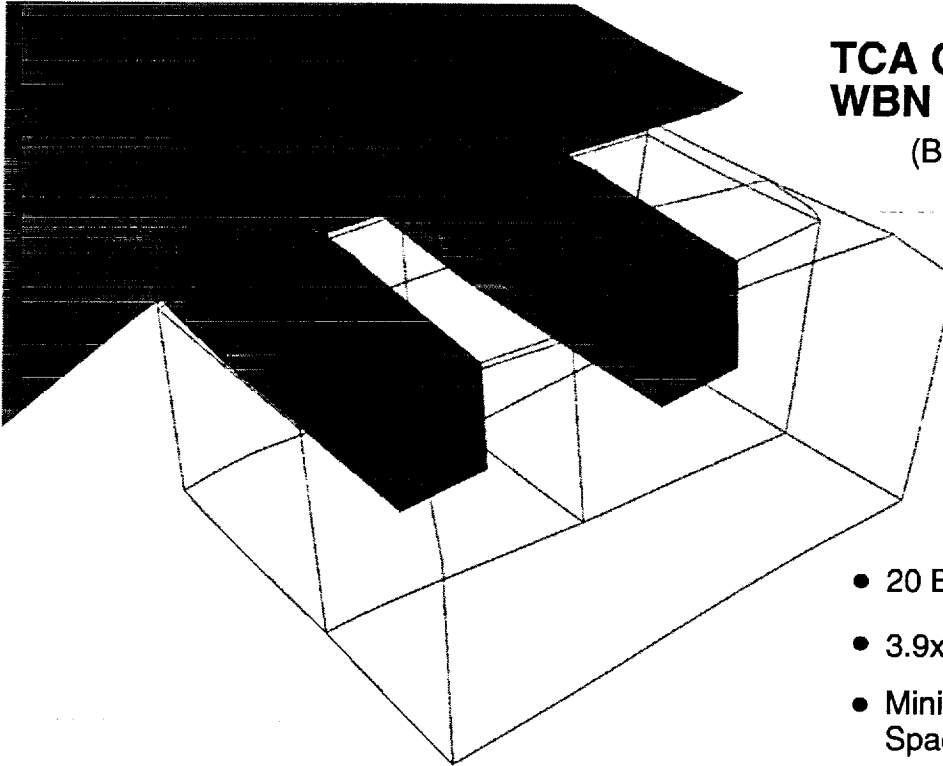
TCA Clean Wing
WBN N–S Grid
(Back View)

- 20 Blocks
- 3.9×10^6 Grid Points
- Minimum Viscous Spacing 2×10^{-3} in.

The nacelles for the TCA configuration have a rectangular cross-section at the aft portion and diverters have a blunt aft face flush with the wing trailing edge. We therefore use C-grid to cover the bottom and PAI side surfaces of the nacelles and used an H-grid sitting on the top surface of the nacelles. The final TCA clean wing WBN grid has 20 blocks with a total of 3.9 million grid points. Both 1-to-1 match and surface patching are used for block interfaces.

Minimum viscous spacing is maintained at 0.002 inches for the first two cells off the solid surfaces.

TCA Clean Wing WBN N–S Solution

Free stream conditions: Mach = 0.3; Re = 8×10^6; AOA=10 deg.

Turbulence Model: Baldwin–Lomax with Degani–Schiff option

Convergence History
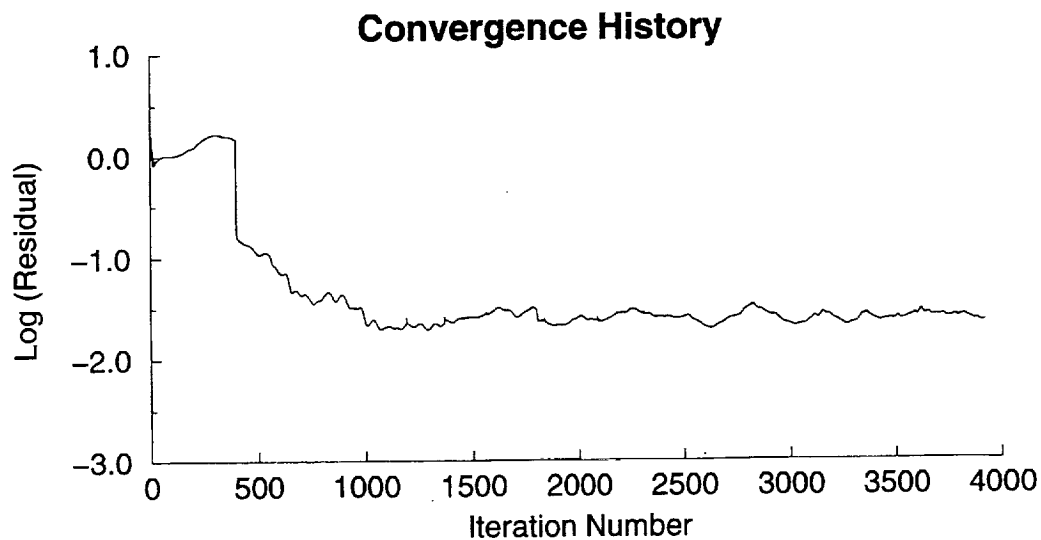
The completed TCA clean wing WBN model is run using CFL3D V.5 for AOA=10 degrees at free stream Mach of 0.3 and free stream Reynolds number of 8 million. Again, Baldwin-Lomax turbulence model with Degani-Schiff option is used. Two level grid sequencing and multi-grid cycles are used. This figure shows the residual history up to 3925 iterations. Again, the residual seems not going to decrease further to a lower level.

ASE Technologies, Inc.

TCA Clean Wing WBN N-S Solution

Free stream conditions: Mach = 0.3; Re = 8×10^6; AOA=10 deg.
Turbulence Model: Baldwin-Lomax with Degani-Schiff option

Convergence History
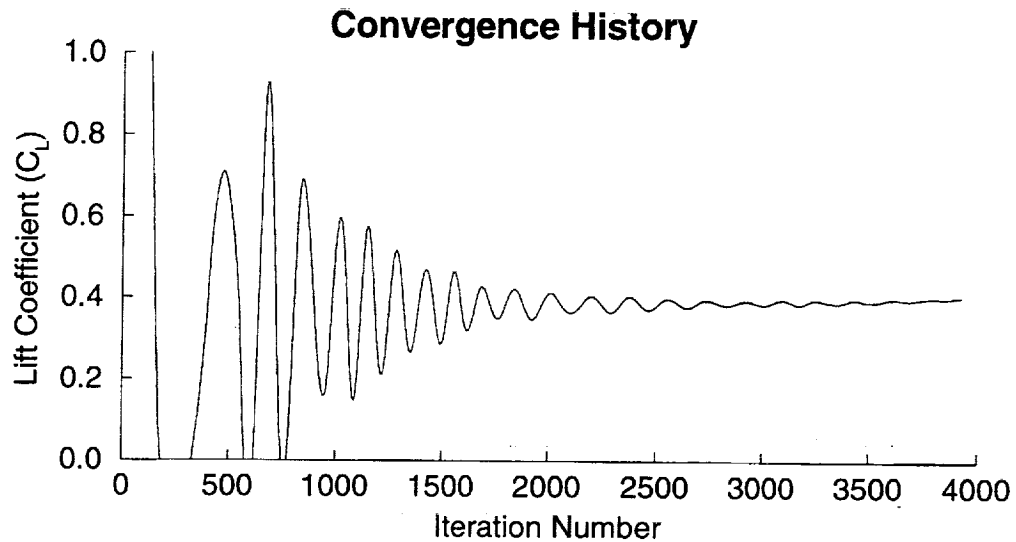
However, the integrated lift coefficient seems to be converging with less and less fluctuations. At the end of 3925 iterations, it appears that C_L is still increasing slightly which indicates that additional runs are necessary for the solution to converge to a steady state. Additional analysis is in progress to obtain a more converged solution.

TCA Clean Wing WBN N–S Solution

AOA=10

Cp
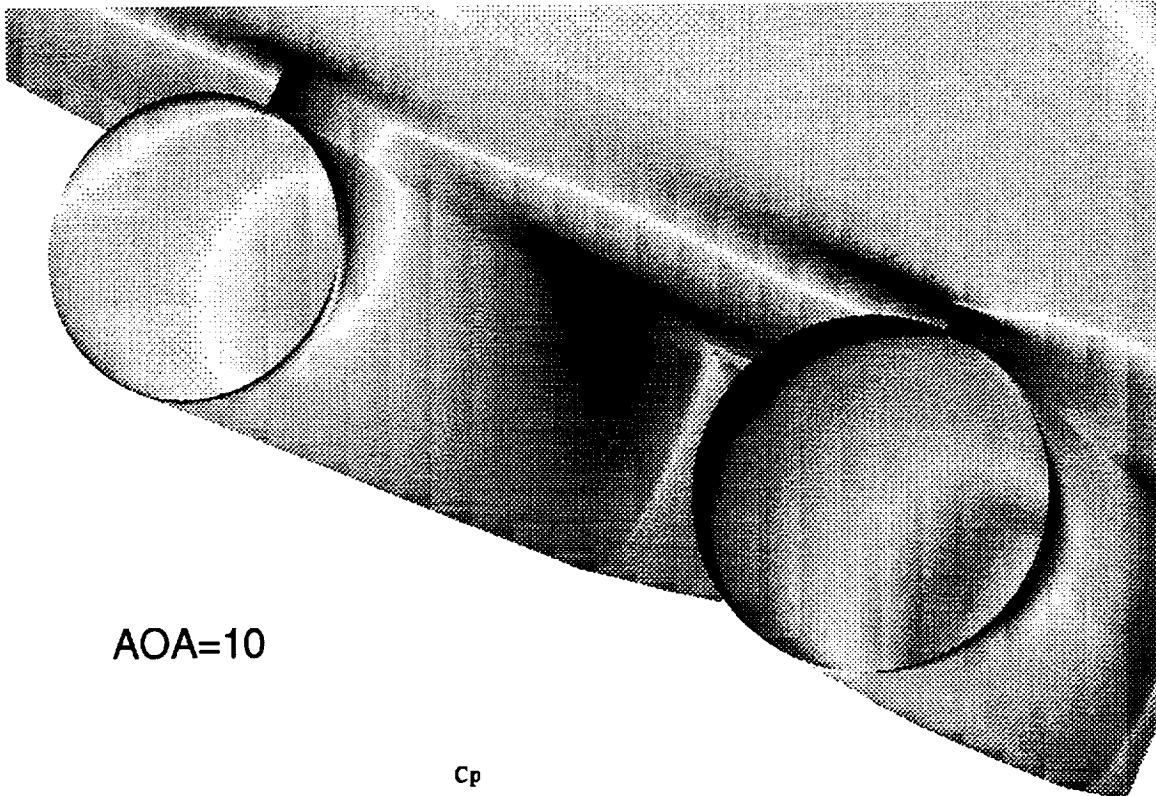
-1.0   -0.5   0.0   0.5   1.0
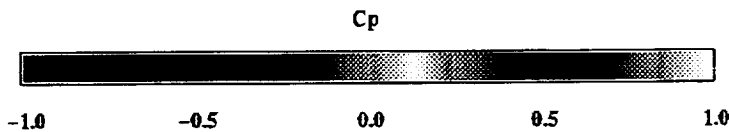
This picture shows the pressure distribution on the WBN lower surface from the latest CFL3D solution. The high pressure and low pressure regions around the leading edge of the nacelles and diverters indicate cross flow in the spanwise direction. Additional post-processing after the fully converged solution is obtained is necessary to clearly understand and describe the flow features in that region.

ASE Technologies, Inc.
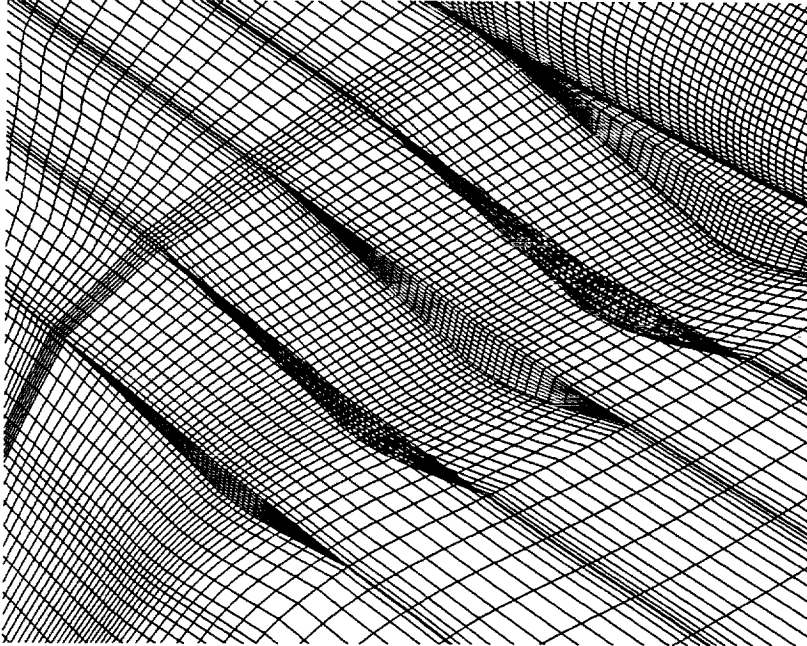
TCA Flaps 30/10 Wing/Body Grid

- Single Block

- C–O Topology

- 289x65x181

- 1–1 match between webs in wing upper and lower surfaces

- More continuous TE flap hinge line

Our next task is to model the TCA WBN configuration with deflected leading and trailing edges. The WB grid in the case of 30/10 has 3.4 million grid points. Once again, webs are used in the WB grid to connect the deflected flap and the undeflected wing segments and 1-to-1 match is established between the webs in wing upper and lower surfaces. In this TCA 30/10 configuration, the TE flap hinge line sweep is more "continuous" in the spanwise direction.

TCA Flaps 30/10 WBN Model

How to model the "web" regions
due to the deflected TE flaps ?

Wing upper surface flap hinge line

Wing lower surface flap hinge line
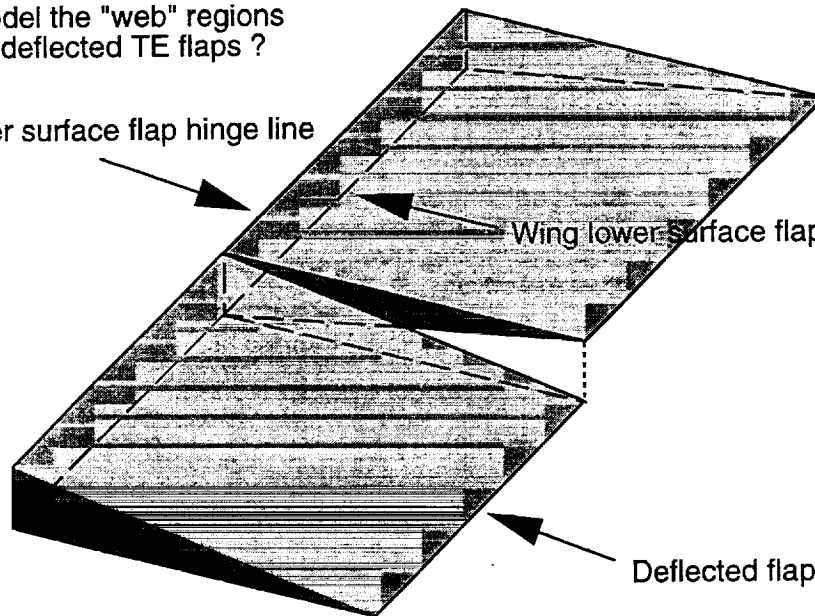
Deflected flap

The most critical question in this task is how to model the web regions due to the deflected TE flaps. This figure shows the geometric mismatch between the wing upper surface web and the lower surface web.

TCA Flaps 30/10 WBN Model

Proposed new approach:

(a) Use wedges above the deflected flap
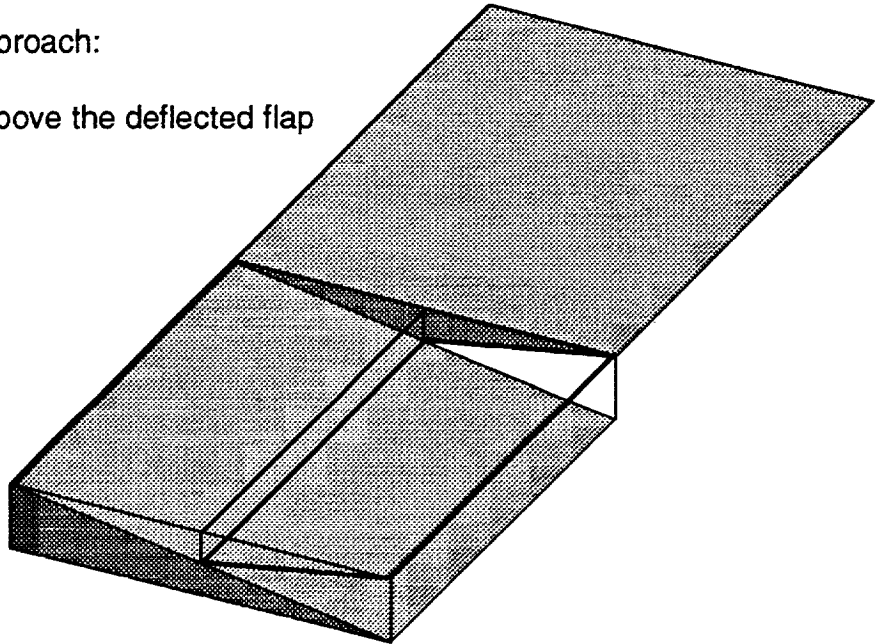
Our proposed new approach to this problem is to use three wedges to fill the space above the deflected flap caused by the TE flap deflection.

ASE Technologies, Inc.

TCA Flaps 30/10 WBN Model

Proposed new approach:

(b) Use wedges under the undeflected
      wing segments
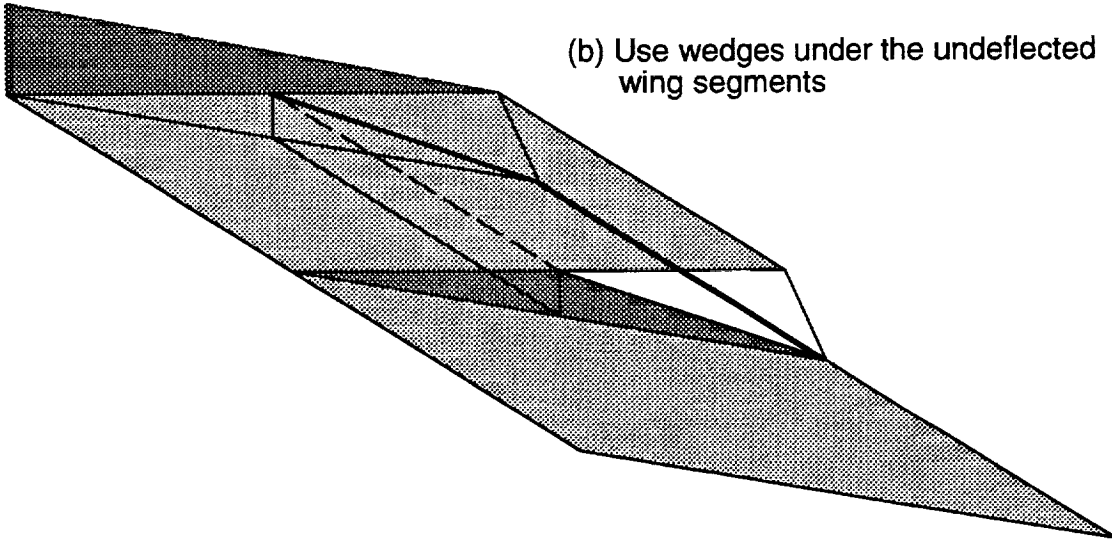
And we will use another three wedges to fill the space underneath the undeflected wing segments caused by the flap deflection. This will enable 1-1 point matching at (wedge) block interfaces as well as an accurate definition of the viscous surfaces at the flap/wing end walls.

The advantages of this new approach include: (1) the geometry in the wing trailing edge region caused by the deflected flaps is modeled more accurately; and (2) exact boundary conditions or block interface can be specified for every face of all the wedge blocks.

All the solid surfaces are accounted for in this approach and exact 1-to-1 match can be established between the side surfaces of the wedge blocks in the "web" region. By adjusting grid spacing in the gap regions, any gap size can be modeled accurately.

ASE *Technologies, Inc.*

Summary

- Obtained viscous CFD solutions for HSCT WBN configurations without deflected trailing edge flaps (Arrow Wing and TCA)

    - To date, comparisons with test data indicate good agreement
    - Predicted flow characteristics may prove helpful for PAI work

- Developed a grid structure for HSCT WBN configurations with deflected trailing edge flaps

Future Plan

- Continue to develop CFD models for HSCT WBN configurations; Currently working on TCA Flaps 30/10 configuration

- Validate CFL3D solutions by further comparison with test data

- Support PAI tasks by quantifying the effect of nacelles on flap aerodynamics and providing flow field details in the vicinity of nacelles

CLF3D/MAGGIE CFD Analysis of a 4%–Scale HSCT Aircraft Model inside a 12–ft Wind Tunnel

by

Chung–Jin Woan
Boeing North American, Inc.
Seal Beach, California

David T. Yeh and Roger W. Clark
McDonnell Douglas Corporation
Long Beach, California

1997 HSR Aerodynamic Performance Workshop
NASA Langley Research Center, Hampton, Virginia
February 25–28, 1997

OBJECTIVES

The objectives of this study are:

1) to develop an integrated wind–tunnel/free–air CFD process to speed up CFD turnaround time in HSCT high–lift configuration development through a direct CFD application to the M2.4–7A Arrow Wing configuration at low speed,

2) to study the effects of wind–tunnel wall on the model aerodynamic characteristics and the combined effects due to the wind–tunnel wall and model supports through direct comparison of CFD calculations, and

3) to obtain CFD results prior to wind–tunnel tests and to validate and evaluate the CFD results by direct comparison with wind–tunnel test data.

Currently, M2.4–7A is still under schedule to be wind–tunnel tested in the NASA/Ames 12–ft tunnel. Therefore, the validation of CFD results against test data will not be included in this paper.

OBJECTIVES

- Develop an Integrated Wind–Tunnel/Free–Air CFD Process to Speed up CFD Turnaround Time in HSCT High–Lift Configuration Development

- Investigate the Effects of Wind–Tunnel Wall and Model Supports on the Model Aerodynamic characteristics

- Validate/Evaluate the CFD Resluts by Comparison with the Wind–Tunnel Test Data

1885

DEFINITIONS OF PROBLEMS

This view graph shows three CFD configurations of the Arrow Wing M2.4-7A: the full-scale free-air configuration, the 4%-scale model/wind-tunnel configuration, and the 4%-scale model /wind-tunnel/support configuration. The model used has deflected LE (Leading Edge) and TE (Trailing Edge) flaps of 40 and 10 degrees, respectively. The shape of the tunnel wall section is the NASA/Ames 12-ft tunnel test section.

The free-air CFD simulation has been done elsewhere and available to our present study. In the rest of our discussion, we will focus on the last two wind-tunnel configurations with assumption that the free-air CFD grid is given.

DEFINITIONS OF PROBLEMS

1. M2.4–7A Free–Air CFD

NASA/AMES
12–ft Tunnel

NASA/AMES
12–ft Tunnel

Fore Post

Aft Post
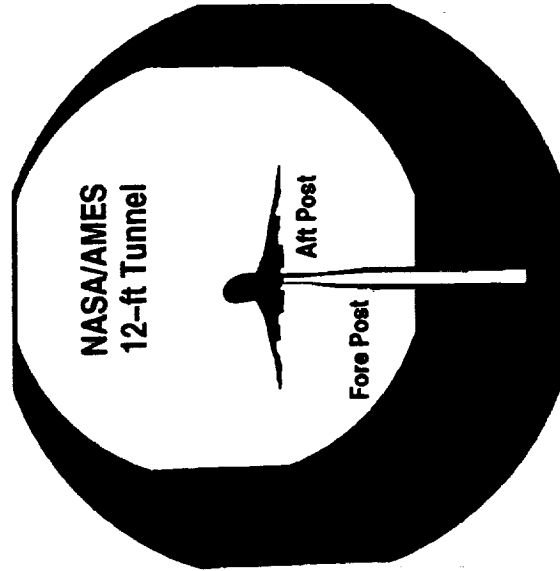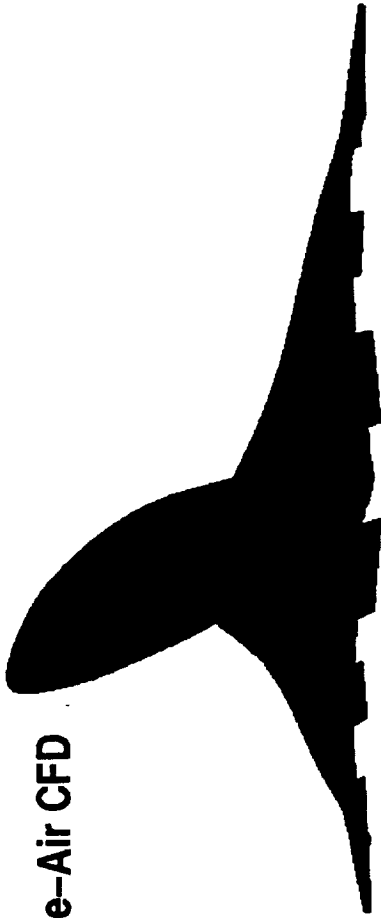
2. 4%–Scale M2.4–7A/Tunnel CFD   3. 4%–Scale M2.4–7A/Tunnel/Support CFD

APPROACH

Our approach is a simple direct application of CFL3D/MAGGIE CFD package developed at NASA/LaRC to our problems with chimera (overset or overlapping) grid option. CFL3D is a Reynolds–Averaged thin–layer Navier–Stokes flow solver. The version currently in use is Version 5.0. MAGGIE is a CLF3D grid pre–processor for constructing the needed chimera grid in flow simulation.

A chimera grid is a grid consisting of two or more grids having overlapping regions between adjacent grids for information exchange during flow solution updating. The chimera technique was developed to alleviate the difficulty of generating structured CFD grids for complex configurations by allowing a CFD grid to be constructed from a series of simple, independently generated, component grids.

APPROACH

- **Use Chimera (Overset or Overlapping) Grid CFD Technique**

  - Component grids may be generated independently of others

  - Component grids may be easily added to and/or subtract from the existing grid

  - The same free–air grid can be used directly in wind–tunnel CFD, hence, the need of regenerating tunnel grid is eliminated

- **Employ MAGGIE Code**

  - A CFL3D grid pre–processor for constructing chimera grid

- **Employ CFL3D Code**

  - Has been Widely used in aerospace industry

  - Has been and is being used in HSCT CFD applications

  - Has a good documentation and Government support

CHIMERA METHOD AND CONCEPT

The basic concept of chimera method is illustrated in this and the next two view graphs. There are Two basic steps in grid generation. One is to generate component grids. Another is to construct a composite grid by hole creations and fringe point interpolations as shown in this figure.

Here, we have tow independently generated Circle grid and Rectangle grid. An overset grid is constructed by creating a hole inside the Circle grid and blanking out all the grid points outside a specified interior circle of Circle grid. The resulting overset grid is shown in the right figure. The grids in black are the fringe points of Circle grid and those in green are the fringe points of Rectangle grid. The grids in blue and red are the field points of Circle grid and Rectangle grid, respectively. This represents an application of overset grid to eliminate singular axis from flow solver calculation. A singular axis often degrades flow solution convergence rate.

A *hole point* is a grid point that has been blanked (specified) to be within a hole. This point is considered to be out of the computational domain. A *fringe point* is a hole boundary point that will receive flow information from the adjacent grid during flow solution update. A *field point* is a grid point within computational domain that is updated by the flow solver or boundary conditions. A *hole* is simply a collection of hole points that have been blanked.

It is noted that all the fringe points must be created such that they reside entirely within the field point regions of the adjacent grids. That is, they must receive information from the field points. Otherwise, they would become the so called "*orphan*" points.

CHIMERA METHOD AND CONCEPT

1. Component grid generation
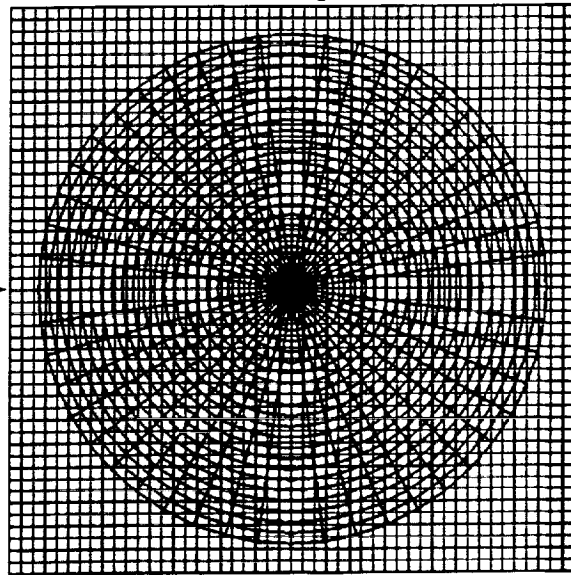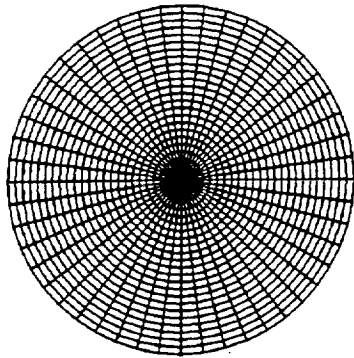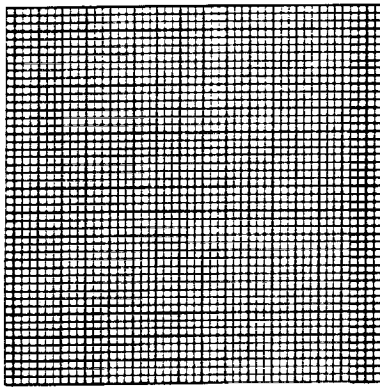
2. Composite grid creation

Blocked Grids
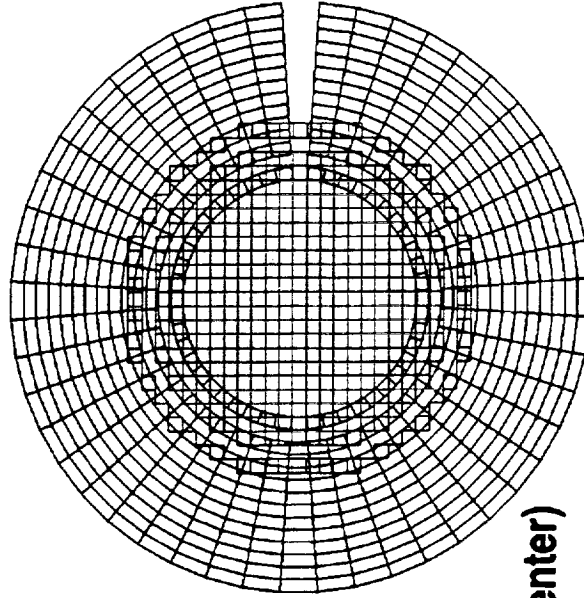
(Cell Center)

Composite Grid

CHIMERA METHOD AND CONCEPT (CONTINUED)

In this and the next view graphs, a chimera grid is constructed for a 4-element airfoil. The independently generated grids include 3 C-grids for elements 1, 2, and 3, an O-grid for element 4, and an H-grid (Cartesian grid) to serve as a farfield (outer) grid.

CHIMERA METHOD AND CONCEPT
(CONTINUED)

Given Configuration

Element 2

Element 3

Element 4

Element 1

1. Component Grid Generation

Element 1

Element 2

Element 3

Element 4

Added Outer Grid
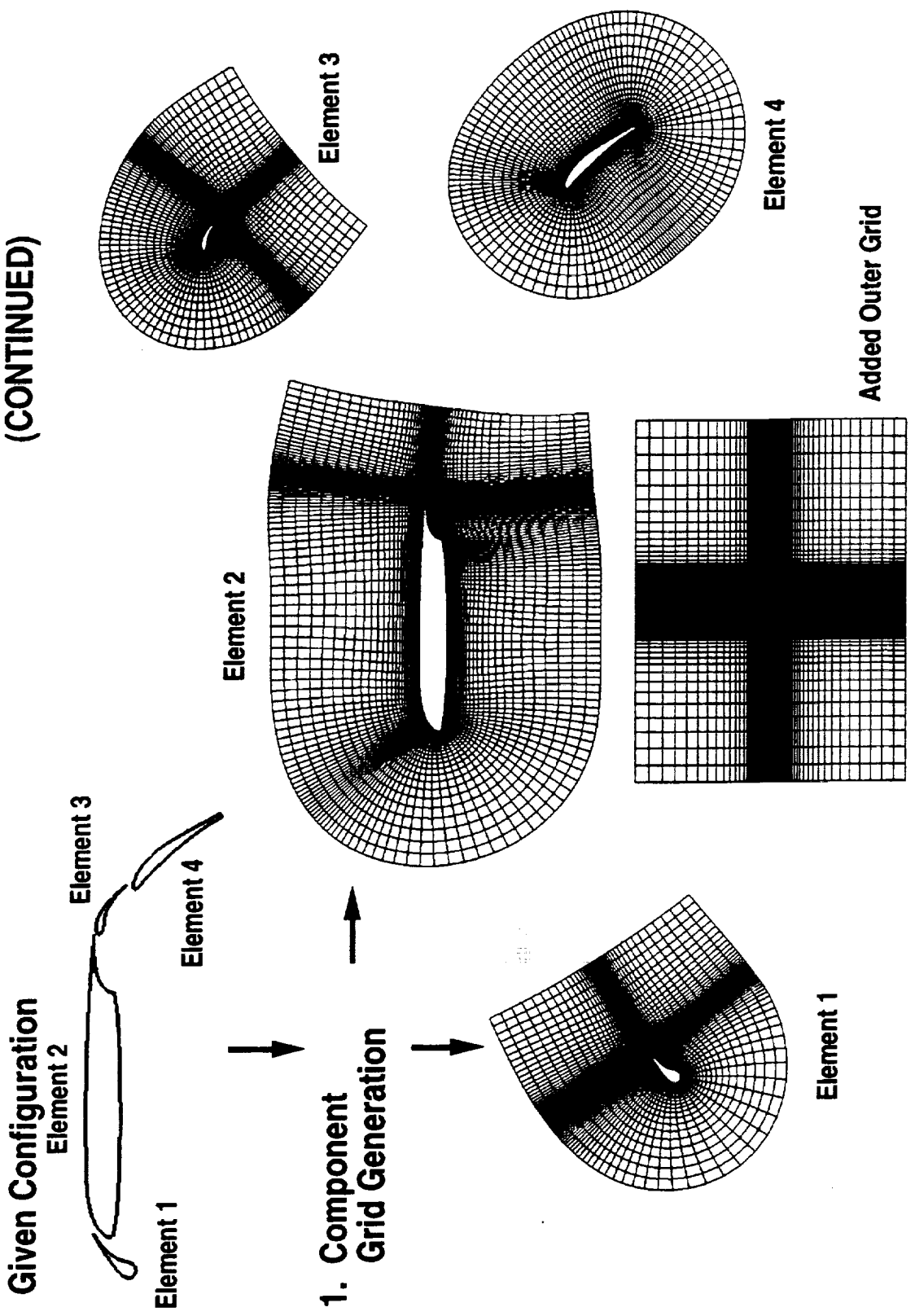
CHIMERA METHOD AND CONCEPT (CONCLUDED)

The right figure shows the constructed chimera grid of the 4-element airfoil.

The use of chimera grid may be identified as:

1) to alleviate the difficulty of generating a conventional structured grid, and

2) to optimize the number of grid points by using an H-grid with coarser grid density in the farfield.

1894

CHIMERA METHOD AND CONCEPT
(CONTINUED)

1. Component Grid Generation (Continued)
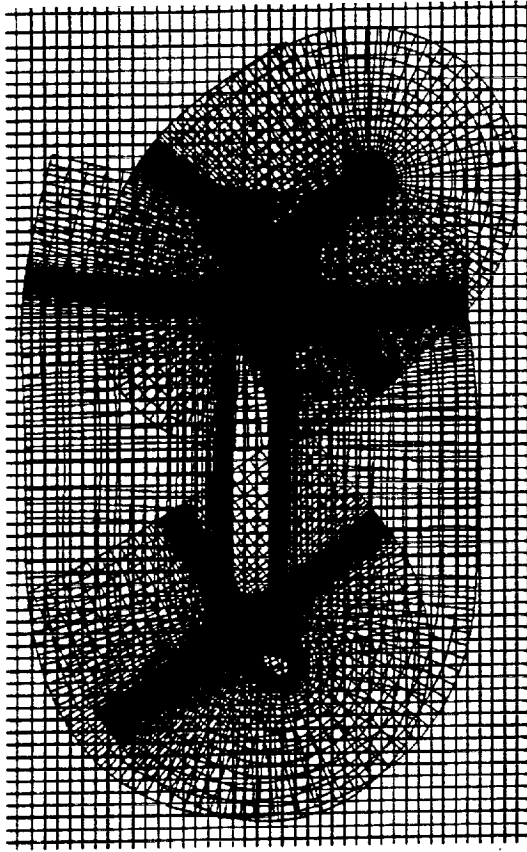
2. Composite Grid Creation
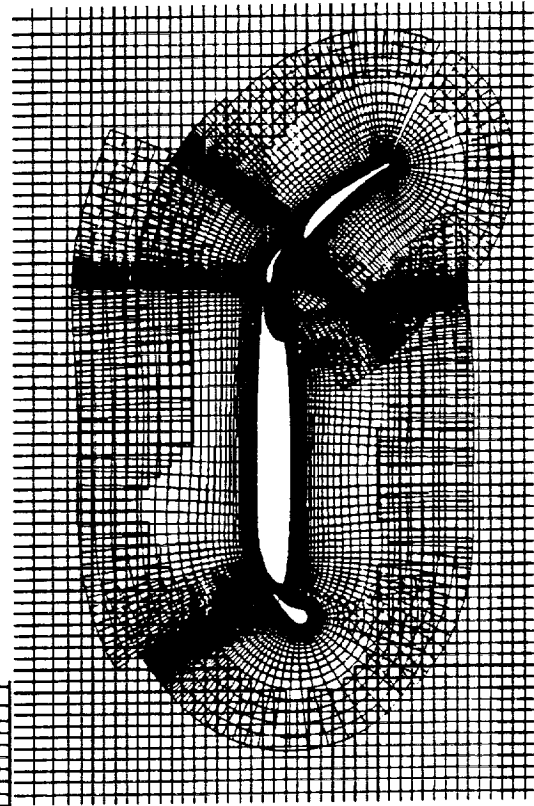
Blocked Grids

MAGGIE – AN OVERSET GRID PRE–PROCESSOR OF CFL3D

MAGGIE can be found in the CFL3D distribution package. MAGGIE is a CFL3D grid pre–processor to construct the needed chimera grid by flow solver.

Some limitations we have experienced and some modifications and enchancements we made during our applications are summarized in the following.

Limitations in the current version

1) Automatic minimax check: A hole can not be created outside a hole creation boundary.

2) Closed hole creation boundary assumption: In practical applications, there exist many situations where a well defined closed boundary is simply doesn't exist.

3) Intolerable CPU time required for a hole creation for a large grid: a single hole creation could take one CPU hour or so on Cray C90. This was mainly due to that MAGGIE checks every grid point for the hole creation. This is a very time consuming process.

Modifications and enchancements

1) User–controlled minimax check and fringe point computation: This eliminates limitation 1

2) Multi–stage hole point blanking: A hole may be created by a process of hole point elimination as done in PEGSUS. This has relaxed limitation 2.

3) Index minimax box (i–box) hole point blanking and searching: A hole may be specified directly by a set of minimax index values. It can be either inside or outside the i–box. Similarly, the grid points to be searched may be limited inside or outside the i–box during the regular MAGGIE hole creation.

4) xyz minimax box (r–box) hole point blanking and searching: A set of xyz minimax may be specified to work in a similar fashion as the i–box. Enhancements 3 and 4 have greatly reduced the number of grid points to be searched and cured limitation 3.

MAGGIE

AN OVERSET GRID PRE-PROCESSOR of CFL3D

● **Limitations in the current version**

- Automatic minimax check
- Closed hole creation boundary
- Intolerable CPU time required for hole creation for large grids

● **Modifications and enhancements**

- User-controlled minmax check and fringe point computation
- Multi-stage hole point blanking to provide PEGSUS like approach to hole creation
- Index minmax box (i-box) hole point blanking and searching
- xyz minmax box (r-box) hole point blanking and searching

MAKING MAGGIE MORE USER-FRIENDLY IN THE FUTURE

To make MAGGIE more user-friendly, the following capabilities are recommended to be implemented in the future:

1) Solution update capability: This will allow a chimera grid to be built up gradually region by region over a series of separate runs to avoid many unnecessary computations. Currently, one either has a solution or has no solution at all regardless how many computations have been done for a given run. If the solution is not completed, the entire computations must be repeated. Each run can be hours of CPU time on Cray C90 for practical problems.

2) Including the block face grids in the cell center grid: This can greatly minimize or totally eliminate the possibility of having orphan points near the block face regions due to incompatibly grid spacings used in the two adjacent grids.

MAKING MAGGIE MORE USER–FRIENDLY IN THE FUTURE

- **Solution update capability**
  - Allow a solution to be built up gradually region by region over separate runs to avoid many unnecessary computations

- **Including the block face grids in the cell center grid**
  - Can greatly minimize or totally eliminate orphan points near block boundaries

1899

DEFINITION OF PROBLEM: 4%-SCALE M2.4-7A/WIND-TUNNEL CFD

The problem of 4%-scale M2.4-7A/wind-tunnel CFD is illustrated in this view graph. The top left figure shows the model surface grid and the top right figure show the grid on the symmetry plane. The tunnel wall surface grid and the grid on the plane of symmetry are shown in the lower figure.

1900

4%–SCALE M2.4–7A/WIND–TUNNEL CFD
DEFINITION OF PROBLEM

Given:
- Free air grid of M2.4–7A
- NASA/Ames 12–ft tunnel section
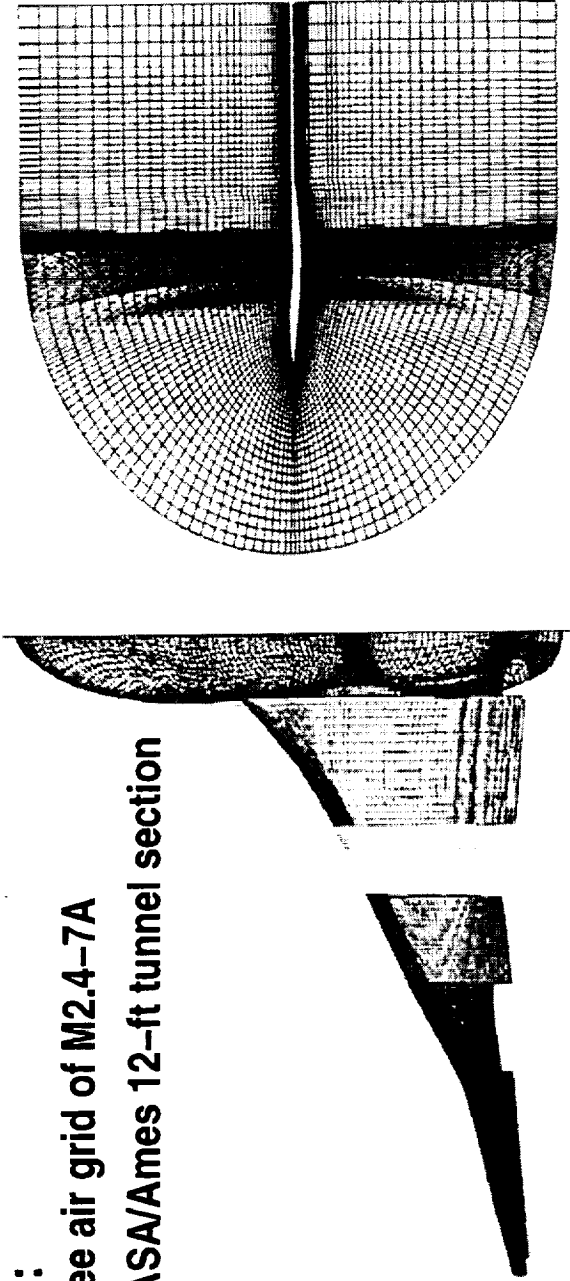
Find:
- CFD solution of 4% model inside tunnel
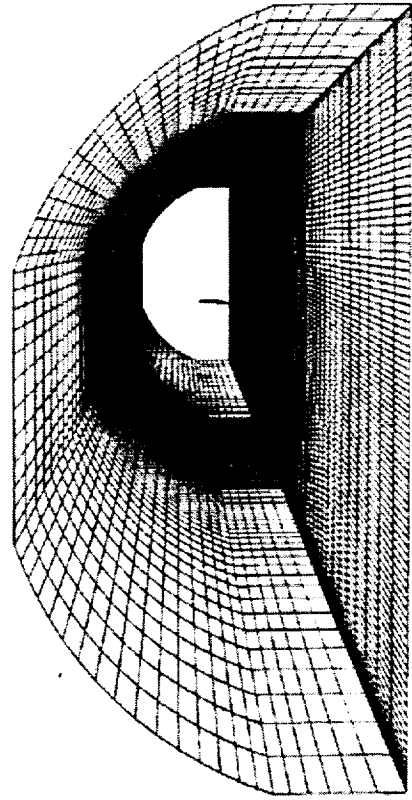
DEFINITION OF PROBLEM: 4%–SCALE M2.4–7A/WIND–TUNNEL CFD (CONCLUDED)

The free–air grid has a trailing gap due to the finite thickness of fuselage as shown in the upper figure. This gap is not suitable for creating a chimera grid at angle of attack inside the tunnel since the grid must be rotated to achieve the desired angle of attack. A mushroom grid was added to the end of the fuselage to eliminate the problem as shown in the lower figure in blue. In addition, an O–type tunnel grid was generated to complete the grid needed by flow solver as shown in green.

4%–SCALE M2.4–7A/WIND–TUNNEL CFD

Blue: 0°
Red: 10°
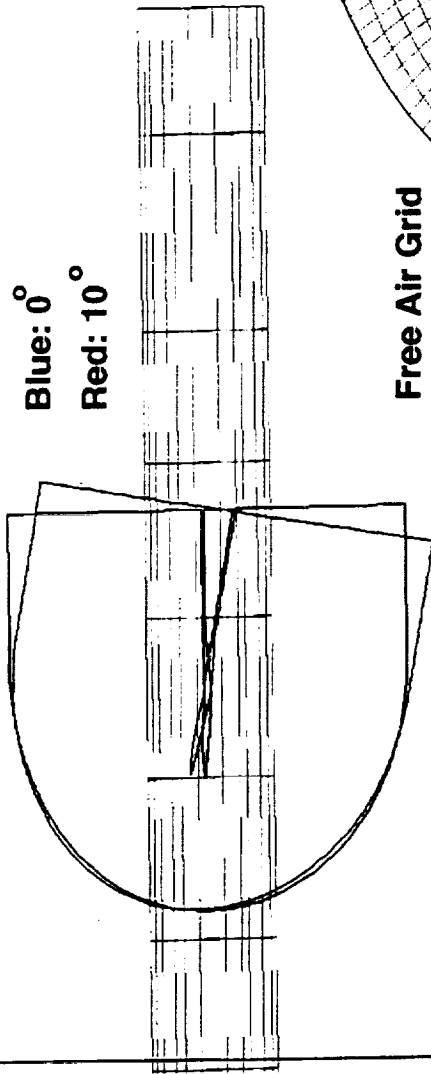
Effect of AoA on Grid

Free Air Grid
(Red)

Mushroom Grid
(Blue)

Tunnel Grid
(Green)

3 Blocked Grids

- ● Add
  - ● A tunnel grid
  - ● A mushroom grid
- ● CFL3D/MAGGIE
  - ● Chimera method

MAGGIE CALCULATED OVERSET GRID: M2.4–7A MODEL/NASA/AMES 12–FT TUNNEL

Shown in this view graph is the MAGGIE constructed overset grid in the plane of symmetry and an axial view of sectional grids. Both the field points and fringe points are shown. The grids in black are the fringe points of the model grid and those in yellow are the fringe points of the tunnel grid. The field grids are in red, blue, and green for the model, tunnel, and mushroom grids respectively.
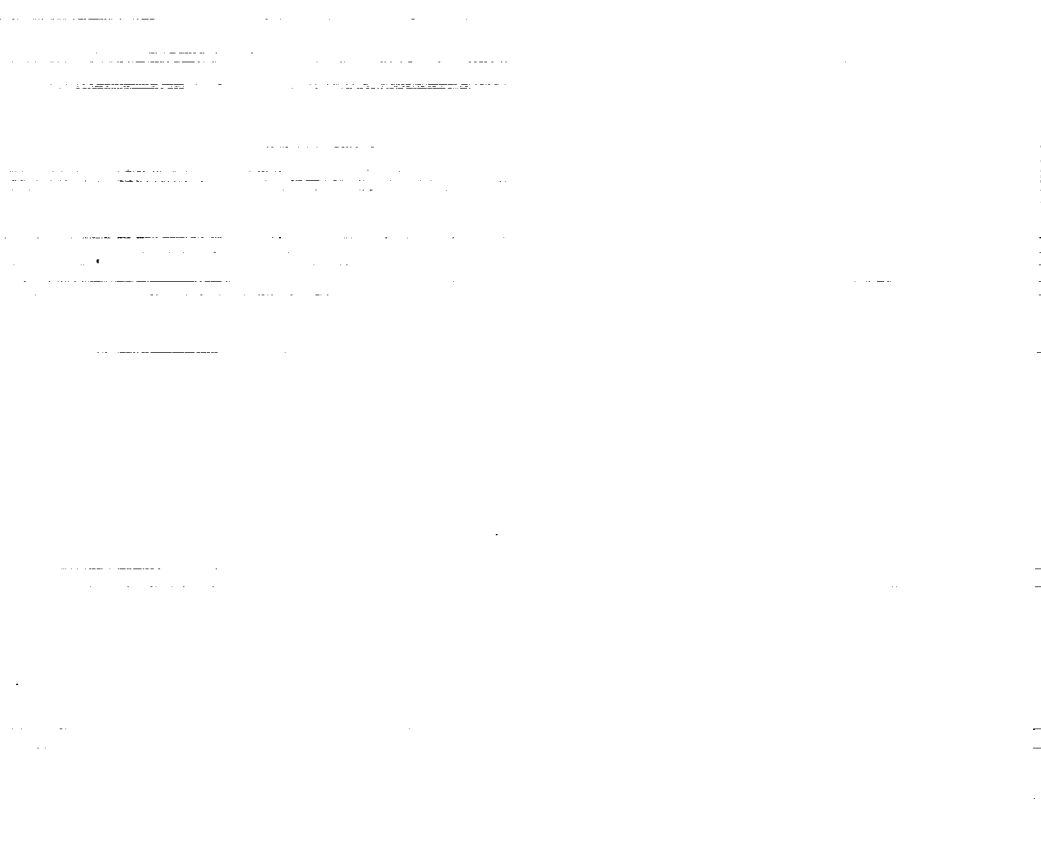
MAGGIE CALCULATED OVERSET GRID
M2.4-7A Model/NASA/AMES 12-FT TUNNEL
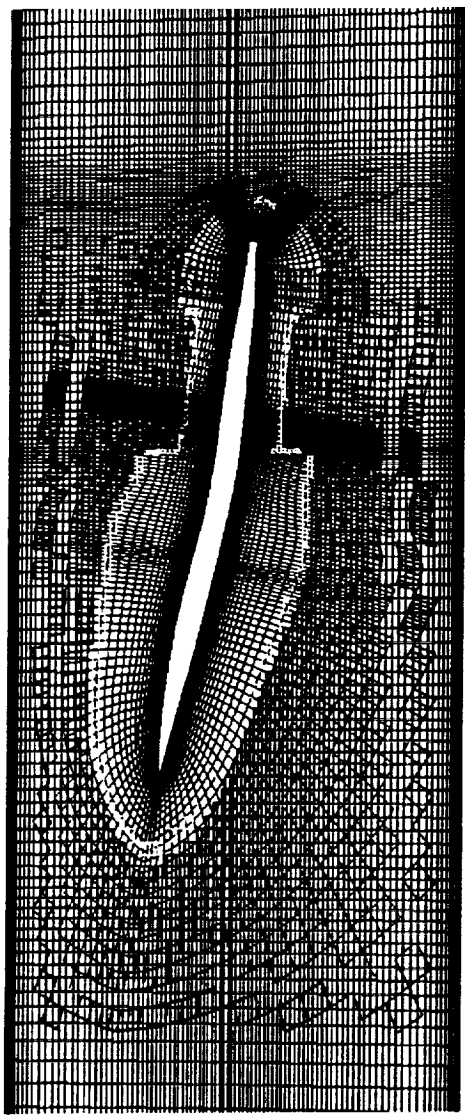
Plane of Symmetry
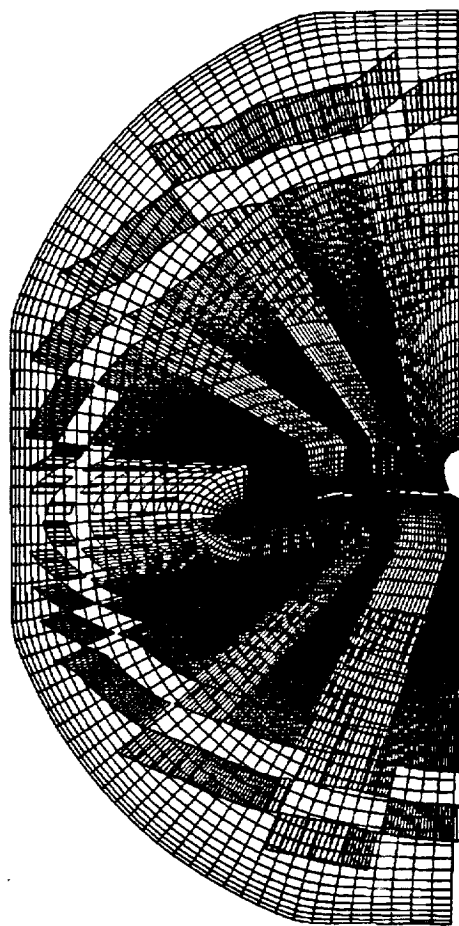
Axial View of Sectional Grids

MAGGIE CALCULATED OVERSET GRID: M2.4-7A MODEL/NASA/AMES 12-FT TUNNEL (CONCLUDED)

This is a 3D view of the chimera grid inside the NASA/Ames 12-ft wind tunnel. Only the field grids are shown.
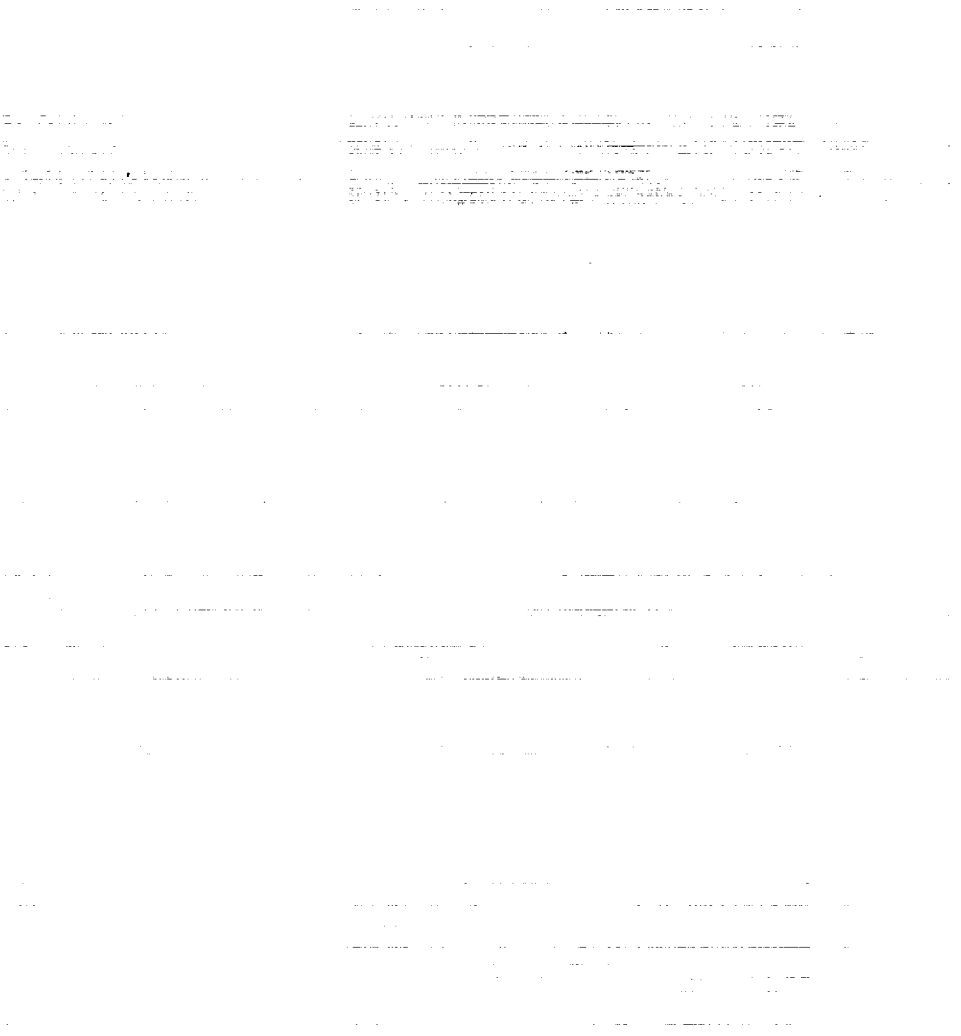
MAGGIE CALCULATED OVERSET GRID
M2.4–7A Model/NASA/AMES 12–FT TUNNEL
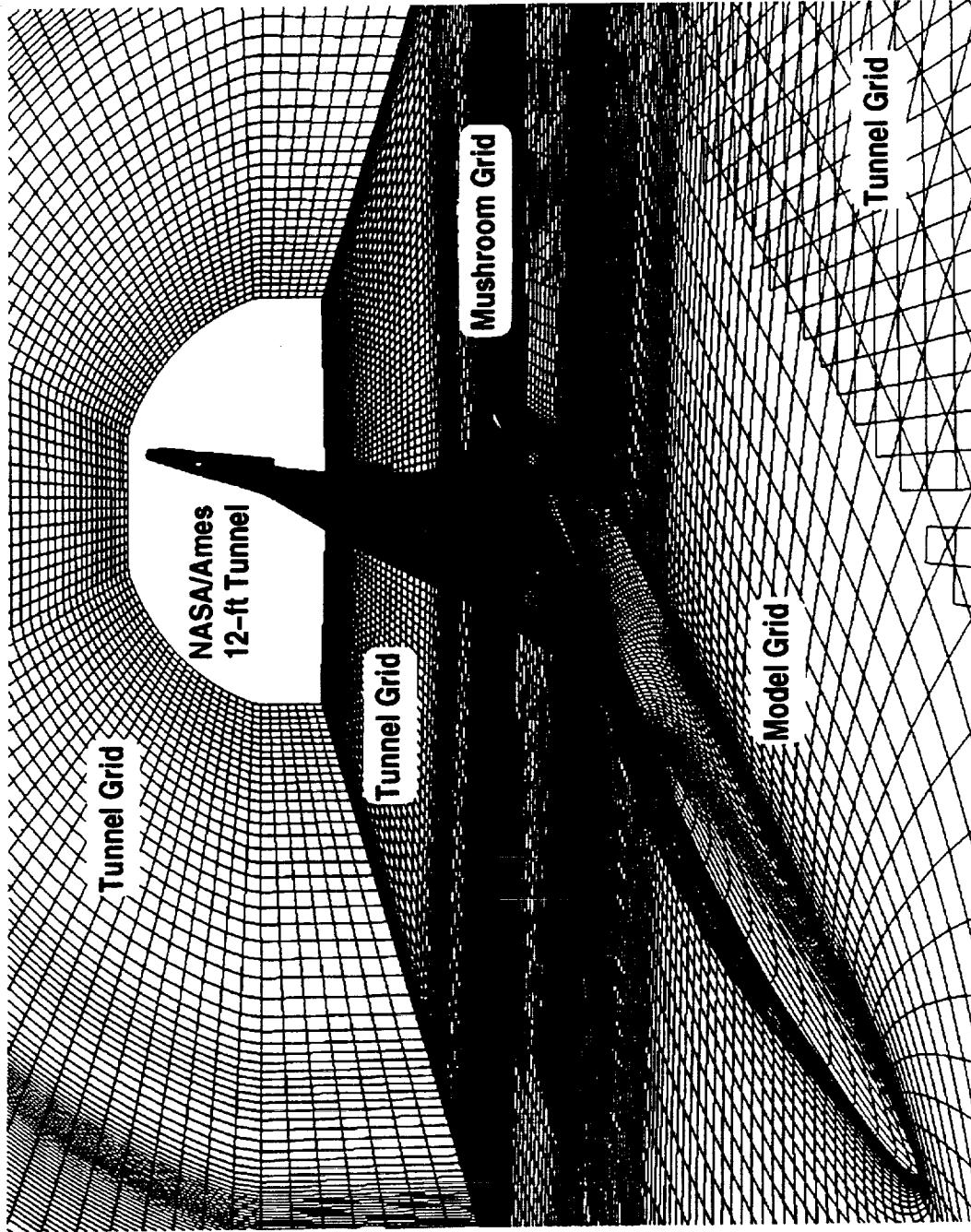
DEFINITION OF PROBLEM: 4%-SCALE M2.4-7A/WIND-TUNNEL/SUPPORT CFD

The problem of 4%-scale M2.4-7A/wind-tunnel/support CFD is illustrated in this view graph. Here, two posts were added to the model/tunnel configuration. Six grids were added to the model/tunnel grid. They are two post grids (in blue) of circular cylinder type and four collar grids (in red). It was found necessary to dense both the model and tunnel grids in the post regions in order to provide adequate overlapping regions for construction of a chimera grid.
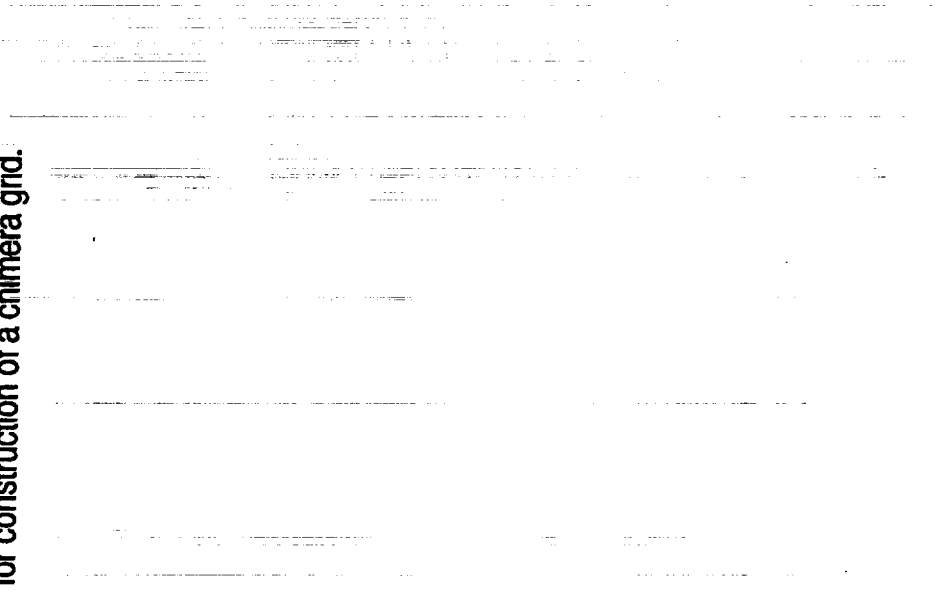
4%-SCALE M2.4-7A/WIND-TUNNEL/SUPPORT CFD
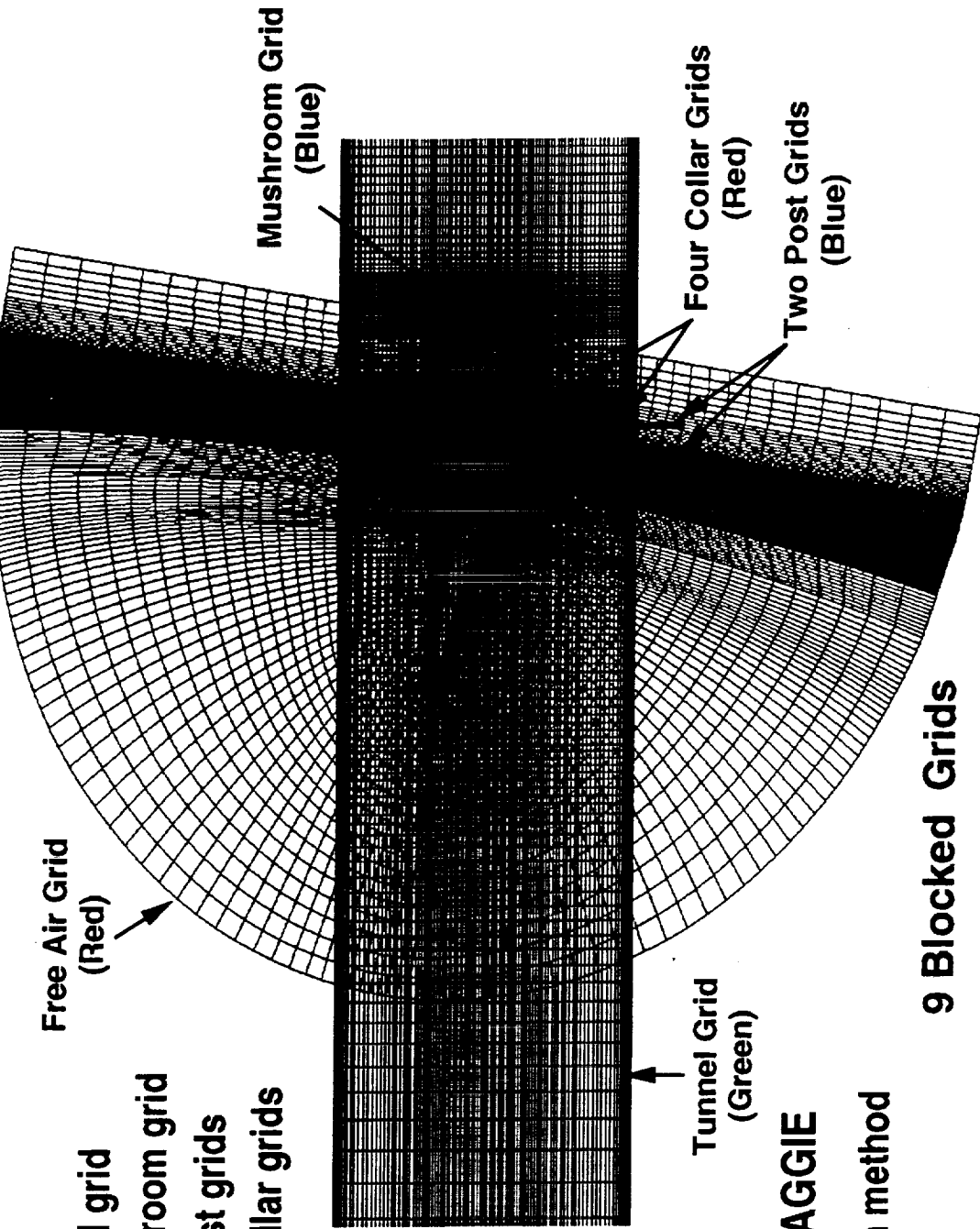
- Add
  - A tunnel grid
  - A mushroom grid
  - Two post grids
  - Four collar grids

- CFL3D/MAGGIE
  - Chimera method

Free Air Grid
(Red)

Mushroom Grid
(Blue)

Four Collar Grids
(Red)

Two Post Grids
(Blue)

Tunnel Grid
(Green)

9 Blocked Grids

MAGGIE CALCULATED OVERSET GRID: M2.4–7A MODEL/TUNNEL/SUPPORT CFD

Shown here is the MAGGIE constructed overset grid in the plane of symmetry for the model/tunnel/support case. For purpose of clarity, the fringe points are not shown. The grid consists of 9 blocked grids as indicated in the figure.
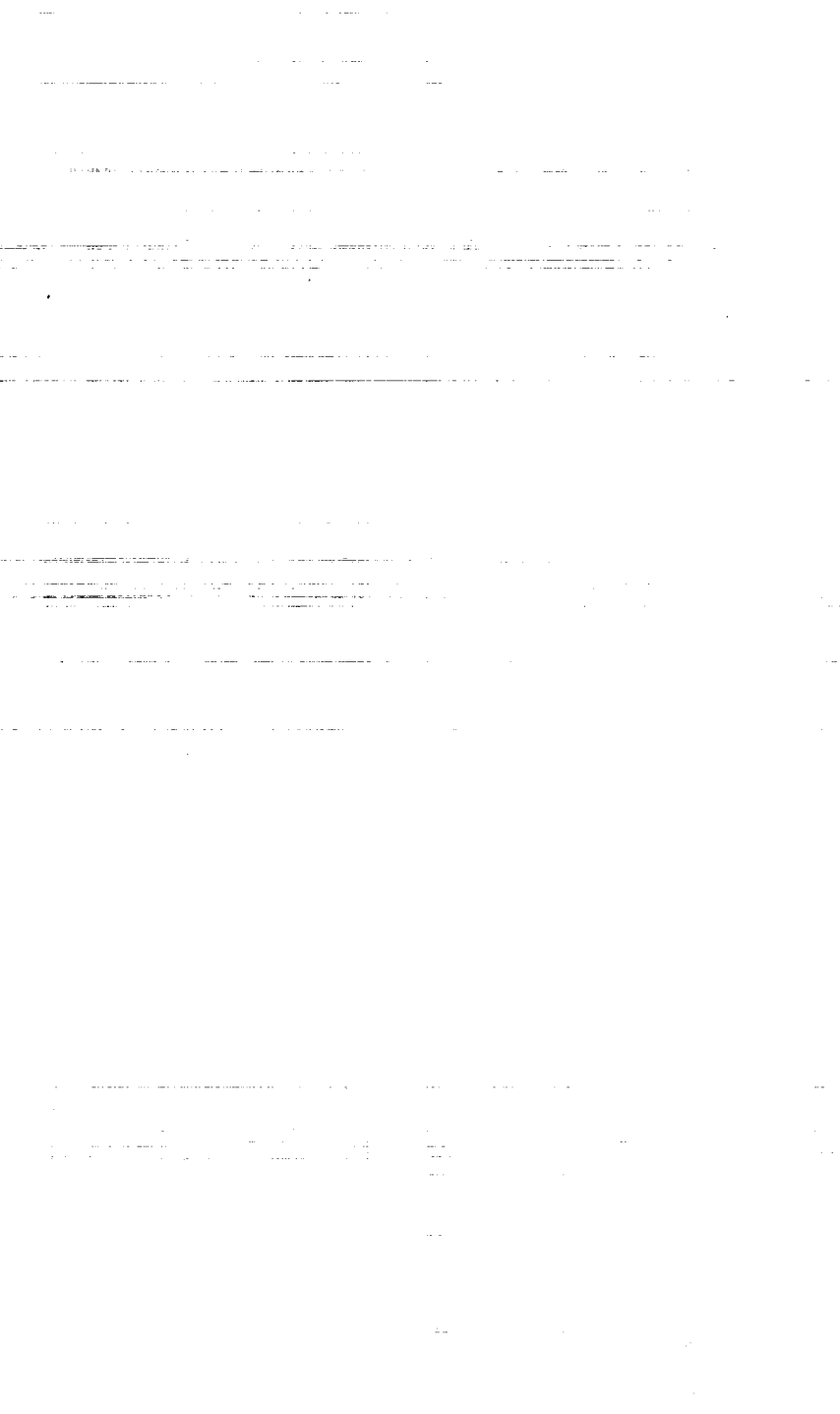
MAGGIE CALCULATED OVERSET GRID
M2.4–7A Model/TUNNEL/SUPPORT CFD

Plane of Symmetry

Tunnel Grid

Mushroom Grid

Collar Grid

Post Grid

Collar Grid

Aft Post

Collar Grid

Post Grid

Collar Grid

Fore Post

Model Grid
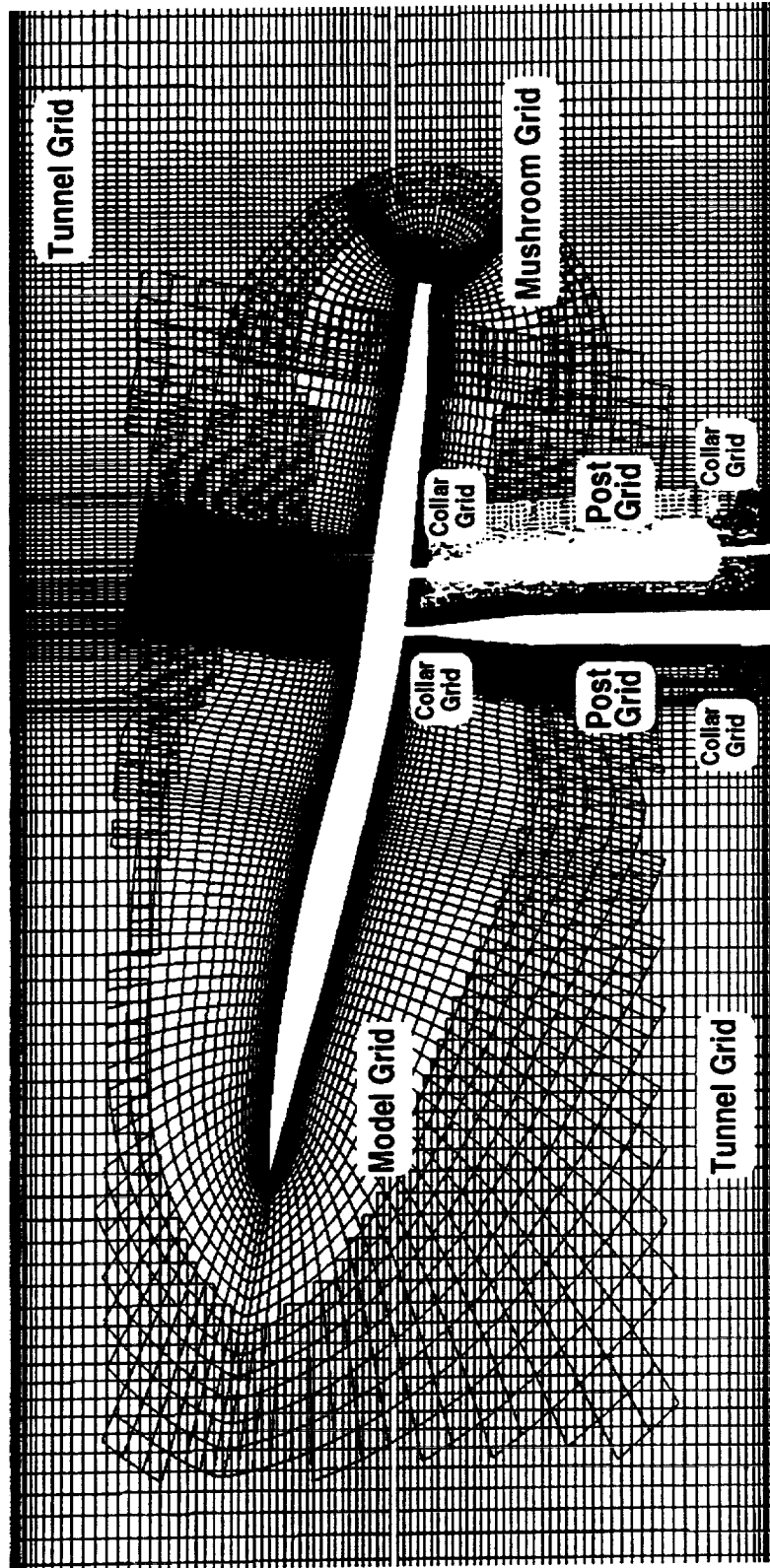
Tunnel Grid

MAGGIE CALCULATED OVERSET GRID: M2.4–7A MODEL/TUNNEL/SUPPORT CFD COLLAR GRIDS (CONTINUED)

Collar grids are used to join the post grids and model grid as shown in the left figure. The right figure shows how the post grids are joined with tunnel grid using collar grids. All the collar grids are shown in green. In general, a collar grid is a good grid topology to use at the intersection of two walls and is particularly suitable for viscous turbulent flow modeling since both walls are joined to form a single grid surface as shown in the figure.
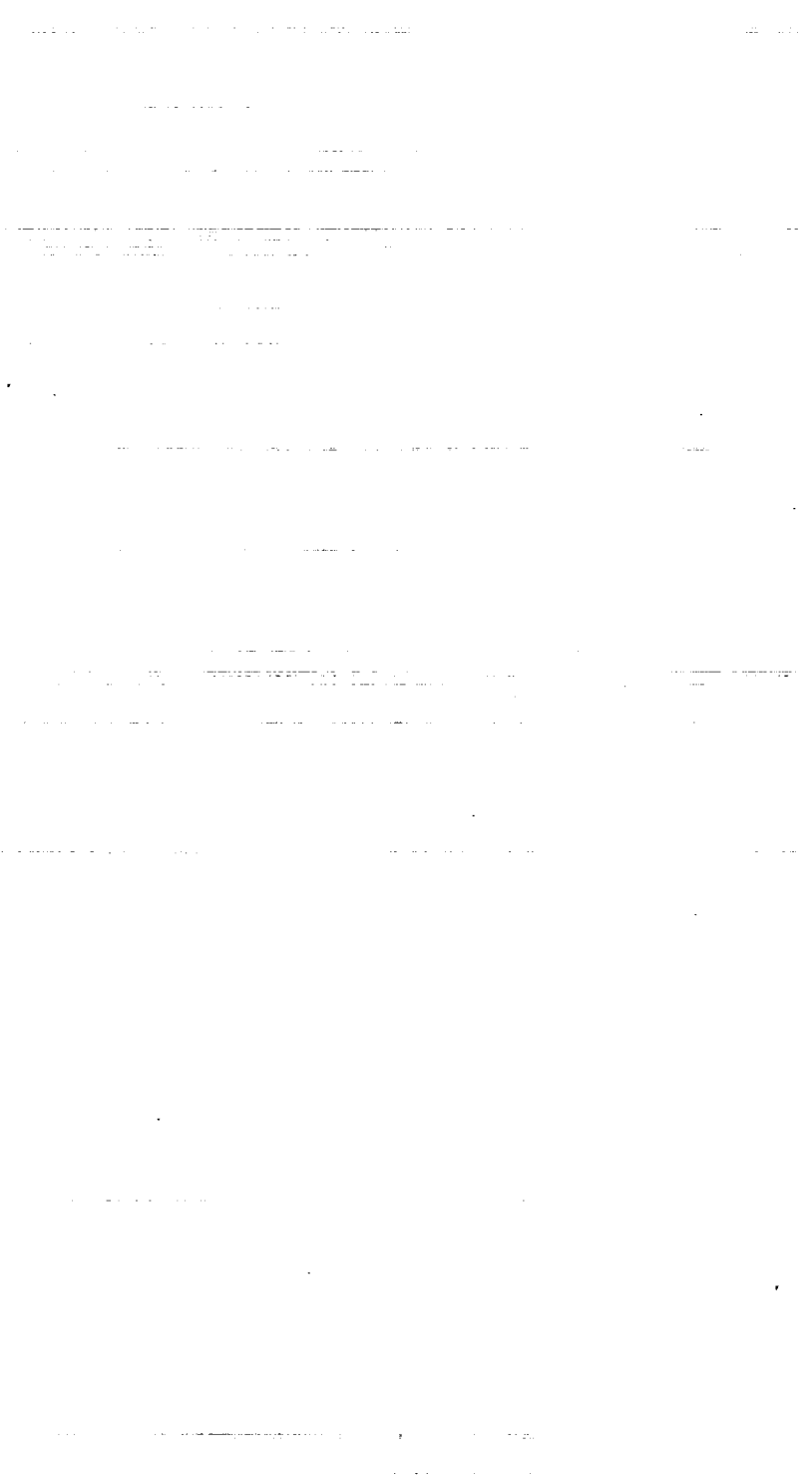
MAGGIE CALCULATED OVERSET GRID
M2.4–7A Model/TUNNEL/SUPPORT CFD

Collar Grids

Aft Post Grid

Collar Grid

Collar Grid

Fore Post Grid

Tunnel Wall Surface Grid
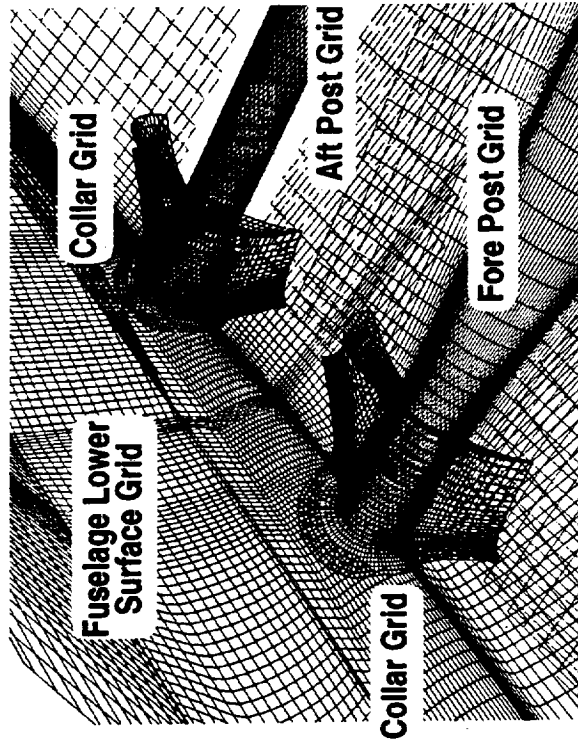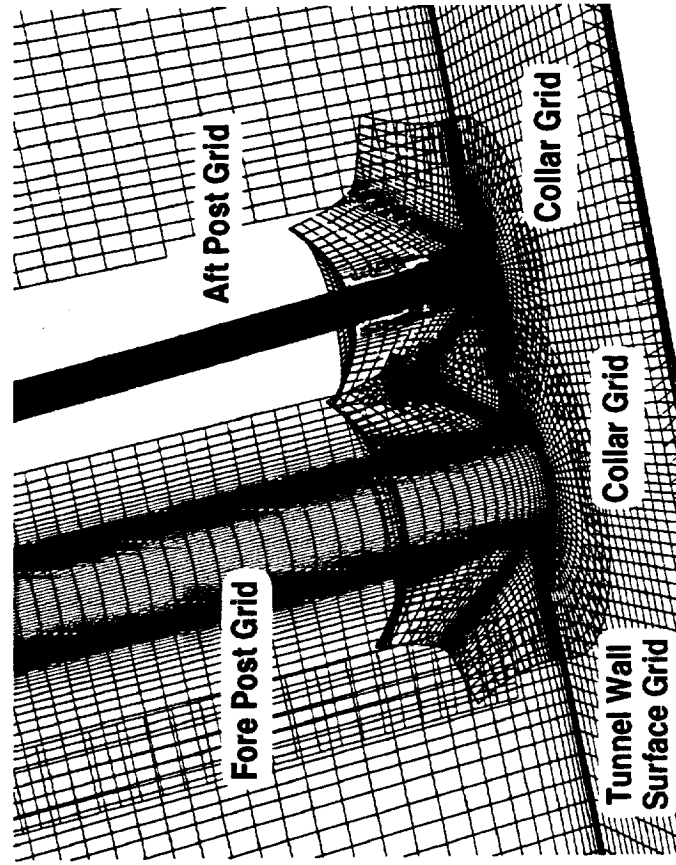
Joing Tunnel Wall and Posts

Collar Grid

Aft Post Grid

Fore Post Grid

Fuselage Lower Surface Grid

Collar Grid

Joing Model and Posts

MAGGIE CALCULATED OVERSET GRID: M2.4–7A MODEL/TUNNEL/SUPPORT CFD (CONCLUDED)

This is a 3D view of the chimera grid in the plane of symmetry inside the tunnel. The model grid is in red, the tunnel grid in green, the mushroom grid in blue, the fore post grid in cyan, and the aft post grid in yellow. For purpose of clarity, the fringe points are not shown. The model surface , the tunnel wall, and the post surfaces are shown in shadded form.

MAGGIE CALCULATED OVERSET GRID
M2.4–7A Model/TUNNEL/SUPPORT CFD

Tunnel Wall

NASA/Ames
12–ft Tunnel

Tunnel Grid

Mushroom Grid

Aft Post and Grid

Collar Grids

Fore Post and Grid

Collar Grids

Model Grid

Tunnel Grid

Tunnel Wall
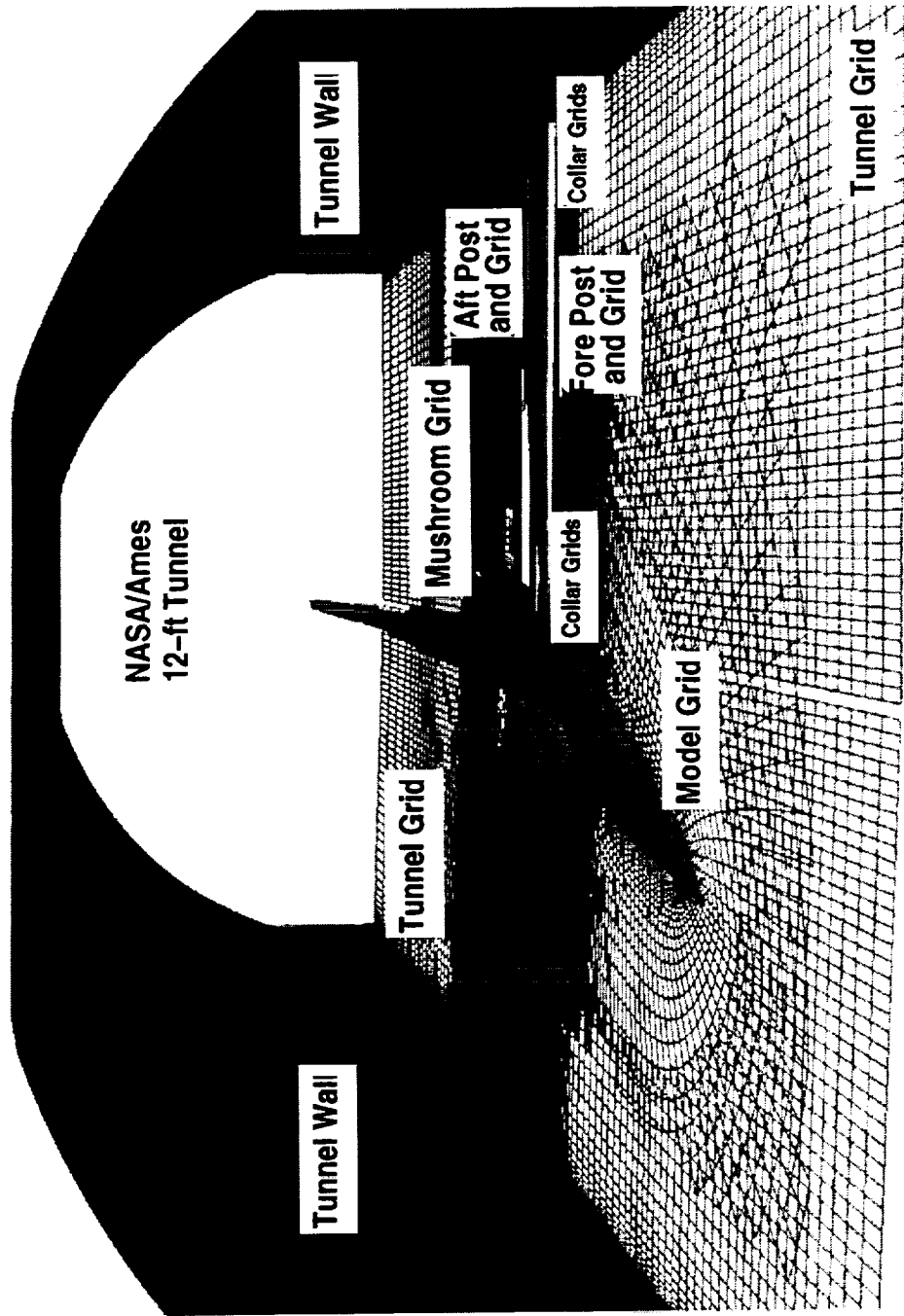
CFD PARTICLE TRACES OF 4%–SCALE M2.4–7A MODEL inside NASA/Ames 12–ft Tunnel

A CFL3D navier-stokes solution has been obtained for the 4%–scale M2.4–7A model/tunnel Configuration at Mach = 0.3, α = 10 deg. and Reynolds number of 8 million. The model has deflected LE and TE flaps of 40 and 10 degrees, respectively. This figure shows a 3D view of particle traces near the wing/body surfaces. As shown in the figure, the leading–edge vortex flow is clearly indicated by the particle traces. Also shown is the surface pressure contour with the blue color representing the low pressure and the red the high pressure.

CFD PARTICLE TRACES of 4%–SCALE M2.4–7A MODEL
Inside NASA/Ames 12–ft Tunnel
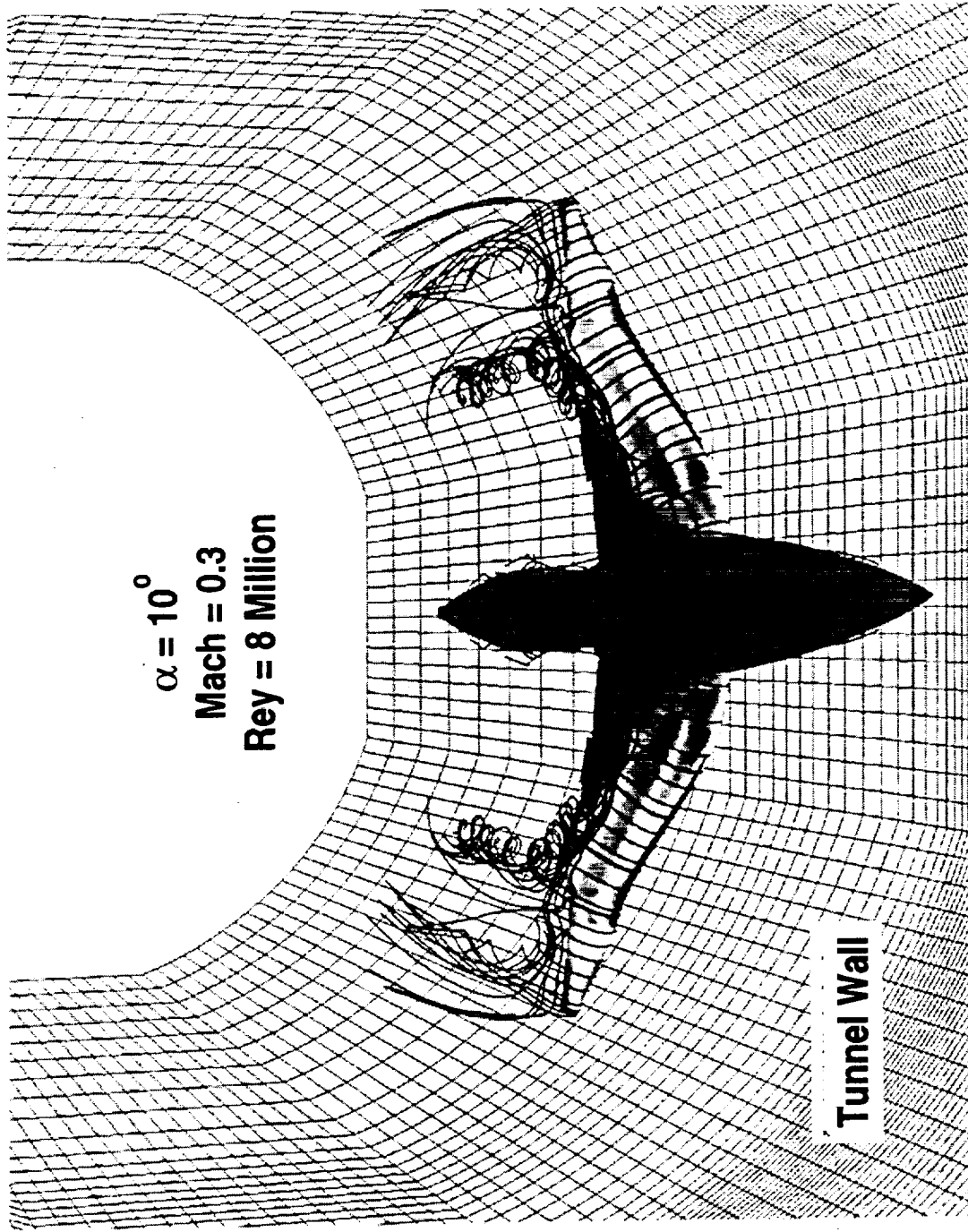
$\alpha = 10^{o}$
Mach = 0.3
Rey = 8 Million

Tunnel Wall

CFD PARTICLE TRACES OF 4%-SCALE M2.4-7A MODEL inside NASA/Ames 12-ft Tunnel (CONCLUDED)

This is a view of the particle traces from the back of the airplane.

CFD PARTICLE TRACES of 4%–SCALE M2.4–7A MODEL
Inside NASA/Ames 12–ft Tunnel

Mach = 0.3, $\alpha = 10^{\circ}$, and Rey = 8 million
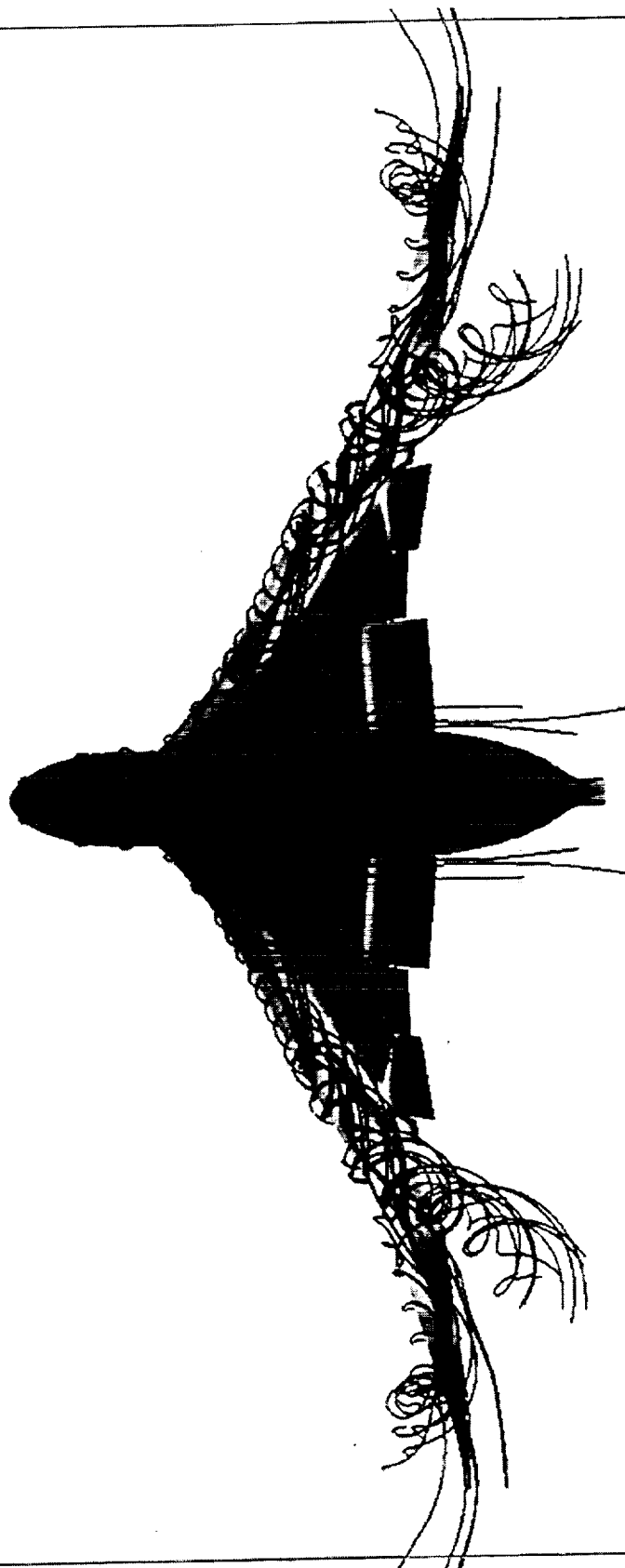
COMPARISON OF FREE–AIR AND WIND–TUNNEL CFD SIMULATION OF M2.4–7A CONFIGURATION

This figure compares the M2.4–7A upper surface pressure contours of the free–air and tunnel CFD simulations. As shown in the figure, the two surface pressure distributions look very much alike.
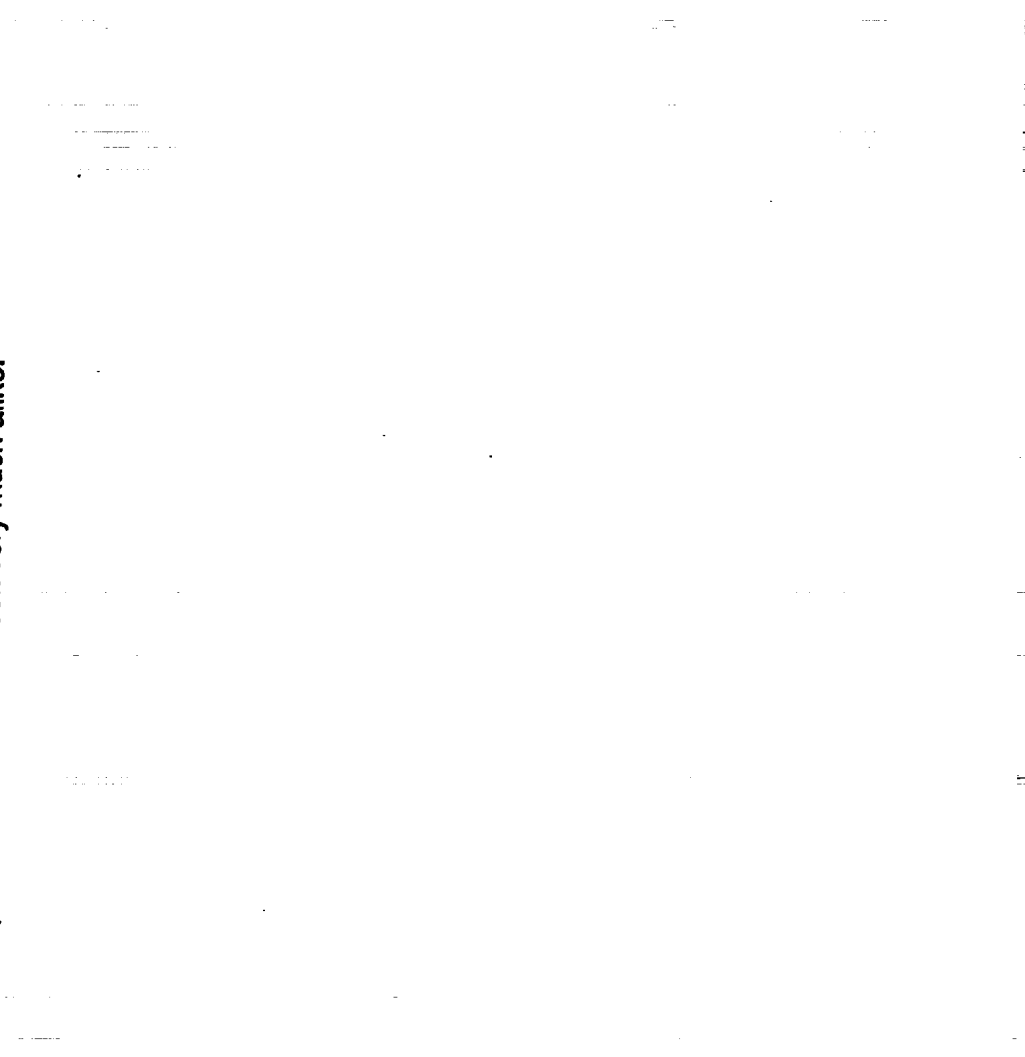
COMPARISON OF FREE–AIR AND WIND–TUNNEL CFD SIMULATIONS OF M2.4–7A CONFIGURATION

Mach = 0.3 and $\alpha = 10^\circ$

Free–Air Case

4%–Scale Model/Tunnel Case

Cp

-2.8 -2.4 -2.0 -1.6 -1.2 -0.8 -0.4 0.0 0.4 0.8

1921

COMPARISON OF CHORDWISE Cp
between Free–Air and Tunnel Cases for M2.7–7A

This figure compares the chordwise Cp distributions between the free–air and tunnel cases at 3–span stations (z = 115.25", 372.25", and 715.00"). The solid lines represent the free–air solution and the solid symbols represent the tunnel CFD solution. As shown in the figure, at each span station, both solutions, in general, agree well overall the entire chord.
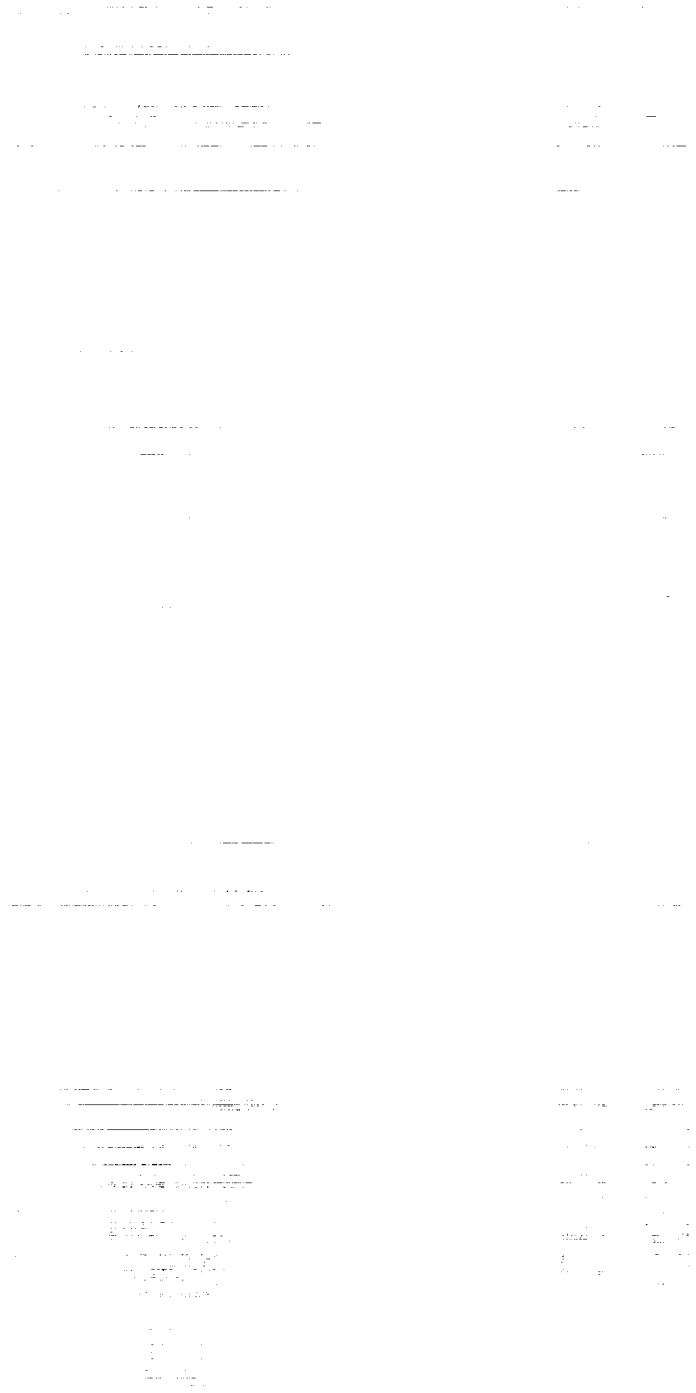
COMPARISON OF CHORDWISE Cp
between Free Air and Tunnel Cases for M2.7-7A
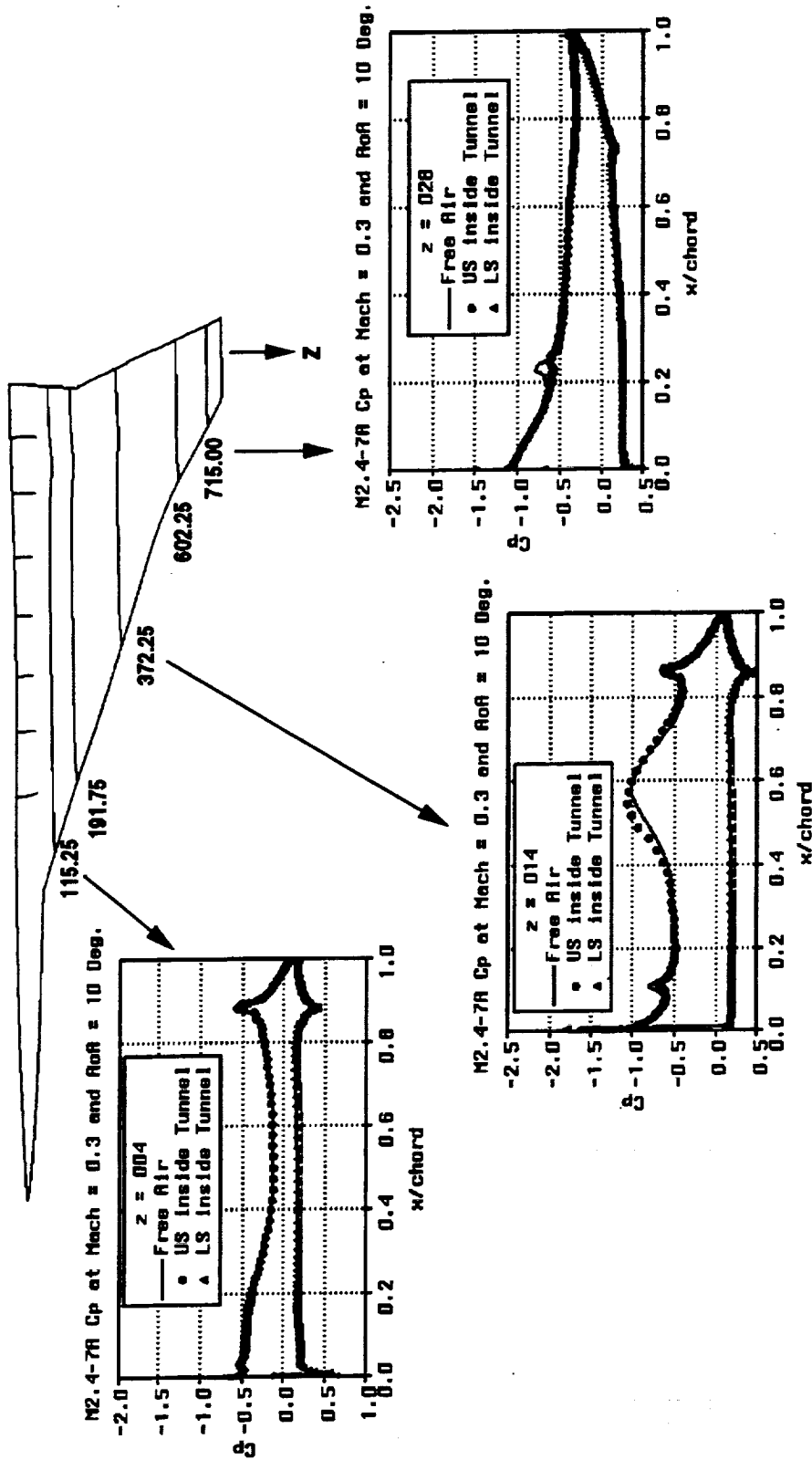
COMPARISON OF SPANWISE Cp
between Free–Air and Tunnel Cases for M2.7–7A

This figure compares the spanwise Cp distributions between the free–air and tunnel cases at 3–axial stations (x = 1546", 2227", 2445", and 2879"). The solid lines represent the free–air solution and the solid symbols represent the tunnel CFD solution. As shown in the figure, at each axial station, both solutions agree well overall the entire span except in the region near z =300" where the tunnel case predicts higher suction than the free–air case.

1924

COMPARISON OF SPANWISE Cp
between Free Air and Tunnel Cases for M2.4-7A
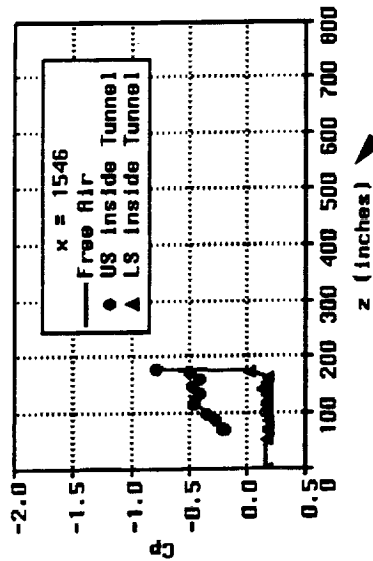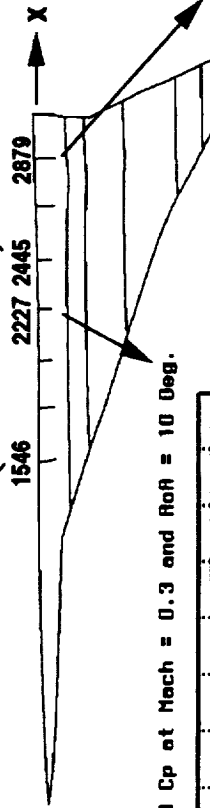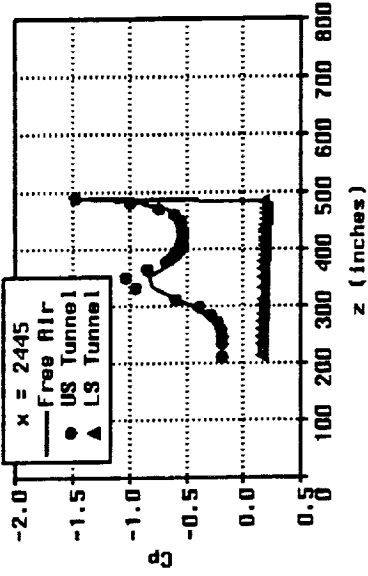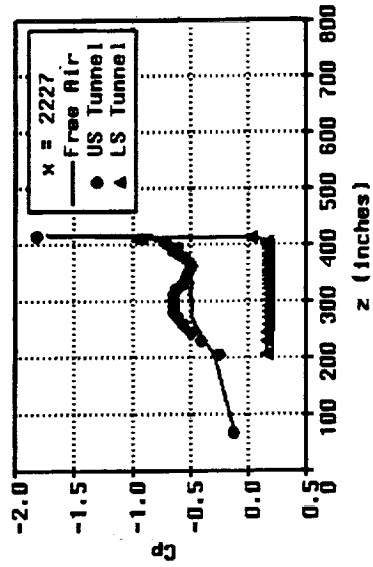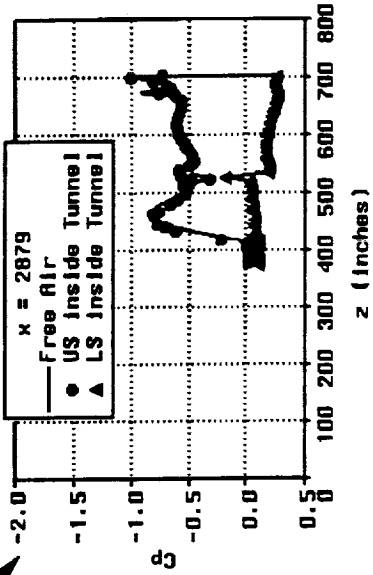
COMPARISON OF CFL3D CONVERGENCE HISTORY
between Free–Air and Tunnel Cases for M2.7–7A

The CFL3D solution convergence histories are compared here for the free–air and tunnel cases in terms of CL, Cd, Cm, and residuals. As shown in the figures, the convergence rate of the tunnel Case is slower than that of the free–air case. This is mainly due to the reflections of the waves of the initial flow disturbance at the tunnel wall.

COMPARISON OF CFL3D CONVERGENCE HISTORY
between Free Air and Tunnel Cases for M2.7-7A

CFL3D CL Time History of M2.7-7A

M = 0.3 AoA = 10 Deg
—— Free Air
······ Inside Tunnel

0.4946
0.5184

nt (Time Step)

(a) CL history

CFL3D Cd Time History of M2.7-7A

M = 0.3 AoA = 10 Deg
—— Free Air
······ Inside Tunnel

0.07147
0.07594

nt (Time Step)

(b) Cd history

CFL3D CM Time History of M2.7-7A

-0.01399
-0.07919

M = 0.3 AoA = 10 Deg
—— Free Air
······ Inside Tunnel

nt (Time Step)

(c) Cm history

CFL3D Residual Time History of M2.4-7A

M = 0.3 AoA = 10 Deg
—— Free Air
······ Inside Tunnel

nt (Time Step)
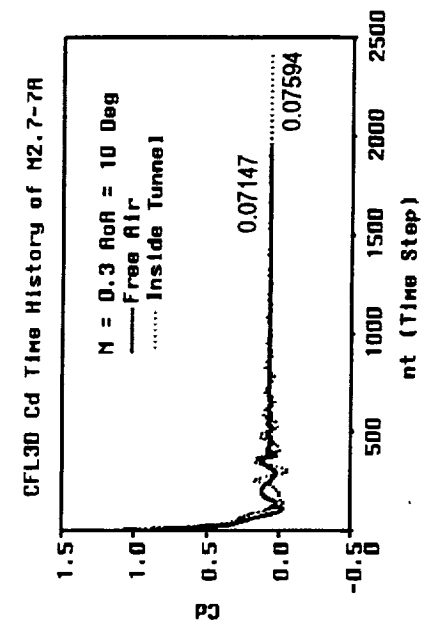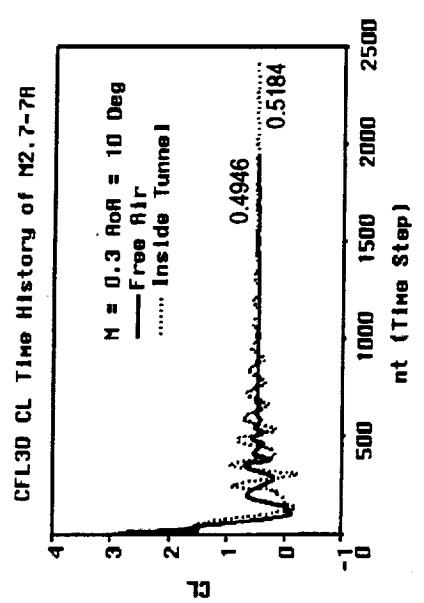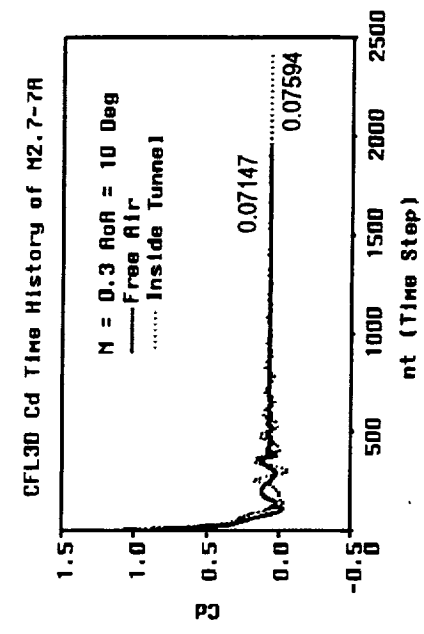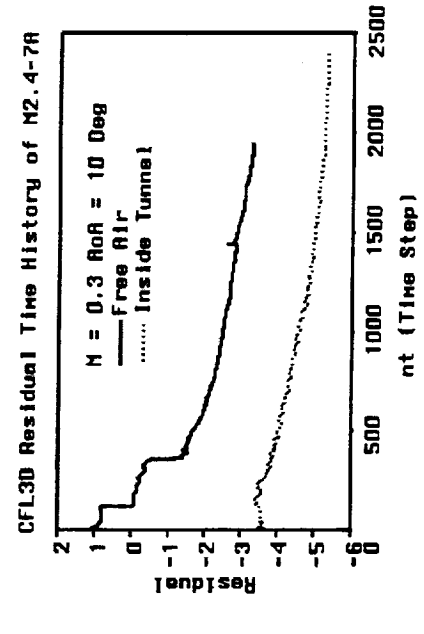
(d) Residual history

STATISTICS OF COMPUTATIONS

This table summarizes some statistics of computations for both model/tunnel case and model/tunnel/support case. The grid used in the model/tunnel case has 3 blocked grids with a total number of grid points 3,689,755. It took MAGGIE 0.93196 CPU hour on NASA/Ames NAS Cray C90 to construct a chimera grid. It took CFL3D 21.33 CPU hours on NASA/Ames NAS Cray C90 to obtain the solution presented here with 2412 time steps. The Baldwin–Lomax turbulent model was used in the flow simulation.

The grid used in the model/tunnel/support case has 9 blocked grids with a total number of grid points 6,214,873. It took MAGGIE 1.92277 CPU hour on NASA/Ames NAS Cray C90 to construct a chimera grid. Effort is currently being undertaken to perform CFL3D calculation.

The integrated CL, Cd, and Cm are also compared in this table for the free–air and model/tunnel cases. The calculated CL and Cd are higher in the tunnel case than in the free–air case and Cm is more negative in the tunnel case than in the free–air case.

STATISTICS OF COMPUTATIONS

Case	Number of Blocks	Number of Grid Points	MAGGIE CPU Time (Hrs on C90)	CFL3D CPU Time (Hrs on C90)	CFL3D Time Steps
Model/Tunnel	3	3,689,755	0.93196	21.33	2412
Model/Tunnel and Posts	9	6,214,873	1.92277	N/A	N/A

Case	CL	Cd	Cm
Free–Air	0.4946	0.07147	-0.01399
Model/Tunnel	0.5184	0.07594	-0.07919
Model/Tunnel and Posts	N/A	N/A	N/A

1929

CONCLUDING REMARKS AND FUTURE WORKS

An integrated wind–tunnel/free–air CFD analysis process has been presented and demonstrated using the 4%–scale M2.4–7A Arrow Wing configuration. The chimera grid technique has been shown to be a useful tool in our present study. A CFD grid can be built up form independently generated component grids. Therefore, a grid can be reused in various CFD configurations.

A Navier–Stokes solution for the 4%–scale M2.4–7A/wind–tunnel configuration has been obtained and compared to the free–air solution in terms of CL, Cm, Cd, and solution convergence histories.

The future works will include the completion of a Navier–Stokes solution for the M2.4–7A/wind–tunnel/support case and validation/evaluation of the CFD calculations by comparison with wind–tunnel test data.

CONCLUDING REMARKS AND FUTURE WORKS

- An integrated wind–tunnel/free–air CFD analysis process has been presented and demonstrated using the 4%–scale M2.4–7A Arrow Wing configuration

- The chimera grid technique has been shown to be a useful tool in our present study

- A Navier–Stokes solution for the 4%–scale M2.4–7A/wind–tunnel configuration has been obtained and compared to the free–air solution in terms of CL, Cm, Cd, and solution convergence histories

- The future works will include the completion of a Navier–Stokes solution for the M2.4–7A/Wind–tunnel/support case and validation/ evaluation of the CFD calculations by comparison with wind– tunnel test data

THIS PAGE IS INTENTIONALLY LEFT BLANK

RESULTS OF A WINGDES2/AERO2S FLAP OPTIMIZATION FOR THE TCA

Steven F. Yaros

Aero- and Gas- Dynamics Division

Subsonic Aerodynamics Branch

NASA Langley Research Center

February 25, 1997

Steven F. Yaros
Mail Stop 286
NASA Langley Research Center
Hampton, VA 23681-0001

757-864-3050
757-864-8192 (FAX)
s.f.yaros@larc.nasa.gov

Bibliography

- *Design of Supersonic Transport Flap Systems for Thrust Recovery at Subsonic Speeds;* Mann, Michael J., Carlson, Harry W., and Domack, Christopher S.; NASA/TP-1999-209536, December 1999.

- *Survey and Analysis of Research on Supersonic Drag-Due-to-Lift Minimization with Recommendations for Wing Design;* Carlson, Harry W. and Mann, Michael J.; NASA TP 3202, September 1992.

- *Validation of a Computer Code for Analysis of Subsonic Aerodynamic Performance of Wings with Flaps in Combination with a Canard or Horizontal Tail and an Application to Optimization;* Carlson, Harry W., Darden, Christine M., and Mann, Michael J.; NASA TP 2961, January 1990.

- *Validation of a Pair of Computer Codes for Estimation and Optimization of Subsonic Aerodynamic Performance of Simple Hinged-Flap Systems for Thin Swept Wings;* Carlson, Harry W. and Darden, Christine M.; NASA TP 2828, 1988.

- *Applicability of Linearized-Theory Attached-Flow Methods to Design and Analysis of Flap Systems at Low Speeds for Thin Swept Wings with Sharp Leading Edges;* Carlson, Harry W. and Darden, Christine M.; NASA TP 2653, 1987.

There are many documents that describe the theory and usage of the linearized-flow approach over the years. The author feels that the documents listed above are chronologically significant in the history of the development of the codes, including many successful optimizations. The first document was found to be especially interesting, since the configurations described therein were similar to the TCA configuration. The method used herein is essentially identical to the method used in that report. Many of the authors are still available for consultation, and thus technical help was easy to obtain.

Analytical Background of Computer Codes

- Two codes, WINGDES2 and AERO2S, based on linear, attached-flow theory

- Nearly-attached flow ⟶ high aerodynamic efficiency

- Estimate of attainable leading-edge thrust and representation of vortex forces

- Actual performance comparable to that of a flat wing with full leading-edge thrust

NASA Langley Research Center
Hampton, VA 23681-0001

The assumption is made that a high level of aerodynamic efficiency results from a flow that is nearly as attached as possible, minimizing the real-world effects of flow separation.

The method includes an estimate of attainable leading-edge thrust and an approximate representation of vortex forces.

The combination of attainable leading-edge thrust and dustributed thrust produces performance comparable to that of a flat wing with full leading-edge thrust.

WINGDES2

- Mildest camber surface that will produce optimum performance

- A "design moment coefficient" is determined from an initial "whole-wing design"

- Subsequent runs are carried out with flap areas specified

- Result is set of flap deflections that approximate the optimum camber design

- Does not make a performance analysis based on the wing with deflected flaps

NASA Langley Research Center
Hampton, VA 23681-0001

The code defines the mildest camber surface at specified values of lift and pitching moment.
The "whole-wing design", with no pitching moment constraint, is used initially in order to improve trailing-edge flap specifications.

AERO2S

- Used to estmate the aerodynamic performance of the wing with deflected flaps

- Results are modified to include attainable leading-edge thrust and the forces due to vortices

- Measure of performance is the Suction Parameter, which compares the drag of the configuration with upper and lower bounds

$$S_s = \frac{C_L \tan(C_L/C_{L_a}) - \Delta C_D}{C_L \tan(C_L/C_{L_a}) - C_L^2/(\pi AR)}$$

- AERO2S runs are made at a matrix of multiples of leading-edge and trailing-edge flap deflections

- Optimum flap defections chosen from the maximum Suction Parameter point on a contour plot whose axes are the multiples of the nominal flap deflections

5 of 14

NASA Langley Research Center
Hampton, VA 23681-0001

The forces due to vortices are produced by leading-edge flow separation.
The upper bound of the Suction Parameter is the drag of a flat wing with no leading-edge thrust and no vortex force. The lower bound is the drag of a wing with an elliptical spanwise load distribution and full leading-edge thrust.

INPUT DATA

- Data for both codes were obtained from LaRC data files that were extracted from Boeing data generated during lofting

sfy 24may96 020 TCA-6 Flopt 01 Cldes=0.5, Cmdes=-0.0141

$INPT1

NPLOT=1, PFILE='wdes_020.xyp', ELAR=1.,

XM=.35, JBYMAX=18, CLDES=0.50, CMDES=-0.0141, IPRSLD=0, IVOROP=1,

RN=210., IEMPCR = 0, CBAR= 94.952, XMC=190.38, NGCS=0, IFLPDES = 1,

NLEY=20, NTEY=20, XMAX= 247.4100, SREF= 8500.0000, NYC=20,

NPCTC=20, NYR=20,

TBLEY= 0.0000, 1.6400, 3.2810, 5.6660, 5.6670, 7.3750, 9.8330,

15.4840, 17.0920, 19.6890, 22.9710, 26.2520, 29.5340, 30.8580, 35.7900,

...

NASA Langley Research Center
Hampton, VA 23681-0001

Thanks to Lori Ozoroski, NASA Langley Research Center, for providing the data files for both the WINGDES2 and AERO2S codes. The automatic production of the data files during lofting computations saved a great deal of tedious data extraction and specification.

TCA Wing Planform with Part-Span Flaps
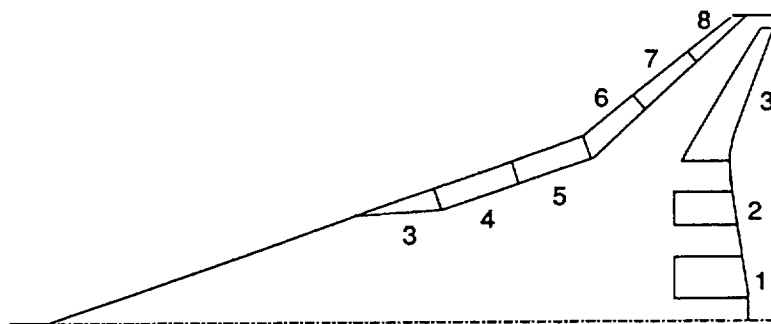
NASA Langley Research Center
Hampton, VA 23681-0001

The numbering system of the flaps has occasionally var-
ied. The system shown above will be used in this paper,
along with an extended version of it for the full-span flaps.
Identical flap numbers will be differentiated by specifying
"leading-edge" or "trailing-edge".

Optimized Distribution of Part-Span Flaps
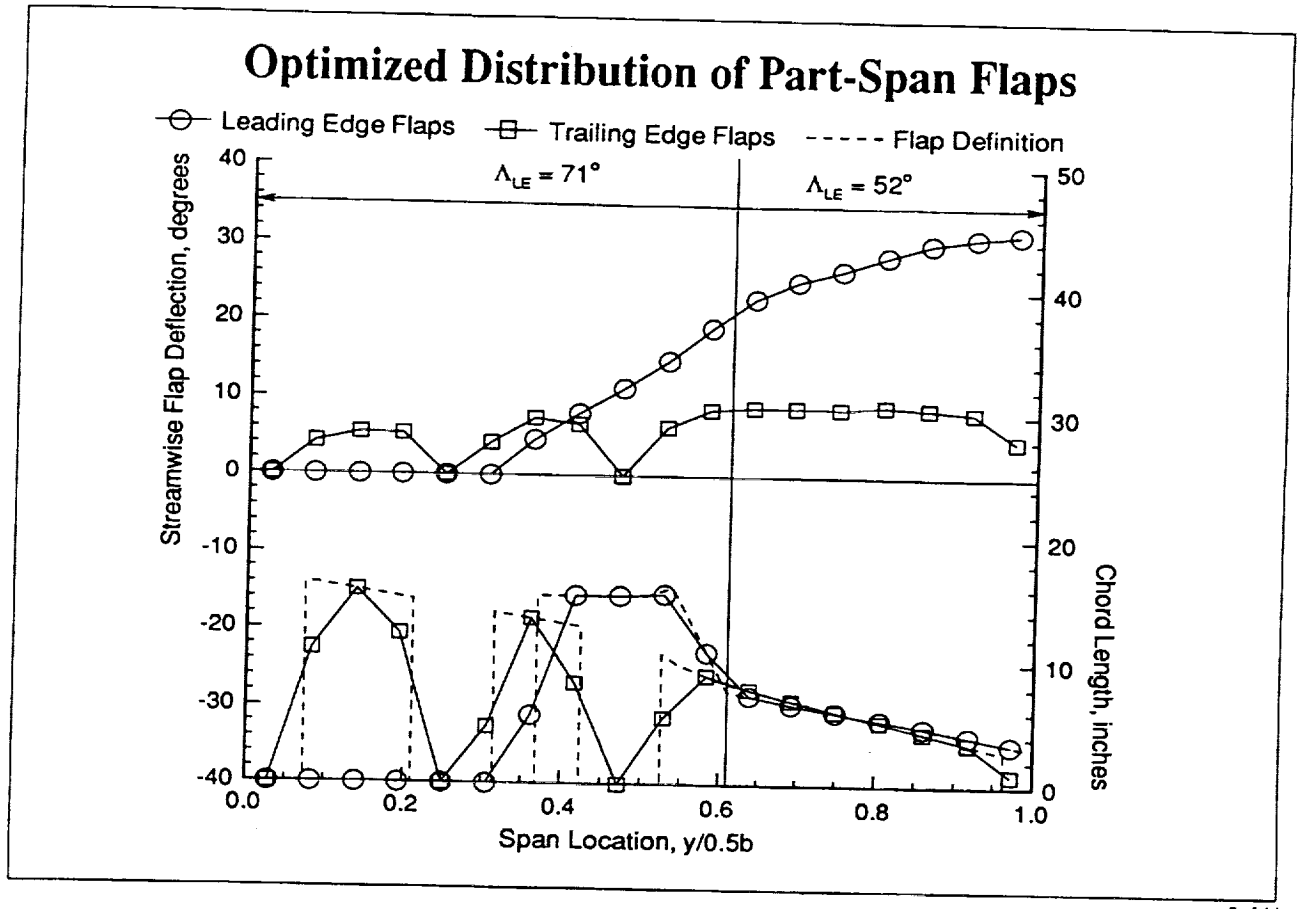
NASA Langley Research Center
Hampton, VA 23681-0001

The upper curves correspond to the left-hand-side axis, and the lower curves to the right-hand-side axis.
Since the span of the wing is divided into a finite number of strips for the flap analysis, strips that include non-flap areas show their chord lengths reduced accordingly.
The flaps angles are measured in the streamwise direction.

Flap Deflection Schedule Used in AERO2S
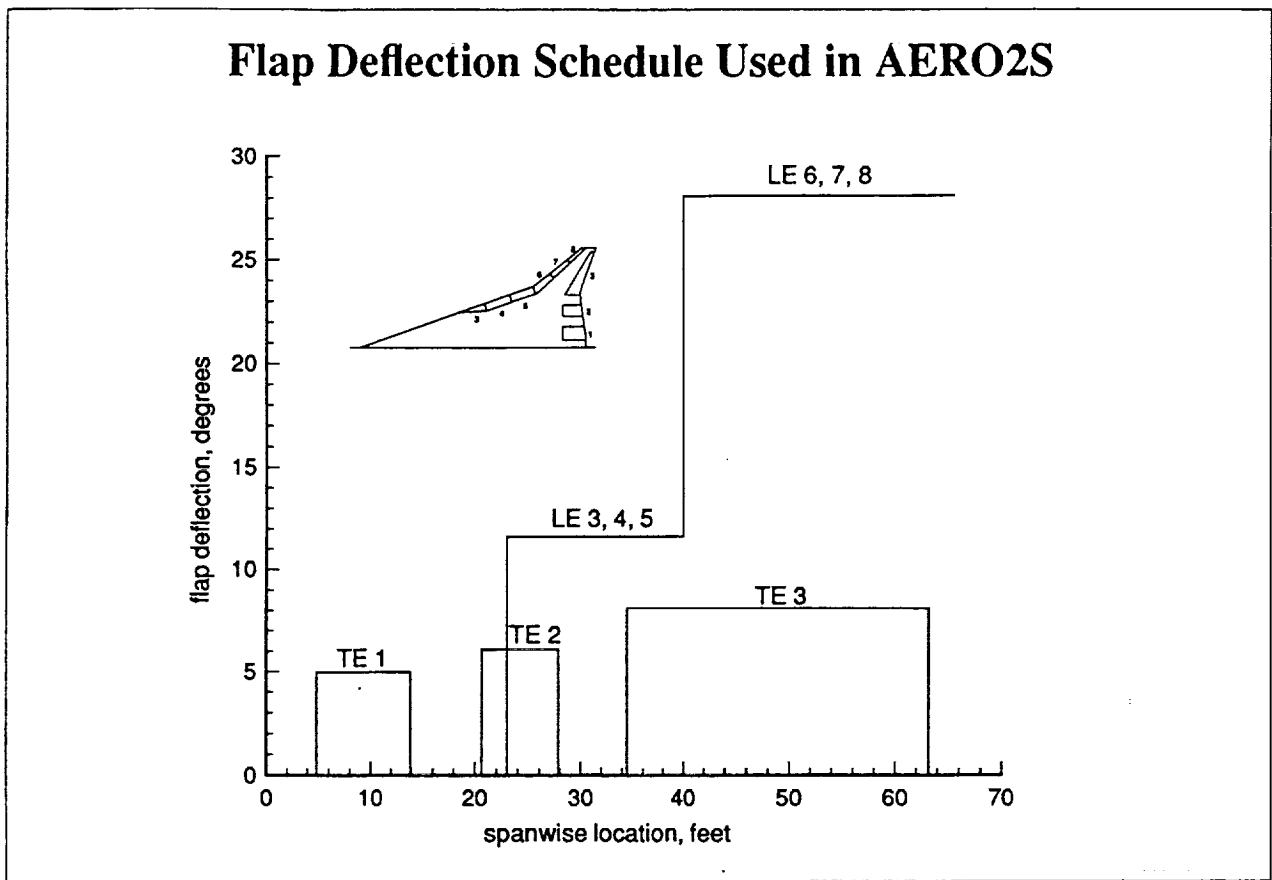
The average value of flap deflection was calculated and specified as the nominal value for that flap. Flap deflections are still specified in the streamwise direction.

Suction Parameter Contours
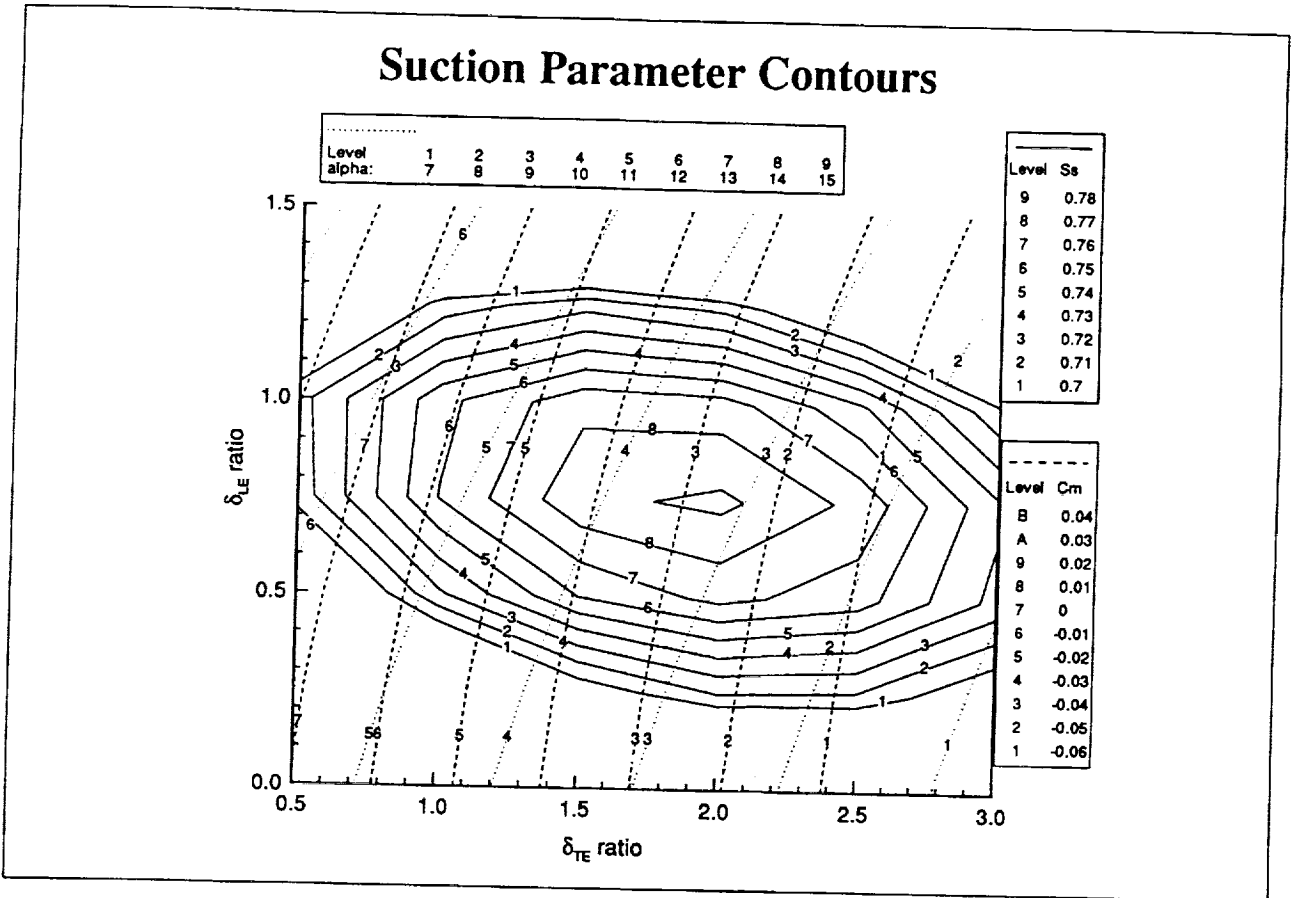
The nominal values of the flap deflections are multiplied as TE and LE groups by weighting factors ranging from 0 to 3 (for this configuration) to obtain deflection ratios δ_{TE} and δ_{LE}. The resulting Suction Parameters are plotted against these ratios. An optimum Suction Parameter is apparent near $\delta_{TE} = 2$ and $\delta_{LE} = 0.75$. Also plotted are angle of attack and pitching moment coefficient.

The large number of individual calculations were carried out in a day or two, as AERO2S ran very quickly on our mainframes.

TCA Wing Planform with Full-Span Flaps
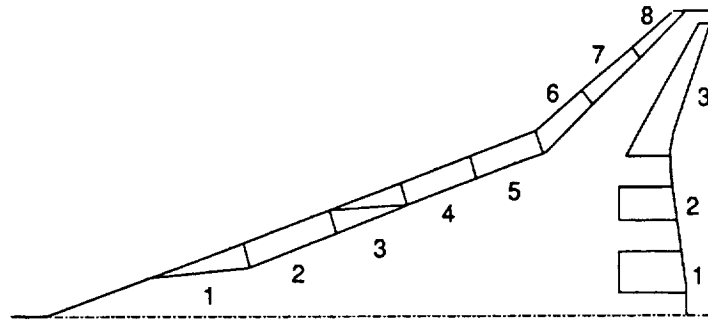
NASA Langley Research Center
Hampton, VA 23681-0001

A second configuration was analyzed, the full-flap config-
uration, in which LE flap 3 is made a full flap, and LE
flaps 1 and 2 are added. All of the leading-edge flap deflec-
tions were then re-optimized, as were the trailing-edge flap
deflections. The trailing-edge flap configuration remained
the same in extent.

Optimized Distribution of Full-Span Flaps
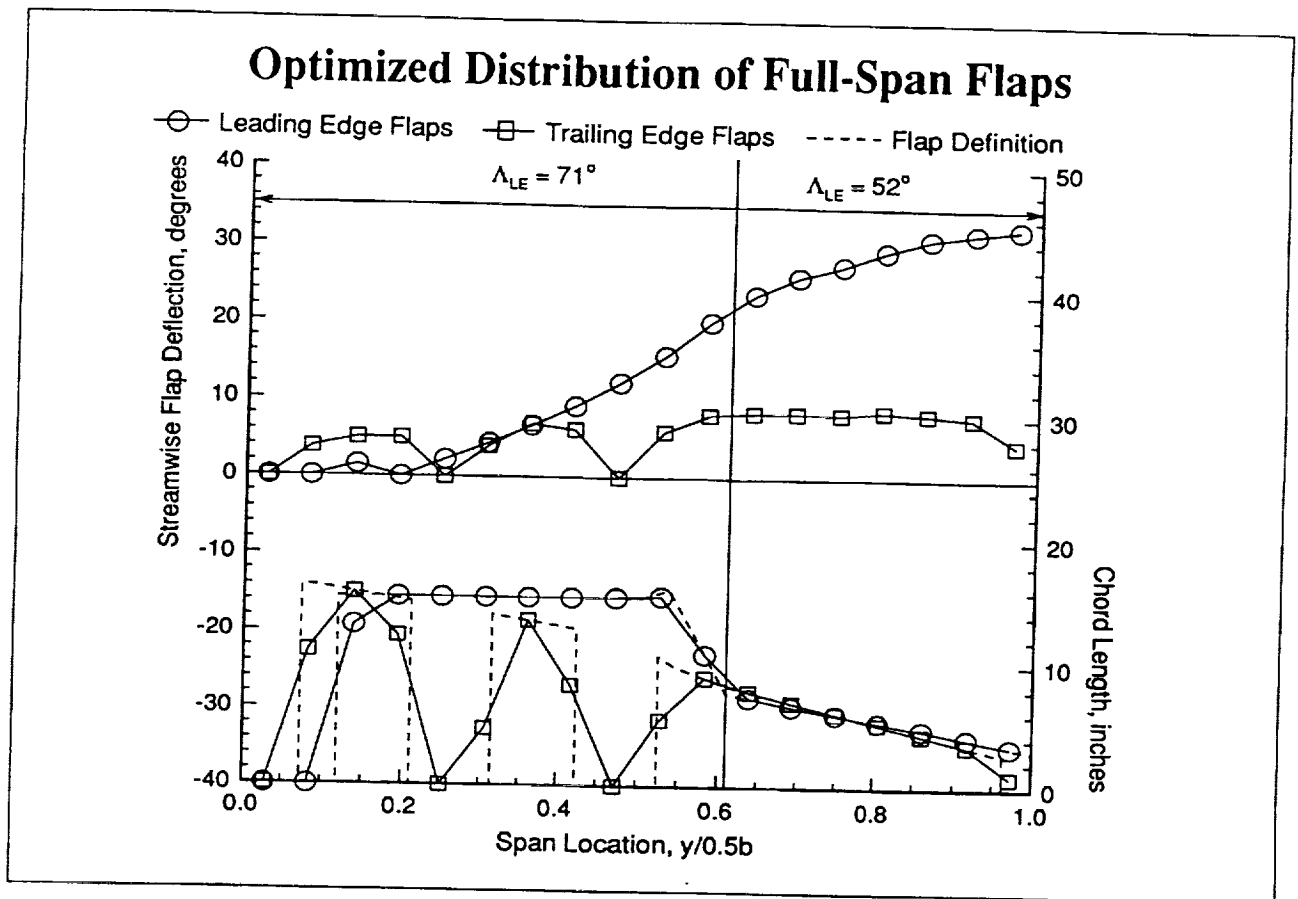
The resulting optimized distribution is very similar to the part-span flaps. Likewise, the ratioing of the deflections and optimization of the Suction Parameter resulted in similar numbers.

Application of Results to TCA

- Average deflection for each flap was calculated
- Streamwise deflection values changed to values normal to the hinge line of the flap using $\delta_n = \operatorname{atan}\left(\frac{\tan \delta_s}{\cos \Lambda_{hl}}\right)$

- Flap values rounded to the nearest 5°
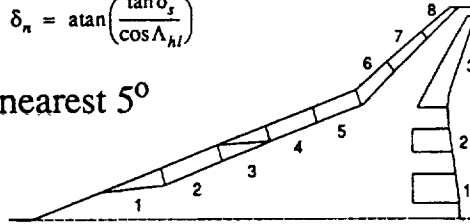
Final Flap Deflection Values (degrees)

	LE Flaps								TE Flaps		
	1	2	3	4	5	6	7	8	1	2	3
Part	0	0	45	25	25	30	30	30	10	10	20
Full	5	10	20	35	35	30	30	30	10	10	20

13 of 14

The final flap deflection schedule, after reference to the local hinge lines of the flaps, indicates a great deal of similarity between the part-span and the full-span distributions. The Suction Parameters obtained were also very similar in value. Values compare very reasonably with previous flap deflection schedules derived by other means.

Conclusions and Comments

- The codes WINGDES2 and AERO2S were easy to obtain, and technical help was readily available

- The codes have a long, well-documented history of successful optimizations of various aircraft configurations

- The codes were easy to use, although specification of input data was time-consuming

- Run times were short, allowing the many runs necessary for the Suction Parameter matrix to be accomplished within a day or two

- Results of the optimization appear to be reasonable

NASA Langley Research Center
Hampton, VA 23681-0001

Flow Simulation About A High-Lift High Speed Civil Transport Using TetrUSS

1997 AP High Lift Workshop

by

Victor Lessard

Vigyan, Inc.

v.r.lessard@larc.nasa.gov

OutLine

⬙ **Description of TetrUSS**
- Grid generation
- Flow Solver
- Postprocessing

⬙ **TetrUSS Euler application to TCA High-Lift configurations**
- Grid study
- Flap effectiveness study

⬙ **TetrUSS viscous application to TCA configurations**

Baseline
- Grid generation
- Near wall grid spacing study
- Comparison to structured grid N-S solution and LaRC 16 FT data.

High-Lift-30/10 configuration
- Grid generation (modified TE flap geometry)
- Viscous solution (hopefully)

v.r.lessard@larc.nasa.gov

1948

Tertrahedral Unstructured Software System
TetrUSS

(1996 NASA Software of the year)

△ **Geometry Setup: GRIDTOOL**-*developed by Dr. J.A. Samareh (CSC)*
-interactive program for defining surface from CAD and point data
-surface projection method for assuring that triangles lie on the surface

△ **Grid Generator: VGRID**-*developed by Dr. Shahayar Pirzadeh (ViGYAN, Inc.)*
-triangular surface and tetrahedral volume grid by advancing front method
-viscous grids generated both advancing layer and front technology

△ **Flow Solver: USM3D** -*USM3D developed by Dr. Neal T. Frink (NASA LaRC)*
-tetrahedral cell-centered, finite volume, RFDS and VLFVS
-2nd order accurate spatial reconstruction
-Spalart-Allmaras turbulence model with **wall function**

△ **Analyzing Solutions: VPLOT3D** -*developed by Dr. Paresh Parikh*
-interactively display grid and flow solution
-particle traces, vectors and surface data probing and more

-TECPLOT and FAST can be used as well

v.r.lessard@larc.nasa.gov

TeTrUSS refers to the Tetrahedral Unstructured Software System. This system was developed at NASA Langley with the collaboration of several local contractors. TeTrUSS won the 1996 NASA software of the year award. It is made up of four main codes. They are GRIDTOOL, VGRID/POSTGRID, USM3D and VPLOT3D.

TetrUSS Euler Application to TCA High-Lift Configurations

△ **Objective**

  -Perform a flap effectiveness study to support upcoming wind tunnel test in the 14x22 Foot Tunnel in March

v.r.lessard@larc.nasa.gov

1950

TCA High-Lift Configuration
Flap Settings Studied

TCA Config.	Leading-Edge Flaps								Trailing-Edge Flaps		
	1	2	3	4	5	6	7	8	1	2	3
TCA-1	30	30	30	30	30	30	30	30	10	10	10
TCA-2	0	0	30	30	30	30	30	30	10	10	10
TCA-3	0	0	40	40	40	40	40	40	10	10	10
TCA-4	0	0	50	50	50	50	50	50	10	10	10
TCA-5 *	0	0	45	25	25	30	30	30	10	10	20

* optimized setting from AERO2S

sketch
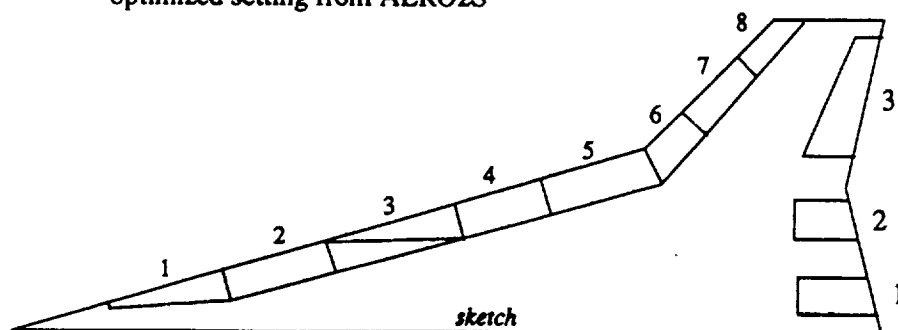
v.r.lessard@larc.nasa.gov

Unstructured grid Euler calculations are done for five TCA high-lift configurations. The table shows the leading- and trailing-edge flap settings for the five configurations given the naming convention TCA-1 through TCA-5. Note, the naming convention is different than for the wind tunnel configurations which have similar nomenclature. The sketch shows the locations of the flaps.

TCA-1 Unstructured Euler Grid

Coarse Grid
660.803 cells
41.486 boundary faces
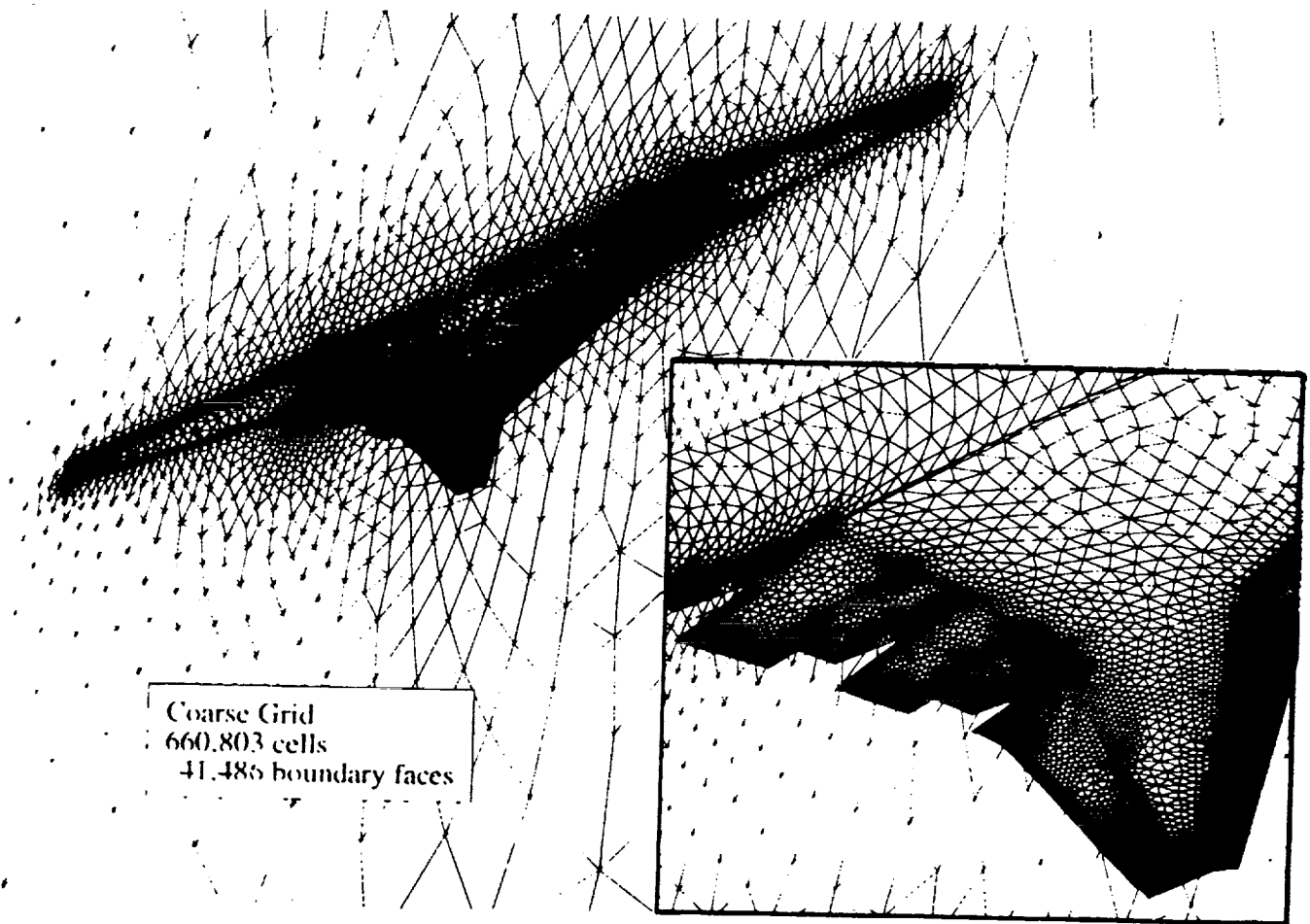
Grid generated using VGRID

This figure shows the features of the unstructured Euler grid for TCA-1 high-lift configuration. This grid is typical of all the high-lift configurations grids. The red triangles lie on the symmetry plane. A close up view in the right lower corner shows the details of the surface triangles at the trailing-edge in the vicinity of the segmented flaps.

TCA-1 Configuration Grid Refinement Study

Euler Grids
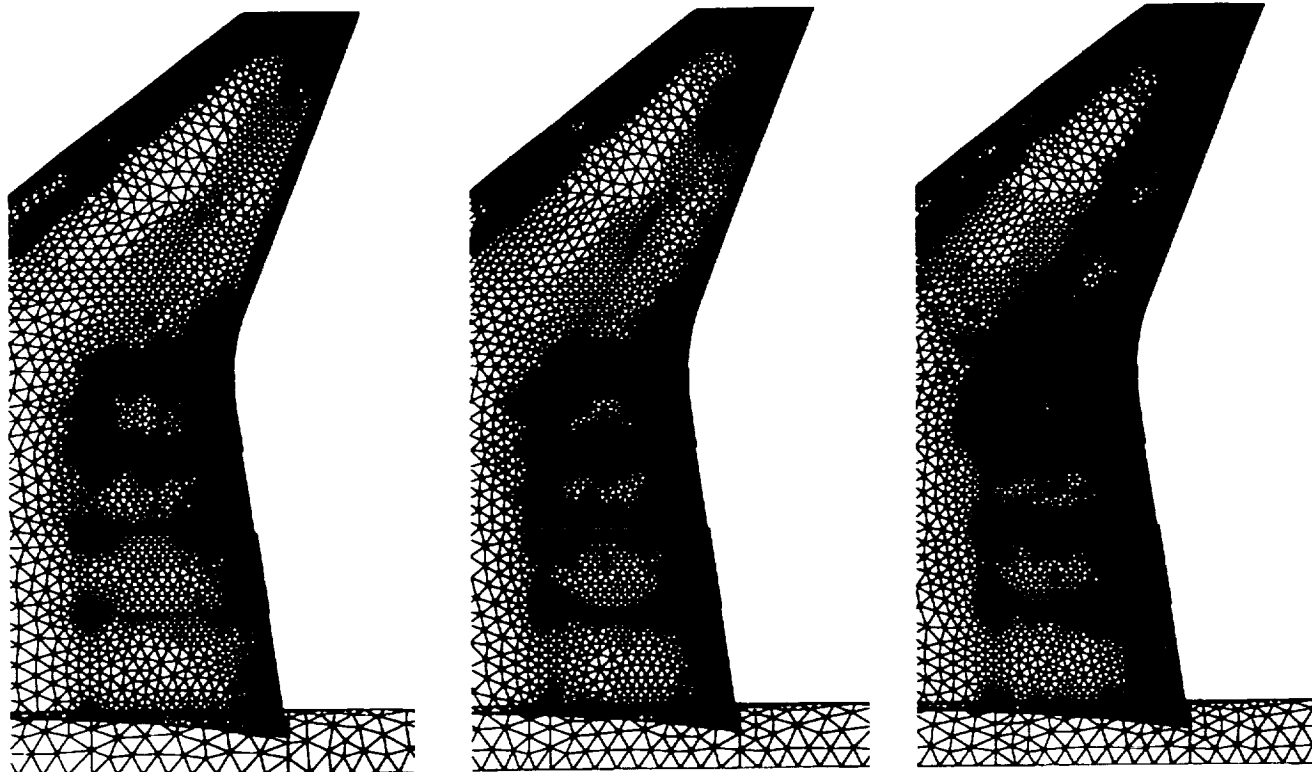
Coarse Grid
660.803 cells
41,486 bndry faces
109 MW memory

Medium Grid
887,010 cells
49,698 bndry faces
147 MW memory

Fine Grid
1,236,752 cells
61,848 bndry faces
205 MW memory

Grids generated using VGRID

Euler calculations for TCA-1 high-lift configuration were done on three grids to access the grid convergence quality of the solution. This figure shows the surface triangulations in the vicinity of the segmented trailing-edge flaps for three grids. They are the coarse, medium and fine grids. The total number of tetrahedral cells range from 0.66 million to 1.2 million going from the coarse to fine grids. The amount of resources in terms of memory to run USM3D for the grids ranged from 109 megawords to 205 megawords for the coarse and fine grid, respectively.

TCA-1 Configuration Grid Convergence Study

USM3D-Euler
M=0.24, α=8°
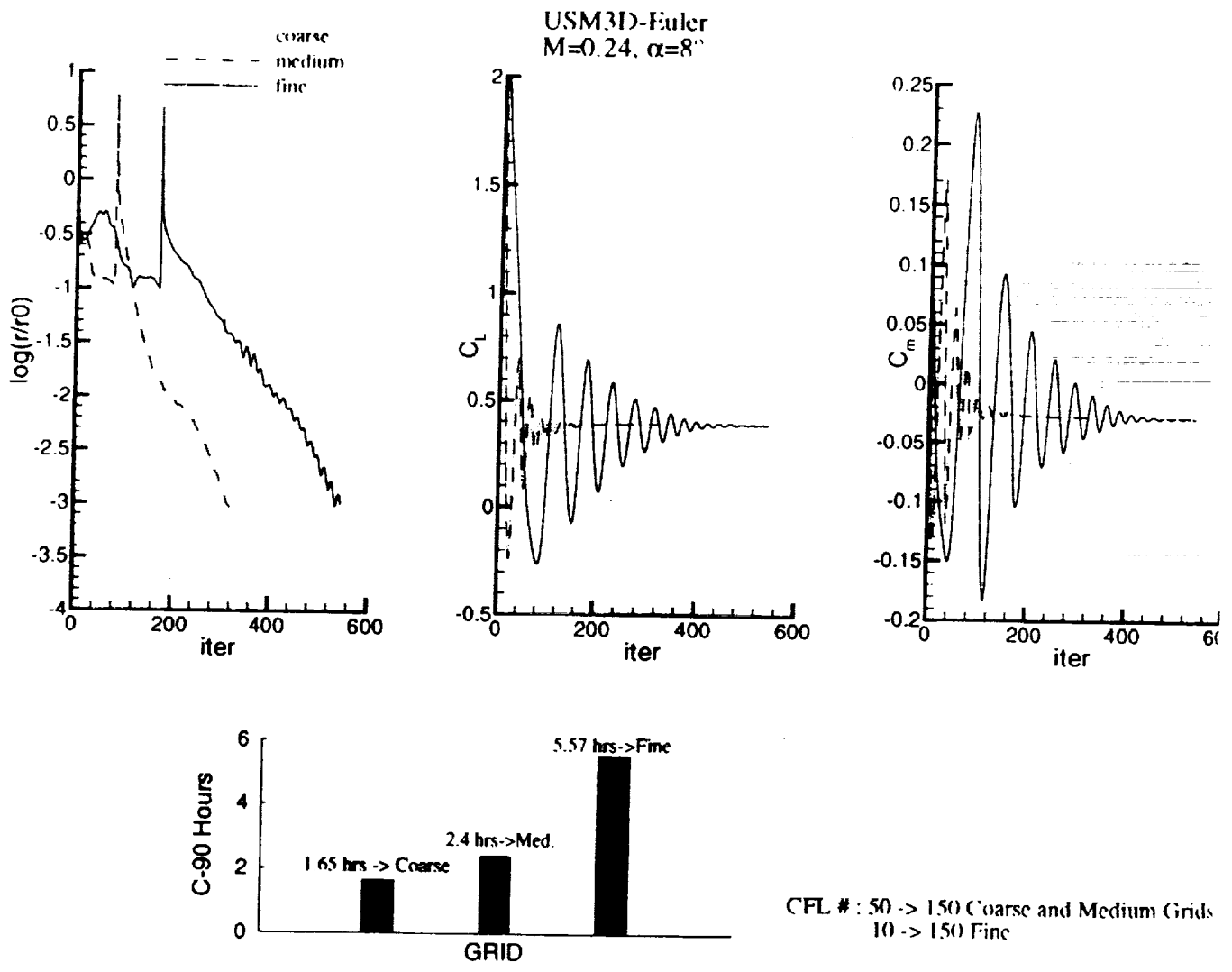
This figure shows the solutions convergence history for the TCA-1 high-lift configuration on the three grids; the coarse, medium and fine. The convergence rate for the coarse and medium grids are nearly the same where there is a drop of three orders of magnitude for the residual (r/ro) within approximately 300 iterations. The fine grid took almost 2 times the number of iterations to reach the same level of residual. The bar chart shows the differences in C-90 run times between the three grids. The lift and pitching moment coefficients history curves show the state of the converged solutions as well. From this study of the convergence history curves it can be seen that there is a definite advantage if the results from the coarse or medium grid are good enough.

TCA-1 Unstructured Grid Refinement Study

USM3D-Euler

M=0.24, α=8°
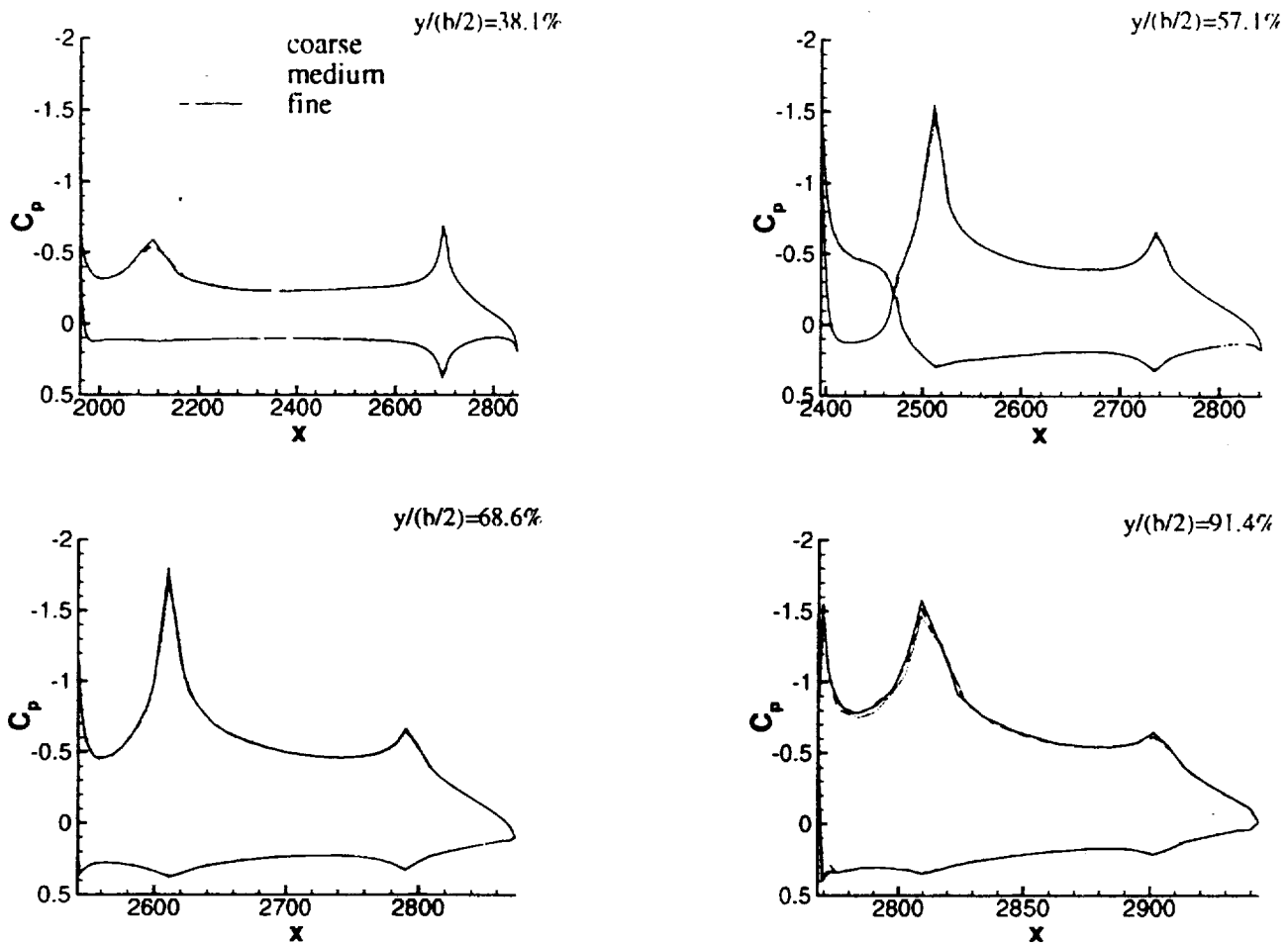
Predicted pressure coefficients for the coarse, medium and fine grid of the TCA-1 high-lift configuration is shown at 4 constant spanwise stations. The flow conditions are M=0.24 and an angle-of-attack (AOA) of 8 degrees. The pressure coefficients are essentially the same for the three grids with the exceptions at the leading-edge flap hinge-line where the more fine grid produces the higher suction peaks.

TCA-1 Configuration Grid Refinement Study

USM3D-Euler
M=0.24

C_{D_p} = pressure drag coefficient

Legend:
- ──□── Fine
- ──△── Medium
- ▽ Coarse
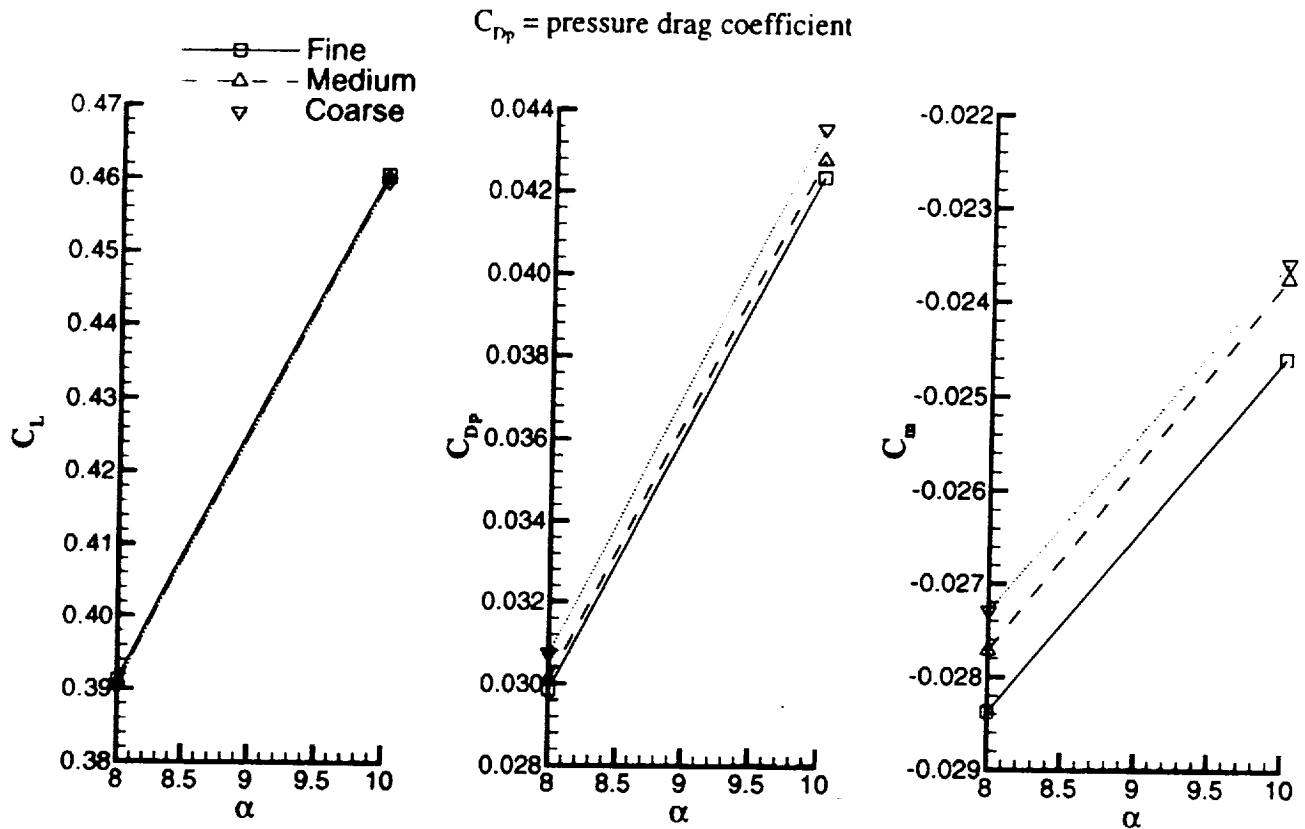
As part of the grid refinement study the predicted lift, pressure drag, and pitching moment coefficients are presented for AOAs of 8 and 10 degrees for the coarse, medium and fine grids of the TCA-1 high-lift configuration. As suspected from the surface pressures plots of the previous page, the integrated lift for the three grids are very close where the fine grid lift is the greatest. The integrated pressure drag decrease with increase in grid refinement and appears to be approaching a grid convergence. However, the pitching moment is increasing in the negative sense at a geometric rate with each grid refinement. Further grid refinement is needed to obtain a true grid refinement.

TCA High-Lift Configurations Euler Calc.

TCA-1 (δ_{LE}=30°, δ_{TE}=10°)

TCA-2 (δ_{LE}=30°, δ_{TE}=10°)

C_p
0.01
-0.35
-0.71
-1.07
-1.42
-1.78
-2.14
-2.50

TCA-3 (δ_{LE}=40°, δ_{TE}=10°)

Under the assumption that the fine grid of the TCA-1 high-lift configuration was sufficient, Euler calculations for the other four TCA flap setting (TCA-2,3,4,5) were done for grids of comparable densities. Upperwing surface pressures results for the five high-lift configurations are shown on this page and the next page. The flow conditions are M=0.24 and an AOA of 12 degrees. Differences in the surface pressure can be seen due to the different leading- and trailing-edge flaps deflections. Most notable differences can be seen between the TCA-1 flap setting where the entire leading edge is deflected at 30 degrees and the other configurations where the flaps 1 and 2 are undeflected. The TCA-5 configurations shows the greatest wing loading on the outboard wing section. This is due to the increase in flow circulation caused by the trailing-edge flap 3 deflected at 20 degrees. This outboard loading is expected to over predicted because the Euler calculations cannot predict the trailing-edge separation on the outboard flap.

TCA High-Lift Configurations Euler Calc.

USM3D-Euler: M=0.24, $\alpha=12°$

TCA-4 ($\delta_{LE}=50°$, $\delta_{TE}=10°$)

TCA-5 ($\delta_{LE}=45°$, $25°$, $30°$, $\delta_{TE}=20°$)
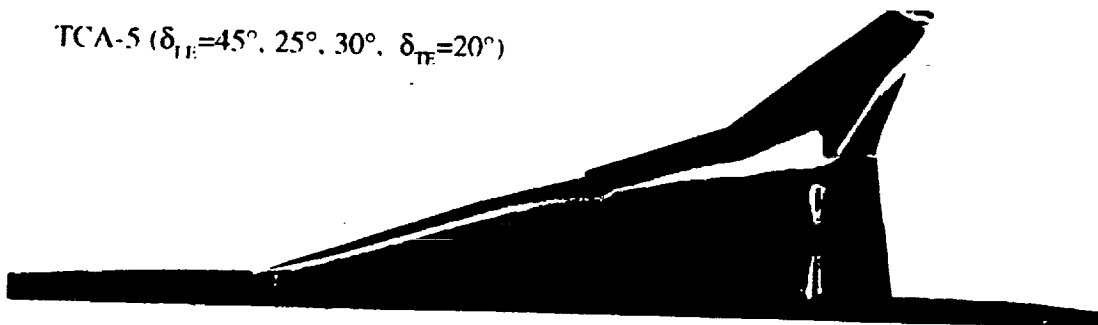
C_p
0.01
-0.35
-0.71
-1.07
-1.42
-1.78
-2.14
-2.50

Predicted Forces and Moments of High-Lift TCA Flap Configurations
USM3D-Euler Results
M=0.24

TCA-1
TCA-2
TCA-3
TCA-4
TCA-5

$\Delta C_l = C_l(TCA\text{-}\#) - C_l(TCA\text{-}2)$

diverging solution point (dp)

$\Delta C_m = C_m(TCA\#) - C_m(TCA\text{-}2)$
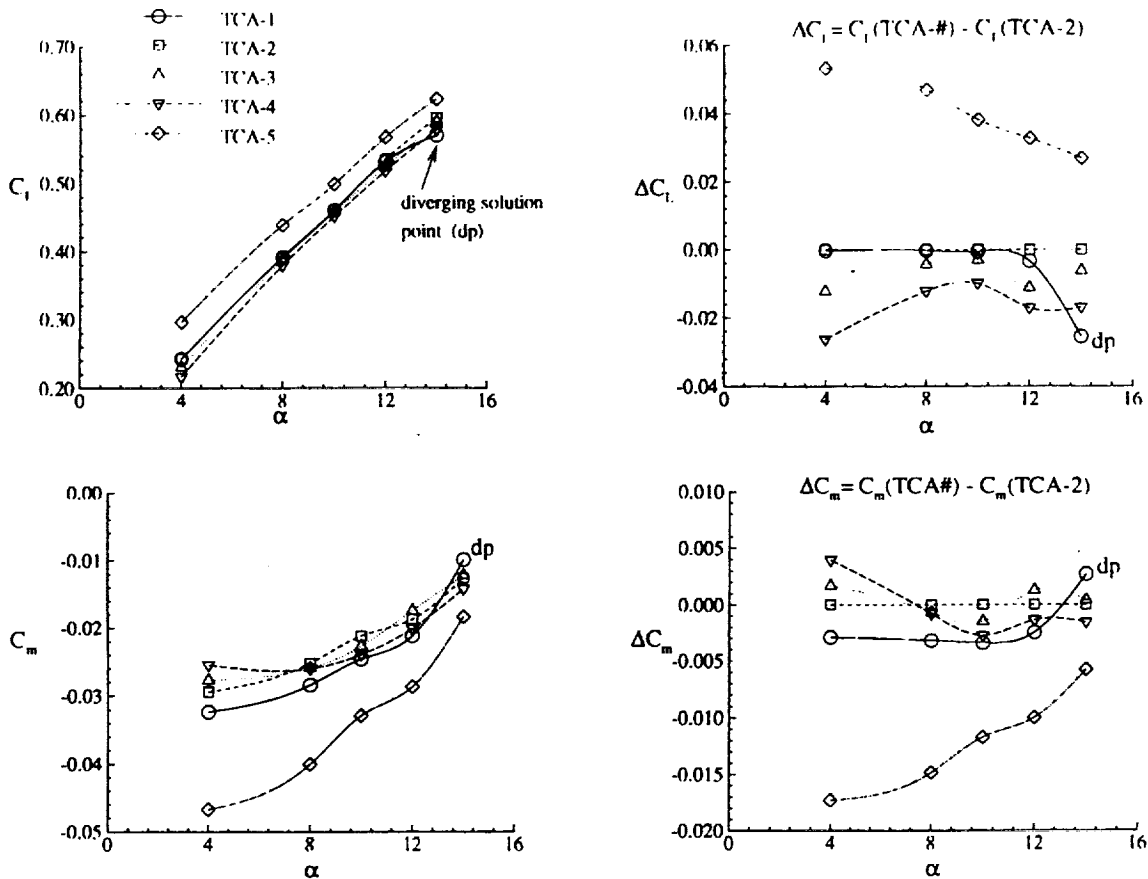
The predicted lift and pitching moment coefficients and their deltas between the different configurations are plotted verses AOA in this figure. The TCA-2 configuration is used as the reference point for computing the deltas. TCA-2 configuration produced more lift than the TCA-1,3,4 configurations. The solution for the TCA-1 configuration at AOA of 14 degrees did not converge but is shown for completeness. The TCA-5 configuration produced the greatest lift over the AOA range and this is due the outboard flap being deflected at 20 degrees. The exact increase in lift should be taken lightly because the Euler calculations cannot predict trailing-edge flow separation. The pitching moment for TCA-1 through TCA-4 configurations were similar while the TCA-5 configuration has a dramatic increase in the negative sense because of the outboard wing loading being behind the moment reference location.

TetrUSS Viscous Application To TCA Baseline Configuration

⬙ **Objective**

-Evaluate the TetrUSS viscous technology for wing/body TCA baseline configuration

-In the process, evaluate effects of near wall grid spacing on the solution using the Spalart-Allmaras turbulence model and the Spalding wall function

v.r.lessard@larc.nasa.gov

1960

TCA Baseline Configuration Unstructured Viscous Grid

anisotropic stretching at LE

advancing layer

1,190,951 cells   440,835 viscous cells   40,918 boundary triangles   Generated using VGRID
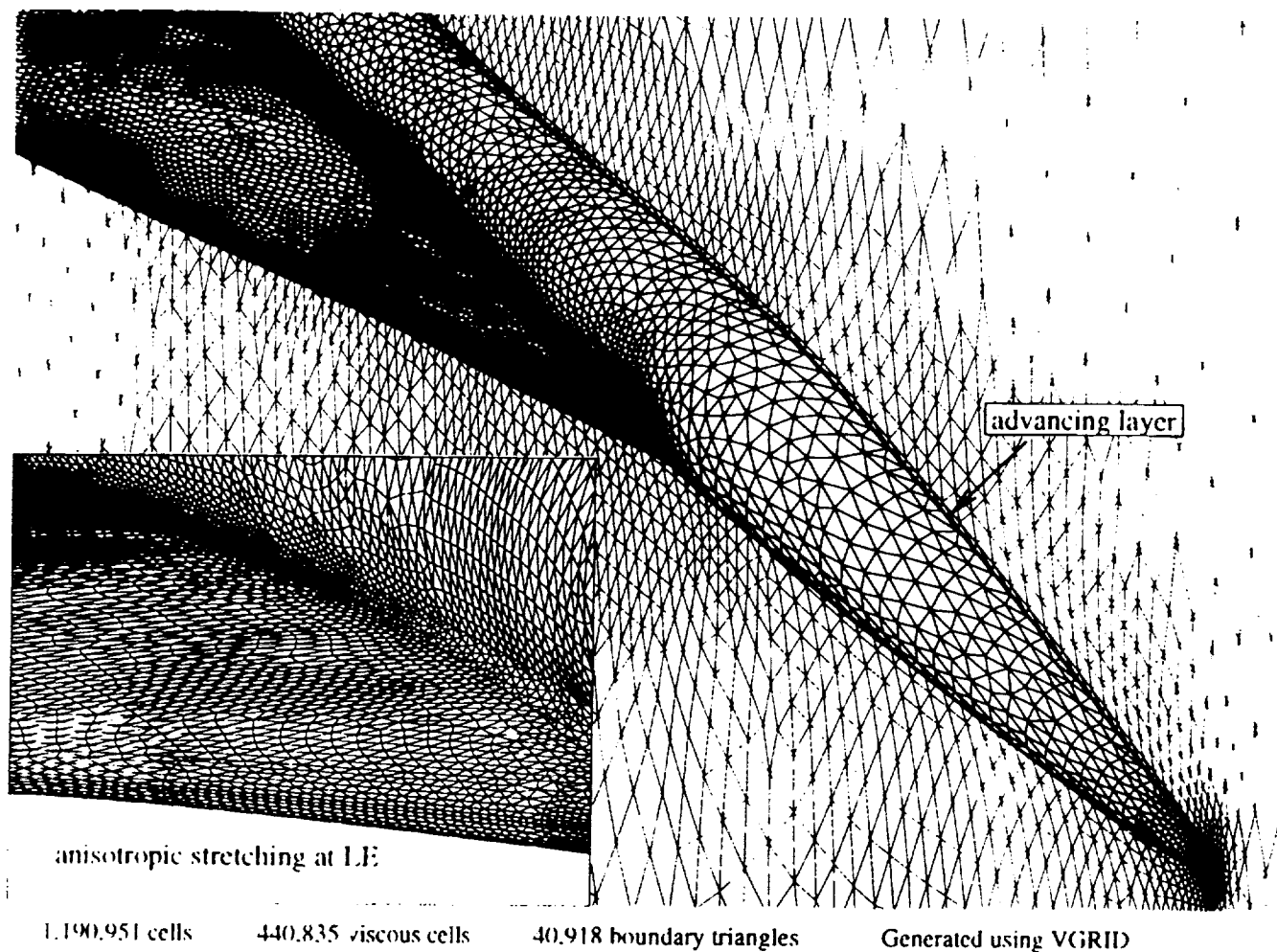
A typical viscous unstructured grid for the TCA baseline configuration is shown where the red lines are on the symmetry plane. The viscous layer which was generated by the advancing layer method can be seen on the symmetry plane near the surface. A close-up view of the leading edge is shown in the left lower corner of the figure. Anisotropic stretching of the surface triangles is done to reduce the number of surface and volume points in the grid.

Thin-Layer Tetrahedral Grids
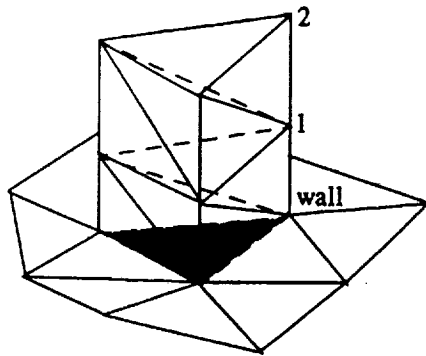
Grid	Near Wall Spacing (y+)	Nodes
1	50	6
2	30	6
3	15	6
4	15	8
* 5	15	6

* grid adapted to vortices

1 prism cell (or 1 node) = 3 tetrahedral cells in viscous layer

v.r.lessard@larc.nasa.gov

The unstructured viscous layers are generated by projecting the surface triangles approximately normal to the surface, and thus, producing a prism cell. The prism cell is then divided into three tetrahedral cells. Hence, for a single prism cell (or grid node) off the surface there are three viscous tetrahedral cells. To study the effects of near wall grid point spacing on the Navier-Stokes solutions using the Spalart-Allmaras turbulence model with the wall function 4 different grids with different wall spacing and nodes was generated. The wall spacing and number of nodes are listed in the table.

Typical USM3D-Viscous Solution Convergence History For TCA Baseline Configuration

M=0.24, Rn=8 million, α=6.94
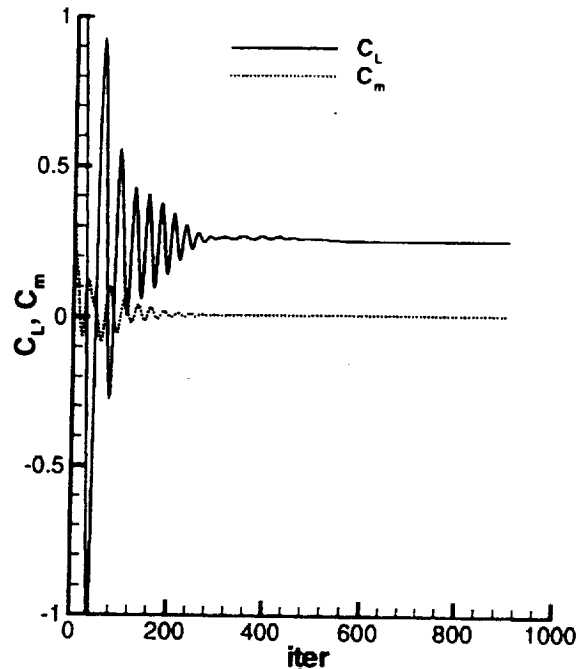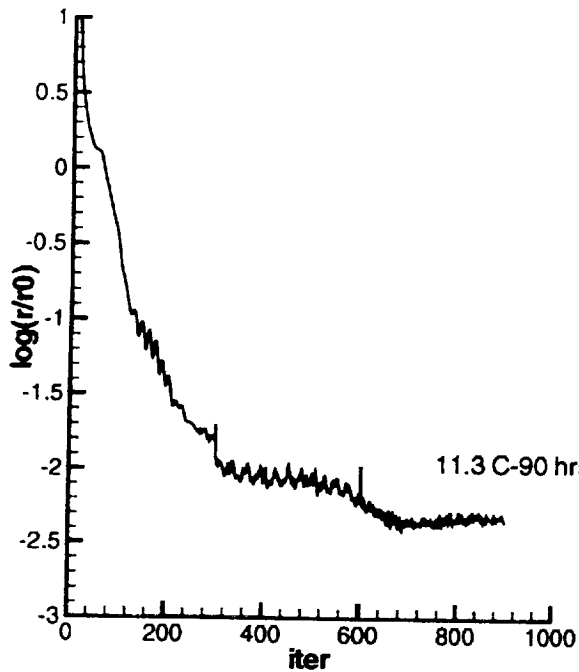
Grid Info.
========
1,190,951 cells
440,835 viscous cells
40,918 boundary face

11.3 C-90 hrs.

CFL #: 50 -> 150 first 200 iter.
        150   201 -> 900 iter.

A typical USM3D-viscous solution convergence history curve for the TCA baseline configuration is shown in this figure. This figure shows that the residual reduced approximately 3.5 order of magnitude in about 900 iterations. The total C-90 run time was approximately 11.3 hours. The lift and pitching moment convergence history curves are also shown.
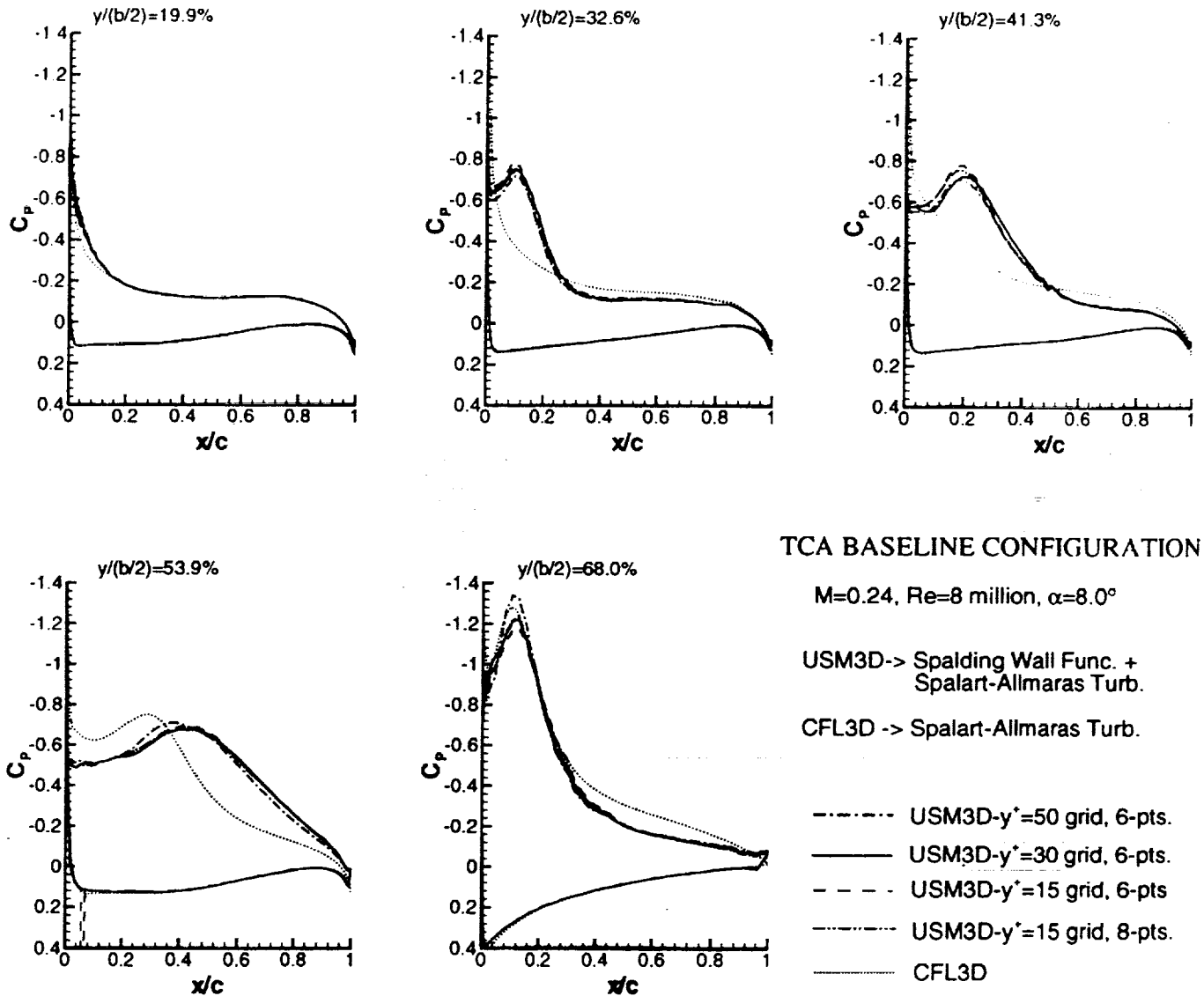
y/(b/2)=19.9%   y/(b/2)=32.6%   y/(b/2)=41.3%

y/(b/2)=53.9%   y/(b/2)=68.0%

TCA BASELINE CONFIGURATION

M=0.24, Re=8 million, α=8.0°

USM3D-> Spalding Wall Func. +
            Spalart-Allmaras Turb.

CFL3D -> Spalart-Allmaras Turb.

— ·· — ·· — USM3D-y*=50 grid, 6-pts.
————— USM3D-y*=30 grid, 6-pts.
— — — · USM3D-y*=15 grid, 6-pts
— · — · — USM3D-y*=15 grid, 8-pts.
————— CFL3D

Predicted surface pressure coefficients for the near wall grid spacing study are compared. The flow conditions are M=0.24, Re=8 million and AOA of 8 degrees. Results from a structured grid CFL3D solution is shown for comparison purposes as well. Comparsions are similar to the AOA case of 6.94 degrees.
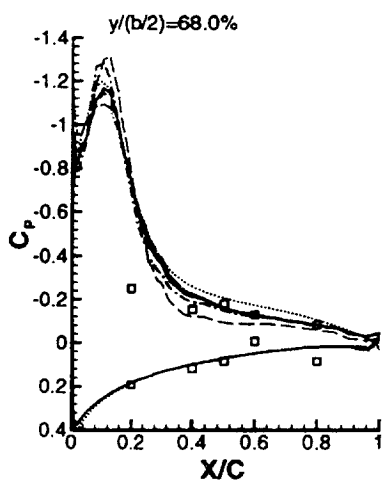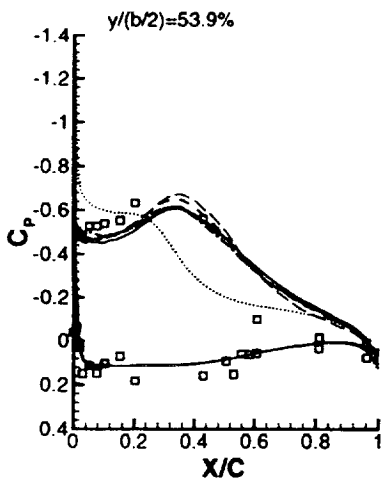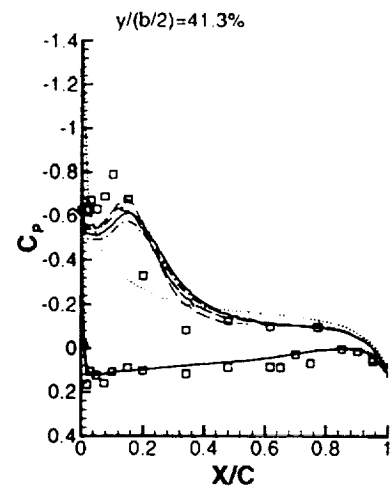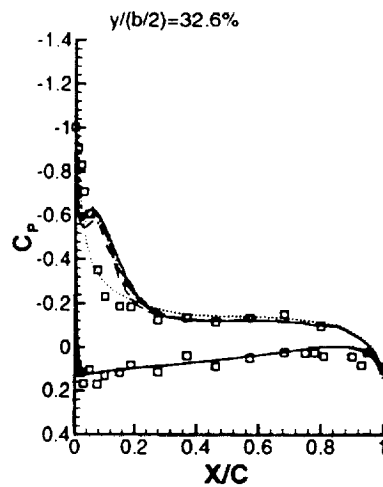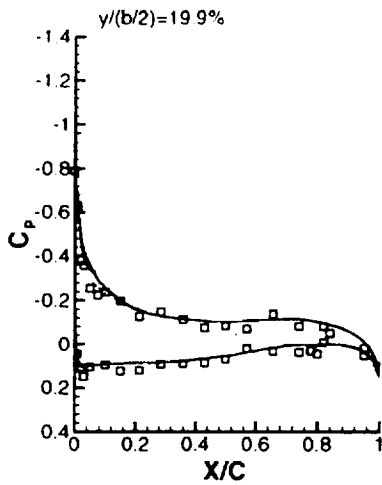
y/(b/2)=19.9%

y/(b/2)=32.6%

y/(b/2)=41.3%

y/(b/2)=53.9%

y/(b/2)=68.0%

TCA BASELINE CONFIGURATION

M=0.24, Re=8 million, α=6.94°

USM3D-> Spalding Wall Func. +
Spalart-Allmaras Turb.

CFL3D -> Spalart-Allmaras Turb.

— - — - — · · USM3D-y*=50 grid-6 points
———— USM3D-y*=30 grid-6 points
— — — · USM3D-y*=15 grid-6 points
— · · — · · — · · · USM3D-y*=15 grid-8 points
— — — · USM3D-y*=15 grid-6 points, adapted to vortices
———— CFL3D
☐ Experiment (LARC 16 FT)

Predicted surface pressure coefficients for the near wall grid spacing study are compared with LaRC 16 Foot experimental data for five constant spanwise locations. The flow conditions are M=0.24, Re=8 million and AOA of 6.94 degrees. Results from a structured grid CFL3D solution is shown for comparison purposes. In general, the different wall spacings and number of viscous nodes of the unstructured grids produced similar results. The unstructured viscous calculations of the different grids captured the inboard and outboard vortices in essentially the same locations noted by the suction peaks. Although, the suction peaks varied slightly with the near wall spacings. The results y+=15 grid and y+=30 grid is thought to be better than that of the y+=50 grid. Higher suction peaks are achieved by adapting the y+=15 grid with 6 nodes to the vortices.

TCA BASELINE CONFIGURATION

USM3D-viscous solution

M=0.24, α=6.94°, Rn=8 million

pO 0.710 0.714 0.719 0.723 0.728

y⁺=15 Grid, 1.2 million cells
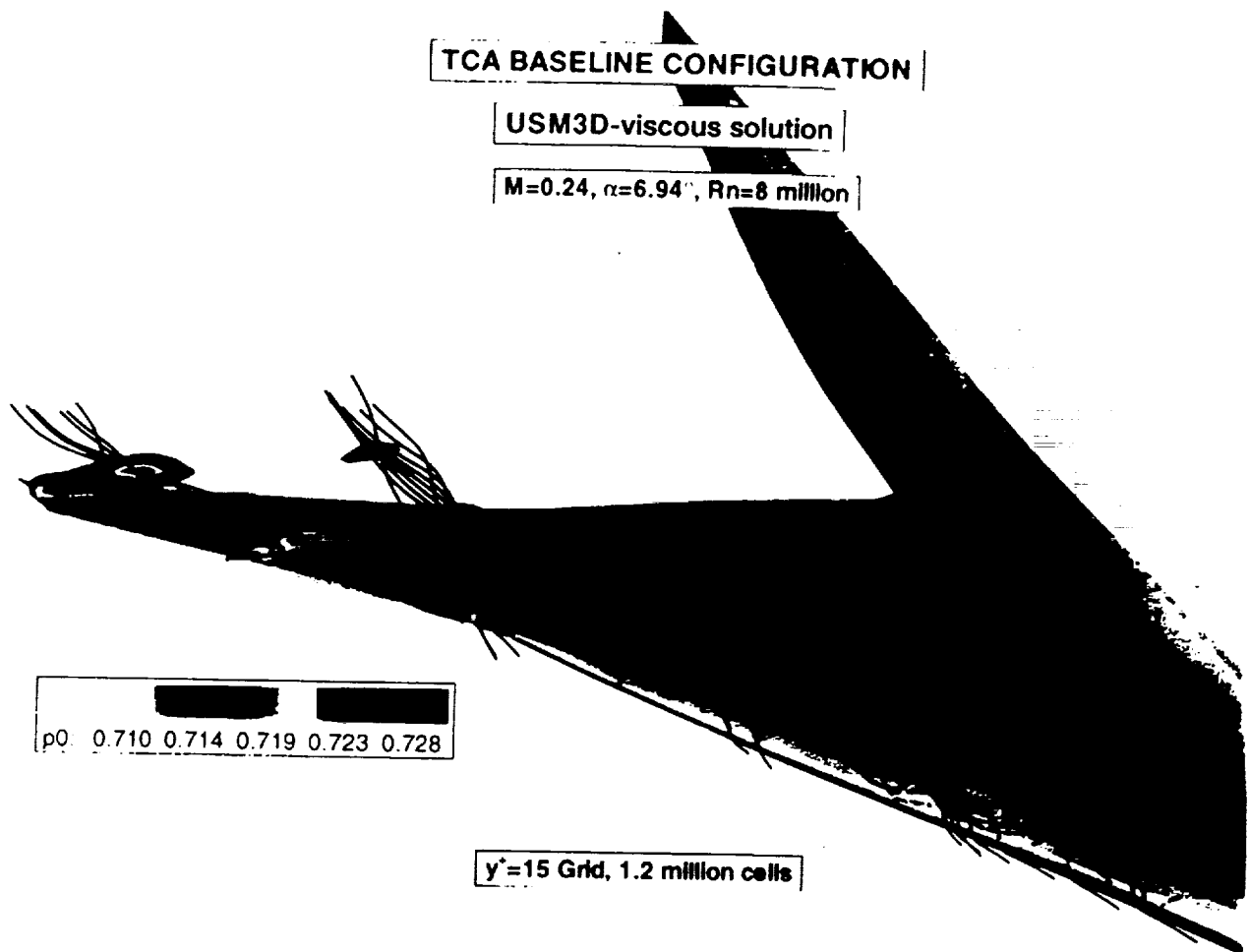
This figure shows predicted total pressures contours off the surface and particles traces following the inboard and outboard vortices for the baseline TCA configuration. The flow conditions are M=0.24, Rn= 8 million, AOA=6.94 degrees. The unstructured viscous grid that the solution was obtained on was the y+=15 grid with 6 boundary layer nodes.

Force and Moments for the TCA Baseline Configuration Near Wall Spacing Study

M=0.24, Re=8 million

α	C_L	C_D	C_{Df}	C_M	Comments
6.94	0.25477	0.030308	0.008788	0.011805	USM3D-y+=50, 6-pts
6.94	0.25551	0.031708	0.009863	0.012233	USM3D-y+=30, 6-pts
6.94	0.25584	0.030521	0.008826	0.011631	USM3D-y+=15, 6-pts
6.94	0.25573	0.031564	0.009927	0.012053	USM3D-y+=15, 8-pts
6.94	0.25653	0.030307	0.008687	0.011876	USM3D-y+=15, 6=pts, adapted grid to vortices
6.94	0.24112	0.028977	0.010117	0.015388	CFL3D
6.90	0.24647	0.028210	**********	0.012743	Experiment (M=0.30)

reference center: based on 50% MAC

v.r.lessard@larc.nasa.gov

Predicted forces and moments for the unstructured viscous grids are compared with LaRC 16 Foot experimental data and the structured CFL3D results for the TCA baseline configuration. The flow conditions are M=0.24, Re=8 million and AOA=8 degrees. Overall the unstructured viscous grids lift and drag coefficients were overpredicted. The predicted pitching moments compared well with experiment and was better than the CFL3D results.

TetrUSS Viscous Application To TCA High-Lift (30/10) Configuration

Objective

-Evaluate the TetrUSS viscous technology for TCA high-lift configuration

-Overcome the viscous unstructured grid obstacle for simple segmented flaps

v.r.lessard@larc.nasa.gov

1968

TCA High-Lift Configuration Unstructured Viscous Grid

$\delta_{1} = 30^{\circ}$, $\delta_{11} = 10^{\circ}$
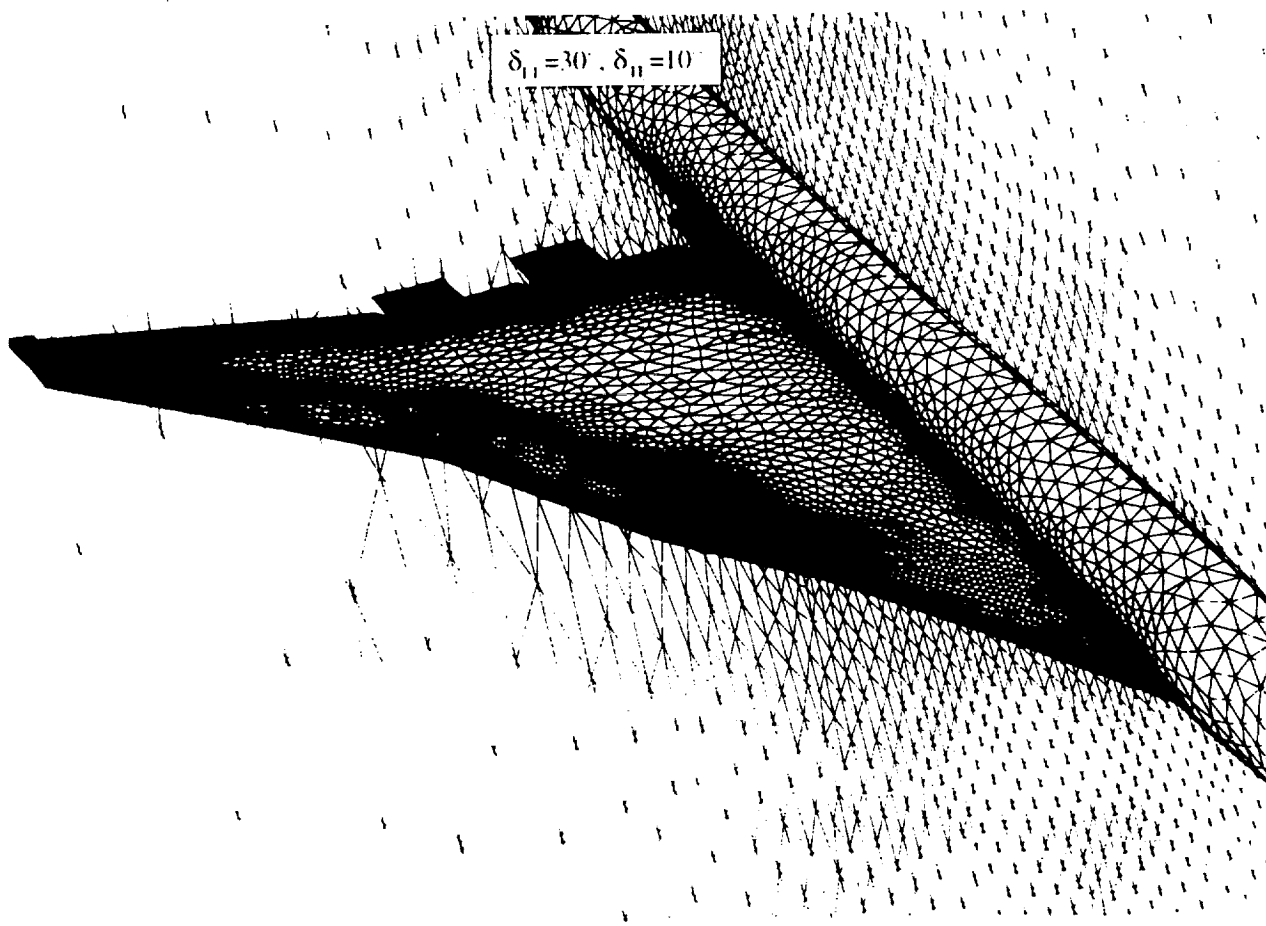
1,493,814 cells   512,974 viscous cells   46,512 boundary triangles   (Generated using VGRID)

The unstructured viscous grid for the TCA (30/10) high-lift configuration is shown. This configuration is the same as the TCA-2 configuration used in the Euler calculations. The viscous layer is seen on the red symmetry plane near the fuselage. The grid contains 1.5 million cells with approximately 513 thousand of those cells in the boundary layer.

TCA High-Lift Configuration Unstructured Viscous Grid

$\delta_{LE}=30^\circ, \delta_{TE}=10^\circ$

1.493,814 cells   512.974 viscous cells   46.512 boundary triangles   Generated using VGRID
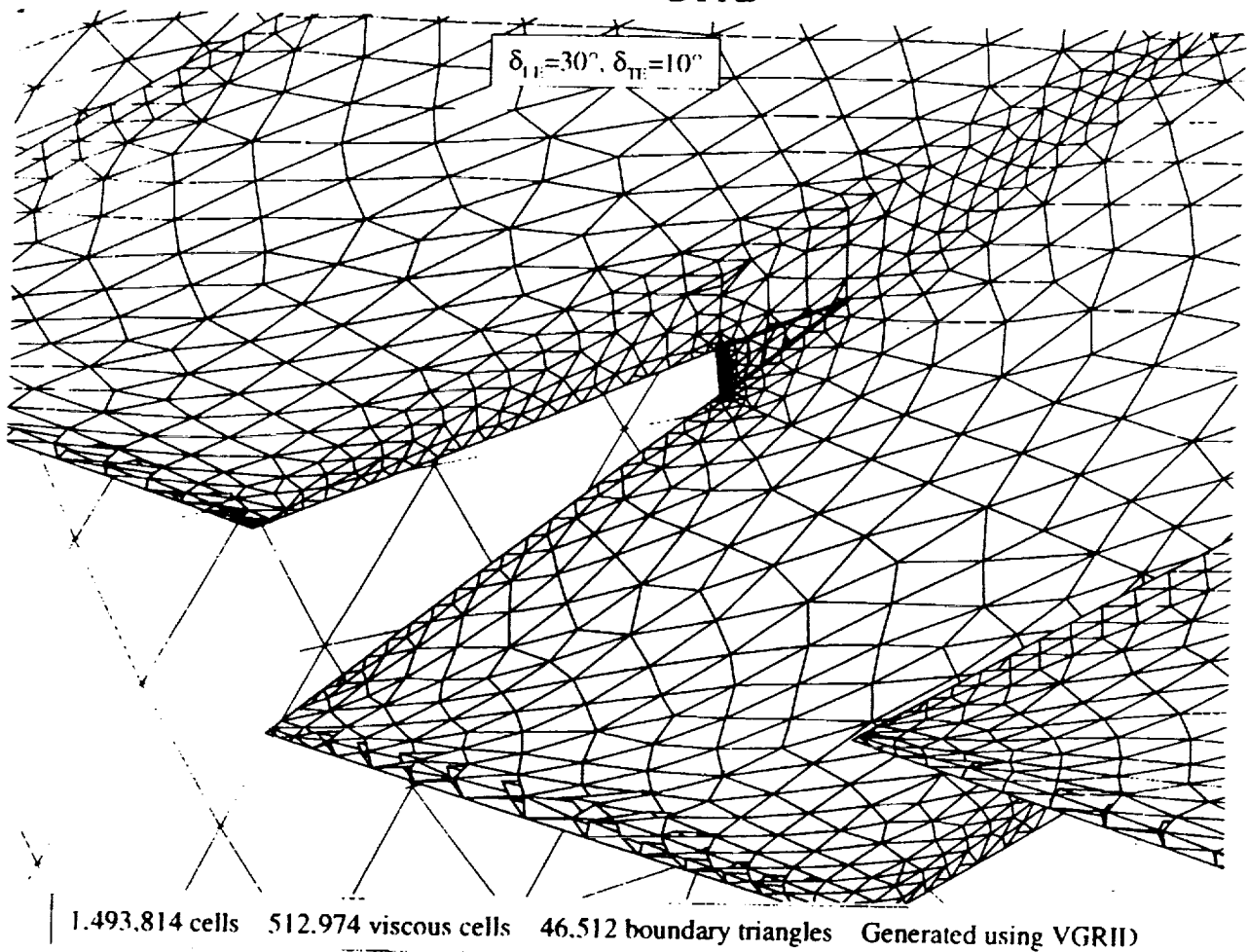
A close-up view of the trailing-edge segmented flaps with a geometry modification is shown in this figure. The geometry modification is shown within the green lines near the intersection point between the undeflected trailing-edge surface and the flap. This was done to remove the singular point for growing the viscous layer. This modification is local and is believe to have little effect on the global results.

TCA High-Lift Configuration Unstructured Viscous Grid

$\delta_{1.}=30^\circ, \delta_{\text{II}}=10^\circ$

1.493.814 cells   512.974 viscous cells   46.512 boundary triangles   Generated using VGRID
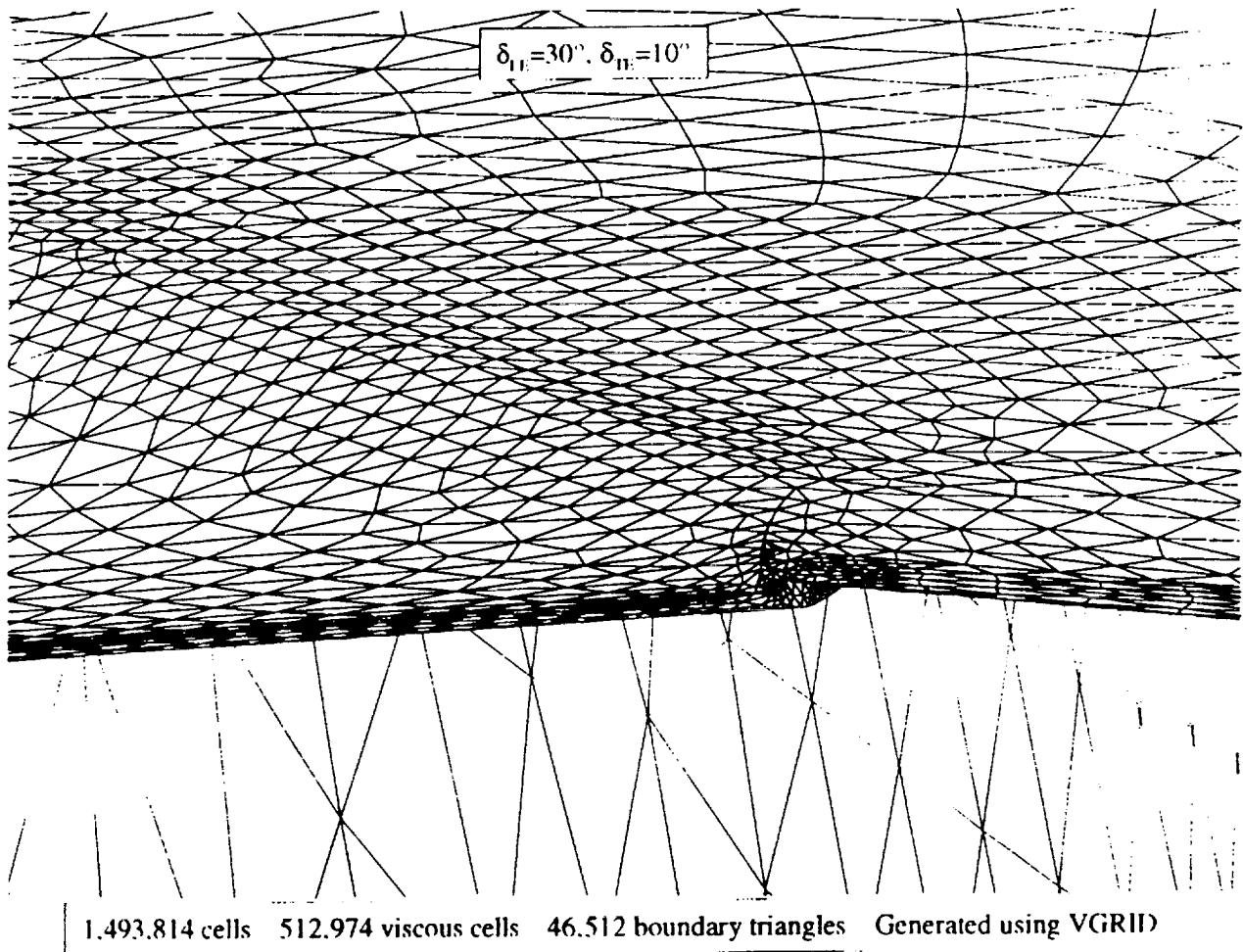
One of the strengths of unstructured grid is that more details in the geometry can be modeled more easily. For example, this figure shows the forward facing step generated when the leading-edge flap 3 is deflected 30 degrees. The edge of the flap is very difficult to model with structured grid technology but is fairly simple with unstructured grid methods. In fact, most structured grids would be generated by smoothing this step between the surfaces.

TCA High-Lift Configuration Convergence History

$\delta_{LE}=30°$, $\delta_{TE}=10°$

M=0.24, Rn=8 million, $\alpha=10°$
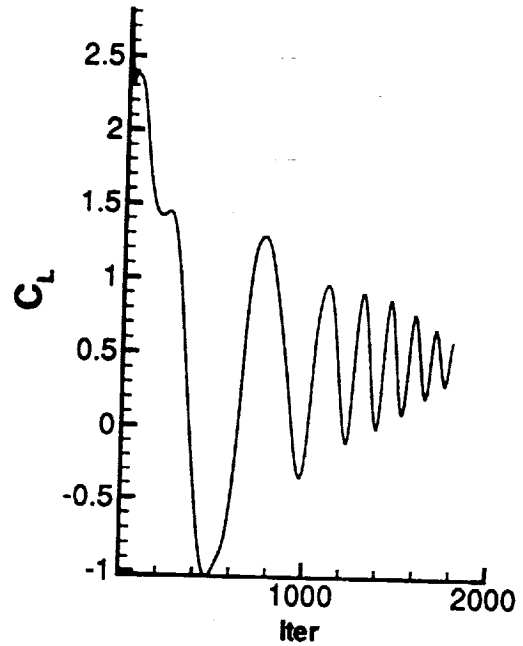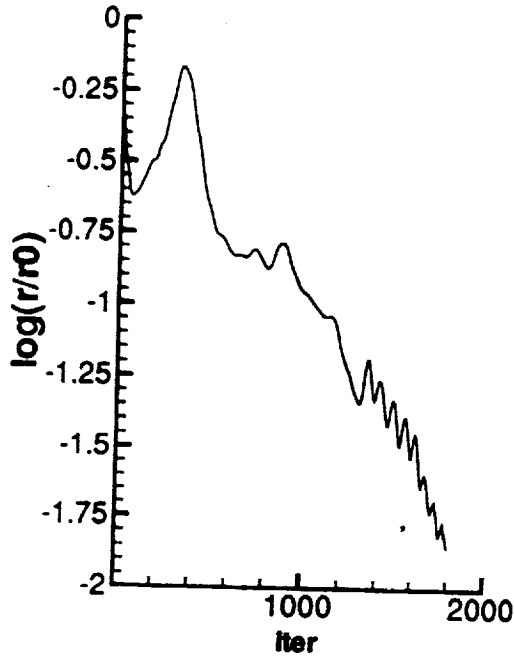
The convergence history for the TCA (30/10) high-lift configuration calculation at AOA=10 degrees is shown. Currently the solution is not converged and is being run more.

TCA (30/10) High-Lift Configuration

USM3D-viscous

M=0.24, Rn=8 million, α=10°

!! WARNING: SOLUTION NOT CONVERGED!!

C_p
-0.03
-0.55
-1.06
-1.58
-2.09
-2.61
-3.13
-3.64

!! WARNING: SOLUTION NOT CONVERGED!!
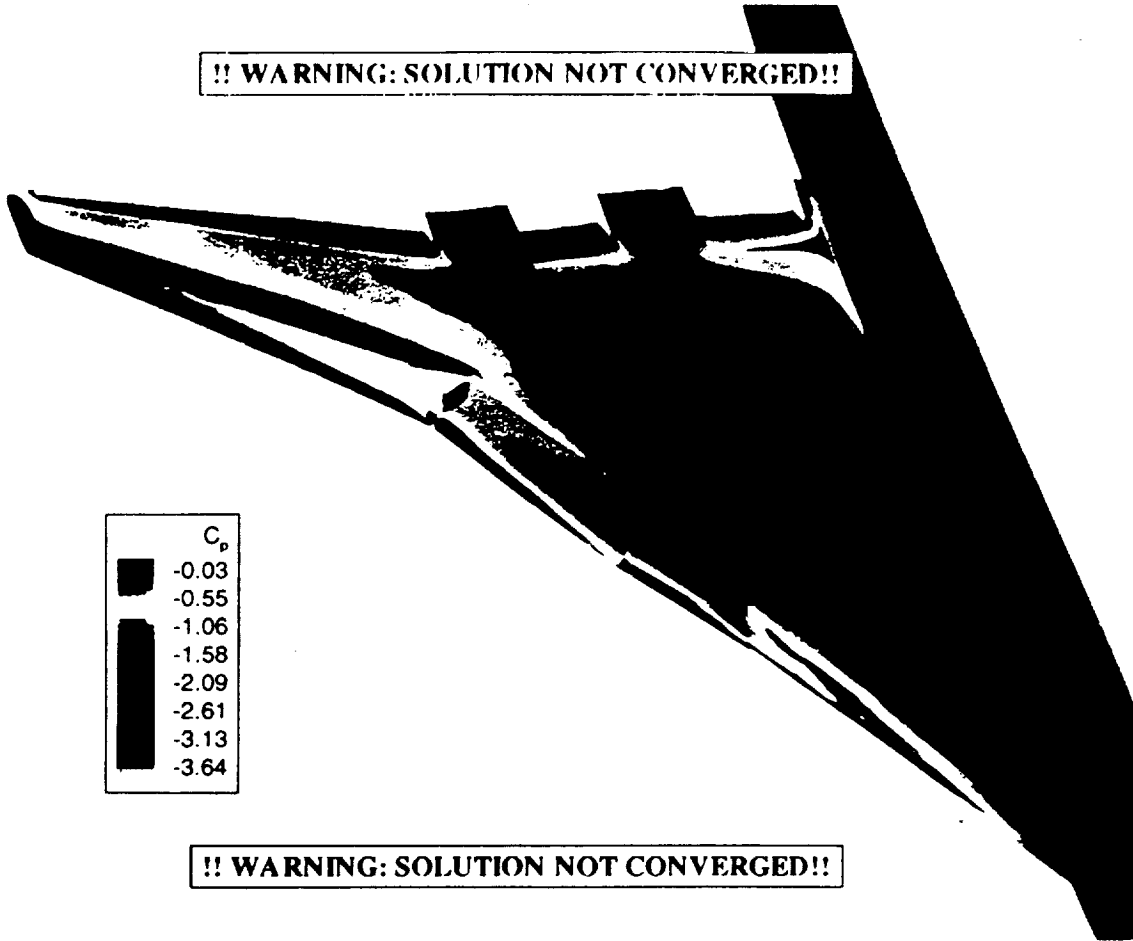
Surface pressure contours of the high-lift TCA configuration for the unconverged solution at AOA=10 degrees is shown in this figure. Because the solution is not converged no significant information can be obtained from this plot.

Conclusions

- TetrUSS unstructured grid generation for both Euler and viscous calculations of high-lift HSR configurations is both fast and straight forward.

- The flap effectiveness study shows the potential of using unstructured Euler calculations as a part of the preliminary design process.

- USM3D viscous calculations on the baseline TCA configuration compared well with the limited experimental data.

- USM3D has the potential of handling complex viscous flow fields.

v.r.lessard@larc.nasa.gov

1974

A CFD Assessment of Several High-Lift Reference H Configurations Using Structured Grids

Aerodynamic Performance Workshop

February 25-28, 1997

Wendy B. Lessard

NASA LaRC

HSR H-L CFD

Objective

Solve the viscous subsonic flowfield for the high-lift RefH configuration and determine the ability of an existing structured Navier-Stokes code to accurately predict this flow

Outline

- Grids
- Flow solver
- Results

  – Convergence and resources used

  – Force and moment comparisons

  – Pressure data correlations

  – Off-surface and surface flow viz

- Conclusions

HSR H-L CFD

The objective of this study is to calibrate a Navier-Stokes code for a high-lift Reference H configuration using structured grids.

The outline of this presentation will first include a brief description of the grids used and the flow solver. Next the results will be presented in terms of convergence and resources used on the C-90. Predicted force and moment and surface pressure results are compared to experiment and off- and on-surface flow viz is discussed.

Concluding remarks follow.

GRIDS

Three grids were generated of the high-lift ($\delta_{LE} = 30°$ / $\delta_{TE} = 10°$) Reference H config by Langley's Geometry Lab

Geometry	Blocks	Grid Pts	Patched	Pt-Pt
w/b	14	3,988,514	2	23
w/b/n/ht	37	4,595,343	38	83
w/b/n/emp	74	7,085,708	96	163

GEOLAB generated three RefH high-lift configurations, which are shown in the table. The leading- and trailing-edge flaps were deflected 30° and 10°, respectively. (All the leading-edge flaps were down). The full-span configuration was generated for side-slip calculations, and this grid was actually a coarsened version of config2 (with the vertical tail attached) and mirrored to the other side.

1977

Reference H Grid Topology

O-H

C-O
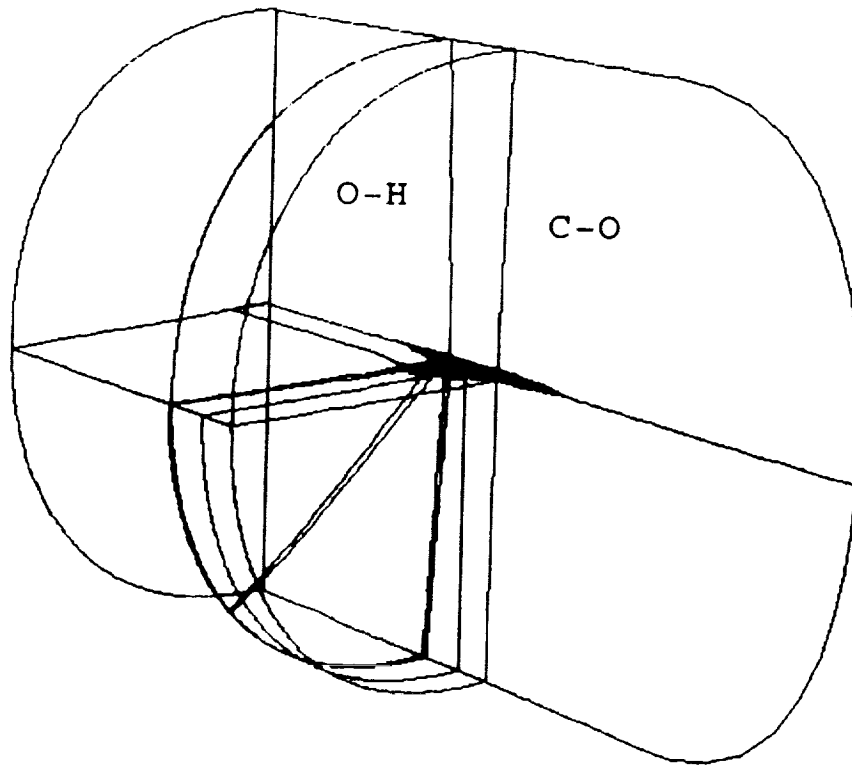
This figure shows the outline of the multi-block grid which was used for all the grids. The basic gridding topology was C-O for the forebody and O-H for the wing/fuselage and aftbody.

Reference H Block Details Around Trailing-Edge Flaps and Nacelles
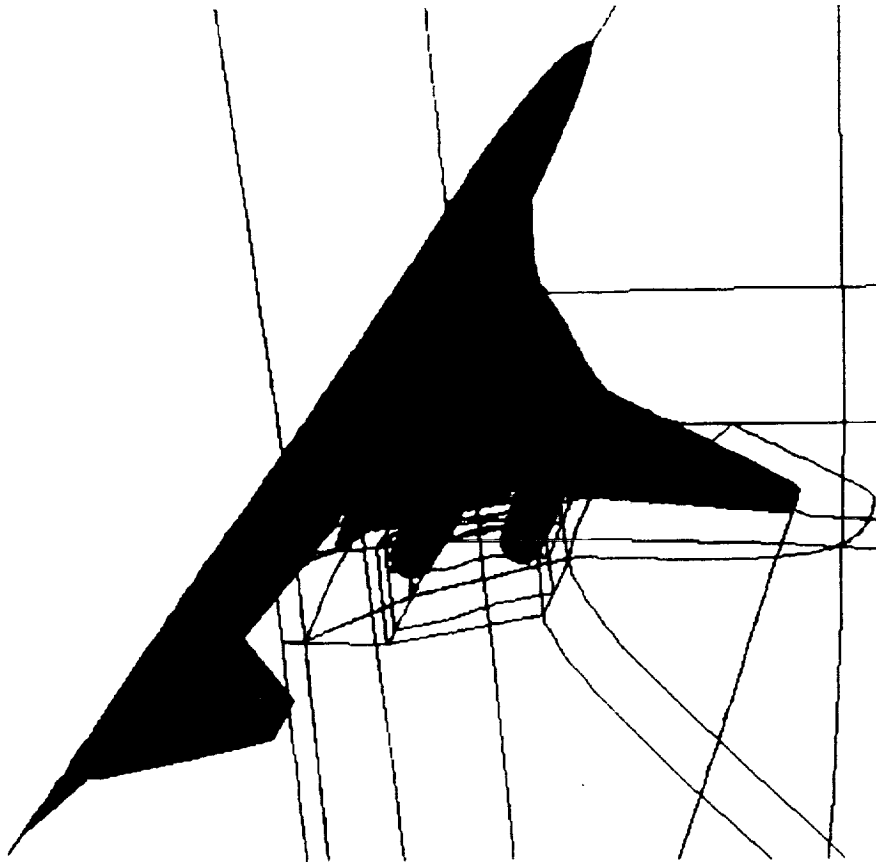
A close-up view of the high-lift RefH grid is shown in this figure, which details the complex blocking structure around the nacelles. An additional 23 blocks were added to the wing/body case in order to model the nacelles.

Side of flap walls

Flow through region
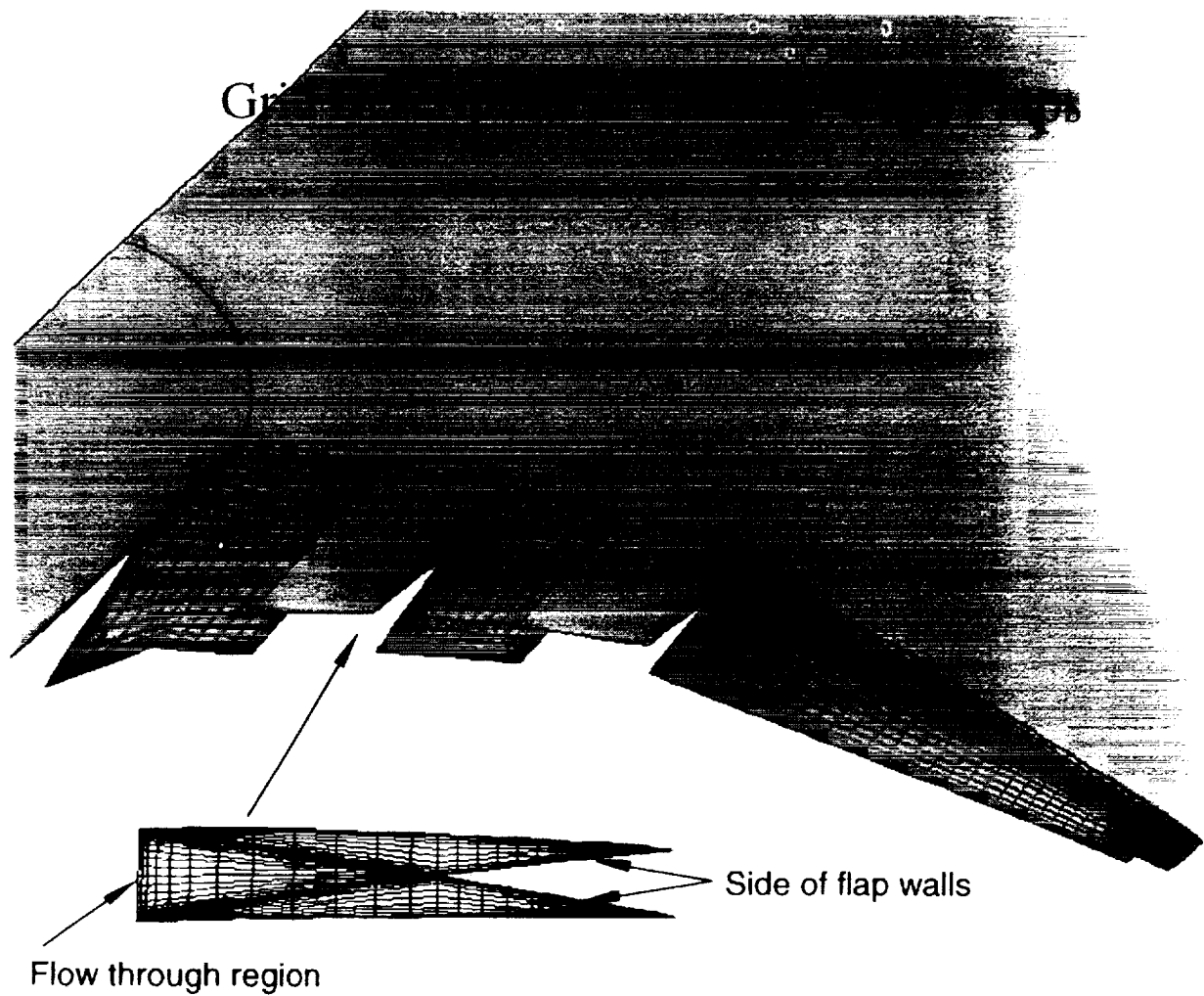
This figure highlights the surface grids on the RefH trailing-edge flaps and the gridding strategy used to model the sides of the flap regions. As shown in the insert, two small triangular grids were generated which model the sides of the flap walls. And the middle triangular region simulated flow through, which maintained point-to-point matching across the interface.

CFL3D

- Solves the time-dependent Reynolds-averaged Navier-Stokes equations on structured grids.

- Multigrid and mesh sequencing for convergence acceleration.

- Baldwin-Lomax with Degani-Schiff turbulence model.

- Multitasked for use on several processors with an average speed-up time of 1.5.

HSR H-L CFD

The slide is self-explanatory

RESOURCE REQUIREMENTS

All cases were run on the C-90 at NAS

Alias	RefhH Geom	Cases	Memory	Avg Run
config1	w/b	$\alpha=6,8,10,12,15$	170 mw	15 hrs
config2	w/b/nac/htail	$\alpha=8,10,12$	180 mw	18 hrs
config3	w/b/nac/emp full-span	$\alpha=8$ $\beta=0,6,12,18$	260 mw	25 hrs

HSR H-L CFD

The resource requirements using CFL3D on the C-90 at NAS are shown in the following table, which summarizes the memory required and the average run time for all the cases considered.

Convergence Characteristics for H-L Reference H, w/b/n/htail at α = 10°
M = 0.24, Re = 8 mil
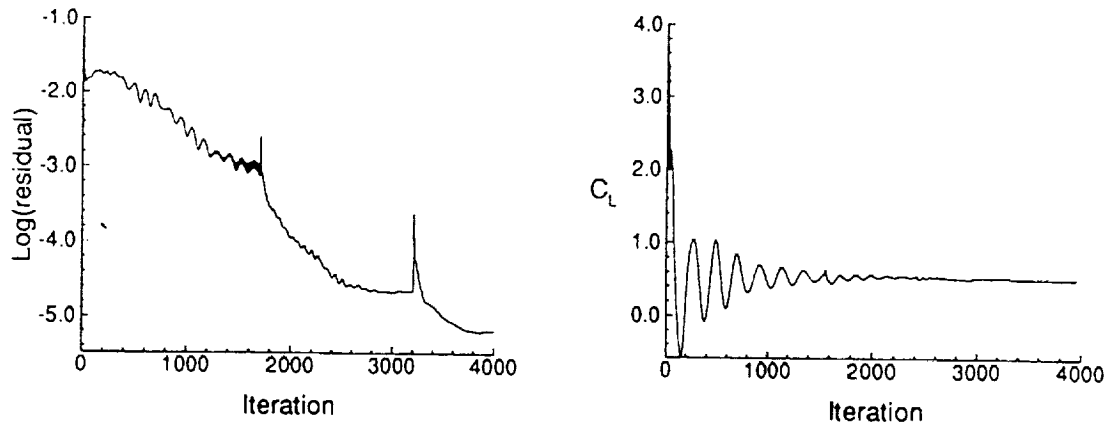
Convergence Characteristics for H-L Reference H, w/b/n/emp at α = 8°, β = 12°
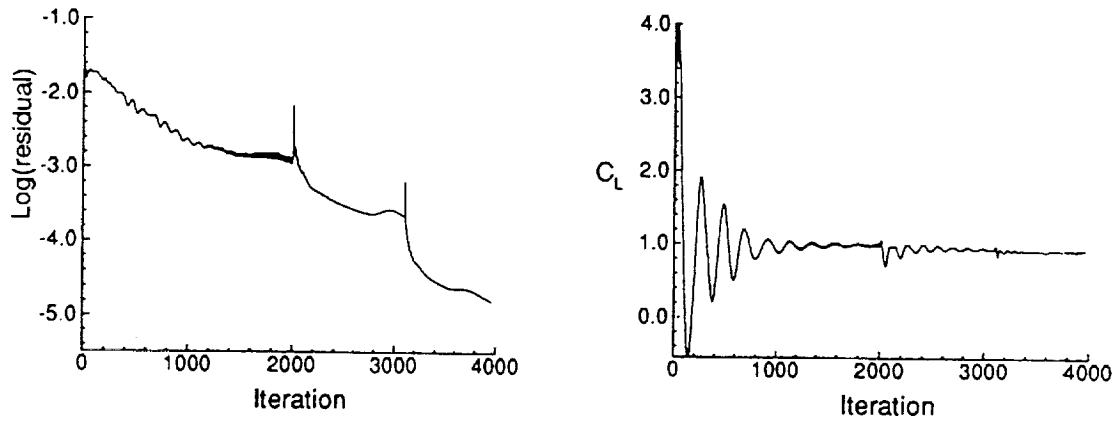
Residual and lift histories for the config2 case at α = 10° and the full-span config3 case at α = 8° and β = 12°, M = 0.24 and Re = 8.0 million. Both show approximately 3.5 order reduction in residual magnitude with negligible oscillations in C_L

Forces and Moments for Reference H w/b
M = 0.24, Re = 8 mil
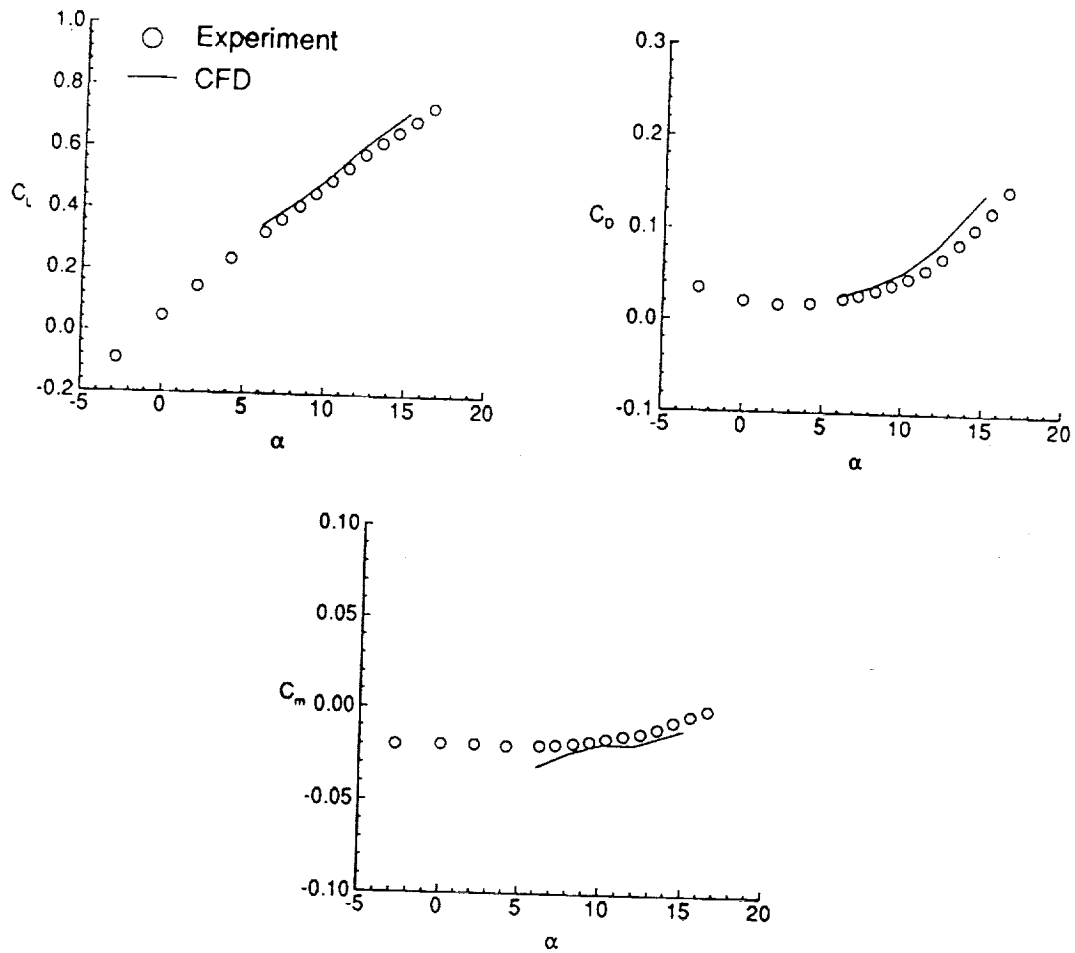
This figure shows the predicted forces and moments compared to experiment for config1, which it the RefH high-lift wing/body configuration. Good correlations are seen, though there is some overprediction of the lift and drag. The pitching moment trend is good but questionable $\alpha = 6°$.

Reference H C_p Comparisons at $\alpha = 6°$

$M = 0.24$, $Re = 8$ mil

The predicted chordwise pressure distributions extracted from the solution shown on the previous slide are compared to experiment and show very good correlation.

Crossflow P$_t$ Contours for RefH 30 /10

M = 0.24, Re = 8 mil, α = 6

P$_t$

- 0.7
- 0.71
- 0.70
- .0.68
- 0.66
- 0.64
- 0.62
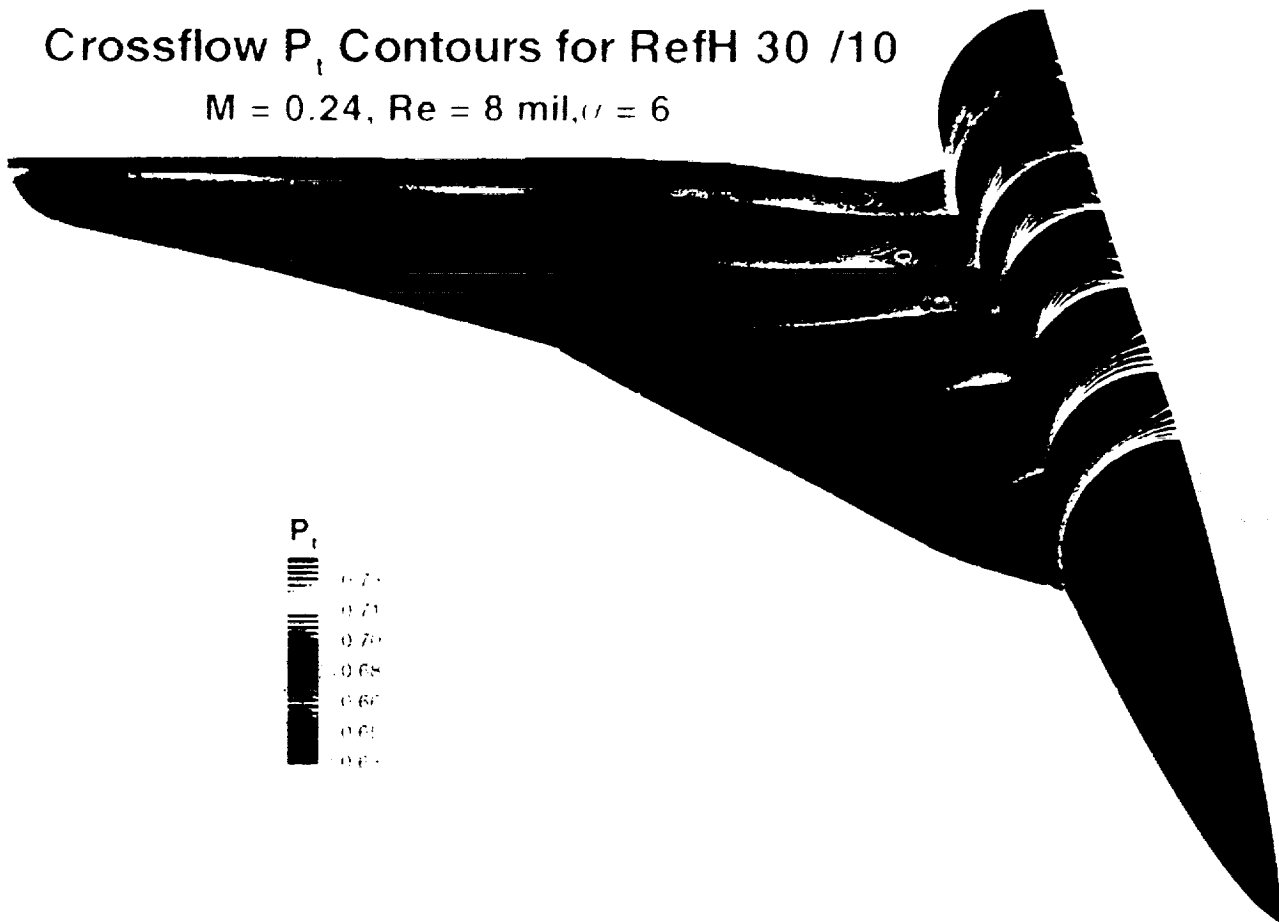
Total pressure contours are plotted in six crossflow planes at α = 6 for the RefH wing/body configuration. In general, the flow on the wing is attached except for a small inboard vortex, which emanates from the apex of the wing.

1986
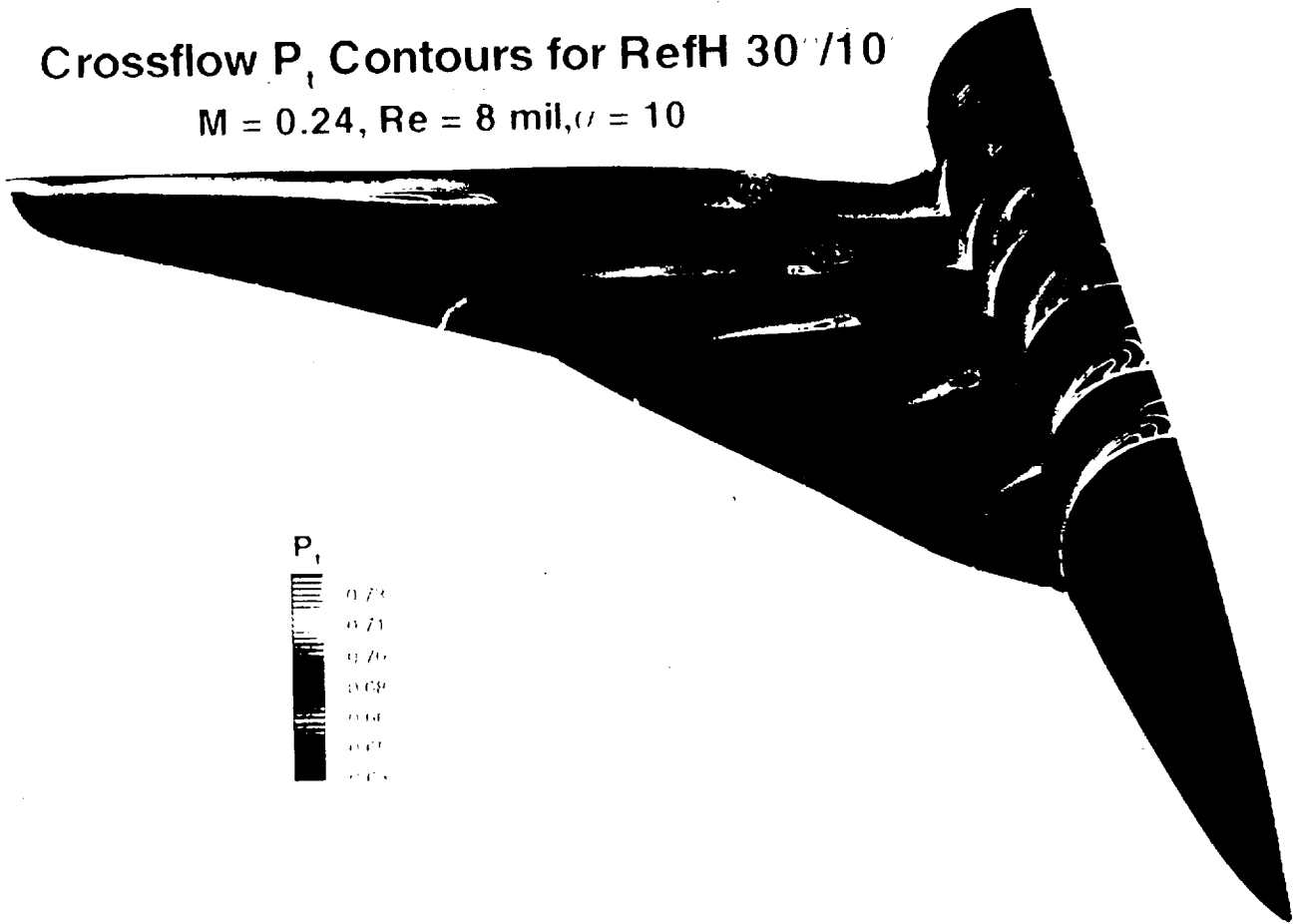
Total pressure contours are plotted in six crossflow planes at $\alpha = 10°$ for the RefH wing/body configuration. Another vortex has formed outboard of the apex vortex, and this elongated vortex emanates from the leading-edge hingeline. A weak crank vortex has developed and appears confined to the leading-edge flap region as it propagates downstream. A fuselage vortex has also formed.

Reference H C$_p$ Comparisons at $\alpha = 10°$

M = 0.24, Re = 8 mil
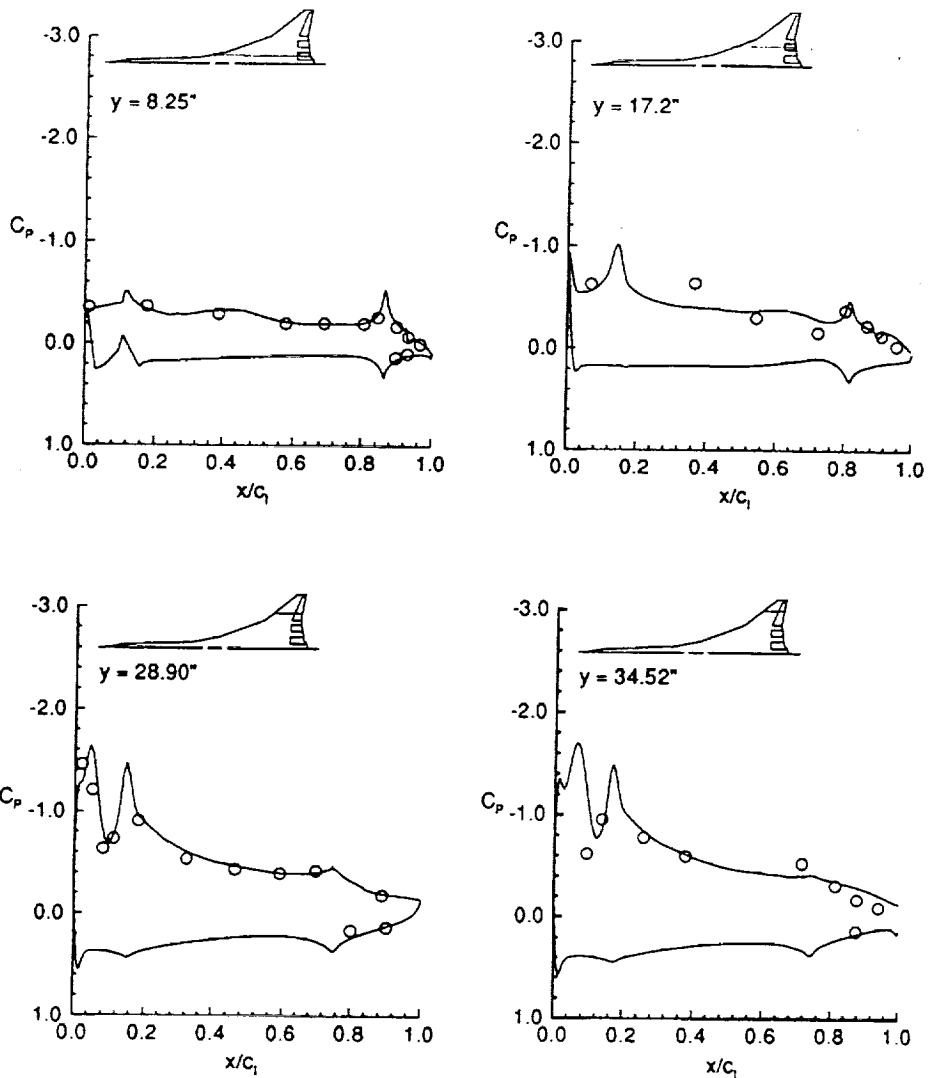
The predicted chordwise pressure distributions extracted from the solution shown on the previous slide are compared to experiment and again show good correlation, though some discrepancies are seen on the trailing-edge flap at y = 34.52"

Crossflow P$_t$ Contours for RefH 30°/10

M = 0.24, Re = 8 mil, α =15

P$_t$
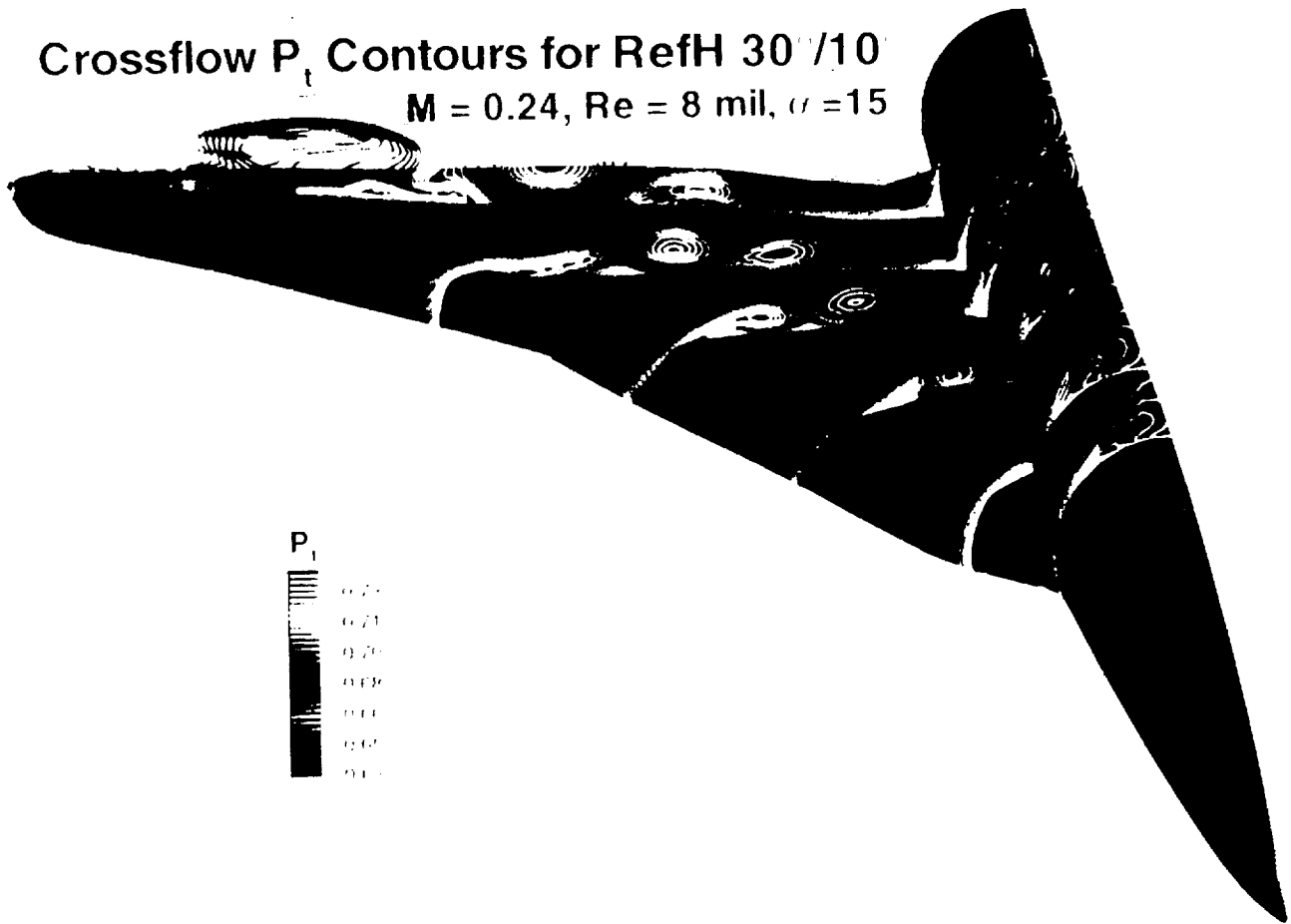
Total pressure contours are plotted in six crossflow planes at α = 15° for the RefH wing/body configuration. A very complicated vortical flow pattern has developed, and all the vortices that were present for the α = 10° case have increased in size and strength. The crank vortex merges with a leading edge vortex which develops just upstream of the crank. This combined vortex moves inboard onto the wing as it travels downstream where it begins to dissipate near the trailing edge.

1989

Reference H C_p Comparisons at $\alpha = 15°$

M = 0.24, Re = 8 mil
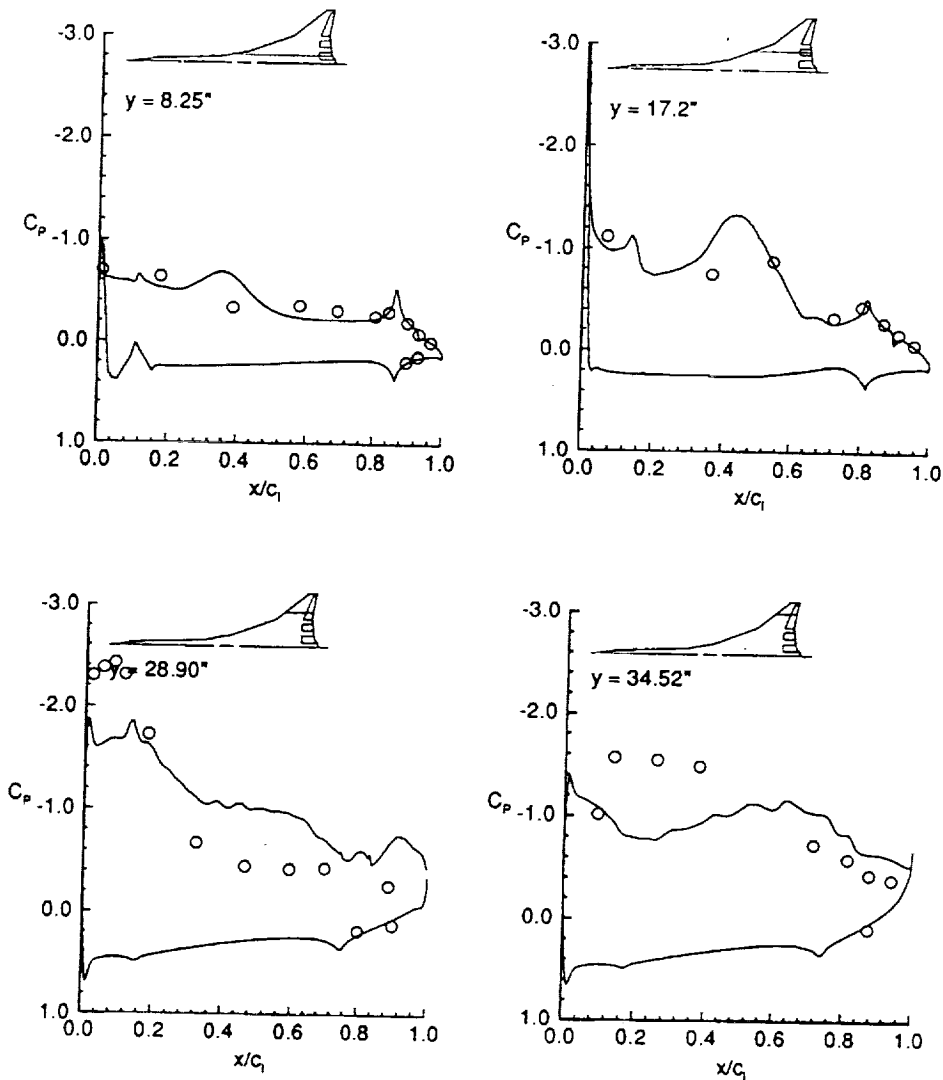
The predicted chordwise pressure distributions extracted from the solution shown on the previous slide are compared to experiment and correlate well for the first two chordwise stations. However due to the massive flow separation on the outboard of the wing, the predicted pressure distributions show poor comparisons. Note in particular the decrease in the predicted suction peak values at the leading-edge.

1990

Forces and Moments for Reference H w/b/nac/htail
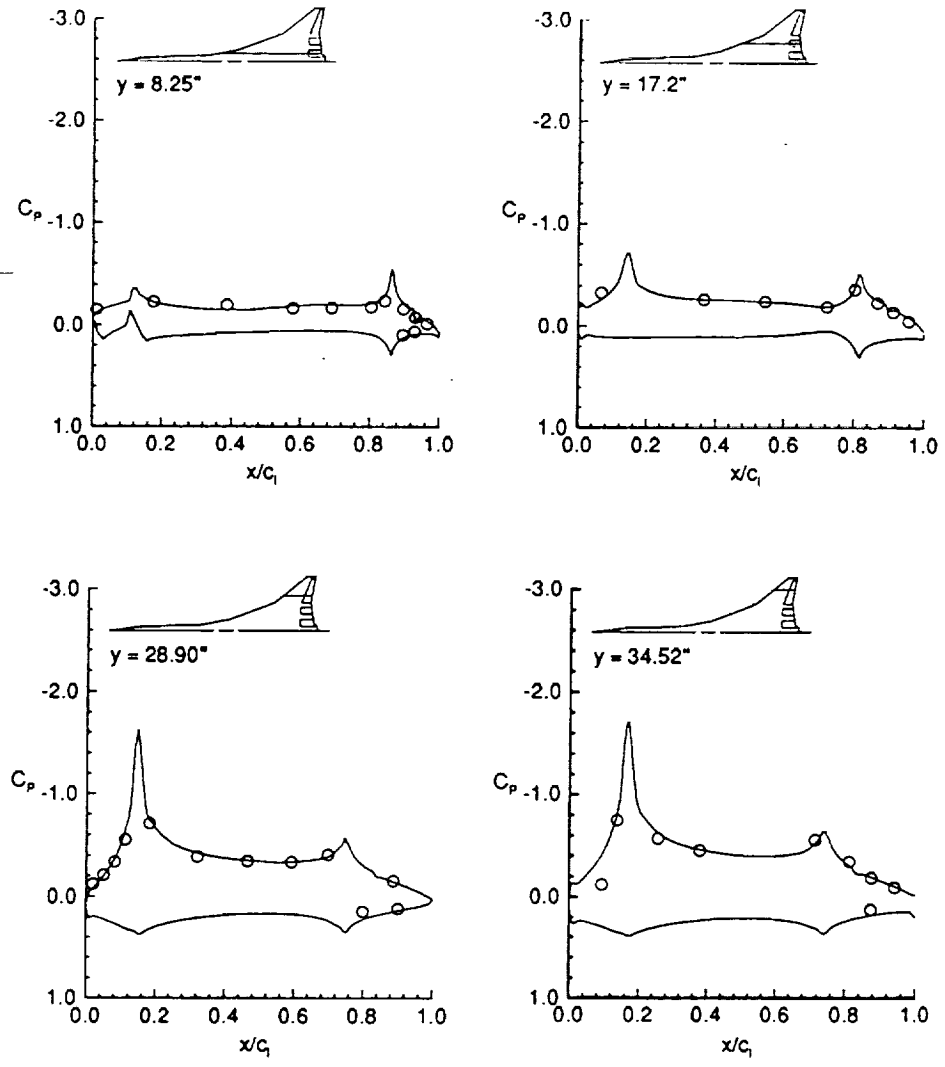### M = 0.24, Re = 8 mil
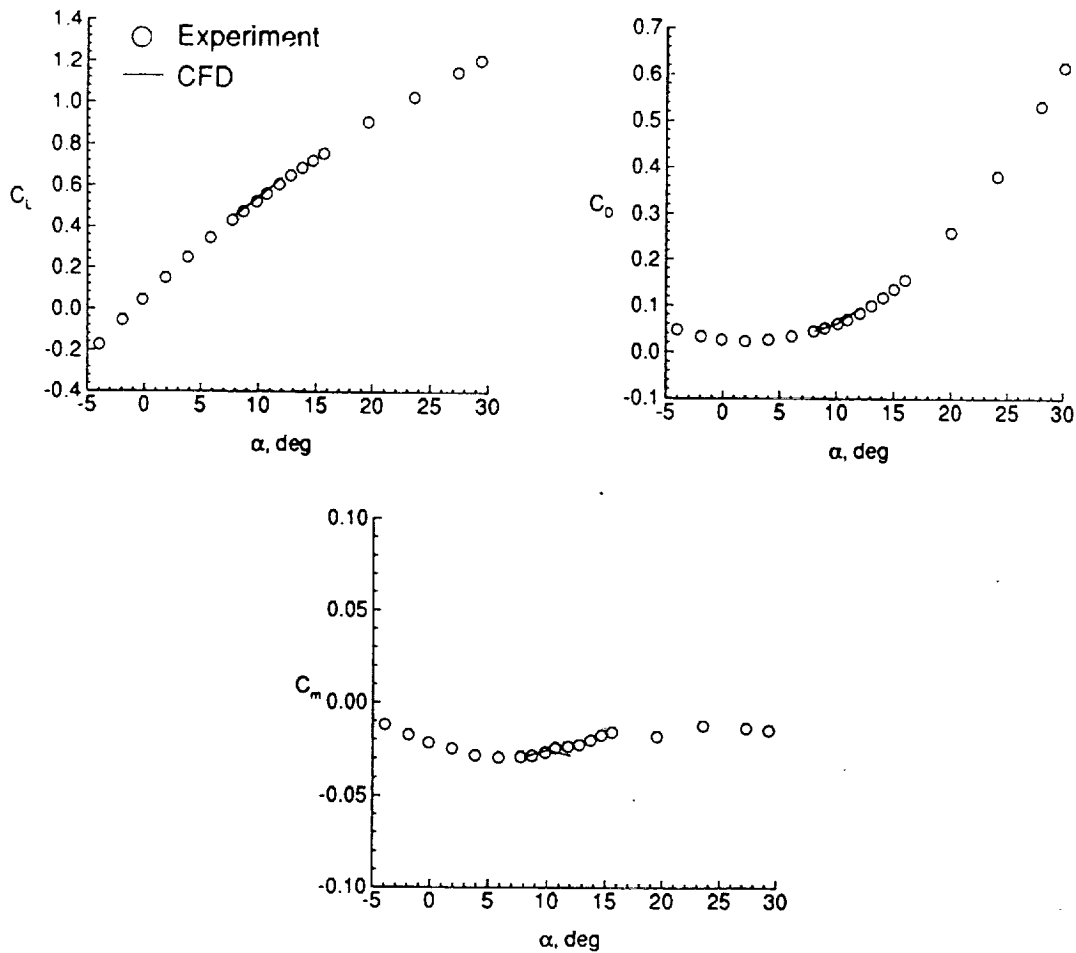
This figure shows the predicted forces and moments compared to experiment for config2, which is the RefH high-lift wing/body/nac/htail configuration. Very good correlations are seen. Since the surface pressure distributions were similar for both config1 and config2, no C_p comparisons are shown for config2. Off-surface contours on the wing were also similar for both cases, though some differences are noted in the wake region.

Full Span RefH 30°/10° Surface Grid
w/b/nac/emp
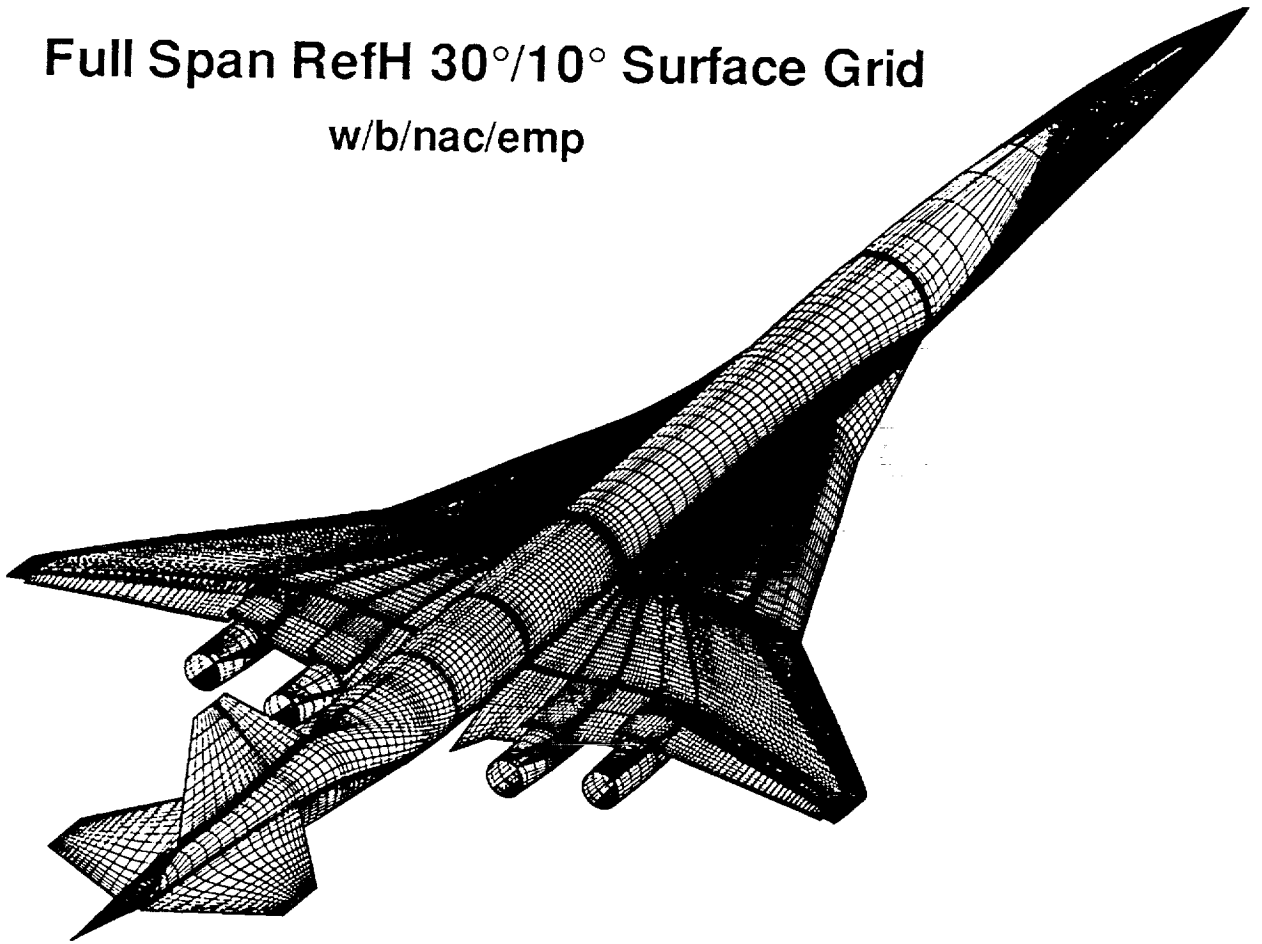
The full-span Reference H (30/10) wing/body/nacelle/empennage surface grid is shown here. This grid contains over 7.0 million points and has 74 blocks. Lateral performance calculations were made using this grid at $\alpha = 8°$, and $\beta = 0°, 6°, 12°,$ and $15°$.

Forces and Moments for RefH w/b/nac/emp
M = 0.24, Re = 8 mil
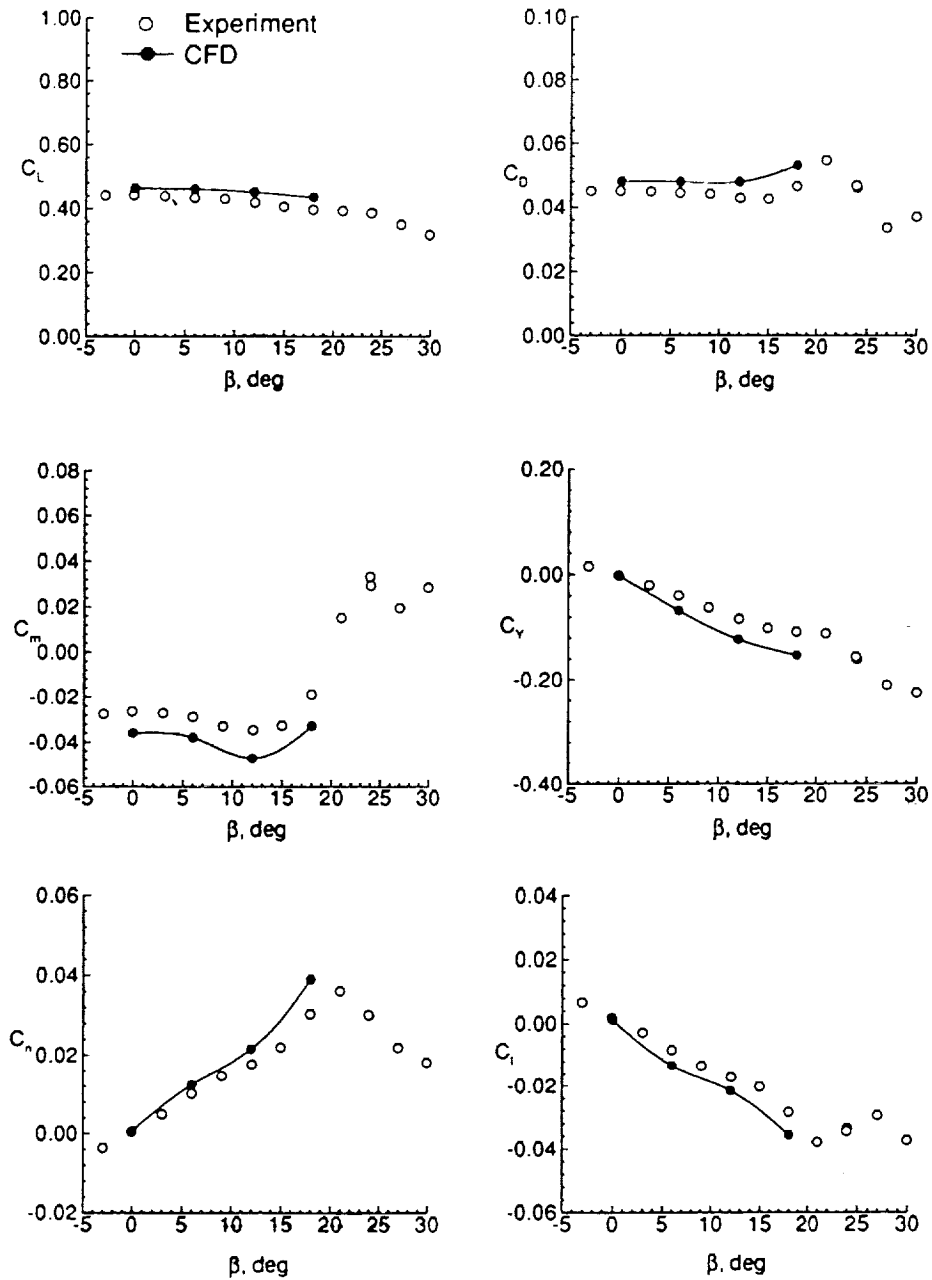
The computed forces and moments for the full-span RefH configuration obtained at a sideslip angle of $12°$ and at $\alpha = 8°$ are compared to experiment. The lateral performance trends are well predicted, though the point values tend to deviate more than the previous cases. This could be due to the coarseness of the grid.

Contours on RefH Upper Surface
M = 0.24, Re = 8 mil, β = ...

C_p Contours on RefH Lower Surface
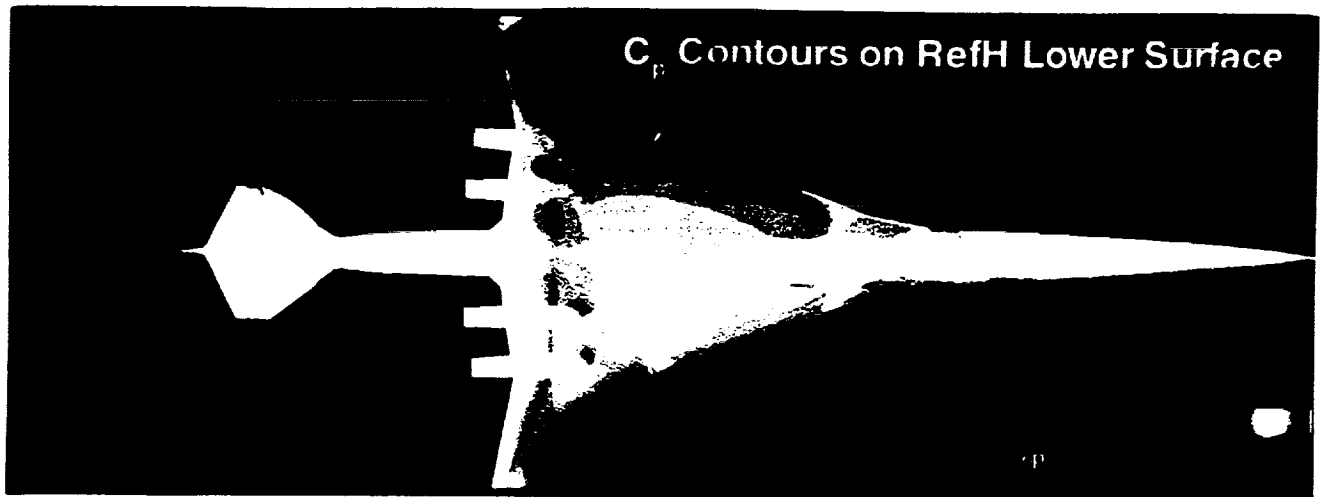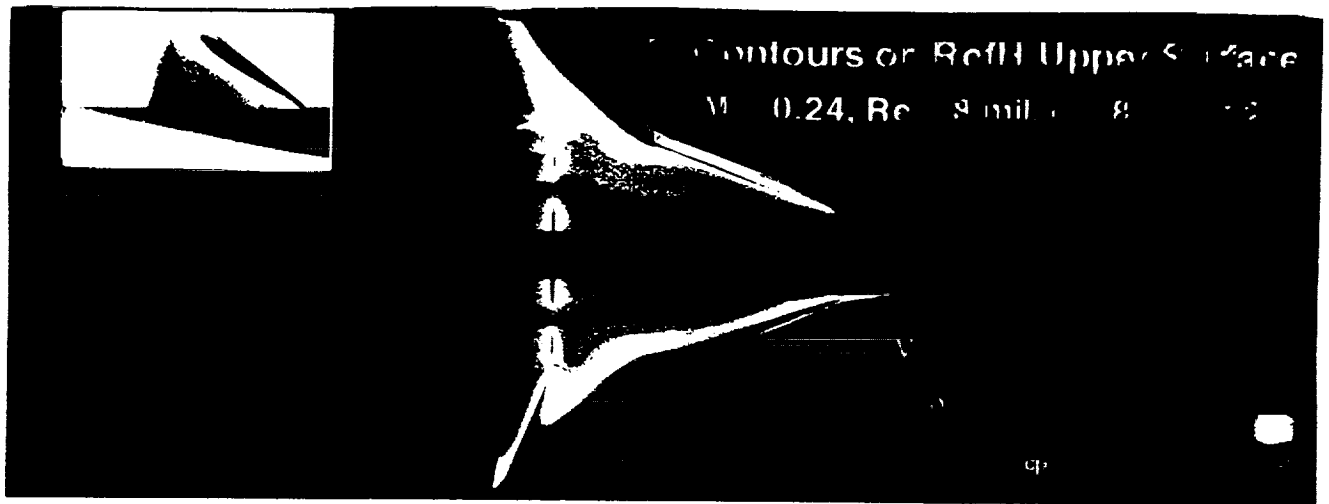
Surface pressure contours for the upper and lower surfaces of the RefH at a 12°
sideslip angle are shown. Note the higher loading of the right wing, which is
characterized by higher suction peaks compared to the left wing. A vortex has also
formed on the leading-edge of the vertical tail.

RefH C_p Comparisons at $\alpha = 8°$, $\beta = 12°$

M = 0.24, Re = 8 mil
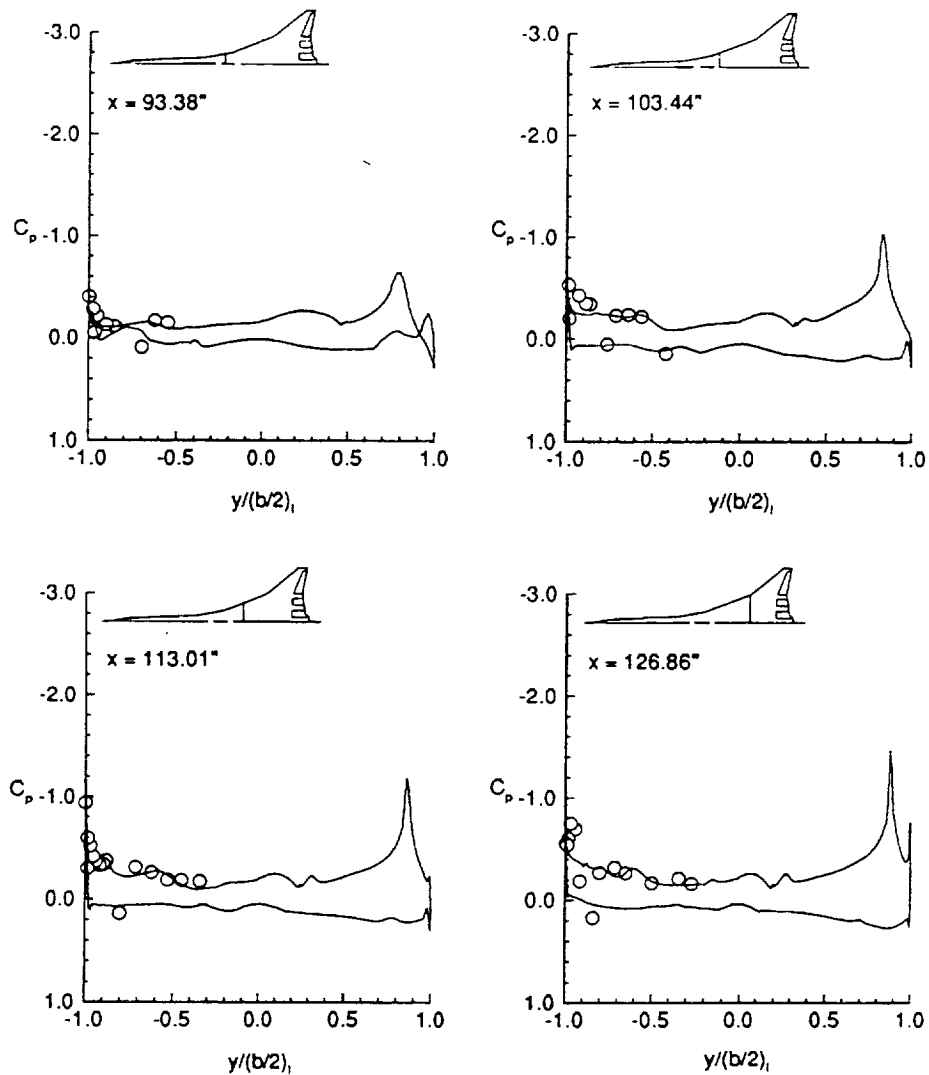
This figure shows C_p comparisons for the full-span configuration at four fuselage stations. The spanwise distance on each plot ranges from -1.0 to +1.0, where the 0 to -1.0 interval represents the left wing and the 0 to +1.0 interval represents the right wing. Note the asymmetry of the pressure distribution curves and the higher suction peaks that occur on the right wing. Correlations are fair and could probably be improved with more grid resolution in the leading edge regions.

RefH C_p Comparisons at $\alpha = 8°$, $\beta = 12°$

M = 0.24, Re = 8 mil
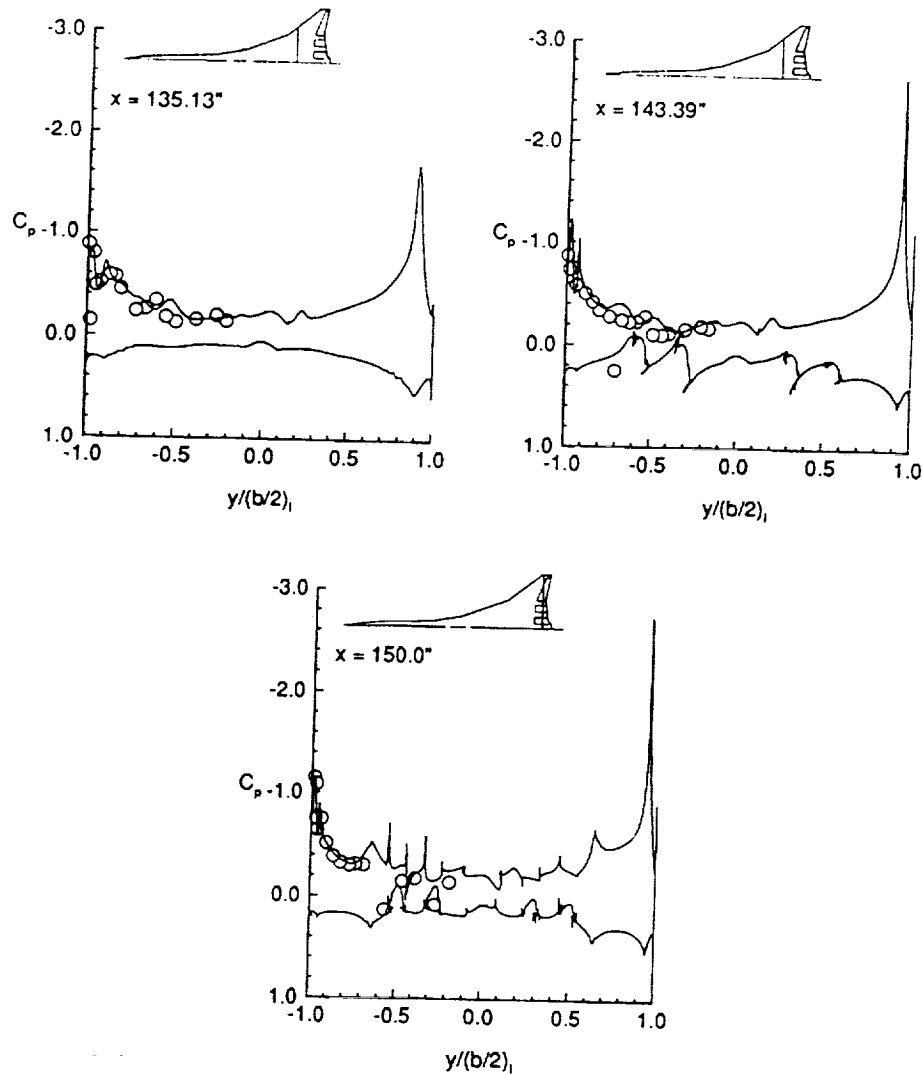
This figure shows C_p comparisons for the full-span configuration at three downstream spanwise stations. Fair to good correlations are noted. The nonsmooth lower surface pressures at x = 143.39" are due to the alternating high pressure. low pressure effects that occur on the nacelles at a 12° sideslip angle. Likewise the choppy pressure distributions depicted at x = 150" were expected since the pressures were extracted on and around the trailing-edge flaps.

RefH C_p Comparisons at $\alpha = 8°$, $\beta = 12°$
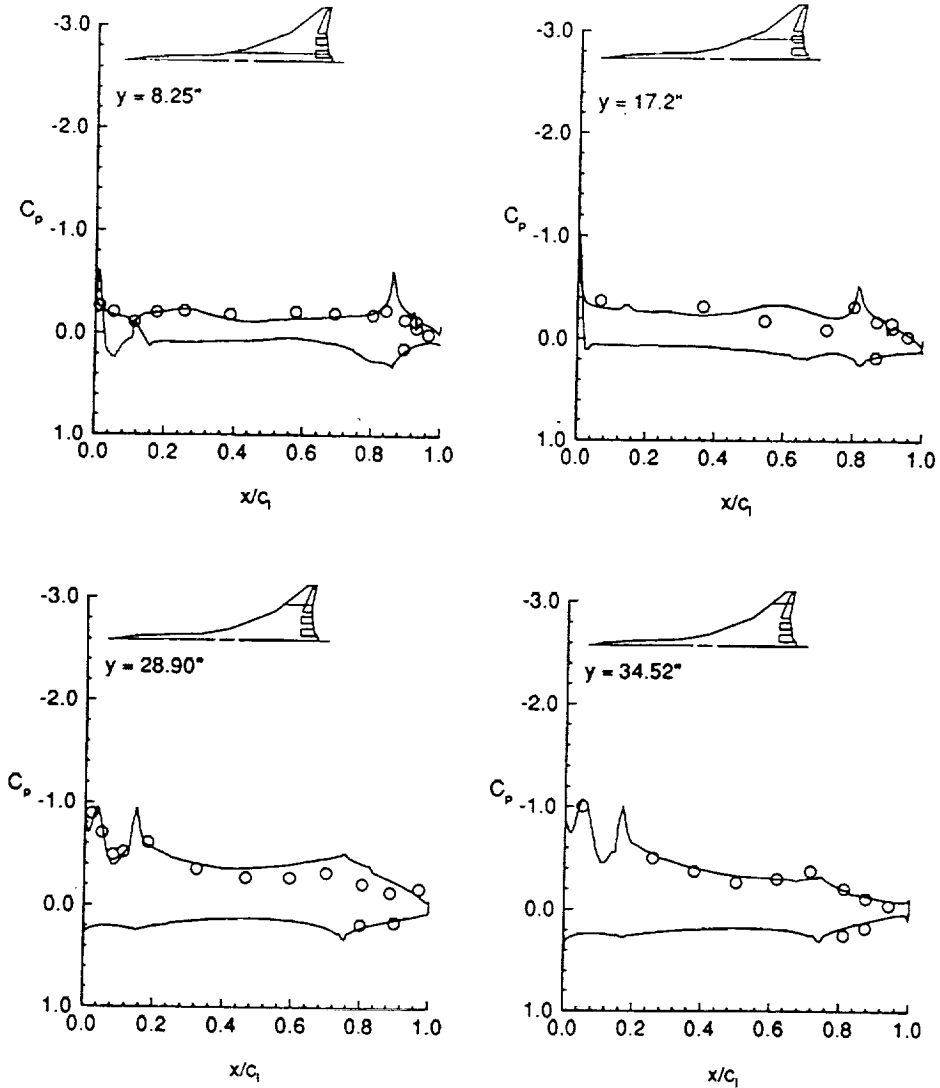
M = 0.24, Re = 8 mil

This figure shows C_p comparisons at four chordwise stations ancd correlation between computation and experiment are good.

Reference H C_p Comparisons with Two Different Grids
M = 0.24, Re = 8 mil, $\alpha = 8°$, $\beta = 0°$

○   Experiment
———   CFD (w/b/nac/emp)
· · · -   CFD (w/b/nac/htail
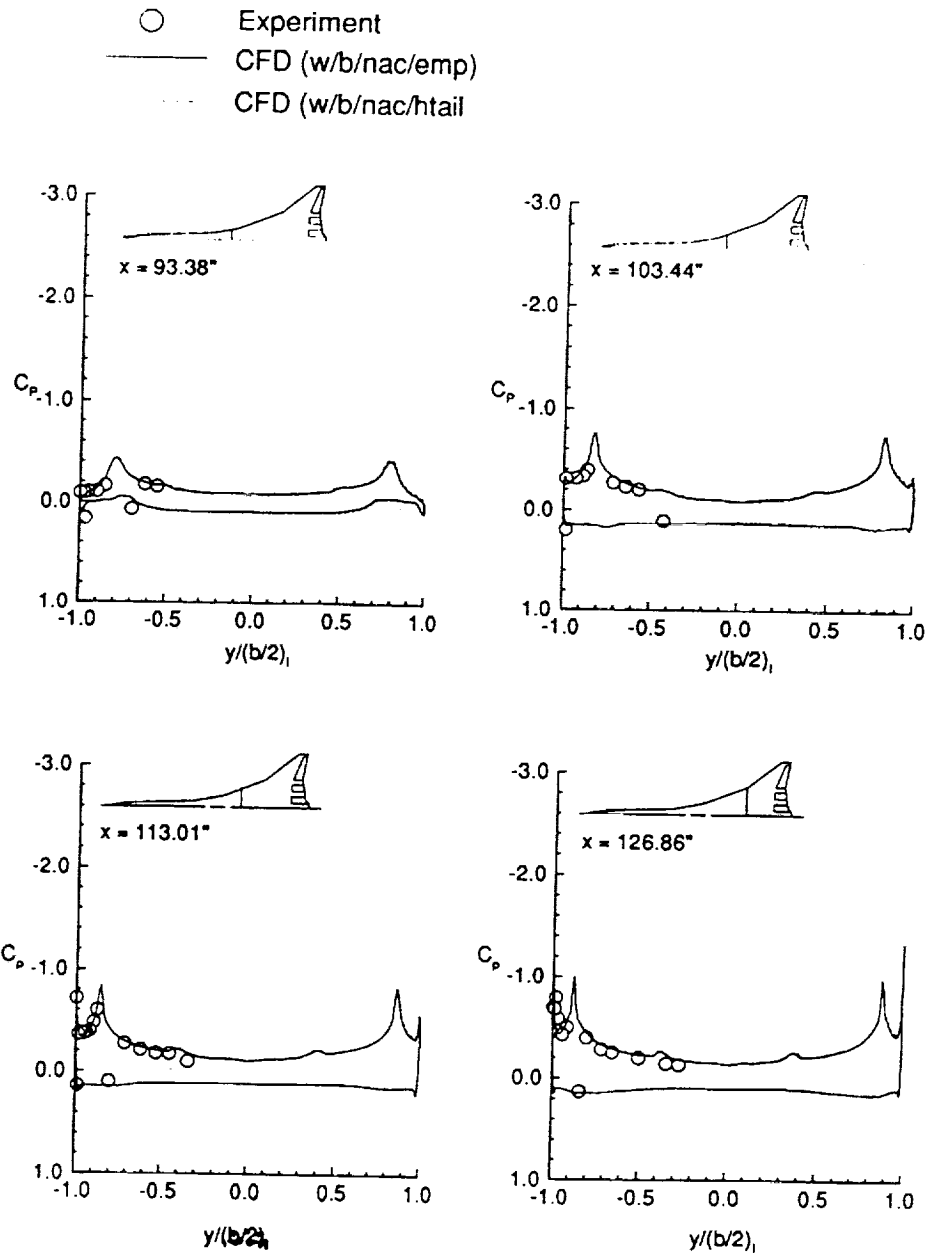
Since the full-span high-lift RefH grid (config3) was a mirrored coarser version of config2, C_p comparisons were made at the various chordwise and spanwise stations to address any grid effects in the sideslip solutions. This figure shows the pressure distributions at four spanwise stations obtained by the two grids; the experimental values are also plotted. Excellent agreement is seen between the two CFD solutions using the different grids, and correlation with experiment is also good. **1998**

Reference H C_p Comparisons with Two Different Grids
M = 0.24, Re = 8 mil, α = 8°, β = 0°

○ Experiment

——— CFD (w/b/nac/emp)

- - - - - - CFD (w/b/nac/htail

C_p comparisons made at three additional downstream spanwise stations show a slight deviation in pressures at the inboard suction peak at approximately $y/(b/2)_i = 0.40$. Correlaton with experiment shows good agreement.

CONCLUSIONS

- Computational results correlated well with experimental force and moments data and were capable of predicting the longitudinal and lateral performance trends.

- Predicted surface pressures compared well to experiment except when the flow began to develop extensive outboard separation.

- Predicted off-surface and surface flow viz offers insight into the flow physics and continues to provide important details that the wind-tunnel does not.

- Multi-block structured grids for high-lift w/b/nac/emp HSCT configuration is still a time consuming process in terms of grid generation and code set-up/debugging.

HSR H-L CFD

The slide is self-explanatory
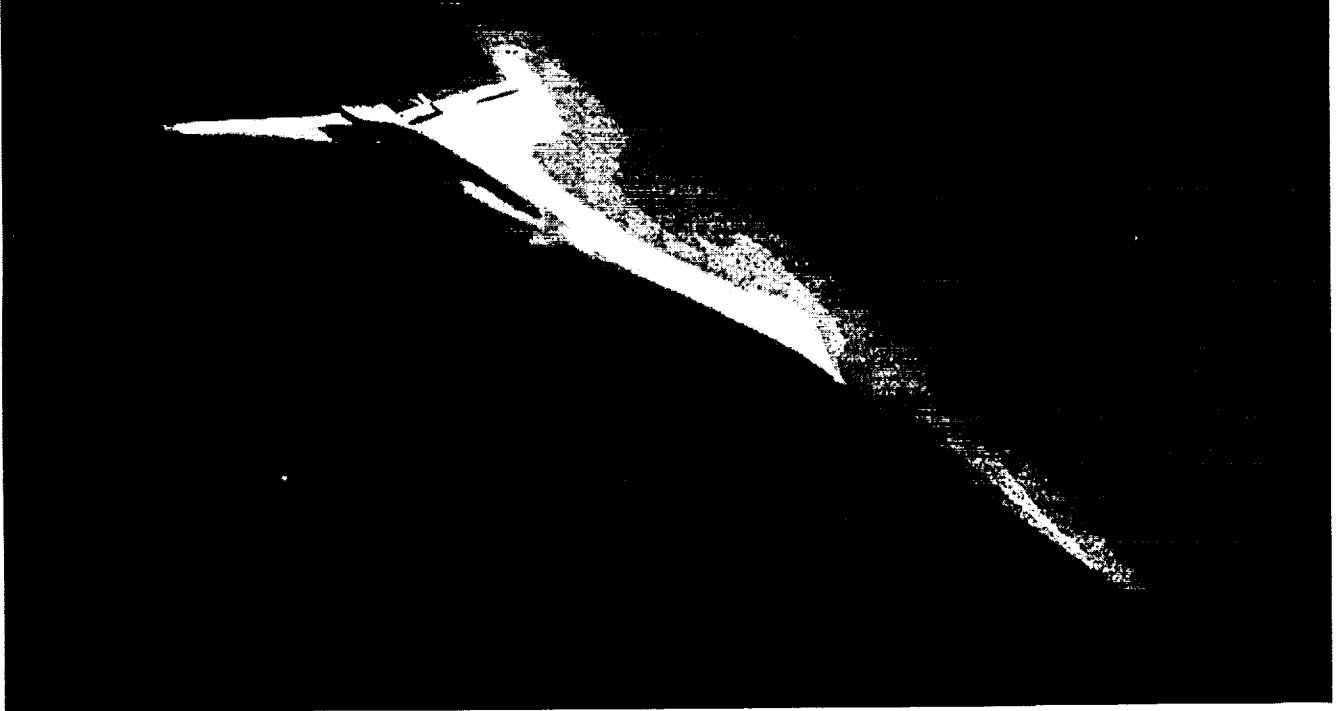
Future work will include solving the high-lift flow about the Technology Concept Airplane (TCA) using CFL3D. Surface pressure contours are shown in this figure at $\alpha = 10°$.

This page intentionally left blank.

ASSESSMENT AND APPLICATION
OF CFD METHODS
FOR HSCT HIGH-LIFT AERODYNAMICS

Allen Chen

Boeing Commercial Airplanes Group

High Speed Research Program

Aerodynamic Performance Technology Workshop

February 26, 1997

2003

- Quick review of various types of CFD codes.

- Issues and recommendations are intended to generate discussions either inside or outside meeting rooms.

2004

Outline

- ## Review of CFD Codes

- ## Overview of CFD Activities

- ## The Process

- ## Results

- ## Issues

- ## Conclusions and Recommendations

- All these types codes are CFD codes. Some people have forgot that linear codes such as AERO2S are CFD codes too. Good aerodynamic work is accomplished by appropriate combination of various tools.

- Euler codes are not used extensively at Boeing. Full potential codes are. TRANAIR was used in assessing power effect in defining the 5% TCA high-lift model. TRANAIR was also used in assessing the tunnel floor boundary layer characteristics prior to Test 437 conducted at NASA-Langley's 14- by 22-ft Wind Tunnel. The results are not to be presented here.

2006

Review of CFD Codes

CFD (Computational Fluid Dynamics)

- # Navier-Stokes

- # Euler

- # Full potential

- # Linear

2007

- Boeing provides geometry, test data. It is a non-trivial task.

- Geometry is provided as either surface definitions such as bicubic spline patches or grids.

Overview of CFD Activities

- ## BCAG

  Process improvement, quality improvement, etc.

  Coordination with Dynacs and LMAS

- ## Dynacs

  Evaluation of various codes (1995)

  Reynolds number effect, transition location effect (1996)

- ## LMAS

  T.E. flap deflection effect, ground effect (1996)

2009

- Examples of objectives include:

- How well do the CFD results match test data?

- Can CFD predict Reynolds number effects, transition location effects?

- Can CFD predict performance of various high-lift systems such as simple flap versus sealed flap?

- Can CFD predict LE and TE flap deflection effects?

- Can CFD predict ground effects?

- It is non-trivial to prepare a case because test data and geometry need to be identified and located.

- It is important for the CFDers to know something about the test.

- Accurate test log helps tremendously in identifying the geometry and flight conditions.

2010

The Process

- Identify the objectives

- Identify the test data

- Locate the test data and the geometry

- Prepare the input

- Postprocessing

- More Navier-Stokes results will be shown than linear results.

Results

- ## Navier-Stokes

- ## Linear

- This is where we were.

2014

Review of Run Matrix (Navier-Stokes)

(Reported in September, 1995)

- Mach 0.24, 6% scale

- All turbulent

- Ref. H wing/body flaps up
  (α 6°, 10°)

- Ref. H w/b flap LE 30°/outb'd TE 20°
  (α 10°)

2015

- We continued and expanded the scope.

- We are still learning.

2016

Review of Run Matrix (Navier-Stokes)

(1996 Results)

- Mach 0.24, 6% scale

- Ref. H w/b flap LE 30°/outboard TE 20°
  (α 6°, 10°, 12°, 14°, 16°)

- Flap ends treatment variations

- Grid density variations

- The activity was to support the NTF Test 089 where the modified 2.2% Ref. H model with the TCA planform was tested. The outboard wing is entirely TCA. The inboard is a blend of Ref. H and TCA to save cost in model design and fabrication.

2018

Review of Run Matrix (Linear)

- Mach 0.3, $-2° < \alpha < 22°$

- Ref. H wing/body

- Modified Ref. H wing/body with TCA planform

- Flaps 0/0, 30/10

2019

- Most of the test data were acquired to support developing high-lift technology.

- Various groups, such as configuration and stability and control, compete for test time. Very little was left to generate data for CFD validations.

- CFDers need to learn how to match the geometry in wind tunnel test. Nacelle effects may be small but nacelles are on for most of the runs.

2020

Review of Run Matrix (Test Data)

- Most of the test data were acquired with nacelles on

- CFD models tried to match the test configuration as much as possible

2021

- Forces and moments are more important than surface pressures for airplane designers. Surface pressures are useful when the geometry needs to be reshaped for better performance.

- Surface velocity vectors are to be compared with mini-tufts pictures. The question is which layer of the Navier-Stokes solution from which the velocity vectors are to be extracted.

- Many more properties are available from Navier-Stokes solutions that are not available from tests. Examples are: vortices, total pressure maps, skin frictions, etc.

2022

CFD/Test Comparisons (Navier-Stokes)

- Forces and moments

- Wing pressures

- Wing surface velocity vectors

- NASA-Langley 14x22ft W. T. Test 404

2023

- Points are concentrated near the leading edge and the trailing edge, with spacings learned from the high-speed subsonic transports.

- Points are also concentrated near the flap hinges.

- Points are concentrated near the TE flap ends in anticipation of drastic local changes. This is done also for the undeflected inboard trailing edge flaps in anticipation of deflecting them for later runs.

- Numbers of cells are divisible by 8 for multi-gridding.

- Stretchings between two neighboring cells are kept small to minimize numerical errors.

2024

Surface Grid for Ref. H W/B LE 30°/Outb. TE 20°

2025
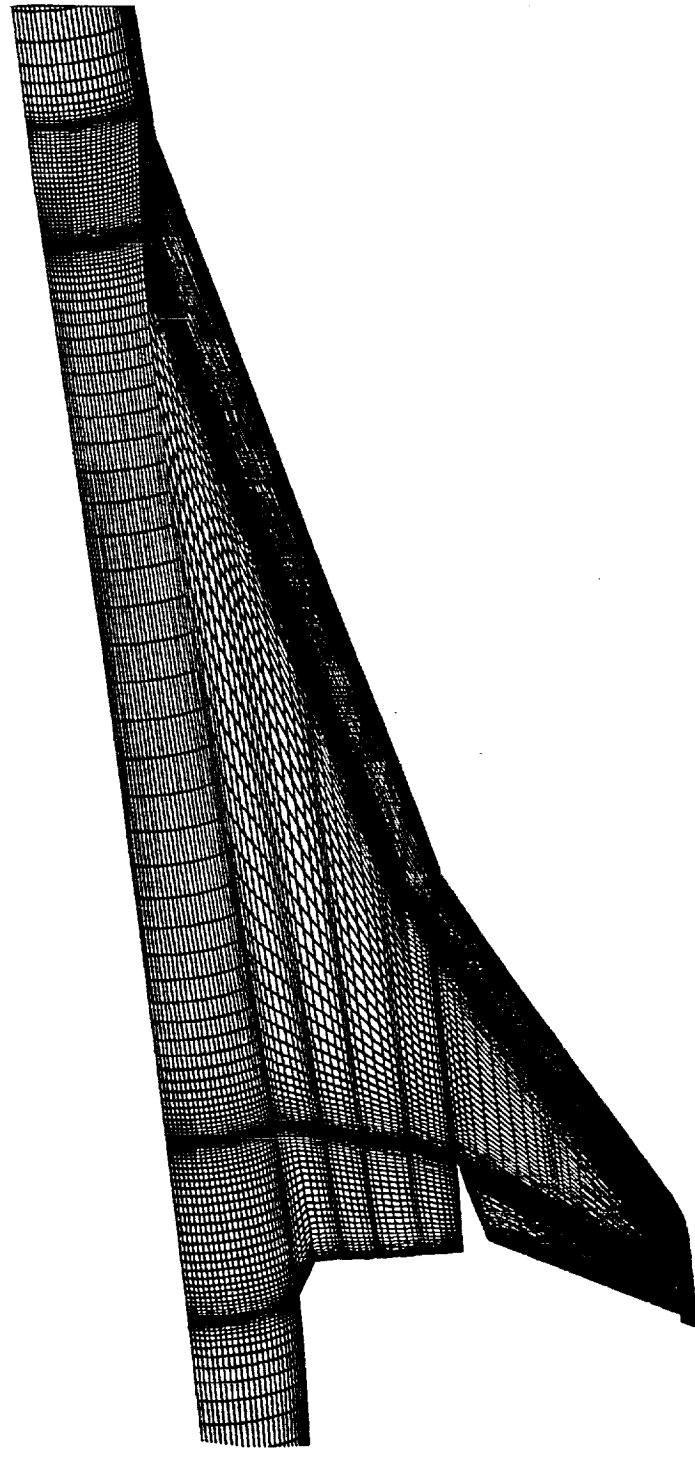
- Constant-K lines are not smooth across the wake. 20 negative cells are present.

Field Grid in the Wake I (JMAX = 73)
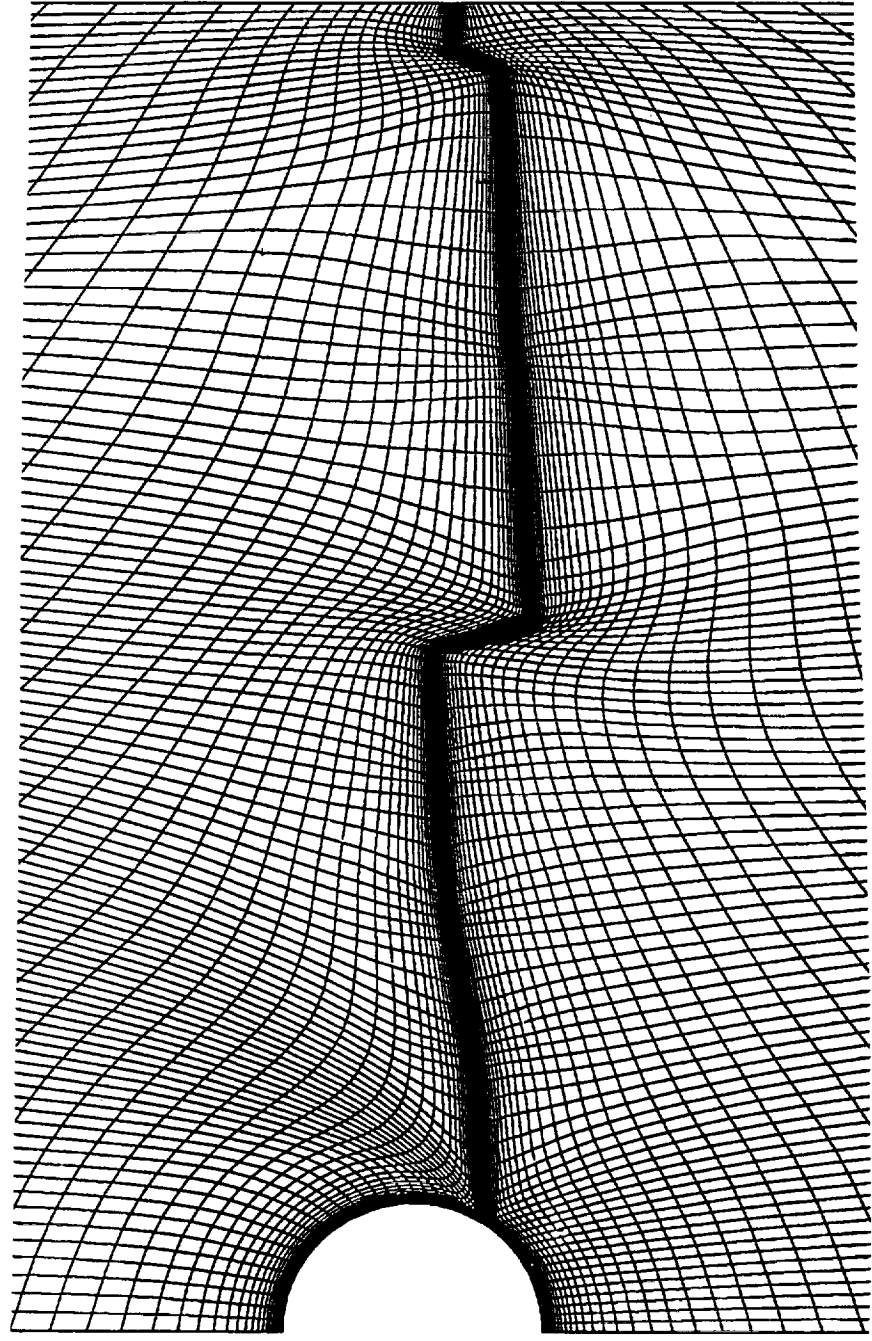
- Constant-K lines are smooth across the wake. No negative cells are present.
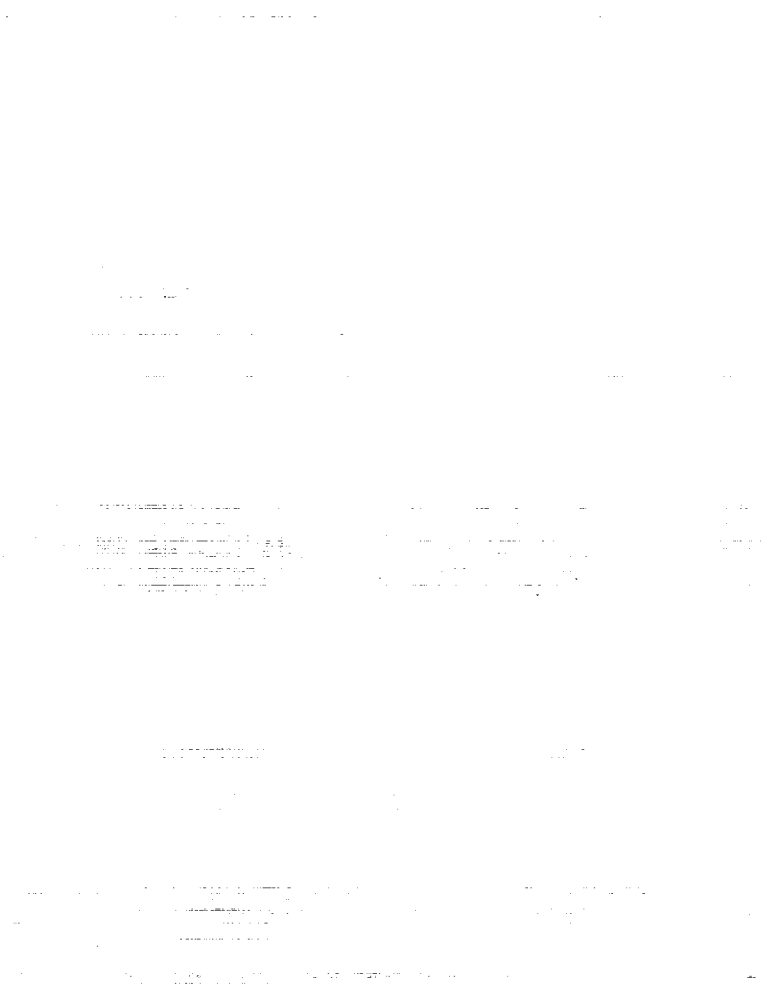
Field Grid in the Wake II (JMAX = 129)
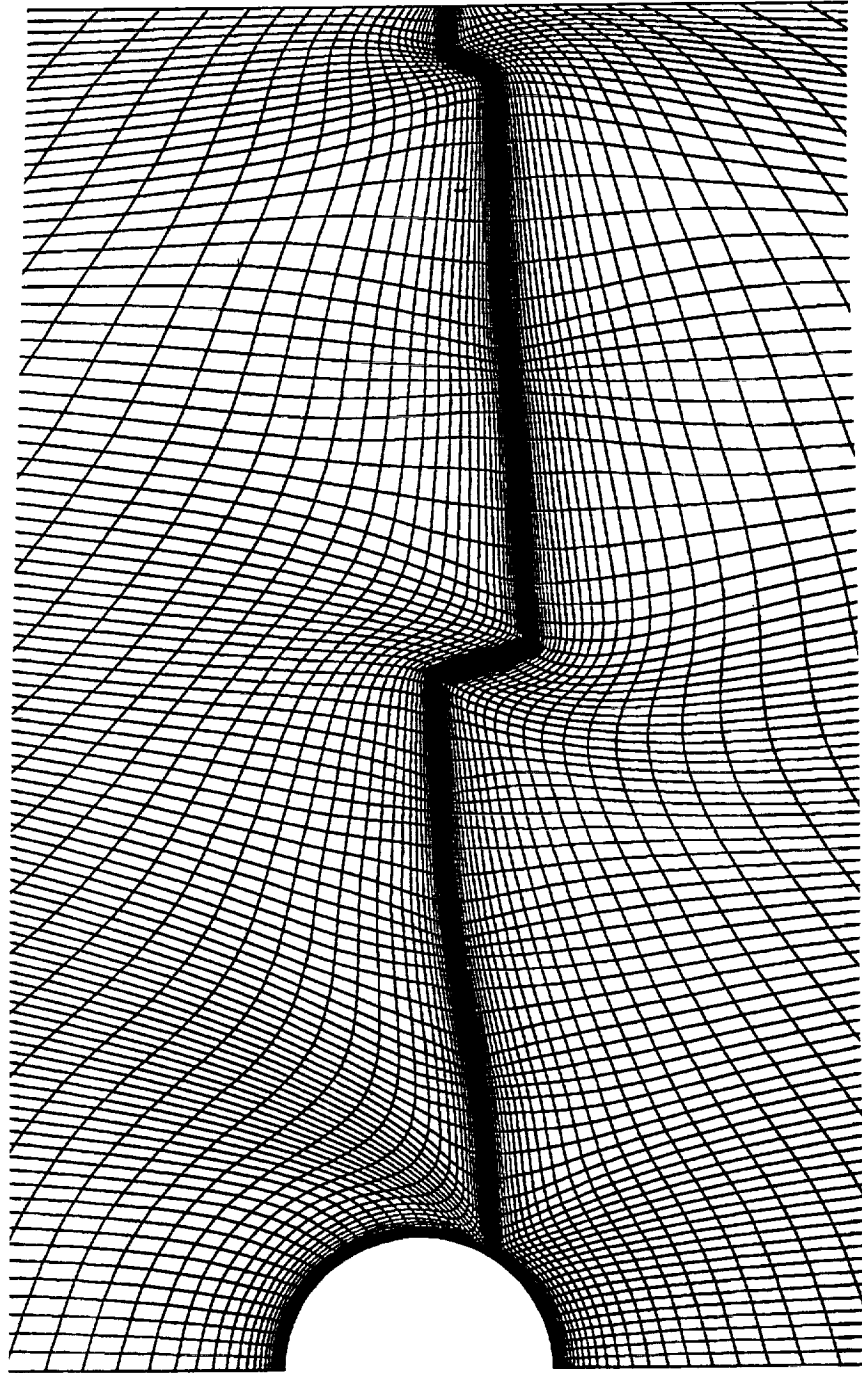
- Solutions depend on the codes. They depend on how the codes were used too.

Forces and Moments from Various Codes I

Ref. H Wing/Body Flaps LE 30, Outboard TE 20, Mach 0.24
Viscous CFD vs NASA-Langley 14x22 Test 404, Run 195

- CFL3D Dynacs
- CFL3D LMAS
- TNS3DMB BCAG
- OVERFLOW Dynacs
- TNSMB Dynacs
- Test data
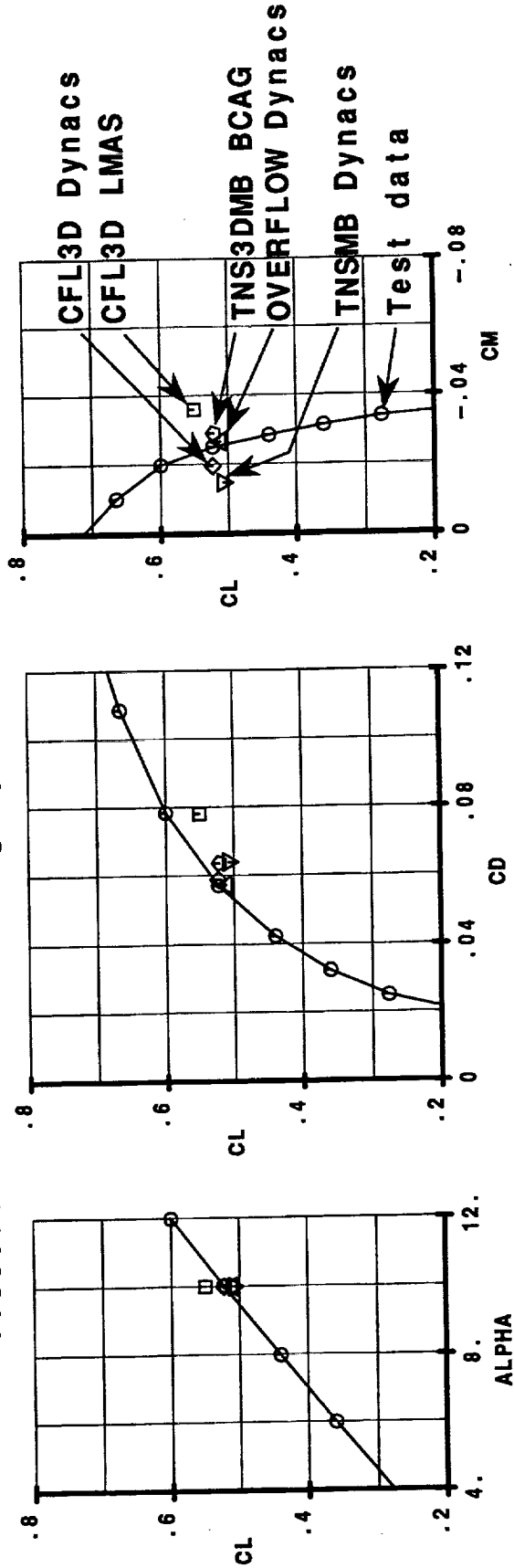
NOTE: Dynacs results were based on 1994 single-block grid
LMAS CFL3D was based on 1995 14-block grid
BCAG TNS3DMB was based on 1996 4-block grid

- All TNS3DMB codes originated from the same place. Enhancements by users made differences in the results.

Forces and Moments from Various Codes II

Ref. H Wing/Body Body Flaps LE 30, Outboard TE 20, Mach 0.24
TNS3DMB vs NASA-Langley 14x22 Test 404, Run 195
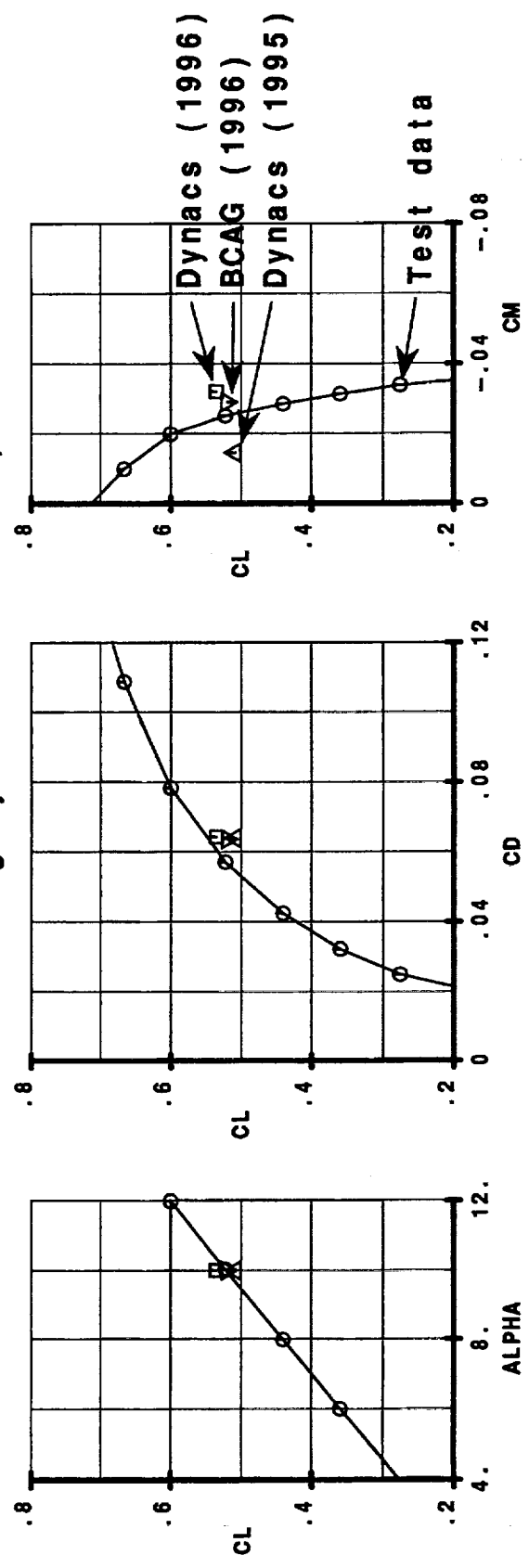
NOTE: 1996 Dynacs results and BCAG results were based on 1996 4-block H-H grid

1995 Dynacs results were based on 1994 single-block O-H grid with a differenct point distribution

- Test/theory comparisons need to be made at various conditions. An angle of attack sweep is an important first step. The code is not doing too well for C_L and C_D for $\alpha > 12°$. The pitching moment trend is not well predicted even for lower angles of attack.

- Mini-tuft pictures (to be shown later) show strong spanwise flows at similar conditions. The geometry for mini-tuft runs did not match CFD model.

- 'Endplating' the trailing edge flap ends increased the lift, as expected. It also lowered the drag, probably due to a more continuous spanload.

CFD Alpha Sweep and Effect of Endplating

Ref. H Wing/Body Flaps LE 30, Outboard TE 20, Mach 0.24
BCAG TNS3DMB vs NASA-Langley 14x22 Test 404, Run 195

TE flap ends flow-through

TE flap ends 'endplated'

Test data
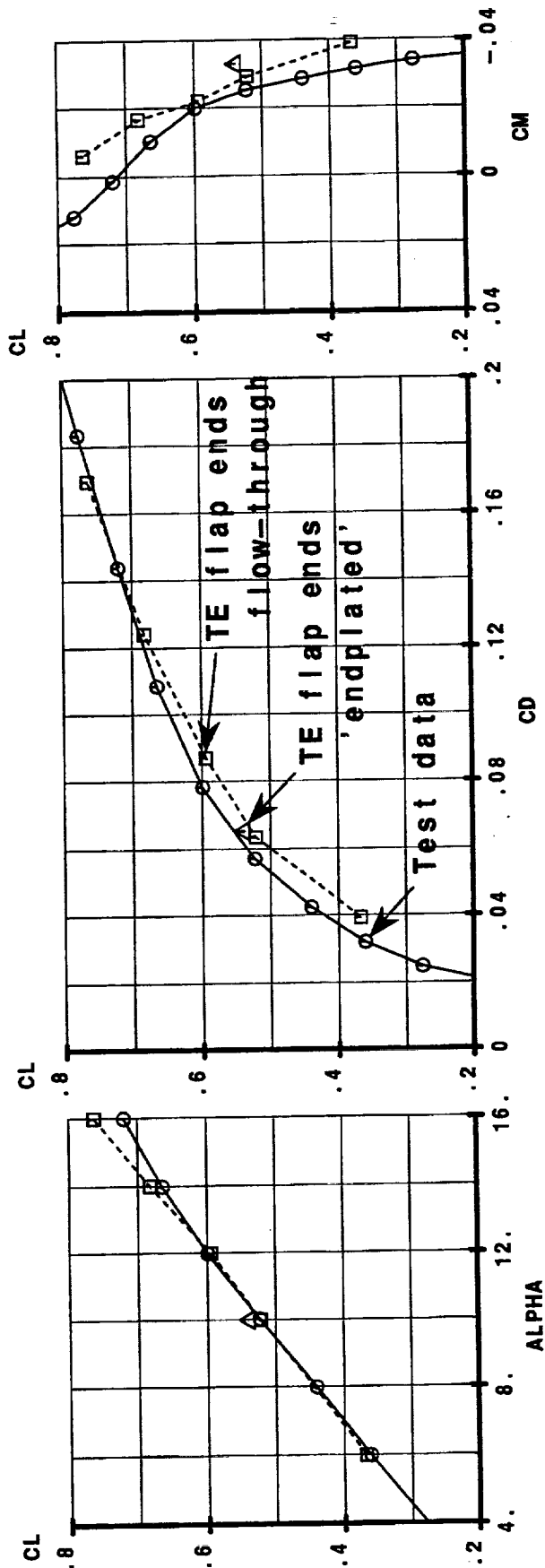
- Increasing the number of grid points normal to the wing surface did not affect the lift and drag significantly. Better pitching moment trend was obtained, however.

Effect of JMAX on Forces and Pitching Moment

Ref. H Wing/Body Flaps LE 30, Outboard TE 20, Mach 0.24
BCAG TNS3DMB vs NASA-Langley 14x22 Test 404, Run 195

JMAX=129
JMAX=73

Test data
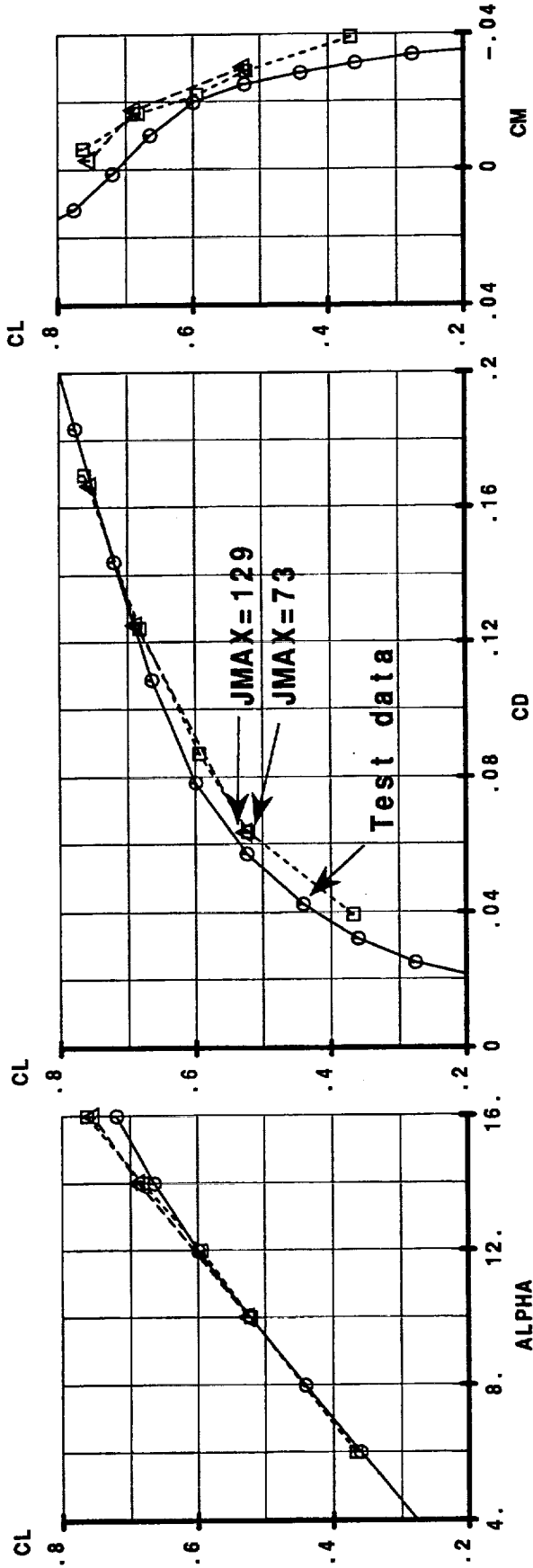
Note: The JMAX 129 case also had a smooth grid in the wake

- The first cell near the wall for the Re independent grid was sized for 90 M Re. The boundary layer thickness was estimated for 8.4 M Re.

- The results are very good for the pitching moment, slightly better than before for drag, rather disappointing for lift.

- Convergence was studied, but not thoroughly.

2038

Forces and Moment from a Re Independent Grid

Ref. H Wing/Body Flaps LE 30, Outboard TE 20, Mach 0.24
BCAG TNS3DMB vs NASA-Langley 14x22 Test 404, Run 195
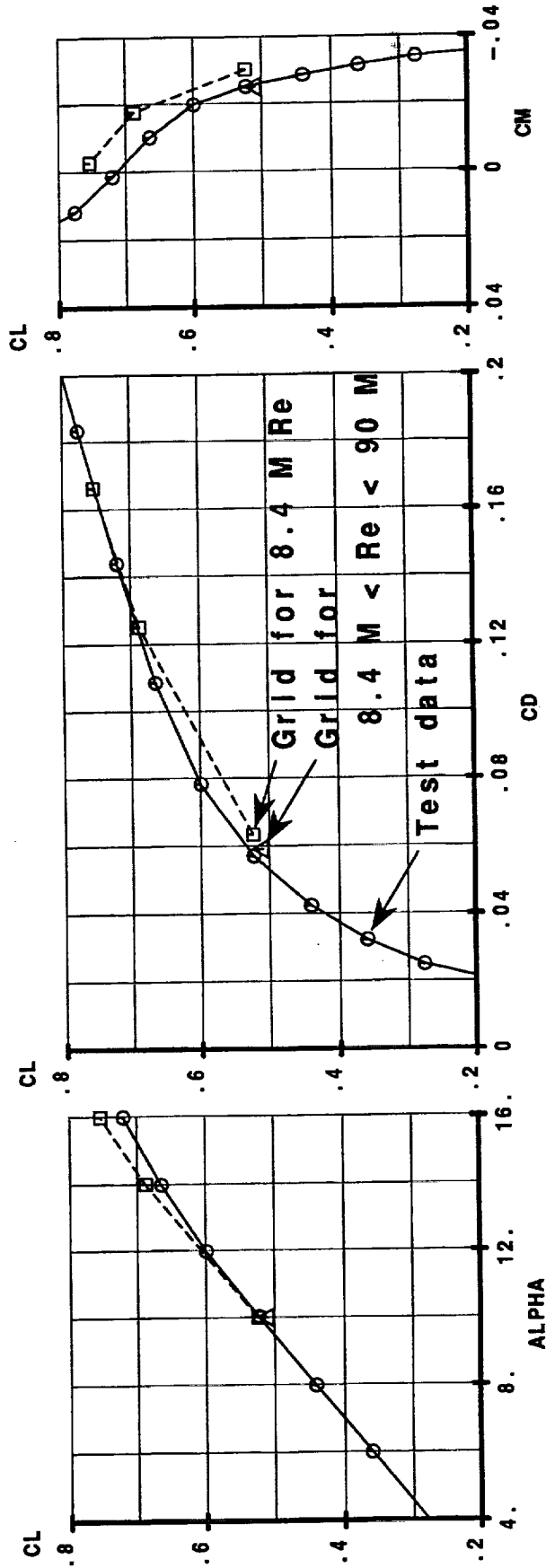
Note: JMAX=129 above the wing and JMAX=129 below for 8.4 M grid
JMAX=97 above and JMAX=81 below for 8.4 M < Re < 90 M grid

awc_vufoil.doc
page 19

- Forces and pitching moment computed by the code for displaying the convergence history had problems with the scale. Results shown on previous charts were obtained by postprocessing.

- Lift and pitching moment were still changing at the end of the analysis for all three grids.

- Both total drag and skin friction drag were changing at the end of the analysis for the grids that were made for 8.4 M Re. Total drag for the Re independent grid has stabilized but the skin friction and the pressure drag seem to be trading with each other.

2040

Convergence with Different Grids

Ref. H 6% W/B, Flaps LE 30, Outboard TE 20, Mach 0.24, Alpha 10 Degrees

A: 72 cells normal to wing surface, first cell for Re 8.4 M

B: 128 cells normal to wing surface, first cell for Re 8.4 M

C: 96/80 cells normal to wing upper/lower surface, first cell for 90 M
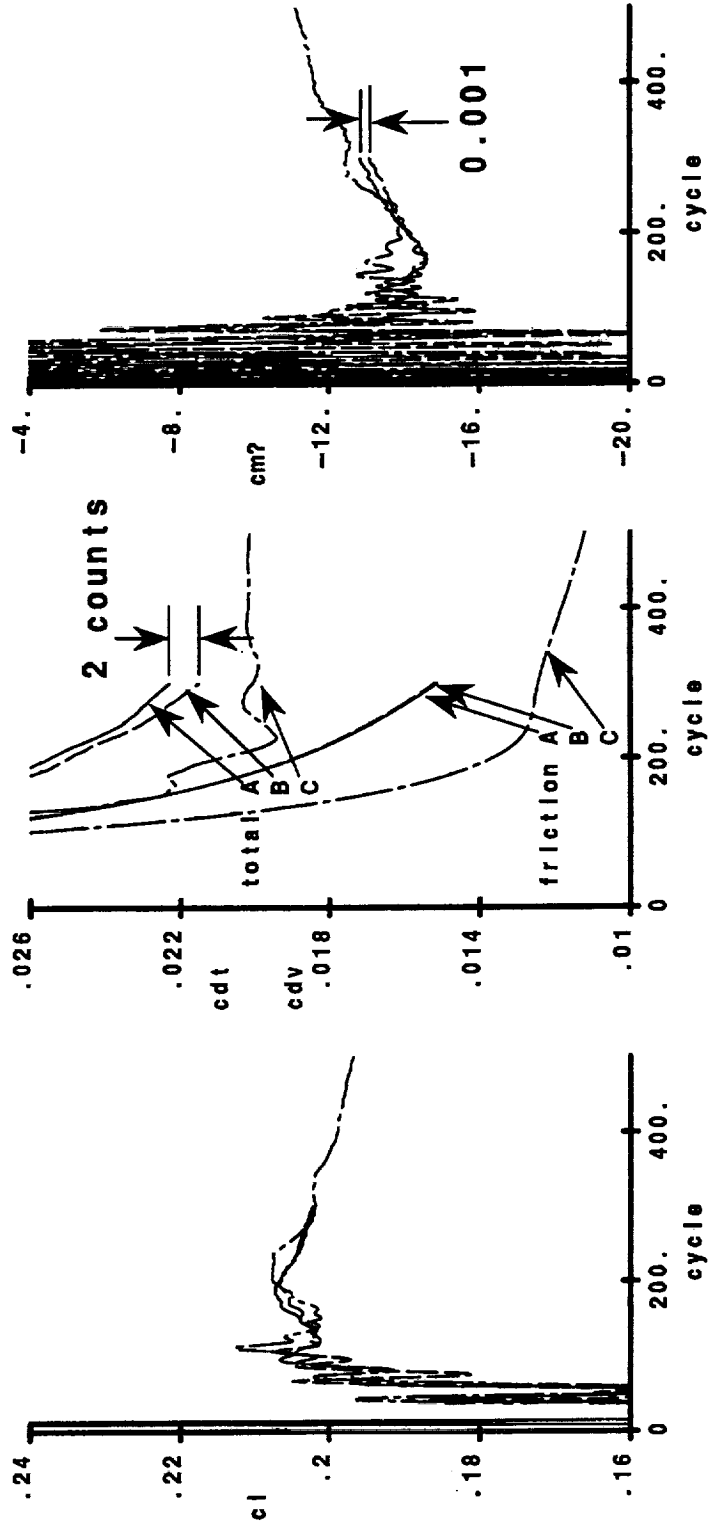
- Convergence in average dρ/dt was not well behaved and became worse with increasing angle of attack.

- The total drag still changes at the end of the analysis for all three angles of attack.

Convergence with Grid 1 for 3 Angles of Attack

6% Ref. H, W/B, Flaps LE 30, Outb TE 20, M 0.24
4-Block Viscous TNS3DMB, JMAX=73 with Non-smooth Wakes

16 deg. alpha
14 deg. alpha
10 deg. alpha
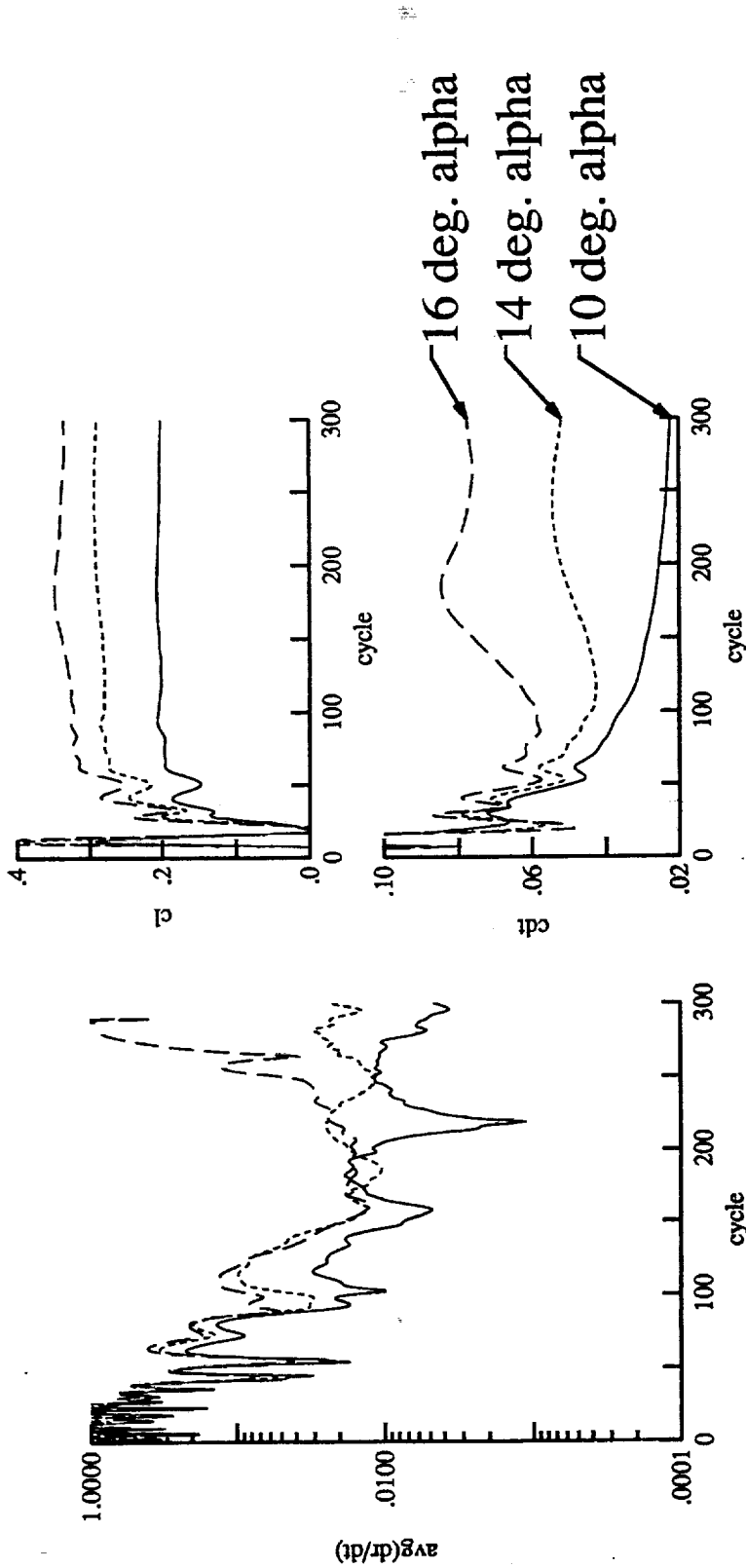
- Convergence in average dp/dt was better than before. However, there does not seem to be significant impact on the convergence of lift and total drag.

Convergence with Grid 2 for 3 Angles of Attack

6% Ref. H, W/B, Flaps LE 30, Outb TE 20, M 0.24
4-Block Viscous TNS3DMB, JMAX=129 with Smooth Wakes

16 deg. alpha
14 deg. alpha
10 deg. alpha
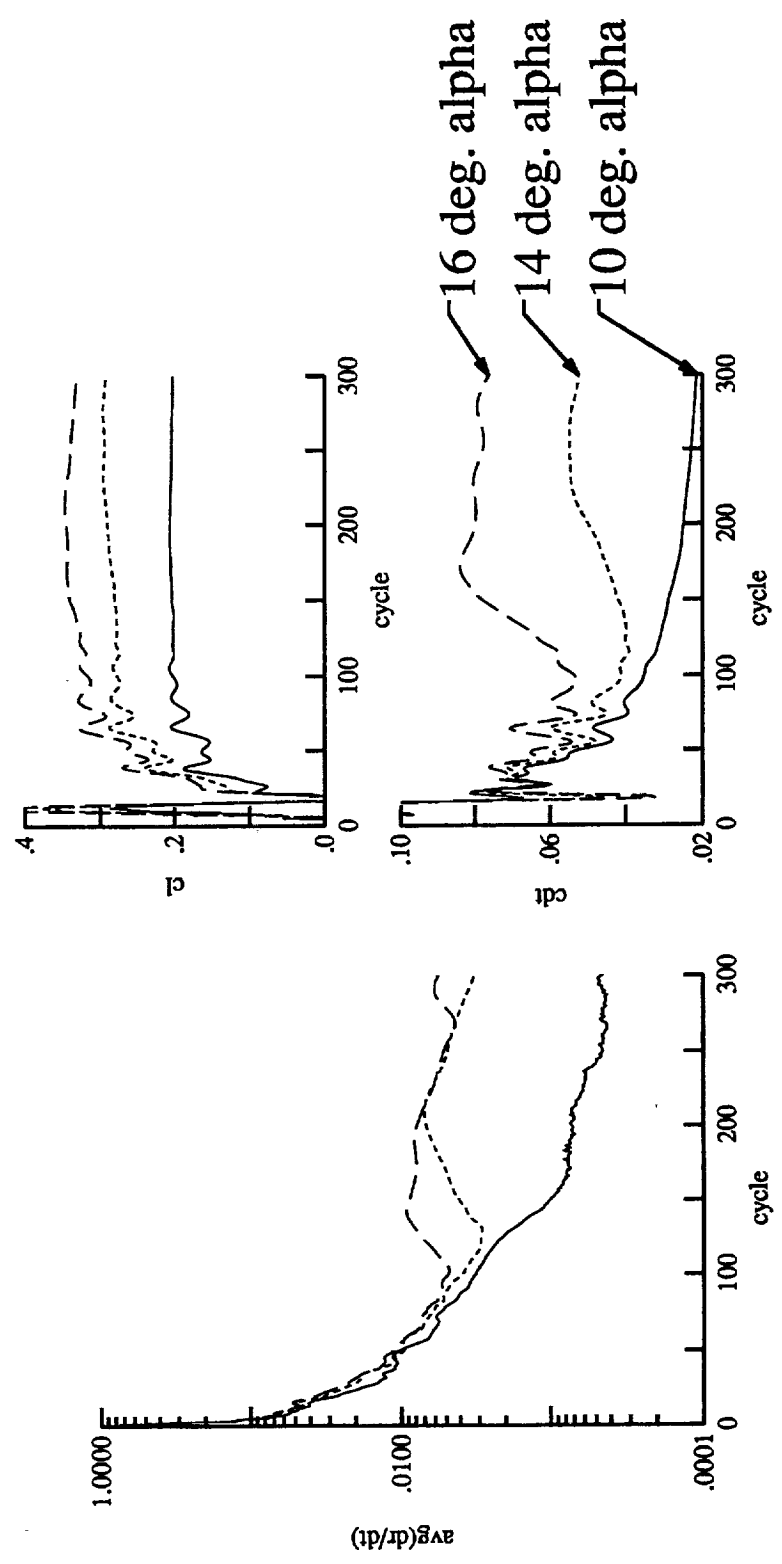
- Convergence in average dp/dt has slowed down to a very painful crawl for the Re independent grid.

Convergence with Grid 2 and Grid 3

6% Ref. H, W/B, Flaps LE 30, Outb TE 20, M 0.24, Alpha 10 Deg
4-Block Viscous TNS3DMB

Grid for 8.4 M < Re < 90 M

Grid for Re 8.4 M

2047
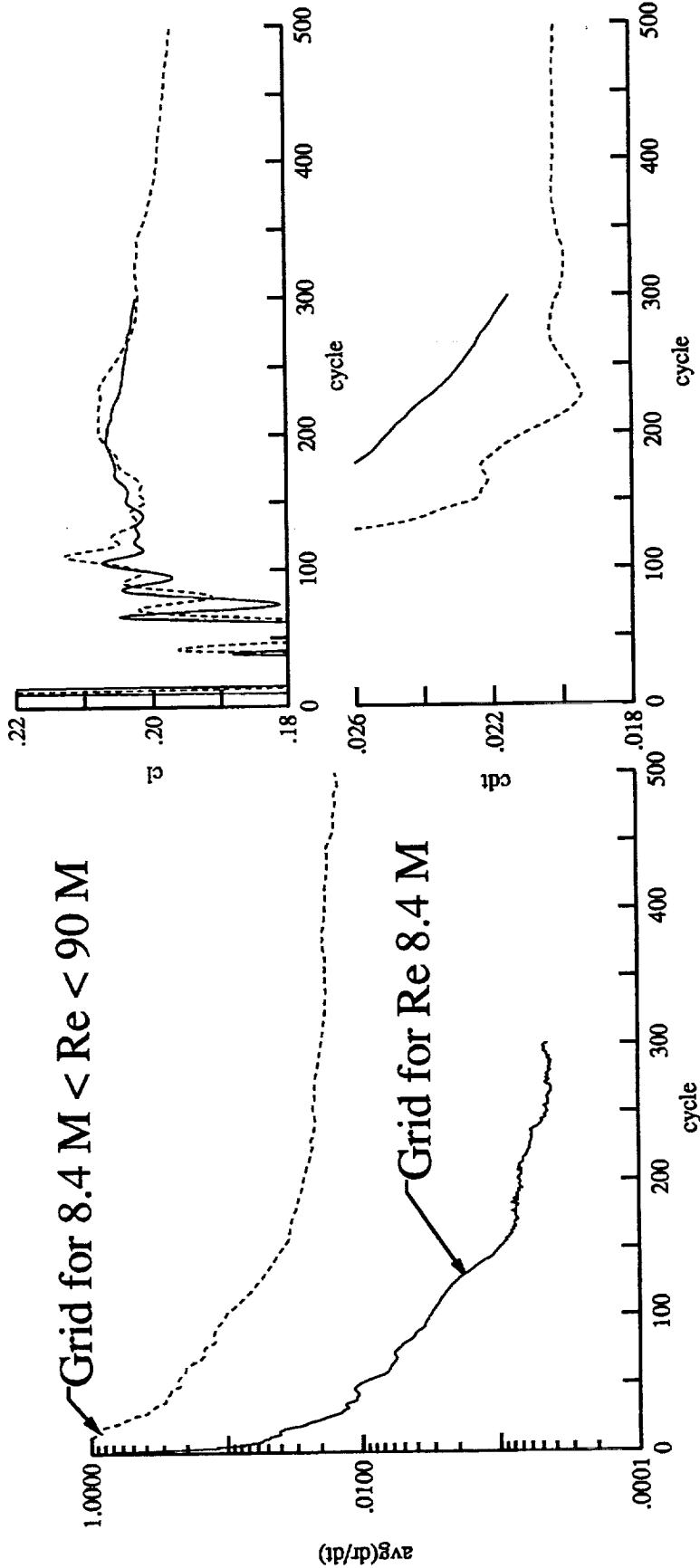
- Only selected pressure distributions are presented.

- Differences in computed spanwise wing surface pressures are noticeable only at this last station.

- 'Endplating' increased the load, as expected.

Effect of Endplating on Wing Pressures I

6% Ref. H, W/B, Flaps LE 30 Outboard TE 20, Mach 0.24, Alpha 10 Degrees
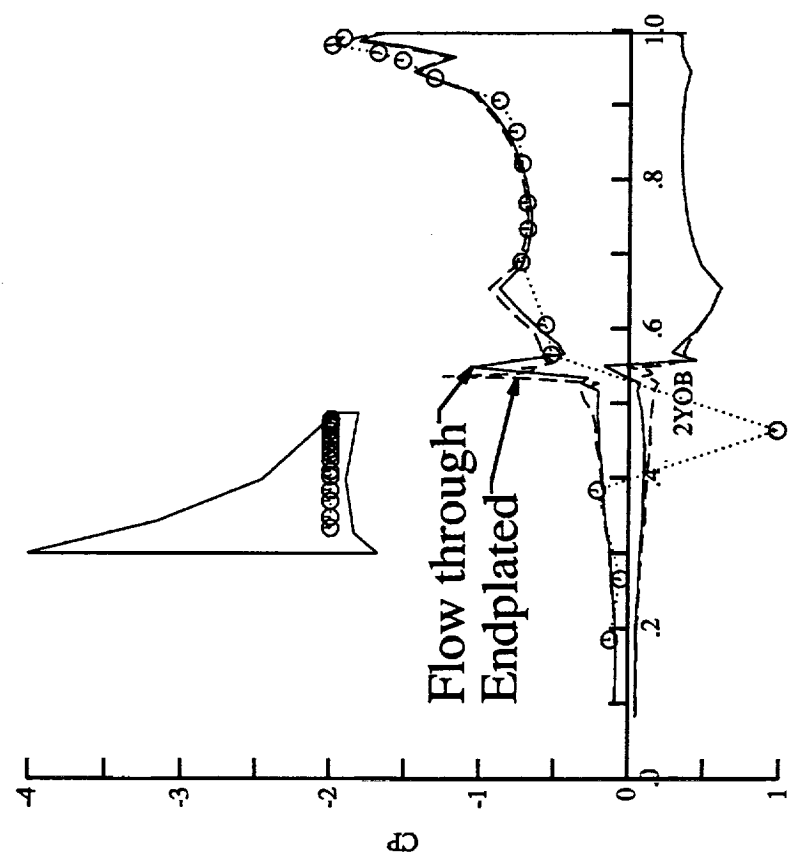
- The effect of 'endplating' seems to be traveling in the spanwise direction.

Effect of Endplating on Wing Pressures II

6% Ref. H, W/B, Flaps LE 30 Outboard TE 20, Mach 0.24, Alpha 10 Degrees
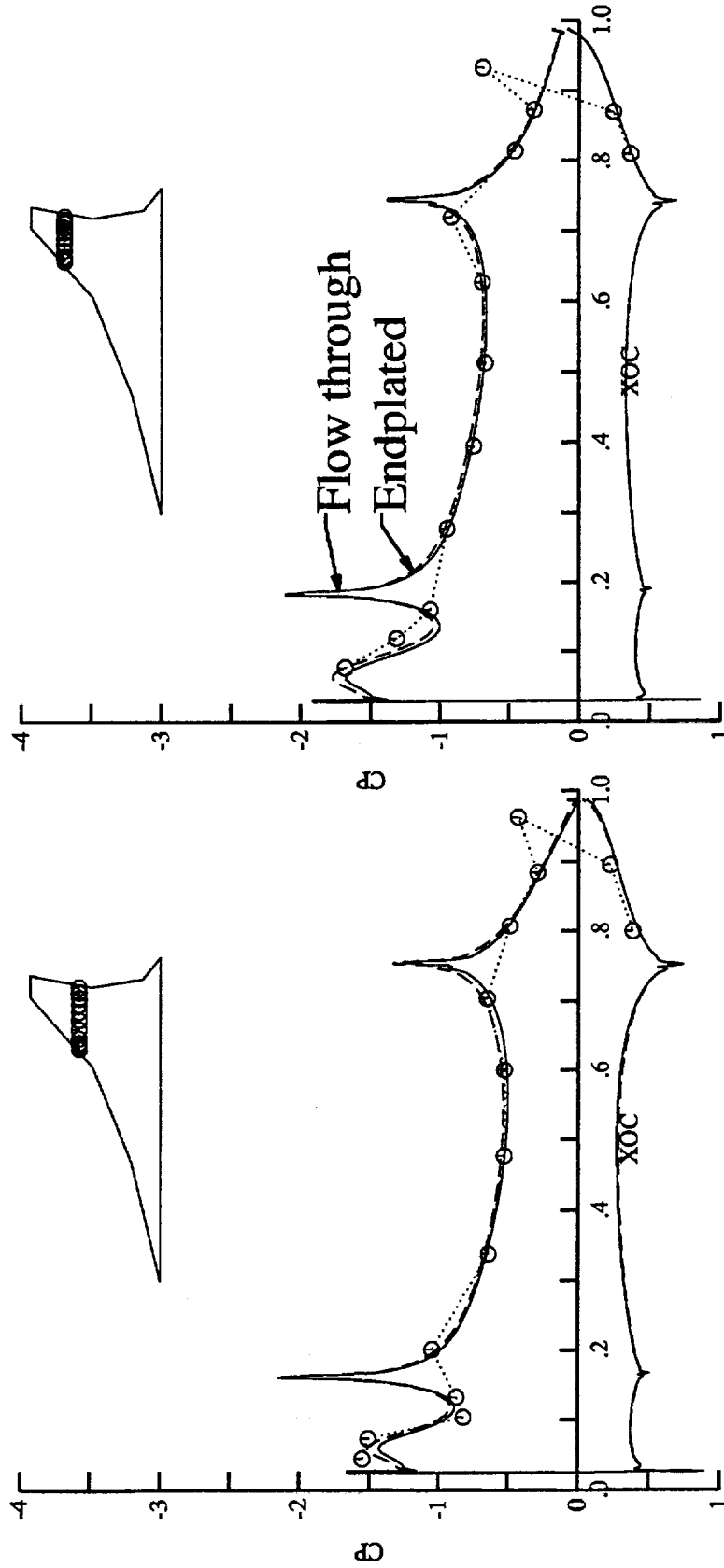
- The effect of 'endplating' seems to be traveling in the spanwise direction.

- The mismatch between the CFD results and the measured pressures for x/c < 0.2 could be caused by the difference in locations where these data were extracted from. CFD results were extracted along a buttock line cut that has a constant Y coordinate. Pressure ports on the wind tunnel model are on a buttock line only when the flap is not deflected.

Effect of Endplating on Wing Pressures III

6% Ref. H, W/B, Flaps LE 30 Outboard TE 20, Mach 0.24, Alpha 10 Degrees

Flow through

Endplated

CP

x/c
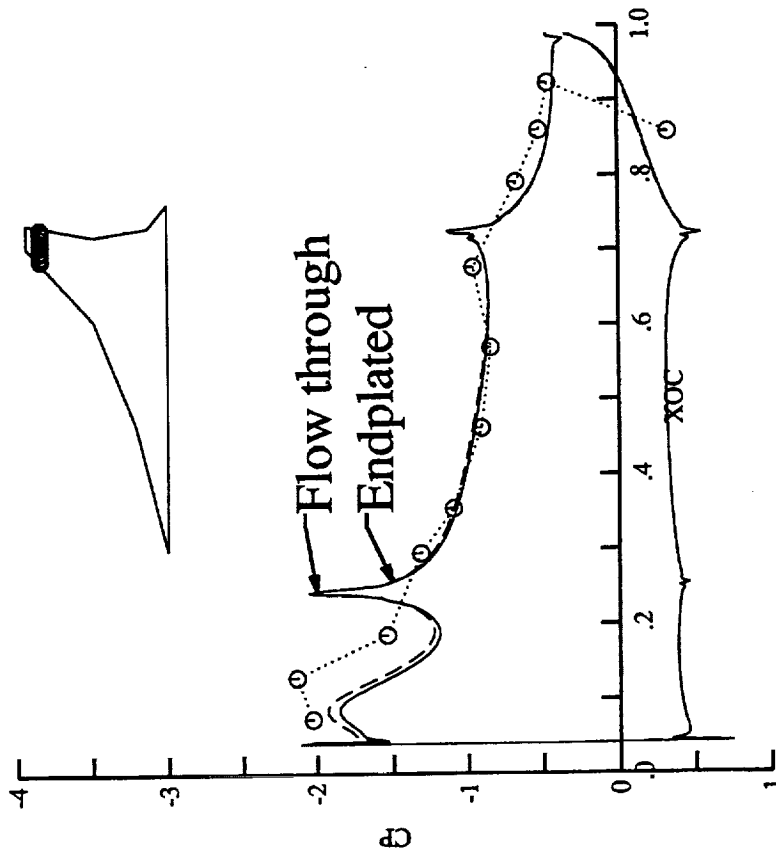
- Effect of JMAX on wing pressures are the greatest at the outboard streamwise stations, especially around the TE flap hinge of the last measuring station.

Effect of JMAX on Wing Pressures at α = 10°

6% Ref. H, W/B, Flaps LE 30 Outboard TE 20, Mach 0.24, Alpha 10 Degrees

JMAX=129

JMAX=73
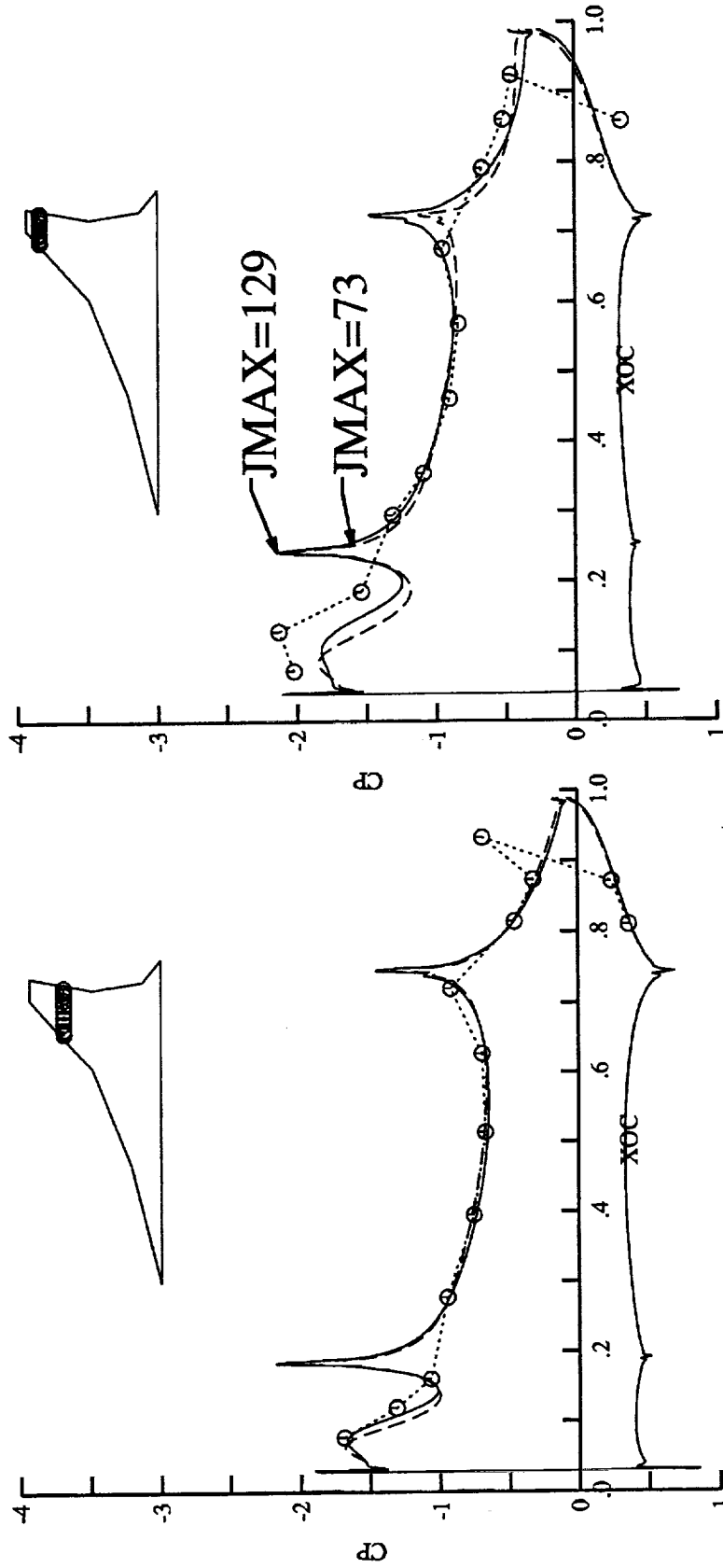
- It is difficult to match the measured wing surface pressures at this angle of attack. More multi-grid cycles may help. On the other hand, the problem could have come from the inboard wing.

Run 191
Alpha 14
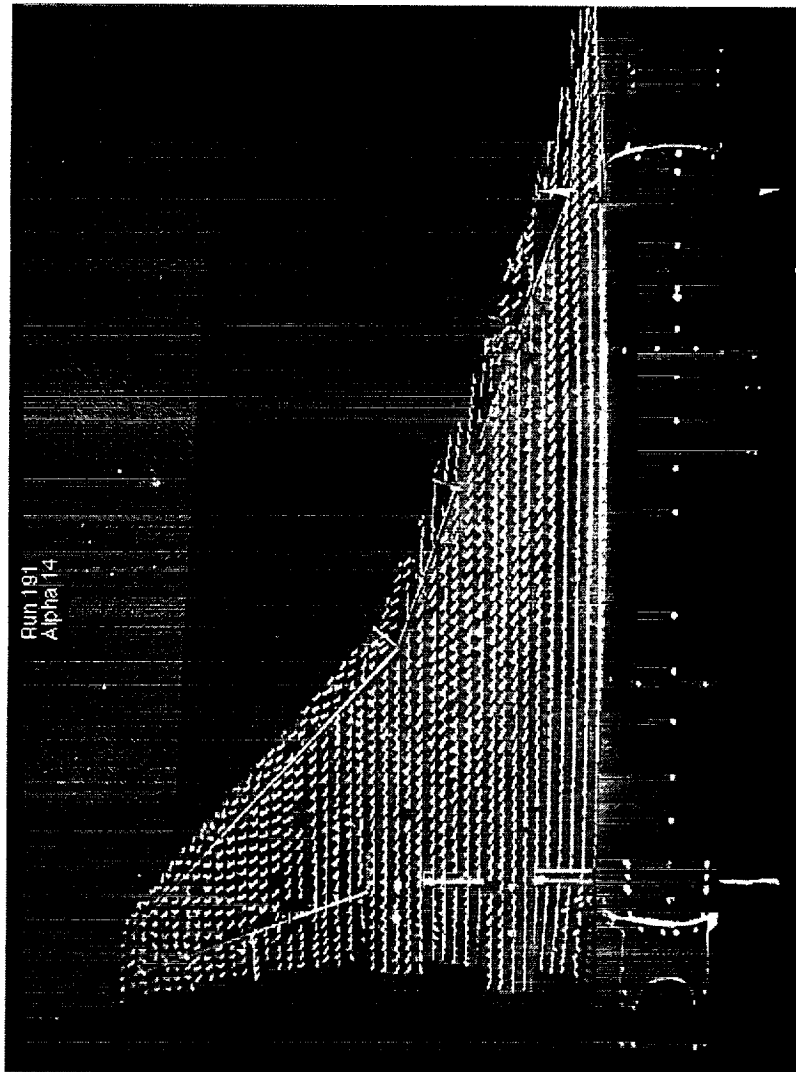
Effect of JMAX on Wing Pressures at $\alpha = 14°$

6% Ref. H, W/B, Flaps LE 30 Outboard TE 20, Mach 0.24, Alpha 14 Degrees

JMAX=129
JMAX=73
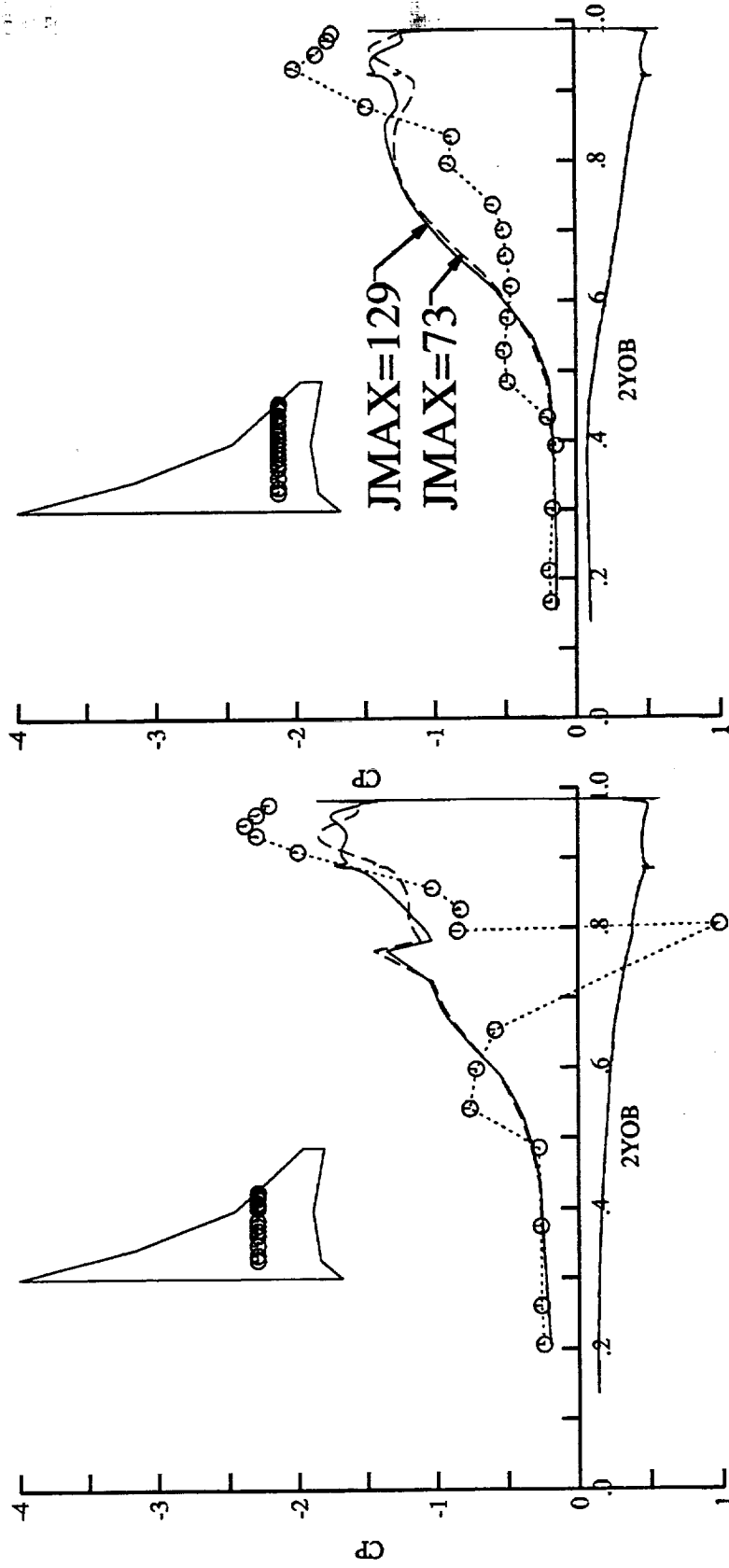
- Lower surface pressures match well with the very limited measured values.

Effect of JMAX on Wing Pressures at $\alpha = 14°$ II

6% Ref. H, W/B, Flaps LE 30 Outboard TE 20, Mach 0.24, Alpha 14 Degrees
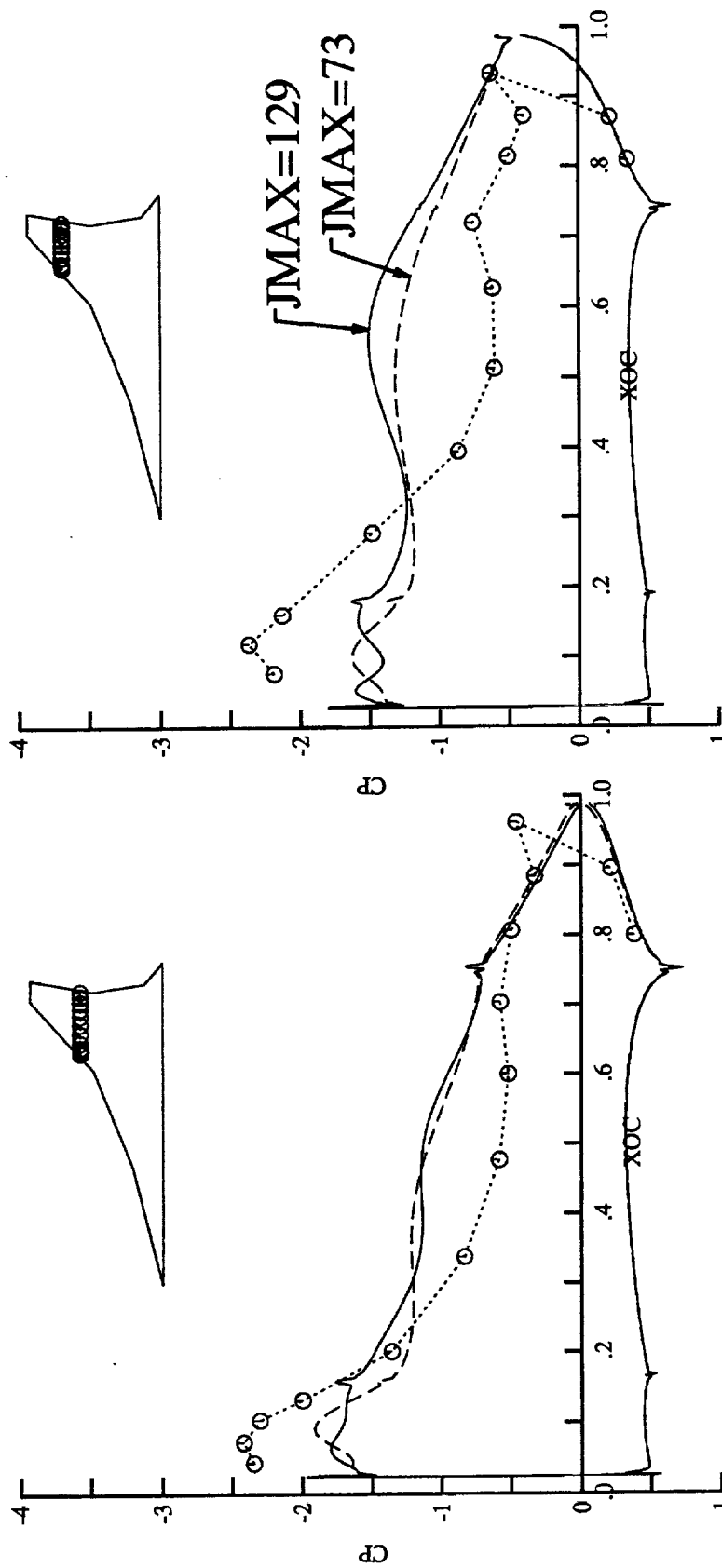
- The flow has totally separated. The Navier-Stokes may need a lot of help to match the measured wing surface pressures.

Effect of JMAX on Wing Pressures at $\alpha = 14°$ III

6% Ref. H, W/B, Flaps LE 30 Outboard TE 20, Mach 0.24, Alpha 14 Degrees

JMAX=129

JMAX=73
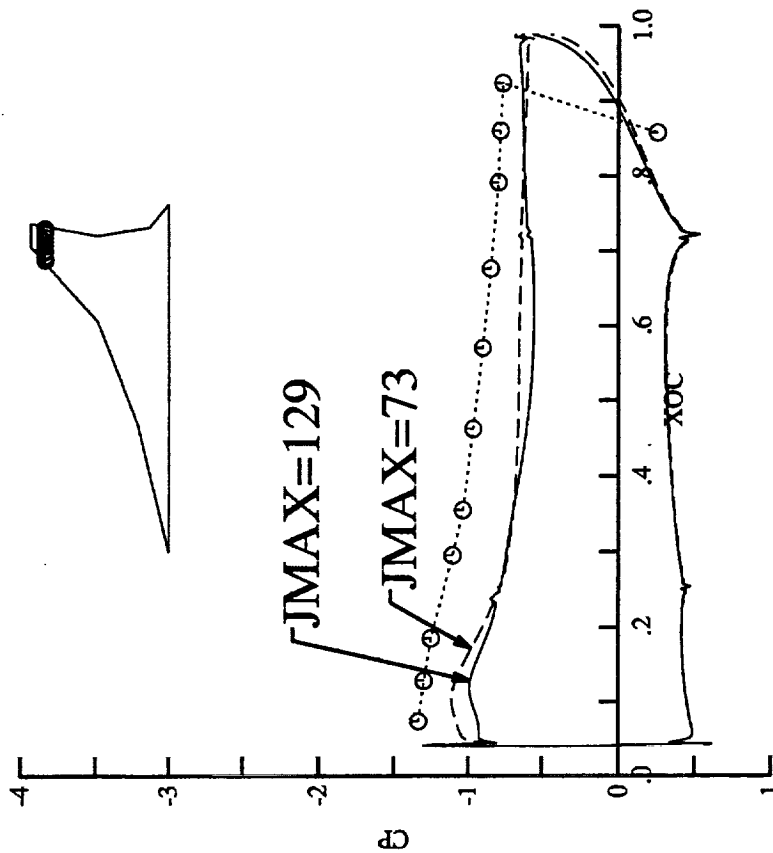
- Pretest estimate for the modified 2.2% NTF model with the TCA planform was made using AERO2S and the test data from NTF Test 078. The results are compared with data from NTF Test 089.

- AERO2S analyses were made for Ref. H and the modified Ref. H with partial span inboard leading edge flap. The increment was then applied to the test data from NTF Test 078.

- Partial span inboard leading edge flap was the configuration defined for TCA in April, 1996.

CFD/Test Comparisons (Linear)

- ## Forces and pitching moment

- ## NTF Test 089

- Test data were reasonably predicted for $C_L < 0.5$.

- Mismatches for $C_L > 0.5$ could be attributed to the fact that NTF Test 078 data were acquired with a full span inboard leading edge flap while the AERO2S model for the modified 2.2% model had the partial span inboard leading edge flap.

Mod. Ref. H with partial span inboard LE flap

Mod. Ref. H with full span inboard LE flap

NTF 089
LE: 30°
TE: 10°
Run: 346
Re: 9.30 M
Mach: 0.30
AOA: 13.87

NTF 089
LE: 30°
TE: 10°
Run: 351
Re: 9.50 M
Mach: 0.30
AOA: 13.81
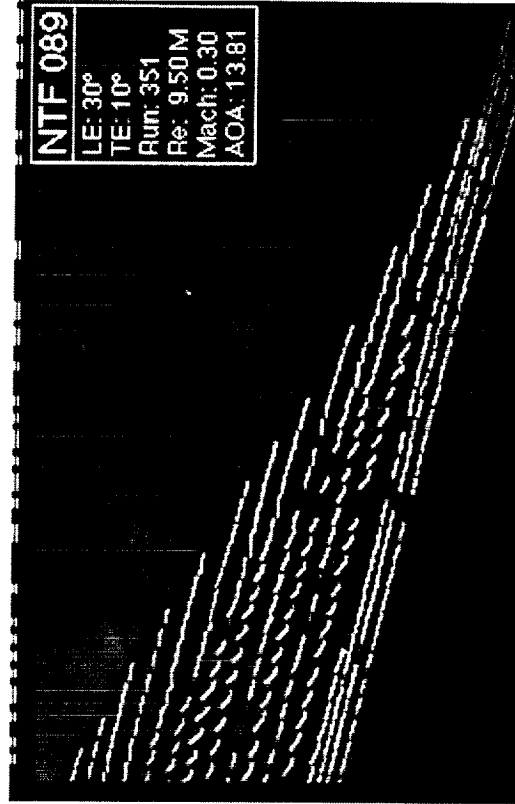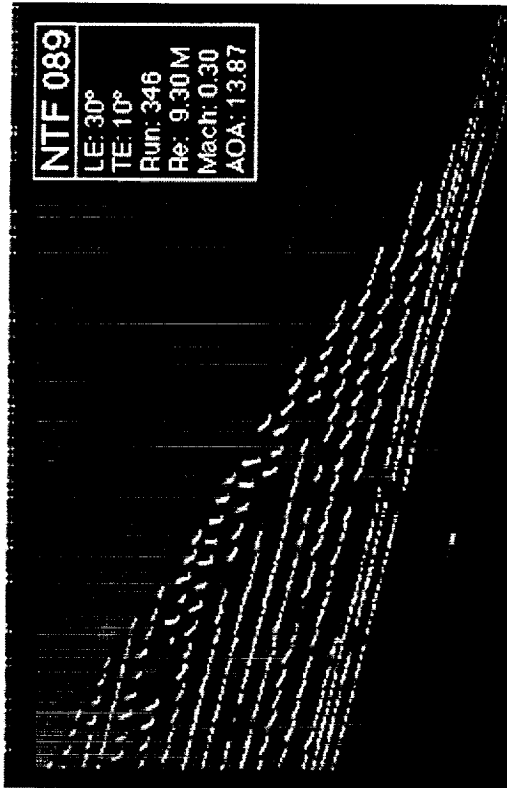
NTF Test 089 - Prediction and Data

Modified Ref. H W/B/N, Flaps 30/10
Partial Span Inboard LE Flap, TCA LE radius
Mach 0.3, Re 99 Million

Data
Prediction

CL1

ALPHA

CD1

CM1

LOD
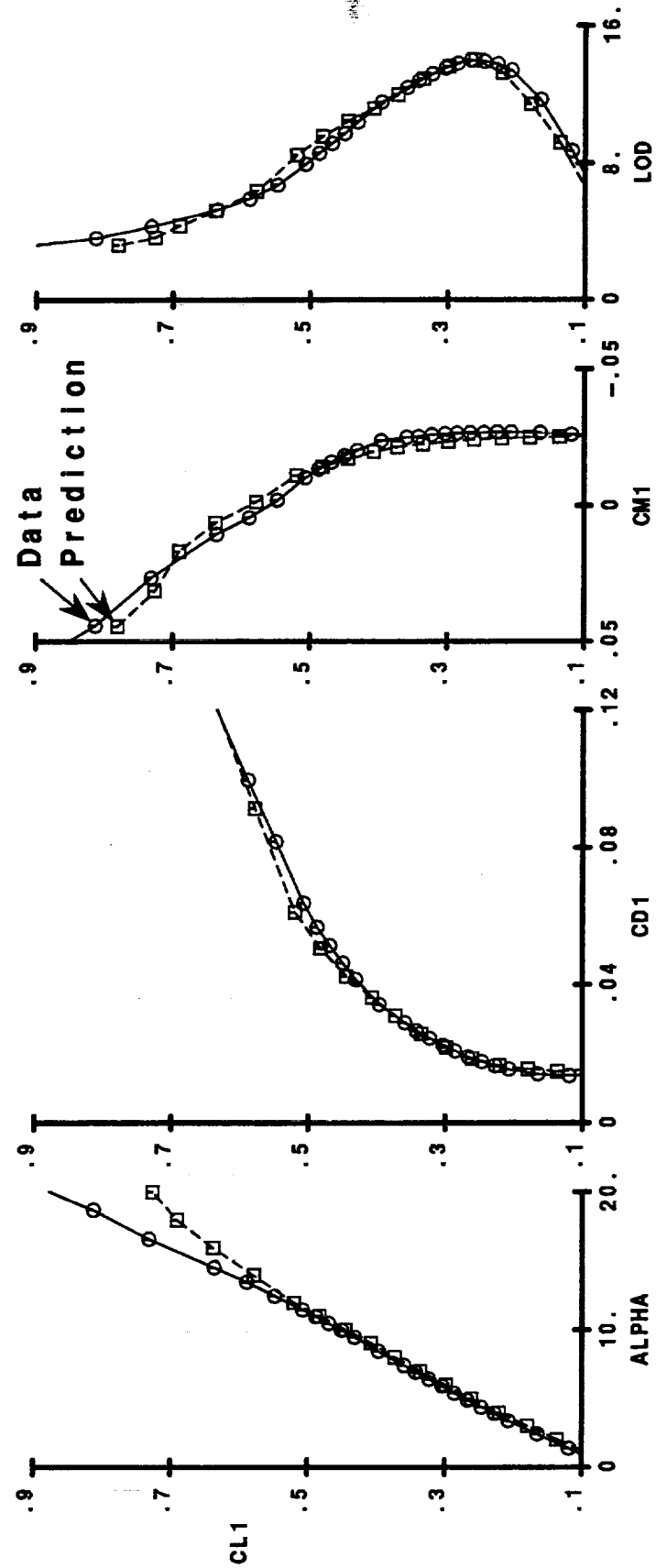
- Can TNS3DMB benefit from the low Mach number pre-conditioning?

- H-H? O-H? Overset? Which grid is the most appropriate one?

- von Neumann gets overloaded when deadlines approach.

- Not many tests were planned with the CFDers' requests in mind. HSR is better than other programs. Recent experience in NTF Test 089 with mini-tufts is a good example of acquiring critical data that will be useful for CFD validations.

Issues

- Convergence

- Grid topology

- Availability of computer

- Availability of test data

2067

- A third bullet may be added later if we need hours and hours of C-90 time to reach converged solutions.

Conclusions - Navier-Stokes Codes

(Reported in September, 1995 and have not changed)

- Reveal flow details

- Too much work in preparing input, e.g., surface grid, Reynolds number dependent volume grid, connectivity file for multi-block codes, etc.

- Previous experience in preparing pretest estimates for 14x22 Test 429 indicates that AERO2S is very useful in ranking wings that generate similar flow patterns.

- Current application reinforces the fact that the usefulness of linear codes such as AERO2S vanishes when flow separations such as vortices begin to appear.

Conclusions - Linear Code

- Input relatively easy to generate, though not fully automated yet

- Good for estimating performance of similar configurations

- No surface pressures

- Some are in progress already. Some need the help from code developers.

- X along the body axis seems to be universal. Y or Z for spanwise is still system dependent. The user is in good shape as long as he/she stays with only one system.

Recommendations

- **Develop utility tools to reduce the flow time for grid generation**

- **Develop/improve tools to generate input for grid generation and/or flow solvers**

- **Unify coordinate system**

- **Improve output data and postprocessing**

- Work is cut out for code developers and test technique developers.

Recommendations - concluded

- Develop boundary layer transition prediction/measurement capabilities

- Obtain surface pressure data on the outboard wing for high Reynolds numbers

This page intentionally left blank.
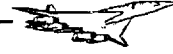
Recent High Lift System and
Alternate Control Test Results

G. H. Wyatt
Boeing Commercial Airplane Company

High Speed Research Program
Aerodynamic Performance Technology Workshop

February 26th, 1997

6% HSCT Pitch Control Summary
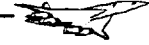
Topics

- Baseline high lift performance and technology projections for TCA
- Recent high lift system improvements to ref H
- Review of alternate pitch control results from 6% ref H model
- Technology projection and alternate controls impact
- 14x22 test results w/ canards and high lift system improvements
- Conclusions
- Recommendations

- Baseline high lift performance for TCA - For reference, todays status and how it compares with our technology projection for year 2001.

- Recent high lift system improvements to ref H. Based on 14x22 facility tests of the 6% model, describe improvements to the leading edge flap system which bring us closer to our technology projection.

- Review of alternate pitch control results from 6% ref H model

- Technology projection and alternate controls impact

- 14x22 test results w/ canards and high lift system improvements

- Conclusions

- Recommendations

2078
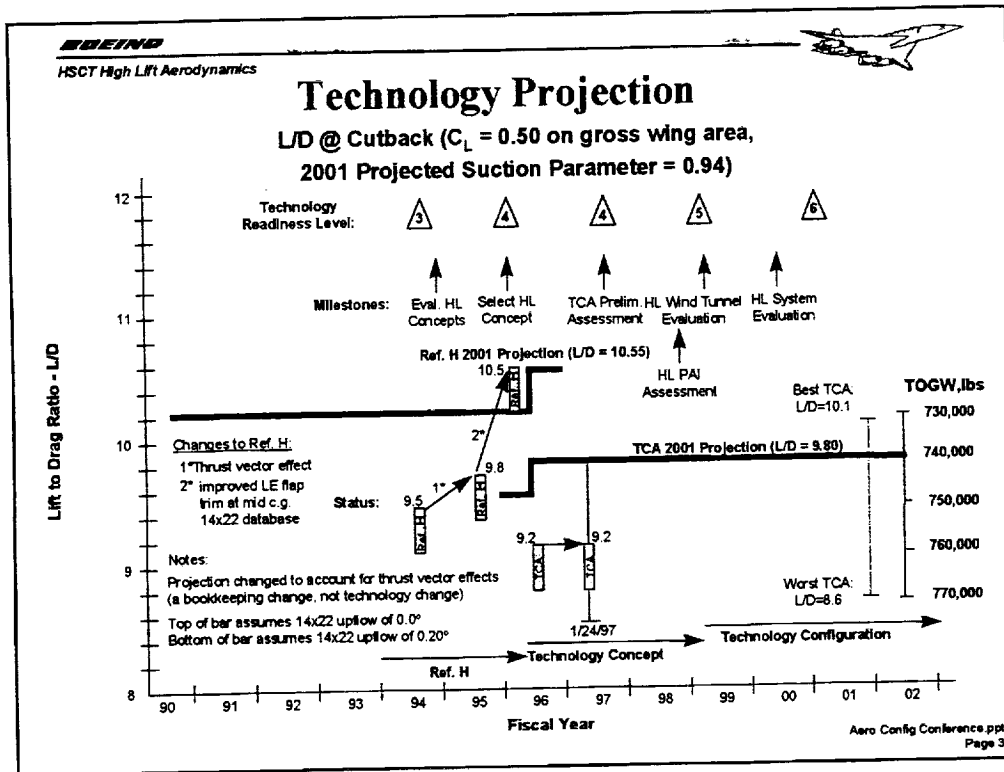
This figure shows the 1997 high lift technology projection for climbout L/D. It shows trimmed L/D at climbout as a function of Fiscal Year. The HSR II program ends in 2001. The technology projection for climbout L/D is 9.8 for the TCA. The current status is 9.2. The chart also shows high lift program milestones and major phases of the program. At the top in triangles is the technology readiness level. The green bars are the current status for this metric with an uncertainty band. At the right is an uncertainty band on the final outcome and an estimate of the TOGW impact for this metric. This chart shows that we need to get from 9.2 to 9.8 trimmed L/D for the TCA to meet program goals by the year 2001.
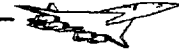
Technology Projection

TCA Technology Projections

S_{ref}=8500. ft^2

$$L/D_{ideal} = \frac{CL}{CDo+(CL^2/\pi AR)}$$

Target 9.8

Status 9.2

Ideal

Target programmed flaps

Programmed Flaps

Fixed Flaps 30/10

L/D including Thrust

C_L including Thrust
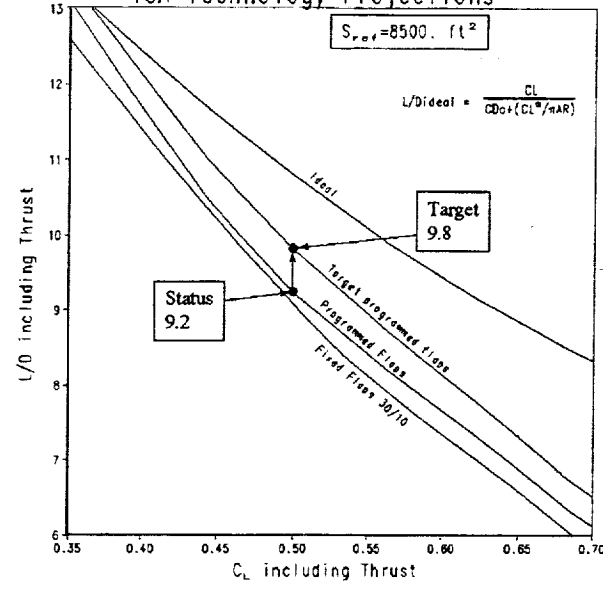
This figure also shows the technology projection. It is a plot of trimmed L/D versus CL for the TCA configuration. Shown for reference is the theoretical ideal L/D. The use of programmed flaps helps bring the status up from the fixed flap level. At the cutback CL=0.50 we need to improve by 0.6 units in L/D to meet the technology projection..

Sizing Constraints and Thumbprint

December '96 TCA Update
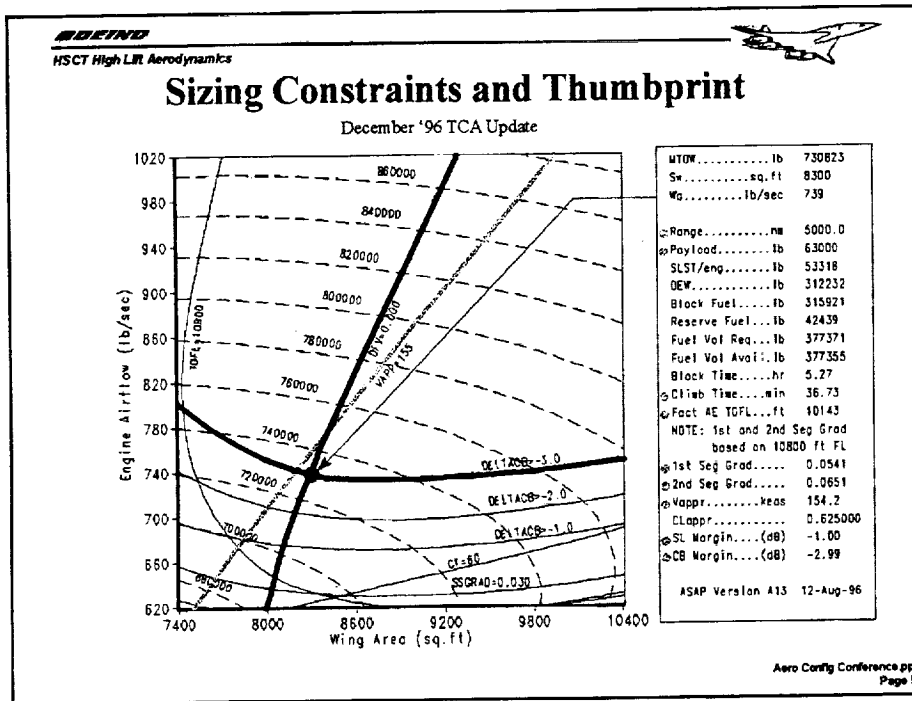
This figure shows the sizing thumbprint for the December 1996 TCA update baseline. It is better than the previous TCA by 200 square feet wing area and about 10,000 lb lighter. The improvements are the result of the propulsion nozzle team making improvements to their technology projections, specifically nozzle performance.

Mission constraints are range, payload, climb time, TOFL, climbout gradients, approach speed, sideline noise, and community noise.

The TCA is sized by noise at cutback (Stage III - 3db), blue curve, and the fuel volume required to meet the mission, red curve.

The approach speed line is very close to being a constraint, this is based on a maximum approach speed of 155 knots, green curve. This airplane has a 154.2 knot approach speed. Approach speed is a function of lift in ground effect and aft body or nacelle margins to ground contact.

The TOFL line is below the sized configuration and is not currently sizing the configuration.

The airplane is very highly low speed sized.
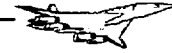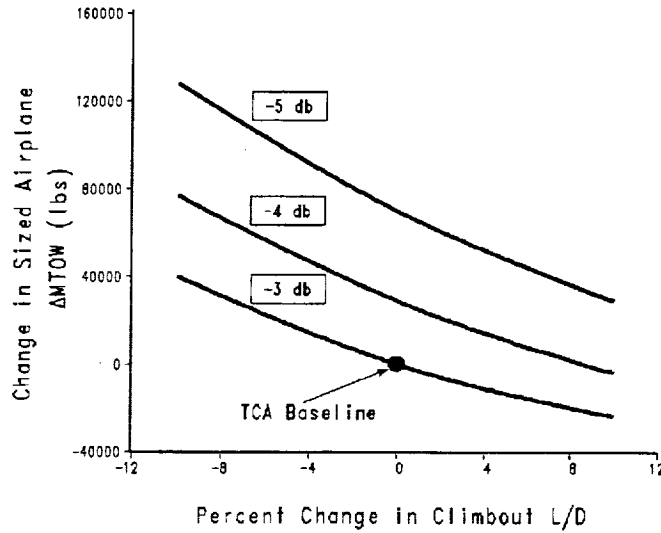
This figure shows the sensitivity of MTOW to changes in climbout L/D for different noise levels. Currently we are sizing to Stage III - 3db. A future goal is probably going to be Stage III -5db. As regulations get more stringent the MTOW sensitivity to L/D variation increases, moving from the -3db line to the -5 db line.

Recent High Lift System Improvements
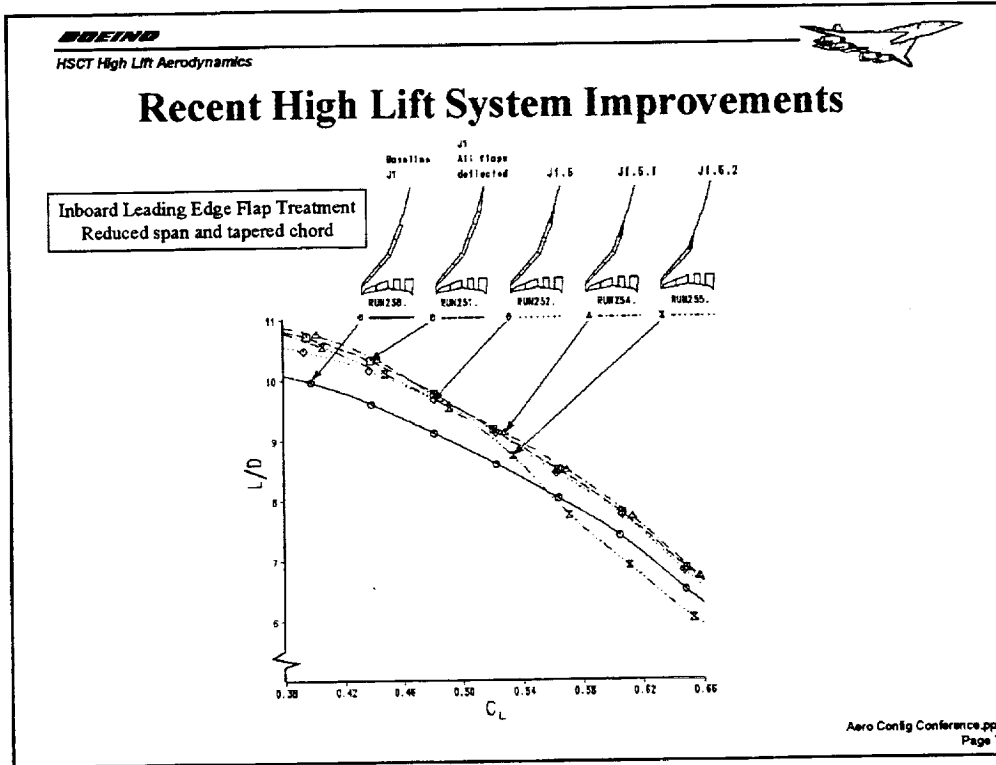
This figure shows recent improvements to the high lift system of the ref H. This data shows an optimization of the inboard flap span coverage and a new inboard flap chord that tapers to zero inboard. The flap labeled J1.6.1 is the one down selected for the ref H model. It provides about 0.5 units L/D improvement at CL=0.55, which is the cutback CL for the ref H. The system may also be lighter since it covers less span that the previous baseline flap.

This concept has been applied to the baseline TCA configuration with unknown results as of today. The new TCA model will be tested in March of 1997.

HSCT High Lift Aerodynamics

Recent High Lift System Improvements
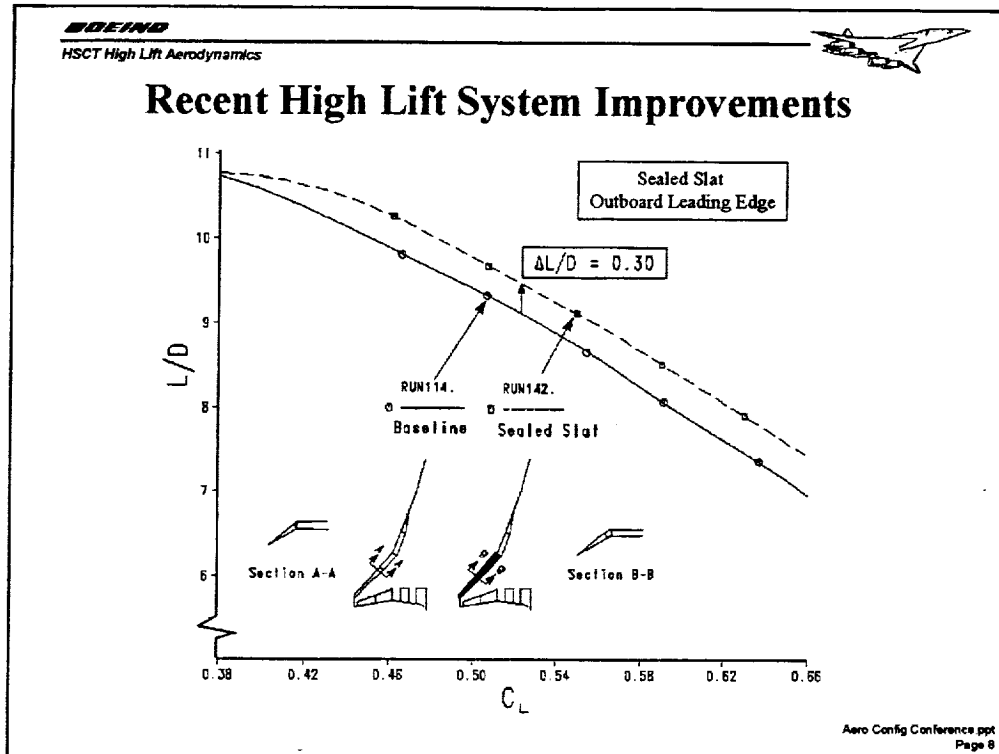
This figure shows the improvements in cutback L/D that an outboard leading edge flap modification can provide. This concept is the sealed slat. The sealed slat has a hingeline external to the wing. The hingeline of the sealed slat is below the wing, creating fowler motion with deflection, which adds a small amount of wing area, this helps to reduce the angle of attack. The radius over the upper surface at the hingeline is very generous and helps the flow negotiate the hingeline. The baseline flap has a relatively sharp corner at the upper surface above the flap hingeline, and is the source of flow separations.

The sealed slat concept provides about 0.3 units in L/D improvement over the baseline LE flap.
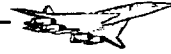
Potential for Gains in Climbout L/D

Previous wind tunnel data suggests a potential for increased low speed L/D for configurations with a canard instead of a tail.

The potential is at least 0.5 units in trimmed L/D over the aft tail baseline.

As will be seen data from 14x22 test NASA421 shows a potential for increased low speed performance relative to a tailed configuration. The performance benefit is sensitive to CG position, at an aft CG the tail can provide trimmed L/D's as high as that of the best canards, but the aircraft is typically unstable here. As the CG moves forward canards get better performance and that benefit is as large as 0.5 units in L/D.
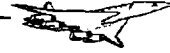
Canards and the Technology Projection

The sharp leading edge of the outboard wing causes early flow separation.

If we achieve the technology projection, then the flow on the outboard panel will likely be attached during climbout.

The outboard sealed slat helps achieve this goal.

A canard will also help achieve this goal.

We are not sure if the benefits of a canard and a sealed slat are synergistic.

Aero Config Conference.ppt
Page 10

Wind tunnel observations of flow on the outboard wing of the ref H at operating angles of attack is known to have regions of leading edge separation. This is due to early flow separation either at the sharp leading edge or over the upper surface at the flap hingeline.

One of the goals for achieving the technology projection is to develop a high lift system which keeps the flow attached on the outboard wing during climbout.

The outboard sealed slat achieves this goal.

The canard also helps improve flow over the outboard wing, this may be due to a reduced angle of attack for the wing.

We are not sure if the benefits of a canard and a sealed slat are synergistic. They both may promote attached flow on the wing thus achieving the same goal. For this reason we don't know if the benefits of both can be claimed.... yet.
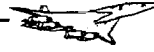
Takeoff and Touchdown Lift

The TCA baseline is sized by noise at cutback and fuel volume required for the mission.

When the common performance process is implemented for mission sizing, lift levels will decrease.

Information in the literature indicates that for slender wings, the favorable ground effect may be as little as 1/2 the static ground effect.

If these two effects were combined, it could cause both the TOFL and VAPP lines to be mission sizing critical.

A canard configuration can reduce trimmed angle of attack.

Currently the baseline TCA is sized by noise at cutback and fuel volume required for the mission. The approach speed constraint of 155 knots or less is currently not sizing the configuration, but the line is close. Approach speed is determined by touchdown attitude limits in ground effect accounting for a 3% speed bleed during flare.

When the common performance process is implemented for mission sizing, lift levels will decrease. This is because the ref H database has lower lift levels than that predicted by AERO2S.

Information in the literature indicates that for slender wings, the favorable ground effect may be as little as 1/2 the static ground effect which we are currently using.

These two effects if combined could very well cause both the TOFL and VAPP lines to be critical to sizing.

A canard configuration can reduce trimmed angle of attack for most useable CG locations.

HSCT High Lift Aerodynamics
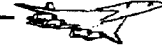
Brief Review of Available Canard Test Data

The following few charts are extracted from previously published analysis, and are shown for review.

The following charts are from the NASA421 test analysis of alternate pitch control devices. They are shown here for a reference point for and to tie into new data from NASA442.

Model Geometry

6% Model reference dimensions
Sref   = 25.56 sqft
Cbar   = 61.937 inches
Span   = 93.343 inches
Length = 226 inches
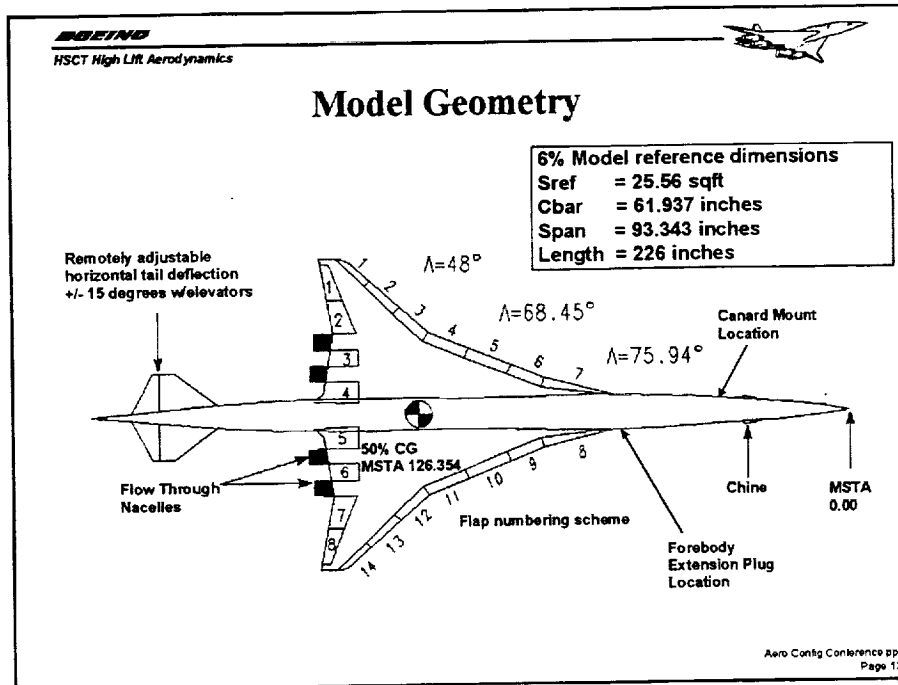
This figure shows the geometry of the 6% ref H low speed model. The figure shows the flap system layout and location of the horizontal tail and canard mount. The horizontal tail is remotely adjustable as is the canard when mounted. The forebody has extension plugs to simulate aft wing shift when canards are tested. (Plugs are not shown).

Summary of Configurations Tested at the 14x22 with the 6% ref H Model
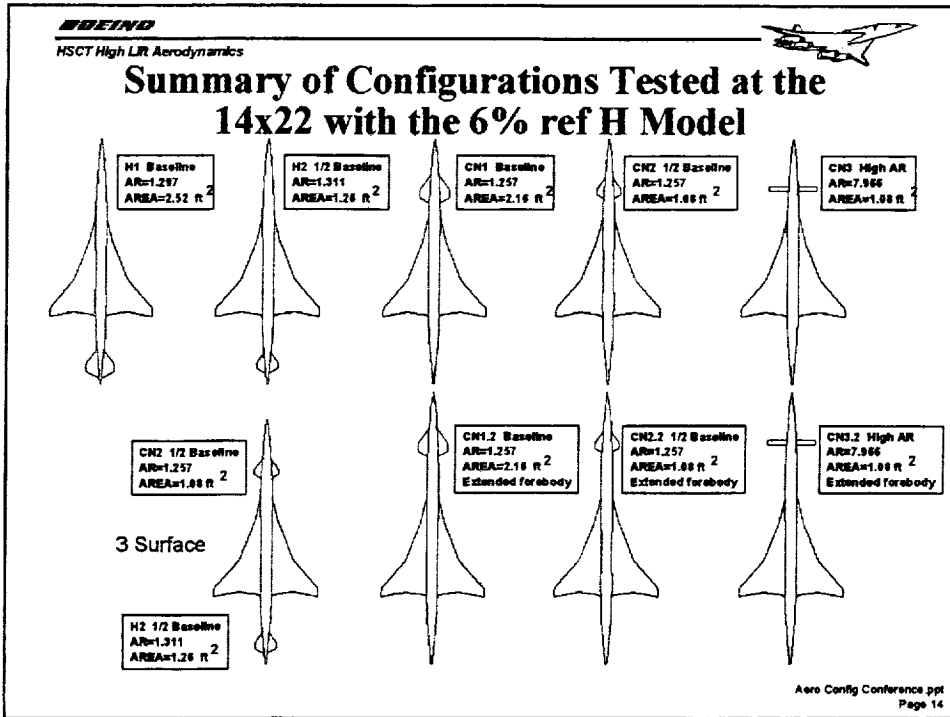
This figure shows the various alternate control configurations that have been tested at the 14x22 facility using the 6% ref H model. All of the control devices tested previously were simple slab surfaces with no high lift systems or elevators.
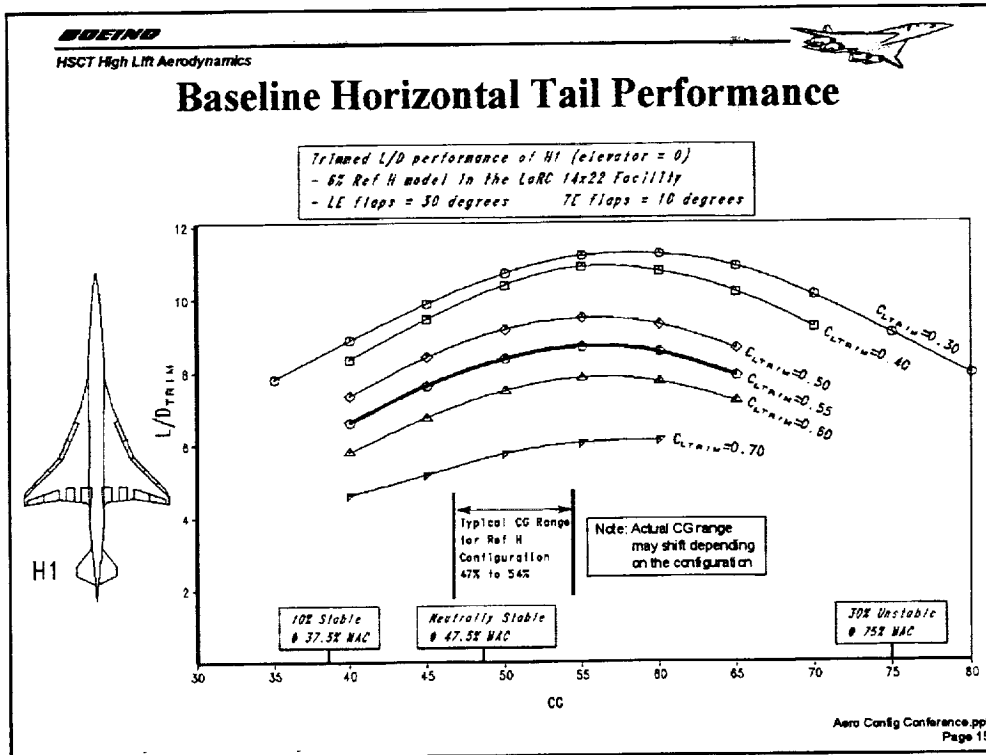
Baseline horizontal tail trimmed L/D is shown here as a function of CG position. This configuration is neutrally stable at 47.5% MAC. L/D's get better when the CG is located aft of this location. This is due to the pitching moments at aft CG's requiring less tail down load and possibly tail lift for trim. Typical CG range for the ref H configuration is 47 to 54% MAC.
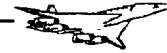
Best Canard Configuration Performance
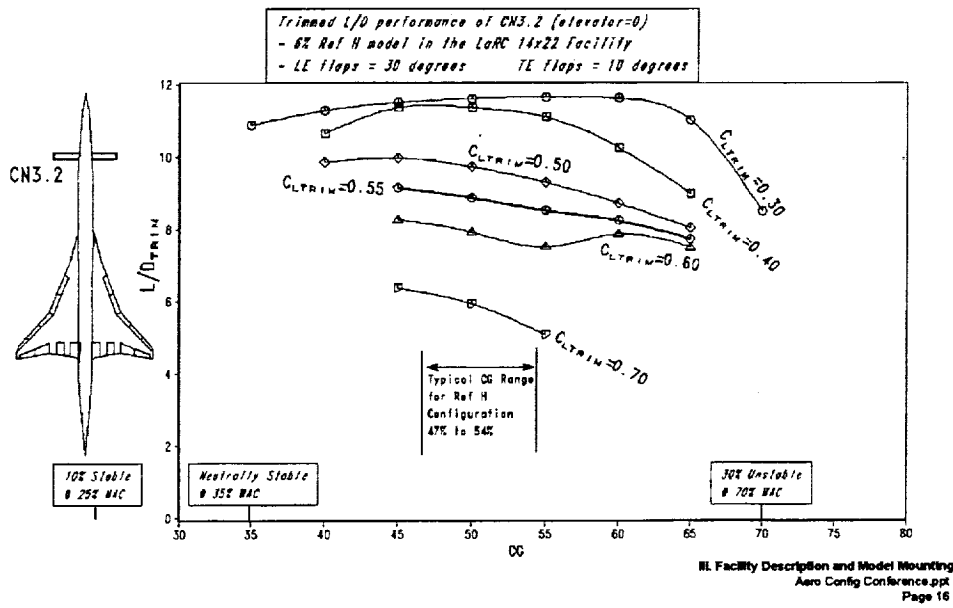
The best canard in terms of trimmed L/D is shown here as a function of CG position. This configuration is the high AR canard mounted low on the extended forebody, this simulates an aft wing shift. This configuration is neutrally stable at 25% MAC. This is far forward of typically achievable L/D's. This configuration gets better at more forward CG locations. For the canard to trim more forward CG locations will require either less trailing edge flap to reduce the canard lift requirement, or an efficient high lift system on the canard so it can generate higher CLmax.

Trimmed L/D Comparison at Common Stability Levels
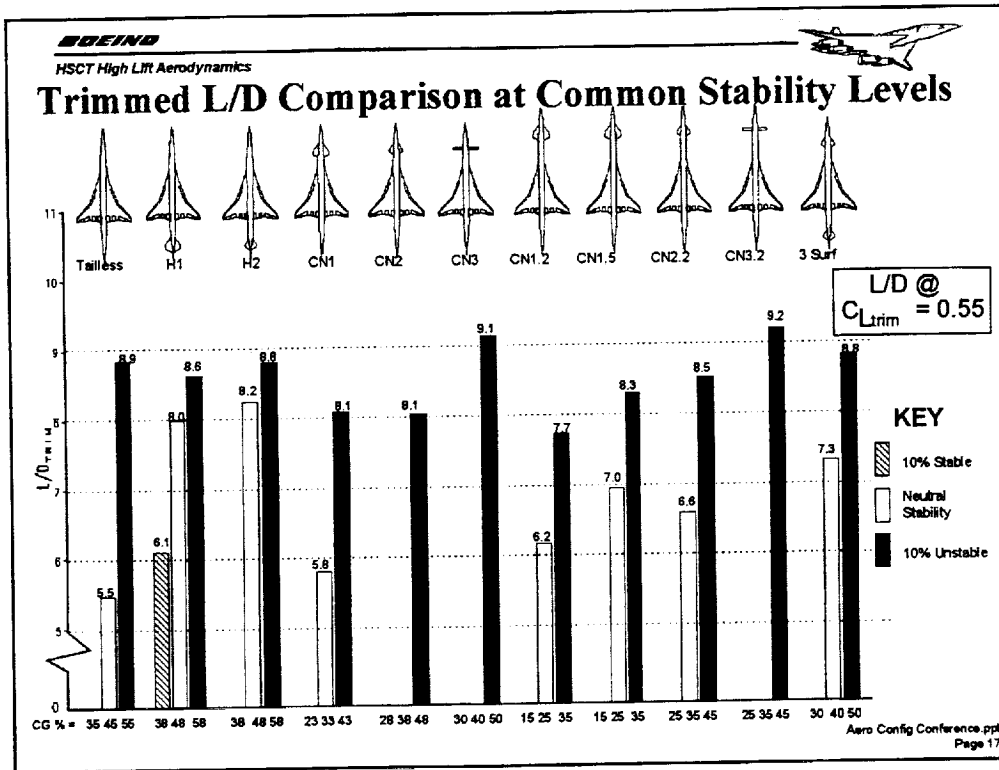
This figure summarizes all the configurations tested previously at the 14x22 facility on the 6% model. The chart shows trimmed L/D at cutback, CL=0.55, for each configuration at common stability levels. The black bars indicate trimmed L/D at 10% unstable CG locations. The baseline ref H is 10% unstable at 58% MAC. White bars are for trimmed L/D at neutral CG locations. For the baseline ref H this is 48%. The two high AR canards show L/D gains of roughly 0.5 units in L/D. The relative location of the 10% unstable CG is 58% for the tail, 50% for the high AR canard on the baseline forebody, and 45% for the high AR canard on the extended forebody.
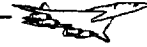
Trimmed Angle of Attack

Baseline tail compared with high AR canard
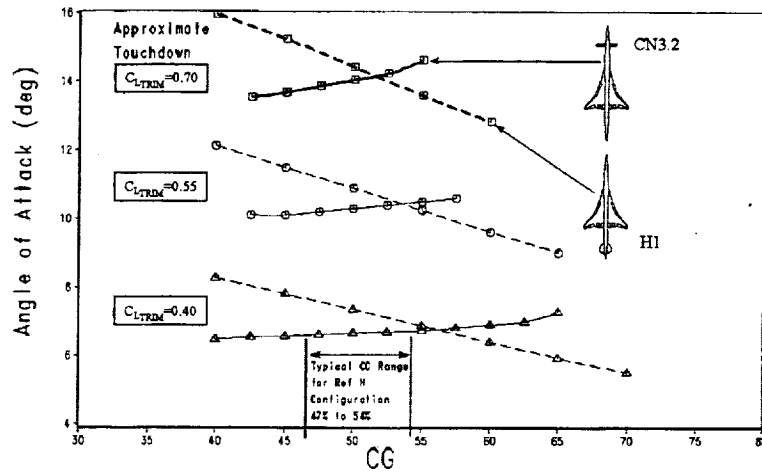
Trimmed angle of attack changes with CG position. As the CG moves forward or aft airplane pitching moments rotate. This rotation changes the lift (or download) required to trim. Forward CG's mean the pitching moments are more nose down for a fixed flap setting. This required a tail down load to trim. At a constant CL if the tail is pushing down for trim the wing has to work harder by carrying the lift lost due to tail down load for trim. This results in a higher angle of attack and more induced drag from the wing. The same is true of the canard, but as the CG moves forward the canard has to trim the configuration by carrying an up-load. This allows the wing to fly at a lower angle of attack for a constant CL.

2094
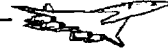
**Additional Canard Positions
and Configurations Tested During NASA 442**

CN3
High AR

High

Low
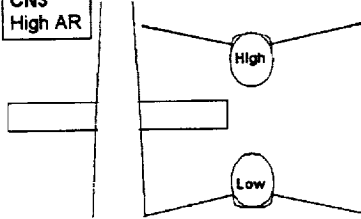
- Test 421 tested clean canards only (no high lift system)
- Test 421 tested the high AR canards in the the low position only
- Test 442 tested the high AR canard with LE droop and 15 degrees of elevator
- Test 442 tested the high AR canard in the high position both forward and aft

Leading edge droop with dowel and clax

15 degree elevator

CN4
Geometry approximate

Aero Config Conference.ppt
Page 19
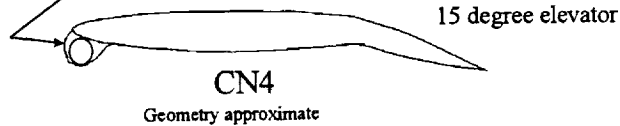
This figure shows additional canard configurations tested during NASA 442. Test to test repeat runs were made for selected configurations. The high AR canard was tested in the fore and aft positions both high and low. In addition, a leading edge flap system was simulated by the use of a dowel positioned under the LE as shown. This configuration was also tested with a 15° deflected elevator.

Test to Test NASA421 to NASA442

Trimmed L/D vs. CG

Solid symbols - TEST442
Open symbols - TEST421

$C_{L_{TRIM}}=0.40$

$C_{L_{TRIM}}=0.55$

$C_{L_{TRIM}}=0.70$

Typical CG Range
for Ref H
Configuration
47% to 54%

L/D_TRIM

CG

H1

Aero Config Conference.ppt
Page 20
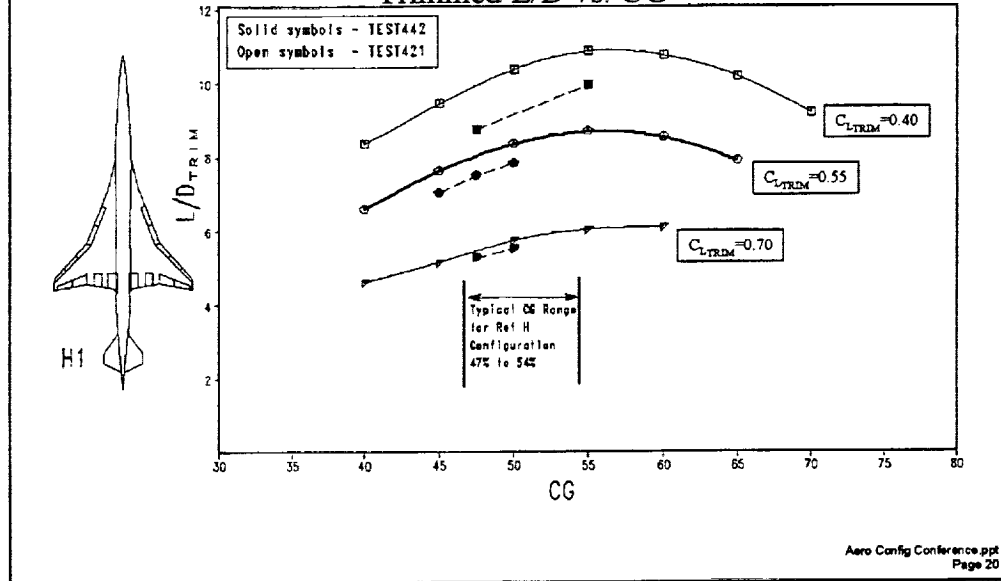
This figure shows the test to test trimmed L/D levels between NASA 421 and NASA 442 for the baseline horizontal tail. Repeatability is very poor, but is somewhat better at high CL's. The data from the most recent test is not as robust because only a couple of tail deflections were flown. It was expected that the new test data would be at a higher L/D level than the 421 data, because the inboard leading edge flap had the new span and taper configuration which was worth roughly 0.5 units in L/D. The fact that the data is down by ~0.5 units at CL=0.55 means that the levels are really down by 1.0 units. This is a big difference.
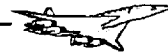
Test to Test NASA421 to NASA442
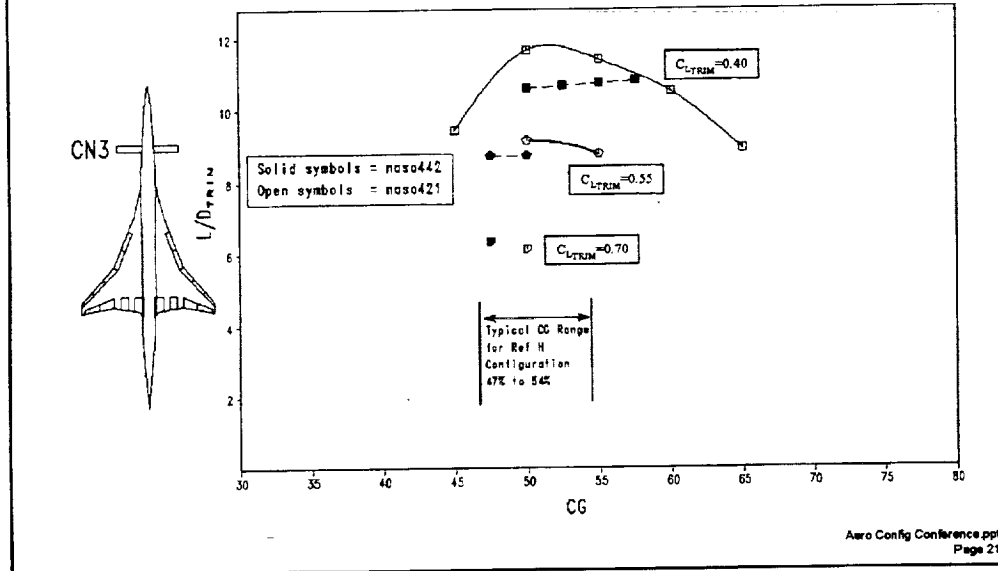
Trimmed L/D vs. CG

This figure shows the test to test trimmed L/D levels between NASA 421 and NASA 442 for the high AR canard in the aft low position. Repeatability is very poor, but is somewhat better at high CL's. The data from the most recent test is not as robust because only a limited number of canard deflections were flown. It was expected that the new test data would be at a higher L/D level than the 421 data, because the inboard leading edge flap had the new span and taper configuration which was worth roughly 0.5 units in L/D. The fact that the data is down by ~0.5 units at CL=0.55 means that the levels are really down by 1.0 units. This is a big difference.
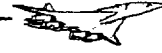
Test to Test Comparison

Although the data is still somewhat preliminary, it should be OK to use for increments

- New turbulence screens
- New tunnel calibration
- Different balance
- Different inboard leading edge configuration
- Different mount to model seal
- New data system
- Different years

The data is preliminary and should be used with caution at present, aside from the previous two charts it will be used only for increments from here on out.

Possible reasons for the poor test to test could be attributed to:

New turbulence reducing screens, after test 421 the screens in the 14x22 facility were removed as they were worn out. Test 442 had new screens in place which could change the tunnel calibration.

Test 442 was flown with a different balance than test 421. Checkloads during both tests were taken, no major problems were noted in the run logs.

Different inboard leading edge configuration. The previous test (421) had a much dragier leading edge flap on the inboard wing than test 442. This should have nudged the data in the better direction though.

The seal at the post to model interface was different. Test 421 used a rubber boot for a seal, test 442 used no seal.

A new data system is now in place - the bugs are being worked out.

Different year, season, personnel, - lots of other variables.

Effect of Mount Position
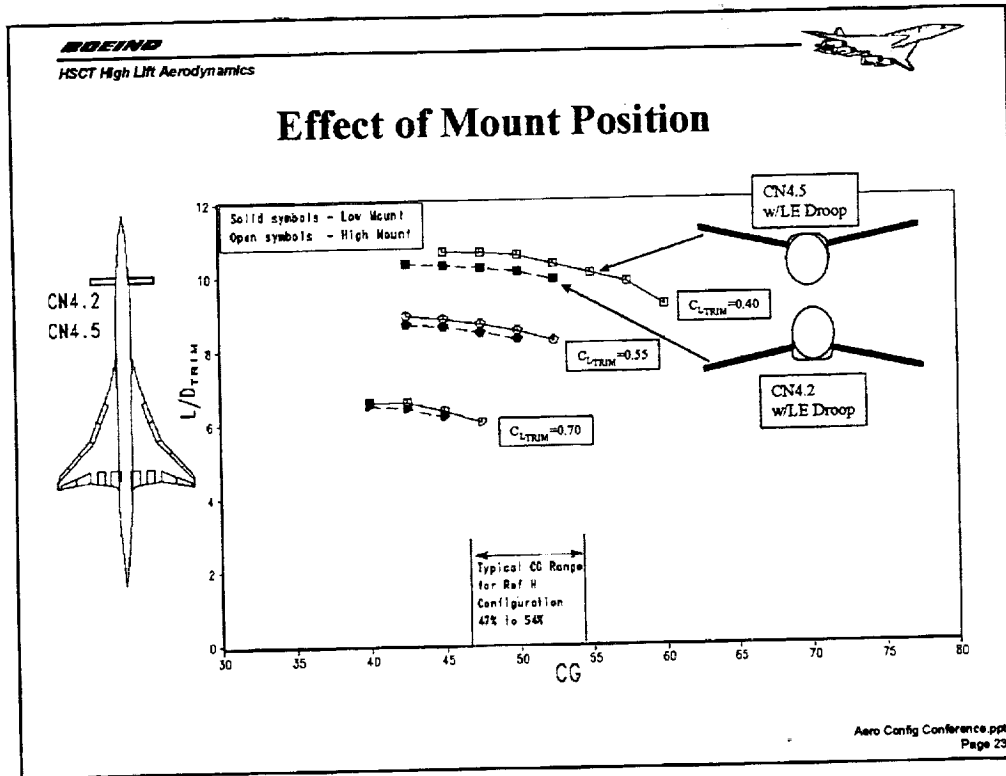
This figure shows the effect of high / low mount position for the high AR canard with the drooped LE. This data is new from test442. It shows that a high mount can provide from 0.2 to 0.5 units in L/D depending on CL. This data is for the forward mount position with the extended forebody. With the canard in the forward position the moment arm is greater and lift required to trim becomes less than canards mounted in the aft locations.
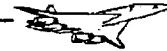
Effect of Canard Mount Position and LE Droop
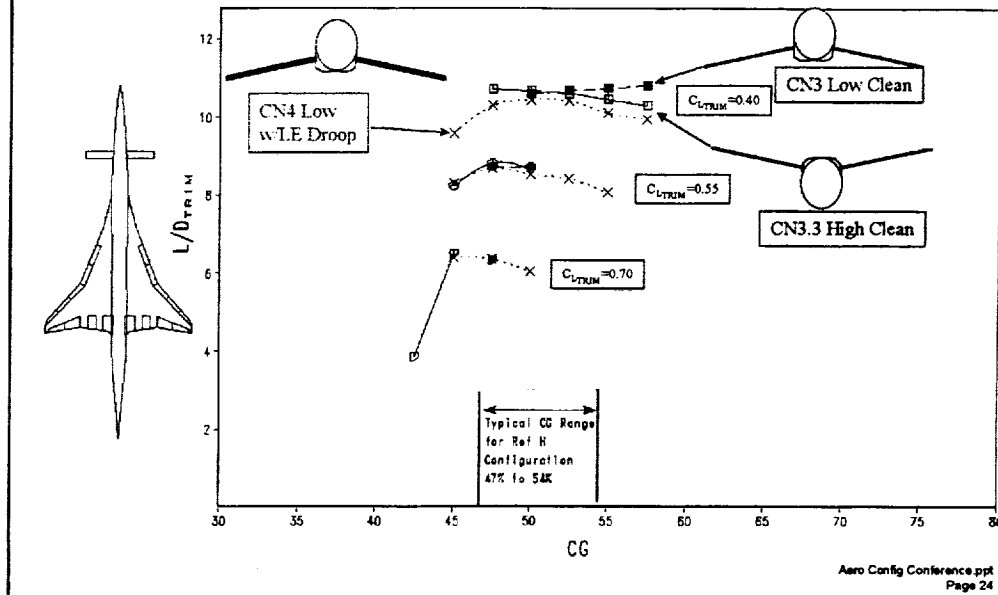
This figure shows the effect of canard mount position and the effect of the LE droop for the aft mount position. This data is for the high AR canard. In the aft position any benefit seen for the high mount has disappeared. In fact the low mount is better at aft CG's, and the high mount is better at forward CG's. The dotted lines with x symbols is the low canard with LE droop. Here we see that by simply adding LE droop we make the configuration worse. A high lift system on the canard needs to be designed in detail to get better results than this.

Effect of Canard Elevator

High AR Canard with LE Droop

CN4.2

Low mount on extended forebody

$C_{L\,TRIM}=0.40$

$C_{L\,TRIM}=0.55$

$C_{L\,TRIM}=0.70$

CN4.2
w/LE Droop

CN4.2
w/LE Droop
and 15° elevator

L/D_{TRIM}

Typical CG Range
for Ref H
Configuration
47% to 54%

CG

Aero Config Conference.ppt
Page 25
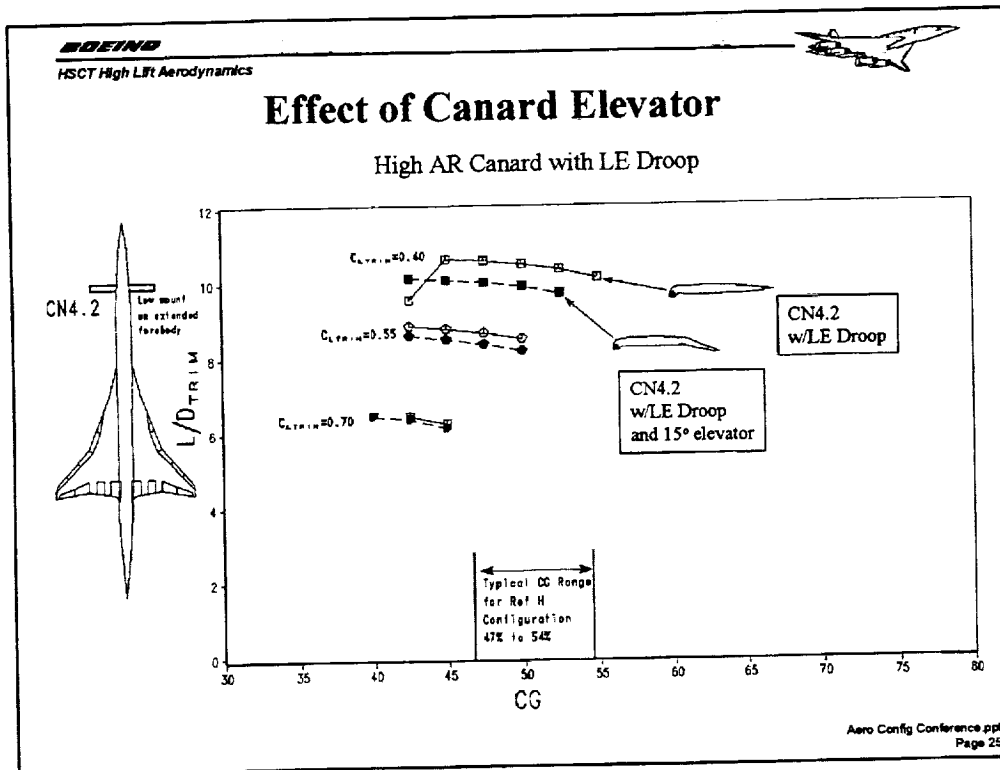
This figure shows the effect on trimmed L/D of deflecting the canard elevator 15°. Both configurations are the high AR canard mounted low on the extended forebody. Both configurations also have the LE droop. The configuration with deflected elevator is worse than the undeflected. The only point where the canard w/ elevator deflection is better is at CL=0.4 in the most forward CG. Again the high lift system of a canard like this one is going to require more thought in the design to get the desired results of high lift with low drag.

Effect of Canard and Sealed Slat

Baseline clean high AR canard

CN3

L/D$_{TRIM}$

$C_{LTRIM}=0.40$ — Section A-A

$C_{LTRIM}=0.55$ — 40° Sealed Slot Outboord LE

$C_{LTRIM}=0.70$ — Baseline Outboord LE

Typical CG Range
for Ref H
Configuration
47% to 54%

CG

30 35 40 45 50 55 60 65 70 75 80

Aero Config Conference.ppt
Page 26
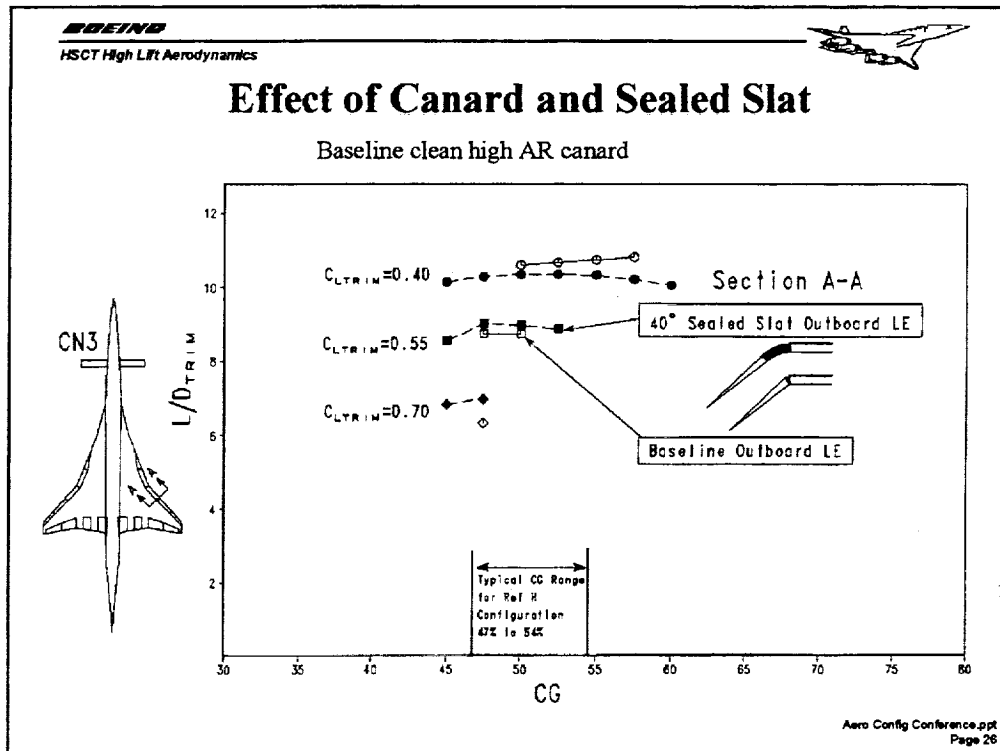
This figure shows the effects of the sealed slat leading edge flap in combination with the "best" canard configuration, the clean high AR canard mounted low on the baseline forebody. As can be seen the sealed slat adds approximately 0.3 units in trimmed L/D over the baseline outboard LE flap. This is approximately the same as shown in a previous slide (0.30 units improvement for the sealed slat over the baseline outboard leading edge flap). It appears that the sealed slat can be used in combination with canards and the L/D benefits of both can be expected.

The sealed slat is worse for the low CL case because it is over deflected, 40 degrees is too much for CL=0.40.
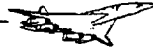
Conclusions

- High lift performance continues to be critical to the HSR program.

- Lift at takeoff and touchdown could become more critical to mission sizing.

- High lift systems on canards will need to be worked harder to get the desired lift with minimum drag.

- The basic wing produces generous amounts of induced drag with lift.

- A high mount canard may provide up to 0.5 units improvement in trimmed L/D.

•High lift performance continues to be critical to the HSR program. Currently the baseline TCA is sized to Stage III -3db at cutback. A more aggressive noise goal of Stage III -5db will make achieving the technology projection for L/D at cutback more critical.

•Lift at takeoff and touchdown will be reduced when the new common process is finished. The use of wind tunnel data instead of AERO2S will reduce lift levels. This will also make the TOFL and VAPP constraints more critical.

•As the literature suggests dynamic ground effect may be as little as 1/2 of static ground effect. We currently are using static ground effect. If dynamic ground effect considerations are required, then lift will be even more critical to mission sizing.

•High lift systems on canards will need to be worked harder to get the desired lift with minimum drag. The simple attempt to improve the high AR canard with dowels and clax did not work. We have to do our homework in this area to produce an efficient highly loaded canard.

•The basic wing produces lots of induced drag with lift, by reducing wing lift and carrying the lift reduction from the wing on a high AR canard with better induced drag characteristics leads to a more efficient system.

•A high mount canard may provide up to 0.5 units improvement in trimmed L/D, this benefit seems to diminish as the canard is mounted longitudinally closer to the wing.

2103
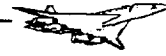
Recommendations

- Continue the research into alternate controls, benefits in both L/D and angle of attack can be obtained.
- Since wind tunnel resources are scarce, use CFD to develop an efficient high lift system for a canard.
- After the CFD analysis is complete build several canards to be flown on the 5% TCA model next year.
- Since the sealed slat provides L/D benefits with and without canards, a systems study is needed to evaluate the viability of the concept.
- Continue to work recent 14x22 data to understand the large differences between tests, as this could impact our performance buildups.

Aero Config Conference.ppt
Page 26

•Continue the research into alternate controls, benefits in both L/D and angle of attack can be obtained.

•Since wind tunnel resources are scarce, use CFD to develop an efficient high lift system for a canard.

•After the CFD analysis is complete build several canards to be flown on the 5% TCA model next year.

•Since the sealed slat provides L/D benefits with and without canards, a systems study is needed to evaluate the viability of the concept.

•Continue to work recent 14x22 data to understand the large differences between tests, as this could impact our performance buildups. Data from the 14x22 tunnel is the basis of the new common process. The large shifts in data levels will lead to huge uncertainties in our performance levels.

LOCKHEED MARTIN

An Approach to Modeling HSR Configurations With Control Surface Deflections

Tom Kinard

Lockheed Martin Aeronautical Systems

Marietta, Georgia

1997 HSR Aerodynamics Performance Workshop

NASA Langley Research Center

February 25 - 28, 1997

Outline

For the past three years Lockheed Martin Aeronautical Systems (LMAS), Marietta, Georgia, has conducted CFD analysis of the Reference H configuration. The data shown in this presentation resulted of some of this work. The presentation is broken down into six main topics. The first section will describe the objective of this work. The second section will be a brief description of the flow field being modeled. The next section will describe the grid-generation method used to model part span flaps. The next two sections will show applications to Reference H in and out of ground effect. The last presentation will conclude with some observations gathered to date.

Outline

- Objective

- Flow Field Characteristics

- Approach used to Model High Lift Configurations

- Application to Reference H

- Application to Ground Effect Study

- Concluding Remarks

Objective

The overall objective of this work is to evaluate state-of-the-art CFD methods for application to high speed research configurations. The tools will be evaluated as to their ability to produce good flow field predictions for use in preliminary and detailed design studies.

The current focus of the work is on high lift configurations of the Reference H aircraft. Particular attention is placed on the ability of structured grid methods to predict the flow field around wings with deflected flaps.

The objective of the first study presented here is to assess the ability of the CFL3D code to predict the forces and moments due to multiple trailing edge flap deflections.

The objective of the second or ground effect study is to evaluate the current state-of-the-art in predicting aerodynamic characteristics of a HSR configuration operating in close proximity of the ground. An exhaustive examination of this topic is beyond the scope of current funding, therefore a limited study involving only a few configurations has been undertaken.

2108

Objective

- To assess the effectiveness of structured CFD in predicting integrated forces and moments to support preliminary design needs.

- Focus on High Lift Configurations
  - Full/Part span leading and trailing edge flaps
  - Low speed landing and takeoff configurations
  - Aerodynamic characteristics in close proximity to the ground

Flow Field Characteristics

The flow field being modeled in these studies is quite complex. When leading or trailing edge flaps are deflected, large slope discontinuities develop in the surface geometry. These discontinuity can and do produce rapid changes in surface pressure and near field velocities. Many of the flow features being modeled here are viscous dominated. Most notable are flow separation, reattachment, and secondary vortical structures. Along with rapid changes in surface pressures, vortices develop along the leading edge, tip and trailing edge wing flap gap intersection regions. Strong spanwise flow is also present in the flow field and should to be properly modeled in order to obtain good quantitative agreement with experiment.

Flow Field Characteristics

- Strong Flow Gradients due to Slope Discontinuities

- Viscous Dominated

- Can have Strong Vortex Interactions

- Large Regions of Strong Spanwise Flow

Approach & Tools

In the studies conducted by LMAS, only structured grid methods were examined. Several characteristics of structured grid solvers make them good candidates for the analysis undertaken here. Most structured grid codes have efficient flow solvers with a wide variety of turbulence models. Since much research and development has been invested in this type of solver, there is a wide experience base to draw upon when problems occur.

There are several disadvantages associated with structured grid methods. The first and foremost is grid generation. Even with programs such as Gridgen, which have reduced the time to generate grids around complex geometries, it still takes on the order of weeks to produce good quality grids. After a structured grid is constructed, manipulation of the mesh can be time consuming or impractical.

For the present studies, the Gridgen software package was used to generate and modify all the grids that were needed.

The flow solver chosen for this study was CFL3D. CFL3D provides a robust solution algorithm with a wide variety of turbulence models and boundary conditions.

Solutions from CFL3D were post processed using a number of programs. For examination of overall data, FAST and PLOT3D were used. For 2D plots and graphs TECPLOT was extensively employed.

Computer time used in these studies was furnished by NAS.

2112

Approach & Tools

- Use State-of-the-Art Structured Grid Solver

  Advantages

  - Efficient Solver Algorithms
  - Multiple Turbulence Models
  - Established Experience Base

  Disadvantages

  - Lengthy Grid Generation Time
  - Slow Geometry Manipulation

- Grids Generated using GRIDGEN

- Flow solutions generated by CFL3D on NAS Cray C-90

- Post-processing assisted by FAST, PLOT3D,and TECPLOT

2113

Desired Grid Characteristics

At the onset of these studies, some basic requirements considered desirable for good quality solutions were set forth for the grids that were to be constructed. None of these requirements were mandetory to run the flow solver.

The first requirement was to generate grids with no pole boundaries. The mesh can contain singular points but no singular lines. This was done to reduce the errors associated with computations around pole boundaries. CFL3D can and does handle singular lines, but errors do occur near these lines.

The second grid characteristic was to have all point match boundaries at zone interfaces. This was more a function of the grid generator rather than the flow solver. The current version of Gridgen will only generate point continuous block interfaces. The developers are aware of the need for non point match boundaries and are expected to release a version soon.

Since more than one flap deflection was to be considered for analysis, the blocking structure needed to be set up such that individual block would be placed at each flap interface. This allowed for the surface grids to be projected to new "database" files with only minor changes to the rest of the grid. This would save many man hours that would have been required to "start from scratch" for each new flap deflection.

For all analysis and especially viscous analysis, there needs to be a high degree of surface modeling integrity. If care is not taken, surface meshes can float away from the prescribed databases. With Gridgen, lines generated on database entities are held to the database. The domain grids can deviate from the prescribed database when TFI or ellipitc smoothing is employed. At the end of the grid generation process the surface domains **must** be projected to the database entities.

For viscous analysis, grid lines need to be as orthogonal to the surface as possible. This can be achieved by applying ellipic smoothing to faces of the grid which are normal to solid surfaces. At corners and other breaks in the geometry, there is often a need to relax this requirement in order to achieve an acceptable grid.

Most viscous flow solvers, which do not have wall functions, need to have a Y+ on the order of 1 or less in order to have accurate resolution of the boundary layer regions. For the present analyses, a value of 5 was set as a target. Most of the grids were able to meet this target with the exception of small regions in the grid where geometry changes occured.

2114

Desired Grid Characteristics

- No Pole Boundaries

- Point Match or Subset Block Boundaries

- Flexible Blocking Strategy for "Efficient" Geometry Manipulation

- High Surface Modeling Integrity

- Orthogonal Grid lines Near Solid Surfaces

- Normal Spacings Such That Y+ Less Than 5

Modeling of Flap Deflections

The first challenge associated with these analyses, was how to grid the deflected flaps. The major requirements of any scheme that could be considered for use would be: (i) generate grids with high surface grid integrity, (ii) produce a low number of skewed cells, and (iii) easily adaptable to different flap settings. Several schemes were explored and will be described here. Each scheme has advantages and disadvantages which were weighed in the selection process.

2116

Modeling of Flap Deflections

- How to model Deflected Wing Surfaces?

- Desired Characteristics

  High Surface integrity

  Low numbers of Skewed Cells

  Easily Manipulated

- Several Schemes Are Available

2117

Exact Modeling of All Surfaces

The first scheme considered was one that exactly models all exposed surfaces. Using this approach would produce the highest surface integrity, but would produce some unwanted side effects. The first problem is that it produces a large number of singular lines, including singular lines that lie on solid surfaces. Singular lines on solid surfaces have caused problems in some flow solvers. Associated with the use of singular lines, the number of highly skewed cells would be large if care is not taken to properly distribute points along and normal to the singular lines. This scheme was not chosen for any of the analyses shown in this presentation, in accordance with the basic requirements for grid discussed earlier.

Exact Modeling of All Surfaces
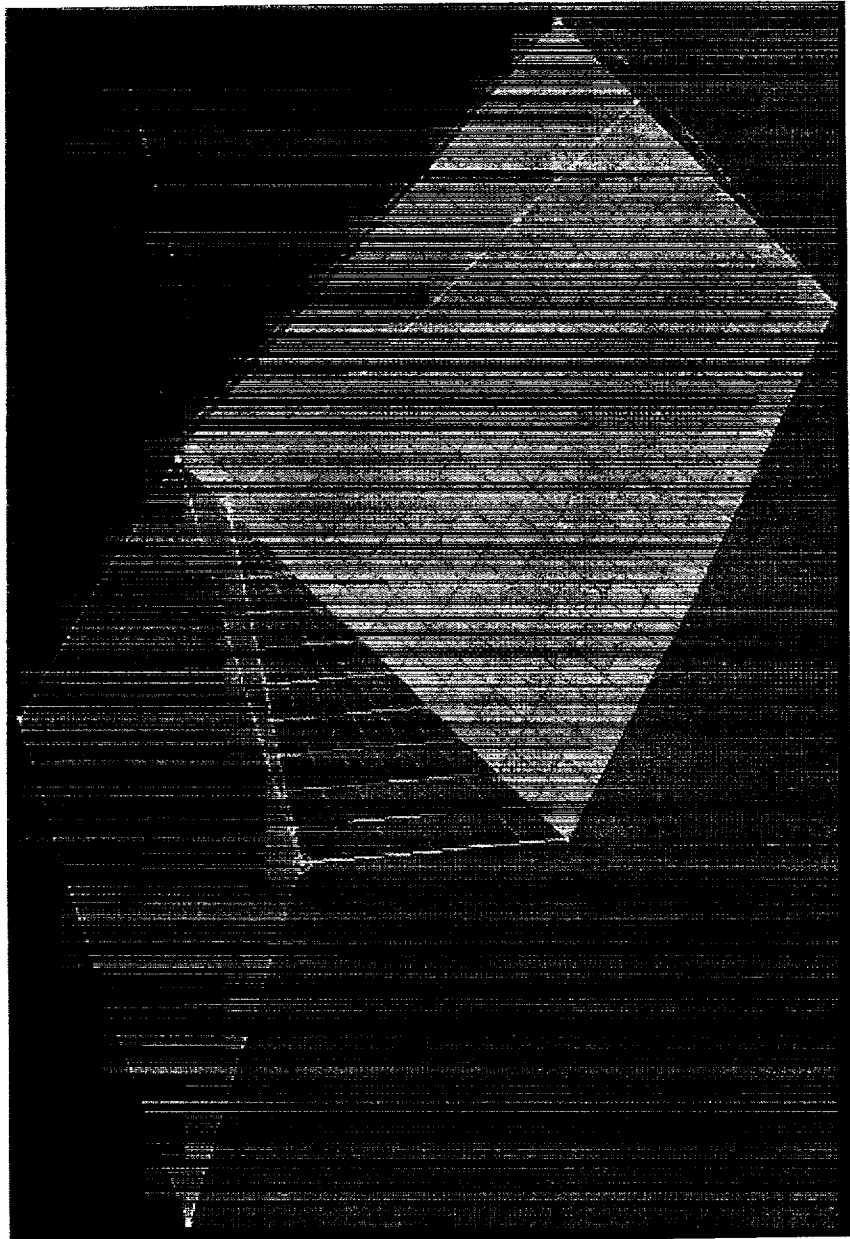
Sheared Grid Scheme

The second scheme examined was a sheared grid scheme. Using this scheme, the blocks associated with the control surfaces would be simply rotate by the amount of deflection. This would provide a grid that was easily manipulated, but the zone interfaces would have to have special treatments. The mis-match could potentially introduce errors into the solution in regions of high gradients. Therefore, this method was not chosen.

Sheared Grid Scheme

"Point Match" Web

The final scheme considered was to place a point match Web between the deflected flap surface and the undeflected wing. This type of procedure required that a spanwise gap be created between the wing and deflected surface. This scheme allowed for easy modification to new geometries. There is an associated error in using this method. The solver is "fooled" into believing that the web on the upper and lower surface are in fact one surface yielding a point match zone interface, even though the surfaces do not physically collapse. The use of this scheme allows for the creation of a grid with all point match interfaces. A quantitative estimate of this error is not available. It is *assumed* that since these regions are small and the distance between the webs is small compared to the characteristic length of the configuration, that the error introduced by these webs will be small.

"Point Match" Web

Application to Reference H

Only the wing and body of the Reference H configuration was modeled in this analysis. The leading edge flap was deflected 30 degrees down and all of the trailing edge flaps were deflected 5,10 and 15 degrees, trailing edge down. Computations were executed with a Mach number of 0.24 and Reynolds number of 1.7million/ft. This yielded a condition which was close to the wind tunnel condition for a dynamic pressure of 85psf. Three angles of attack were executed. They were 6,10 and 14 degrees.

2124

Application to Reference H

Reference H Configuration and Conditions

- Reference H Configuration Used In Analysis;

  Wing + Body

  Leading Edge Flaps (full span) Deflected 30°

  Trailing Edge Flaps (part span) Deflected 5°, 10°, and 15°

- Analysis Conditions:

  Mach = 0.24

  Reynolds Number = 1.7million/ft

  Alpha = 6°, 10°, and 14°

Application to Reference H

An H-H topology was chosen for all the grid used in this analysis. This topology provides the easiest layout for making subsequent changes to the final grid. Some disadvantages are that the wing leading edge will not have a continuous patch which could introduce errors where the wing leading edge is round. Also the orthogonality of the grid around the body is not optimal.

The final grid consisted of 13 point match zones. No pole boundaries were used in any part of the grid, although some singular points do exist in the mesh. A total of 5,690,702 nodes were constructed in the entire grid. The dimensions of the grid were chosen such that a minimum of three multi-grid levels were possible.

In order to reduce the amount of time necessary for new grids to be constructed for additional flap deflections, sub-blocks were created along the trailing edge regions. This allowed for the construction of the grid used for the trailing edge deflection of 5 degrees to be subsequently modified for the 10 and 15 degree case.

No attempt was made to achieve an optimal grid for the analysis conditions. The number of points chosen were selected to produce a grid that "looked" acceptable.

Application to Reference H

Computational Grid Characteristics

- H-H Grid Topology

- 13 Point Match Zones

- No Pole Boundaries

- 5,690,720 Nodes With 3 Levels of Multigrid Possible

- Sub-Blocks Around Flaps for Easy Manipulation

- Original Grid Constructed for 5° Trailing Edge Flap Deflection

- Subsequent Grids Constructed as Perturbations of Original

2127

Application to Reference H

Force and moment data generated by the CFD runs are shown in comparison to test data. Quantitative comparisons of the integrated forces, moments, and surface pressures were conducted against data measured in the NASA Langley 14 x 22 wind tunnel. The flow and reference conditions are also shown here. It should be noted that all dimensions are in model scale, and all computations were done at model scale.

All three angles of attack were run on the 5° trailing edge deflection case. But due to the limited amount of computer time, only the 10° angle of attack was run on the other two configurations. The data collected shows mixed results. For lift, the CFD and experiment show good agreement. For drag and moment, the absolute comparisons are not that good. Several possible causes for this disagreement are the lack of resolution of vortical structures, and poor resolution of surface slope discontinuities.

Application to Reference H

Force and Moment Comparisons

- Test Data From NASA Langley 14 X 22 Tunnel Test 437
- Mach = 0.24, Reynolds Number = 1.7 Million/ft
- Sref = 1840.32 in^2, Cref = 61.94in, Bref = 46.67in
- XMC = 126.354, YMC = 14.486, ZMC = 13.44
- All Dimensions Model Scale

	CL		Δ Difference	CD		Δ Difference	CM		Δ Difference
	CFD	TEST	ICFD - TESTI	CFD	TEST	ICFD - TESTI	CFD	TEST	ICFD - TESTI
5° Deflection									
α = 6	0.2837	0.28123	0.0025	0.02806	0.025152	0.00291	-0.01081	-0.0053348	0.00548
α = 10	0.4553	0.45227	0.0030	0.05695	0.047298	0.00965	-0.002264	-0.0013111	0.00095
α = 14	0.6428	0.63216	0.0106	0.1237	0.10070	0.0023	+0.01636	+0.0072413	0.00912
10° Deflection									
α = 10	0.5299	0.52217	0.0077	0.07122	0.058043	0.01318	-0.02013	-0.019314	0.00082
15° Deflection									
α = 10	0.5943	0.6090	0.0147	0.08746	0.075844	0.01162	-0.0357	-0.040966	0.00527

2129

Application to Reference H

A plot of the computed lift vs experiment is shown here. The absolute agreement is very good except for the 15° flap deflection case. At the 5° deflection case the lift curve slope is predicted well.

Application to Reference H

Lift Comparison

Legend:
- TE 5 Test
- TE 10 Test
- TE 15 Test
- ● TE 5 CFD
- ■ TE 10 CFD
- ◆ TE 15 CFD

Axes: CL (vertical), ALPHA (horizontal)
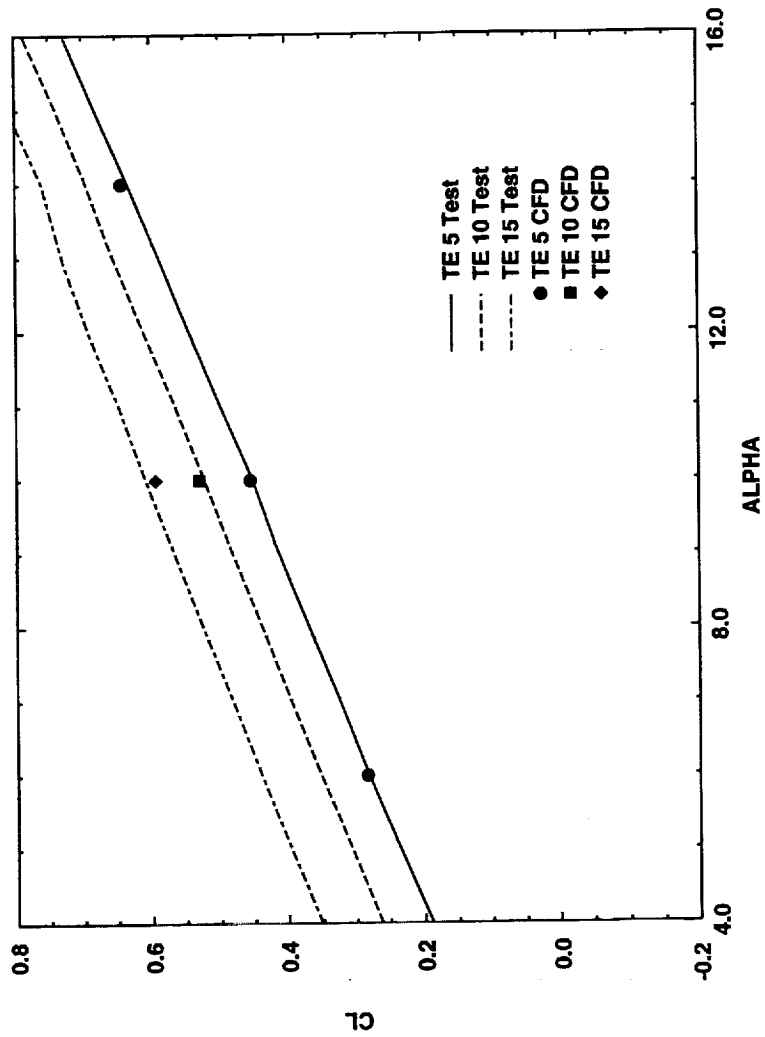
Application to Reference H

A plot of drag vs lift for this configuration is shown here. The trend in drag is predicted well for the 5°case. The absolute agreement to the test data is not as good. This was most likely due to the lack of resolution of vortical structures present in the flow field.

Application to Reference H

Drag Comparison
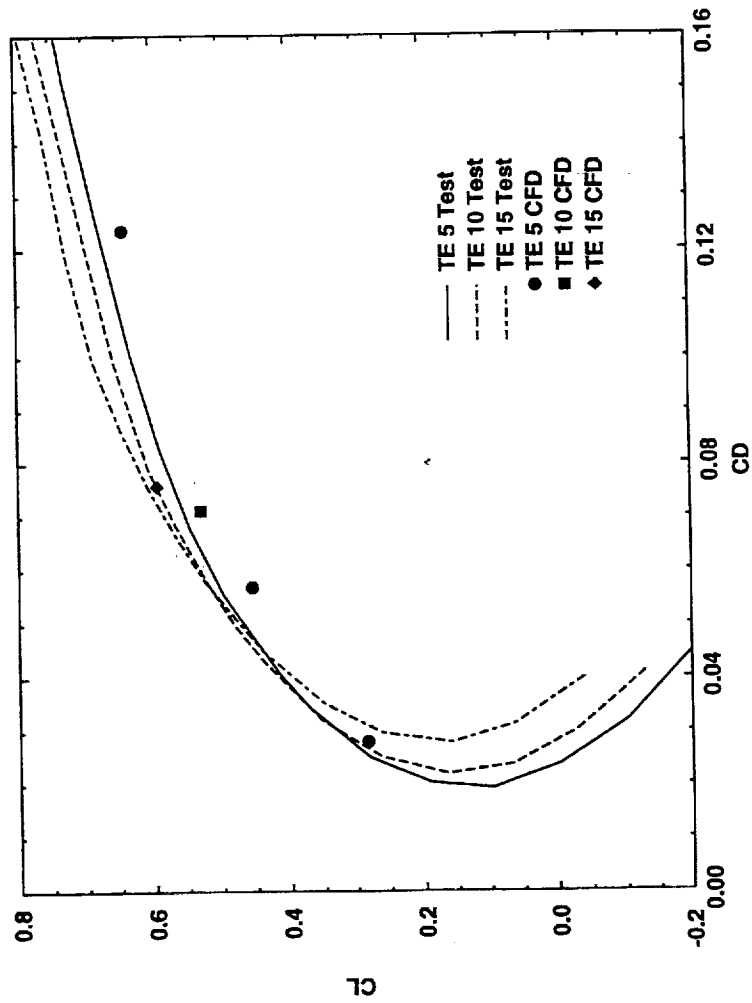
Application to Reference H

The plot of pitching moment vs lift is shown here. For the most part the correlations are not good. The 10° angle of attack case for the 5 and 10 degree deflection case do agree well with the test data. The trend for the 5° flap deflection case is not predicted well.

Application to Reference H

Pitching Moment Comparison
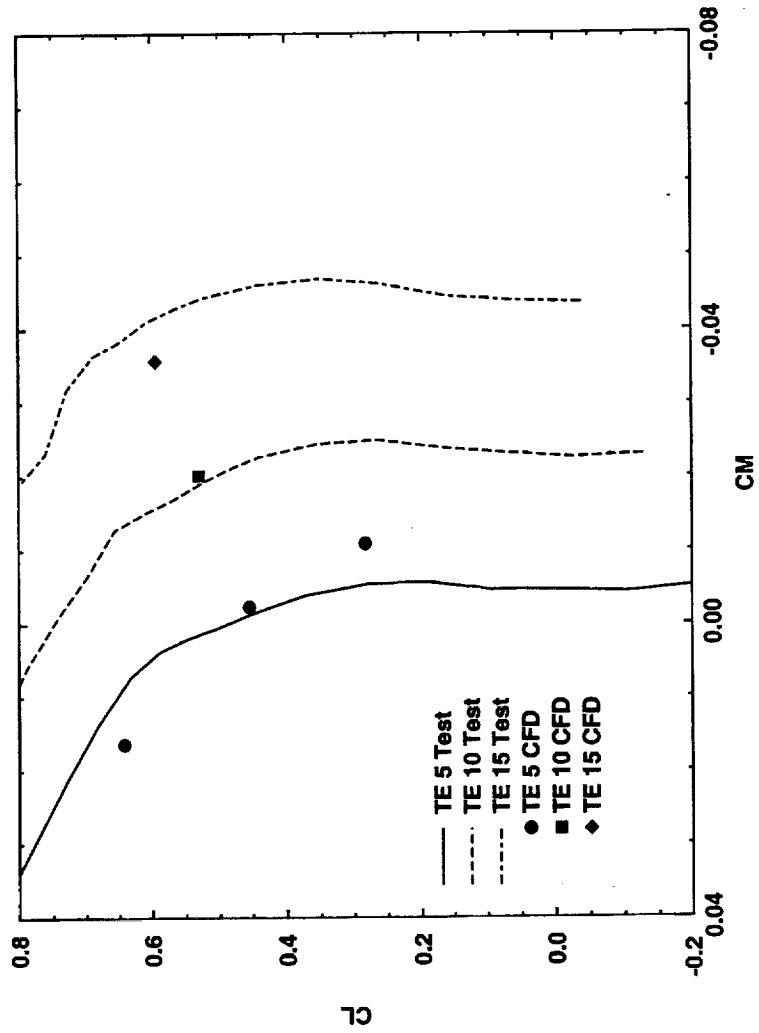
Application to Reference H

A plot of pressure coefficient vs XOC is shown here for a span station just aft of the wing break. At this span station the wing has a sharp leading edge. The pressure distributions indicate that the grid resolution around the wing leading edge was not adequate to resolve the flow structures. The sources of disagreement further aft of the leading edge need to be further investigated.

Application to Reference H

Surface Pressure Coefficient Comparison

Legend:
- CFD TE 5
- CFD TE 10
- CFD TE 15
- Run 177
- Run 157
- Run 167
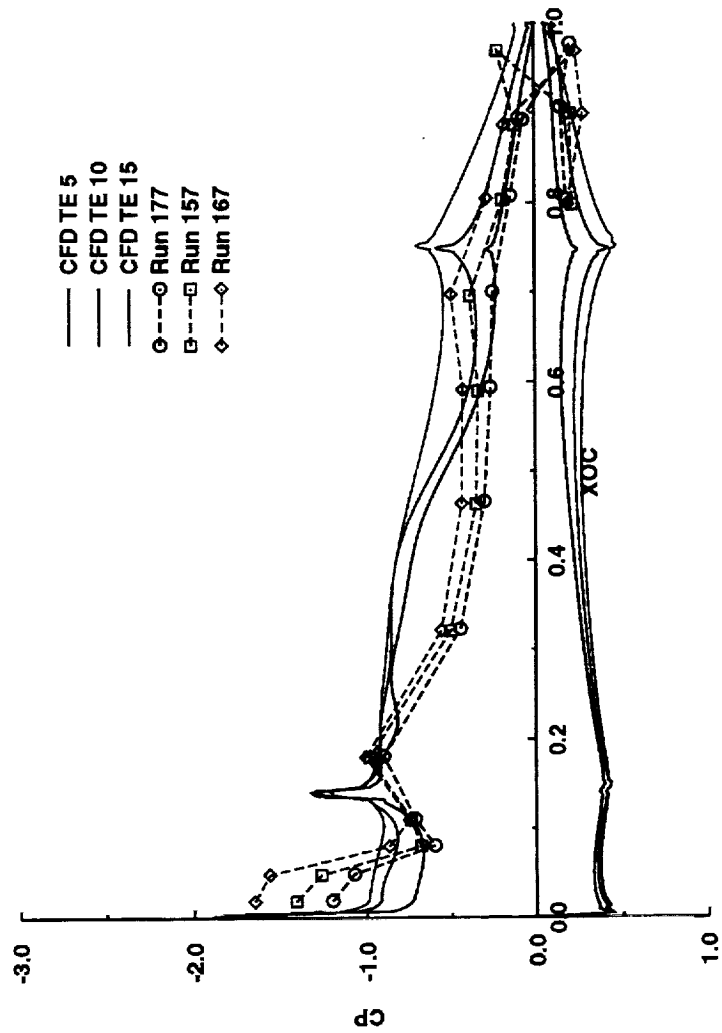
Application to Reference H

This plot gives an overall feel for the flow structures predicted by the CFD runs. This plot is for the 15° flap deflection configuration at an angle-of-attack of 10°. The foot print of two main streamwise vortices can be seen in this plot. Also visible in this plot are the slope discontinuities at the trailing edge flaps.

Application to Reference H

Surface Pressure Coefficient for Trailing Edge Deflection of 15°and Alpha of 10°

Cp
7.450E-8
-0.2
-0.4
-0.6
-0.8
-1
-1.2
-1.4
-1.6
-1.8

2139
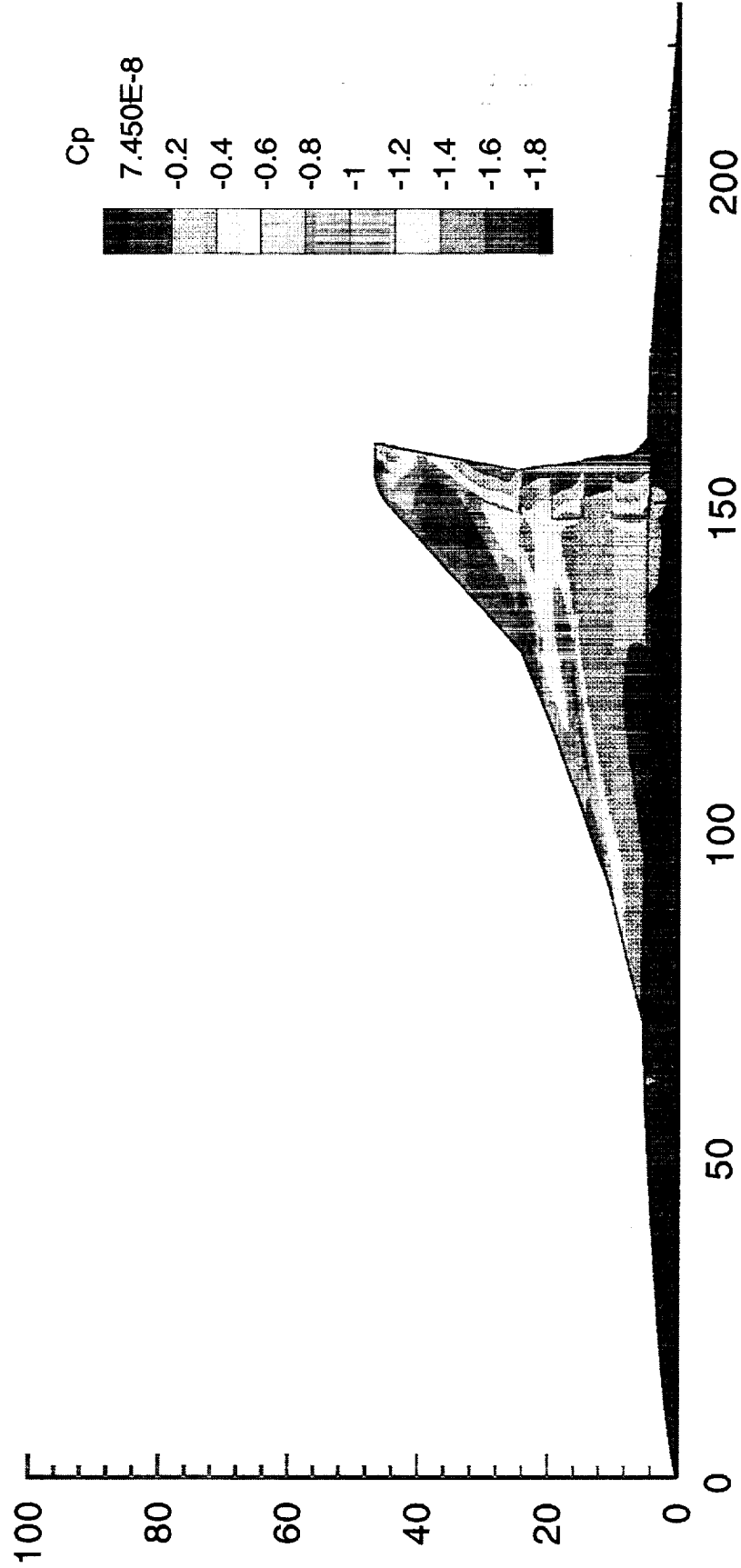
Ground Effect Study

The data shown here is preliminary since this is an ongoing effort.

The approach in assessing the current methodologies was to first conduct a "free air" analysis of Reference H with trailing edge flaps set in landing flare position. The next two analysis conditions will be to lower the configuration to a height of 24 inches and 12 inches above the ground. The heights are given in model scale. The two ground height solutions were carried out with the aircraft stationary with respect to the ground. The second part of the analysis will be to rerun the 12 and 24 inch ground heights with the ground moving with respect to the aircraft.

For all the analysis conducted thus far the Mach number is 0.24 with and angle of attack of 7.7°, at a Reynolds number of 1.7million/ft.

Ground Effect Study

Approach

- Aircraft in Free Air
  Two Ground Heights with A/C Fixed with Respect to the Ground
  Two Ground Heights with A/C Moving with Respect to the Ground

- Analysis Conditions
  Mach = 0.24
  Reynolds Number = 1.7million/ft
  Alpha = 7.7°

2141

Ground Effect Study

The grids used in this study were constructed using an H-H topology. Similar to the grids generated for the previous analysis, there are no pole boundaries. When completed, the free air grid contained 10 zones. Sub-blocks were placed around the trailing edge flaps. The free air grid was constructed such that the two ground heights were included in the grid as block boundaries. By taking the time to do this up front, the two ground height grids were ready to run as soon as the blocks below each ground height were removed. As in the previous analysis all dimensions for the grid were chosen such that a minimum of three levels of multi-grid are possible.

2142

Ground Effect Study

- H-H Grid Topology

- 10 Point Match Zones

- No Pole Boundaries

- Grids Built with 3 Levels of Multigrid Possible
  - Free Air Grid 4,062,170 Nodes
  - 24in Ground Height 2,642,650 Nodes
  - 12in Ground Height 2,097,625 Nodes
  - *Ground Heights measured vertically from A/C moment center (model scale)*

- Both Ground Heights Built into Grid as Block Boundaries

Ground Effect Study

This figure shows the body of Reference H with the two ground planes. As stated before these planes are in the free air grid. When the 24 inch ground height case was ready to be run, the blocks below the farthest ground plane were removed and a solid boundary condition was applied to the block boundary. In a similar procedure the 12 inch ground height grid was constructed. Constructing a grid in this fashion not only reduces the total grid generation time, but the surface grid and the grid close to the geometry also remain exactly the same for all computations, thereby reducing the number of uncertainties in the solutions. If a different angle of attack were to be prescribed, the ground planes and the associated blocks below the aircraft would have to be modified. This procedure has not been fully exercised.

Ground Effect Study

GROUND PLANE PLACEMENT IN COMPUTATIONAL GRID
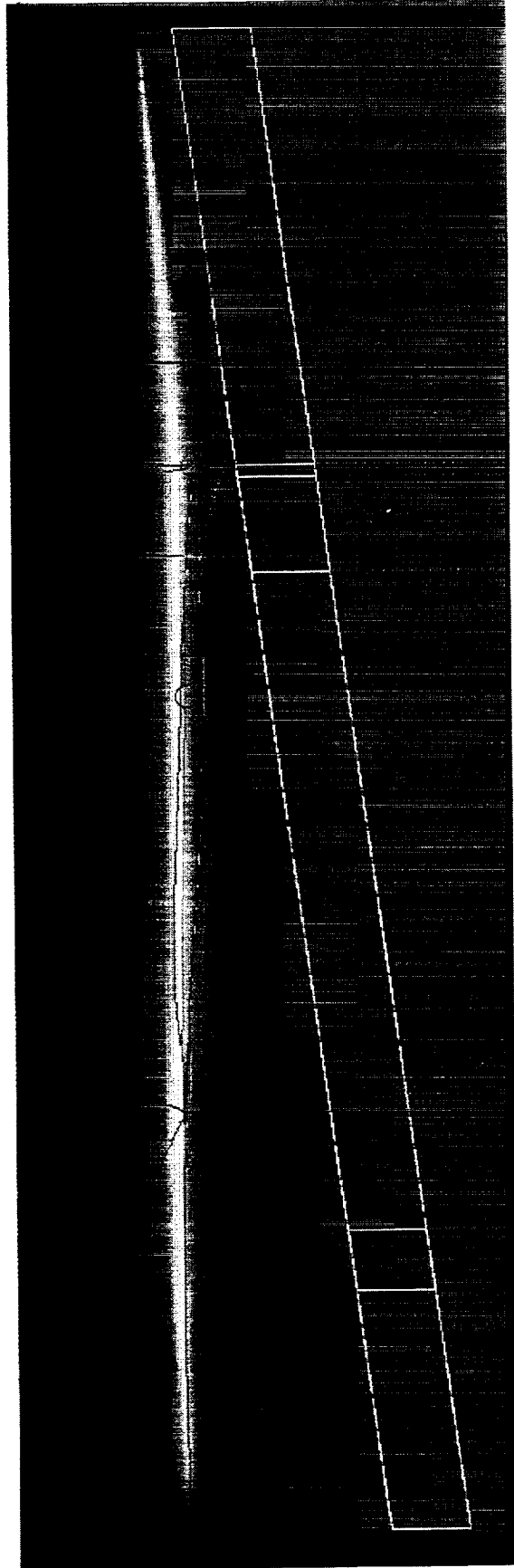
Ground Effect Study

The preliminary forces and moments for the free air case, 12 and 24 inch ground height are shown here. For the free air and 24 inch ground height cases, lift grows as the aircraft approaches the ground. The 12 inch ground height does not follow this trend. This anomaly is seen in the drag and pitching moment as well. Further investigation needs to be conducted to resolve this discrepancy. As mentioned above these are preliminary numbers and do not represent the final results of this study.
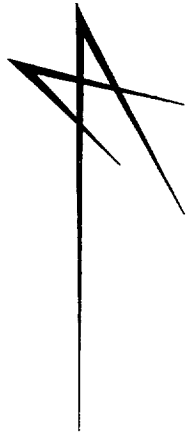
Ground Effect Study

Force and Moment Summary for Ground Effect Study 1997
Mach=0.24, Alpha=7.7, Reynolds Number=1.7million/ft
Sref=1840.32, Cref=61.937, Bref=46.672
XMC=126.354, YMC=14.486, ZMC=13.44

CASE	CL	CD	CM
FREE AIR	0.6781	0.1236	-0.06431
24 INCH HEIGHT	0.7086	0.1229	-0.06420
12 INCH HEIGHT*	0.6164	0.1010	-0.04238

Ground Effect Study

One possible reason for the lift of the 12 inch ground height to be in error can be seen from this chart. This is a plot of the computed Mach number at the symmetry plane. The ground plane for this and the 24 inch ground height run from the inflow boundary to the outflow boundary. Having such a large plate ahead of the aircraft, produced a thick boundary layer. This boundary later interacted with the aircraft lower surface changing the integrated forces and moments. Several ideas are being explored to better model this case such as making the entire wall inviscid, or applying suction to the plate upstream of the aircraft or a combination of inviscid,suction, and viscous boundary conditions.

Ground Effect Study

Symmetry Plane Computed Mach Number Contours
For 12 Inch Ground Height Case

Mach
0.24
0.22
0.21
0.19
0.18
0.16
0.14
0.13
0.11
0.10
0.08
0.07
0.05
0.03
0.02
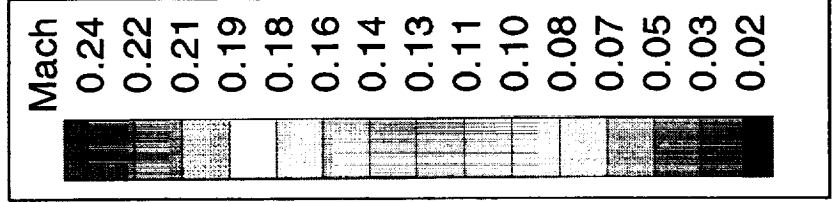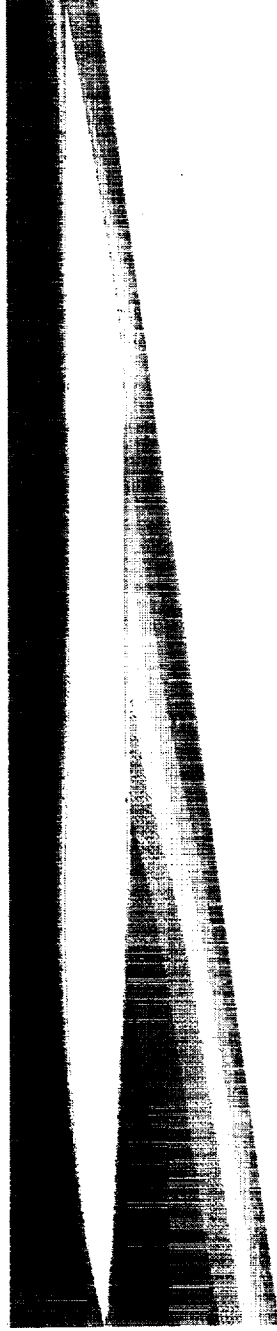
Ground Effect Study

One more example of the effect of the thick boundary layer on the lower surface pressures can be seen in this plot. The pressure contours are very different for the two ground heights. The flow shows the tendency to actually slow down as the ground is brought closer to the aircraft.

Ground Effect Study

Lower Surface Computed Pressure Coefficient

Ground Height = 12 inches

Ground Height = 24 inches

Cp: -0.20 -0.10 0.00 0.10 0.20 0.30 0.40
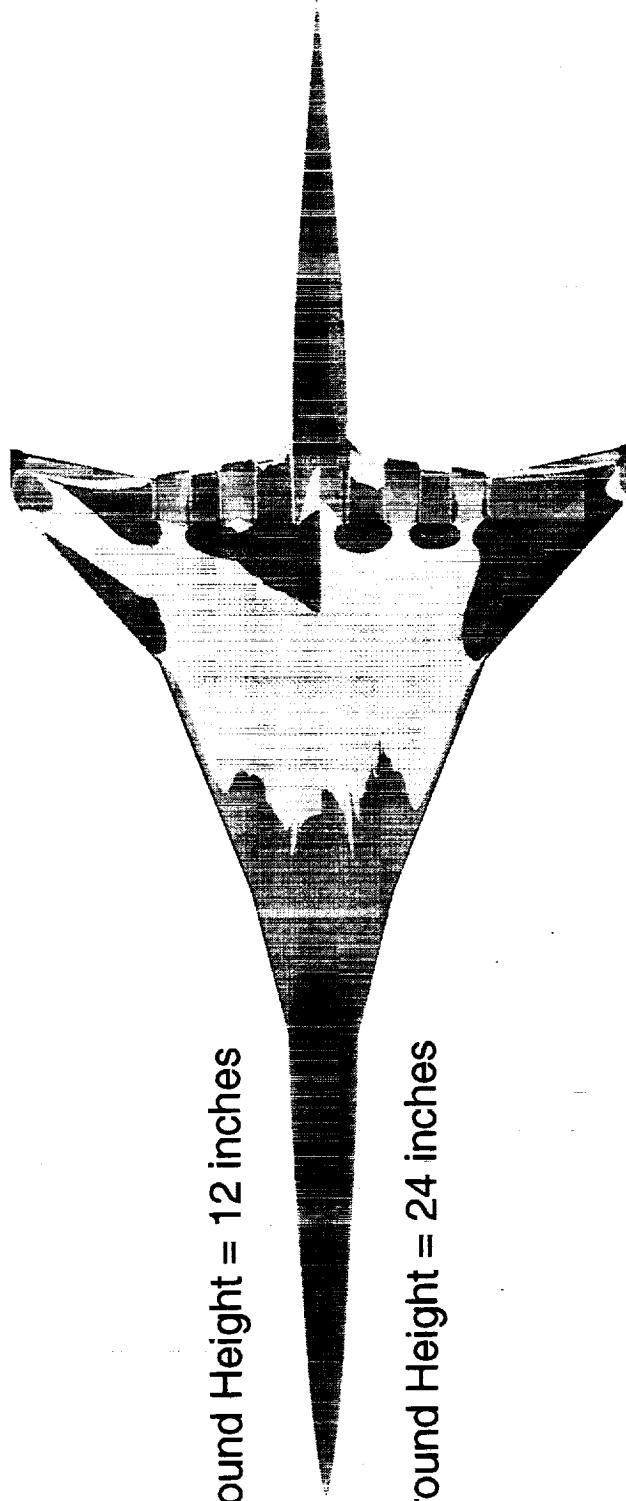
Concluding Remarks

From the solutions presented here, the use of a webbed closure for part span flaps appears to be a good strategy of modeling high lift configurations. Studies should be conducted to assess the error associated with using this strategy.

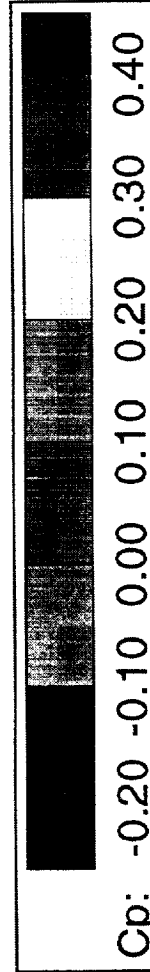With good grids, the use of structured flow solvers can produce reliable force and moment data for preliminary design needs. The current state of the art solvers can predict the effects of multiple part span flaps on aerodynamic coefficients.

Even though structured flow solvers can provide good prediction of forces and moments, thein effective use in the preliminary design arena is hampered by the long set-up time. The generation of good quality grids consumes a large amount of time. New methods have reduced this set up time but more work need to be expended in this arena in order to make this type of analysis more applicable to the design environment.

A first cut at modeling high lift configurations in ground effect has been attempted. Anomalies have been seen in the solution which need to be resolved by further investigations.

Concluding Remarks

- "Webbed" closures provide a good strategy to modeling wings with part span flap deflections

- Structured grid flow solver such as CFL3D can provide good predictions of integrated forces and moments for HSR configurations with flap deflections

- Effective use of structured grid methods still hampered by lengthy set up time

- Grid sensitivity studies need to be conducted for high lift configurations

- More work is being done on strategies for modeling configurations in ground effect

2153

This page intentionally left blank.

MCDONNELL DOUGLAS

HSCT

HIGH-SPEED CIVIL TRANSPORT
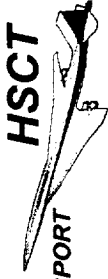
Automated Flap Deflection Procedures for HSCT High-Lift Aerodynamics

David T. Yeh

Roger W. Clark

February 25-28, 1997
HSR Workshop
at
LaRC, Hampton, VA

Outline

This report starts with the statement of the objective for the HSCT high-lift aerodynamics, followed by the description of the need for automatic flap modeling procedures for high-lift applications. The flap layout and arrangement for HSCT high-lift configurations are described. The detailed methodologies and gridding techniques incorporated in the flap deflection procedures are discussed. The numerical capability of the flap procedures is demonstrated for a number of HSCT high-lift configurations. Sample solutions and code validation are presented followed by a summary.

OUTLINE

- Objectives - HSCT High-Lift Aerodynamics
- Need for Grid Modification Procedures
  - LE & TE Hinged Flaps
- Flap Arrangement and Layout
- Flap Deflection Procedures & Issues
  - Pre-Process Procedure
    - LE Flaps
    - TE Flaps
- Sample CFL3D Solutions and Code Validation
- Summary

Objective

The objective of the HSCT high-lift effort is to analyze and optimize the aerodynamic performance. To achieve the objective, it is necessary to develop and validate the numerical methods required for analysis of the high-lift systems.

The computational emphases are focused in the following areas:

1. Conduct Numerical simulations of the high-lift configurations for wind-tunnel support;

2. Assess the numerical capability in capturing the flow physics under high-lift, low-speed conditions;

3. Complement wind-tunnel results in deriving an optimal high-lift system through parametric studies.
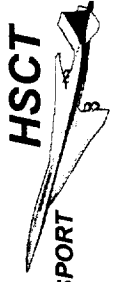
OBJECTIVE - HSCT HIGH-LIFT AERODYNAMICS

Analyze/optimize high-lift performance

- increase L/D -> lower power -> less noise

Develop/validate the numerical methodologies required for analysis of the high-lift system of HSCT configurations

• Perform pre- and post-test analysis for WT support

• Validate/evaluate current CFD code for analysis

• Conduct parametric studies for optimal performance

Numerical Process

Design and analysis of HSCT high-lift configurations require the modeling of the LE and TE flaps with a wide range of planforms and angular deflections. In order to make the numerical process feasible and efficient for the high-lift applications, an automated flap deflection process has been developed which would automatically modify the baseline CFD grid to account for multiple LE and TE flap deflections. Once the numerical results are obtained, they can be utilized for performance study and wind-tunnel support in an effort to derive an optimal high-lift system.

Automated Flap Deflection Modeling for HSCT High-Lift CFD Analysis
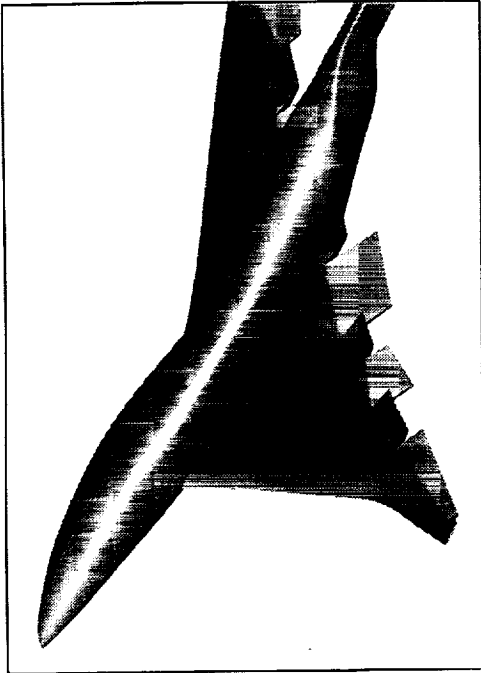
- ● **Baseline Model w/ or w/o LE Deflection**

M2.4-7A MODEL

- ● **Flap Deflections**

Flap Schedule
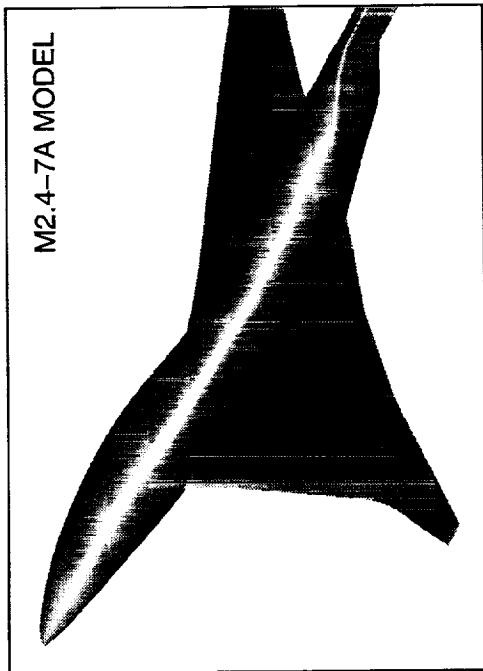
Automated Procedure

- ● **Grid Modification**

At the TE

Flap

Flap

Flap

$\underline{\text{C}}$L
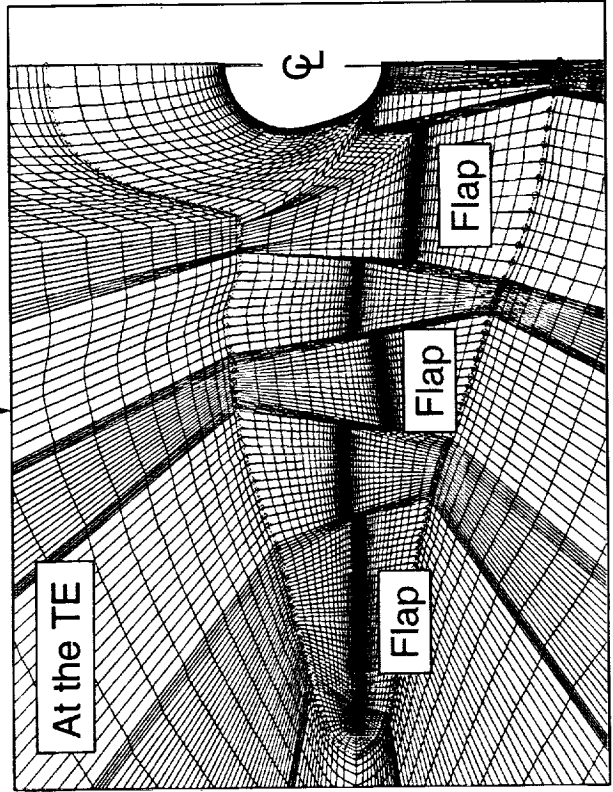
CFD Analysis

- ● **Performance Study / Wind-Tunnel Support**

Pressure & Traces

≥ 0.00
-0.20
-0.40
-0.60
-0.80
-1.00
≤ -1.20
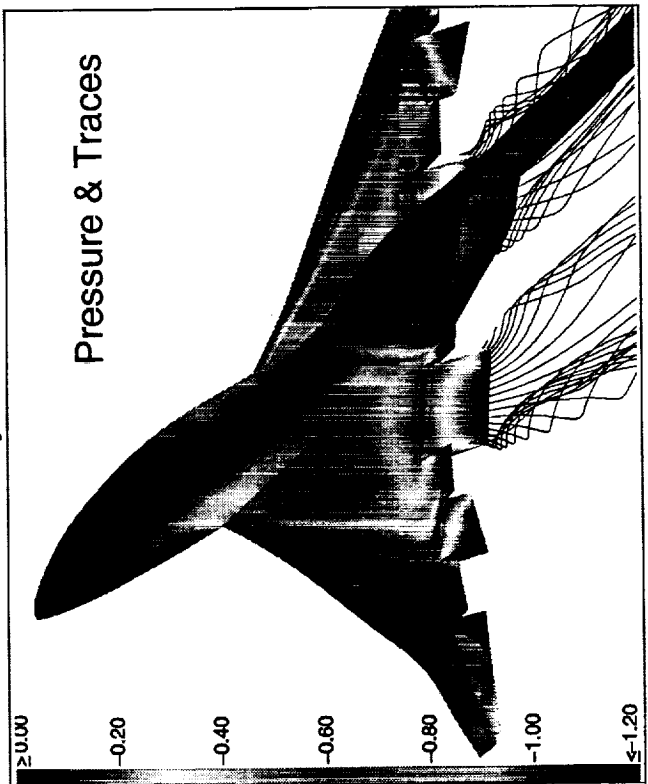
Purpose

The automated flap deflection procedures are developed to modify the baseline grid to account for multiple LE/TE flap deflections with minimal user interface. These numerical procedures are applicable for high-lift analysis and optimization including wind-tunnel support, parametric studies and flap optimization applications.

Automated Flap Deflection Procedures

- Modify HSCT baseline grid for multiple LE/TE flap deflections
- Reduce the regridding process & minimize user interface

Applications:

- Support W-T tests - Wide range of flap deflections
- Parametric studies of the effects of LE & TE flap deflections
  - Deflection angles
  - LE Flap chord lengths
  - LE Flap spanwise extent (i.e., full span vs. part span)
  - LE radius
- Optimize Aero Performance
  - Flap schedule
  - LE Flap planform

User Friendly

The flap deflection procedures are easy to use once the flap system has been defined. These procedures have been implemented in such a way that only flap deflection angles are required to generate a modified grid for CFD analysis. In doing so, the regridding process for different flap deflections is eliminated.

Automated Flap Deflection Procedures Reduce Turn–Around Cycle for Performance Analysis and Flap Optimization

Start with a Clean Grid (No Flaps)

1 Specify Flap Deflections
  (LEI, LEO, TEI, TEM, TEO)

2 Run Flap Deflection Procedures

3 Obtain a Modified Volume Grid

LEI

LEO

TEI

TEM

TEO
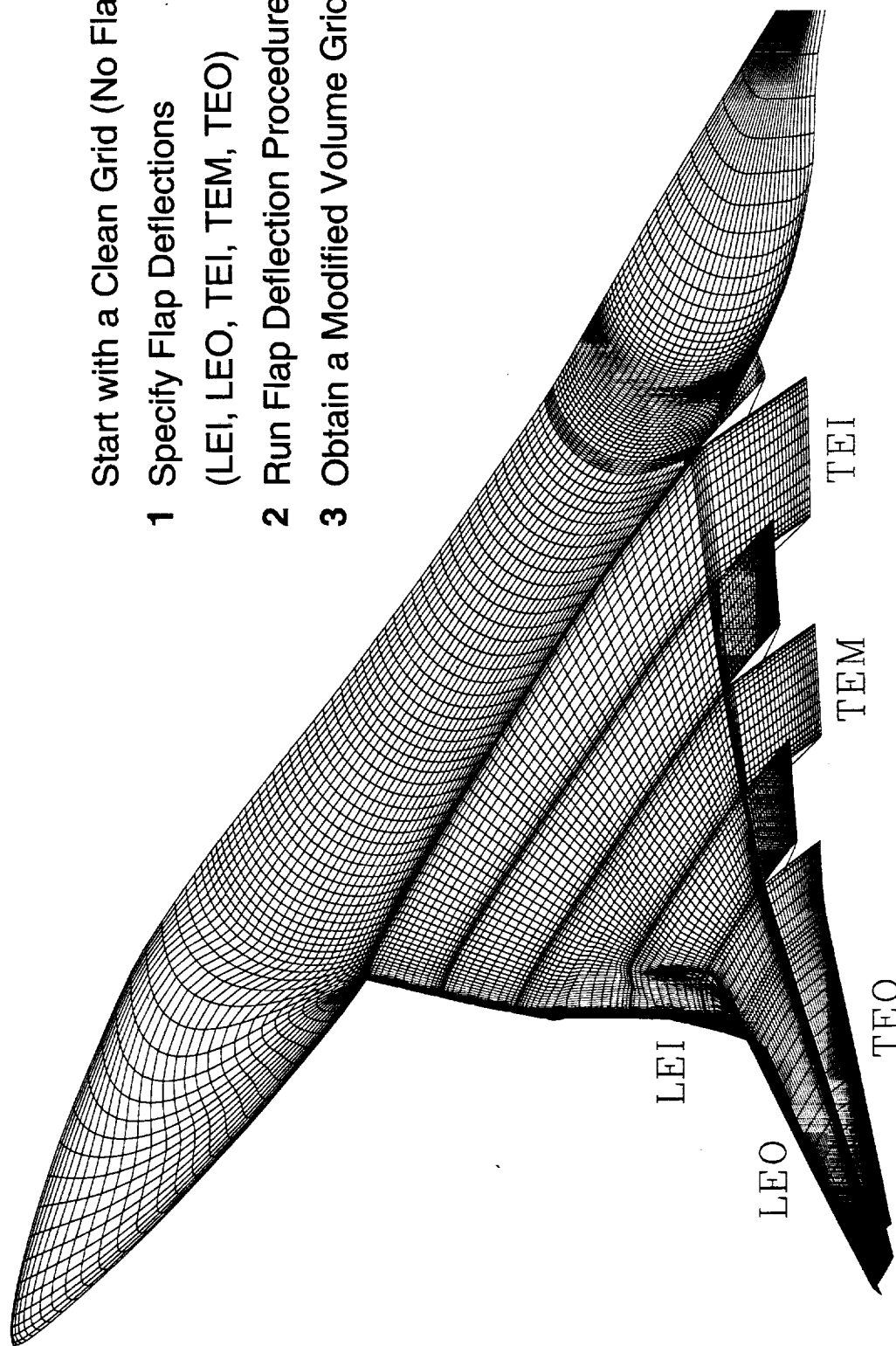
Flap Arrangement

An overview of the flap layout and arrangement will be presented for 2 HSCT high-lift configurations including the M2.4-7A (Arrow Wing) and TCA configurations.

Flap Arrangement and Layout

M2.4-7A Layout

This chart shows the Arrow Wing Configuration with the layout of the flap segments. The flap system for this configuration consists of either part-span or full-span hinged LE flap segments that extend all the way out to the wing tip. These LE flap segments are arranged such that there is no spanwise gaps across the flap segments.

This configuration has 4 flap surfaces at the TE which consists of an inboard, a middle and 2 outboard flaps. In order to simulate the 3-D edge effects on the TE flap surfaces, it is necessary to model the spanwise gaps across the TE flap surfaces and the wing.

M2.4-7A Configuration Layout

Baseline Inboard tapered flap

Option 1

Option 2

Nose strakes
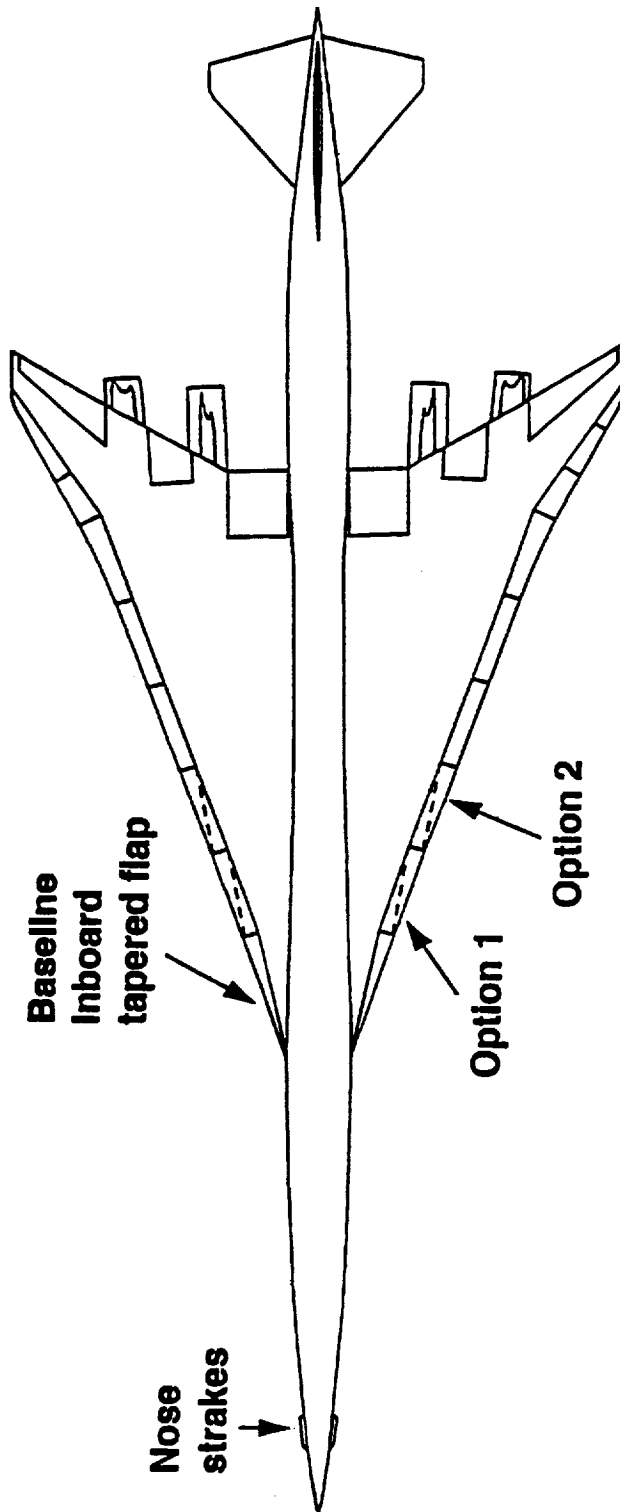
TCA Flap Definition

The TCA configuration has a similar flap arrangement as that for the Arrow Wing. The essential information required to model the flap surfaces is to obtain the coordinates of the corner points of the flap elements and their corresponding hinge lines. These information are required for both the LE & TE flap surfaces.

Technology Concept Airplane TCA - Flap Definition
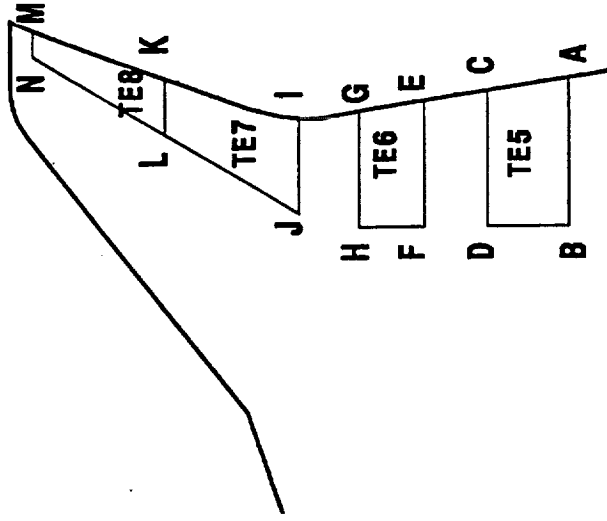
TE Flaps
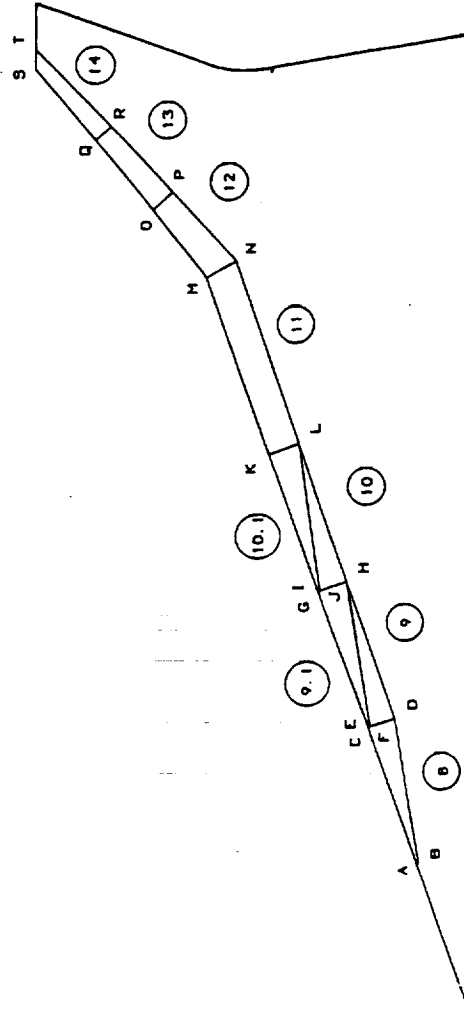
LE Flaps

Flap Deflection Flow Chart

The automated flap deflection procedures consist of 3 procedures: a pre-processor, LE flap and TE flap deflection procedures. For the cases where only the LE flap deflection is required, the pre-processor is bypassed and the process goes directly to the LE flap deflection procedure. The pre-processor is only used to line up the grid lines with TE flap edges whenever the TE flap modeling is needed. The running process for using these procedures has been automated for a number of HSCT High-Lift Configurations.
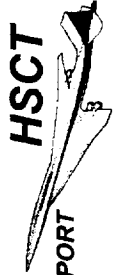
Flap Deflection Flow Chart
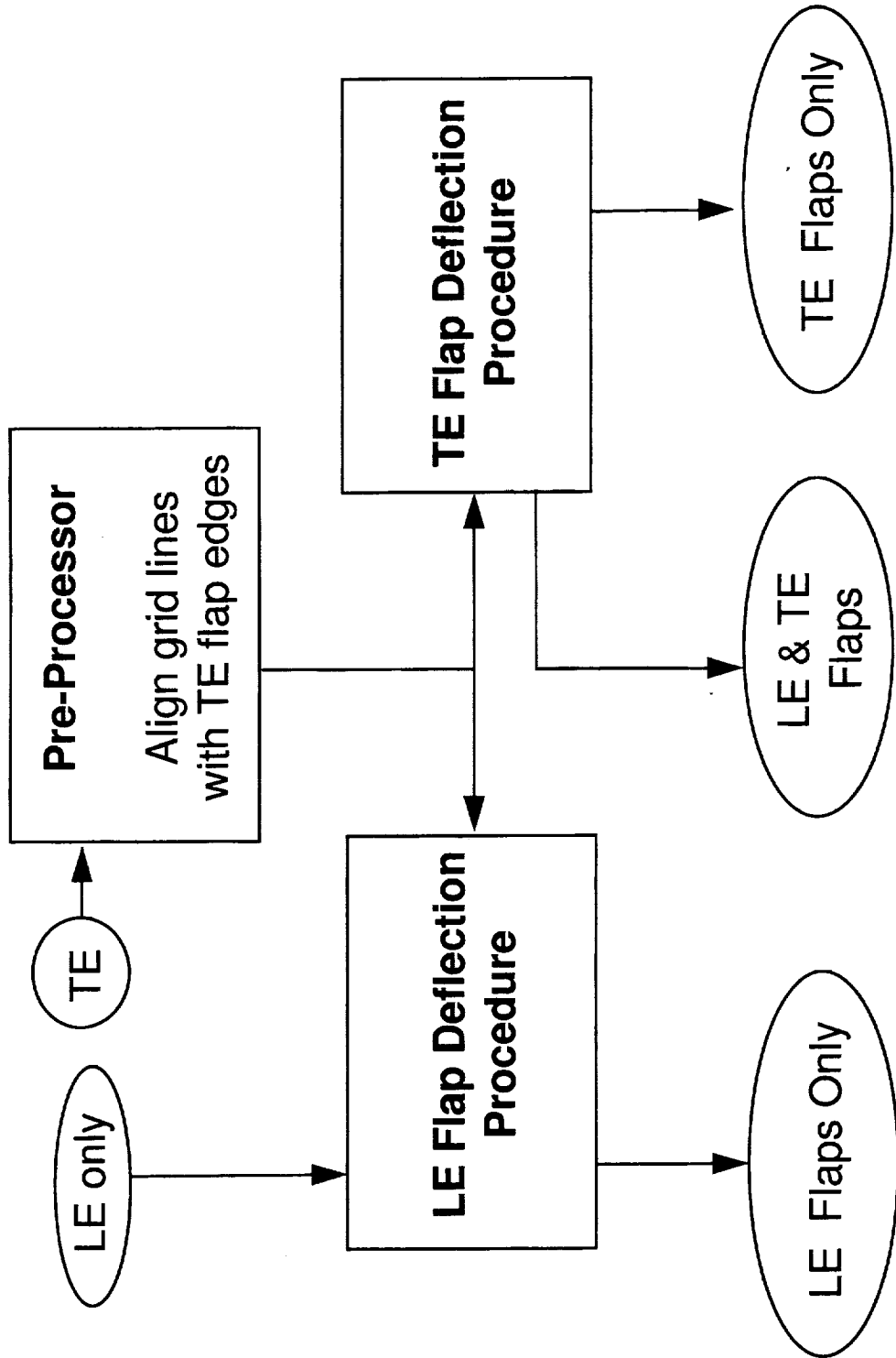
Pre-Processor

The pre-processor is provided for the convenience of the users where the surface grid lines of arbitrary distribution are adjusted to line up with the TE flap edges. The corresponding volume grid is also modified in the process through parametric linear interpolation (along each spanwise curve). The use of the pre-processor is required only once for a new configuration or grid of interest.

Pre-Process Procedure for Modeling Trailing-Edge Flaps
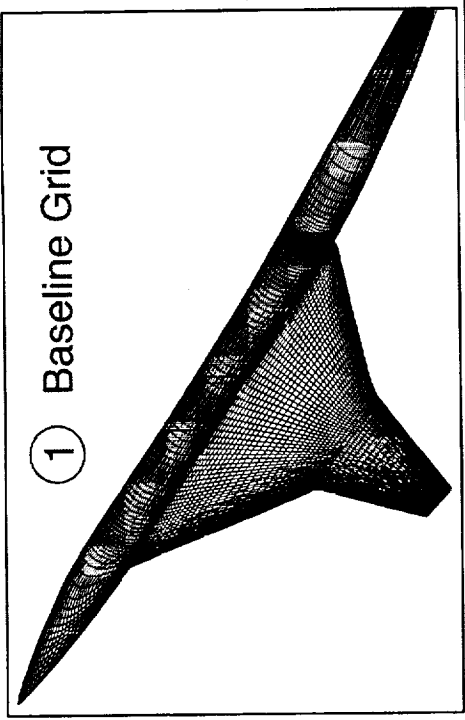
- Align Grid Lines with TE Flap Edges
- Modify Corresponding Volume Grid

① Baseline Grid

② Spanwise Definition

③ Chordwise Definition

TE Flaps

Modify Volume Grid

Modify Volume Grid

Resultant Spanwise Distribution

Resultant Chordwise Distribution
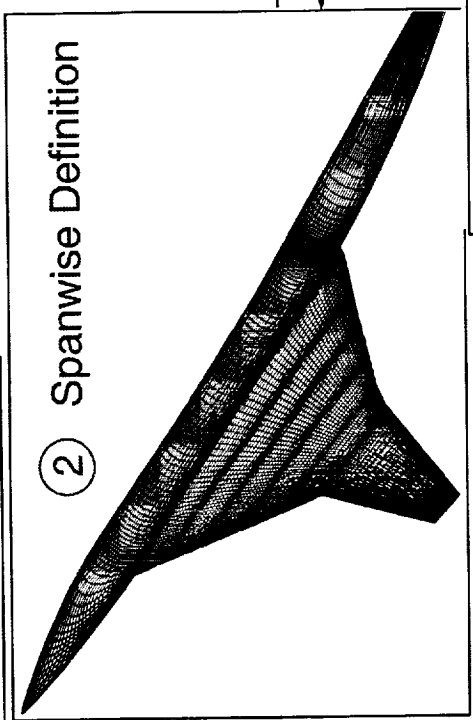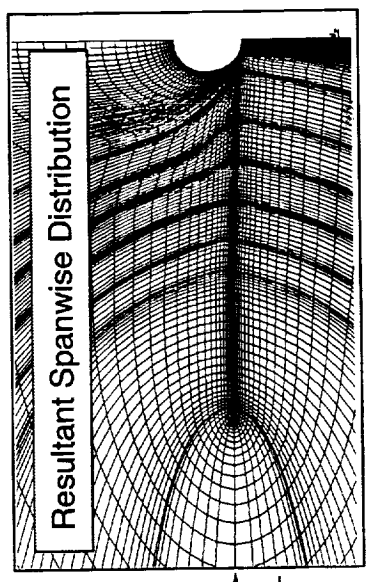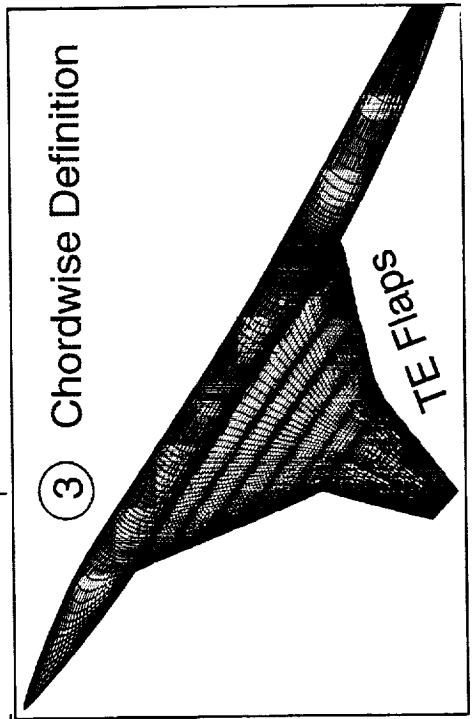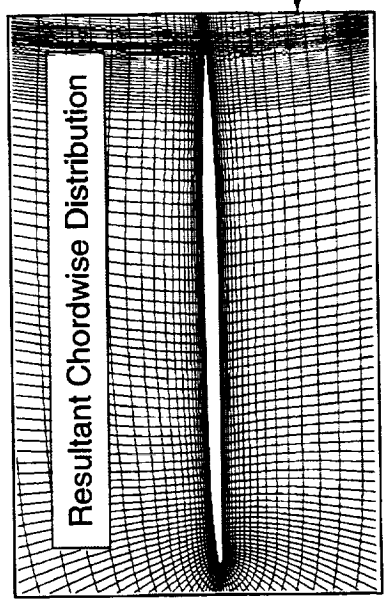
LE Flaps

The following next few charts will be focused on the gridding techniques that are incorporated in the LE flap deflection procedure.

LE Flap Deflection Procedure

LE Flap Deflection Procedure

The LE flap deflection procedure consists of a series of mapping, grid modification and smoothing techniques that modifies a baseline grid to account for LE flap deflections. The basic idea is to isolate the LE flap geometry so that the flap geometry can be rotated about the hinge axis of an arbitrary orientation, or can easily be modified in the design process. Once a desirable flap rotation/geometry is determined, the surface grid points upstream of the hinge line are mapped onto the new flap surface. The corresponding volume grid is then generated for the CFD analysis, or is used in the TE flap deflection procedure for simultaneous LE/TE deflections.

2178

Automated Grid Modification Procedure for Modeling Leading–Edge Flap Segments

4. Hinge–Line Surface Smoothing

Spline

Interpolation

δ_f

5. Mapping

Relaxed to the original grid

TE

Distribution for TE Flaps

Deflected LE

6. Grid Modification & Clustering

1. Identify Flap Segments

TCA Configuration

2. Generate Flap Geometries

Inboard

Additional cuts for better accuracy

Tip

3. Rotate about Hinge Lines

Hingewise Rigid Body Rotation

LE Flap Segments

The first step to generate the LE flap geometry is to obtain the definition of the flap segment breaks based on the wind-tunnel model. The LE flap geometries are then generated at the breaks based on the baseline grid definition. The option of additional subcuts are generated as necessary between the breaks to accurately model the geometry in the high twist regions. These subcuts are used as the segment breaks for generating a high fidelity LE flap surfaces.

Generation of the Leading–Edge Flap Segments

- Based on 1. Flap Segment cuts
         2. Clean Baseline Surface Grid

Baseline Grid
(M2.4–7A–mod3)
& LE Flap Segment Cuts

Create LE Flap Geometry at
the Break Locations Based
on the model Definition

Wing Root

Wing Tip
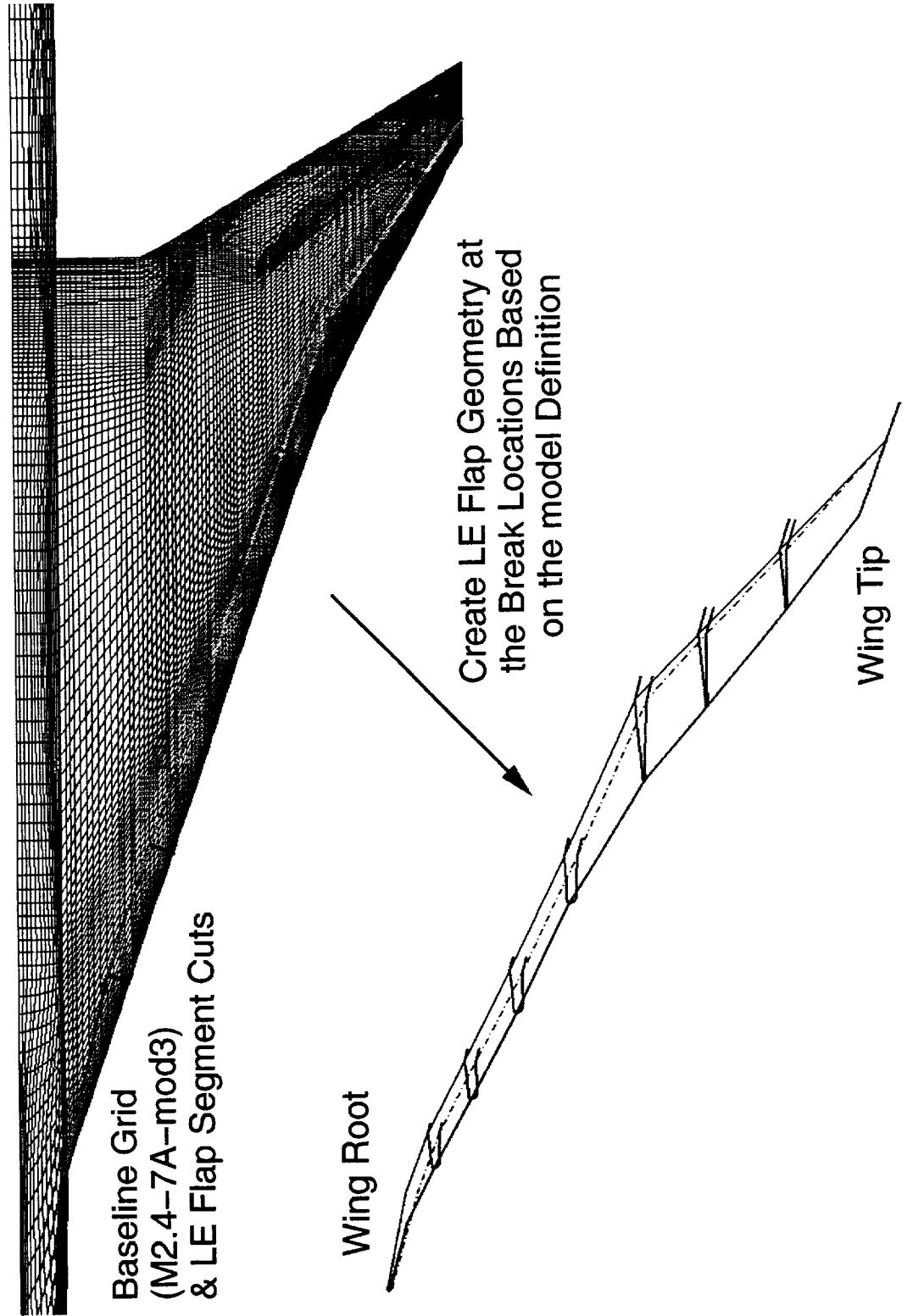
LE Flap Modification

Once an isolated LE flap geometry is generated, this geometry can easily be modified for various LE radii or shapes. The numerical LE flap geometry can be described as interchangeable model parts that often used in the wind-tunnel testing.

LE Geometry Modification Using Flap Segment Definition

Modified LE

Original LE

- Modify the LE Geometry Directly From the Model Definition

- Utilize the New Goemtry for CFD Analysis

- Provide New LE Geometry for Construction of Future Models
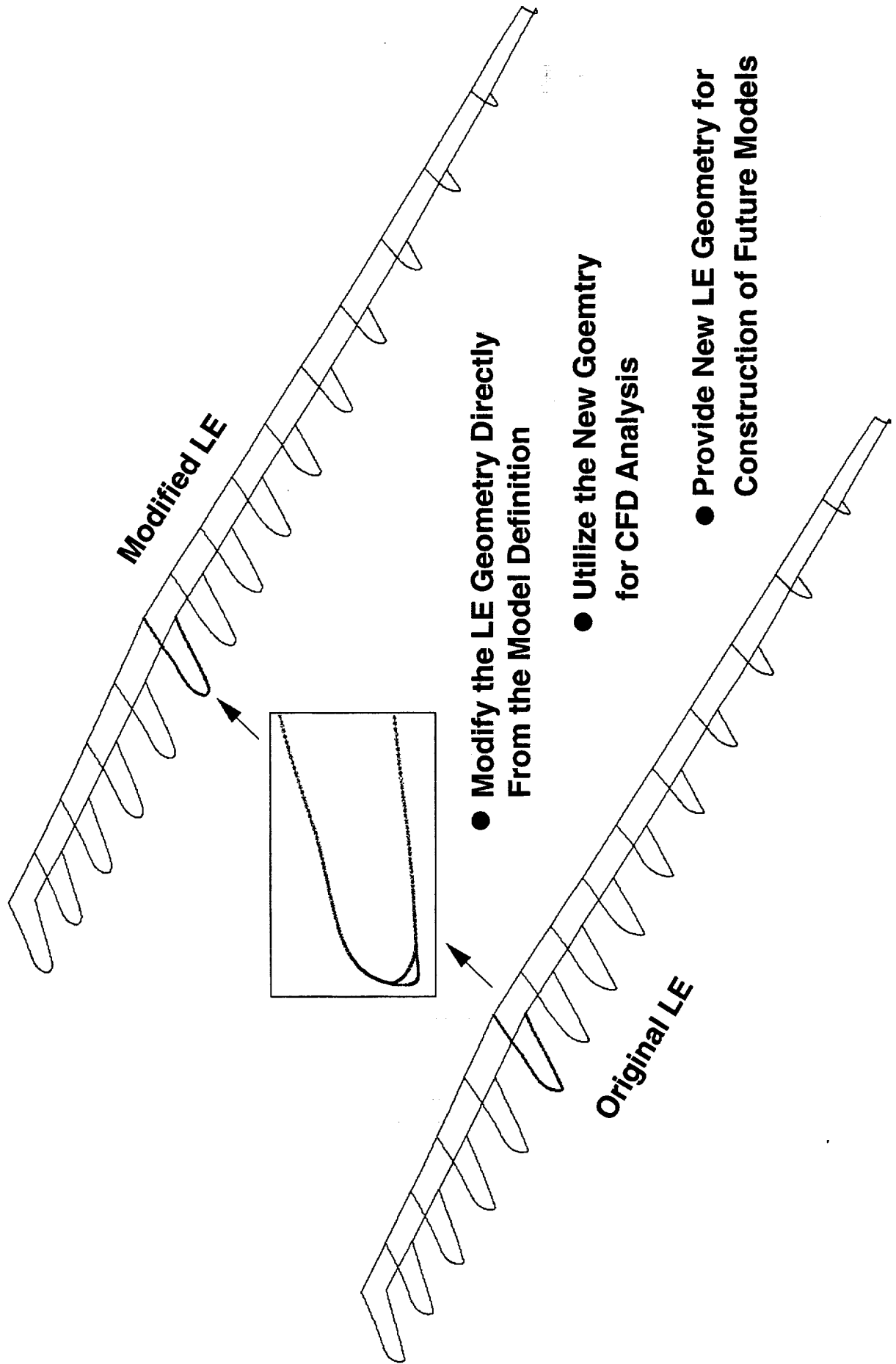
Variable LE Flap Chord

Variable LE flap chord can be easily modeled through the expansion or contraction of the flap segment cuts. These new cuts will then be utilized for generating the LE flap geometry as described earlier. Since the flap breaks are approximately normal to the LE, the resultant flap-to-wing chord ratio in the streamwise direction may not be the same as the specified ratio along the flap breaks depending on the LE sweep angle.

Numerical Procedure for Modeling Variable LE Flap Chord

Original LE Flap Segments

Extend Flap Chord

Streamwise Cut

TE

$C_{flap}\big|_{Baseline}$

$Frac \times C_{flap}\big|_{Baseline}$

LE

2185
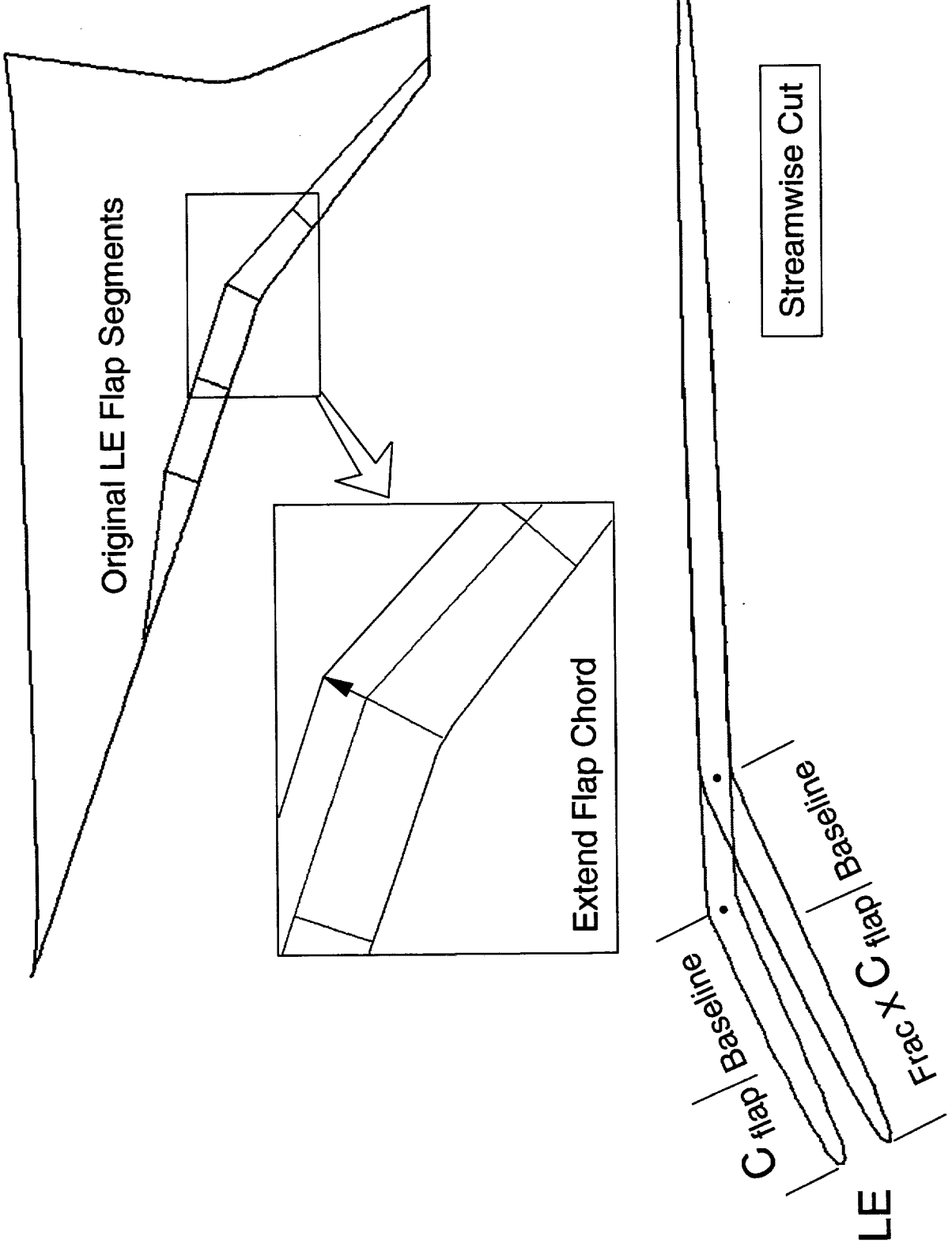
Flap Deflection

The flap deflection is performed by rotating each of the flap segment about an user specified hinge-line axis(two points). The rigid body rotation is performed in the three-dimensional space so that it is not limited to the hinge line sweep angle. Once the rotation is completed, a cubic spline fit is used to smooth out the upper surface while a linear interpolation is performed for the lower surface. The lower surface near the hinge line region is often over hung by the wing box unless the rotational axis is located exactly on the lower surface.

Flap Segment Deflection and Geometry Modeling
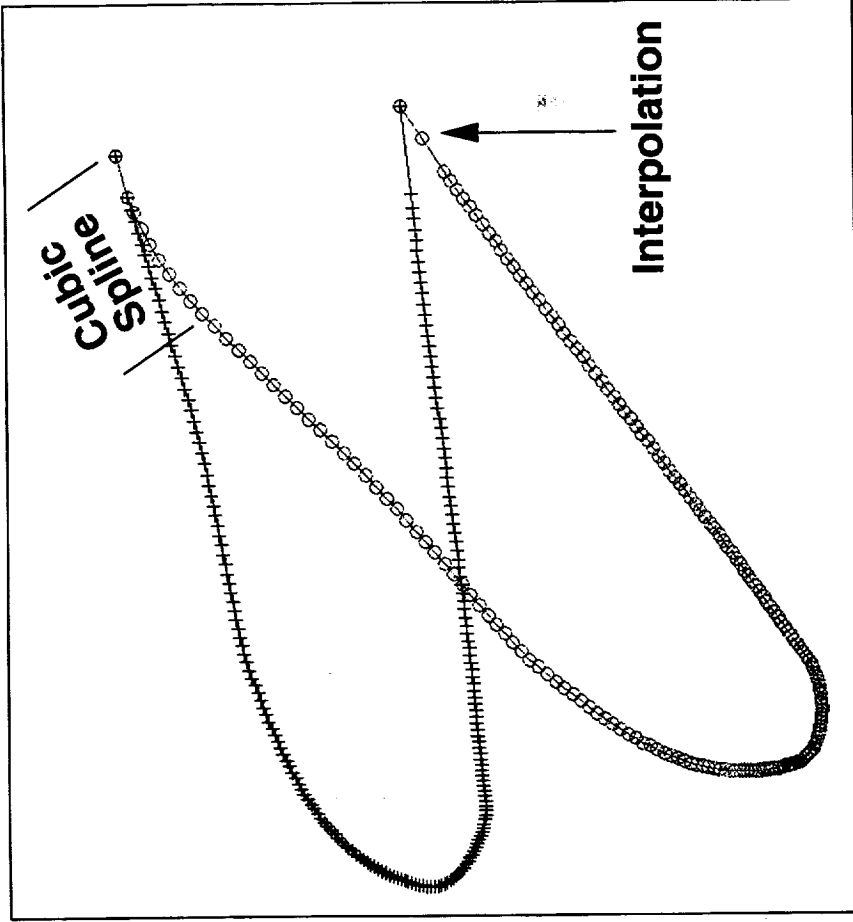
● **Flap rotation about the hinge axis**

● **Surface Smoothing**
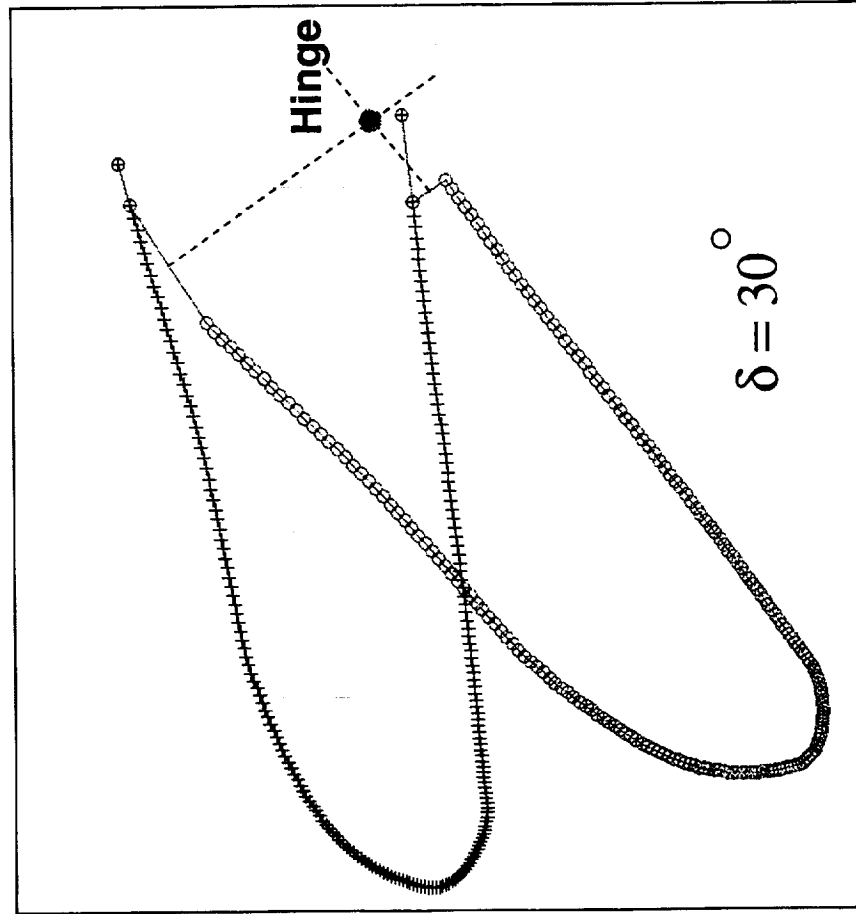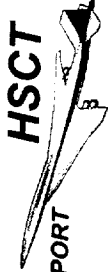
Surface Mapping

Once the flap deflection is completed, the baseline surface grid located upstream of the hinge lines will be mapped onto the new flap geometry. In order to avoid the surface grid clustering to a point near the inboard triangular (tapered) flap element, the grid distribution is relaxed to the original grid in a specified inboard region. The grid distribution in the TE region is retained to maintain the TE flap edge definitions. It is interesting to note that double deflection angles may occur for the streamwise cut that cuts through multiple flap segments with different hinge-line sweep angles.

M2.4-7A-Mod3 Surface Grid with Leading-Edge Flap Deflection

Relaxed to the original grid

Double deflections – Streamwise cut of the flap segments with different hinge line sweep angles

Retain the original grid distribution for trailing-edge flap definition

2189
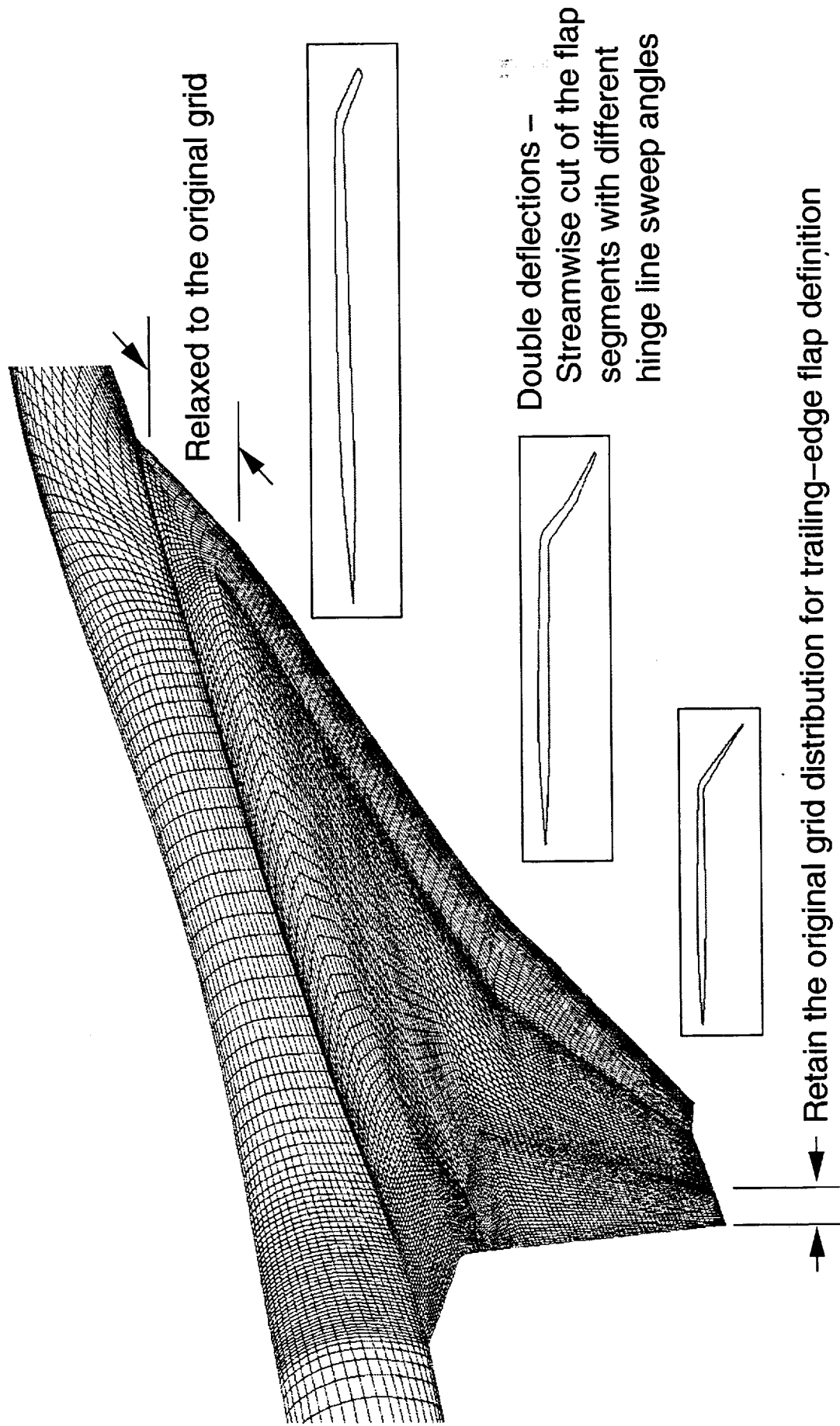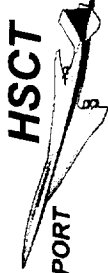
Volume Grid Modification

The baseline volume grid is modified to account for the modified surface grid on the deflected LE flap. The volume grid modification is performed through a linear combination of translation based on the surface grid displacement and rotation based on the streamwise deflection angle. The grid perturbation is controlled by a decay function that gradually relaxes the grid to the original distribution in the far field. A chordwise weighting factor controls the amount of the rotation to avoid grid crossover near the lower hinge line region.

Volume Grid Modification Procedure for LE Flap Deflections

Relaxed to the original grid

$\overrightarrow{ds}_{i,j} = \{0\}$

Original Grid Line

$\overrightarrow{ds}_{i,j} = \{0\}$

Modified Grid Line

θ
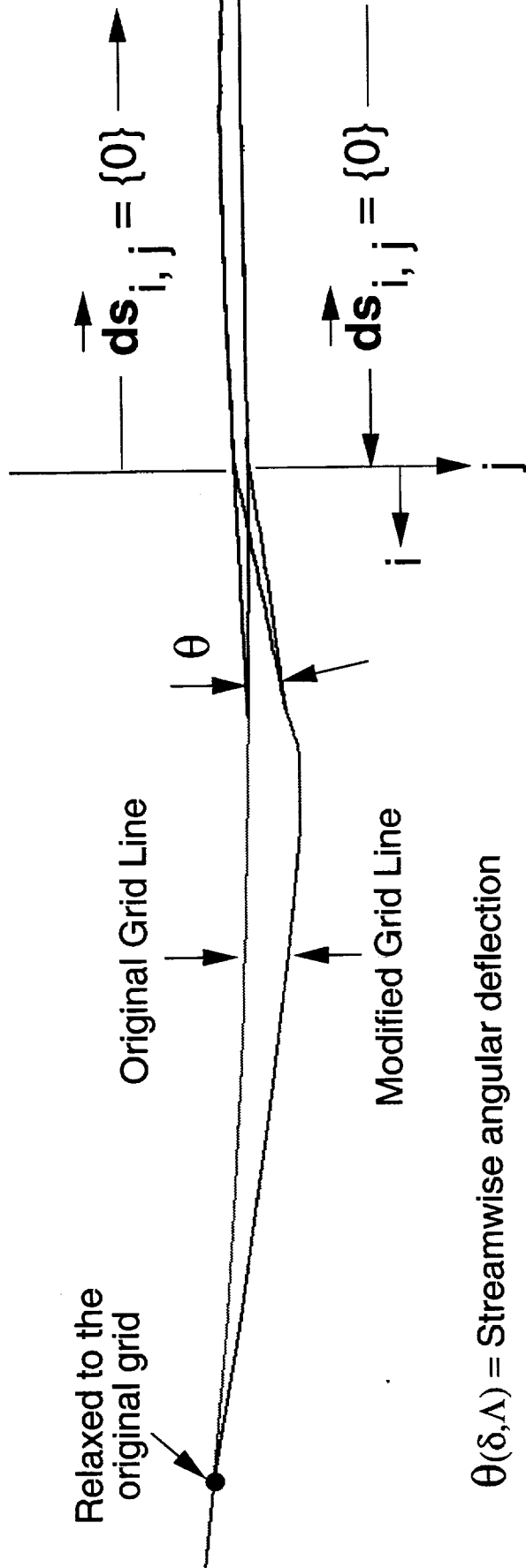
$\theta(\delta, \Lambda)$ = Streamwise angular deflection
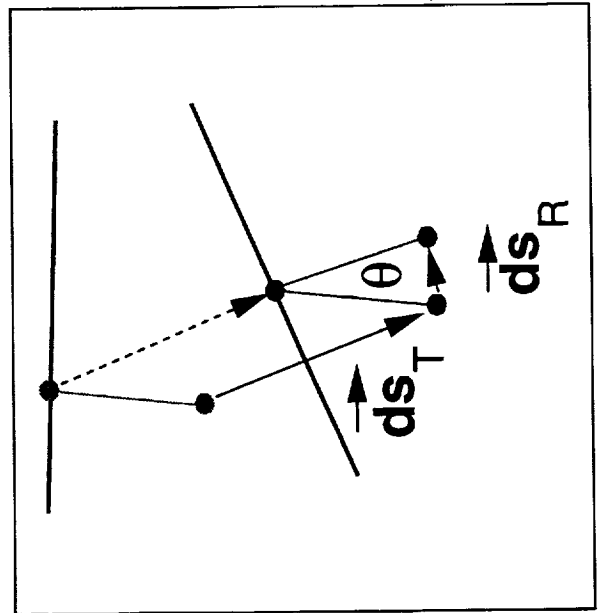
$$\overrightarrow{ds} = (\overrightarrow{ds}_T + \overrightarrow{ds}_R * W_i) * F(l)$$

Translation · Rotation

W_i = Chordwise Weighting Factor

$F(l)$ = Field Decay Function

$\overrightarrow{ds}_R$

$\overrightarrow{ds}_T$

θ

Modified Volume Grid

This figure shows the modified field grid in the streamwise direction. In the inboard region, the field grid has been 'pulled' toward the LE due to two factors. One factor is that the same number of grid points are placed in the most part of the LE flap except near the inboard region. The second factor is due to the decrease in flap-to-wing chord ratio. As a result, more grid points are placed near the LE as compared to the original grid.

It is interesting to note that the surface grid shown for the mid-section consists of a double angular deflection. This is a direct result of a streamwise cut that cuts through 2 flap segments with different hinge-line sweep angles.

Typical Cross-Sectional Grid for the M2.4–7A Mod3 Configuration with Leading–Edge Flap Deflection ($\delta=40°$)
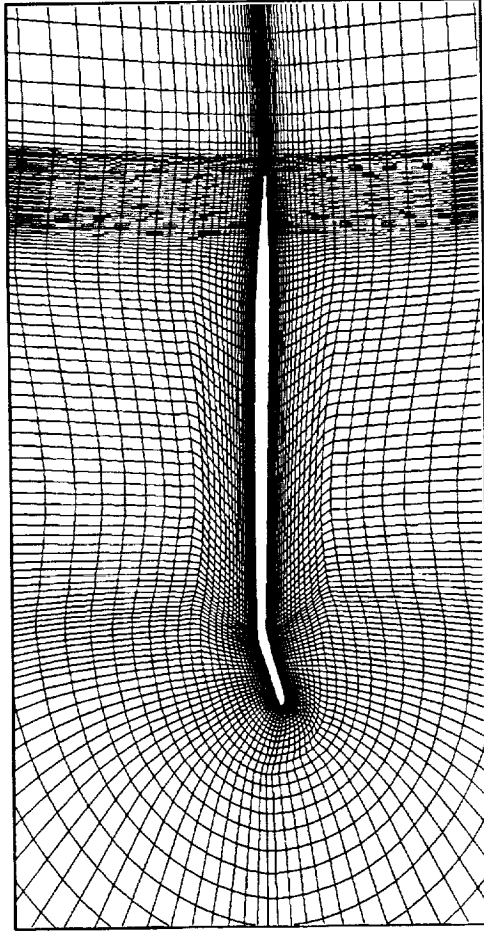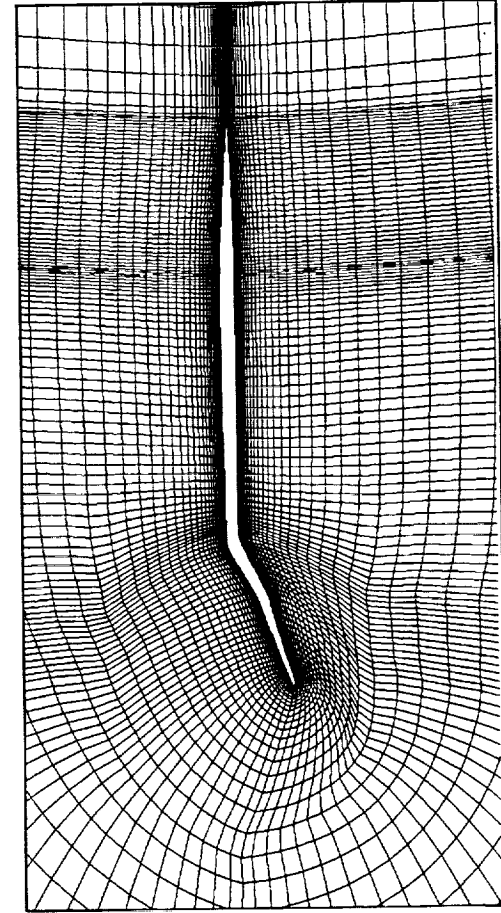
- Inboard Region
- Mid–Section
- Outboard Region
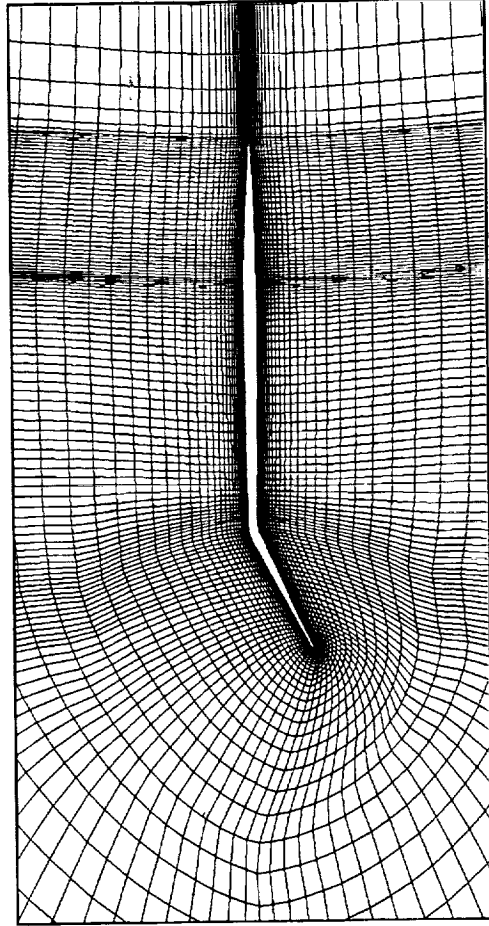
TE Flap Deflections

The following next few charts will be focused on the grid modification techniques that are used for the TE flap deflections.

TE Flap Deflection Procedure

TE Flap Deflection Overview

A grid modification procedure for modeling the TE flap deflections has been developed. This chart illustrates the overview of the regridding process. This procedure consists of 6 computer codes that are used sequentially to modify a baseline volume grid through grid revision techniques. These techniques consist of blocking and regional regridding near the flap region; spanwise wing/flap gap modeling; rigid-body-rotation about user specified axes; volume grid perturbation; upper surface smoothing and lower surface interpolation near the hinge line; and grid clustering for viscous calculations.

Automated Grid Modification Process for TE Flap Deflections

3. Flap Rotate

$V_3 = V_1 \times V_2$

$V_2 = V_1 \times Z$

V_1 = hinge axis

4. Grid modification

S_n

S_1

$S_n = S_1 \cdot fac$

δ

2. Gap modeling

Wing

Flap

Wing/flap

①

Wing

Flap

Gap

②

5. Surface smoothing

J−2 J−1

J+1 J+2

Cubic Spline

Original
Fitted

Interpolation

1. Blocking / Regridding
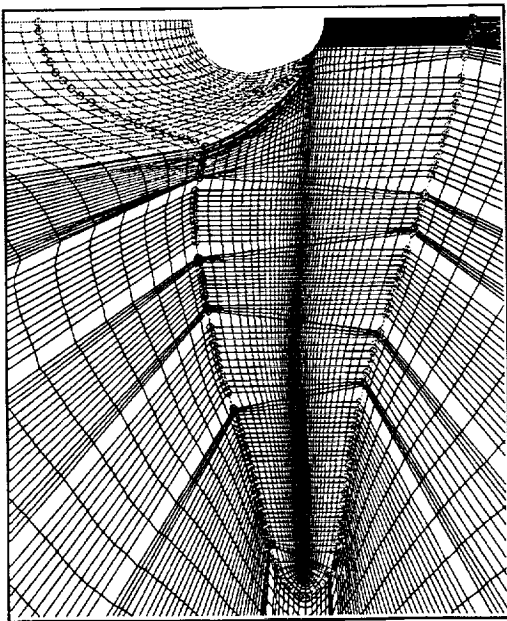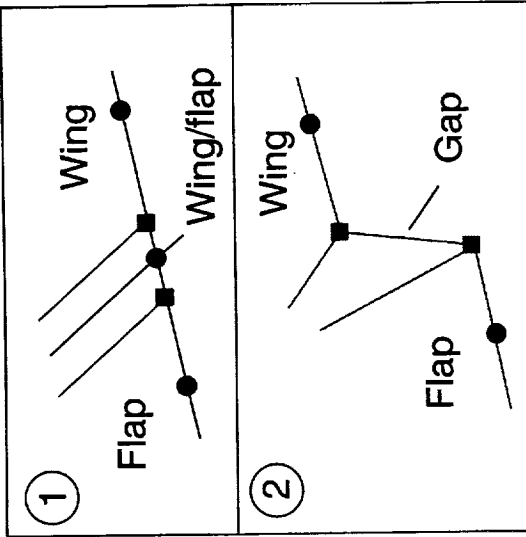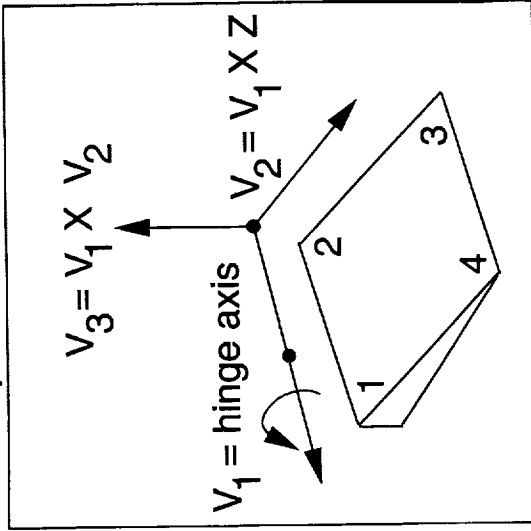
6. Grid Clustering
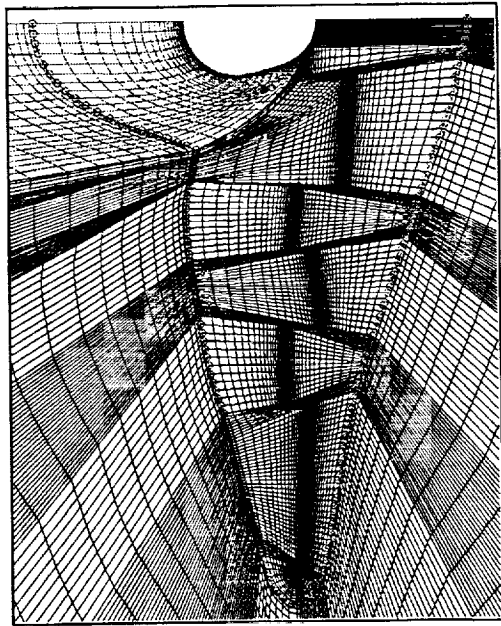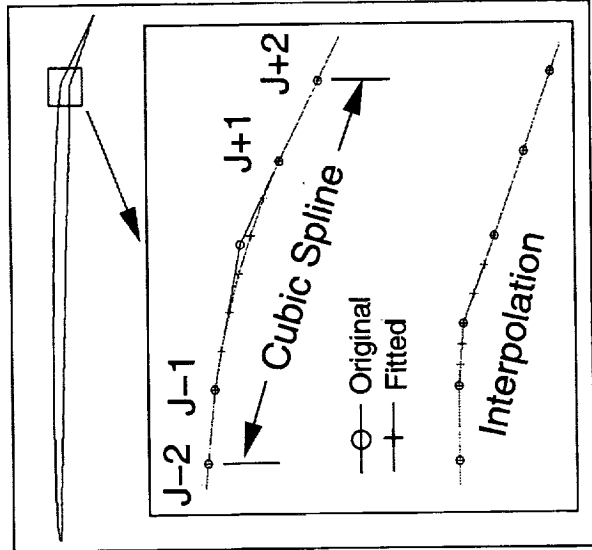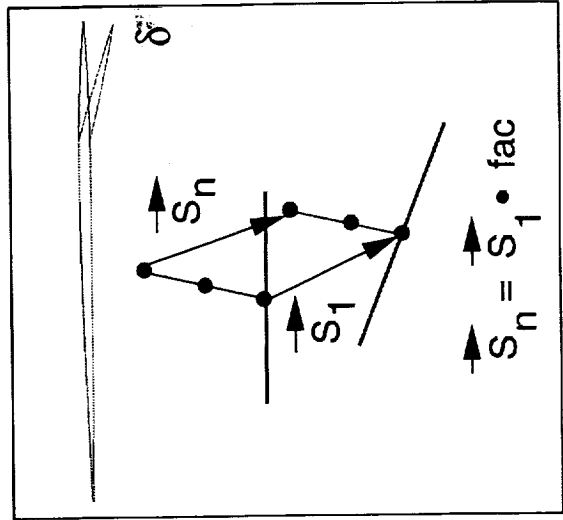
Baseline grid

A typical HSCT baseline grid generated at MDC consists of a single-zone with an C-type topology in the chordwise direction and an O-type topology in the spanwise direction. Due to the nature of the C-O grid topology, TE flap deflection always cause the grid lines to cross with one another. To easily model multiple TE flap deflections, it is desirable to have the grid lines that extend vertically well beyond the downward flap displacement before turning outboard.

Baseline Grid Modification for Modeling TE Flap Deflections

Baseline Surface Grid (M2.4-7A)
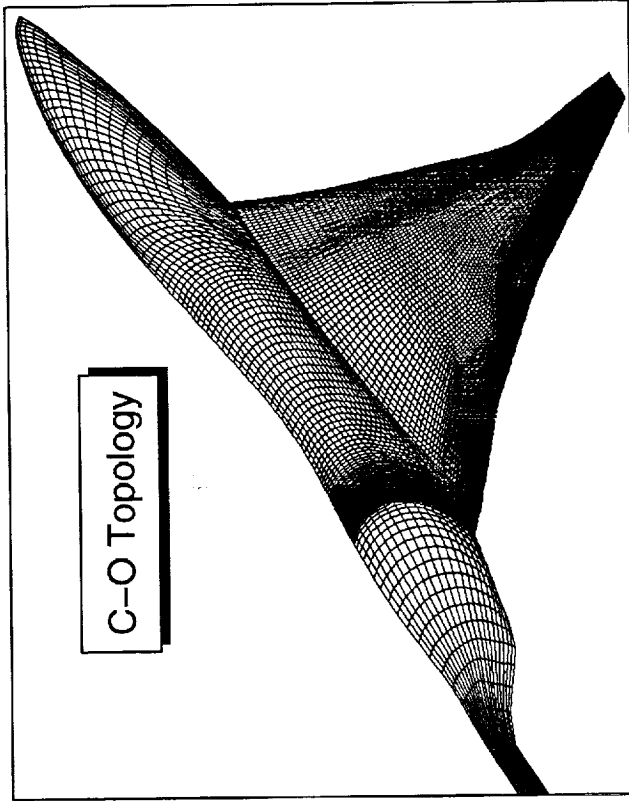
C-O Topology

Baseline Cross Sectional Grid

at TE

Flap

Flap

Flap

TE Flap Modeling $\longrightarrow$ Regional Regridding is Needed to Avoid Grid-Line Crossing

Blocking and Regridding

A regional blocking strategy was developed to provide a better control of the grid orientation as illustrated in the figure. A spanwise reference curve is first identified which divides the inner and outer regions. The K=20 grid line curve was arbitrarily chosen which is far enough to model the flap deflection angle up to 40 degrees. Once the boundary is defined, the inner region is subdivided into 14 blocks for 3 TE flap surfaces, to guide the orientation of the grid lines. The block edges are defined such that the grid lines will not cut through the corners (i.e. flap corners). Because the wing is located at the lower half of the fuselage, the grid generation for the upper fuselage requires more than a simple algebraic approach. Therefore, the grid distribution in the region between the upper centerline and the fuselage/wing junction is retained from the baseline grid.

The regional blocking and regridding are used only near the TE flap region. The final volume grid is constructed by a linear combination of the baseline grid and the modified grid so that the flap region will be fully modified while the original baseline grid will gradually prevail in the region away from the flap for smooth transition.

Regional Blocking and Regridding for Modeling
Trailing–Edge Flap Deflections

2201

Flap Rotation

Once the TE flap is separated from the wing with the spanwise gaps, the flap deflection is performed by rotating the flap surface about the user-defined hinge-line axis (two points). All the TE flap surfaces can be rotated independently at different angular deflection.

Surface Grid Modification for Modeling Multiple Deflected TE Flaps

- Flap Deflection About an Arbitary Hinge Line

- Modified Surface Grid with Deflected Trailing-Edge Flaps

$V_3 = V_1 \times V_2$

$V_2 = V_1 \times +Z$

$V_1 = $ Hinge Line

2
3
4
1

Inboard Flap

Middle Flap

Outboard Flaps

2203
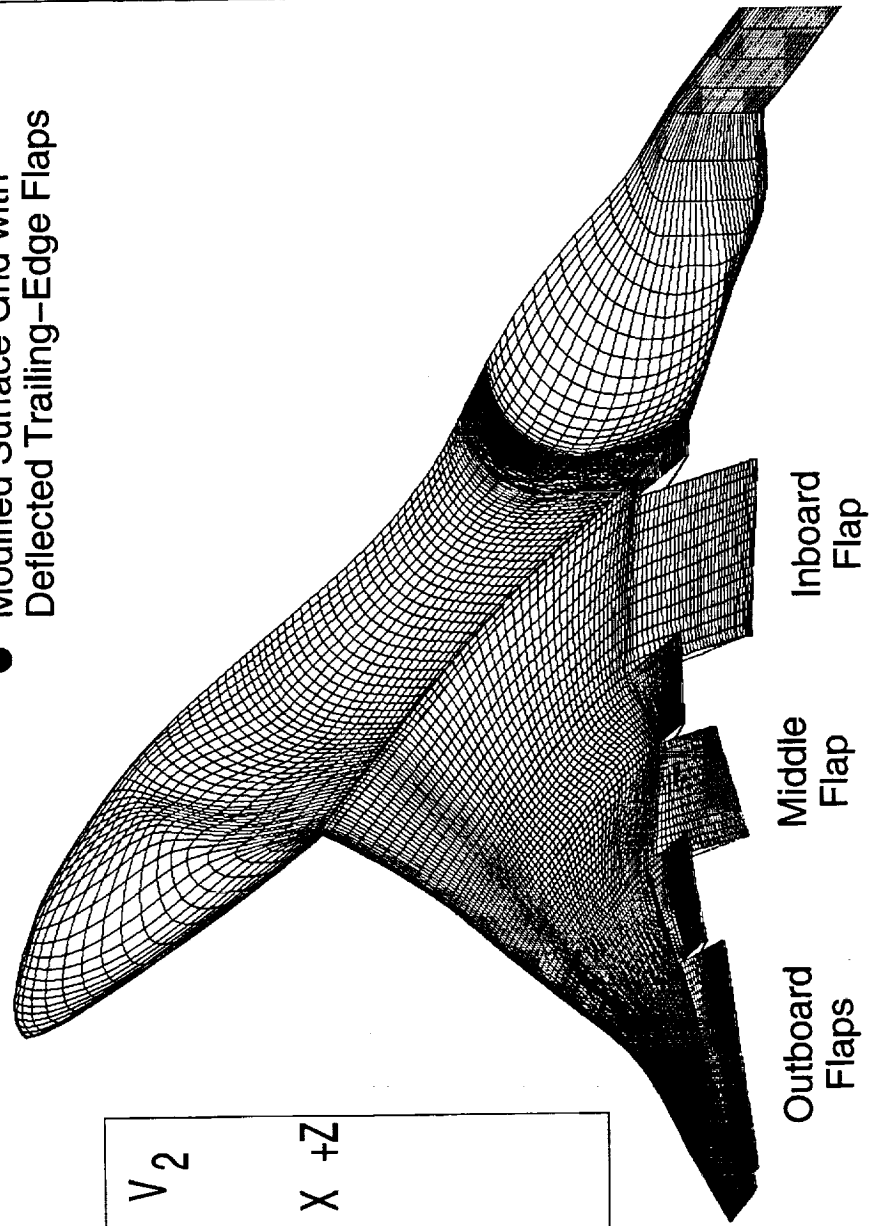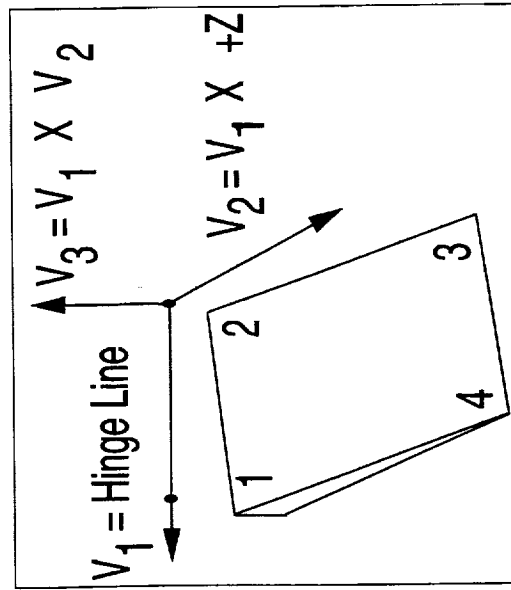
Surface Smoothing

To model a smooth upper surface near the TE hinge line, a cubic spline fit was performed on the upper surface. The fitted curve was defined by the 4 points located forward and backward of the first chordwise point on the flap surface as shown in the figure. Using the spline fit, by definition, will provide a continuous slope variation across the wing and flap surfaces. The number of the additional nodes used to define the upper surface can be specified by the user which are placed on the fitted curve for smooth transition. A simple interpolation was performed for the lower surface which is representative of a sharp corner of the actual test model.

Surface Modeling Near the Hinge Line of a Deflected TE Flap

Original
Fitted

Cubic Spline

J-2
J-1
J
J+1
J+2

Added New Points

δ

Interpolated New Points

Trailing-Edge Flap

2205
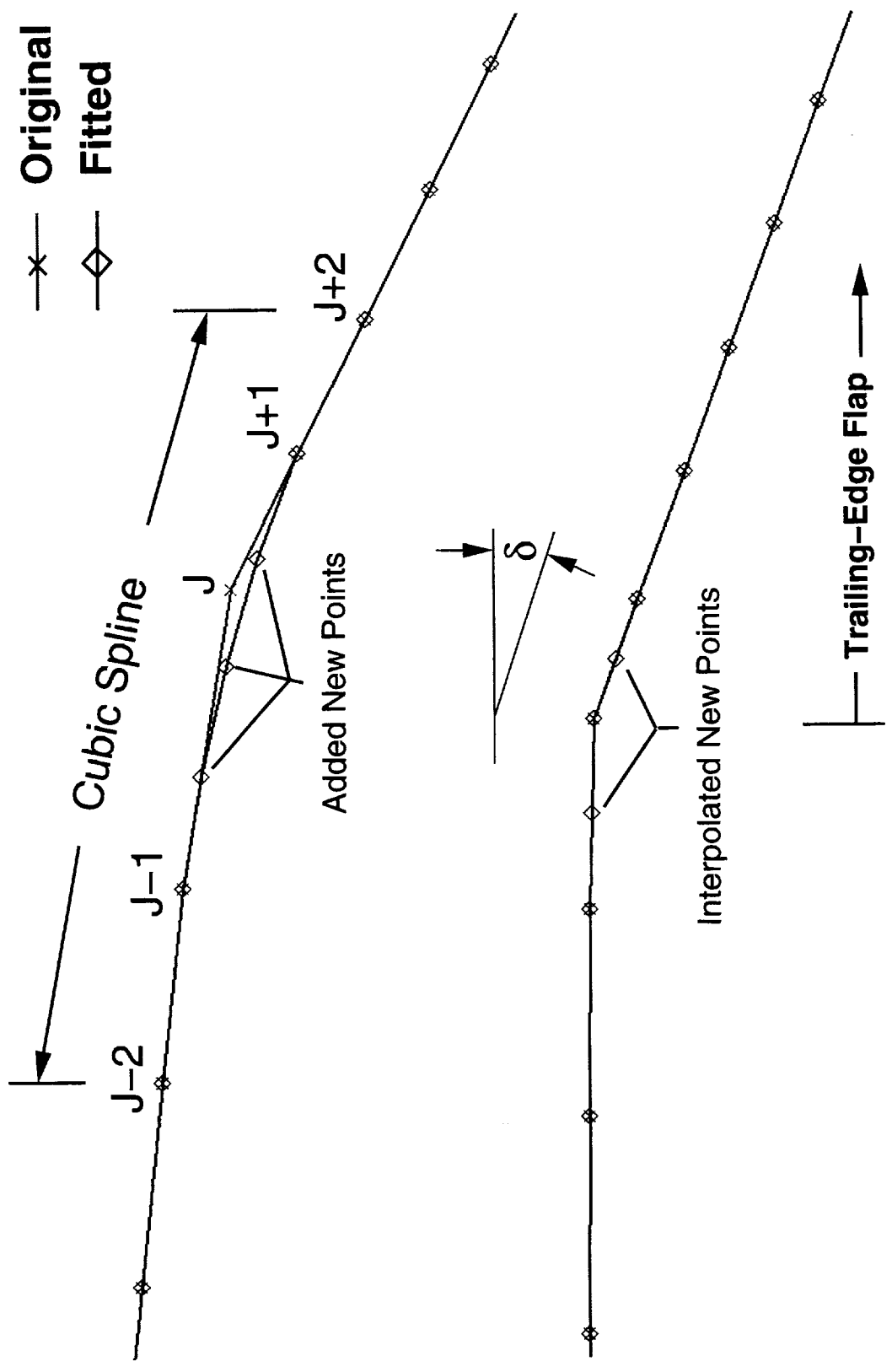
Grid Clustering

This figure shows the modified viscous grid at the TE station with deflected flaps. An exponential stretching was performed for both the inner and the outer regions. The minimum spacing for the outer region was chosen to be the minimum of the outermost cells in the inner region.

Cross Sectional Grid at the Trailing-Edge Station

Grid boundary (Original grid)

$ds_{min} = .002$ in

36 Points

Grid boundary (Original grid)

30 Ponts

Flap

Flap

Flap

2207
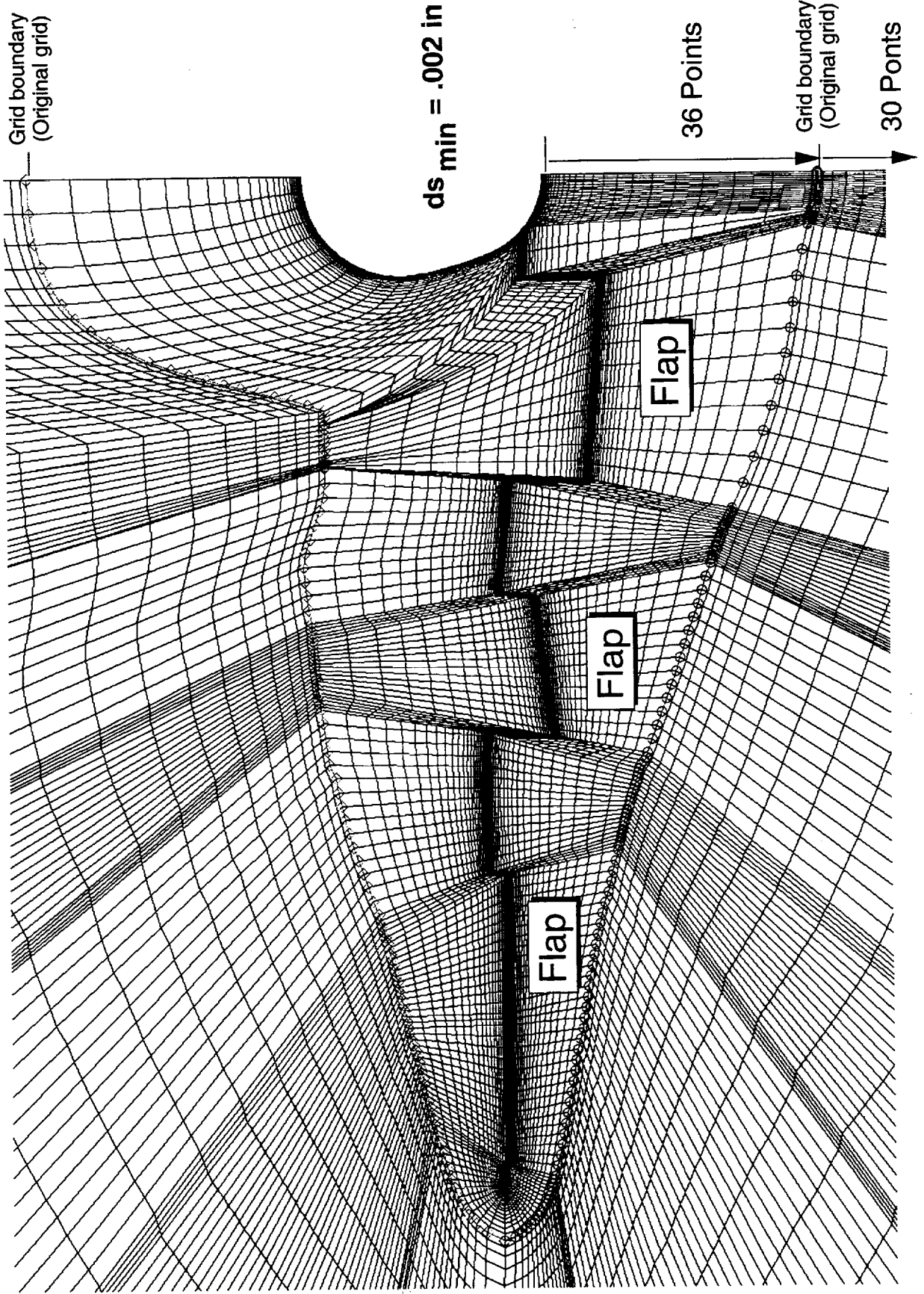
Chordwise Field Grid

The final volume grid is constructed by a linear combination of the baseline grid and the modified grid so that the flap region will be fully modified while the original baseline grid will gradually prevail in the region away from the flap. The wake region is also modified based on the flap TE locations and is gradually relaxed to the original grid locations at the downstream boundary.

Chordwise Grid Distribution with Trailing-Edge Flap Deflections

Inner & Outer Zonal Boundary

Modified Wake Region for Flap Deflections
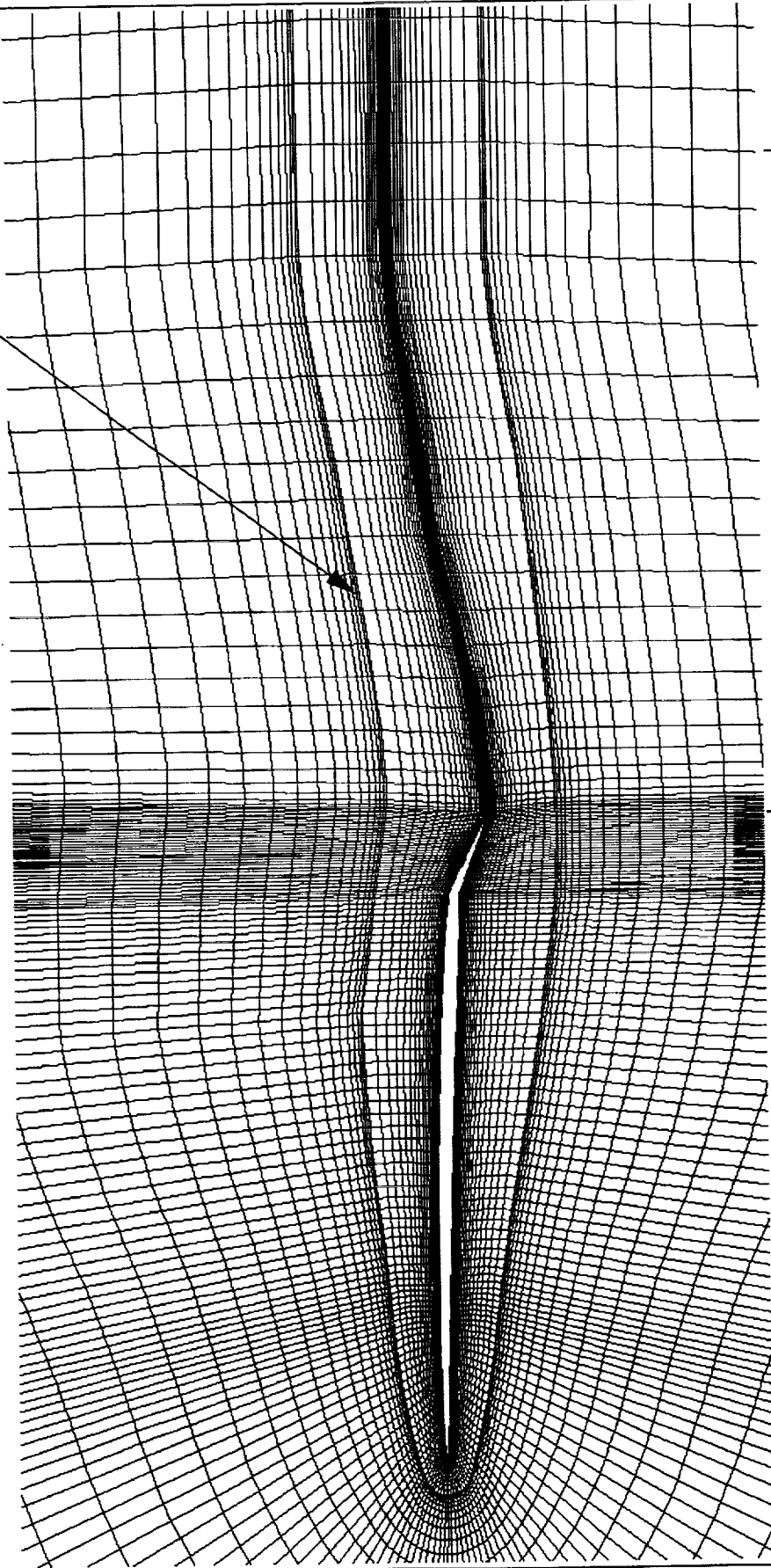
Modified Wing Region for Flap Deflections

2209

Spanwise Gap Modeling

The spanwise gaps across the wing and flap surfaces are modeled by stretching the gap grids as shown in the figure. Numerical simulation of the flap deflections and gap regions are accomplished through interpolation of the flow solutions across the gap grids where the flow information is propagated between the upper and lower surfaces.

The spanwise total pressure contours at the TE station is shown in the figure, which indicates the total pressure loss across the boundary layer and shear layers in the subsonic flows. It illustrates the continuity of the solution across the gap interface boundary.

Spanwise Gap Modeling for Trailing-Edge Flap Deflections

- Spanwise gaps across the wing and flap surfaces are modeled by stretching the gap grids
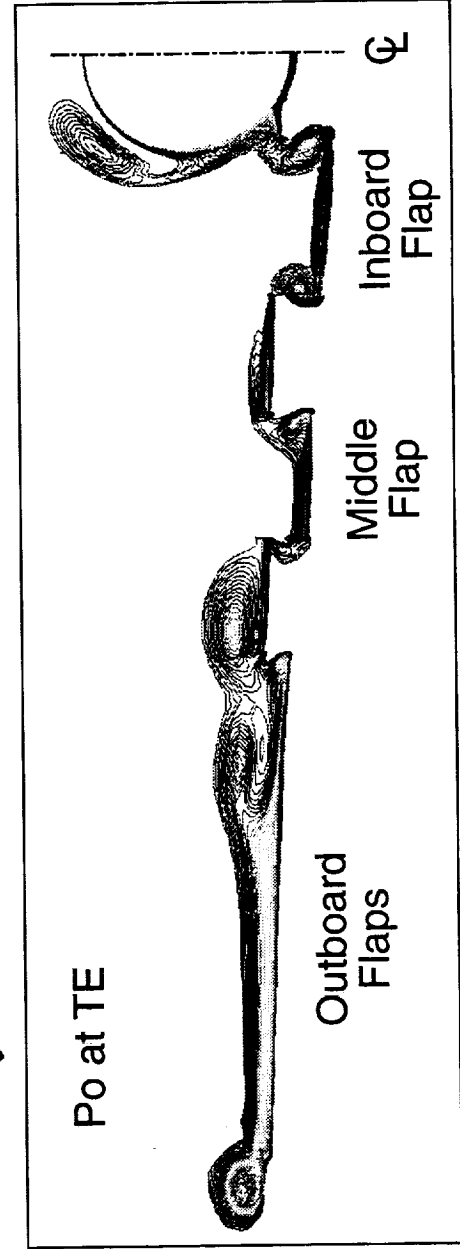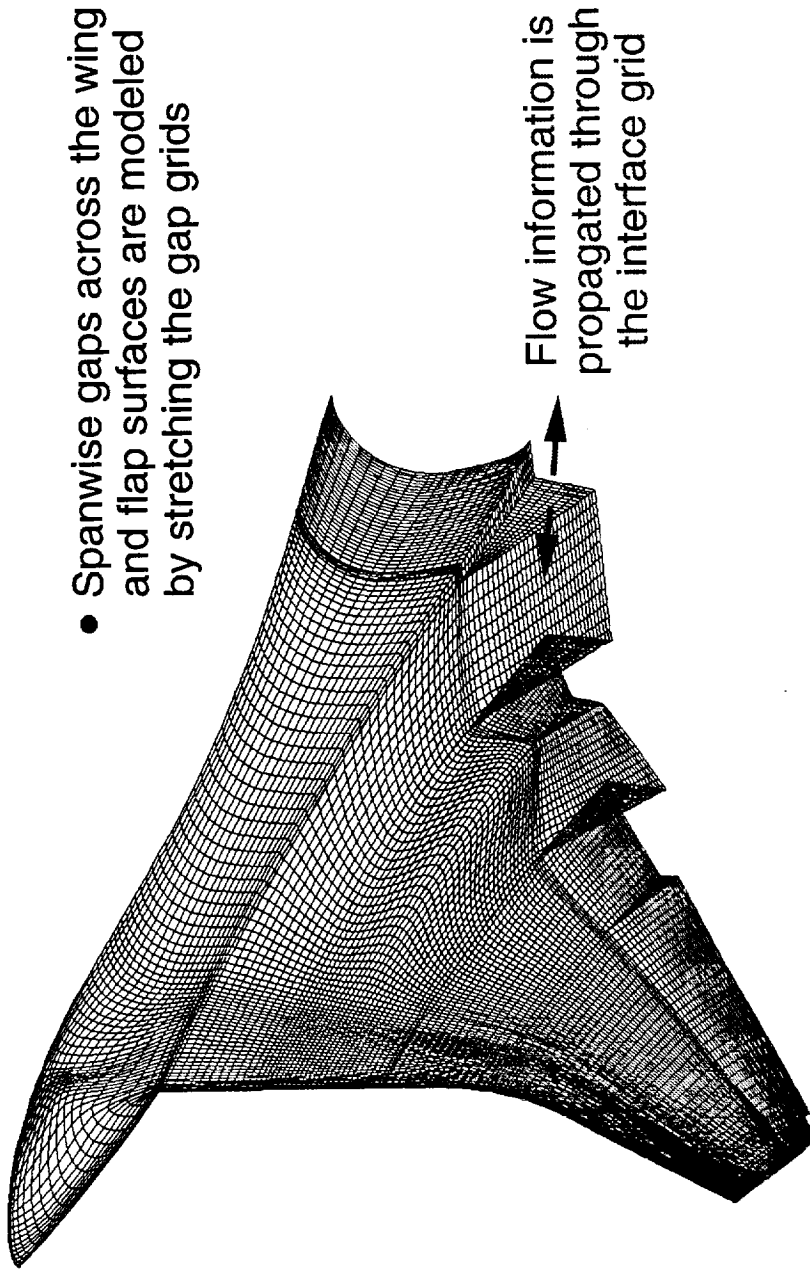
Flow information is propagated through the interface grid

Po at TE

Outboard Flaps

Middle Flap

Inboard Flap

$\mathcal{C}_L$

TYPICAL COMPUTATIONAL MODEL

A typical grid consist of a single-zone with approximately 3.3 million grid points for a half-body model. The spanwise gaps across the wing and TE flap surfaces are modeled through 'web grids' where flow interface is imposed. The number of grid points in each direction and subregion are arranged such that 3-level of multigrid option can be specified for convergence expedience.

Typical HSCT High–Lift Computational Model

- Single Zone Consists of 3.3 Million Grid Points for the Half–Body (305X65X169) : (Chordwise X Radial X Spanwise)

- C–O Grid Topology (C : Chordwise; O–Spanwise)

- Spanwise Gaps are Modeled through 'Web Grid' for Flow Interface

- Grids are Generated for 3–Level of Multigrid Calculation for Each Sub–Region (Fuselage, Wing, Flap, Gaps *etc.*)
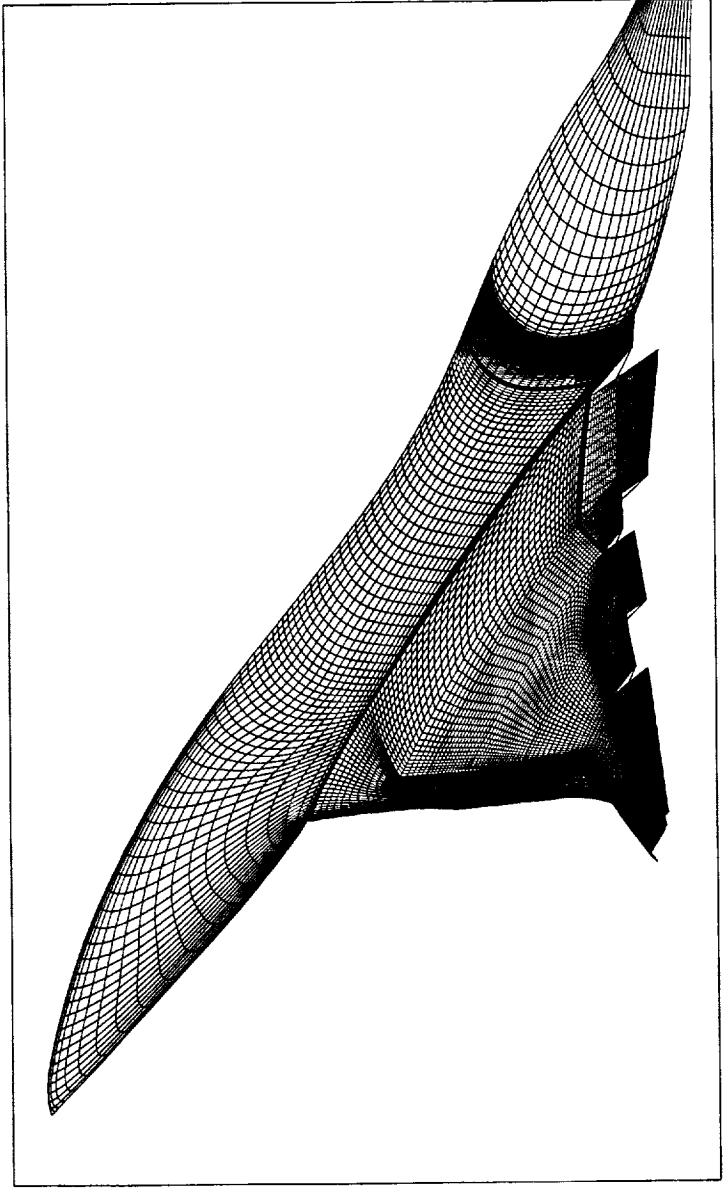
Sample CFL3D Solutions

Sample CFL3D solutions will be presented using the modified grids generated by the automated flap deflection procedures. The numerical results consist of the M2.4-7A Opt2A, M2.4-7A Mod3 and the TCA configuration with a part span LE flap.

Sample CFL3D Solutions

M2.4-7A Opt2A-Effects of TE Flaps-Upper Surface

This chart shows the upper surface pressure of the M2.4-7A Opt2A configuration at M=0.3, alpha=10 for 2 TE flap deflections (10, 20 deg). These solutions were obtained using the Baldwin-Lomax turbulence model with Degani-Schiff modification.

Similar vortex induced low pressure regions and corresponding locations are observed for both cases at a constant angle-of-attack. A lower pressure near the hinge line is clearly visible at a higher flap deflection angle (20) case. As the flap-to-wing chord ratio increases near the wing tip, the influence of the TE flap deflection on the upstream increases as indicated by the lower pressure near the outboard LE.

Predicted Surface Pressure for the M2.4–7A Opt2A Configuration at M = 0.3, α = 10 degrees, Re=8 million

CFL3D and Baldwin–Lomax Turbulence Model with Degani–Schiff Modification

(a) $\delta_{flap} = 0^\circ/10^\circ$

(b) $\delta_{flap} = 0^\circ/20^\circ$

M2.4-7A Opt2A-Effects of TE Flaps-Lower Surface

Using the same flow solutions shown in the previous chart, this chart shows the lower surface pressure of the M2.4-7A Opt2A configuration at M=0.3, alpha=10 for 2 TE flap deflections (10, 20 deg).

Similar pressure patterns can be seen for both cases except near the hinge lines where a higher pressure is observed for the higher flap deflection case (20 deg). It also shows a stronger flap influence on the lower surface of the wing near the TE flap regions.

Predicted Surface Pressure for the M2.4–7A Opt2A Configuration at M = 0.3, α = 10 degrees, Re=8 million

CFL3D and Baldwin–Lomax Turbulence Model with Degani–Schiff Modification

Cp

≥0.50

0.00

≤-0.50

(a) $\delta_{flap} = 0^{\circ}/10^{\circ}$

(b) $\delta_{flap} = 0^{\circ}/20^{\circ}$
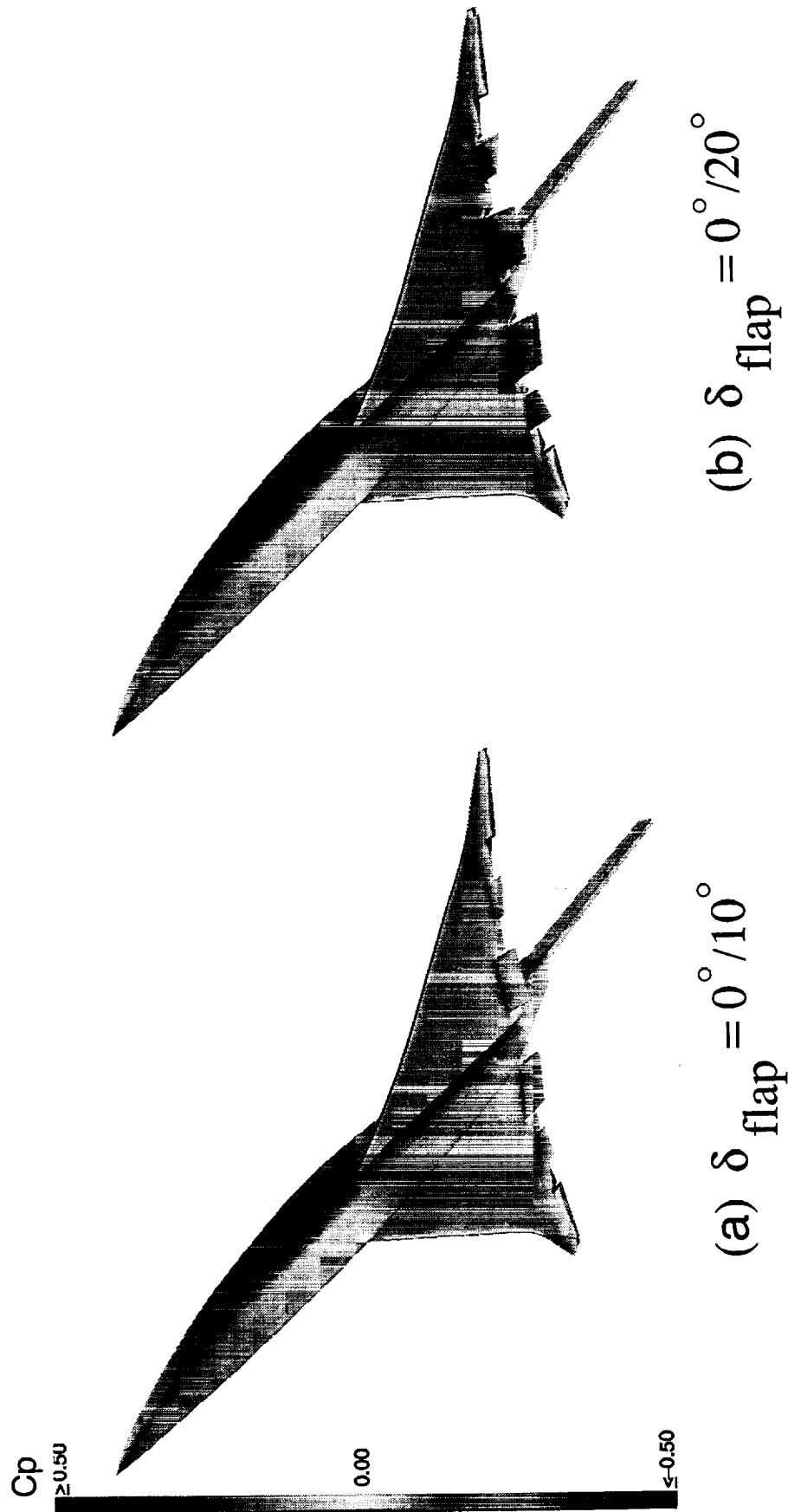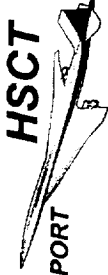
M2.4-7A Opt2A-Force Comparison

The predicted drag polar for the M2.4-7A Opt2A with TE flap deflection of 10 and 20 deg. are compared with the test data. The comparison shows a good agreement both in the linear as well as nonlinear regions.

Comparison of Test Data and CFD Results

LaRC 428 and CFL3D N-S Solution

M2.4-7A Opt2A

HSCT
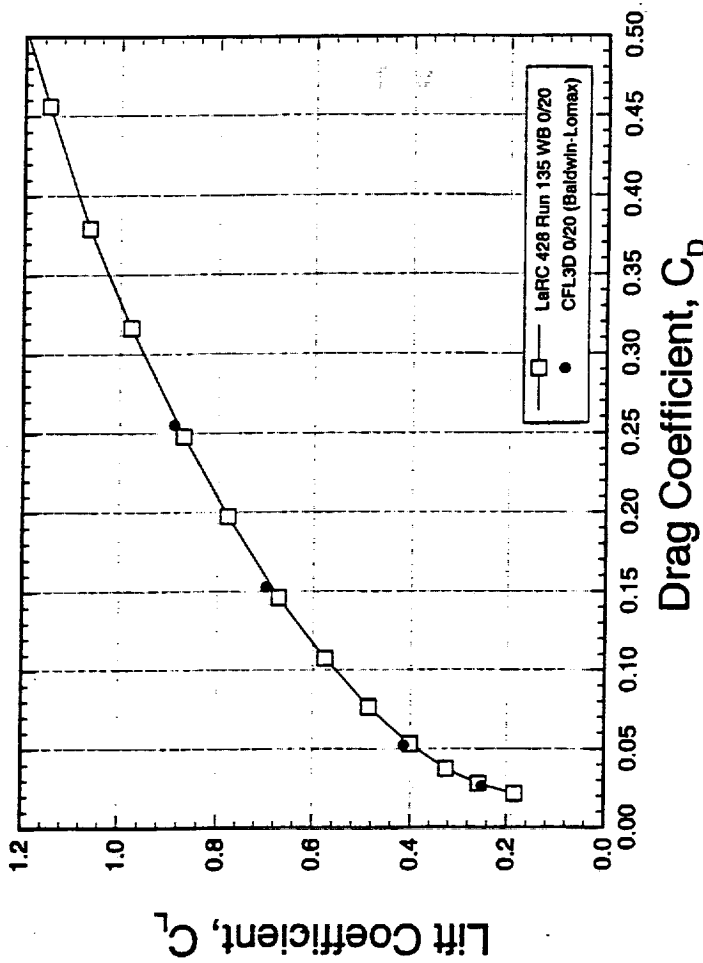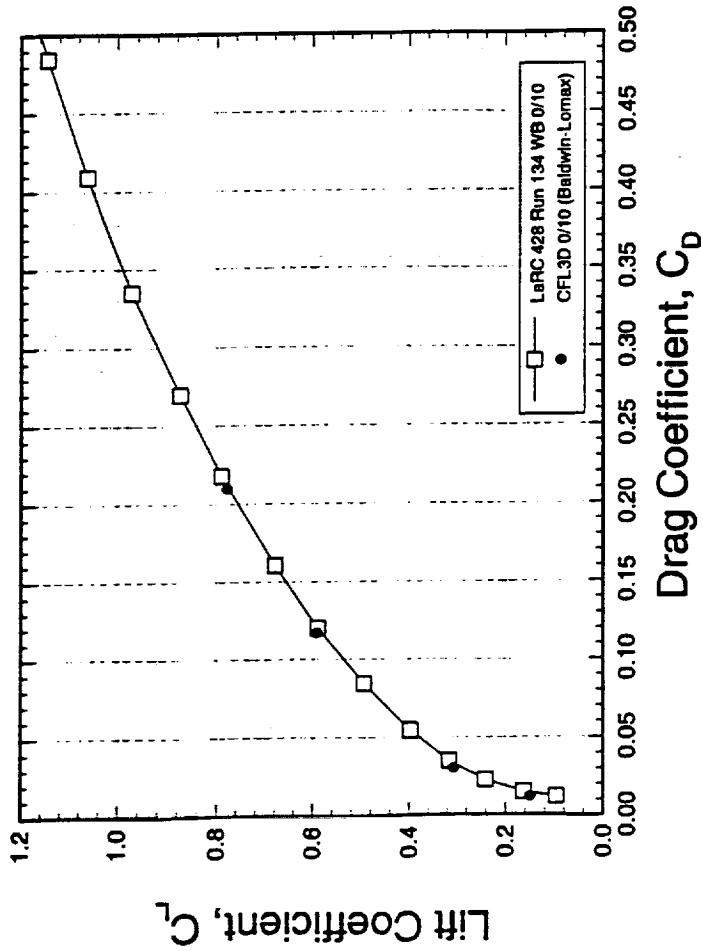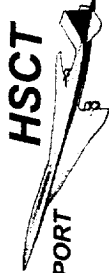
M2.4-7A Mod3 40/10 Configuration

The second configuration in the study is a modified Arrow Wing (M2.4-7A Mod3) with a larger inboard LE radius. Creating a more rounded LE is intended to promote attached flow to maximize L/D at high-lift conditions. This configuration is currently being tested in the 12-ft tunnel at NASA ARC.

Predicted Surface Pressure for the M–2.4–7A Mod–3 Configuration
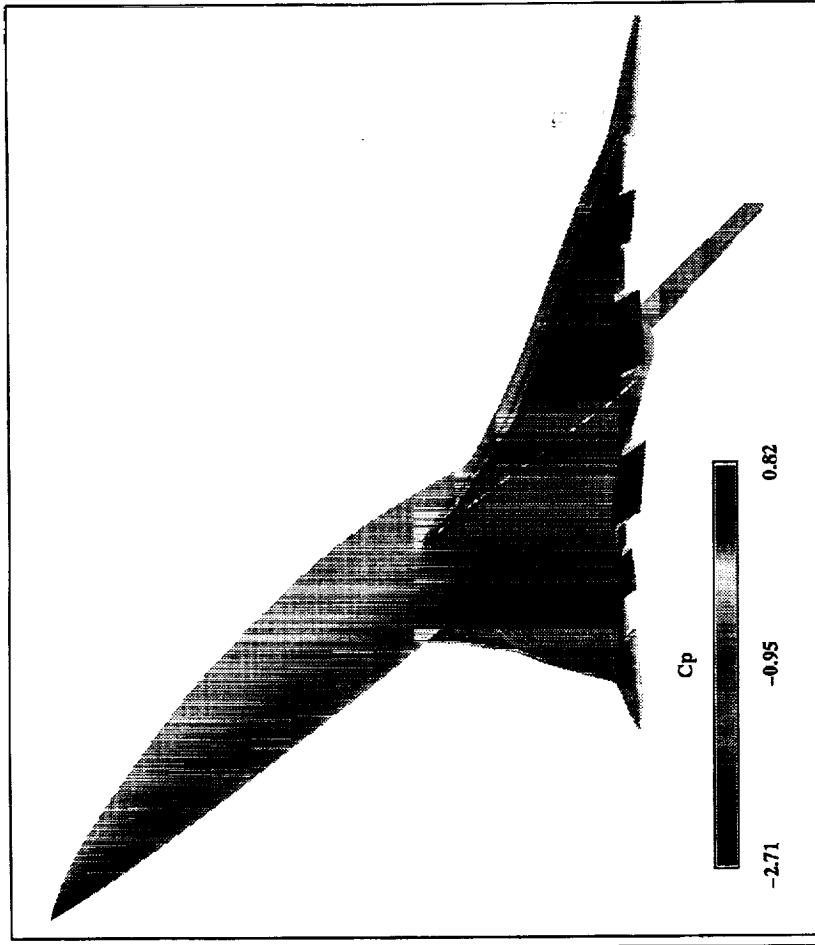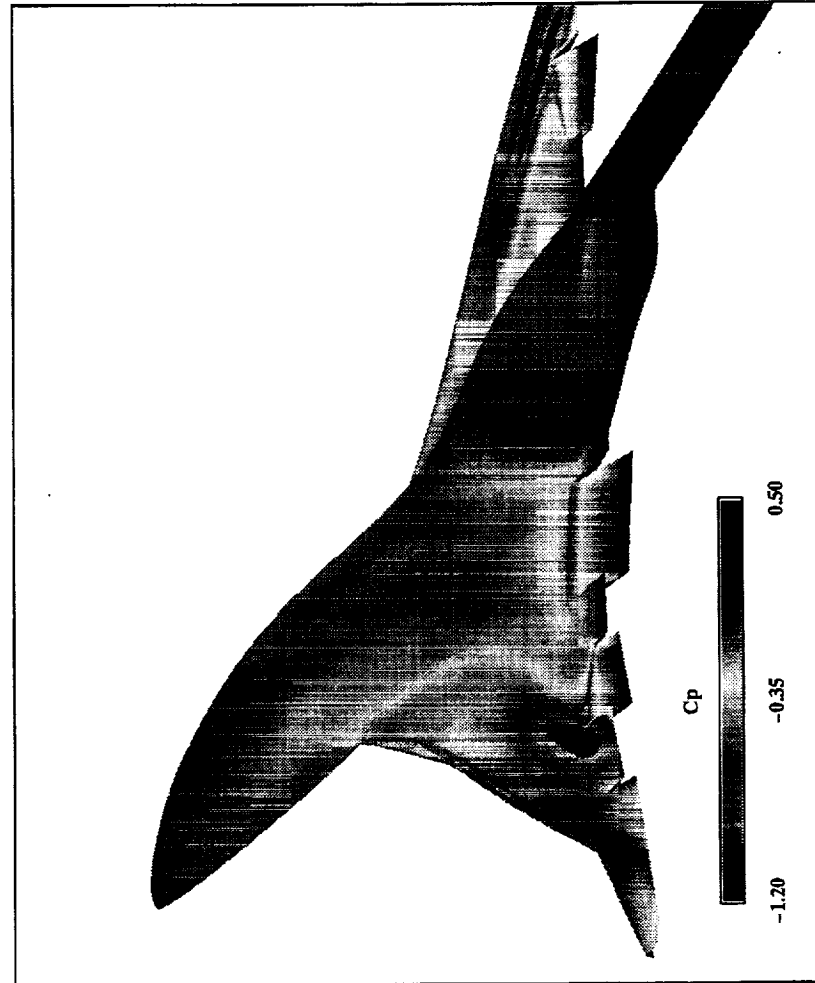
M=0.3, α=10°, δ (LE/TE)=40°/10°

TCA 30/10 Configuration

The technology concept airplane (TCA) model is the current baseline configuration which is the primary focus of the numerical studies. This figure shows the predicted surface pressure for the TCA 30/10 part span LE flap configuration at alpha=10. Currently, the full span LE flap model is being generated.

Predicted Surface Pressure for the TCA Configuration (Part Span)

δ(LE/TE)=30°/10°, M=0.3, α=10°, Re=8 million

Cp

0.50

−0.35

−1.20
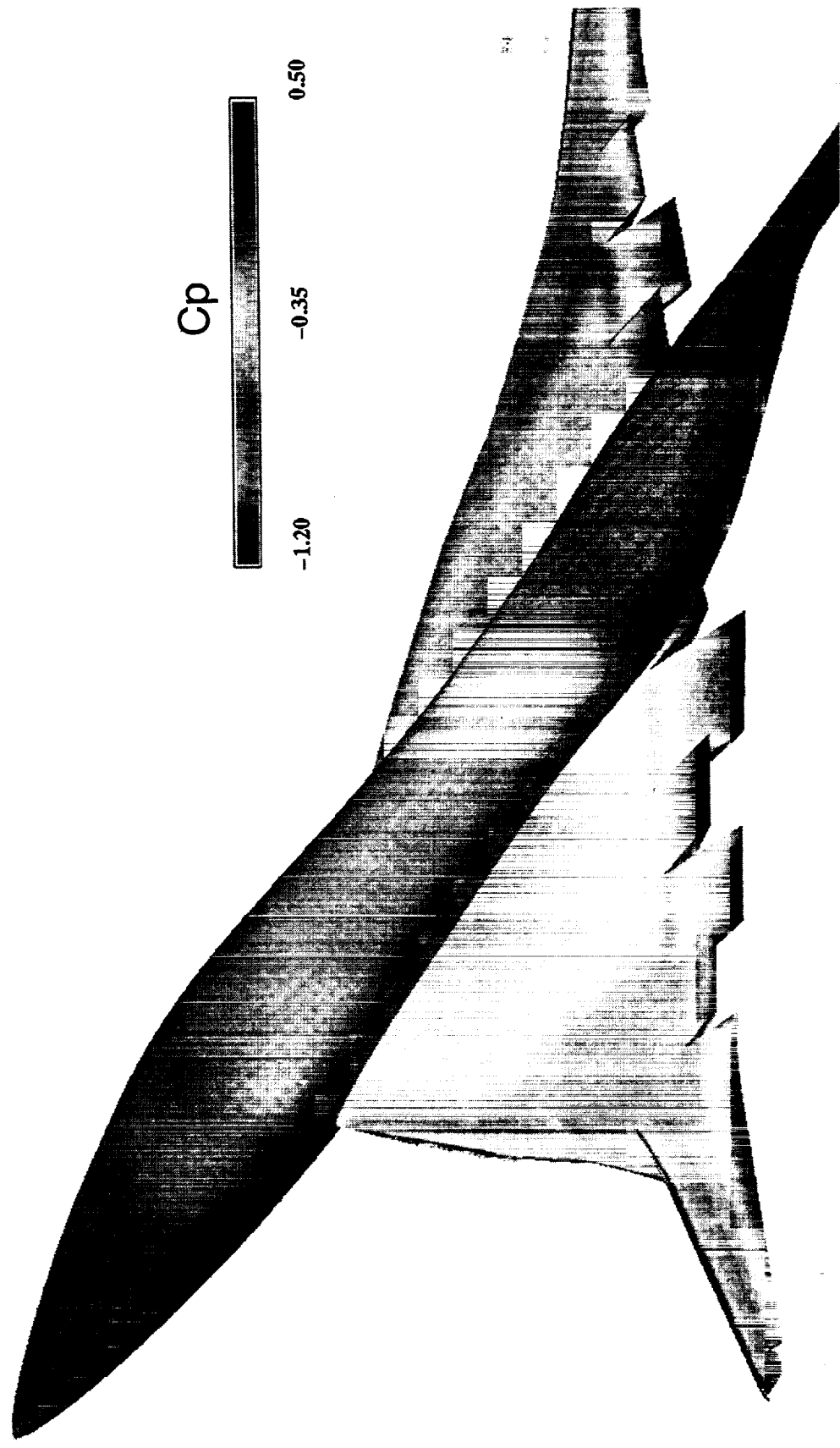
Summary - LE Flap Deflection

The LE flap deflection procedure has been developed to efficiently model the HSCT high-lift configurations. Geometric perturbation techniques have been incorporated in the process which can be utilized in the parametric and flap optimization studies.

SUMMARY - LE Flap Deflection Procedure

Modifies a clean (no flaps) volume grid to account for:

- Multiple flap segments

- Multiple LE sweeps

- Variable LE flap chord length and spanwise extent (part span vs. full span)

- Quadrilateral and triangular(tapered) flap segments

- Flap rotation about arbitrary hinge axes

- User specified deflection angles (inboard and outboard)
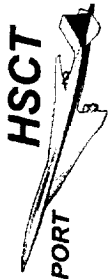
Summary - TE Flap Deflection

The TE flap deflection procedure has been implemented to efficiently model the HSCT high-lift configurations. A pre-processor is also provided in the process for the convenience of the users in defining the TE flap geometries.

These automated flap deflection procedures also have been successfully applied to the surface grid generation with multiple control surfaces for panel method calculations.
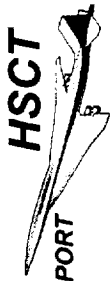
SUMMARY - TE Flap Deflection Procedure

Modifies the volume grid with/without LE flap deflection to account for:

- Multiple TE flaps

- Spanwise gap modeling for 3-D effects

- Rigid-body-rotation about arbitrary hinge axes

- User specified flap deflection schedule
  - Each flap is deflected independently

Pre-Processor - Modifies surface & volume grids for TE flap definition

This page intentionally left blank.

A New Approach to Constrained Induced and Trim Drag Optimization

Winfried M. Feifel
The Boeing Company
Seattle WA
(206) 965-0561

THIS PAGE IS INTENTIONALLY LEFT BLANK

Background
- Need to analyze wind tunnel data
- Determine tail downwash / trim drag

WMFFIT Aerodynamic Potential Flow Model
- Convert CFD data into small matrices of 'super influence coefficients'
- Compute induced drag, moments, aero surfaces deflection angles

Application of WMFFIT to Ref.H NASA437 Wind Tunnel Data
Trim tail-off data using:
- Conventional Tail
- Canard
- Tri-Surface

Explain performance differences between canard and conventional tail

Future Additions to WMFFIT

Summary

A new numerical method has been developed which allows the easy construction of a complete induced drag and pitch trim model for fully three-dimensional aircraft configurations comprised of an arbitrary number of lifting surfaces. The induced drag is described as a function of a small number of parameters, such as lift, canard, wing, and tail incidence angles, and the deflection angles of trailing edge flaps. Combined with constrained optimization the method allows optimal trim of multi-surface configurations with minimum computational effort on a PC.

Ref.H trailing edge flap positions have been experimentally optimized -tail off- as part of the NASA437 test series conducted in the NASA Langley 14x22 wind tunnel. Generally, the untrimmed 'optimum' configurations exhibited large pitching moments. The above described method accepts experimentally acquired data as constraints and thus can be used to determine trimmed model performance characteristics.

The analyses indicate that the trimmed optimum performance greatly depends on the type of trim surfaces used. At the lift coefficients of interest a canard configuration exhibits $\Delta L/D = 0.7$ higher lift/drag ratio than the conventional tail configuration. Only about 1/3 of the canard performance gain is shown to be the result of savings in induced drag. The balance of the gain is attributed to changes in wing viscous drag. Compared to the conventional tail configuration the performance of the canard is shown to be less sensitive to migration of the airplane center of gravity. Only small further performance improvements seem to become available from a tri-surface configuration.

Which configuration is best when the airplane is trimmed in pitch?

CLSAC VERSUS CMSAS0   LODC VERSUS CLSAC

10/15 Trailing Edge Flap Angles

Baseline J1.6.1
LE/TE 30%X

20/15

15/15

10/15

Untrimmed Lift Coefficient (vertical axis, left plot)

Pitching Moment, CM₅₀ — Pitching Moment, CM_{50}

CMSAS0

12-FEB-96 16:31:15

Untrimmed L/D (vertical axis, right plot)

CLSAC

Untrimmed Wing Lift Coefficient

12-FEB-96 15:22:11
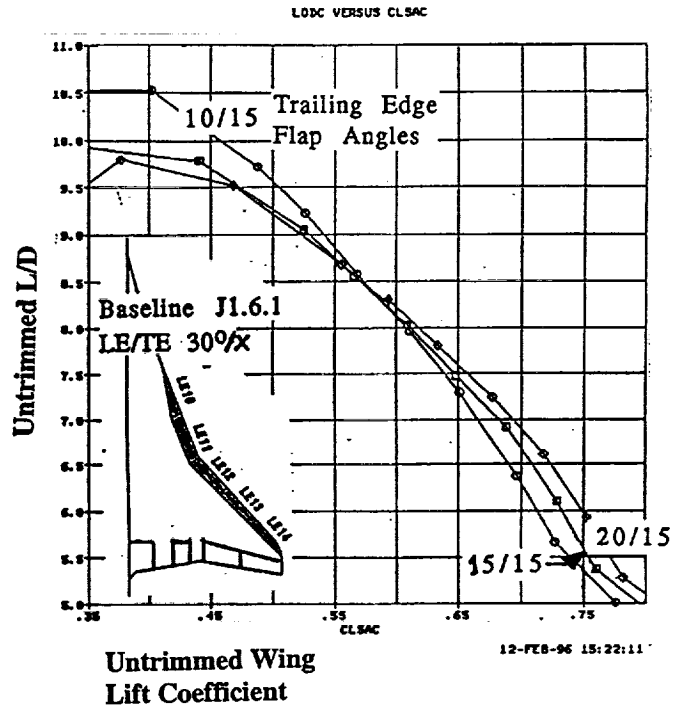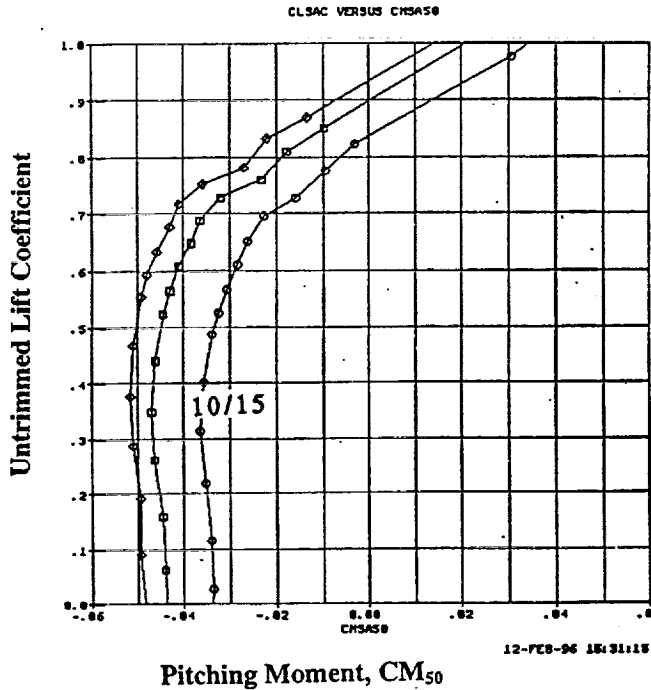
A 6% scale wind tunnel model of the Ref.H supersonic transport configuration was evaluated (Test NASA437) in the NASA 14'x 22' wind tunnel. A limited amount of the test time was used for optimization of the trailing edge flap settings. The figure shows the L/D performance of the 'best' untrimmed (tail off) configurations. The outboard flaps were set at 15 degrees, the deflection of the two inboard flaps was varied. Varying the inboard flap deflection is seen to affect both L/D performance and pitching moment characteristics.

It is not at all obvious which of the configurations will be best once the airplane is trimmed in pitch. For an accurate prediction of trim drag of a conventional tail the down wash needs to be known as a function of wing lift and flap settings. Conversely, the interactions between the wing and the canard needed to be accounted for if a canard is used as the trimming device. To facilitate the pitch trim study, a fast, easy to use potential flow based method was developed which calculates the above parameters.

Objective
Recast CFD results in into a function of the few parameters of interest
- Lift
- Moments
- Aero Surfaces Deflection Angles

Fully 3-dimensional
No loss in accuracy

Approach
Method of span load mode functions

Use linear CFD to determine the mode shapes and the associated geometry changes

Results
WMFFIT is exact - not a curve fit

Small matrices fully describe airplane linear aerodynamics

Can be used for constrained induced drag optimization

Span load distributions are a 'by-product' of the analysis procedure

Computer usage reduced by orders of magnitude

A FORTRAN procedure (WMFFIT) was developed with the objective to recast the results of a series specific CFD analyses of a particular airplane configuration into a form which requires as input only the few parameters of practical interest (wing, canard, tail lift coefficients, deflection angles, etc.).

The computer program and the underlying theory will be discussed in the next slides.

Subsequently, a few applications of the new method will be shown with special emphasis on pitch trim of the Ref.H configuration.
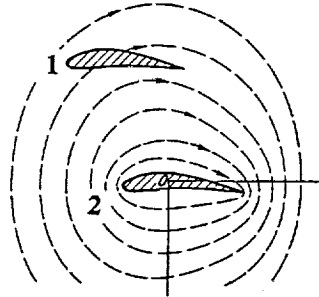
Munk's Biplane Theory:

D_{11} = induced drag of isolated wing #1
D_{22} = induced drag of isolated wing #2
D_{12} = drag of wing #1 due to upwash of wing #2
D_{21} = drag of wing #2 due to downwash of wing #1

Total Induced Drag:

$$D_i = D_{11} + D_{12} + D_{21} + D_{22}$$

Implied Assumptions:

-The mutual induced interference between the wings does not change the shape of
the spanwise load distributions.

-The angle of attack of the wings is adjusted so that their lift remains unchanged, i.e.

$L_1 = L_{11}$, and

$L_2 = L_{22}$.

W.M.Feifel Feb.97

The new computer program determines lift, induced drag, moments, and the associated geometric angle of attack changes of the aerodynamic surfaces involved. Induced drag is calculated using an analogy to Munck's biplane theory which breaks the configuration total drag down into the drag of each of the two wings alone and the drag due to the interactions between the two wings.

Extending Munck's theory, induced drag is obtained by summation of the drag contributions of a series of isolated spanwise load distributions, and their mutual interactions. Determining the shapes of these spanwise load distributions is one of the major tasks to be resolved.

Synthesis of Spanwise Load Distributions by Mode Shape Functions

BOEING
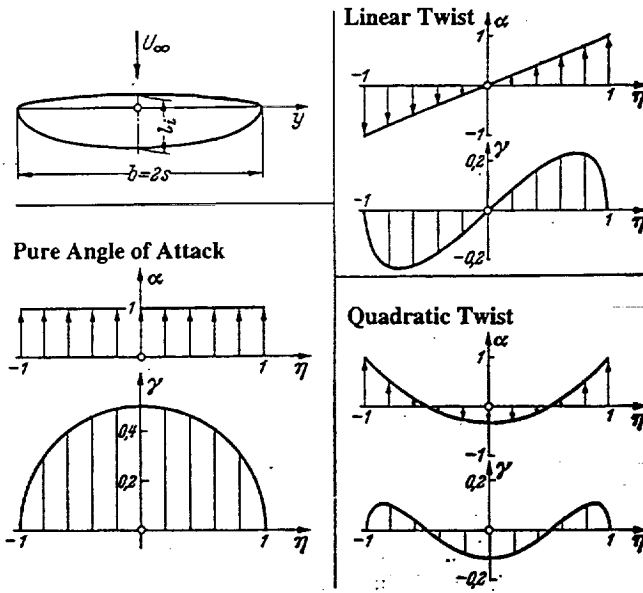
Trefftz's & Glauert's Synthesis of Spanloads:

-Complex span loads can be synthesized from
a series of spanload mode shapes

-Multhopp's approximation by Fourier series

-Arbitrary spanload mode shapes can be used

Problem to be solved:

Find useful mode shapes which fully describe the spanloads of complex airplane configurations.

W.M.Feifel Feb.97

Complex spanwise load distributions can be composed using a series of simpler mode shape functions. A mode shape is defined as a span load the shape of which changes proportional to a single feature, for example the amount of wing twist. The spanwise load distribution an a wing can be composed of many mode shapes, such as a series of sine or cosine functions. For many applications only those mode shapes are useful for which a corresponding wing geometric feature can be determined. The next page will describe an approach to developing mode shapes for complex airplane configurations with an arbitrary number of lifting surfaces.

PANEL MODEL FOR A372 POTENTIAL FLOW
ANALYSIS YIELDS:
1) INDUCED DRAG INFLUENCE COEFF.
2) PITCHING MOMENT INFLUENCE COEFF.
3) SURFACE ORIENTATION CHANGE COEFF.
4) GENERIC SPANLOAD FUNCTIONS

TAIL CL
DELALPHA

7.5

6.5

5.5

4.5

#1

#2

#3

FLAP #4

WING CL
DELALPHA
TWIST

3.5

2.5

1.5

TWO VARIABLES/FLAP:
FLAP DEFLECTION
DELALPHA

1) Wing Lift Coefficient
2) Canard Lift Coefficient
3) Horizontal Tail Lift Coefficient
4) Inboard Flap Deflection Angle #1
5) Nacelle Flap Deflection Angle #2
6) Outboard Flap Deflection Angle #3
7) Aileron Deflection Angle #4
8) Wing Twist

CANARD Cl
DELALPHA

.5

WMF97

The process of creating the mode shapes for an arbitrary airplane configuration is most easily explained using an actual data case as an example. The figure shows the Ref.H wing in conjunction with a horizontal tail and a canard as control surfaces for pitch trim. In addition, four trailing edge flaps can be independently deflected. The present slide shows the airplane geometry, the next slide the associated mode shape functions. The mode shape functions are the results of CFD analyses. The potential flow load distribution of the entire airplane configuration is described by $N = 8$ load functions.

Mode shape #8 describes the load distribution due to wing aerodynamic twist and camber with the canard, wing, and tail incidence angles selected such that none of the three surfaces carries any lift. The shape of this load distribution is directly proportional to the amount of wing aerodynamic twist.
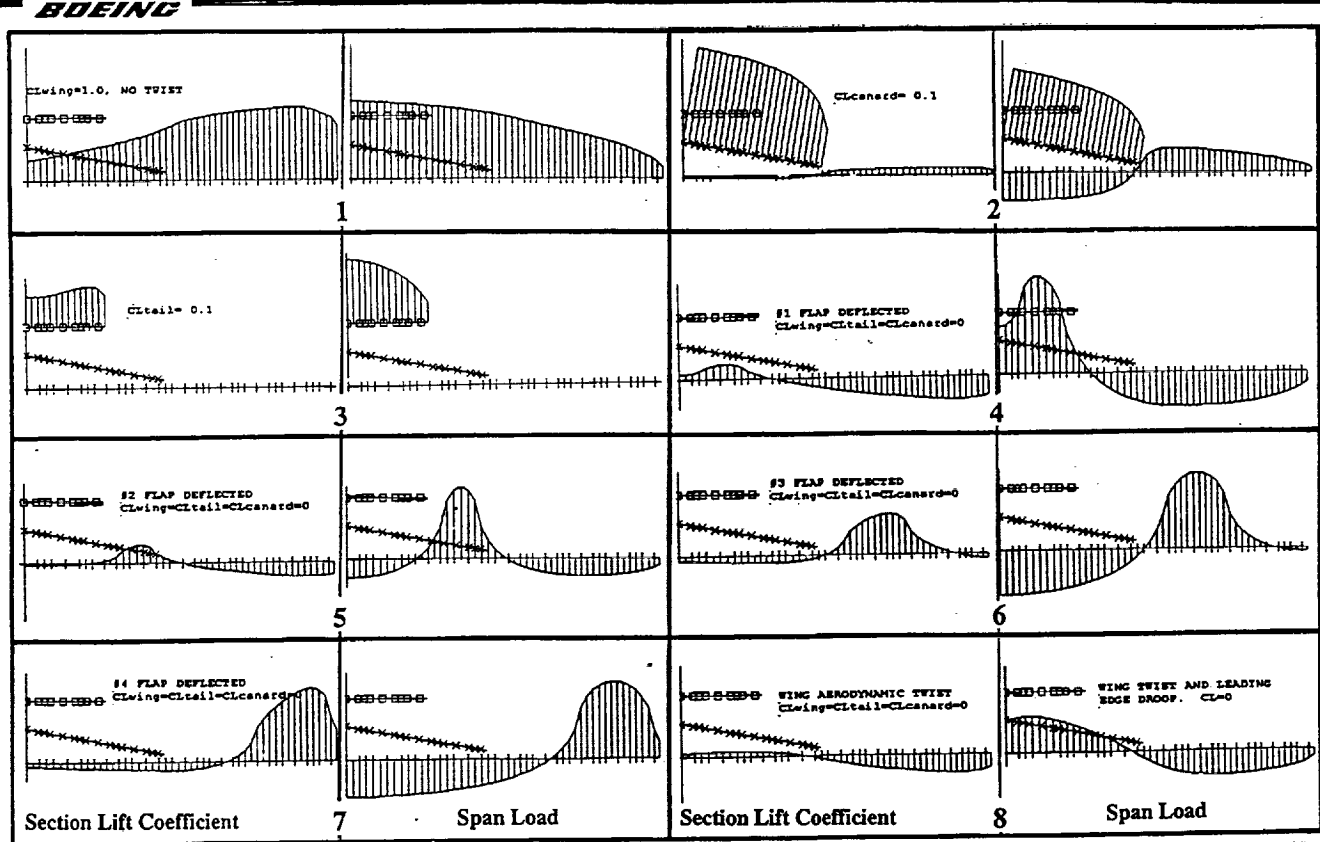
W.M.Feifel Feb.97

The other seven load functions involve only the untwisted and uncambered ('planarized') wing:

Load function #1 describes the wing flaps up span load at $CL_{wing} = 1.0$ with the canard and the tail set at their respective zero lift incidence angles.

Load function #2 comprises the canard load distribution at a lift coefficient $CL_{canard} = 1.0$., and the zero lift span loads induced on the wing and the tail by the canard. The zero lift condition implies that the incidence angles of both the wing and the tail be adjusted such that there is no net lift force acting on either one of these surfaces.

Load function #3 consist of the horizontal tail span load at $CL_{tail} = 1.0$ with the wing and canard set at their respective zero lift angles of attack.

Load functions #4 through #7 describe the span loads induced by individual 1 degree deflections of the flaps #1 through #4 with canard, wing, and tail each operating at zero lift.

Any rigid airplane load distribution is the result of linear combinations of the above eight mode shapes. For the present analysis the individual lift contributions of the wing, canard, and tail, the deflection angles of the four flaps, and the wing twist have been selected as the eight primary variables. In most analyses the wing twist will be held constant, unless wing twist is to be altered by a proportionality factor.

Tasks for the Aerodynamicist:

-Break the airplane configuration into geometric features which will be changed (angle of attack, control surface deflections, flap deflections, aeroelastic deformations).

-Identify surfaces for which the local lift does not vanish if the overall lift of all individual surfaces is zero (wing twist). These are separate features.

Tasks for CFD analysis:

-Find the span loads, induced drag, moments, and geometry changes associated with each of the above N features, setting all other features to zero.

-Find the induced drag values for all linear combinations of two features at a time.

-Process CFD results to define small the influence matrices which will fully describe the lift, drag, and pitching moment characteristics of the airplane, together with the associated geometry changes (angle of attack, control surface deflections).

N = Number of mode shapes identified

$(N * (N + 1)) / 2$ = Number of CFD solutions to be found

W.M.Feifel Feb.97

Identification of the number, N, of mode shapes needed to describe the load distribution about a complex airplane configuration is the main task for the aerodynamicist. It requires a certain amount of experience. Nearly always will it be necessary to analyze a configuration were the wing is twisted and cambered. A second 'planarized' configuration also be necessary in order to be able to completely isolate the mode shapes. This will be explained further in the next slide.

Once the number and types of mode shapes has been established, CFD analyses will be required to obtain the induced drag, moments and incidence changes associated with each individual mode by itself. All combinations of pairs of modes need to be analyzed to obtain the induced drag interaction terms between the mode shapes. Thus $(N*(N+1))/2$ cases will have to be processed.

The induced drag most likely will obtained from a Trefftz plane analysis which yields a single number: The drag of the entire configuration. The induced drag interaction terms are found by subtracting the isolated drag of each of the two individual mode shapes from the drag value obtained for the two mode shapes combined. This interaction value contains the all mutual interference effects between the two modes. Only a near field drag analysis could provide information about the interference drag experienced by each individual component separately. However, this information is generally not needed.

Twisted and 'Planarized' Airplane Configuration for CFD Analysis
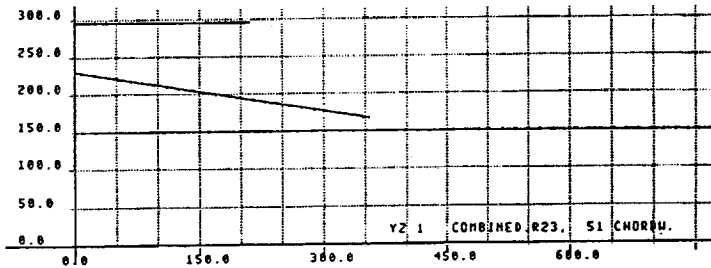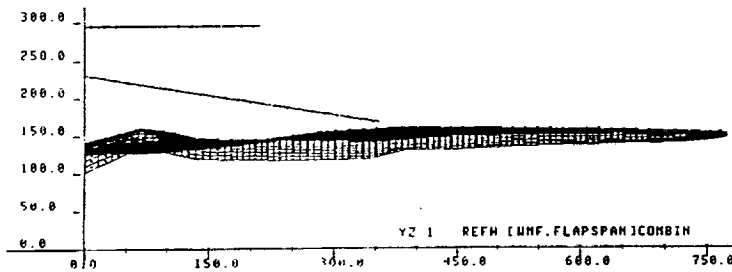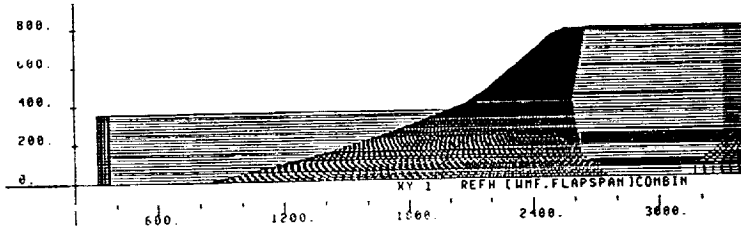
Twisted configuration to obtain interaction between Span-Load-due-to-Twist with other planar mode shapes.

'Planarized' configuration for analyses of mode shapes which are independent of twist and camber.
Note: Only twist and camber are removed. Dihedral and spacing between lifting surfaces must be retained.

W.M.Feifel Feb.97

The majority of the mode shapes describe wing plan form effects and thus require a planar wing arrangement for the analysis. The 'planarized' wings must have twist and camber removed, but wing dihedral and the vertical spacing between wings must be maintained and represent the trailing vortex arrangement in the Trefftz plane. In the example shown only the main wing was cambered.

The twisted / cambered configuration analysis yields the zero lift span load due to twist and the pitching moment associated with twist and camber. Also, the change in the aerodynamic surfaces angles of zero lift due to twist and camber will be a result of the nonplanar analysis.

The CFD code must be able to:

- Generate solutions for pure mode shapes
- Generate solutions containing combinations of two pure mode shapes
- Accurately compute induced drag
- Compute lift and moments
- Provide the relationship between the mode shape and the necessary changes to the configuration geometry

Boeing A372 vortex lattice code is well suited:
- Fully 3-dimensional
- Arbitrary, multi-surface configurations
- Mixed design and analysis boundary conditions
- Constrained induced drag minimization
- Multiple solutions (RHS) in one run
- Only 2 runs needed ('planarized' and twisted configuration)

Post Processor:
- Convert CFD results into influence coefficient matrices describing lift, drag, moments as function of N mode shapes
- Evaluate matrices, provide capability for constrained optimization

W.M.Feifel Feb.97

In principle, any CFD code which yields sufficiently accurate induced drag information can be used for the mode shape analyses. However, isolation of the mode shapes will prove quite cumbersome if the code does not have some design capability.

For the present analyses the Boeing A372 vortex lattice code has been applied. The code has extensive design capability allowing, for example, a direct solution for the incidence angles needed which yield a prescribed canard lift coefficient, $CL_{canard} = 1.0$, while maintaining zero lift on the wing and the horizontal tail, respectively. A372 has the capability to simultaneously process many flow conditions by introducing multiple right hand sides to the system of linear equations to be solved. Therefore, all planar wing mode shapes and their interactions can be obtained in a single computer run. However, twisted/cambered configurations involve a different geometry and thus require a second analysis run. The codes constrained design and induced drag optimization techniques are described in "Vortex-Lattice Utilization', NASA SP-405, 1976. For the present application the code has been slightly modified to create data files which can be read by the WMFFIT computer program.

WMFFIT is the program which generates and operates on the small aerodynamic model constructed from the CFD analyses. It can be used to trim a configuration in pitch, minimize induced drag subject to constraints, and to synthesize span loads.

BOEING

Induced Drag Influence Coefficients:

	Wing CL	Canard CL	Tail CL	#1 Flap	#2 Flap	#3 Flap	#4 Flap	Wing Twist
Wing CL	.136271							
Canard CL	.264612	.325600						
Tail CL	.250220	.372920	1.756640					
#1 Flap	.000114	.000151	.001807	.000006				
#2 Flap	.000024	.000048	-.000347	-.000003	.000004			
#3 Flap	-.000147	-.000145	-.001195	-.000005	-.000002	.000006		
#4 Flap	-.000128	-.000142	-.000843	-.000004	-.000002	.000000	.000006	
Wing Twist	.000808	-.001454	.008812	.000042	.000006	-.000037	-.000028	.00012

Matrix Reference Conditions:

Wing Area	7100 ft^2
Mean Chord	1032 in
CG @ 50% MAC	2106 in
Lift Coeff. CL	1.0
Flap Deflection	1 deg.
Present Ref.H Wing Twist	1.0

Angle-of-Attack Influence Coefficients:

	Wing CL	Canard CL	Tail CL	#1 Flap	#2 Flap	#3 Flap	#4 Flap	Wing Twist
#1 Flap =	24.220580	20.628020	-1.730010	.876703	-.091126	-.099221	-.063145	1.015916
#2 Flap =	24.220580	20.628020	-1.730010	-.123296	.908874	-.099221	-.063145	1.015916
#3 Flap =	24.220580	20.628020	-1.730010	-.123296	-.091126	.900779	-.063145	1.015916
#4 Flap =	24.220580	20.628020	-1.730010	-.123296	-.091126	-.099221	.936855	1.015916
Wing Only=	24.220580	20.628020	-1.730010	-.123296	-.091126	-.099221	-.063145	1.015916
Canard =	-.487780	235.34720	-.139936	.000831	.000630	.000759	.000544	-.000054
Tail =	14.924800	21.637100	231.79700	.104921	-.019194	-.067361	-.047425	.503178

Pitching Moment Influence Coefficients:

	Wing CL	Canard CL	Tail CL	#1 Flap	#2 Flap	#3 Flap	#4 Flap	Wing Twist
CM50 =	.040041	1.456210	-1.139928	-.001274	-.000958	-.001210	-.000941	.005224

RefHmatrix.txt WMF-Feb-97

The three matrices shown fully describe the Ref.H configuration induced drag, aerodynamic surfaces orientation angles required, and the associated pitching moment characteristics as a function of the eight primary variables which include a canard and tail surface for pitch control. Isolated canard or tail configurations are obtained by prescribing zero lift for the unwanted control surface.

The diagonal of the drag matrix defines the influence of each primary variable on itself. Some of the off-diagonal interaction terms carry a negative prefix, indicating a favorable interference between two components.

The angle of attack influence coefficients describe the angle of each aerodynamic surface relative to the free stream velocity vector as a linear function of the eight primary variables. Canard upflow and tail down wash angles are easily derived from this table.

The pitching moment values shown in the table have been computed relative to MAC = 50%. For other moment reference points the moment transfer has to be calculated for the three lift force carrying surfaces only. The flaps, wing twist and camber generate pure moments and thus contribute only to CM_0.

BOEING

- Quick evaluation of trimmed airplane induced drag characteristics

- Constrained minimization of induced drag

- Analysis of Ref.H NASA437 wind tunnel data

The next slides will show some of the capabilities of WMFFIT. However, the main emphasis will be placed on the analysis of the NASA437 wind tunnel data and the evaluation of different methods for pitch trim.

Example of WMFFIT Applications to Airplane Trim and Induced Drag Optimization
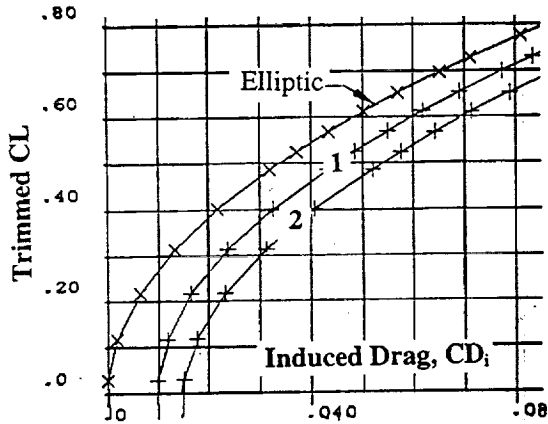
High Drag Emergency Descent:

Flap Schedule:
20/-20/20/-20   20/20/-20/-20
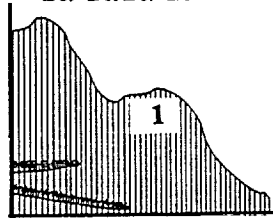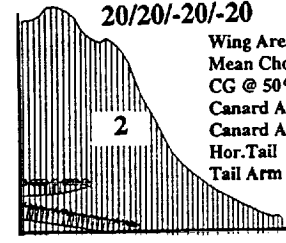
Wing Area (A_{ref})	7100 ft²
Mean Chord (C_{ref})	1032 in
CG @ 50% MAC	2106 in
Canard Area	360 ft²
Canard Arm	1390 in
Hor.Tail	700 ft²
Tail Arm	1193 in

Spanwise Load Distribution, CL=0.48

Trimmed Airplane (Flaps 10/15):

Bad Constraint:

$CL_{wing} = 0.49$ (prescribed)
$CL_{airplane} = 0.42$
$CDi = 0.0294$

Better Constraint:

$CL_{wing} = 0.46$
$CL_{airplane} = 0.49$ (prescribed)
$CD_i = 0.0324$
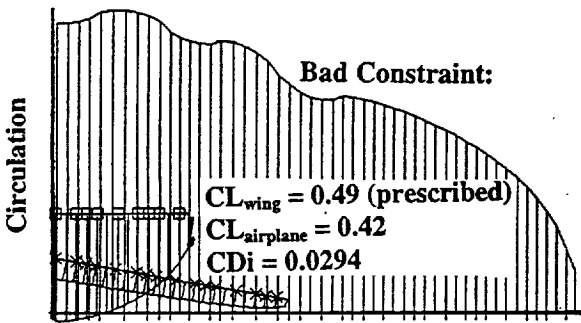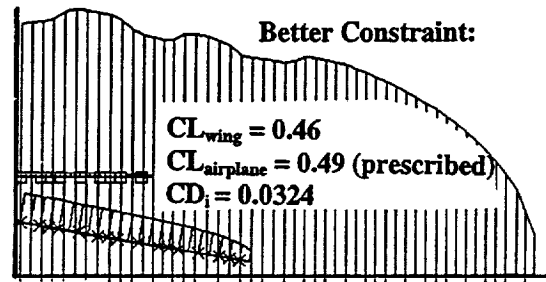
Spanwise Load Distribution

W.M.Feifel Feb.97

Emergency descent from high altitudes is one of the few instances when high drag is desirable. A Ref.H 3-surface configuration was analyzed using different trailing edge flap schedules for the creation of large values of induced drag. Somewhat as a surprise, alternating between upward and downward flap deflection angles produces less drag than deflecting the inboard flaps downward and the outboard flaps upward. A physical explanation for this finding is that the latter configuration reduces the effective wing span with most of the load carried inboard. The span reduction is more effective at creating drag than the ragged span load created by an alternating flap deflection schedule.

The second example illustrates the pit falls common to numerical optimization. In the left hand case the lift of the wing, $CL_{wing} = 0.49$, was prescribed as a constraint. The second constraint was that the airplane be optimally trimmed using the canard and the tail. Minimum induced drag occurs when both the canard and the tail carry a significant downward load, thus reducing the airplane overall lift: A correct, but not a practical result!

A better solution is found when the airplane overall lift is prescribed and the optimizer can distribute the lift between the three aerodynamic surfaces. This example illustrates the inherent difficulty of arriving at the best load split for tri-surface configurations.

- Isolated wing induced drag

- Pitch trim of isolated wing using:
  Conventional Tail
  High Aspect Ratio Canard
  Tri-Surface

- Lift carried by control surfaces

- Changes in induced drag due to pitch trim

- Changes in wing viscous drag due to control surfaces lift

- Canard & Conventional Tail trimmed L/D

- Effect of Center of Gravity location

Note: Control surface viscous drag contributions have been ignored

Analysis of the NASA437 wind tunnel data is broken down into a series of steps which are outlined above. It is important to note that no allowance has been made for the viscous drag of the canard or the horizontal tail. Also, all induced drag analyses are based on potential flow. Loss of leading edge suction due to flow separation is treated as part of the configuration viscous drag.

CDI/CDE VERSUS COLIFT

Induced Drag Increment
$\Delta CD_{i\,ell} = CD_{i\,wing} - CD_{i\,ell}$

Wing Area (A_{ref})   7100 ft^2

T.E. Flaps = 20/15

15/15

10/15

R2581630
R2581640
R2581670

COLIFT

11-FEB-97 87:32:13

Untrimmed Wing Lift Coefficient
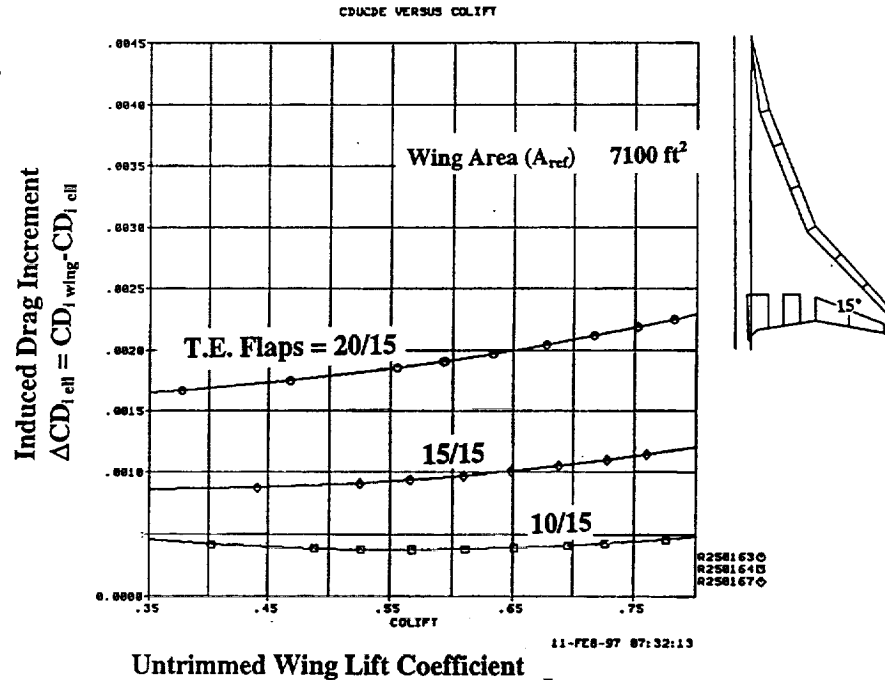
W.M.Feifel Feb.97

The induced drag of the isolated wing is seen to increase with larger inboard trailing edge deflection angles. This increment is associated with the more triangular span load. The outboard flap downward deflection is probably beneficial as it counteracts the wing washout due to twist and the nonelliptic load inherent to the delta wing planform. Isolated wing induced drag, CDi $_{wing}$ rather than elliptic induced drag will be used as reference in the subsequent analyses. This choice was made because the basic wing shape and the flap settings tested were treated as given.

Trimmed Airplane Control Surfaces Lift Coefficient
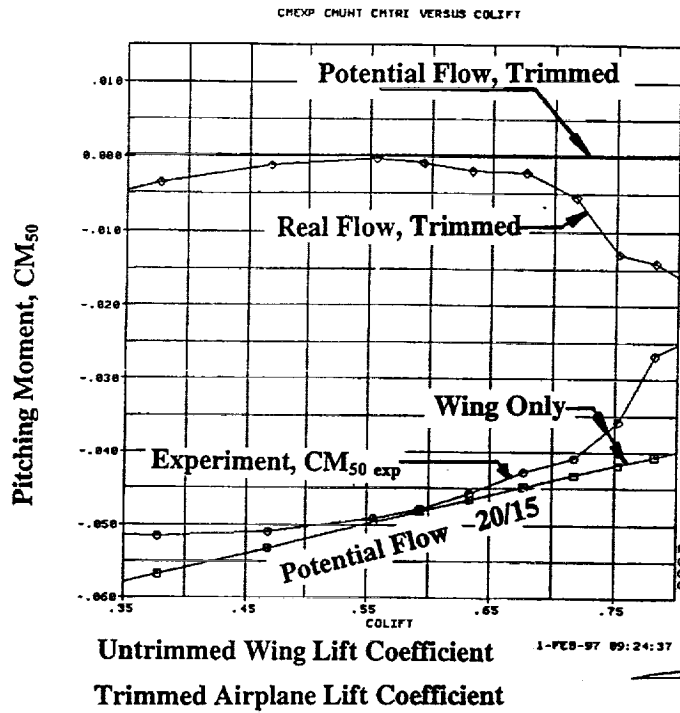
CHEXP CHUHT CHTRI VERSUS COLIFT

Potential Flow, Trimmed

Real Flow, Trimmed

Wing Only

Experiment, CM$_{50\ exp}$

Potential Flow -20/15

Pitching Moment, CM$_{50}$

COLIFT

1-FEB-97 09:24:37

Untrimmed Wing Lift Coefficient

Trimmed Airplane Lift Coefficient

Wing Area (A$_{ref}$)	7100 ft^2
Mean Chord (C$_{ref}$)	1032 in
CG @ 50% MAC	2106 in
Canard Area	360 ft^2
Canard Arm	1390 in
Hor.Tail	700 ft^2
Tail Arm	1193 in

Trim Procedure:

1) Compute wing alone theoretical pitching moment, CM$_{50\ w}$
2) Determine $\Delta CM = CM_{50\ exp} - CM_{50\ w}$
3) Prescribe ΔCM as residual to airplane potential flow trimming procedure

R250163
CHEXP
CHUHT
CHTRI
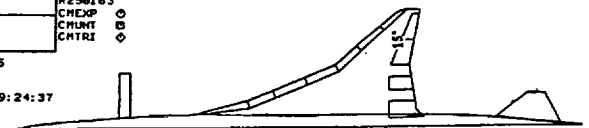
W.M.Feifel Feb.97

The figure shows the tail-off measured pitching moment and the wing alone pitching moment predicted by theory. The excellent agreement between theory and experiment at CL$_{wing}$ = 0.55 must be considered somewhat fortuitous. All experimental pitching moment curves are quite nonlinear, an indication of significant viscous effects.

The nonlinear pitching moment characteristics are accounted for in the WMFFIT pitch trim process by prescribing residuals which correspond to the differences between the wing alone experimental and theoretical pitching moment values. This guarantees that the trimming surfaces carry loads commensurate to trim experimental pitching moments, while accurately calculating the induced drag increments due to trim lift forces.

Trimmed Airplane Control Surfaces Lift Coefficient

CLTTRI CLCCRI CLC3PT CLT3PT VERSUS COLIFT

Control Surfaces Trim Lift (vertical axis)

Canard Only

Canard + Tail — optimized for min CD_i

Horizontal Tail Only

Wing Area (A_{ref})	7100 ft^2
Mean Chord (C_{ref})	1032 in
CG @ 50% MAC	2106 in
Canard Area	360 ft^2
Canard Arm	1390 in
Hor.Tail	700 ft^2
Tail Arm	1193 in

Flaps 20/15

R250163
CLTTRI
CLCCRI
CLC3PT
CLT3PT

COLIFT

11-FEB-97 86:48:48

Trimmed Airplane Lift Coefficient
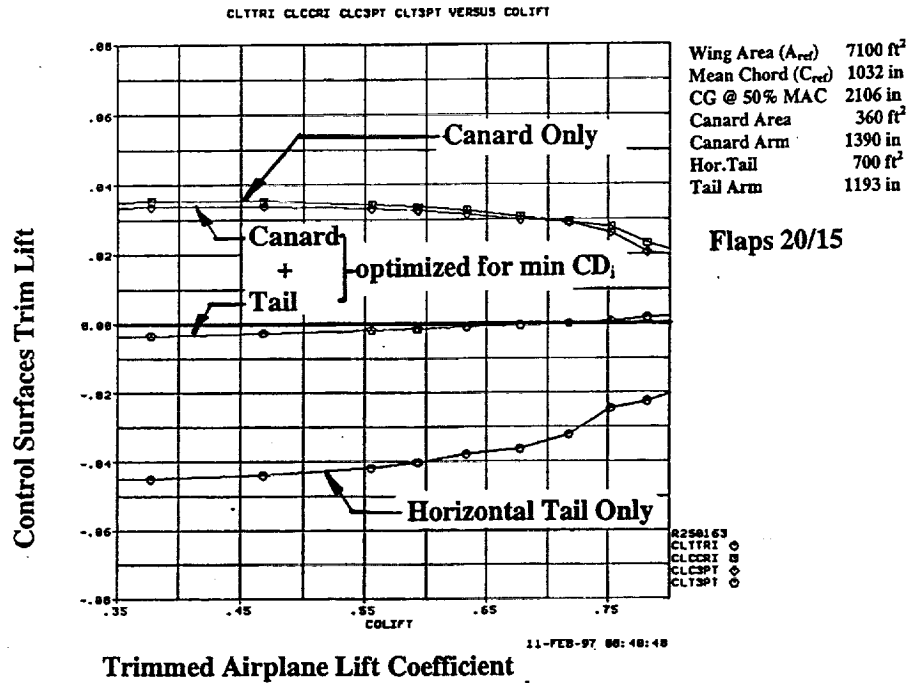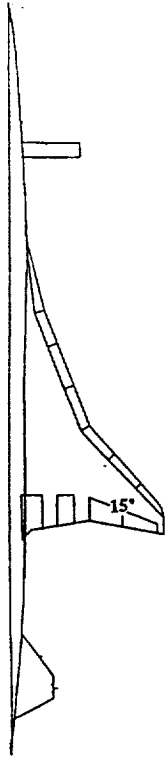
W.M.Feifel Feb.97

The figure shows the variation of control surface trim lift as a function of airplane trimmed lift coefficient. The trim loads become smaller a higher airplane lift coefficients because of the pitch up tendency of the wing. It should be noted that the canard carries upward lift, while the conventional configuration tail carries a significant downward load. Induced drag optimization, which is only possible for the tri-surface configuration with it's additional degree of freedom, yields that most of the trim force should be generated by the canard.

2249

BOEING

Wing Area (A$_{ref}$)	7100 ft^2
Mean Chord (C$_{ref}$)	1032 in
CG @ 50% MAC	2106 in
Canard Area	360 ft^2
Canard Arm	1390 in
Hor.Tail	700 ft^2
Tail Arm	1193 in

DELCDI DCDCRI DCI3PT VERSUS COLIFT

Pitch Trim Induced Drag Increment

$\Delta CD_{i\,trim} = CD_{i\,(trimmed)} - CD_{i\,wing}$

T.E. Flaps =

20/15   Conventional Tail

15/15

30 Drag Counts

Canard
& Trisurface   10/15

R250163
DELCDI
DCDCRI
DCI3PT
R250164
DELCDI
DCDCRI
DCI3PT
R250167
DELCDI
DCDCRI
DCI3PT
DELCDI
DCDCRI
DCI3PT

.35   .45   .55   .65   .75
COLIFT

11-FEB-97 11:38:33

Trimmed Airplane Lift Coefficient
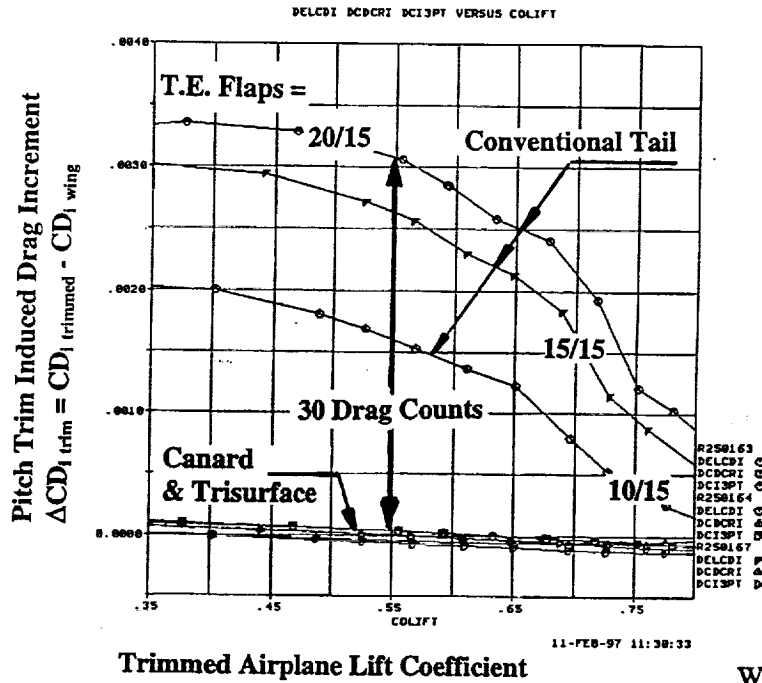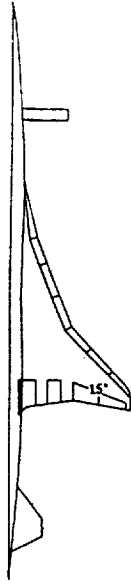
W.M.Feifel Feb.97

This figure shows the increments in induced drag associated with three different settings of the two inboard wing flaps. The trimmed airplane induced drag increment over that of the isolated wing operating at the airplane lift coefficient is seen to be rather large in the case of the conventional tail configuration. Also, tail trim drag is seen to be a strong function of the inboard flap deflection angle. In contrast, the canard and the tri-surface configuration experience virtually no induced drag penalty due to trimming over the whole range of flap settings and lift coefficients.

2250

CDEXP CDPHIN CDIUNT VERSUS COLIFT

Experimental Drag, CD_{exp}

Wing Induced Drag, $CD_{i\,wing}$

Profile Drag, $CD_P = CD_{exp} - CD_{i\,wing}$

T.E. Flaps = -10/15 — 20/15

Experimental Drag

Wing Induced Drag

20/15   10/15

Tail-off Viscous Drag

Wing Area (A_{ref})   7100 ft^2

Untrimmed Wing Lift Coefficient

10-FEB-97 19:40:04

W.M.Feifel Feb.97
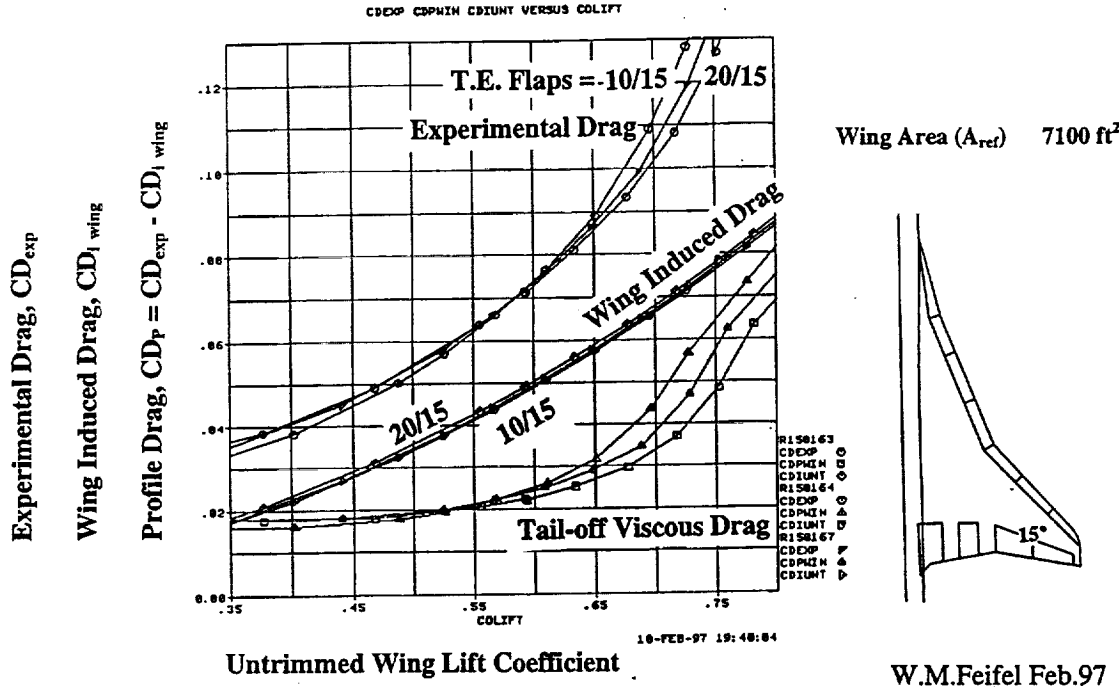
Assuming that the wing isolated induced drag, $CD_{i\,wing}$, is known with sufficient accuracy, the Ref.H tail off viscous drag, CD_P , has been obtained as the difference between the measured drag and theoretical induced drag. Ideally, CD_P should be nearly independent of airplane lift and closely correspond to flat plate skin friction.

The present data, however, show a strong lift dependence of the airplane tail-off viscous drag which must be caused by flow separation or the formation of leading edge vortices. Consequently, there will be a significant viscous drag penalty if the wing is forced to generate extra lift to compensate for a tail downward load. Conversely, the wing viscous drag will be reduced if part of the airplane lift is carried by a canard - assuming that the canard viscous drag is still small.

2251

Change in Wing Viscous Drag Due to Control Surfaces Trim Lift

DVITRI DVICRI DVI3PT VERSUS COLIFT

Wing Viscous Drag Increment, ΔCD_p

Horizontal Tail   20/15

10/15

30 Drag Counts

Canard

Tri-Surface

COLIFT

Airplane Trimmed Lift

11-FEB-97

Wing Area (A$_{ref}$)	7100 ft^2
Mean Chord (C$_{ref}$)	1032 in
CG @ 50% MAC	2106 in
Canard Area	360 ft^2
Canard Arm	1390 in
Hor.Tail	700 ft^2
Tail Arm	1193 in

Assumption:

Wing drag is only a function of wing lift coefficient, CL_{wing}, and is not affected by span load variations induced by canard lift.

R250163
DVITRI
DVICRI
DVI3PT
R250164
DVITRI
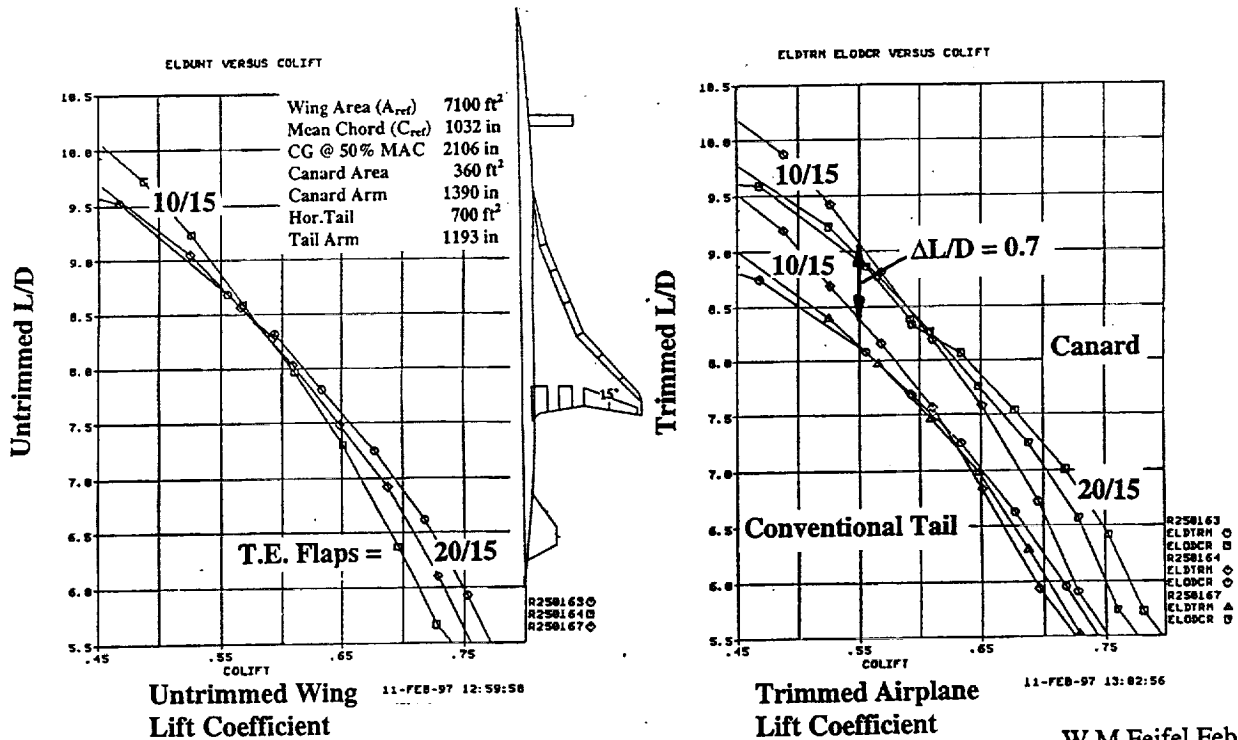DVICRI
DVI3PT
R250167
DVITRI
DVICRI
DVI3PT

W.M.Feifel Feb.97

At a trimmed airplane lift coefficient of CL = 0.55 the added wing lift needed to compensate for the horizontal tail down load is seen to cause a 20 count wing viscous drag increment. Conversely, trimming by a canard reduces the amount of lift carried by the wing and results in a 10 count viscous drag savings compared to the untrimmed isolated wing at CL_{wing} = 0.55. Because of the highly nonlinear viscous drag polar shape of the wing, the canard drag savings are smaller than the viscous drag increments associated with a download carrying horizontal tail.

Only at lift coefficients above the airplane normal operating range does the tri-surface configuration offer drag savings which are appreciably higher than those of a canard.

It must be noted that the wing viscous drag characteristics used for the above estimates are solely based on the tail-off wind tunnel data. No allowance was made to account for changes in viscous drag due the variation in wing span load induced by the canard. Also, changes in CG-location will modify the trim loads and consequently affect both the induced and viscous trim drag increments.

2252

Comparison of Conventional Tail and Canard Trimmed L/D

ELDUNT VERSUS COLIFT

Wing Area (A$_{ref}$)	7100 ft^2
Mean Chord (C$_{ref}$)	1032 in
CG @ 50% MAC	2106 in
Canard Area	360 ft^2
Canard Arm	1390 in
Hor.Tail	700 ft^2
Tail Arm	1193 in

Untrimmed L/D · 10/15 · T.E. Flaps = 20/15

Untrimmed Wing Lift Coefficient

ELDTRN ELODCR VERSUS COLIFT

Trimmed L/D · 10/15 · 10/15 · ΔL/D = 0.7 · Canard · 20/15 · Conventional Tail
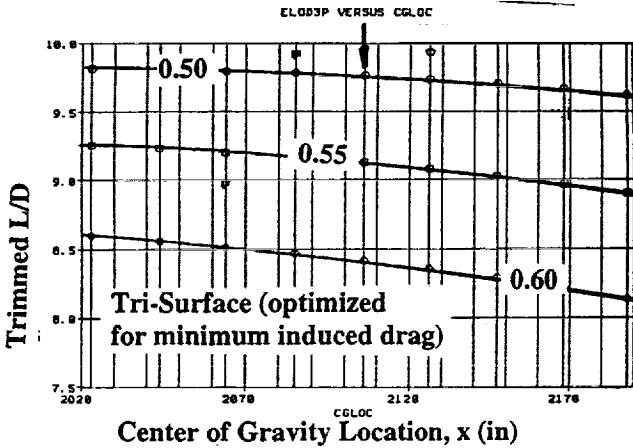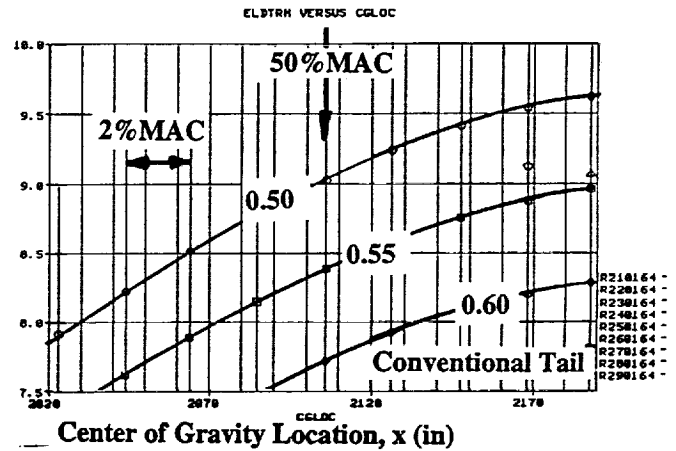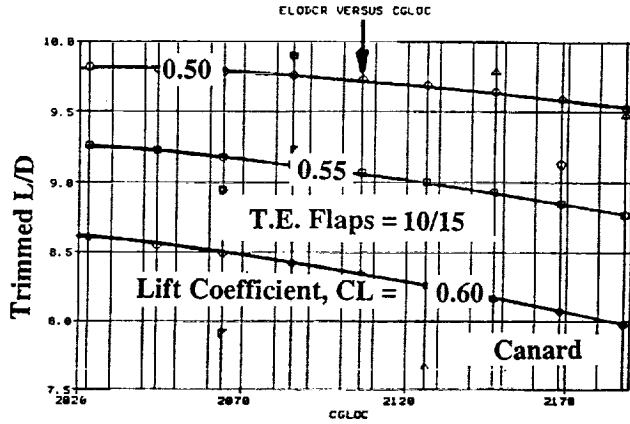
Trimmed Airplane Lift Coefficient

W.M.Feifel Feb.97

The left hand diagram shows the L/D characteristics as measured in the wind tunnel for the tail-off airplane. In the right hand diagram predicted trimmed airplane performance characteristics are presented for both a canard and a conventional tail configuration. The viscous drag of the canard and tail surfaces themselves are assumed to be small and are not included in the above estimates. This assumption will most likely not change the overall ranking between the configurations.

As explained before, the significant performance advantage of the canard over a conventional tail stems only to small extent from savings in induced drag. The majority of the performance benefits identified for this particular airplane configuration are the result of savings in wing viscous drag. If the wing viscous drag level were independent of wing lift, the differences between canard and conventional tail trim performance would be much less pronounced.

Answering the question that triggered the entire study: 10 degrees inboard and 15 degrees outboard appear to be the best flap settings for L/D performance at CL = 0.55.
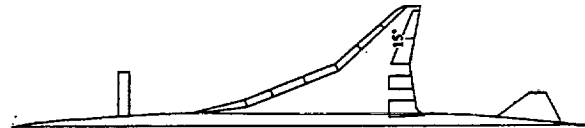
Effect of Center of Gravity Location on Trimmed L/D

ELODCR VERSUS CGLOC

Trimmed L/D

0.50

0.55

T.E. Flaps = 10/15

Lift Coefficient, CL = 0.60

Canard

CGLOC

ELOD3P VERSUS CGLOC

Trimmed L/D

0.50

0.55

0.60

Tri-Surface (optimized for minimum induced drag)

CGLOC

Center of Gravity Location, x (in)

ELBTRH VERSUS CGLOC

50%MAC

2%MAC

0.50

0.55

0.60

Conventional Tail

CGLOC

Center of Gravity Location, x (in)

Note: Stability limits and control surface CL$_{max}$ limits have not been considered.

Wing Area (A$_{ref}$)	7100 ft^2
Mean Chord (C$_{ref}$)	1032 in
CG @ 50% MAC	2106 in
Canard Area	360 ft^2
Canard Arm	1390 in
Hor.Tail	700 ft^2
Tail Arm	1193 in

W.M.Feifel Feb.97

The location of the center of gravity is seen to have a significant impact on the performance of the Ref.H configuration trimmed by a conventional tail. Flying the airplane more unstable by moving the CG aft significantly improves performance. However, this performance gain is entirely the result of reduced down load on the tail.

The L/D performance of the canard configuration is significantly less affect by changes in CG position. Moving the CG forward increases static stability and improves performance. Limits to the aerodynamic load carrying capability will severely restrict the amount of CG travel that can be accepted.

The tri-surface arrangement seems to be least sensitive to CG position.

The above graphs consider only static pitch trim. No checks have been performed to verify that the maximum possible control surface lift coefficients have not been exceeded, or to assure that the configuration is not too stable or too unstable.

Conclusions

- WMFFIT reduces computer usage by orders of magnitude

- Trim procedure used fully accounts for changes in induced drag and wing viscous drag

- At CL = 0.55 Conventional Tail trim drag increment consists of 1/3 induced drag and 2/3 of increased wing viscous drag

- At CL = 0.55 Canard trim does not change induced drag and decreases wing viscous drag

- At CL = 0.55 Canard is better than Conventional Tail by $\Delta L/D = 0.7$

- Only small benefits over a Canard have been found for Tri-Surface configuration

- Compared to Conventional Tail configurations trim drag of Canard and Tri-Surface configurations is less sensitive to CG location

The comprehensive trim drag study required numerous evaluations of different configurations and load distributions. Without the simplifications afforded by use of the WMFFIT procedure the work load would have been prohibitive.

The detailed analysis of the wind tunnel data clearly showed that for this particular configuration superior L/D performance can be achieved using a canard as the pitch trim device. However, the study also indicated that this significant performance gain is to a large extent caused by the poor viscous drag characteristics of the wing and thus should not be interpreted as inherent superiority of a canard as pitch trim device.

- Modify induced drag matrix to account for viscous effects (Oswald efficiency factor)

- Improve accuracy of Trefftz plane induced drag influence coefficients

- Include equivalent flap deflection angles to account for viscous effects on flap efficiency

- Include rolling moment, yawing moment, and hinge moment influence coefficients

- Include aeroelasticity
  - control reversal
  - divergence

- Add non-equality constraints to optimization procedure

At present, WMFFIT computes only induced drag. The dominant coefficients in the induced drag matrix could be adjusted to account for viscous effects and the loss of leading edge suction. These semi empirical adjustments would most likely be valid only over a limited lift or angle of attack range, but would guarantee more realistic results in the prime region of interest.

Accurate determination of the induced drag associated with arbitrary load distribution is a nontrivial task. Improvements in accuracy over that achievable by the A372 concentrated trailing vortex model appears to be a realistic goal.

Flap deflection angles could be empirically adjusted to account for the loss in flap effectiveness at high deflection angles due to viscous effects.

The concepts employed by the present pitch trim method can be easily adapted to include roll and yaw, and to determine hinge moments.

Assuming the availability of a structures model, influence coefficients could be generated to fully account for aeroelastic effects. This would allow the assessment of control surface divergence and divergence.

At present, the optimization procedure accepts only equality constraints. Introduction of inequality constraints would further enhance the power of the method.

High-Lift Engine Aeroacoustics Technology (HEAT) Test Program Overview

Fanny A. Zuniga
Brian E. Smith
NASA Ames Research Center

presented at
High-Speed Research Program
Aerodynamic Performance Technology Workshop
February 25-28, 1997
NASA Langley Research Center
Hampton, VA

Outline

- Introduction
- HEAT 1 Test Overview
    - Objectives and Approach
    - Summary of Results
- HEAT 1A Test Overview
    - Objectives and Approach
    - Measurements and Test Techniques
- Additional Objectives to HEAT 1A Test
    - Large-Scale Geometric-Fidelity Objectives
- Summary

The outline of the presentation is as follows:
- Introduction
- HEAT 1 Test Overview
    - Objectives and Approach
    - Summary of Results
- HEAT 1A Test Overview
    - Objectives and Approach
    - Measurements and Test Techniques
- Additional Objectives to HEAT 1A Test
    - Large-Scale Geometric-Fidelity Objectives
- Summary

Introduction

Customers/Participants
NASA-Ames Research Center, Boeing, Douglas Aircraft Corp.,
Lockheed-Georgia, General Electric, NASA-Lewis Research Center

HEAT 40x80 ft. Wind-Tunnel Tests
- HEAT 1 Isolated Nozzle test
    - GE Gen 1 2-D mixer-ejector nozzle
    - Measured isolated aeroacoustic performance of nozzle
      for HEAT 1 Installed test
    - Summer '94

- HEAT 1 Installed Semi-Span Test
    - 13.5% Semi-Span Boeing Reference H model
    - Gen 1 2-D mixer-ejector nozzle
    - Feb. - May 1995

- HEAT 1A Isolated Nozzle test
    - GE Gen 1 2-D mixer-ejector nozzle

- HEAT 1A Installed Semi-Span Test
    - 13.5% Semi-Span Boeing Reference H model
    - Gen 1 2-D mixer-ejector nozzle

The NASA High-Speed Research program developed the High-Lift Engine Aeroacoustics Technology (HEAT) program to demonstrate satisfactory interaction between the jet noise suppressor and high-lift system of a High-Speed Civil Transport (HSCT) configuration at takeoff, climb, approach and landing conditions. One scheme for reducing jet exhaust noise generated by an HSCT is the use of a mixer-ejector system which would entrain large quantities of ambient air into the nozzle exhaust flow through secondary inlets in order to cool and slow the jet exhaust before it exits the nozzle. The effectiveness of such a noise suppression device must be evaluated in the presence of an HSCT wing high-lift system before definitive assessments can be made concerning its acoustic performance. In addition, these noise suppressors must provide the required acoustic attenuation while not degrading the thrust efficiency of the propulsion system or the aerodynamic performance of the high-lift devices on the wing. Therefore, the main objective of the HEAT program is to demonstrate these technologies and understand their interactions on a large-scale HSCT model.

The HEAT program is a collaborative effort between NASA-Ames, Boeing Commercial Airplane Group, Douglas Aircraft Corp., Lockheed-Georgia, General Electric and NASA - Lewis. The suppressor nozzles used in the tests were Generation 1 2-D mixer-ejector nozzles made by General Electric. The model used was a 13.5%-scale semi-span model of a Boeing Reference H configuration. The tests performed under the HEAT program are listed as follows:
- HEAT 1 Isolated Nozzle test
- HEAT 1 Installed Semi-Span test
- HEAT 1A Isolated Nozzle test
- HEAT 1A Installed Semi-Span test
All the tests were performed in NASA-Ames' 40- by-80 ft. Wind-Tunnel Facility.

First HEAT Entry (HEAT 1)
Installation effects from inboard mixer-ejector nozzle
- Nozzle mixer-ejector entrained-flow effects on high-lift system performance
- Aerodynamic effects on installed noise suppressor performance
- Wing and Trailing-Edge Flap pressures
- Mixer-ejector inflow distortion
- Acoustic signature
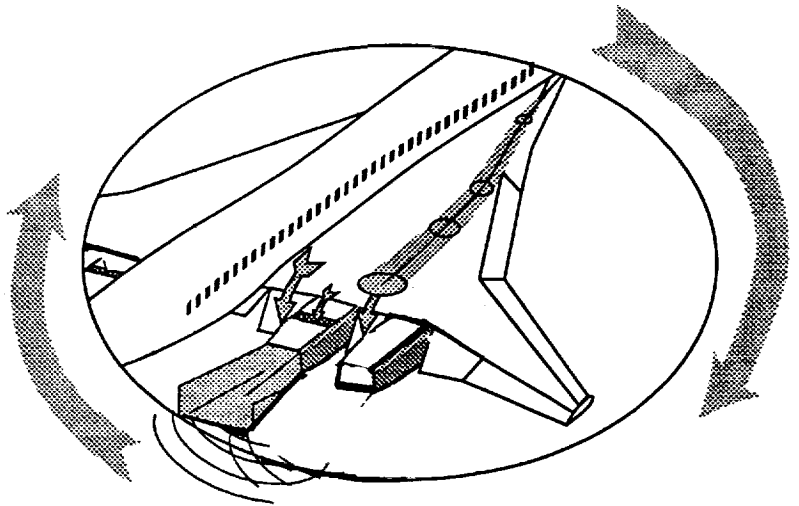
HEAT 1 Test Overview
HEAT 1 was the first entry of the 13.5% Boeing Reference H semi-span model. The model was equipped with an inboard jet flow simulator (JFS) and fitted with GE's 2D suppressor, mixer-ejector nozzles. The outboard station was configured with a flow-through nacelle. The JFS system was supplied with high-pressure air and heated with a propane/burner system that provided high-temperature flows and representative nozzle pressure ratios. The Hot-Aeroacoustic Model (HAM) nozzle was used for the hot-flow aeroacoustic runs. The Cold-Aerodynamic Model (CAM) nozzle was used for the cold-flow aerodynamic runs. Also the CAM nozzle was instrumented with a higher density of static pressures, total pressures and temperature gages than the HAM nozzle.

The purpose of the HEAT 1 test was to examine the installation effects of the mixer-ejector nozzles integrated with the wing high-lift systems. Both the effects of the airframe flowfield on the acoustic performance of the suppressor nozzle and the effects of the nozzle's secondary inlet flows on the aerodynamic performance of the wing high-lift systems were the primary focus of the investigation. In addition, the local flowfield over the wing and flaps was closely examined. Static pressure taps over the wing and flaps were used to study the leading-edge vortex trajectories and trailing-edge flap flows. Boundary-layer rakes upstream of the nozzle's secondary inlets provided a measure of mixer-ejector inflow distortion.

HEAT 1 Objectives and Approach

Test Objectives
- Determine installation effects on high-lift system performance and noise suppressor performance
- Overwing pylon fin effects
- Acoustic fatigue and cabin noise measurements
- Horizontal tail effectiveness and plume impingement

Approach
- Isolated test of suppressor nozzles
- 13.5%-scale semi-span model of Boeing HSCT Ref H configuration
- Inboard nacelle powered by propane-fueled jet flow simulator
- Outboard flow-through nacelle
- Traversing microphones and acoustic array

Schedule
- February - May 1995 (385 runs)

The objectives of the HEAT 1 test were as follows:
- Determine installation effects on high-lift system performance and noise suppressor performance
- Overwing pylon fin effects
- Acoustic fatigue and cabin noise measurements
- Horizontal tail effectiveness and plume impingement

The approach of the test consisted of first measuring the noise suppression of the nozzles in isolation and then integrating the nozzles on to the 13.5%-scale Boeing HSCT Ref H semi-span model. The inboard nacelle was powered by a propane-fueled jet flow simulator. The outboard station was fitted with a flow-through nacelle. Traversing microphones and an acoustic array were used to measure the near-field and far-field acoustic signatures.

The HEAT 1 test was performed during Feb-May 1995 and gathered data for 385 runs.

Summary of HEAT 1 Results

Key Aero-Performance Findings
- Beneficial Aero-Performance installation effect
    - Favorable effect on drag for most configurations
      (up to 20 counts at nominal conditions)

    - Positive increment on L/D varying from 0.3 to 0.15 DL/D
      at nominal conditions (3.6% to 1.8% of L/D at a=10°)

- Data repeatability was $\Delta CD=\pm0.0015$ and $\Delta L/D=\pm0.115$

- Local flowfield pressure data also revealed supporting evidence
  of this beneficial effect on aerodynamic performance

- Flow-visualizations tufts showed dramatic increase in flow angularity
  at outboard secondary inlet location for 10°<a<14°

Key Acoustics Findings
- 1 to 2.3 EPNdB installation effect
- Jet noise shows to be function of flap deflection

Summary of Results

The HEAT 1 test results showed a beneficial aerodynamic performance installation effect for most configurations. This beneficial effect showed a decrease in drag of up 20 counts and an increase in lift-to-drag ratio of 0.3 to 0.15 at nominal conditions. Further evidence of this beneficial effect on aerodynamic performance was supported by examination of the local flowfield pressure data. The installation effect on acoustic suppression showed a loss in suppression on the order of 1 to 2.3 EPNdB. A complete description of these results can be found in Brian Smith's et al paper entitled, "Summary of HEAT 1 Aeroacoustics Installation Effects", presented at last year's HSR Configuration Aerodynamics Workshop, Feb. 27-29, 1996.

Although the results of the test showed much evidence of a beneficial installation effect on aerodynamic performance, these results were hampered by the large uncertainties in the balance data. Repeat runs of the data showed uncertainties in the data of ±15 counts in drag coefficient and ±0.115 in lift-to-drag ratio. It was concluded that in order to verify the results of the first test, a second entry of HEAT model should be performed and the accuracy of the drag measurements should be improved. In addition, the flow-visualization tufts showed a dramatic increase in flow angularity at the outboard secondary inlet location for angles-of-attack greater than 10 deg. This increase in flow angularity could lead to greater installation effects at the outboard nacelle station. Therefore, it was justified that the installation effect at the outboard nacelle should be further examined during the second entry of the HEAT model.

Second HEAT Entry (HEAT 1A)
Installation effects from 2 mixer-ejector nozzles
• Nozzle mixer-ejector entrained-flow
  effects on high-lift system performance
• Wing and Trailing-Edge Flap pressures
• Mixer-ejector inflow distortion
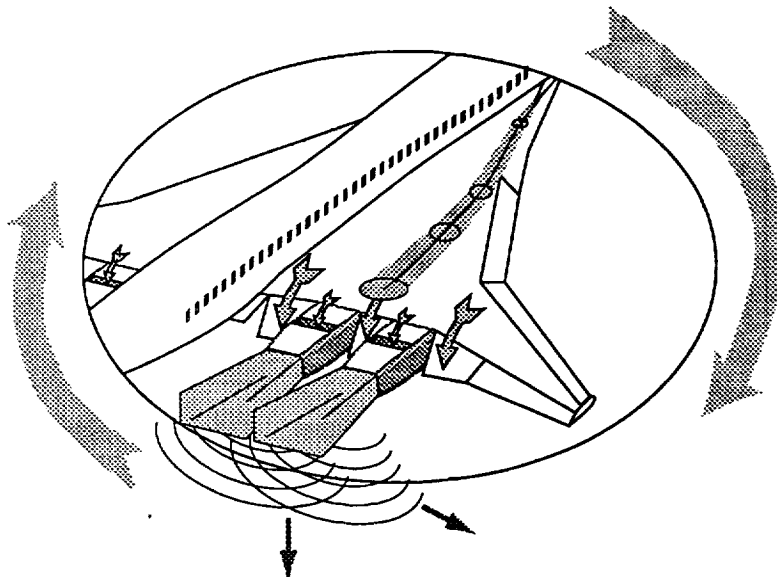
The second entry of the HEAT model or the HEAT 1A test will examine the installation effects from two mixer-ejector nozzles integrated with an HSCT wing and high-lift system. Similar to the first entry, the main purpose of the test is to determine the effects of the nozzle mixer-ejector entrained flow on aerodynamic performance. However, unlike the first test, there will be no acoustic measurements taken in this test. This was decided based on the lack of technical justification, program priority and budget limitations.

HEAT 1A Test Objectives

- Improve accuracy of drag/thrust measurements

- Evaluate high-lift performance increments due to jet flow entrainment from 2 powered mixer/ejector nozzles

- Determine the nozzle aerodynamic performance effects due to interactions between the high-lift system and jet suppressors

- Investigate the local flowfield in the vicinity of the secondary inlets to better understand the interactions between the two flowfields

- Measure hinge-moments on key high-lift system control surfaces

The objectives of the HEAT 1A test are as follows:
- Improve accuracy of drag/thrust measurements

- Evaluate high-lift performance increments due to jet flow entrainment from 2 powered mixer/ejector nozzles

- Determine the nozzle aerodynamic performance effects due to interactions between the high-lift system and jet suppressors

- Investigate the local flowfield in the vicinity of the secondary inlets to better understand the interactions between the two flowfields

- Measure hinge-moments on key high-lift system control surfaces

HEAT 1A Test Approach

Hardware
- Use existing image plane and HEAT 1 semi-span model

- Add a second jet flow simulator to the outboard station of the HEAT model

- Use existing HAM/CAM nozzle hardware at inboard and outboard stations, respectively

Measurement Accuracy
- Refurbish and re-calibrate model support system

- Repeat isolated nozzle thrust performance test of HAM/CAM nozzles to improve accuracy of thrust-removed L/D

- Add instrumentation to image plane to improve aero calibration (buoyancy, blockage and upwash)

- Improve test techniques (add more repeat runs, improve calibration techniques, etc.)

The approach of the HEAT 1A test will be similar to the first entry. The existing image plane, model and HAM and CAM nozzles will be used again in this test. The only change in hardware will be the addition of the outboard jet flow simulator and internal high-pressure air plumbing.

The isolated nozzle thrust performance test will be repeated to improve the accuracy of the thrust-removed lift-to-drag ratios. These lift-to-drag ratios are subtracted from the installed data to give give a net installation effect. Therefore, in order to improve accuracy on the net results, it is necessary to repeat the isolated test with the newly refurbished and re-calibrated model support system. In addition, the change in hardware for the outboard JFS system can also lead to changes in isolated thrust. Therefore, it is justified to repeat this test in an effort to improve accuracy as best possible.

In order to improve the aerodynamic calibration of the buoyancy, blockage and upwash of the test section, instrumentation will be added to the image plane and the calibration for the test section with the image plane will be recomputed. The overall test techniques for aerodynamic calibration and repeatability will also be improved in an effort to improve accuracy.

HEAT 1A Test Approach (cont.)

Systems
• Remotely actuate trailing-edge flaps

• Upgrade high-pressure system to deliver required mass flow rates for 2 JFS systems

Measurements
• Add boundary-layer rakes to outboard nacelle station

• Add hinge-moment instrumentation to outboard flap #3

• Add pressure taps to outboard flaps #3 and #4 to determine hinge-moments and evaluate spanwise loading

• Add five-hole probe to measure downwash angle at tail station during tail-off runs

Flow-Visualization
• Pressure-Sensitive Paint
• Fluorescent Mini-Tufts

There will be two systems added to the HEAT 1A test. These will include: (1) remote actuation of the trailing-edge flaps, and, (2) an upgraded high-pressure system to deliver required mass flow rates for the 2 JFS systems.

The measurements of this test will include all the existing instrumentation of the HEAT 1 test and additional instrumentation as follows:
- boundary-layer rakes on outboard nacelle
- hinge-moment instrumentation on outboard flap #3
- dense number of pressure taps on outboard flaps #3 and #4 to determine hinge-moments and evaluate spanwise loading
- five-hole probe at tail station to measure downwash angle during tail-off runs

Flow-visualization requirements will include the use of pressure-sensitive paint (PSP) and fluorescent mini-tufts. The PSP will be used as another technique to evaluate the hinge-moments on the outboard flaps and tail. PSP will also be applied over upper and lower surfaces of the wing along with the mini-tufts to examine the leading-edge vortex trajectories and trailing-edge flap flows.

Additional Test Objectives

Large-Scale Geometric-Fidelity Objectives
- Leading-Edge Hingeline Step and Gap Size Sensitivity Study
- Wing Crank Flap Gap Sensitivity Study
- Flap Edge/Nacelle Gap Study

Propulsion/Airframe Interaction Objective
- Main Engine Inlet Distortion Measurements

Additional test objectives are being proposed to be merged on to the HEAT 1A test. These objectives are being proposed by the High-Lift ITD team as a result of their survey with Tech Integration, Configuration Aero, Propulsion Airframe Integration and Environmental Impact ITD teams. This survey was conducted to determine what additional technical objectives can be met by large-scale testing and are needed by the technical community to reach the HSRP technology readiness level of 6. This survey was conducted as part of the 4 Engine Propulsion Airframe Integration Configuration (4EPIC) feasibility study. From these efforts, it was concluded that there was not enough technical and program justification for the 4EPIC test but that the program would merit technically by adding on more objectives to the HEAT 1A test.

As a result of this process, the following are a list of technical objectives that can potentially be added on to the HEAT 1A test. They can be categorized as large-scale geometric-fidelity objectives and propulsion/airframe interaction objectives as listed below:

Large-Scale Geometric-Fidelity Objectives
- Leading-Edge Hingeline Step and Gap Size Sensitivity Study
- Wing Crank Flap Gap Sensitivity Study
- Flap Edge/Nacelle Gap Study

Propulsion/Airframe Interaction Objective
- Main Engine Inlet Distortion Measurements

Leading-Edge Hingeline Step and Gap Sensitivity Study

Objective
Determine sensitivity of configuration L/D to details of the leading-edge hingeline geometry especially for outboard wing

Approach
- Generate geometry of representative leading-edge hinge line
- Fit thin upper surface gloves to the leading edge of the wing
- Gather baseline data for smoothly, faired flap-to-wing surface
- Test at two different step sizes
- Obtain aeroperformance data at constant JFS power level and at Re number sweeps and alpha sweeps

Requirement

Determine the sensitivity of configuration L/D to the details of the leading-edge hingeline geometry especially for the outboard wing panel. Maintaining flow attachment on the upper surface may be critical to the outboard wing panel. Vortical structures and local flow separations arising from chordwise leading discontinuities at the hinge line may significantly affect the overall high-lift performance and the flow on the outboard wing panel.

Approach

The geometry of representative leading-edge hinge line details on the upper surface will be generated in consultation with industry flap kinematics and structures personnel. Thin upper surface gloves will be fitted to the leading edge of the wing so that the model can be tested with two step sizes in addition to a smoothly faired, idealized flap-to-main-wing panel surface. If hinged flaps are fabricated for the model, it may be possible to evaluate the effects of gap flows between the slat and main element. L/D and drag polar runs will be made in each configuration at a constant jet-flow simulator (JFS) power level. Since Reynolds number may effect these results, alpha sweeps will be made at a variety of tunnel airspeeds.
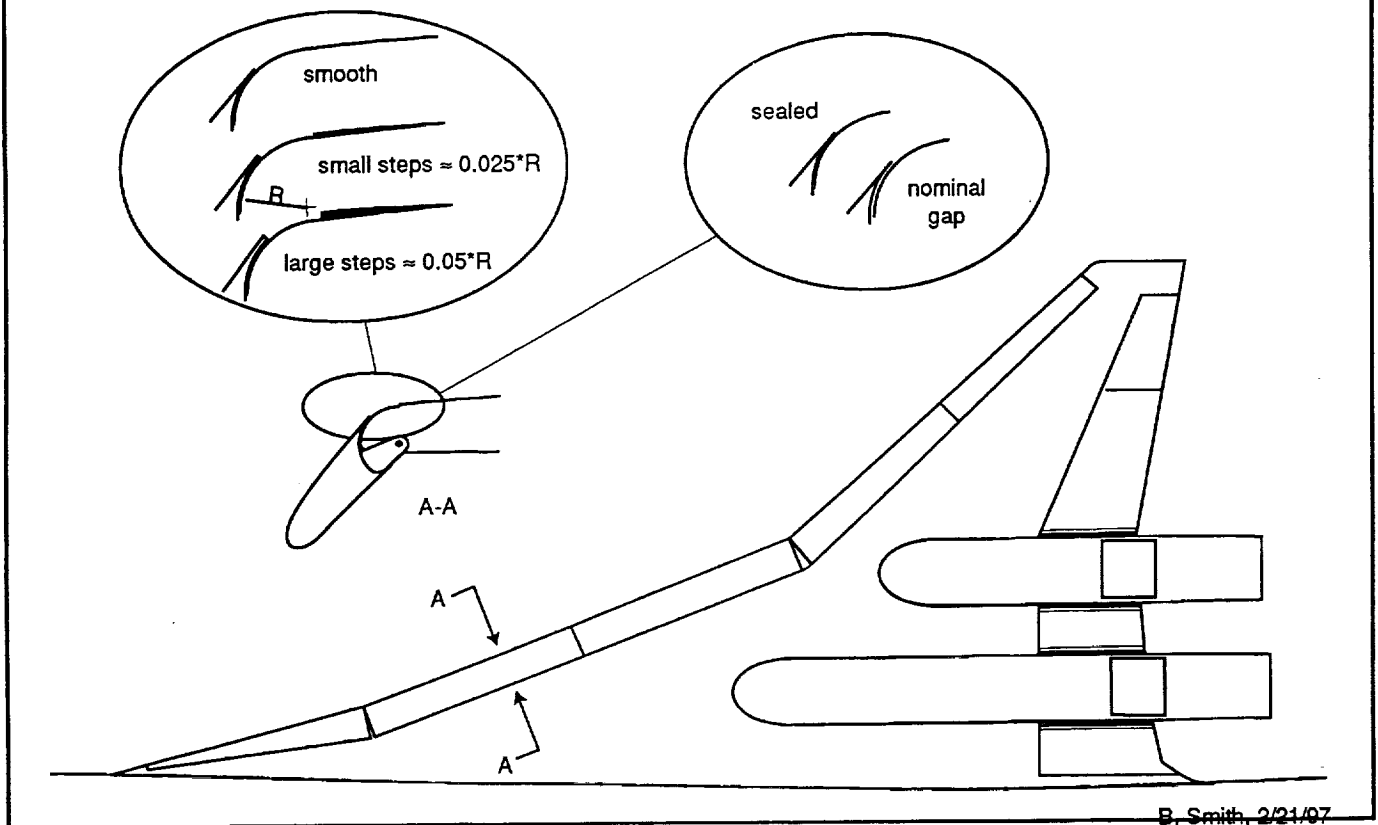
Figure 1 - Leading Edge Hingeline Geometry Effects

Figure 1 above illustrates the HEAT wing planform and the step and gap areas to be examined during the leading-edge hingeline step and gap size sensitivity study. The sizes shown are potential sizes to be tested.

CFD Support Activities

The Low-Speed Aerodynamics Branch here at Ames is working closely with the Applied Computational Aerodynamics Branch to define basic CFD research using generic swept-wing configurations to investigate step (forward- and aft-facing) and cavity effects on curved, accelerating flow fields characteristic of realistic leading edge flap/slat hingeline geometries. Figure x depicts candidate geometries for this area. It is felt that calculations using simplified geometries will provide insight to the physics of these types of flows and will develop CFD technologies applicable to HSCT-class vehicles.

Wing Crank Flap Gap Sensitivity Study

Objective
Evaluate changes in high-lift performance due to effects from leading edge flap-to-flap gaps and discontinuities along span

Approach
- Simulate geometry of the flap-to-flap interface at the wing crank junction
- Test with a smoothly faired, idealized juncture
- Test with simulated "production" gap fairing geometry
- Test with completely unported geometry
- Obtain aeroperformance data at constant JFS power level

Requirement

Evaluate changes to high-lift performance and vehicle drag due to vortical structures and local flow separations arising from leading edge flap-to-flap gaps and discontinuities which exist along the span where the sweep angle changes.

Approach

Accurate modeling of the spanwise discontinuities can be achieved with the large-scale HEAT IA model. An attempt will be made to simulate the geometry of the flap-to-flap interface at the wing crank junction between the inboard and outboard wing panels. This geometry will be generated in consultation with industry flap kinematics and structures engineers. The model will be tested with 1.) the simulated "production" gap fairing geometry, 2.) a smoothly faired, idealized juncture, and 3.) a completely unported geometry which may produce the worst-case performance. In addition to documenting the crank gap effect, candidate mechanization and fairing schemes can be evaluated with the model if the individual leading edge flaps are each hinged separately. L/D and drag polar runs will be made in each configuration at a constant jet-flow simulator (JFS) power level.

**HEAT IA Wing Crank
Flap Gap Sensitivity Study**

**Effect of gaps/fillers arising between adjacent
flap elements due to finite thickness**

hinged
filler wedge

B-B

B

B

B. Smith, 2/21/97
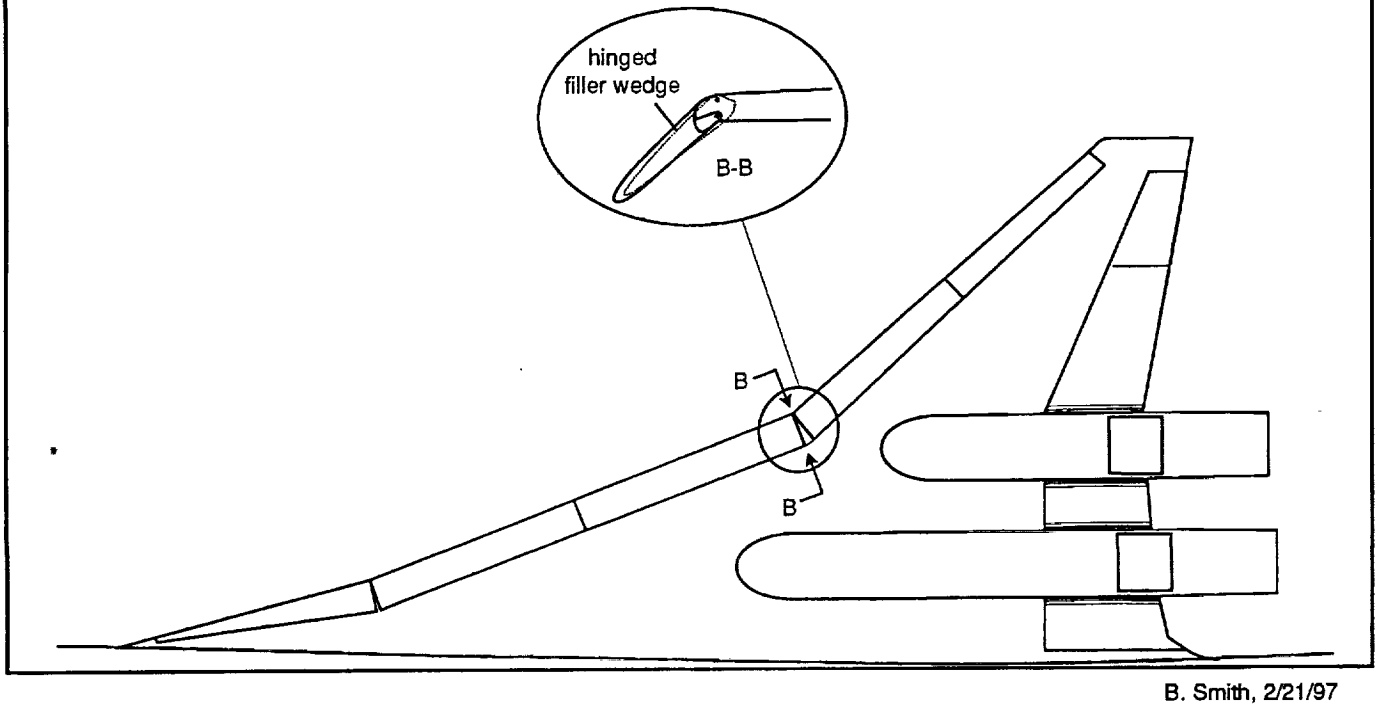
Figure 2 - Effect of Spanwise Discontinuities Along Leading Edge.

Figure 2 above highlights the area to be examined in the wing crank flap gap sensitivity study. The size of the gap in this area will be adjusted to determine the effects of gaps/fillers between these adjacent flap elements.

CFD Support Activities

NS calculations of the full HEAT IA geometry may be able to include studies of the flap-to-flap gap effects. Figure x depicts candidate geometries for this area of the vehicle.

Flap Edge/Nacelle Gap Study

Objective
- Determine sensitivity of configuration L/D to the sizes of gaps between trailing-edge flap edges and nacelles
- Determine critical gap size

Approach
- Use spacer plates between flap edges and nacelle to adjust gap sizes for three inboard flaps
- Obtain aeroperformance data at JFS power level sweeps

Requirement

Determine the sensitivity of configuration L/D to the size of gaps between the streamwise edges of the trailing-edge flaps and vertical sidewalls of the adjacent nacelles. The overall high-lift performance may be significantly degraded and vehicle drag may increase when these gaps are above a certain size. Determining this critical gap size will be crucial to design of candidate high-lift systems for the Technology Configuration.

Approach

The trailing-edge flaps of the HEAT model were designed with this type of system performance study in mind. Thin plates can be bolted to the streamwise edges of the inboard three flaps to produce gaps of various sizes. The configuration tested during the first HEAT entry used a set of plates which produced a minimal gap. L/D and drag polar runs will be made in each gap configuration at a constant jet-flow simulator (JFS) power level. Because of the close proximity of the flap edges to the suction of the ejector suppressor nozzle inlets, it will be instructive to perform some NPR sweeps with the various gap sizes at constant angle of attack and airspeed.

HEAT IA Flap Edge/Nacelle Gap Study

spacer plates providing
reductions of 2.5, 5 & 10%
of local flap span
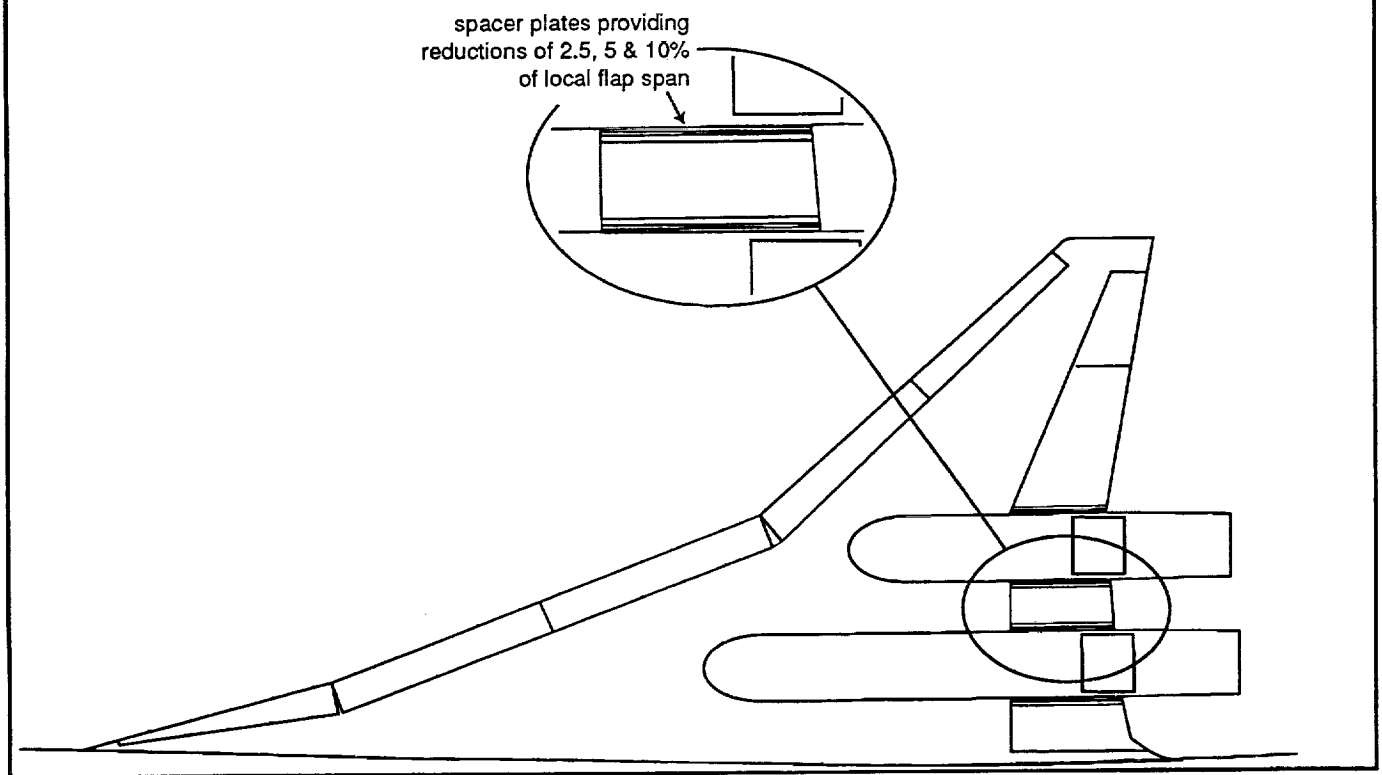
B. Smith, 2/21/97

Figure 3 - Effects of Flap Edge/Nacelle Gaps_

Figure 3 above highlights the area to be examined in the flap edge/nacelle gap study. Spacer plates will be used to adjust the gaps between the flap edges and nacelle walls to determine the effect of these gaps.

CFD Support Activities

A basic building block approach using generic, simplified configurations will be used to determine the incremental effects on lift and drag of the gaps between streamwise flap edges and adjacent vertical nacelle surfaces. The attached figure depicts candidate geometries for this area. The principal CFD investigator at Ames, Ching-Mao Hung, who will be working the HEAT IA problem feels that generic research on this topic will generate technology which can be applied not only to HSRP configurations but also to other aerodynamic problems. The full NS calculations using the complete HEAT IA geometry may be able to investigate these gap effects for select configurations:

Main Engine Inlet Distortion Measurements

Objective
Measure total pressure deficits and flow angles at the inboard and outboard main engine inlet

Approach
- Add 5-hole probe rake arrays upstream of the main engine inlets
- Replace JFS nacelles with flow-through nacelles
- Obtain total pressure and flow angularity distributions at varying angle of attack, airspeeds and leading-edge flap deflections

Requirement

Distortion levels at the location of the main engine inlets due to cross flow on the lower surface of the wing at low-speed, high-alpha, high leading-edge flap deflection conditions may be significantly greater than at the cruise design point. The objective of this investigation will be to measure total pressure deficits and flow angles in a plane at the location of the inboard and outboard main engine inlets.

Approach

Detailed mappings of the total pressure and flow angularity distributions at the locations of the main engine inlets will be made using either a fixed or traversing array of five-hole probes. Flow-through nacelles will be fabricated for use during this portion of the test. The powered nacelle interface with the wing will be redesigned to accept the flow-through nacelles. Surveys of the flowfield at the inlet faces will be made at a variety of angles of attack, airspeeds and leading edge flap deflection angles.

HEAT IA Main Engine Inlet Distortion Measurements

flow-through nacelles

5-hole probe rake arrays
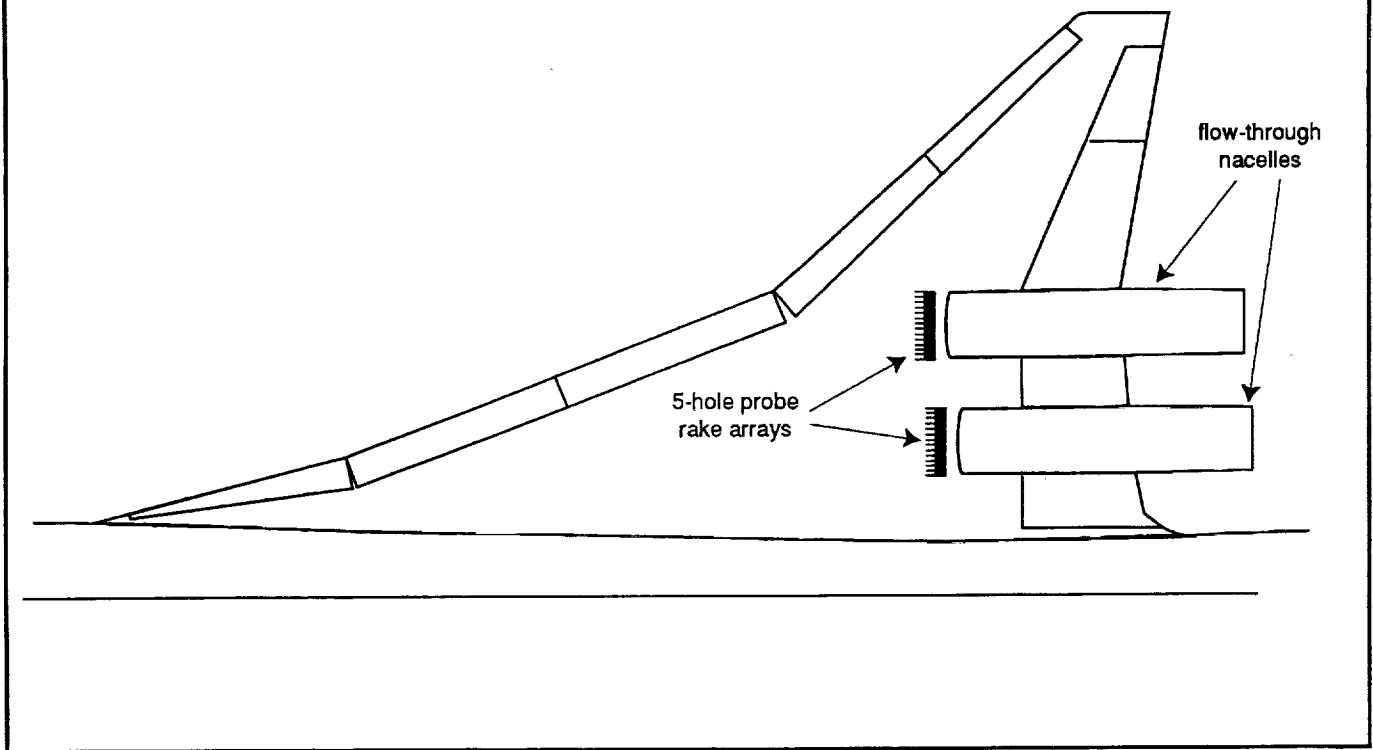
B. Smith, 1/16/97

Figure 4 - Main Engine Inlet Exterior Flowfield Assessments_

Figure 4 above shows the approximate location for the 5-hole probe rake arrays to be added to measure the flow angularity and total pressure deficits at the inboard and outboard main engine inlets.

CFD Support Activities

It may be possible to utilize the NS calculations of the full HEAT IA configuration to predict first-order flow angularities and total pressure deficits downstream of the deflected leading edge flaps with the model at the low angles of attack which might be expected to generate distorted main engine inlet flows.

Summary

- HEAT 1A main objectives and approach have been set

- Measurements and Test Techniques have been reviewed to give improved accuracy on drag/thrust measurements

- Additional large-scale geometric-fidelity objectives are being merged into HEAT 1A test plan where advantageous to program

- Additional Propulsion/Airframe Interaction objective(s) are being examined as potential HEAT 1A objectives

In summary, the justification and motivation for the HEAT 1A test has been presented. The objectives and approach for this test has been reviewed along with the measurements and test techniques to be used in the HEAT 1A test. The importance of improving the accuracy of the drag/thrust measurements for this test was also explained and justified.

The potential additional objectives to be merged in with the HEAT 1A test objectives were presented. The additional objectives were categorized as large-scale geometric-fidelity objectives and propulsion/airframe interaction objectives. These additional objectives are still being reviewed and therefore, the final decision to incorporate them into the test is still pending completion of the review process.

NUMERICAL STUDY OF THE REYNOLDS NUMBER EFFECT AND BOUNDARY LAYER TRANSITION LOCATION EFFECT

Anthony J. Saladino
Dynacs Engineering Co., Inc.
Renton, WA 98055

This presentation summarizes the effects of Reynolds number and boundary layer transition between wind tunnel data and CFD solutions. Computations for a Ref. H wing/body configuration with flaps deflected LE 30°/outboard TE 20° were analyzed for two Reynolds numbers and one trip location. This study will focus on a single Mach number, angle of attack and flap setting to assess the predictive capabilities of CFD. Results are shown for Mach 0.3 and alpha 10 degrees.

The first part of this study evaluated the TNS3DMB CFD code for capturing the influence of Reynolds number variations. Wind tunnel measurements were made in the NTF at chord Reynolds numbers of 30 million and 90 million. Pressure data from NTF test 057 at various spanwise and chordwise stations are compared with CFD; aerodynamic coefficient data from NTF test 060 are compared with CFD.

Based upon the results from the Reynolds number study, it was concluded that there was a need to understand the influence of boundary layer transition effects on the aerodynamic coefficients. Data from NTF test 080 was used to compare with TNS3DMB at a chord Reynolds number of 21.6 million. Comparisons were made with NTF tests without and with trips, and with CFD runs at fully turbulent conditions and with the wing tripped at the leading edge hinge line.

Additional results obtained from CFD include surface plots of pressure coefficient, Y^+, C_f, and velocity vectors.

Two gridding approaches were used to generate the grid. In the first approach Gridgen9.6 was used to construct the surface grid. The transfinite interpolation (TFI) and elliptic smoothing that was used to construct the surface grid did not allow the grid points to be constrained to the data base; projection of the surface grid back to the database was accomplished with GridTool. A single volume grid was developed for both Re = 30 million and Re = 90 million by using a wall spacing of 0.0003 inch. For grid orthogonality and spacing at the surface, thirteen elliptic volume grids were made with 3DGRAPE, with mismatched-point interfaces. There were a total of 3,154,013 points in the grid with an H-H topology, capable of three levels of multi-grid.

The surface grids for six of the thirteen blocks on the outboard wing are shown. The grid density is greater around the leading and trailing edges, as well as around the hinge lines. The 13-block volume grid would model the geometry in accurate details but it also required a great deal of effort.

Dynacs Engineering Co., Inc.

2278

Ref. H, W/B, Flaps LE 30/Outboard TE 20
Surface Grid for 13–Block Grid

LE hinge line

flow–through

TE hinge line

flow–through

Dynacs
ENGINEERING CO. INC.

2279
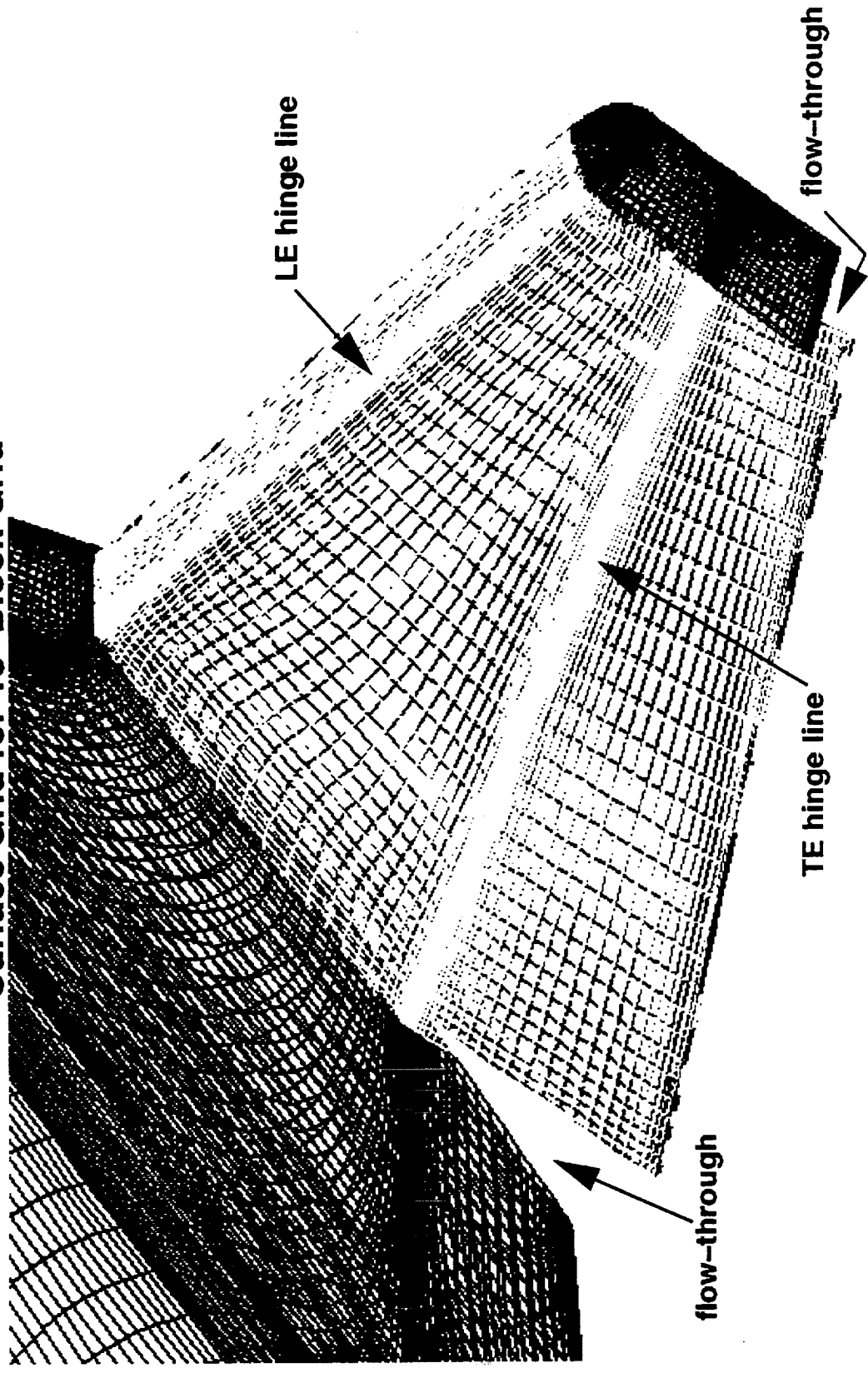
When it became apparent that the flow time was too long, not only for the current task but also for all possible future tasks, a different gridding approach was taken. In the second approach Boeing generated two 4-block volume grids in batch mode, one for Re of 90 million and the other for Re of 30 million. The surface grid was constructed with the BCAG Aero Grid and Paneling System (AGPS). Solid webs connect the side edges of the trailing edge flap, treated in the same way as in 1995. The grid density is greater around the leading and trailing edges, as well as around the hinge lines. The grid spacing near the wall was scaled by the Reynolds number. An H-H grid topology was used with matched-point interfaces for a total of 3,600,652 grid points. Three levels of multi grid were built into the grid.

Dynacs Engineering Co., Inc.

Ref. H, W/B, Flaps LE 30/Outboard TE 20
Surface Grid for 4–Block Grid

LE hinge line

no flow–through

TE hinge line

no flow–through

(red=upper block, green=lower block)

Dynacs
ENGINEERING CO. INC

2281
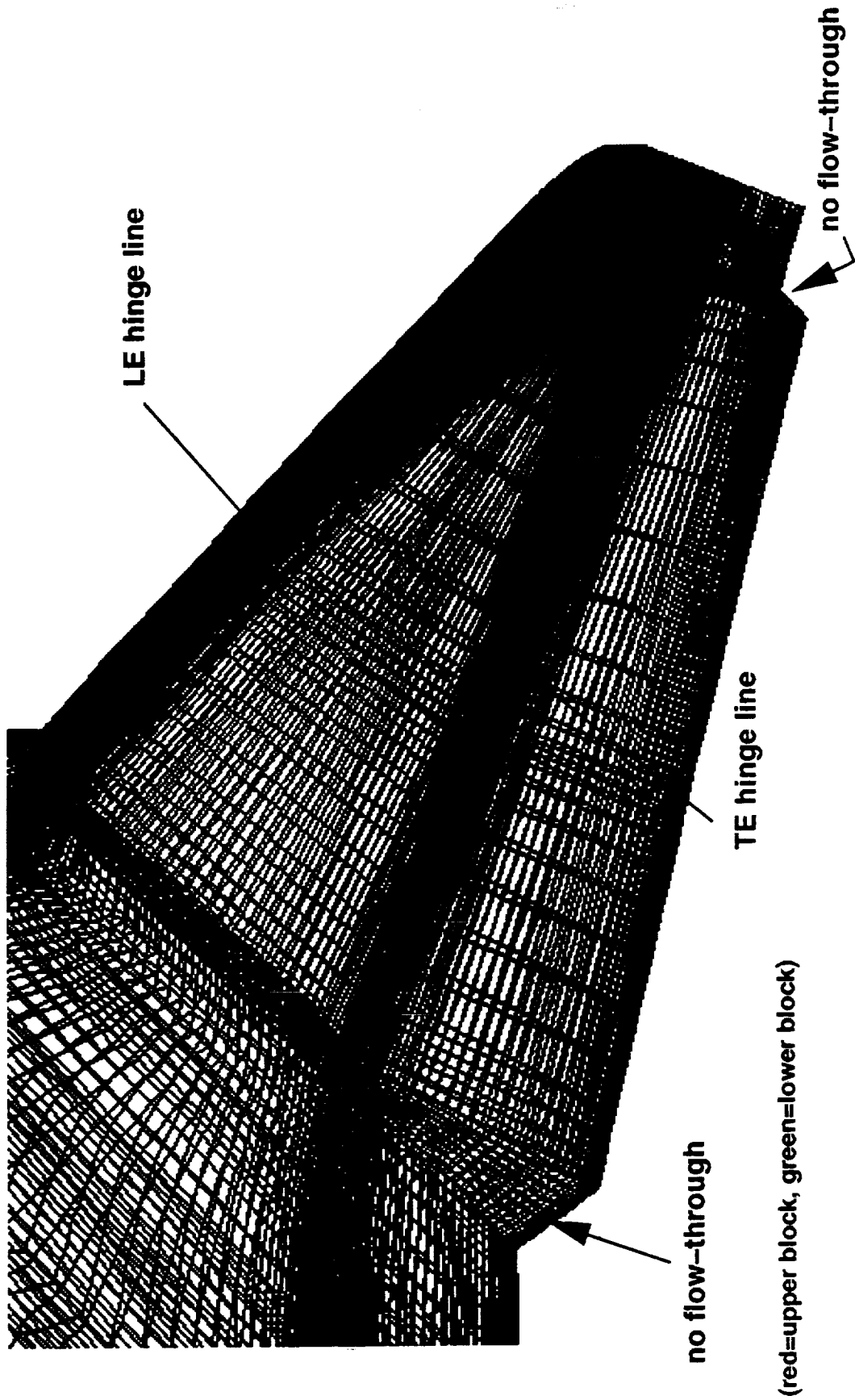
The NTF model is a 2.2% scale of the Ref. H configuration with the TE slightly modified near the body side. The model has several hundred ports distributed on the wing, the fuselage and the nacelle. However, there are five pressure lines that cross the balance, making the force data taken during a pressure run somewhat inaccurate. Hence, force data from Test 060 are used where the pressure lines were cut off during the force runs. The model was not tripped during either of the tests.

The dynamic head q is 817 psf for 30M Reynolds number and 843 psf for 90M. The aeroelastic effect should be small.

Flap deflection angles were the same for both the wind tunnel model and the CFD model, with the exception that the inboard TE flaps were also deflected in the NTF. These NTF test results were chosen in the hope of capturing the transition increments.

Dynacs Engineering Co., Inc.

2282

NTF WIND TUNNEL DATA SOURCES

- Forces and moments
  - Test 060, Runs 129-134 (Re 30M)
  - Test 060, Runs 166-169 (Re 90M)
- Surface pressures
  - Test 057, Run 112 (Re 30M)
  - Test 057, Run 102 (Re 90M)
- Flaps LE 30 deg/ TE 20 deg

Dynacs Engineering Co., Inc.

A TNS3DMB solution was obtained on each of two separate 4-block grids, one for each Reynolds number. Each solution was obtained for the HSCT wing/body, with flap settings of 30° along the leading edge and 20° on the outboard trailing edge, a Mach number of 0.3 and α of 10°. The Spalart-Allmaras turbulence model was used in both cases, and the solutions were obtained for fully turbulent flows. Scalar dissipation was used to attain convergence with three levels of multi-grid. A fully converged solution was obtained by monitoring the residual and the aerodynamic coefficient histories; the viscous drag was the last variable to converge.

In 1995 it was found that matrix dissipation caused the flow to behave erratically when used to initialize the computations. A test case was tried this year in which matrix dissipation was switched on for 50 iterations after the viscous drag had converged with scalar dissipation; the result was that the viscous drag decreased by 0.0005 in magnitude, but the residual increased. Instead of testing for the optimum scalar/matrix dissipation scheduling, and to be consistent with results generated previously, the TNS3DMB solutions were run with scalar dissipation.

Comparisons between CFD and the NTF data are made whenever possible.

Dynacs Engineering Co., Inc.

FLOW CONDITIONS AND CFD SPECIFICS

- Mach 0.3
- Alpha 10 Deg
- Flaps LE 30 deg/outboard TE 20 deg
- Re 30 M and 90 M based on mean aerodynamic chord
- Viscous TNS3DMB: fully turbulent
- Spalart-Allmaras turbulence model

Dynacs Engineering Co., Inc.

2285

Convergence histories of the TNS3DMB runs are presented for both Re of 30 million and Re of 90 million. Three levels of multi-grid were used to speed up the solution convergence. The average (dr/dt) was reduced by 2.5 orders of magnitude, where better error reduction is achieved for the lower Reynolds number. The reduction in average (dr/dt) became very slow after 300 iterations.

Dynacs Engineering Co., Inc.

Ref. H, W/B, Flaps LE 30/Outbd TE 20, Mach 0.3, Alpha 10 Deg Viscous TNS3DMB, Re 30 M (solid lines) and Re 90 M (dashed lines)

Dynacs Engineering Co., Inc
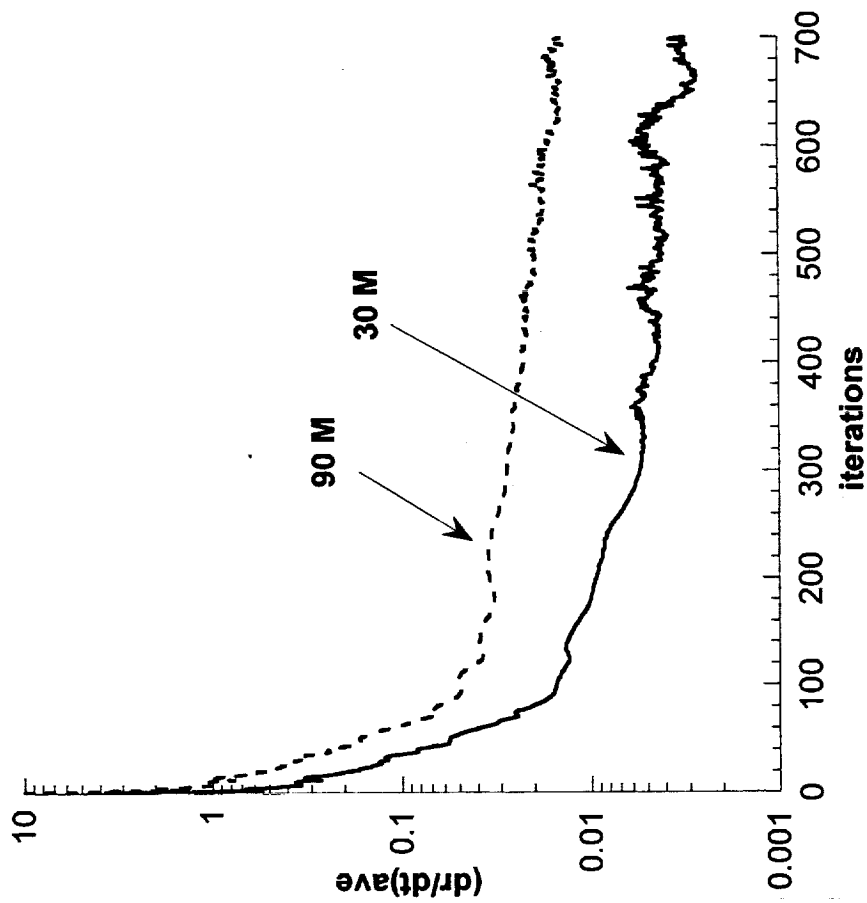
The C_L convergence history is shown for both Re of 30 million and 90 million. The change in C_L from 400 iterations to 700 iterations is approximately 1%.

Dynacs Engineering Co., Inc.

Ref. H, W/B, Flaps LE 30/Outbd TE 20, Mach 0.3, Alpha 10 Deg
Viscous TNS3DMB, Re 30 M (solid lines) and Re 90 M (dashed lines)

Dynacs Engineering Co., Inc
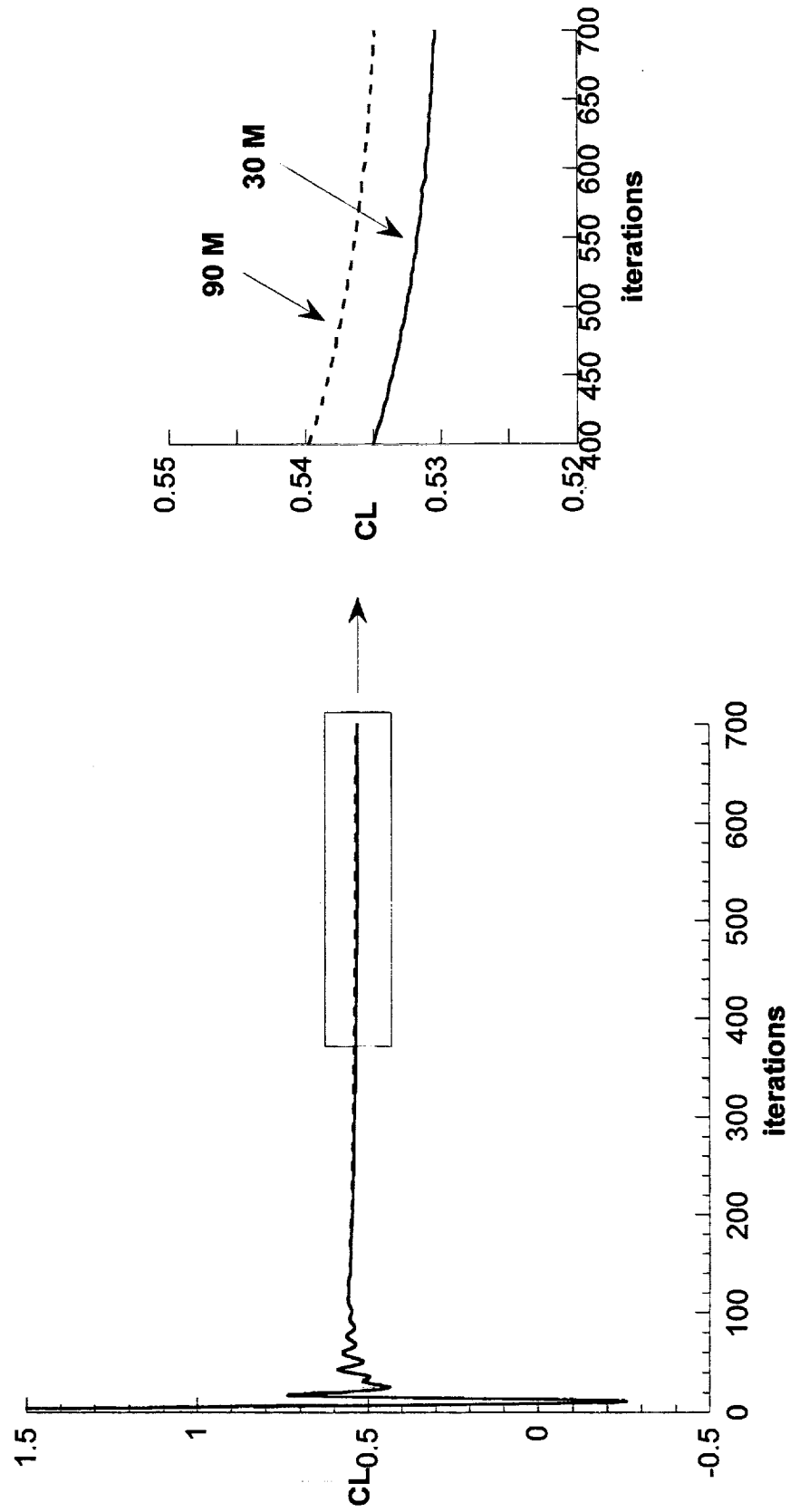
The drag convergence history is displayed for both the components and the total. The presure drag reached a stable level sooner than the viscous drag. The changes in viscous drag coefficient are on the order of 0.0013 for 30M Reynolds number and 0.0016 for 90M. They are not small numbers. This points out the need to find a means to accelerate the convergence. Both the viscous and the pressure drag are smaller for the larger Reynolds number ($C_{DP\_Re\_30M} = 0.05934$, $C_{DP\_Re\_90M} = 0.05108$).

Ref. H, W/B, Flaps LE 30/Outbd TE 20, Mach 0.3, Alpha 10 Deg
Viscous TNS3DMB, Re 30 M (solid lines) and Re 90 M (dashed lines)

2291
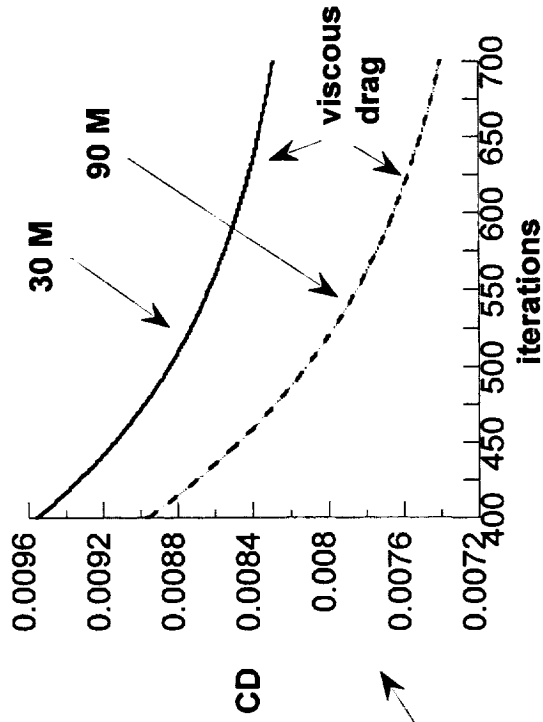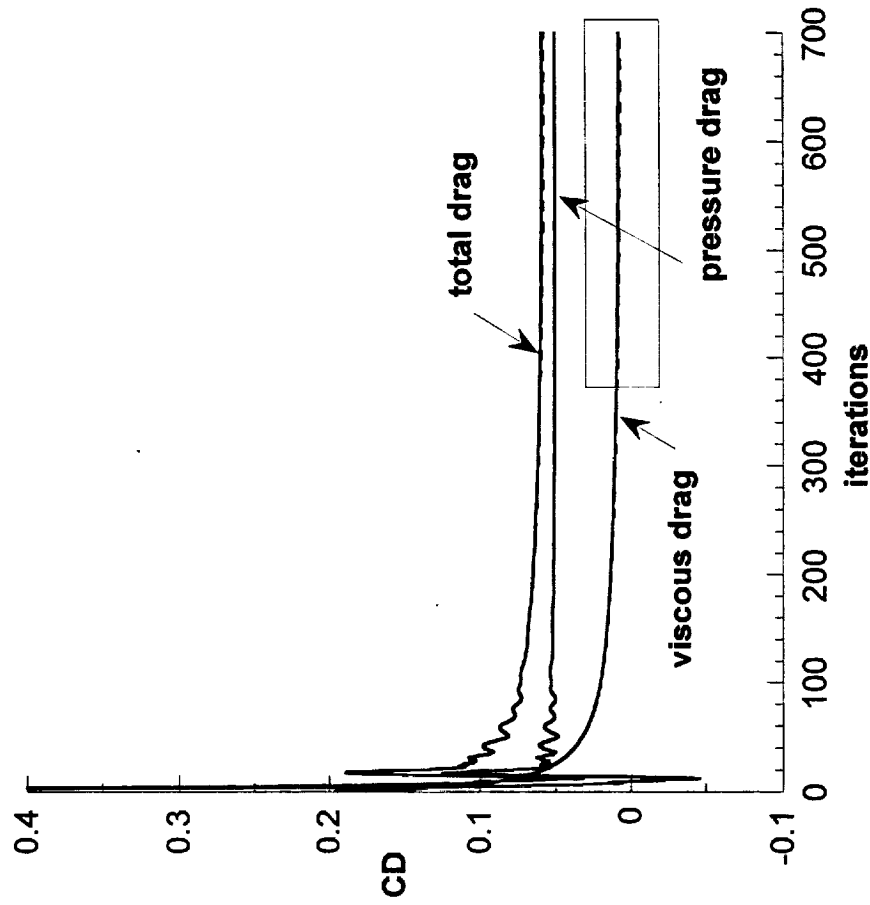
The C_M convergence history for Re of 30 million and 90 million is presented. The change in C_M from 400 iterations to 700 iterations is 0.001, which translates into 0.2° of stabilizer angle, which is not too significant.

Ref. H, W/B, Flaps LE 30/Outbd TE 20, Mach 0.3, Alpha 10 Deg Viscous TNS3DMB, Re 30 M (solid lines) and Re 90 M (dashed lines)

Dynacs Engineering Co., Inc

2293
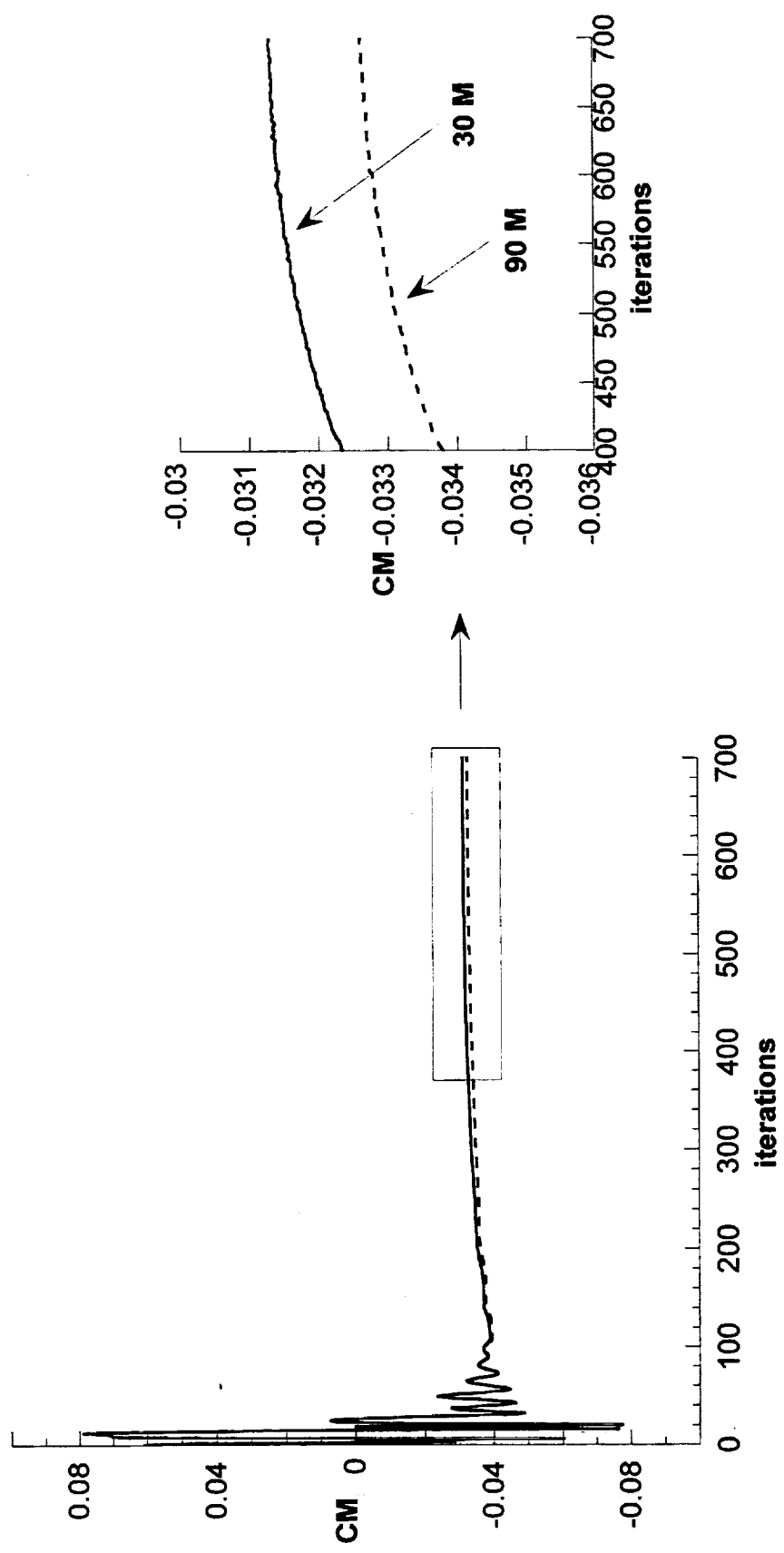
Repeat runs are shown to form tight bands.

The CFD results are for all-turbulent flows while there may be some laminar flows in the NTF, especially for 30M Reynolds number. It is conceivable that there are more flow separations in NTF for 30M Reynolds number than in CFD. That would account for the rather large lift difference between CFD and NTF for 30M Reynolds number. The small difference between CFD and NTF for 90M Reynolds number is about what to be expected. As a result, the measured change in C_L due to the change in Reynolds number is much larger than the computed value.

Dynacs Engineering Co., Inc.

2294

Ref. H, W/B, Flaps LE 30/Outbd TE 20, Mach 0.3, Alpha 10 Deg Viscous TNS3DMB (symbols), NTF Test 060 (lines)

Dynacs Engineering Co., Inc

2295
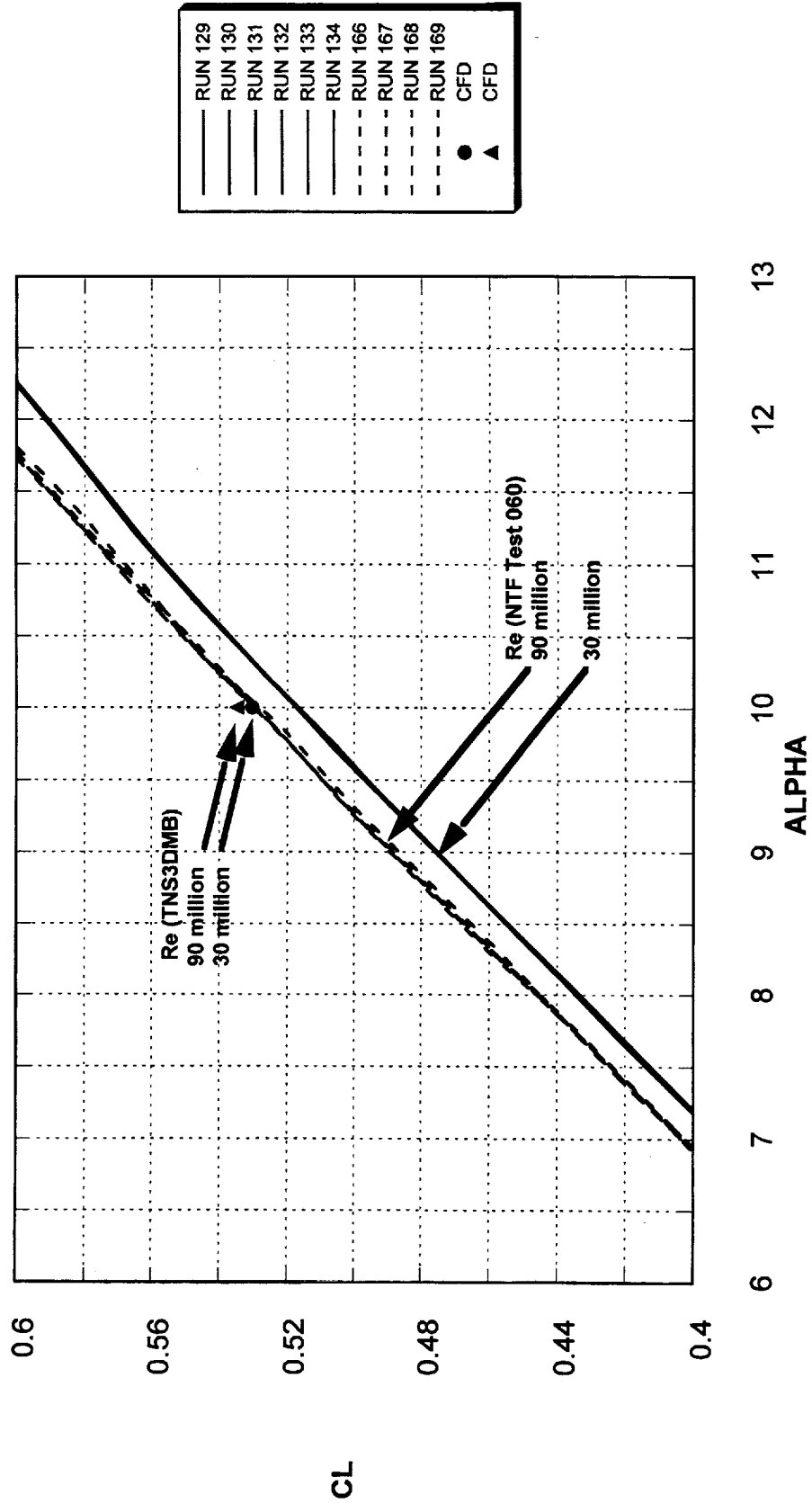
Again, the repeat runs in NTF form tight bands. CFD missed the absolute level of C_D but it captured the increment between 30M and 90M Reynolds number. In the CFD runs, greater drag occurs for the lower Reynolds number, consistent with the NTF results.

Dynacs Engineering Co., Inc.

Ref. H, W/B, Flaps LE 30/Outbd TE 20, Mach 0.3, Alpha 10 Deg
Viscous TNS3DMB (symbols), NTF Test 060 (lines)

RUN 129
RUN 130
RUN 131
RUN 132
RUN 133
RUN 134
RUN 166
RUN 167
RUN 168
RUN 169
CFD
CFD

Re (TNS3DMB)
90 million
30 million

Re (NTF Test 060)
90 million
30 million

CL

CD
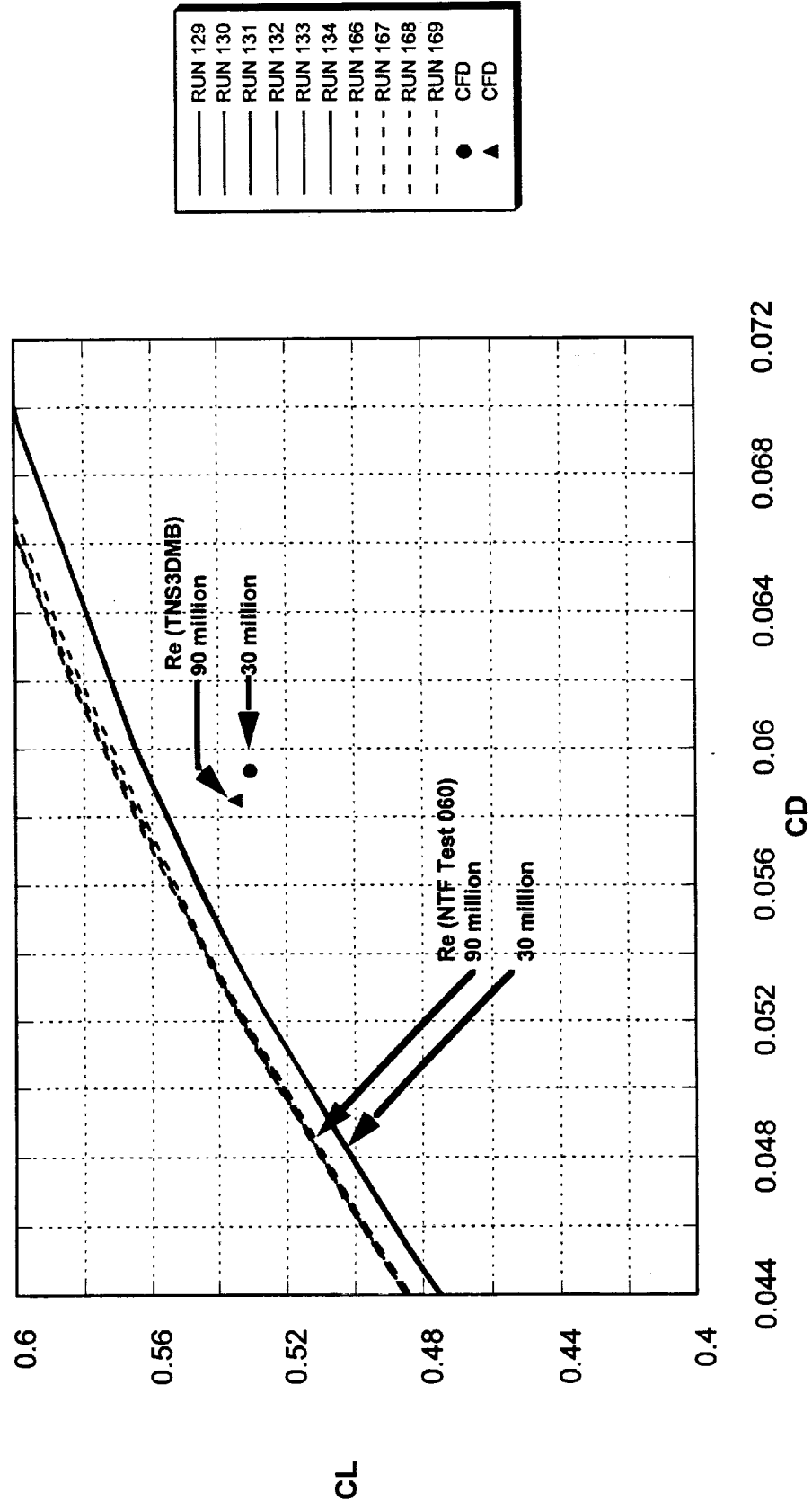
Again, the repeat runs in NTF form tight bands. CFD missed the absolute level of C_M but it captured a portion of the increment between 30M and 90M Reynolds numbers. A change of 0.005 in C_M is equivalent to a 1° deflection in the horizontal stabilizer for Ref. H. Both the NTF data and the CFD solutions predict more pitch-up at the lower Reynolds number.

Ref. H, W/B, Flaps LE 30/Outbd TE 20, Mach 0.3, Alpha 10 Deg
Viscous TNS3DMB (symbols), NTF Test 060 (lines)

Re (TNS3DMB)
90 million
30 million

Re (NTF Test 060)
90 million
30 million

RUN 129	
RUN 130	
RUN 131	
RUN 132	
RUN 133	
RUN 134	
RUN 166	
RUN 167	
RUN 168	
RUN 169	
CFD	●
CFD	◄

CL
CM

Dynacs Engineering Co., Inc

2299
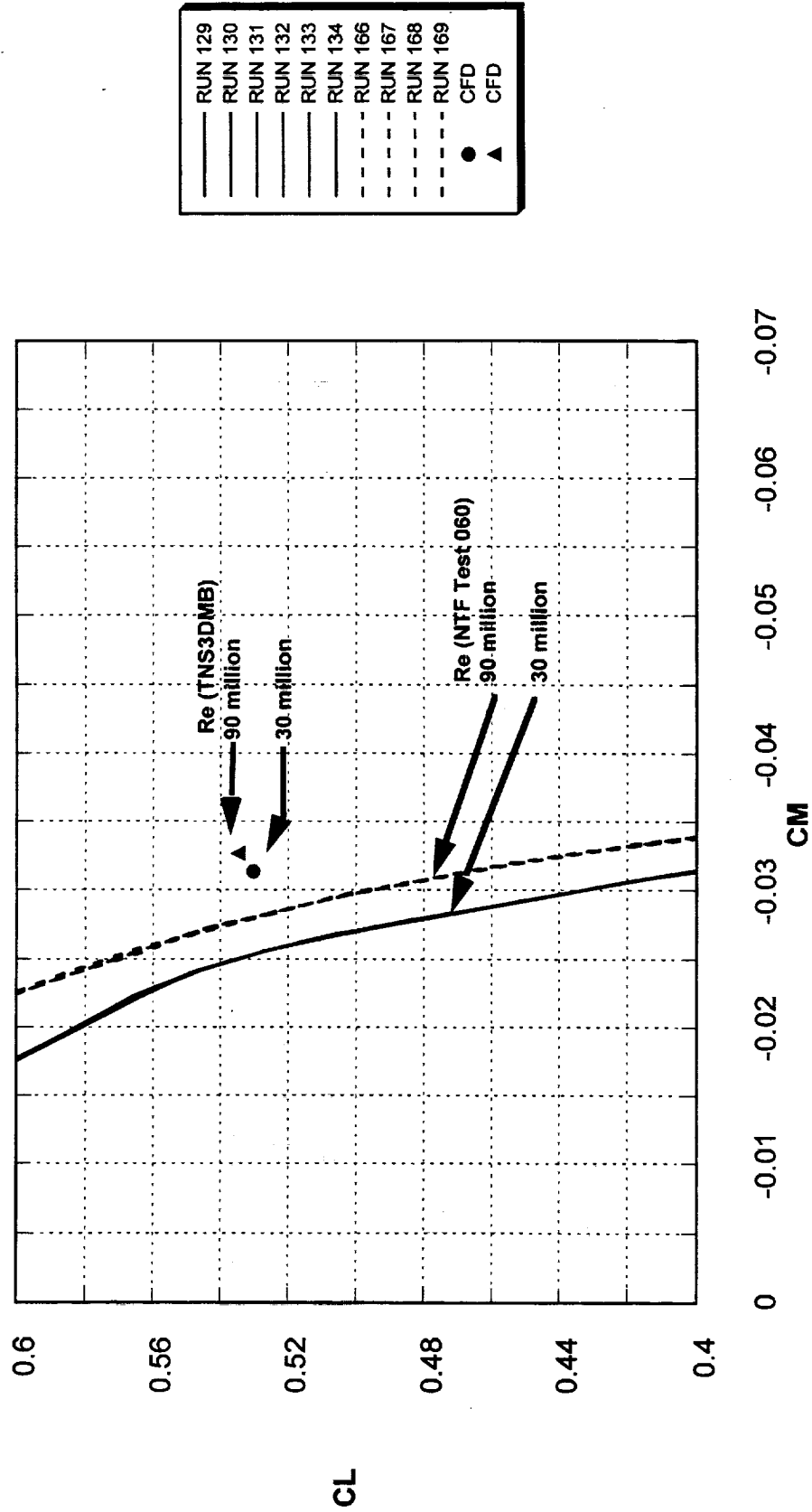
The comparison between CFD and NTF shows some differences at the first station. The mismatch of C_P near 2y/b of 0.8 could be caused by any of the following:

- geometry definition
- grid density
- vortex started from the planform break just upstream of this station
- turbulence model

The code captured one of the leading edge peaks well at the second station. There are some mismatches on the upper surface around 2y/b=0.82. The code generated a local peak where the hinge line is, indicating the flow is still attached. The test data indicated that a vortex could have formed from the leading edge planform break and the core travels downstream not along the hinge line. See also the previous figure.

The mismatch on the lower surface near 2y/b=0.74 for the right plot is caused by a leaky pressure port. The C_P there is zero for both 30M and 90M Reynolds numbers.

Dynacs Engineering Co., Inc.

2300

Ref. H, W/B, Flaps LE 30/Outbd TE 20, Mach 0.3, Alpha 10 Deg, Re 30 M
Viscous TNS3DMB (lines), NTF Test 057, Run 112 (symbols)

Dynacs Engineering Co., Inc

2301
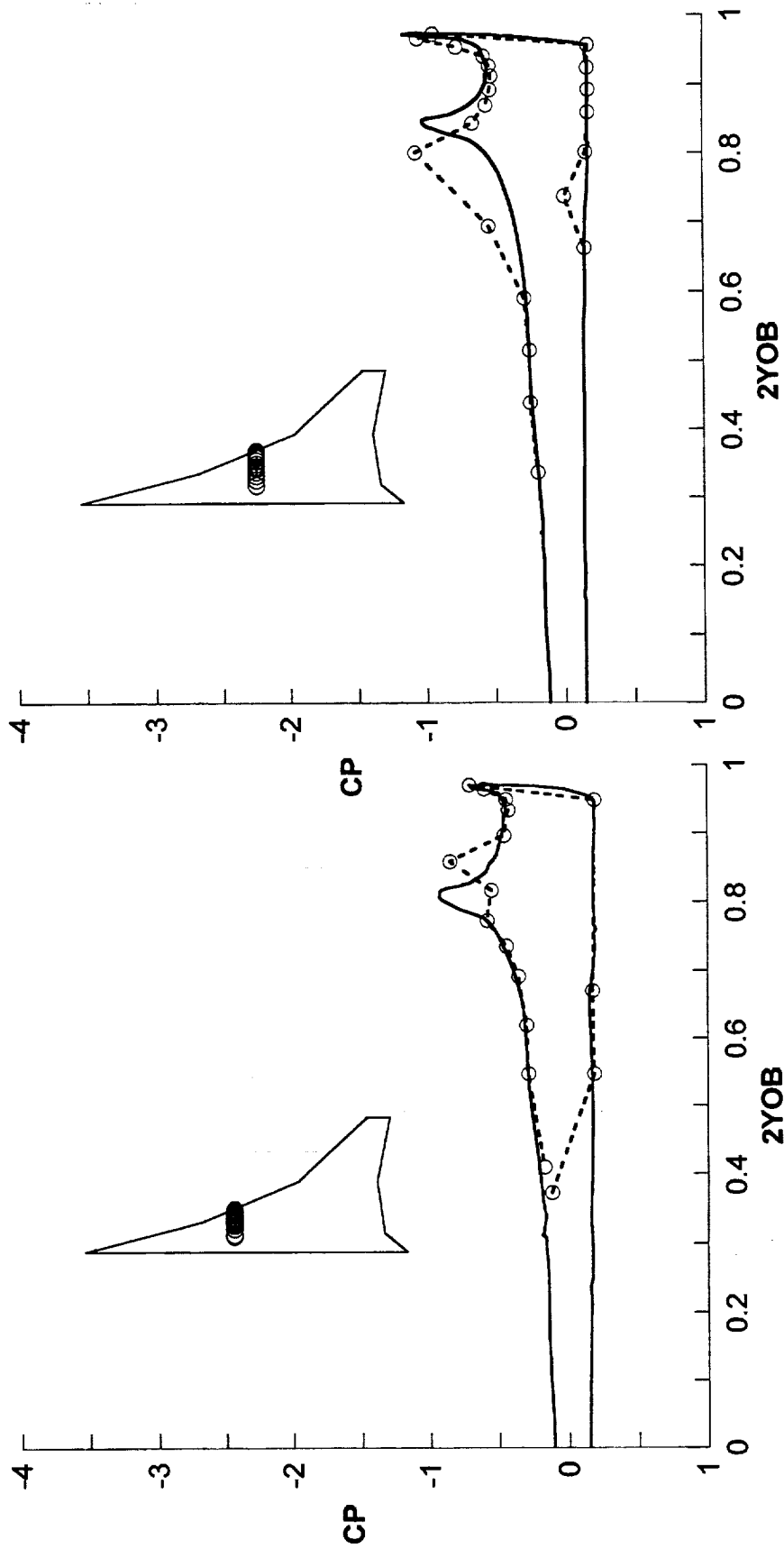
The correlation for the left plot is good with two exceptions:

1. CFD missed the peak near xoc=0.18. This is probably due to the leading edge vortex formed from the planform break.

2. There are too many leaky pressure ports in the test, for 0.02<xoc<0.14 and for xoc>0.83.

There are only a few pressure ports on the outboard wing because of the thinness of the 2.2% model. The pressure ports indicated in the right plot are all on the lower surface. It appears that half of these ports were leaky (0.2<xoc<0.45).

Ref. H, W/B, Flaps LE 30/Outbd TE 20, Mach 0.3, Alpha 10 Deg, Re 30 M
Viscous TNS3DMB (lines), NTF Test 057, Run 112 (symbols)

Dynacs Engineering Co., Inc

The test/theory comparisons are very similar to those seen for the 30M Reynolds number case.

Dynacs Engineering Co., Inc.

Ref. H, W/B, Flaps LE 30/Outbd TE 20, Mach 0.3, Alpha 10 Deg, Re 90 M
Viscous TNS3DMB (lines), NTF Test 057, Run 102 (symbols)

Dynacs Engineering Co., Inc

The test/theory comparisons are very similar to those seen for the 30M Reynolds number case.

Dynacs Engineering Co., Inc.

Ref. H, W/B, Flaps LE 30/Outbd TE 20, Mach 0.3, Alpha 10 Deg, Re 90 M
Viscous TNS3DMB (lines), NTF Test 057, Run 102 (symbols)

Dynacs Engineering Co., Inc
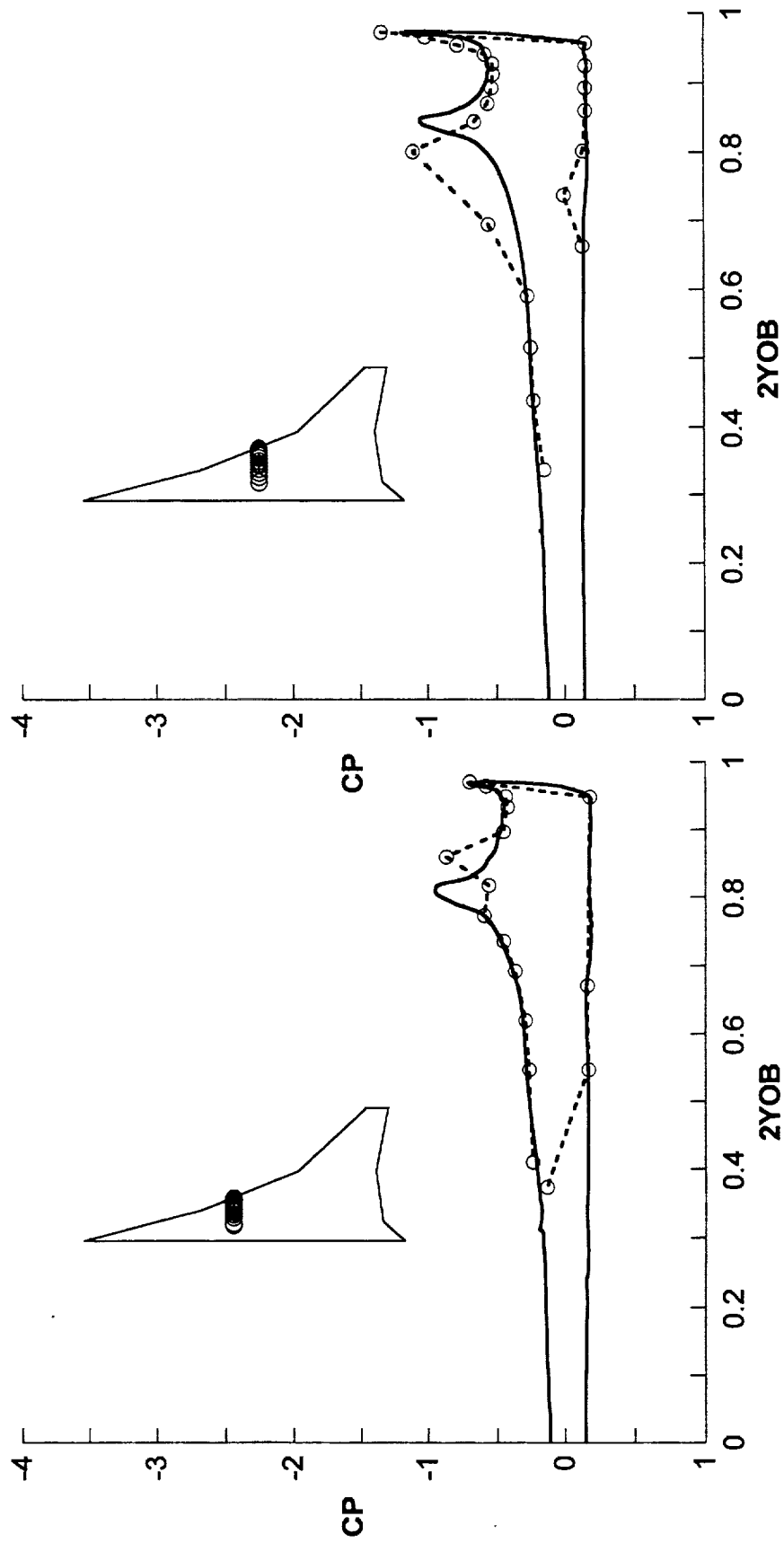
There are very small differences between the test data (left plot) for 30M and 90M Reynolds numbers. CFD (right plot) shows small differences too. This is true for all spanwise stations so only one is shown.

Ref. H, W/B, Flaps LE 30/Outbd TE 20, Mach 0.3, Alpha 10 Deg
NTF Test 057, Re 30 M (Run 112, circles) and Re 90 M (Run 102, squares)
Viscous TNS3DMB, Re 30 M (solid lines) and Re 90 M (dashed lines)
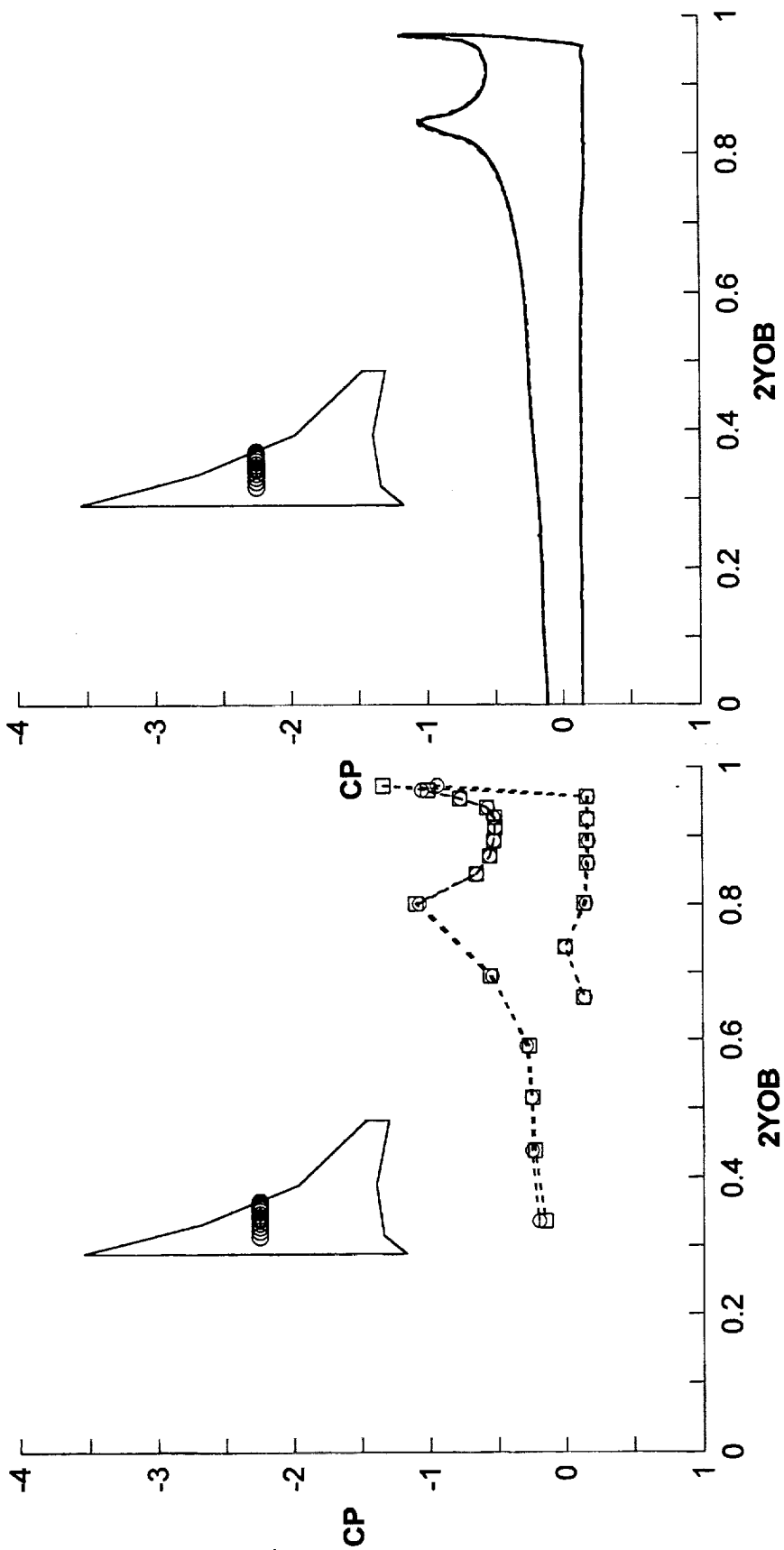
There are very small differences between the test data (left plot) for 30M and 90M Reynolds numbers. CFD (right plot) shows small differences too. This is true for all chordwise stations so only one is shown.

Ref. H, W/B, Flaps LE 30/Outbd TE 20, Mach 0.3, Alpha 10 Deg
NTF Test 057, Re 30 M (Run 112, circles) and Re 90 M (Run 102, squares)
Viscous TNS3DMB, Re 30 M (solid lines) and Re 90 M (dashed lines)

Dynacs Engineering Co., Inc

2311
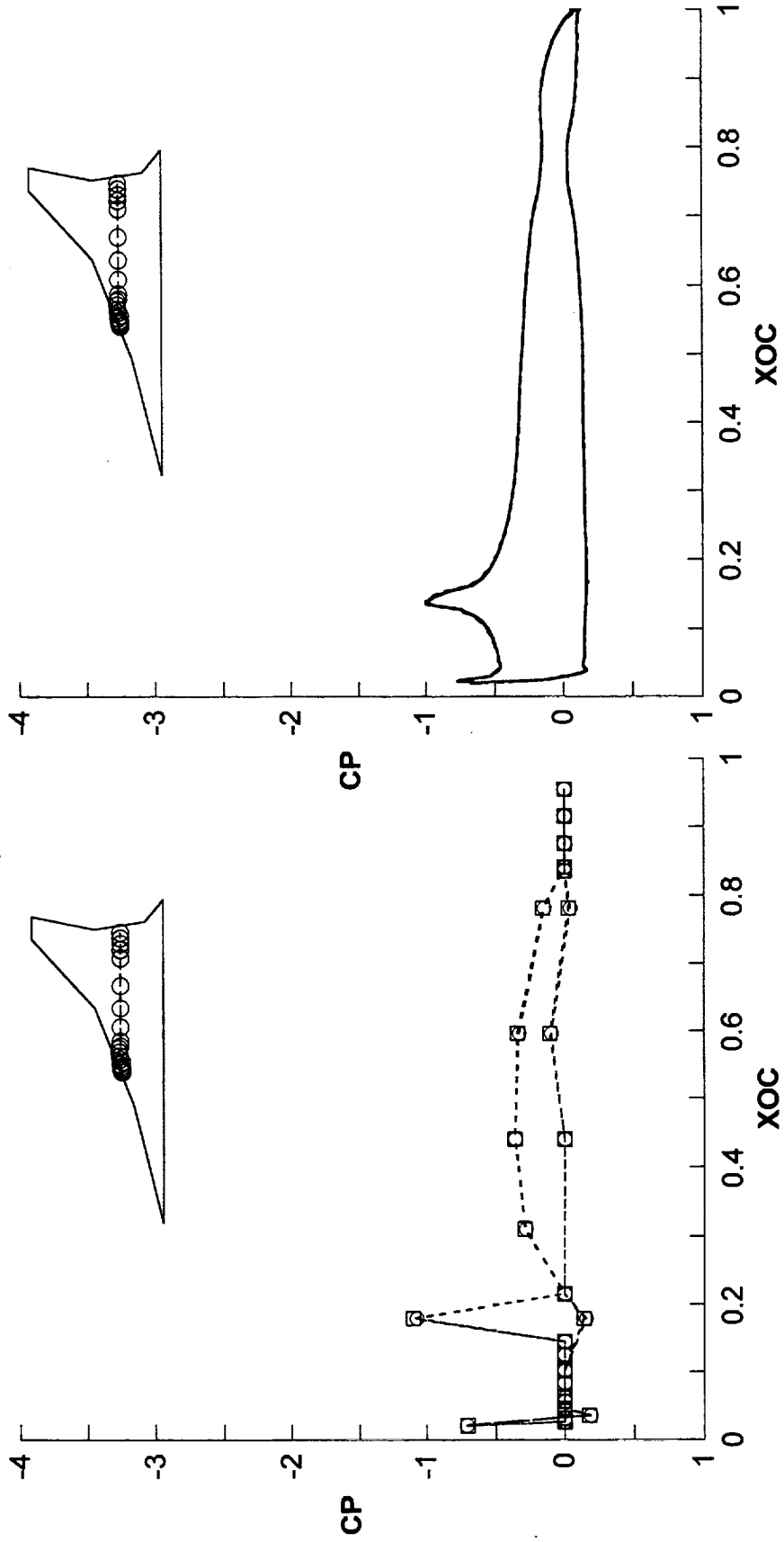
The differences between the 30M and the 90M cases are very small. The software which was used to generate the figure does not allow the reversal of the C_P scale.

2312

Ref. H, W/B, Flaps LE 30/Outboard TE 20, Mach 0.3, Alpha 10 Deg
4–Block Viscous TNS3DMB
Upper Surface Pressure Distribution

CP

0.25
0.00
-0.25
-0.50
-0.75
-1.00
-1.25
-1.50
-1.75
-2.00
-2.25
-2.50

Re = 30 million

Re = 90 million

Dynacs
ENGINEERING CO. INC.

2313
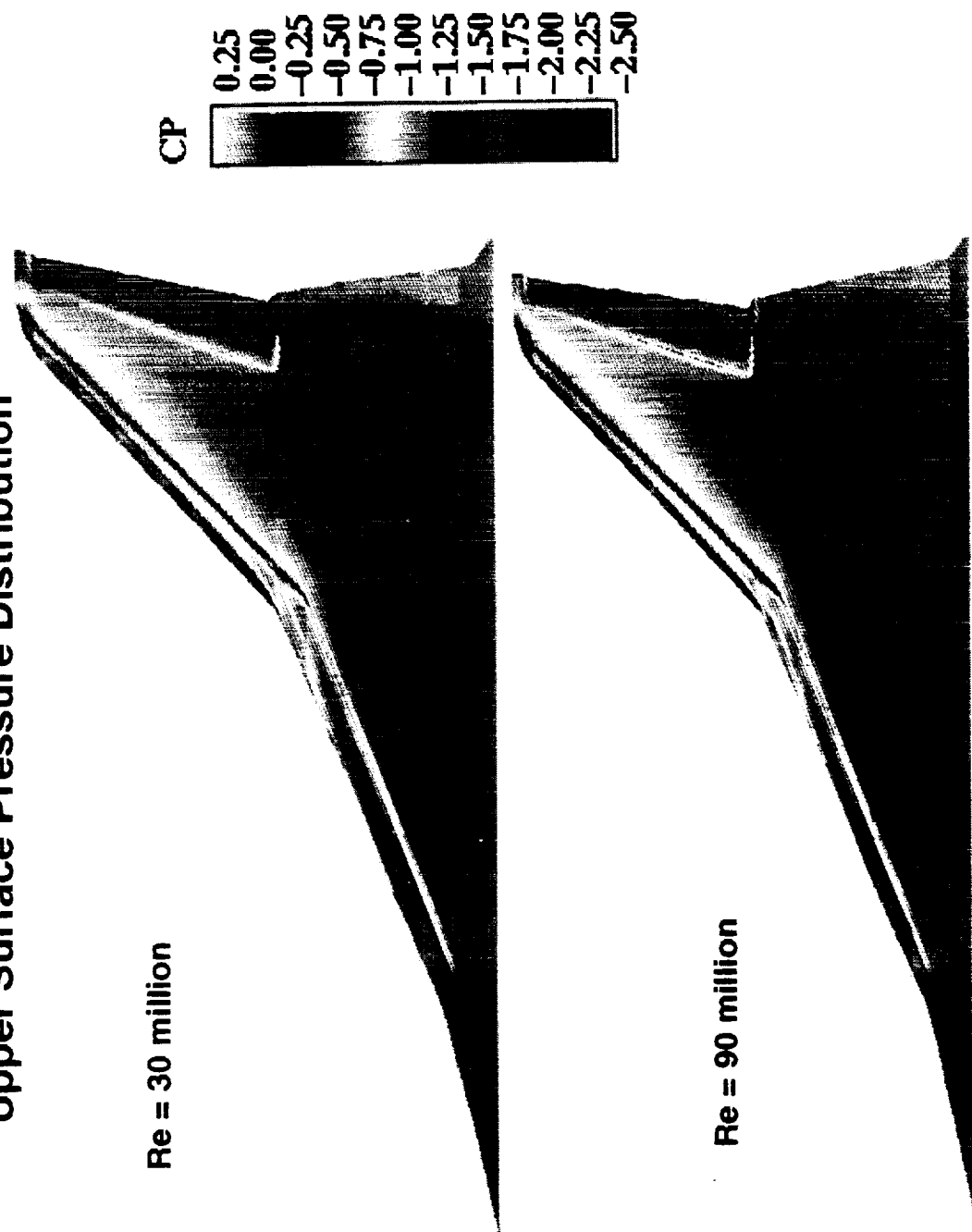
Again, the differences between the 30M and the 90M cases are very small. Notice that a scale which is different from the one used for the upper surface has been used to show the smaller spread of C_P on the lower surface.

2314

Ref. H, W/B, Flaps LE 30/Outboard TE 20, Mach 0.3, Alpha 10 Deg
4–Block Viscous TNS3DMB
Lower Surface Pressure Distribution

CP

0.75
0.50
0.25
0.00
-0.25
-0.50
-0.75
-1.00
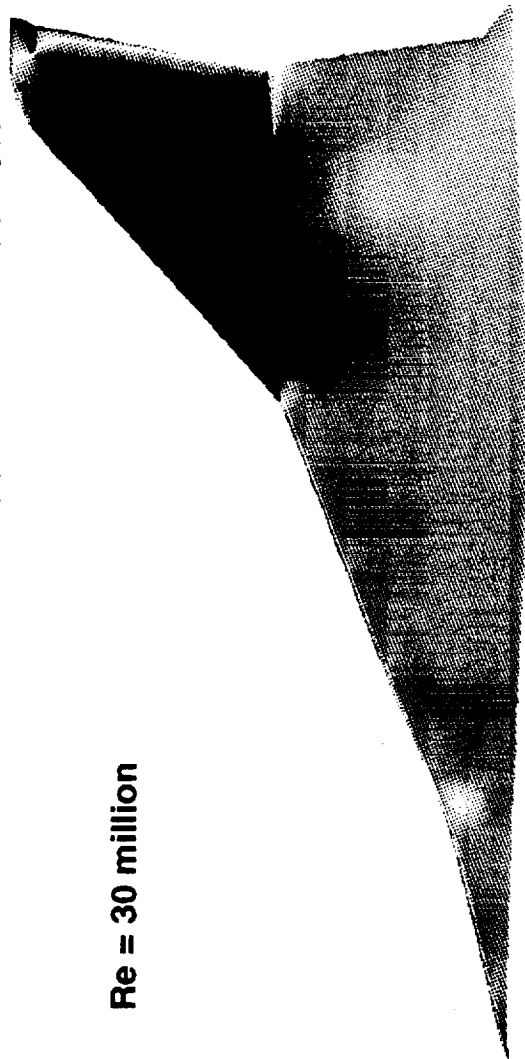
Re = 30 million

Re = 90 million
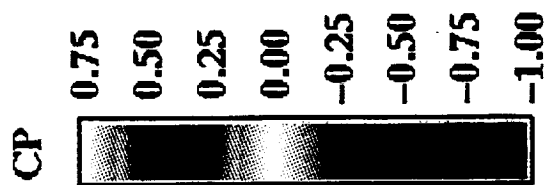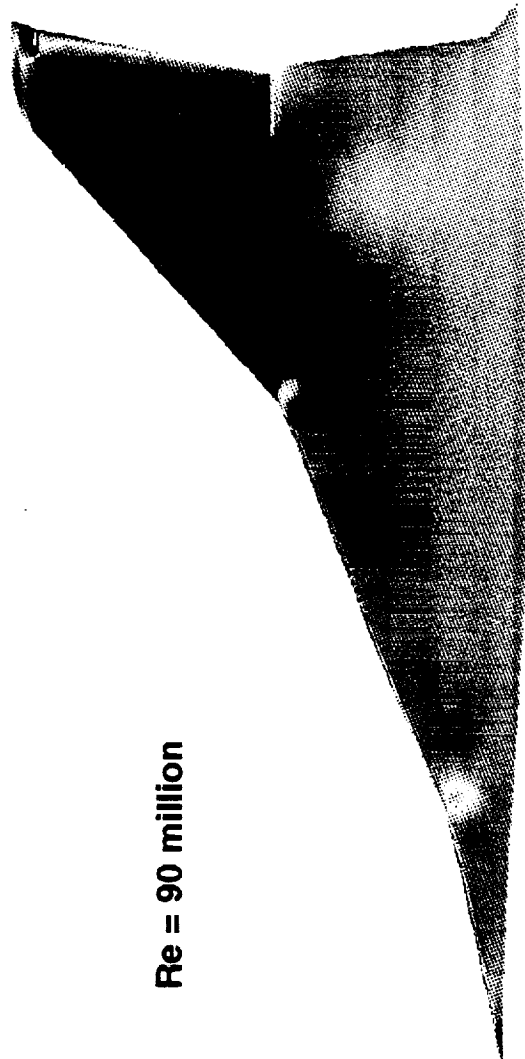
Velocity vectors on a grid layer two cells off the wing upper surface are shown. They look like the mini-tuft pictures. The only NTF test that generated mini-tuft pictures for HSR was Test 078 (December, 1995 - January, 1996). However, LE 30° and outboard TE 20° without the nacelles was not tested and therefore there are no experimental mini-tuft pictures to compare.

There are strong spanwise flows on the deflected outboard TE flap with the flow going toward the wing tip. The flow also tends to be normal to the LE hinge line just upstream of that hinge line because that's the direction of the maximum pressure gradient.

It would be nice if tests can produce information like this so that the CFD streamlines could be evaluated.

The 30M flow pattern is similar and therefore is not shown.

Dynacs Engineering Co., Inc.

Ref. H, W/B, Flaps LE 30/Outbd TE 20, Mach 0.3, Alpha 10 Deg
4-Block Viscous TNS3DMB
Velocity Vectors 2 Grid Cells Above the Upper Wing Surface

Re = 90 million

Dynacs
ENGINEERING CO. INC.
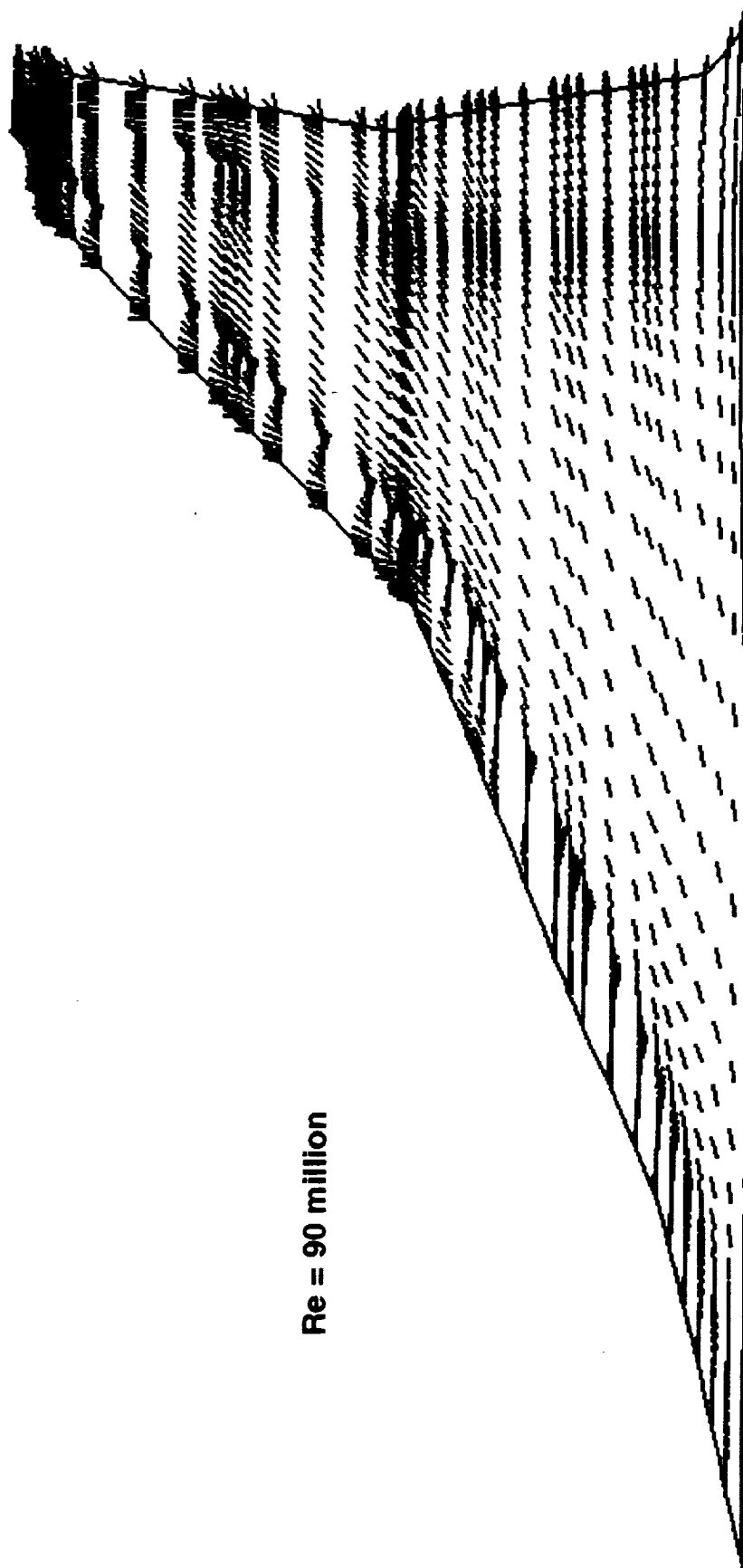
Streamlines on a layer of grid two cells off the wing upper surface show similar patterns for 30M and 90M Reynolds numbers. The flow seems to travel around the leading edge and reattaches on the flap (red lines). On the outboard TE flap the flow is highly separated and flows slightly upstream.

Dynacs Engineering Co., Inc.

Ref. H, W/B, Flaps LE 30/Outboard TE 20, Mach 0.3, Alpha 10 Deg
4-Block Viscous TNS3DMB
Particle Traces 2 Grid Cells Above the Upper Wing Surface

reattachment line

Re = 30 million

reattachment line

Re = 90 million

Dynacs
ENGINEERING CO. INC.
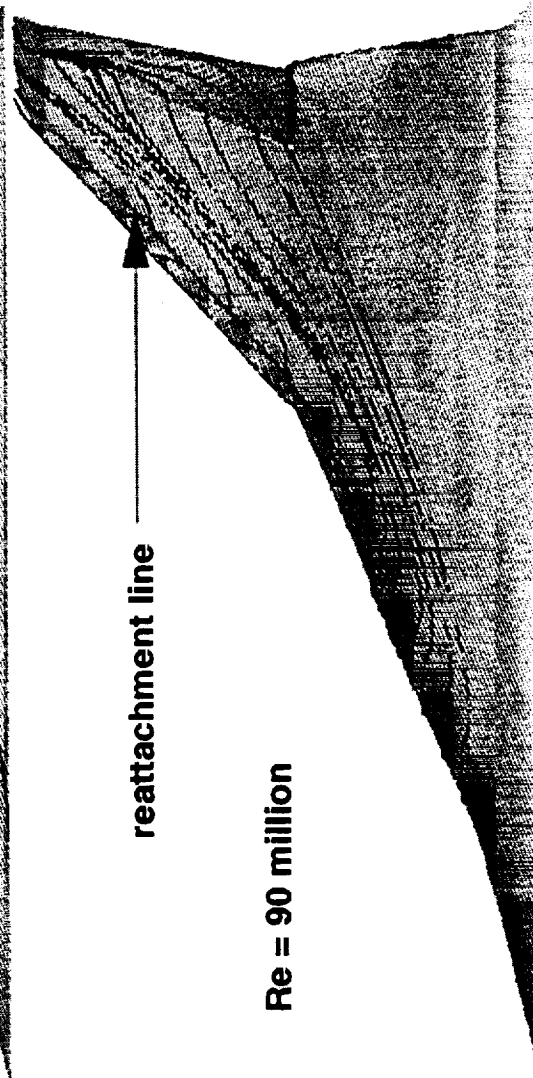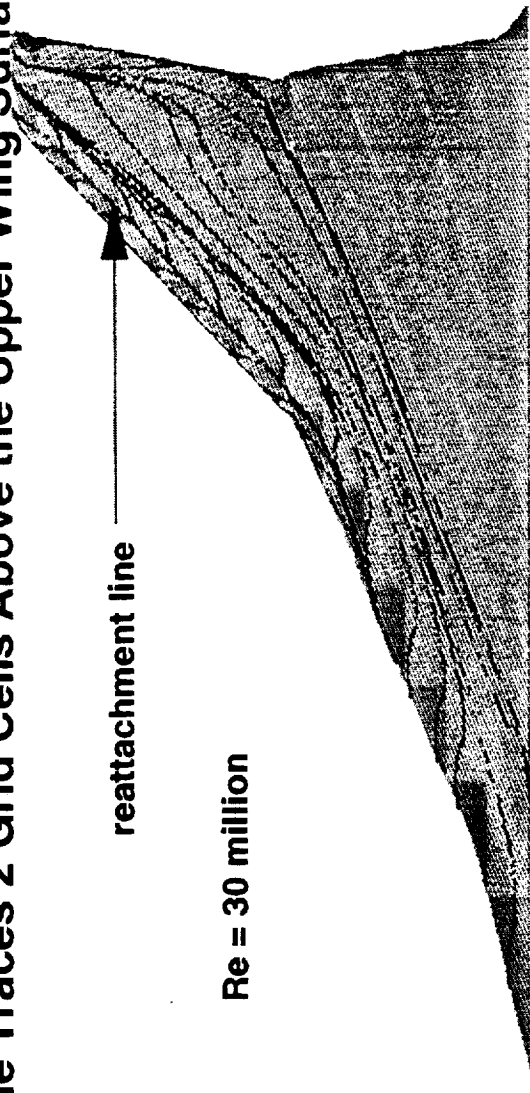
These traces are not limited to a particular grid layer.

The inboard flow seems to be benign. The outboard flow, particularly close to the leading edge, is more violent.

The 30M pattern is similar and therefore it is not shown.

Dynacs Engineering Co., Inc.

Ref. H, W/B, Flaps LE 30/Outboard TE 20, Mach 0.3, Alpha 10 Deg
Inboard and Outboard Wing Particle Traces

Re = 90 million

Dynacs
ENGINEERING CO. INC.

2321

Velocity vectors along grid lines passing through the wing trailing edge near 25% semi-span are shown. Differences between the 30M Reynolds number case and the 90M Reynolds number case are visible, though not obvious.

x-axis is longitudinal

y-axis is spanwise

z-axis is vertical

Velocity Vectors at the TE of 2y/b ~ 0.25
Ref. H W/B, LE 30 Deg., Outboard TE 20 Deg.
Mach 0.3, Alpha 10 Degrees, TNS3DMB

Re 90M

Re 30M
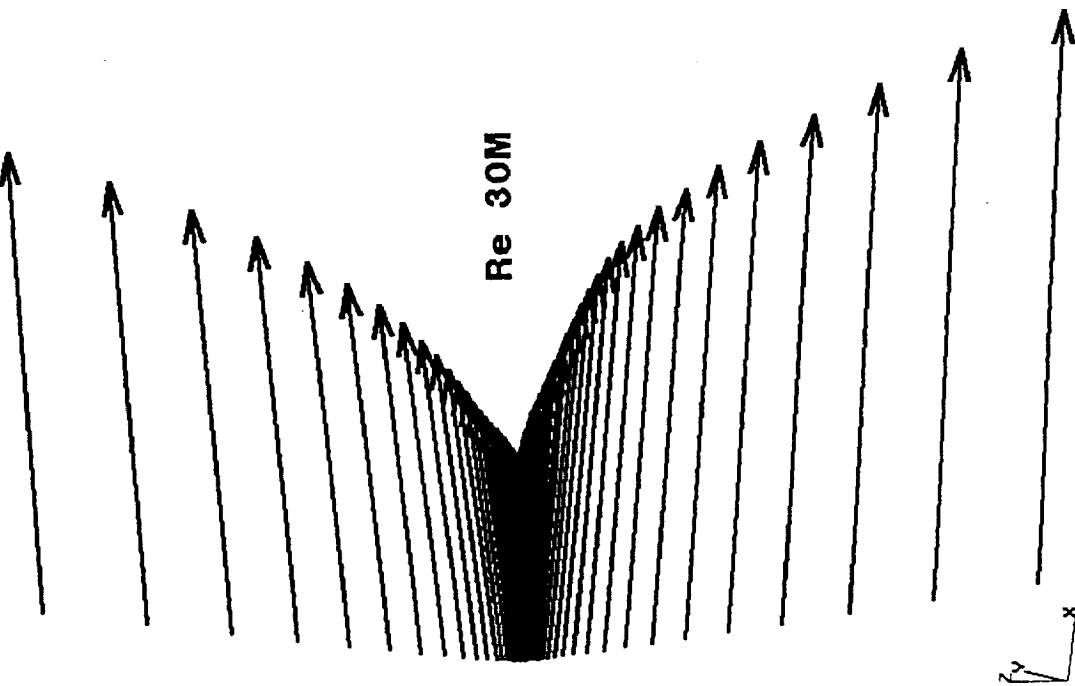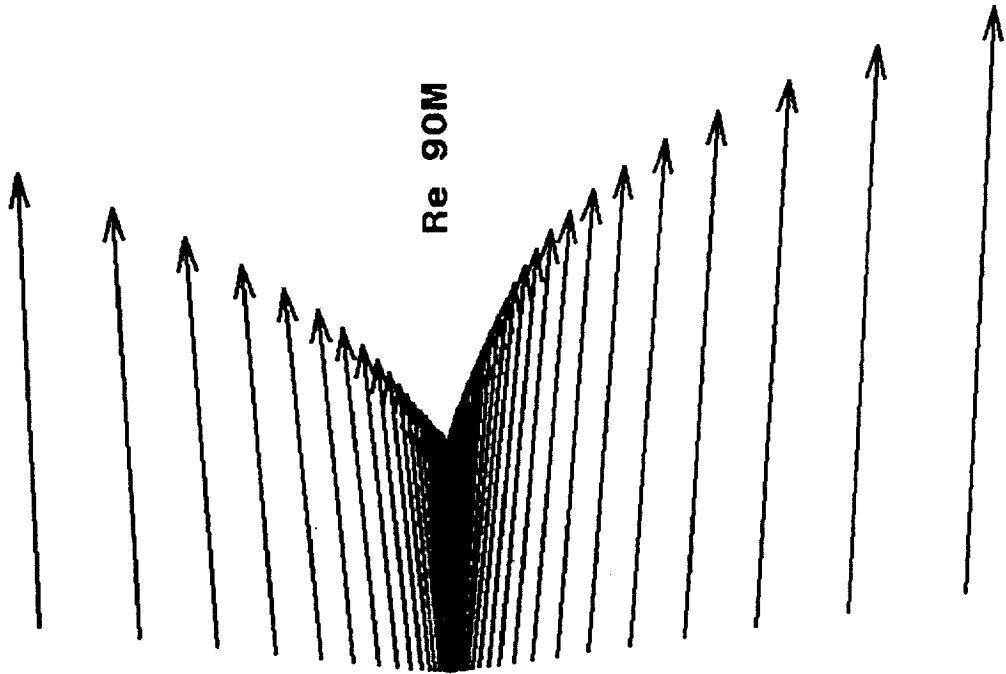
Velocity vectors along grid lines passing through the wing trailing edge near the middle of the outboard trailing edge flap are shown. Differences between the 30M Reynolds number case and the 90M Reynolds number case are more visible than the inboard station shown in the previous figure. It should be pointed out that this is in a highly three-dimensional flow area and as such the velocity vectors change their orientations with respect to the free stream throughout the viscous layer.

Dynacs Engineering Co., Inc.

2324

Velocity Vectors at the TE of 2y/b ~ 0.75
Ref. H W/B, LE 30 Deg., Outboard TE 20 Deg.
Mach 0.3, Alpha 10 Degrees, TNS3DMB

Re 90M

Re 30M
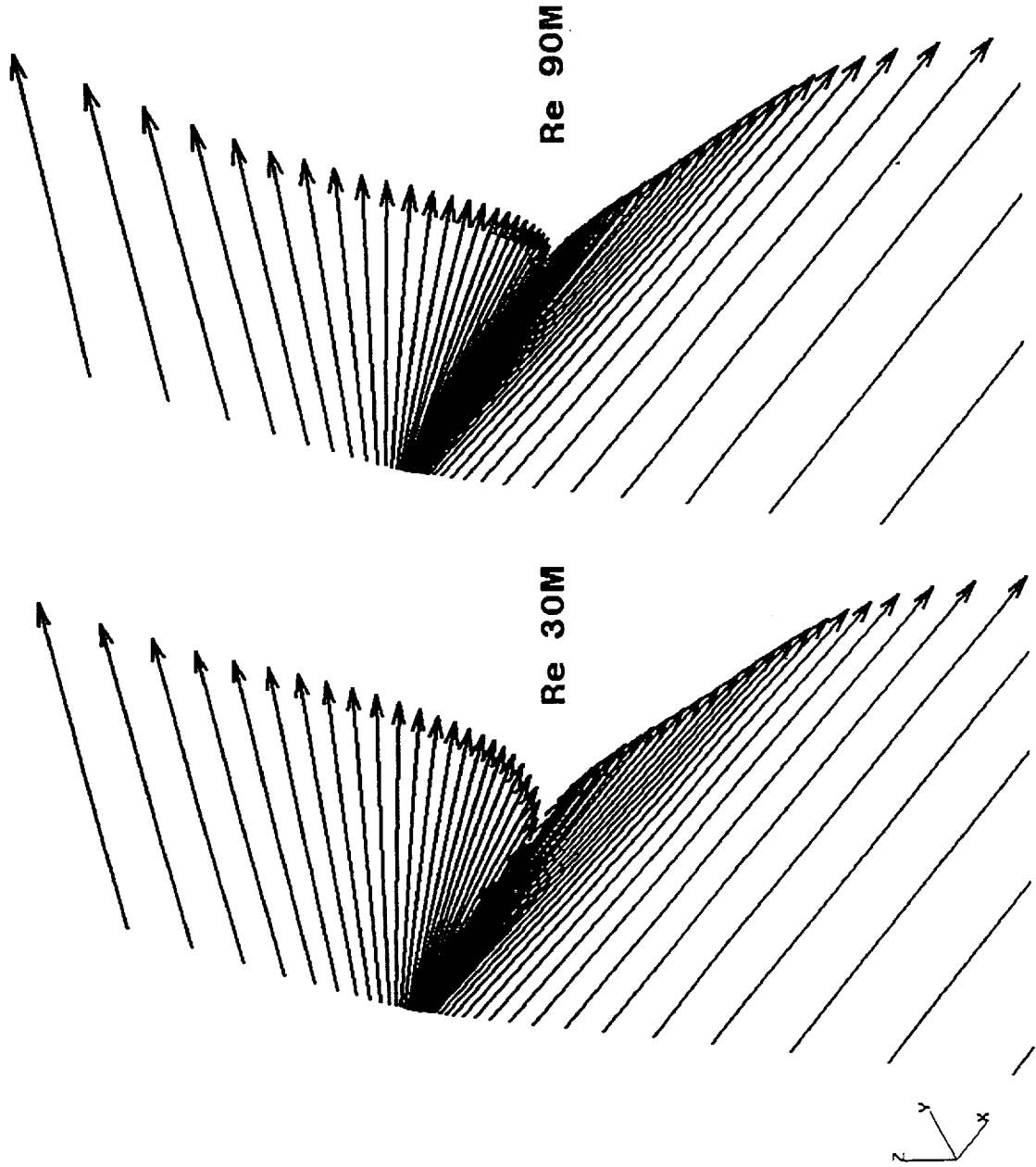
The viscous sublayer thickness or Y^+ is shown in the figure for both Reynolds numbers on the upper wing surface. Values less than one are considered very good for capturing the flow accurately near the surface. Very small differences exist between the two cases at the inboard leading edge hinge line and near the wing root, where the values of Y^+ are lower for the higher Reynolds number. The outboard wing has lower Y^+ values in both cases, which is beneficial for resolving separation and spanwise flow in that region.

Ref. H, W/B, Flaps LE 30/Outboard TE 20, Mach 0.3, Alpha 10 Deg
4–Block Viscous TNS3DMB
Upper Surface Y+

Y+

5.00
4.50
4.00
3.50
3.00
2.50
2.00
1.50
1.00
0.50
0.00

Re = 30 million

Re = 90 million

Dynacs
ENGINEERING CO. INC

2327
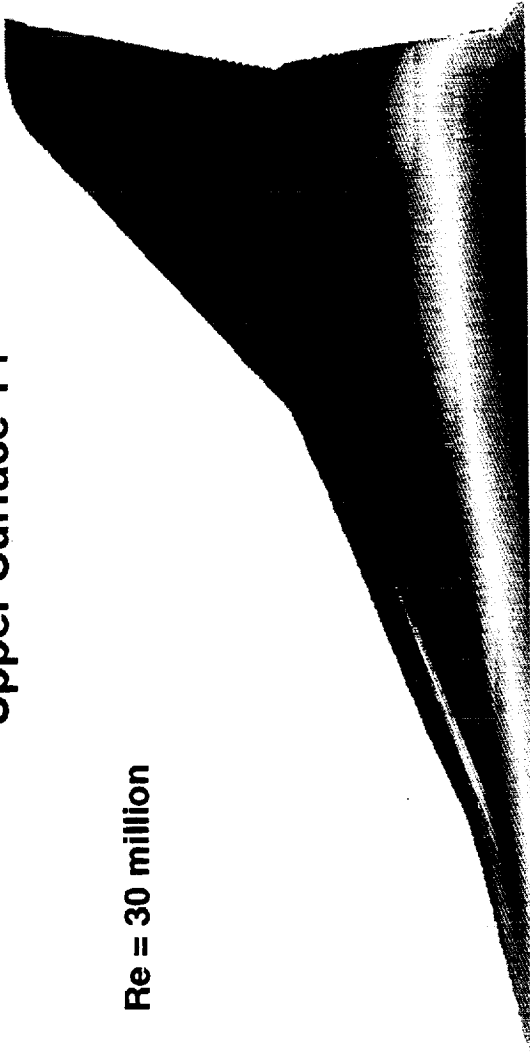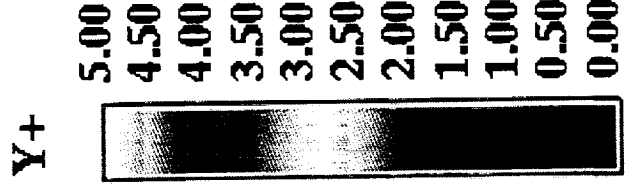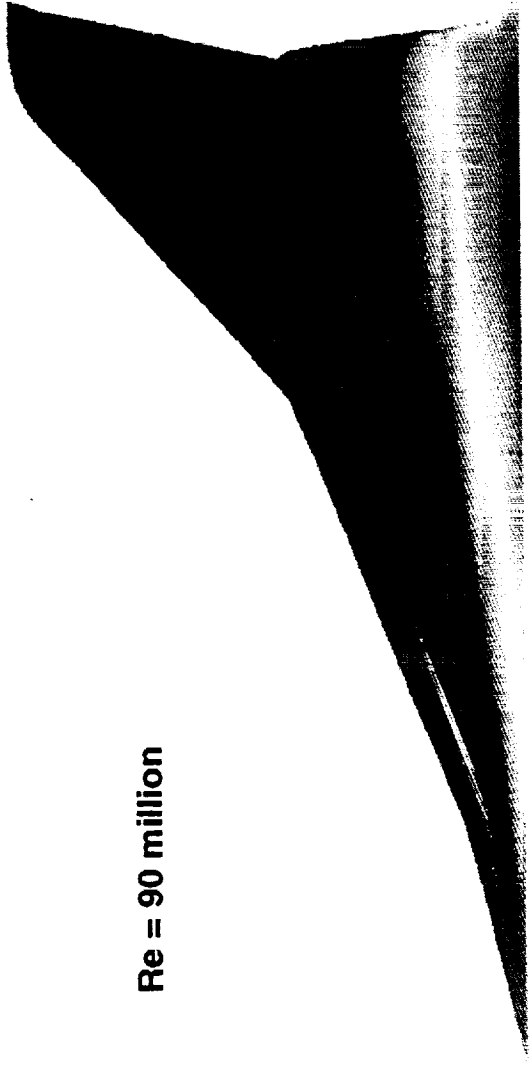
The total skin friction coefficient is higher around the hinge lines, mainly because of the high local velocity outside the boundary layer. The outboard wing has a lower C_f than the inboard wing, with the lowest value appearing right behind the hinge lines.

Ref. H, W/B, Flaps LE 30/Outboard TE 20, Mach 0.3, Alpha 10 Deg
4-Block Viscous TNS3DMB
Upper Surface C_f

C_f

0.010
0.009
0.008
0.007
0.006
0.005
0.004
0.003
0.002
0.001
0.000

Re = 30 million

Re = 90 million

Dynacs
ENGINEERING CO. INC.

2329
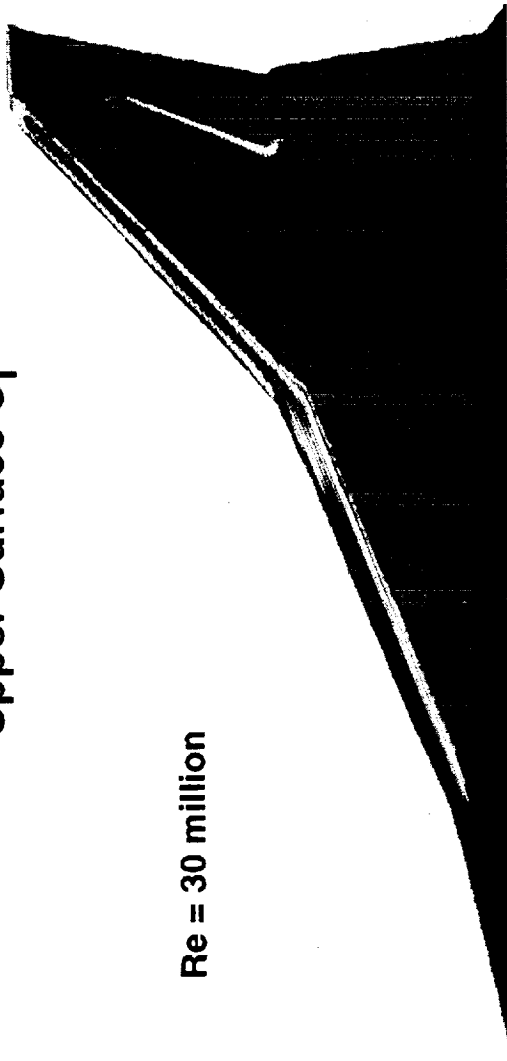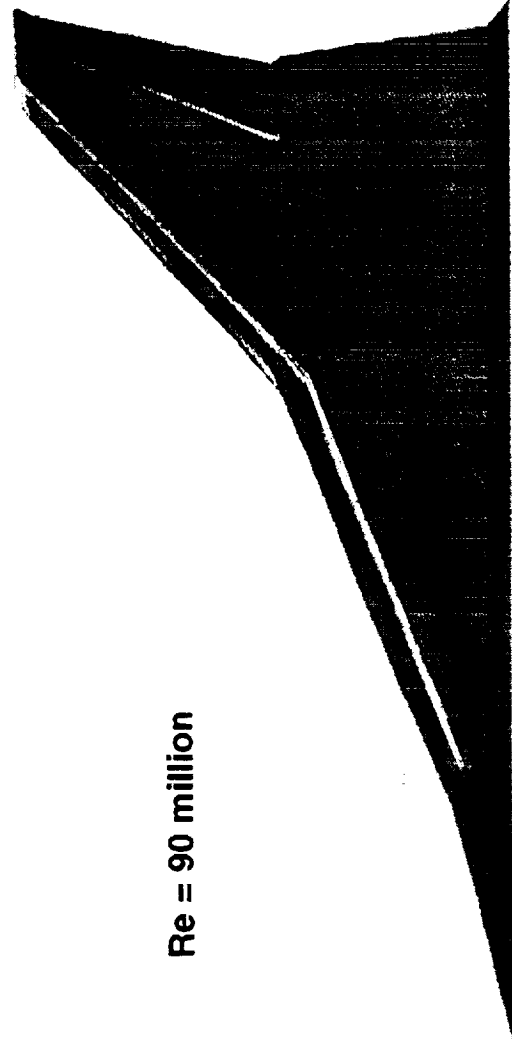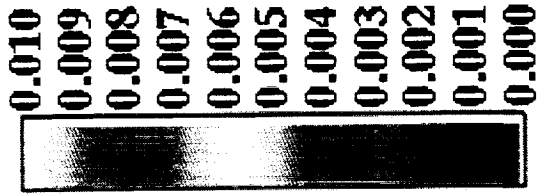
Test data from NTF057 and NTF060 were obtained without the model being tripped. A recent test (NTF080, August-September, 1996) generated some trip-on data for Ref. H. Using NTF080 results to evaluate CFD may answer some of the questions raised by the Reynolds number study, especially at the lower Reynolds number. Wind tunnel data at a chord Reynolds number of 21.6 million will be used for CFD comparisons.

Dynacs Engineering Co., Inc.

TRIP STUDY

- Reynolds Number Study raised questions at Re 30 M

- C_L mismatch between NTF and CFD

  – NTF Test 057 and Test 060 had no trips

  – CFD fully turbulent

- Need to compare CFD trip run with NTF trip data near Re 30 M

Force, moment and pressure data was taken in Test 080. Data were taken with and without trips. To simulate turbulent transition, grit sizes #120 and #150 were applied at a location of 0.625 inch from the wing leading edge (between the LE and LE hinge line). The nose was tripped to provide a fully turbulent fuselage. The flaps were deflected LE 30°/TE 10°. Although the flaps in the CFD grid were deflected LE 30°/outboard TE 20°, the purpose of the study was to capture the trend in the increments; this saved some time by not having to construct a new grid.

NTF WIND TUNNEL DATA SOURCES

- Forces, moments and surface pressure
  - Test 080, Runs 391–395 (Re 21.6M, no trips)
  - Test 080, Runs 404–408 (Re 21.6M, #150 grit)
  - Test 080, Runs 416–420 (Re 21.6M, #120 grit)
- Flaps LE 30 deg/TE 10 deg

Dynacs Engineering Co., Inc.

Two TNS3DMB solutions were obtained, one at fully turbulent conditions, the other tripped. In the latter case the trips were placed at the leading edge hinge line on both the upper and lower surfaces. The laminar region, which is located between the LE and the trip, extended from the surface to 32 grid cells above the surface (TNS3DMB zeroes out the turbulent production term in the laminar region). In addition, the flow was specified to be turbulent on the fuselage, which extended from the surface up to the 32nd grid cell. Each solution was obtained for the HSCT wing/body, with flap settings of 30° along the leading edge and 20° on the outboard trailing edge, a Mach number of 0.3 and α of 10°. The Spalart-Allmaras turbulence model was used in both runs.

Dynacs Engineering Co., Inc.

FLOW CONDITIONS AND CFD SPECIFICS

- Mach 0.3

- Alpha 10 Deg

- Flaps LE 30 deg/outboardTE 20 deg

- Re 21.6M based on mean aerodynamic chord

- Viscous TNS3DMB: fully turbulent and with trip at LE hinge

- Spalart-Allmaras turbulence model

Dynacs Engineering Co., Inc.

2335

Repeat runs are shown to form tight bands.

The NTF data show similar values between non-tripped and tripped cases. In the CFD results, the C_{L_trip} was larger than $C_{L\_fully\_turb}$. Based on the results of the Reynolds number study it was hoped that the C_L for the trip run would be less than C_L for the fully turbulent run.

Not shown are results from a case that was run prior to running the trip case that is plotted above. A case was run where in addition to zeroing out the turbulent production term between the LE and the trip, the eddy viscosity was hard-coded to be zeroed out in the laminar region that extended from the surface to the outer boundary. That method was used as a means of preventing the trip from moving upstream. The C_L turned out to be less than $C_{L\_fully\_turb}$ and the NTF data, in the direction anticipated from the Reynolds number study. However, the C_L for that trip approach was quite low (0.5011), possibly indicating that zeroing out the eddy viscosity may have made the flow too laminar. The two CFD trip approaches induced very different results.

Ref. H, W/B, Mach 0.3, Alpha 10 Deg, Re 21.6M
CFD flaps LE 30/Outbd TE 20; NTF flaps LE 30/TE 10
Viscous TNS3DMB (symbols), NTF Test 080 (lines)

Dynacs Engineering Co., Inc
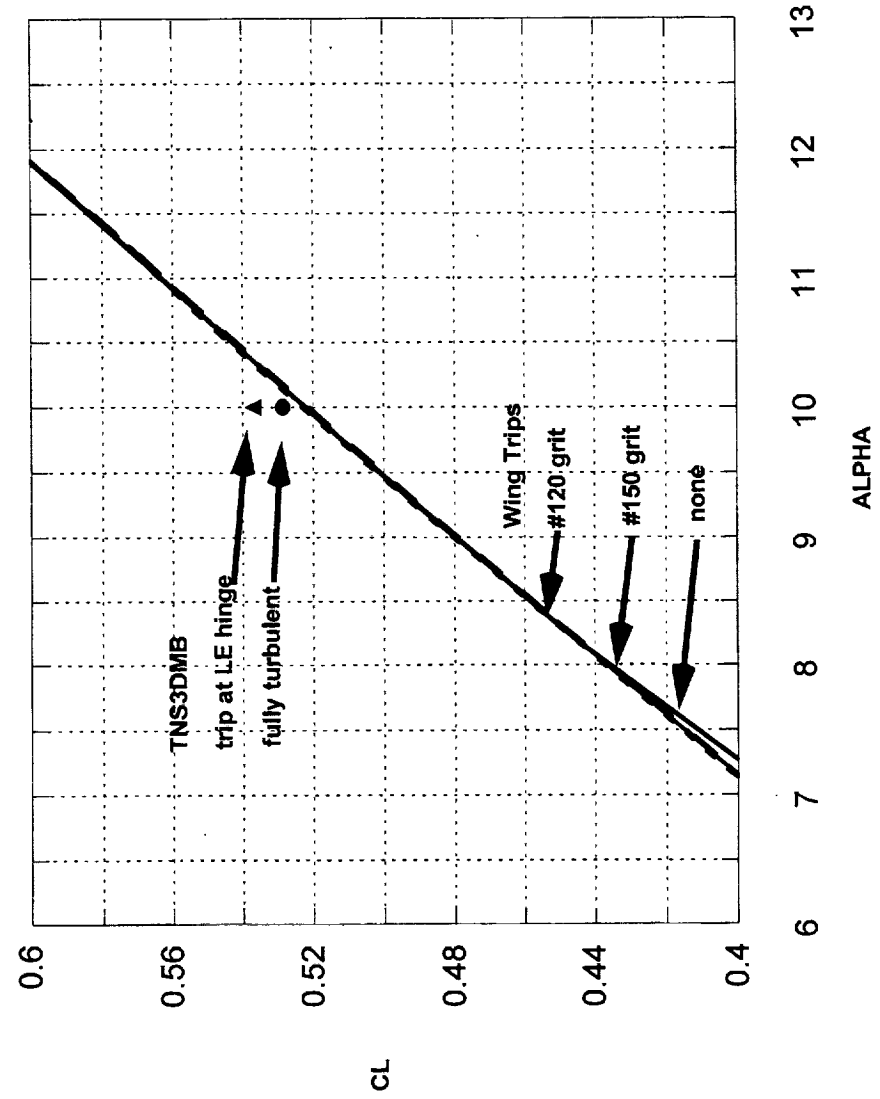
The repeat runs in NTF form a wider band at higher lift coefficients. CFD missed the absolute level of C_D as well as the increment between fully turbulent and trip runs.

Ref. H, W/B, Mach 0.3, Alpha 10 Deg, Re 21.6M
CFD flaps LE 30/Outbd TE 20; NTF flaps LE 30/TE 10
Viscous TNS3DMB (symbols), NTF Test 080 (lines)

RUN 391
RUN 392
RUN 393
RUN 395
RUN 394
RUN 404
RUN 405
RUN 406
RUN 407
RUN 408
RUN 416
RUN 417
RUN 418
RUN 419
RUN 420
CFD
CFD

Wing Trips
#120 grit
#150 grit
none

TNS3DMB
trip at LE hinge
fully turbulent

CL

CD
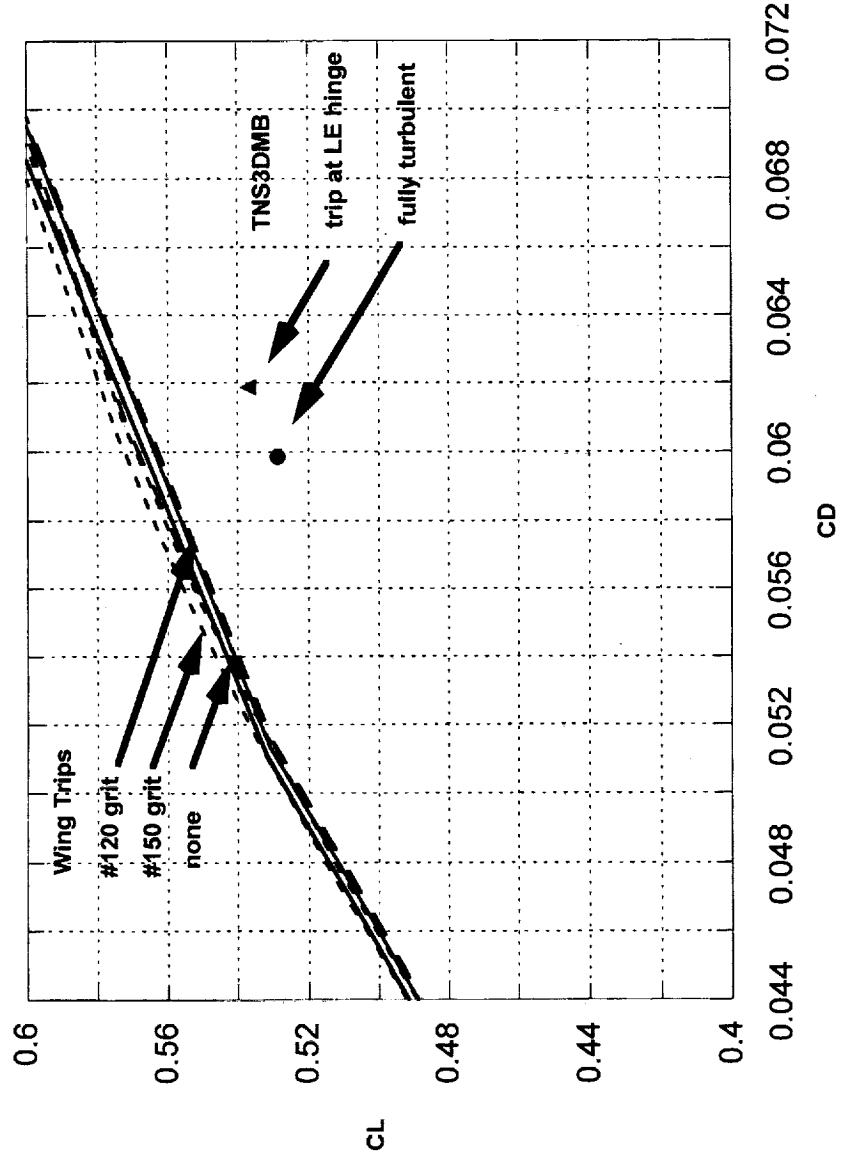
The repeat runs in NTF form tighter bands at the lower lift coefficients. CFD missed the absolute level of C_M and the increment between fully turbulent and trip runs. A change of 0.005 in C_M is equivalent to a 1° deflection in the horizontal stabilizer for Ref. H.

Ref. H, W/B, Mach 0.3, Alpha 10 Deg, Re 21.6M
CFD flaps LE 30/Outbd TE 20; NTF flaps LE 30/TE 10
Viscous TNS3DMB (symbols), NTF Test 080   (lines)

RUN 391
RUN 392
RUN 393
RUN 395
RUN 394
RUN 404
RUN 405
RUN 406
RUN 407
RUN 408
RUN 416
RUN 417
RUN 418
RUN 419
RUN 420
CFD
CFD

Wing Trips
#120 grit
#150 grit
none

TNS3DMB
trip at LE hinge
fully turbulent

CM

CL

Dynacs Engineering Co., Inc

2341
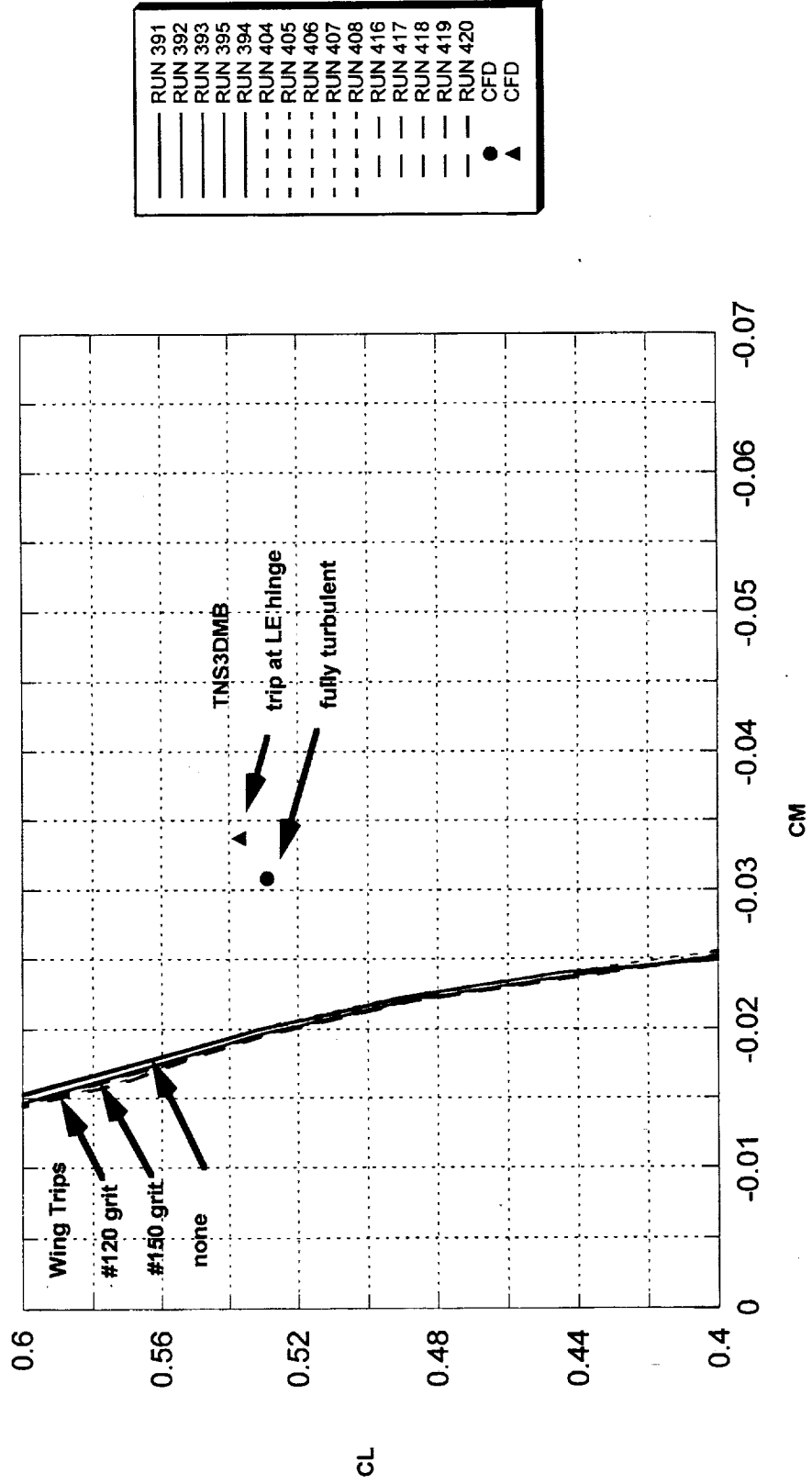
The repeat runs in NTF form tight bands. Values of L/D are largest for the no trip case, with the smallest values occurring at the larger grit size (#120). The TNS3DMB solution shows better agreement with the data than the C_L vs. C_D results had shown.

Ref. H, W/B, Mach 0.3, Alpha 10 Deg, Re 21.6M
CFD flaps LE 30/Outbd TE 20; NTF flaps LE 30/TE 10
Viscous TNS3DMB (symbols), NTF Test 080 (lines)

Wing Trips

#120 grit

#150 grit

TNS3DMB

trip at LE hinge

fully turbulent

RUN 391
RUN 392
RUN 393
RUN 395
RUN 394
RUN 404
RUN 405
RUN 406
RUN 407
RUN 408
RUN 416
RUN 417
RUN 418
RUN 419
RUN 420
CFD
CFD

L/D

CL

0.6
0.56
0.52
0.48
0.44
0.4

4   6   8   10   12   14   16   18

2343
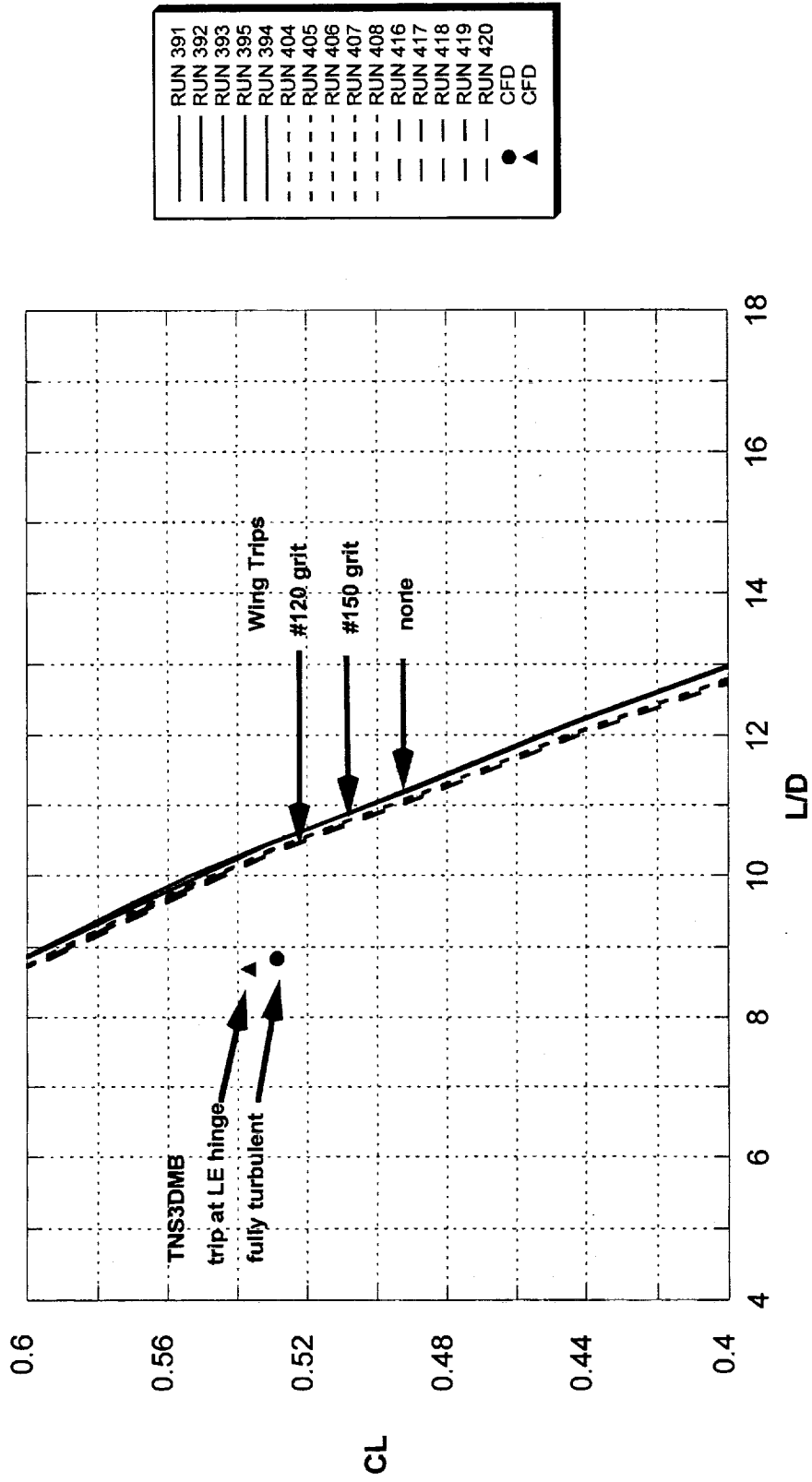
The drag breakdown for all of the cases presented indicates the extent of the pressure drag and viscous drag at various Reynolds numbers. Pressure drag is the greatest and viscous drag is the lowest for the tripped case. The greater lift (from previous C_L vs. $\propto$ plot) and drag in the trip case combined to reduce the differences between CFD and data that were seen in the C_L vs. C_D plot.

Dynacs Engineering Co., Inc.

Drag Coefficient Breakdown
Ref. H, W/B, Mach 0.3, Alpha 10 Deg, Flaps LE 30/Outbd TE 20
Viscous TNS3DMB: trip and fully turbulent

Dynacs Engineering Co., Inc
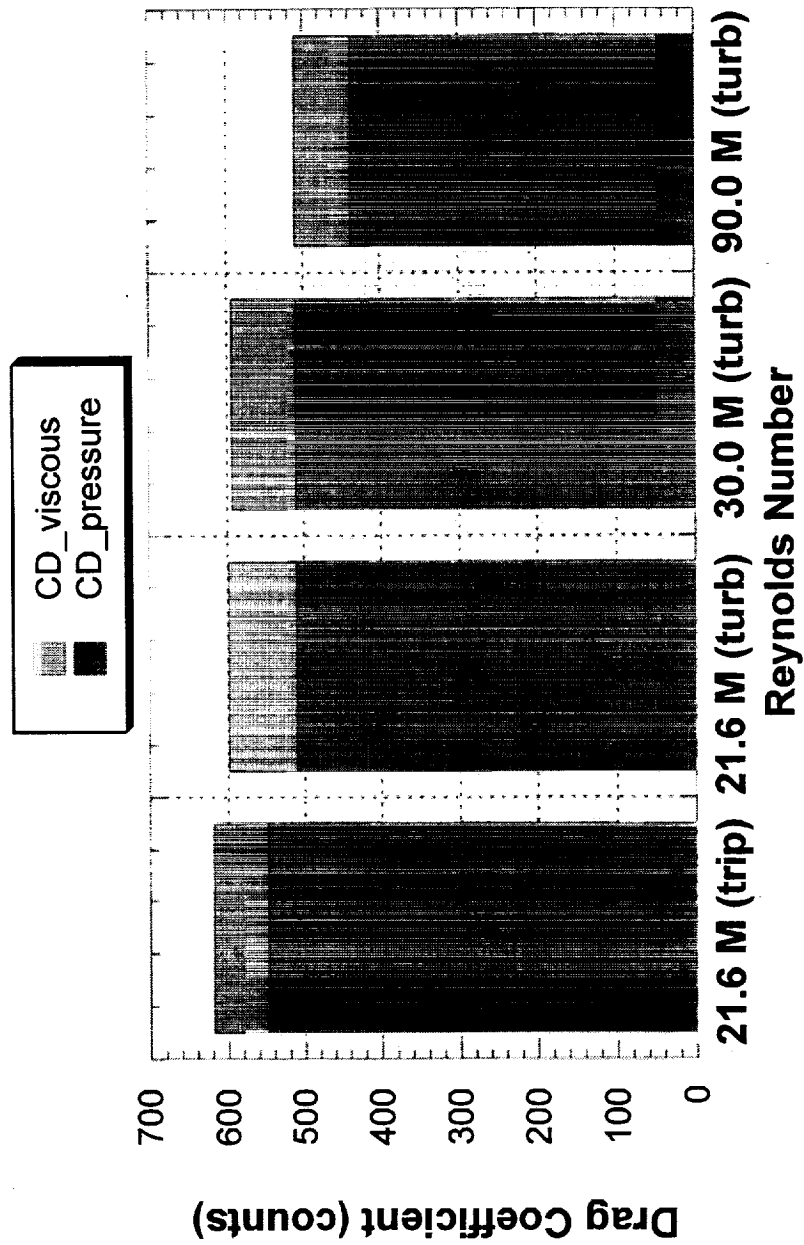
The total skin friction coefficient is plotted for both the fully turbulent and the trip runs made with TNS3DMB. Values of C_f differ between the two cases in the region between the LE and the LE hinge (trip location), where C_f is no greater than 0.001 in the tripped case, compared with values of 0.004 to 0.007 in the fully turbulent case. Other differences occur on the outboard wing, where in the region between the LE hinge and the TE hinge, C_f is 0.004 for the tripped case compared with 0.001 for the fully turbulent case.

Ref. H, W/B, Flaps LE 30/Outboard TE 20, Mach 0.3, Alpha 10 Deg
4–Block Viscous TNS3DMB
Upper Surface C_f

Re = 22 million

C_f

0.010
0.009
0.008
0.007
0.006
0.005
0.004
0.003
0.002
0.001
0.000

fully turbulent

trip at LE hinge

Dynacs
ENGINEERING CO. INC.

2347
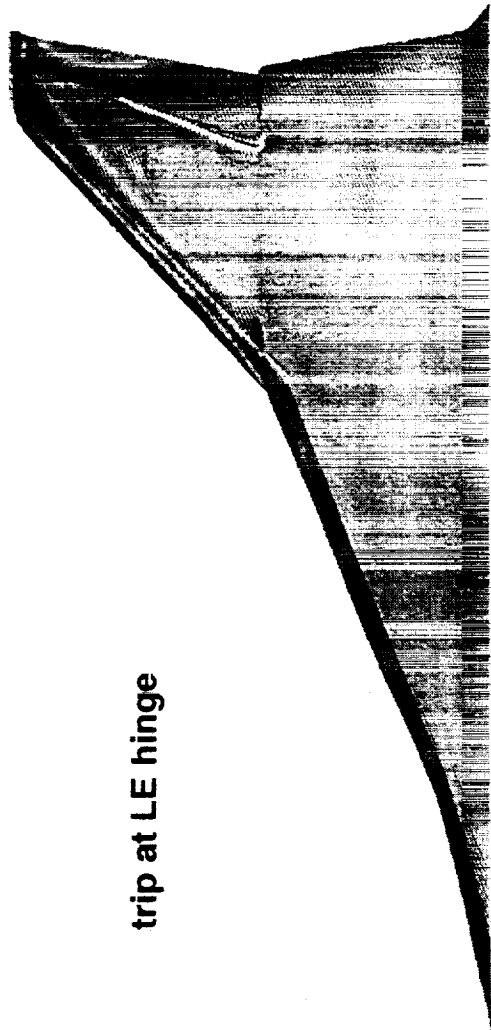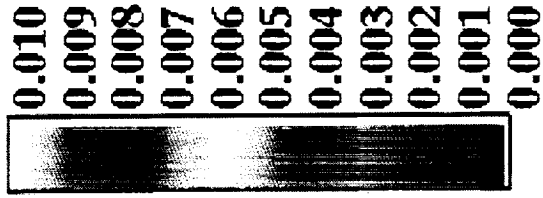
The total skin friction coefficient is plotted at an outboard chordwise station. Both the fully turbulent and the trip runs show a sharp increase in the skin friction coefficient at the LE hinge line. Between the LE and the LE hinge the skin friction coefficient remains lower for the tripped case than for the fully turbulent case. The minimum C_f value at an XOC of 0.05 in the fully turbulent case, and XOC of 0.09 for the trip case, may be the location of reattachment. Directly aft of the LE hinge the magnitude of the skin friction becomes greater for the trip case.

Dynacs Engineering Co., Inc.

2348

Total Skin Friction Cut on Upper Surface
Ref. H, W/B, Mach 0.3, Alpha 10 Deg,, flaps LE 30/Outbd TE 20 Viscous TNS3DMB, Re 21.6

Dynacs Engineering Co., Inc
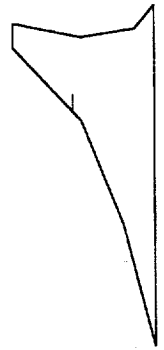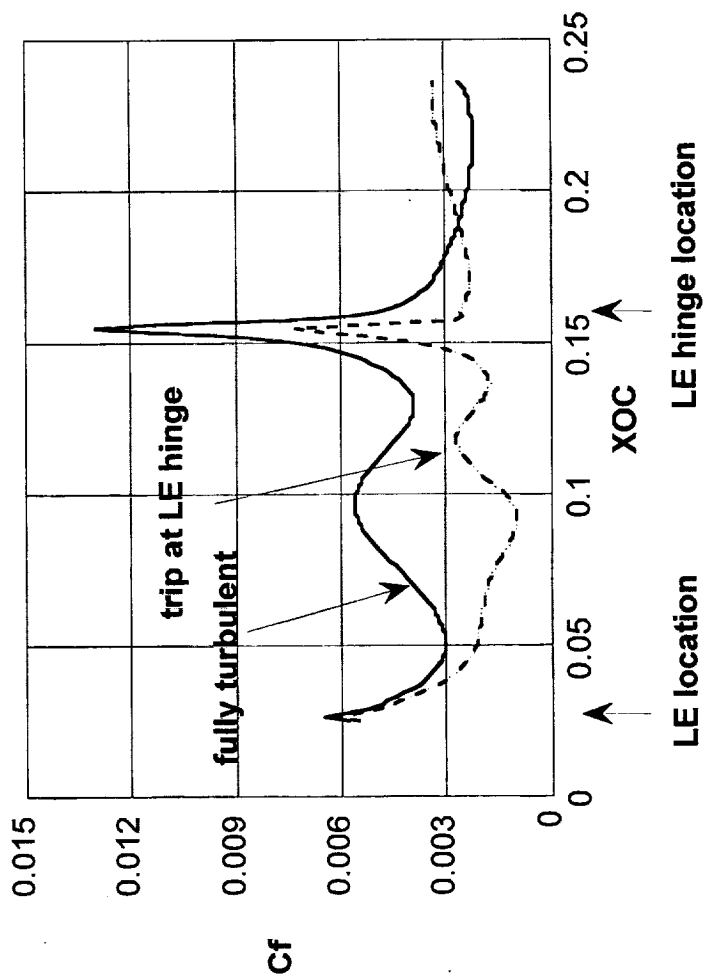
In the Reynolds number study, the increment in C_D was captured well. The increment in C_M was captured, though not as well. The increment in C_L was captured poorly. While there were noticeable differences among the aerodynamic coefficients for Re 30M and 90M, the surface pressure was essentially independent of Reynolds number. Results from the trip study indicate that a different approach may need to be developed for the CFD computation.

Wind tunnel tests provided forces, moments and wing surface pressures but the surface pressures were not sufficient to do a complete CFD assessment. Flow visualization was not available. Skin friction was not measured in the wind tunnel tests. CFD provides much more information about the flow details. There are many CFD parameters, such as total pressure, which are not presented in this report because there are no test data to compare with.

CFD assessment tasks do not end until test/theory comparisons are made and conclusions and recommendations are drawn.

Dynacs Engineering Co., Inc.

2350

CONCLUSIONS

- TNS3DMB captured some of the flow changes as a result of changes in Reynolds number

- Trend in CFD and NTF trip study needs to be understood

- TNS3DMB provides more flow details than testing does

- Test data are not sufficient to evaluate the CFD thoroughly

- Grid generation took too long, especially with Gridgen

- Convergence of the flow solver is too slow

- More time is needed for post-processing and data analyses

Dynacs Engineering Co., Inc.

The 700-iteration solutions presented in this document took 14 hours of C-90 time and there are still some questions as to how well the viscous drag has converged. A combination of scalar dissipation followed by matrix dissipation may help to reduce the computation time and to lower the magnitude of the viscous drag. In order to carry out low-speed Navier-Stokes analyses effectively, the convergence must be sped up. The low Mach pre-conditioning feature developed in recent years may be attractive. Also, NAS seems to encourage multi-tasking. Future Navier-Stokes analyses ought to be performed using codes that can do multi-tasking.

The volume grid used in this study was generated in two calendar days, which may be hard to shorten. The surface grid, on the other hand, could be generated within a shorter time if some efforts are made in improving the AGPS command file.

Dynacs Engineering Co., Inc.

RECOMMENDATIONS

- Grid may need to be refined to capture LE vortex location

- Can try another turbulence model; S-A model may be affecting vortex location

- Speed up the convergence of the flow solver

- Scalar dissipation followed by matrix dissipation study

- Shorten the flow time for grid generation

Dynacs Engineering Co., Inc.

2353

ACKNOWLEGMENT

The velocity profiles at the wing trailing edge and the related facing pages were contributed by Allen Chen of Boeing.

Testing the 2.2% HSR Reference H Model with a Modified Wing Planform in the NTF

Lewis R. Owens, Jr.   NASA LaRC

Richard A. Wahls   NASA LaRC

Marvine P. Hamner   McDonnell Douglas Aerospace

NASA Langley Research Center

February 26, 1997

The HSR program moved into phase two with the selection of a new airplane configuration, the Technology Concept Airplane (TCA). The TCA was designed based on the experiences gained while investigating both the Reference H and the Arrow Wing configurations in different wind tunnels and CFD studies. Part of that investigation included performing extensive high Reynolds number testing on the Reference H configuration in the NTF to provide data for predicting full-scale flight performance, as well as developing techniques for testing these types of configurations in the NTF. With the selection of the TCA configuration, a smaller investigation was designed to examine whether or not the scaling characteristics of the TCA configuration are similar to those observed for the Reference H configuration. This presentation will include a description of the 2.2% Modified Reference H model used in this investigation (highlighting the similarities and the differences when compared to the TCA configuration), the testing objectives, and some preliminary findings that are relevant to the current high-lift system.

Outline

- Objectives
- Background
- Approach
- Model Geometry
- Analysis Approach
- NTF Results
  - planform
  - partial vs full (f/m & minituft)
- Conclusions

As outlined above, this presentation will begin with a statement of the general objectives of the project, followed by background information which led to the initiation of the study, and the approach taken to meet the objectives. Next, the wind tunnel model is described including its relationship to both the Reference H and Technology Concept Airplane (TCA) geometries. Next, the general data analysis approach will be discussed relative to the objectives of this study. Finally, preliminary analysis of results from the experimental part of this study will be discussed. Concluding remarks will close the presentation.

Objectives

- Obtain Rn sensitivity data for representative wing with the TCA planform
- Obtain Rn sensitivity data for partial vs. full inboard LE flap
- Expand subsonic/transonic data base of Rn sensitivities associated with LE radius variations, including the supersonic LE of an outboard wing panel
  - see paper by Wahls,Rivers, & Owens in CA section of this Workshop:
    "Prediction and Assessment of Reynolds Number Sensitivities Associated with Wing Leading-Edge Radius Variations"

The general objectives of the project are shown above. The primary goals included preliminary assessments of the Rn effects associated with the planform change from the Reference H to the TCA and of the corresponding change to the high-lift, inboard LE flap configuration. An additional objective addressed in the course of this study, but not presented herein, included the expansion of the data base showing the effects of LE radius distribution and corresponding sensitivity to Rn at subsonic and transonic conditions. Particular emphasis was placed on the under exploited supersonic LE of the outboard wing panel. This topic was addressed in the experimental portion of the study, and results are described in a separate paper in this workshop (Configuration Aerodynamics Session) entitled:

"Prediction and Assessment of Reynolds Number Sensitivities Associated with Wing Leading-Edge Radius Variations," by Wahls, Rivers and Owens.

Background

- HSR Program
  - Baseline configuration changed from Ref H to TCA
  - Timing issues
    - affect next downselect to Tech. Configuration
    - material availability, new vs. modified model, NTF shutdown
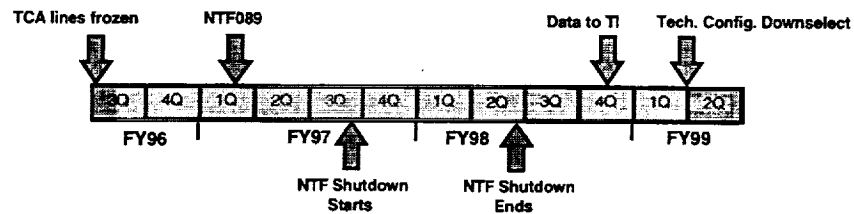
The HSR program is currently in a 3 year phase centered around the evaluation and redesign of the TCA configuration. It was desired to generate Rn effects data on the TCA planform, examine the high-lift LE flap configuration, and demonstrate that a blunt supersonic LE design is worth pursuing in time to provide input to the definition of the follow-on baseline configuration. Given the NTF schedule and major shutdown for upgrade, model material availability, and insufficient funds/support for a new model, the decision was made to target a test window in the NTF in the 1st quarter of FY97 prior to the NTF shutdown.

Approach

- Modify 2.2% Ref H model to TCA planform
  - include alternate LE radius distribution & high-lift flaps
- Perform NTF test
  - Rn effects assessment on TCA planform
  - compare partial vs full inboard flap differences and associated Rn effects

Image 1: 1/17/97
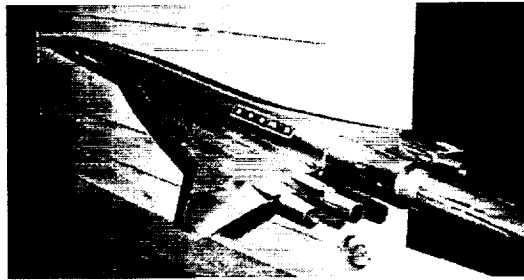
The approach to meet the objectives within the program and facility availability constraints was as follows. First, modify an existing model suitable for the NTF test environment. The obvious choice was the 2.2% HSR Reference H model. Second, perform a test in the NTF at high-lift and transonic conditions to provide a wide range of Rn conditions to allow experimentally based assessments.

Model Geometry I

- Comparison of Modified Ref H and Ref H Models
- Geometric Constants at 2.2% scale

	S_{ref} ft^2 (gross)	mac in.	span in.	AR	LE sweep deg
Ref. H	3.674	22.71	34.23	2.21	76/68.5/48
Modified Ref. H.	4.114	25.07	34.65	2.03	71/52

```
  30
  25 |·····existing body + wing center section
  20 |——TCA planform
  15 |— — ·Ref. H planform
  10
   5
   0
     0   10   20   30   40   50   60   70
                  x, inches
```
y, inches
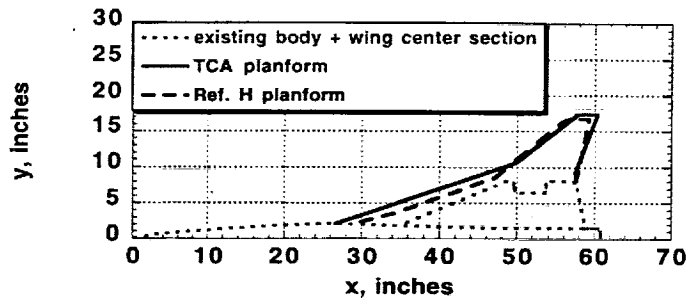
The first step was the modification of the existing 2.2% HSR Ref. H model to represent the TCA wing as closely as possible. Geometric constants are shown above; the Modified Ref. H values are identical to the TCA. Note, that the reference area for the Ref. H is the gross wing area (rather than the wimpress area used during Ref. H testing) to be consistent with the TCA definition. The Ref. H (truncated) body and inboard wing center section and TE (indicated by the dotted lines) were maintained, while the LE and outboard wing panels (indicated by the dashed lines) were not. New LE and outboard wing panels were designed and fabricated to provide the TCA planform while not restricting a return to the Ref. H geometry.

Model Geometry II

- Airfoil modification process was as follows:
  - align TCA & Ref. H TE (inboard sections; existing model)
  - rotate TCA section around TE to align to with existing Ref. H parts
  - blend overlap section between TCA LE and existing Ref. H parts
  - spanwise blending outboard of existing Ref. H parts
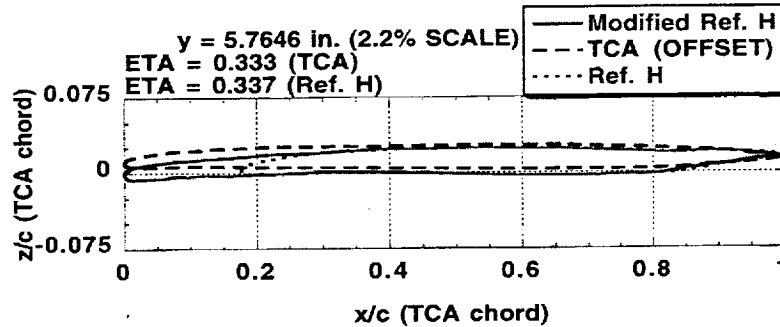
The modification process, or more specifically the blending process, is demonstrated above for a typical inboard airfoil section. First, the TCA section at a given span location is translated to match the TE of the existing Ref. H model hardware. Next, the TCA section is rotated around the TE to align with the existing model parts with emphasis on the upper surface to avoid unwanted surface inflections. Finally, blending occurs over a small region forward of the existing hardware in to the TCA LE region. This sequence was repeated for several airfoils over the span of the existing wing center section/TE hardware; outboard of this point, a small blending region existed in the spanwise direction until the TCA outboard airfoil definitions could be maintained.

Model Geometry III

- Comparison of Modified Ref. H, Ref. H, & TCA Geometries
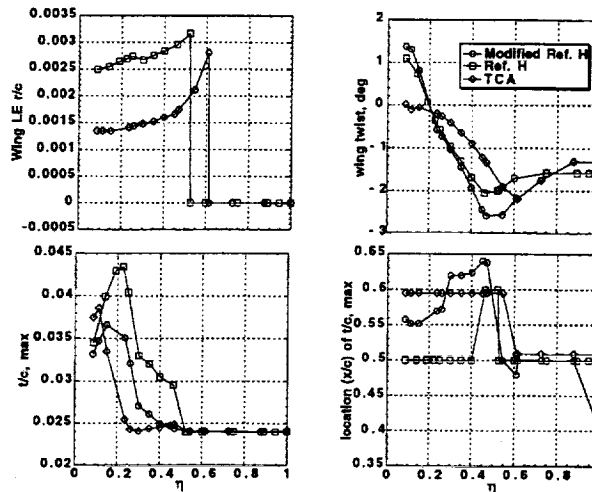
The resulting geometry had the characteristics shown above. Note that wing LE radius distribution of the modified Ref. H is identical to that of the TCA, and that both the TCA and the Ref. H have a sharp LE on the outboard wing panel. Existing Ref. H model hardware inboard drives the differences in wing twist, maximum thickness, and the location of the maximum thickness. Outboard of the pre-existing hardware, the modified Ref. H and TCA geometries more closely match.

The resulting geometry was smooth and sufficient to address the objectives of the study. However, in no way should this geometry be considered optimized aerodynamically.

NTF Test Variables

- Mach = 0.30
- $Rn,mac = 9.4 \rightarrow 100 \times 10^6$
- $\alpha = -3° \rightarrow 24°$
- nacelles on/off
- 0/0 flaps
- 30/10 partial & full span flaps
- baseline & alt. LE radius

- Mach = 0.90
- $Rn,mac = 11 \rightarrow 89 \times 10^6$
- $\alpha = -2° \rightarrow 12°$
- nacelles off
- 0/0 flaps

- baseline & alt. LE radius

The range of test conditions in the NTF test (designated NTF089) pertinent to this study are shown above. All data shown herein were obtained with natural transition on the wing. A complete set of low Rn data with fixed transition was planned but not obtained due to significant facility downtime associated with a pitch system failure. Force and moment data were obtained. Limited pressure data on the existing Ref. H wing center section were also obtained; LE and outboard wing panel pressures were not obtained due to limited funding and design/fabrication time constraints.

Analysis Approach

- Differences in Ref. H & Modified Ref. H (TCA planform)
  - AR, camber + twist = warp, wetted area, thickness distrib., ...
- Linear Theory
  - simple planform (AR) relationship allows lift-curve-slope comparisons
  - $\alpha_{MRefH} = \alpha_{RefH} + \dfrac{C_L}{\pi} \times (\dfrac{1}{AR_{MRefH}} - \dfrac{1}{AR_{RefH}}) \times \dfrac{180}{\pi}$

- Plan to use AERO2S for warp effects

  - drag, pitching-moment, $\alpha_{zero-lift}$, ...
- Compare partial vs full inboard LE flap configuration
  - force & moment data as a function of Rn
  - minituft flow visualization

The analysis approach (work in progress) is outlined above. In order to make comparisons between the Rn trends associated with the Ref. H and those of the modified Ref. H configurations, it is necessary to account for differences in the data due to certain geometric differences. This is a challenging task, and currently only the CL data for the undeflected flaps have been adjusted for AR differences so that comparisons in the lift-curve slope are presented. The AR adjustments are only made to the angle of attack as shown above. Note that this method assumes fully-attached flow, which is not true across the angle-of-attack range tested here. The future analysis plans include modelling camber, twist and wetted-area differences to allow comparisons for drag and L/D. The analysis of the data obtained for the different high-lift flap configurations included making comparisons using the force/moment data as well as the minituft data.

NTF Results I

- Comparison of lift-curve-slope between Ref H & Modified Ref H
  - Mach = 0.3, undeflected flaps
- CL_α trends with Rn differ
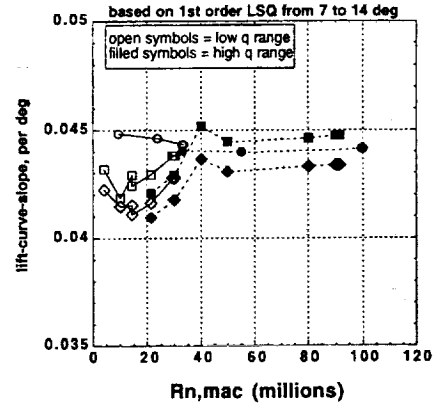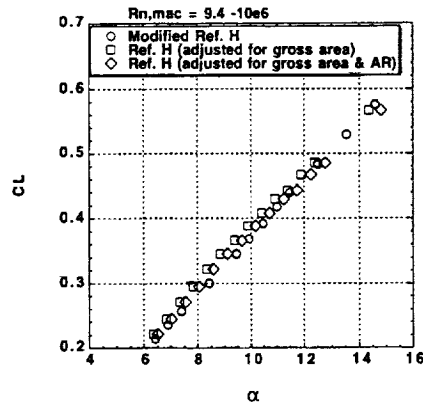
The plot on the left shows the comparison of CL as a function of alpha for the modified Ref. H, Ref. H (adjusted for gross wing ref. area difference), and Ref. H (adjusted for gross wing ref. area and aspect ratio difference) at low Rn. All data shown is for Mach = 0.3 with undeflected flaps. The aspect ratio correction does not fully collapse the differences between the modified Ref. H and the Ref. H lift curves, which may be expected with various LE separations present in this angle-of-attack range. The plot on the right indicates that the lift-curve slopes obtained from a limited angle-of-attack range for modified Ref. H and Ref. H have different sensitivities to Rn, with the Ref. H data showing more sensitivity at low Reynolds numbers.

NTF Results II

- Comparison of lift-curve-slope between Ref H & Modified Ref H
  - Mach = 0.9, undeflected flaps
- CL_α trends with Rn are similar
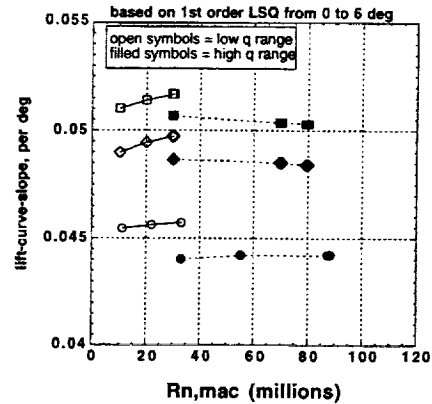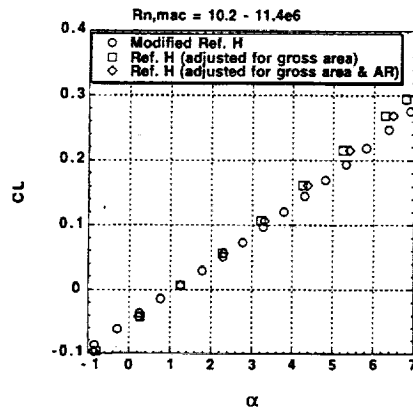
The plot on the left shows the comparison of CL as a function of alpha for the modified Ref. H, Ref. H (adjusted for gross wing ref. area difference), and Ref. H (adjusted for gross wing ref. area and aspect ratio difference) at low Rn. All data shown is for Mach = 0.9 with undeflected flaps. The aspect ratio correction does not fully collapse the differences between the modified Ref. H and the Ref. H lift curves, which may be expected with various LE separations present for alpha greater than approximately 2.5 degrees. The plot on the right indicates that the lift-curve slopes obtained from a limited angle-of-attack range for modified Ref. H and Ref. H have similar sensitivities (small) to Rn. The jump in the lift-curve slope at Rn of about 30 million is associated with the aeroelastic step.

NTF Results III

- Comparison of partial vs full inboard flap deployment on CM
  - Large flap configuration effect
  - Small Reynolds number effect (at least relatively)
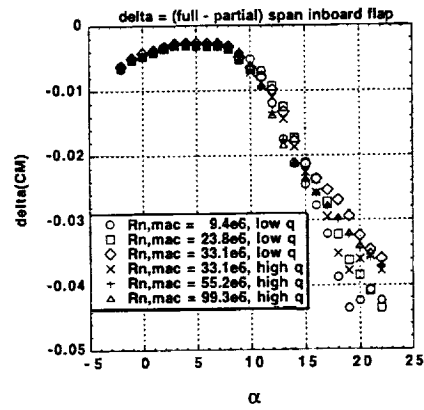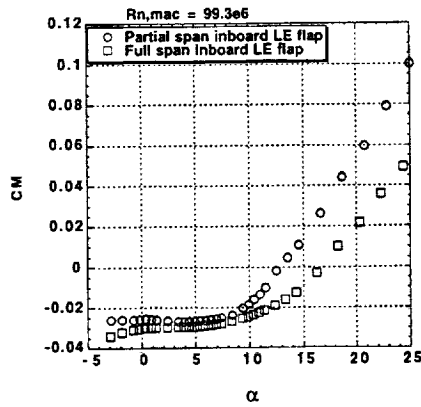
The plot of CM as a function alpha is presented on the left to show the LE flap configuration (partial span vs full span) effect at the highest available Rn test condition. On the right, a plot of the CM difference (full - partial) as a function of alpha demonstrates that the Rn sensitivities are much smaller than the flap configuration effect.

NTF Results IV

- Comparison of partial vs full inboard flap deployment on CL
  - Large flap configuration effect
  - Small Reynolds number effect (at least relatively)
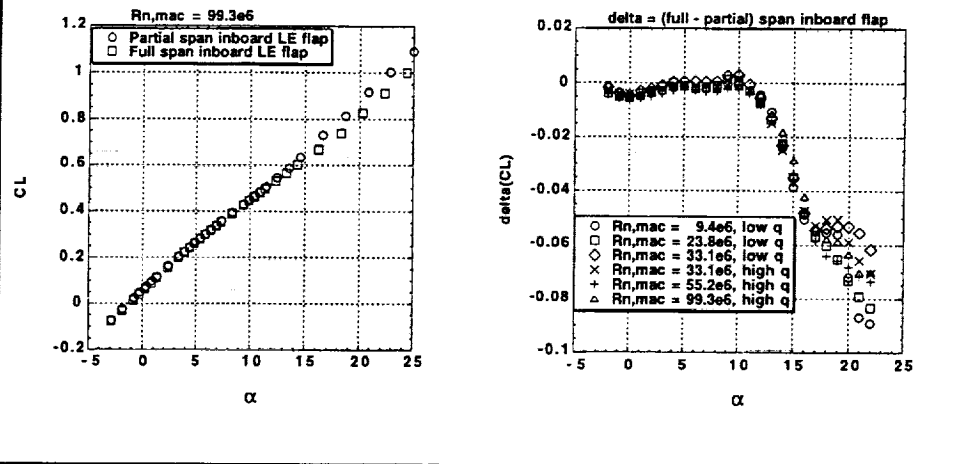
The plot of CL as a function alpha is presented on the left to show the LE flap configuration (partial span vs full span) effect at the highest available Rn test condition. On the right, a plot of the CL difference (full - partial) as a function of alpha demonstrates that the Rn sensitivities are much smaller than the flap configuration effect.

2368

NTF Results V

- Comparison of partial vs full inboard flap deployment on CD
  - Large flap configuration effect
  - Small Reynolds number effect (at least relatively)
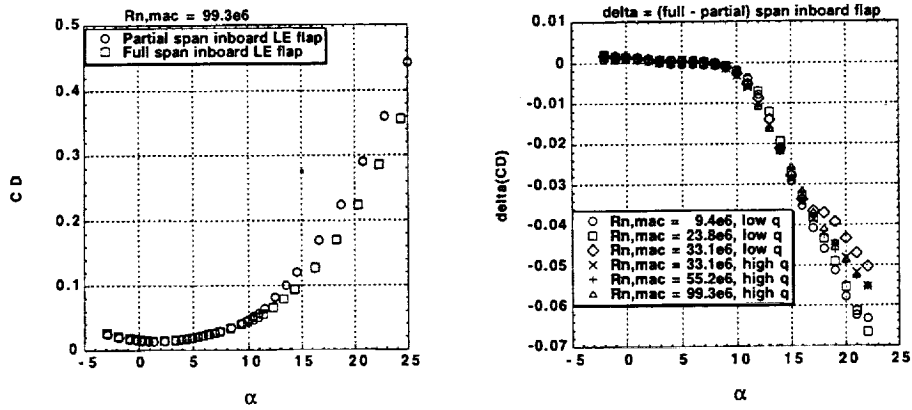
The plot of CD as a function alpha is presented on the left to show the LE flap configuration (partial span vs full span) effect at the highest available Rn test condition. On the right, a plot of the CD difference (full - partial) as a function of alpha demonstrates that the Rn sensitivities are much smaller than the flap configuration effect.

NTF Results VI

- Comparison of partial vs full inboard flap deployment on L/D
  - Large flap configuration effect
  - Small Reynolds number effect (at least relatively)
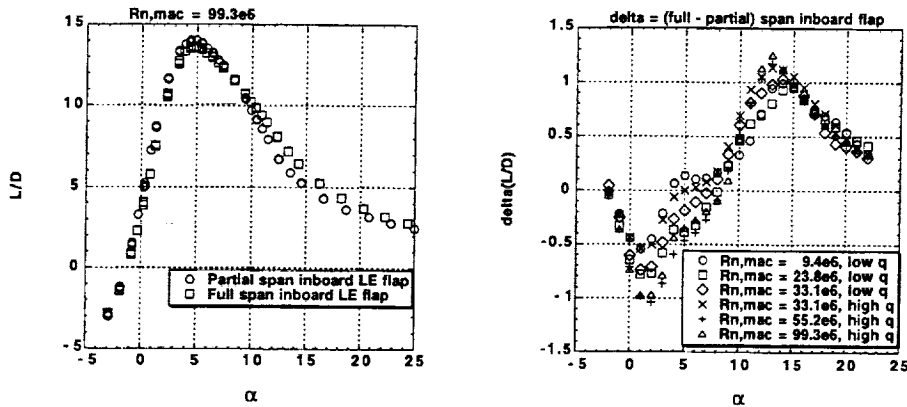
The plot of L/D as a function alpha is presented on the left to show the LE flap configuration (partial span vs full span) effect at the highest available Rn test condition. On the right, a plot of the L/D difference (full - partial) as a function of alpha demonstrates that the Rn sensitivities are smaller than the flap configuration effect.

Camera Views of Minitufts on Wing

- Minitufts applied to left upper wing surface only
  - Camera #14
    - inboard LE near wing/body juncture
  - Camera #1
    - mid span LE covering area where part span LE flap begins
  - Camera #9
    - overall view of wing including outboard wing panel
    - not shown in this presentation
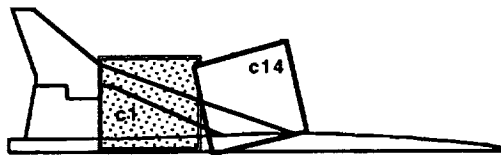
The figure above shows the view orientations for each of the cameras used to obtain minituft data on the inboard, upper surface of the left wing for the modified Ref. H model. The data was obtained at low Rn conditions only. Also, only the Mach = 0.3 data is presented in the next slides to illustrate differences associated with the large LE flap effects shown previously in the force/moment data. The data are grouped by nominal angles of attack (8, 12 and 14 degrees). Multiple angles of attack are presented to give a sense of LE vortex progression.

NTF Results VII-a

- Undeflected flap vs. partial span flap ($\alpha=8°$)
  - c14; inboard near wing/body juncture
  - both LEs -- attached flow character
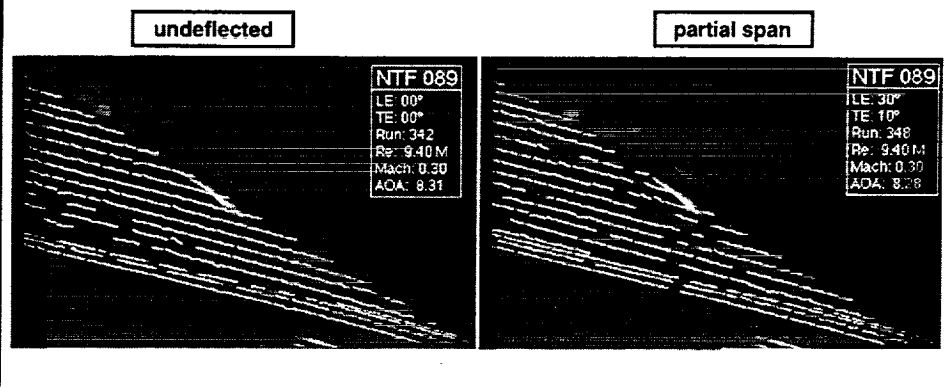
In this figure, the undeflected and partial span LE flaps are compared at an alpha of about 8 degrees. Both configurations exhibit attached LE flow characteristics in this region.

NTF Results VII-b

- Partial span flap vs. full span flap (α=8°)
  - c14; inboard near wing/body juncture
  - both LEs -- attached flow character
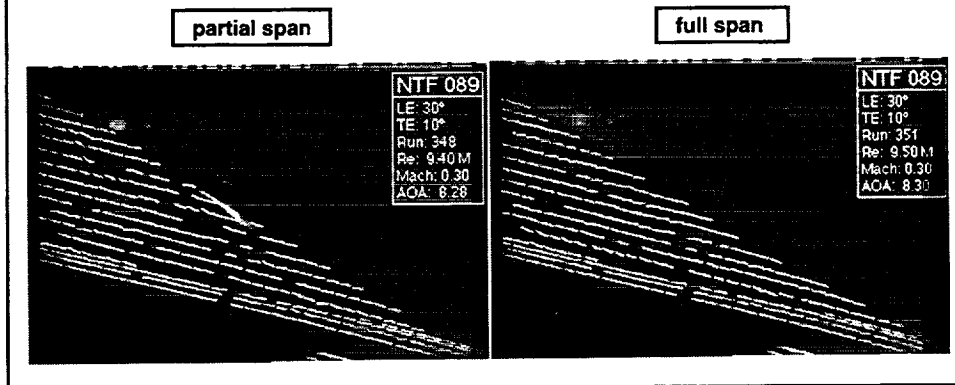
In this figure, the partial and full span LE flaps are compared at an alpha of about 8 degrees. Again, both configurations exhibit attached LE flow characteristics in this region.

NTF Results VII-c

- Undeflected flap vs. partial span flap (α=8°)
  - c01; mid span (inboard of LE crank)
  - undeflected
    - separated flow character beginning
  - partial span
    - attached flow character on LE flap

undeflected
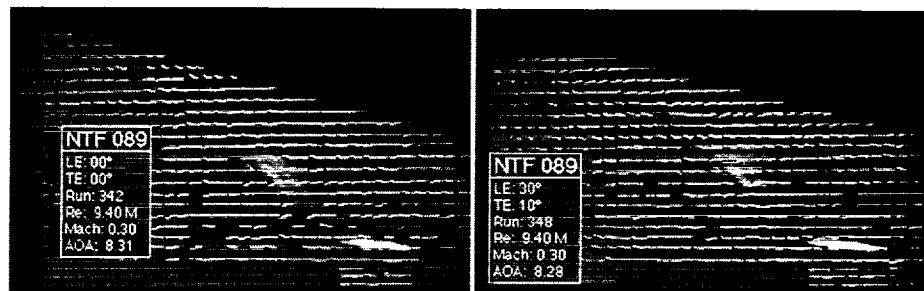
partial span

NTF 089
LE: 00°
TE: 00°
Run: 342
Re: 9.40 M
Mach: 0.30
AOA: 8.31

NTF 089
LE: 30°
TE: 10°
Run: 348
Re: 9.40 M
Mach: 0.30
AOA: 8.28

In this figure, the undeflected and partial span LE flaps are compared at an alpha of about 8 degrees. The undeflected configuration image shows signs of a LE vortex (toward upper, left corner of image). The minitufts that are influenced by separated flow can be identified as those that are not only misaligned with the streamwise direction but must also appear to be a faint blur in the image indicating the dynamic motions of the separated flow. The part span flap does not show any signs of separation.

1997 HSR Aerodynamic Performance Workshop

NTF Results VII-d

- Partial span flap vs. full span flap ($\alpha=8°$)
  - c01; mid span (inboard of LE crank)
  - part span LE
    - attached flow character on LE flap
  - full span LE
    - attached flow character on LE flap

partial span

full span
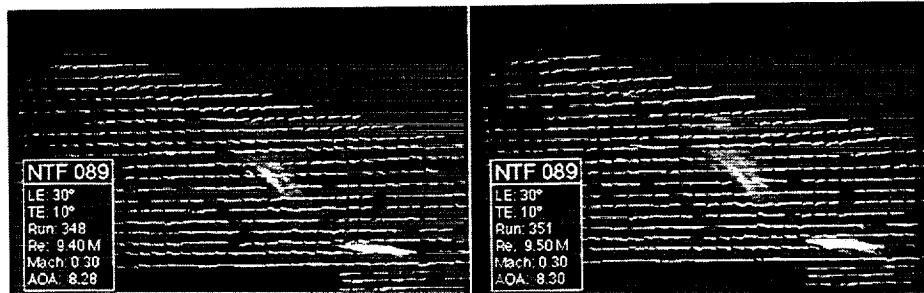
NTF 089
LE: 30°
TE: 10°
Run: 348
Re: 9.40 M
Mach: 0.30
AOA: 8.28

NTF 089
LE: 30°
TE: 10°
Run: 351
Re: 9.50 M
Mach: 0.30
AOA: 8.30

In this figure, the partial and full span LE flaps are compared at an alpha of about 8 degrees. Both configurations exhibit attached LE flow characteristics in this region.

2375

NTF Results VIII-a

- Undeflected flap vs. partial span flap ($\alpha=12°$)
  - c14; inboard near wing/body juncture
  - both LEs -- separated flow character beginning

undeflected
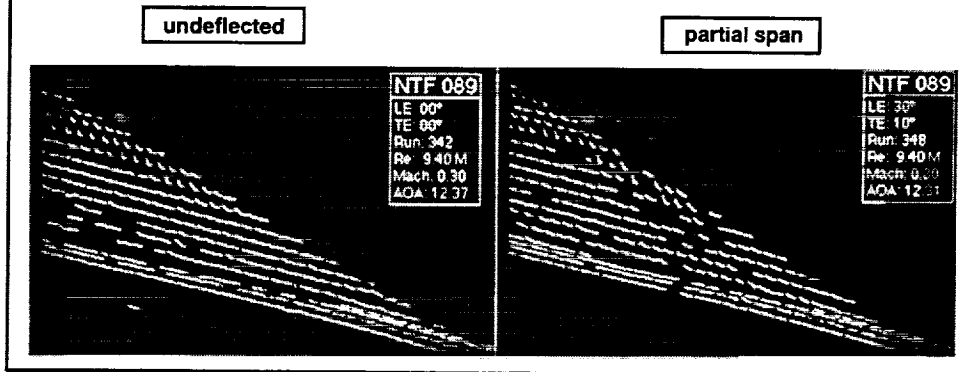
partial span

In this figure, both LE configurations exhibit similar LE separation characteristics at this angle of attack.

NTF Results VIII-b

- Partial span flap vs. full span flap (α=12°)
  - c14; inboard near wing/body juncture
  - part span LE
    - separated flow character on undeflected inboard LE beginning
  - full span LE
    - attached flow character on LE flap
    - separated flow character at flap hingeline
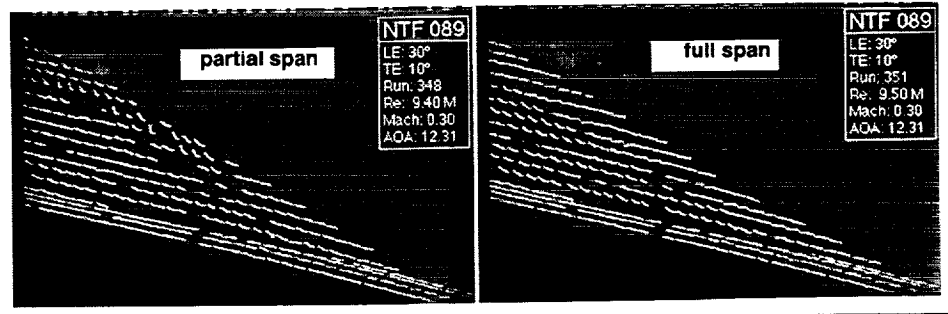
In this figure, the partial and full span LE flap configurations are compared and there is a significant difference in the LE separation characteristics. The flow is attached on the full span LE flap. This difference helps to explain the performance difference between the two flaps, in which the full span flap has lower drag, lower lift, higher L/D and less pitch-up.

1997 HSR Aerodynamic Performance Workshop

NTF Results VIII-c

- Undeflected flap vs. partial span flap ($\alpha=12°$)
  - c01; mid span (inboard of LE crank)
  - undeflected
    - separated flow character established
  - partial span
    - separated flow character on LE flap
    - separated flow inboard of start of part span flap
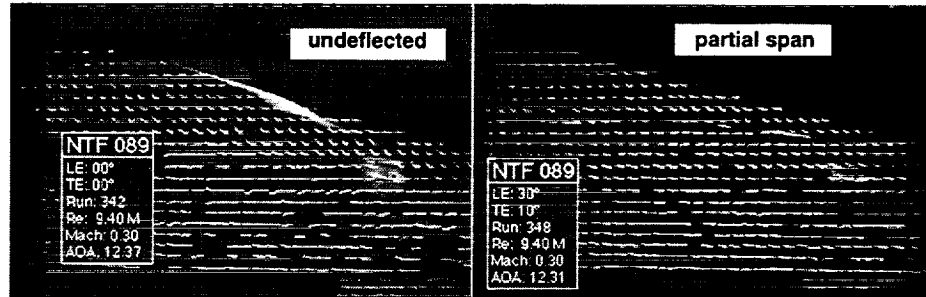
In this figure, the undeflected and partial span LE flap configurations are compared and there is a significant difference in the LE separation characteristics. Note that the comparison of these LE configurations looked very similar in the view near the wing/body juncture. (NTF Results VIII-a slide)

NTF Results VIII-d

- Partial span flap vs. full span flap (α=12°)
  - c01; mid span (inboard of LE crank)
  - part span LE
    - entire LE flap flow separated
  - full span LE
    - separated flow character on beginning on LE flap
    - separated flow character at flap hingeline
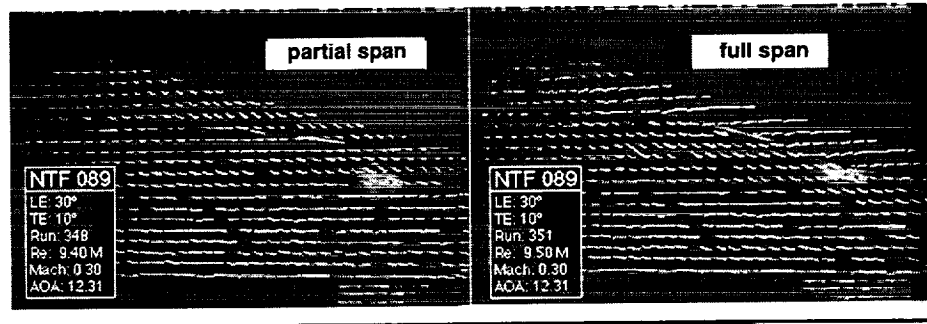
In this figure, the partial and full span LE flap configurations are compared and there is a significant difference in the LE separation characteristics. Again, the full span LE flap has a larger region of attached flow, which helps to explain the performance difference seen in the force/moment data.

NTF Results IX-a

- Undeflected flap vs. partial span flap (α=14°)
  - c14; inboard near wing/body juncture
  - both LEs -- separated flow character established
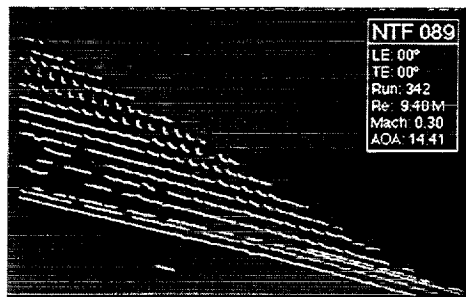
| undeflected | partial span |
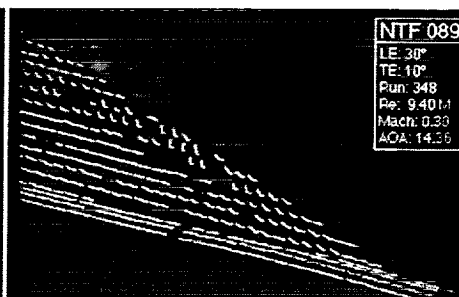
At an angle of attack of 14 degrees, this LE flap comparison is similar to that discussed for 12 degrees. These images were included to give a sense of the LE vortex progression.

NTF Results IX-b

- Partial span flap vs. full span flap ($\alpha=14°$)
  - c14; inboard near wing/body juncture
  - part span LE
    - separated flow character on undeflected inboard LE established
  - full span LE
    - attached flow character on LE flap
    - separated flow character at flap hingeline
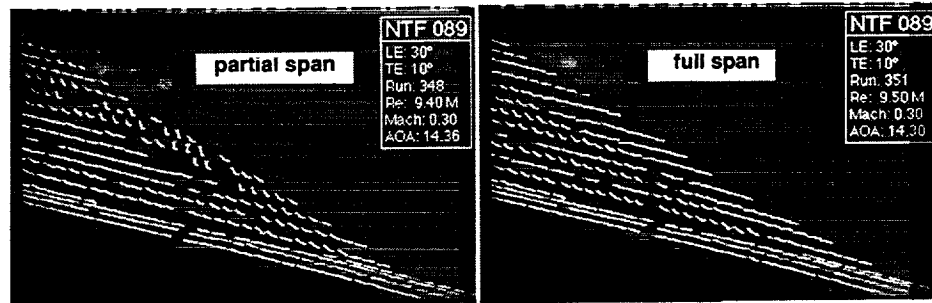
At an angle of attack of 14 degrees, this LE flap comparison is similar to that discussed for 12 degrees. These images were included to give a sense of the LE vortex progression.

NTF Results IX-c

- Undeflected flap vs. partial span flap (α=14°)
  - c01; mid span (inboard of LE crank)
  - undeflected
    - separated flow character established
  - partial span
    - separated flow character on LE flap
    - separated flow inboard of part span flap affects larger area
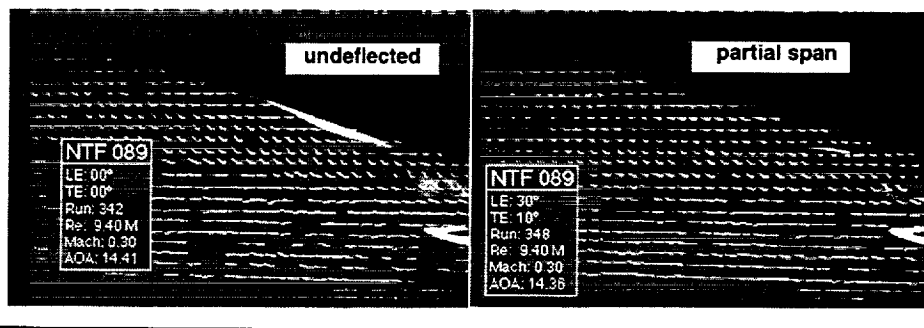
At an angle of attack of 14 degrees, this LE flap comparison is similar to that discussed for 12 degrees. These images were included to give a sense of the LE vortex progression.

NTF Results IX-d

- Partial span flap vs.full span flap (α=14°)
  - c01; mid span (inboard of LE crank)
  - part span LE
    - separated flow region of LE continues to grow
  - full span LE
    - separation onset moves inboard on LE flap
    - separated flow character at flap hingeline
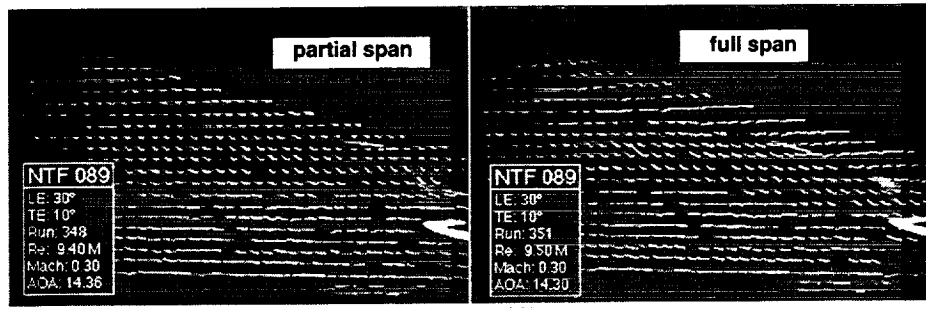
partial span **full span**

NTF 089
LE: 30°
TE: 10°
Run: 348
Re: 9.40 M
Mach: 0.30
AOA: 14.36

NTF 089
LE: 30°
TE: 10°
Run: 351
Re: 9.50 M
Mach: 0.30
AOA: 14.30

At an angle of attack of 14 degrees, this LE flap comparison is similar to that discussed for 12 degrees. These images were included to give a sense of the LE vortex progression.

Conclusions

- Planform Effects (Modified Ref. H vs Ref. H) - 0/0 flaps
  - effectiveness of AR adjustment
    - in general, does not collapse lift curve data
  - CL_α trends with Rn
    - Differ at Mach = 0.3
    - Similar at Mach = 0.9
- Partial vs Full Inboard Flap Differences
  - Large performance difference beginning near design condition
  - Rn effect relatively small in comparison to performance difference
  - Differences driven by separation and vortex formation that Rn changes do not eliminate

In conclusion, the analysis of the planform effects has started with an attempt to adjust the lift data for aspect ratio differences for the undeflected flap configurations. These aspect ratio adjustments have not successfully collapsed the lift-curve data. The lift-curve slope trend with Rn depended on the configuration and Mach number. Further analysis of these planform effects are needed as well as looking at deflected flap configurations.

A large performance difference between partial and full span LE flap configurations was found near the design conditions. The data obtained for each flap configuration showed a relatively small (when compared to the performance difference) Rn effect. The LE flap configuration performance difference is explained by the differences in the amount of attached LE flow regions present on each flap.

2384

High Speed Research Program
Aerodynamic Performance Technology Workshop

High Lift Technology Element

Evaluation of Alternate Control Surface Concepts

Bryan Campbell

NASA, LaRC

Mr. Campbell currently works within the Subsonic Aerodynamics Branch of the Aero and Gas Dynamics Division at the Langley Research Center of NASA.

OUTLINE

Aerodynamic effects of canard longitudinal and height placement, relative area, and aspect ratio on longitudinal aerodynamics.

Potential of asymmetric chine deflection with emphasis on varying forebody location, height, dihedral, and incidence angle.

Advantages of strategically locating wing mounted upper surface fins relative to the local surface flow.

Recommendations

Although several viable concepts have been investigated during recent years, time constraints do not allow for a detailed discussion of each. Therefore, only a small segment of these concepts will be discussed during this workshop. Emphasis will be placed on canards, forebody chines and wing fins.
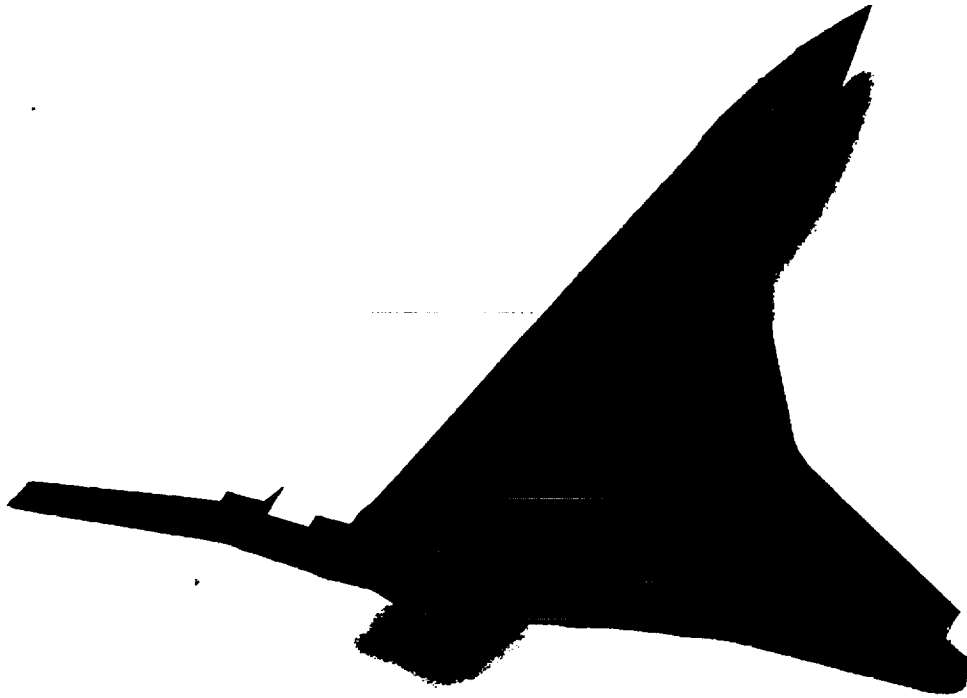
The majority of the data presented were obtained using a 0.01542 scale representation of the HSR Reference-H model. This model was similar in planform, and incorporated full-span leading-edge flaps and segmented trailing-edge flaps. Shown in the photograph is the high-lift configuration of leading-edges at 30°, and trailing-edges at 10°. The wing had no twist or camber. The forebody and fuselage were simple bodies of revolution. A detachable aft fuselage, complete with empennage, was incorporated during the chine study, and removed during the canard tests. The overall length (including aft fuselage) was approximately 58 inches; and the span was 24 inches.

Characteristics of Longitudinal Canard Placement
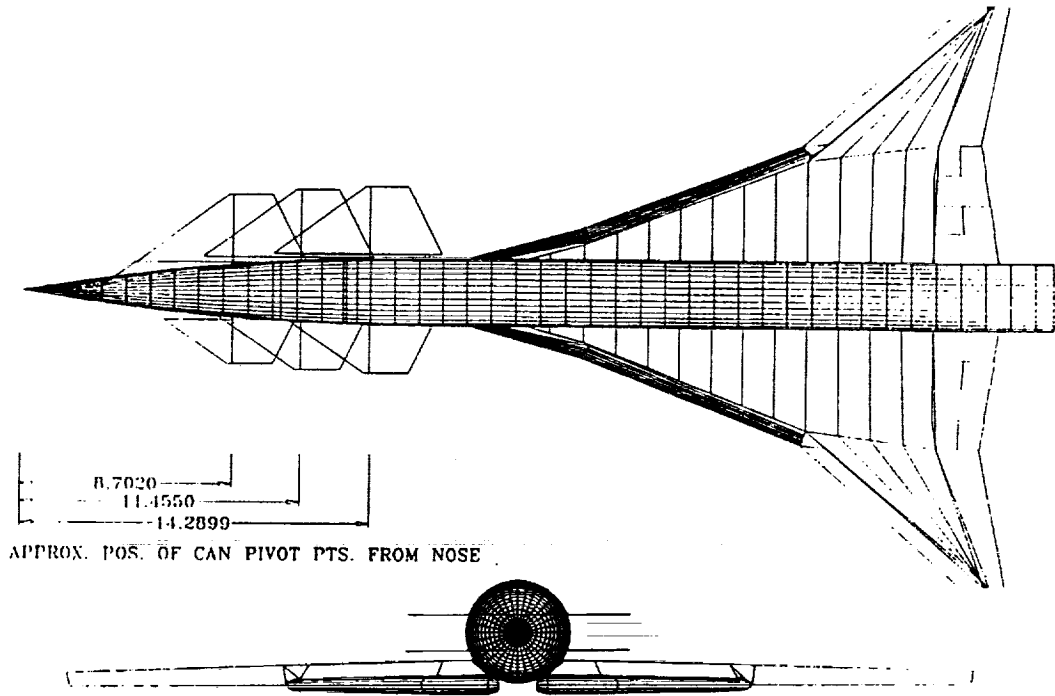

```
         ┌ 8.7020 ───────┘
         └─── 11.4550 ──────────┐
         └──────── 14.2899 ─────────┘
APPROX. POS. OF CAN PIVOT PTS. FROM NOSE
```

The canard investigation looked at the effects of canard longitudinal placement, height, surface area, and aspect ratio. This figure shows the baseline canard, sized to be similar to the Ref-H horizontal tail, compared with one half the surface area. Each canard was capable of a wide range of incidence.

Characteristics of Longitudinal Canard Placement
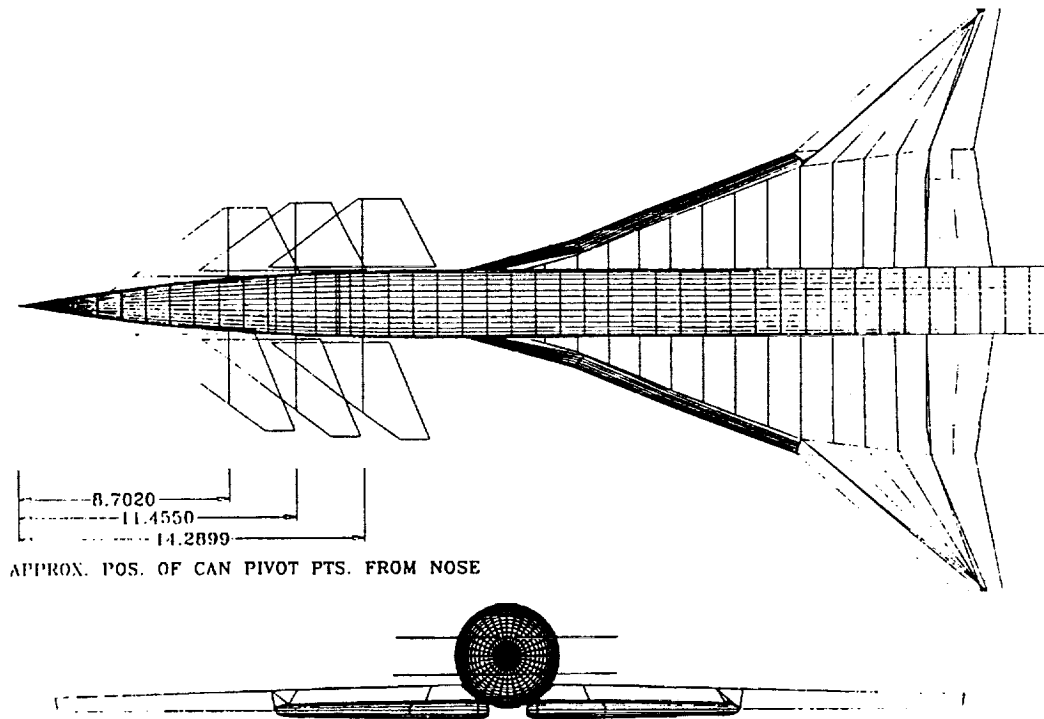

```
|-----8.7020-----|
|-------11.4550------|
|-------14.2899--------|
```

APPROX. POS. OF CAN PIVOT PTS. FROM NOSE

The canard investigation looked at the effects of canard longitudinal placement, height, surface area, and aspect ratio. This figure shows the baseline canard, sized to be similar to the Ref-H horizontal tail, compared with one that is twice the aspect ratio. Each canard was capable of a wide range of incidence.

Aerodynamic Effects of Canard Longitudinal Placement

Baseline Canard, Height = upper, $\delta_c=0^\circ$, Flaps at $30^\circ/10^\circ$, q=25 psf
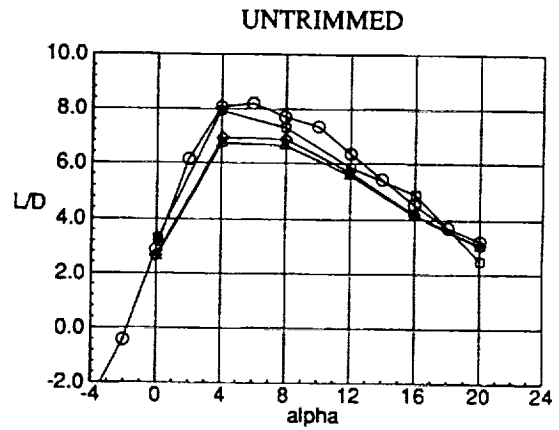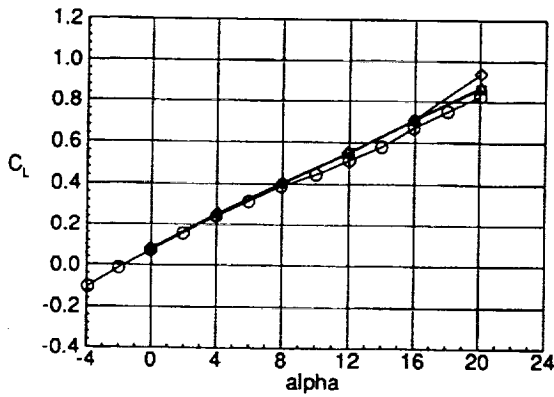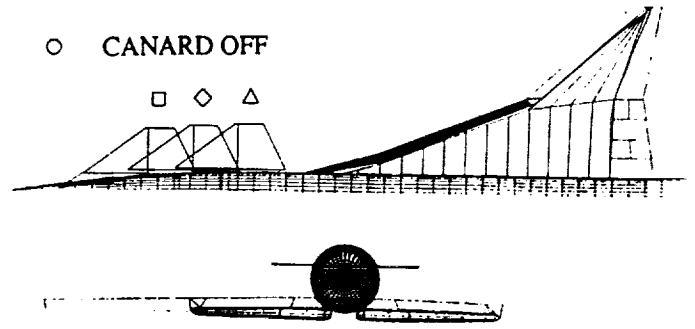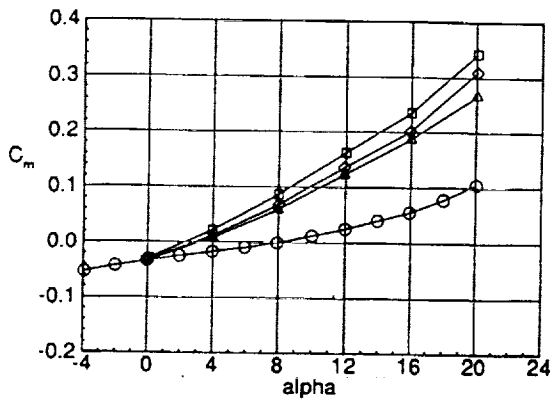
Reducing the canard moment arm has the effect of similarly reducing the overall pitch of the model. Changing this location had little influence on lift; but, as seen in the L/D plot, has an influence on drag.

Control Power Effects of Canard Longitudinal Placement

Baseline Canard, Height = upper, $\alpha=12^{\circ}$, Flaps at $30^{\circ}/10^{\circ}$, q=25 psf
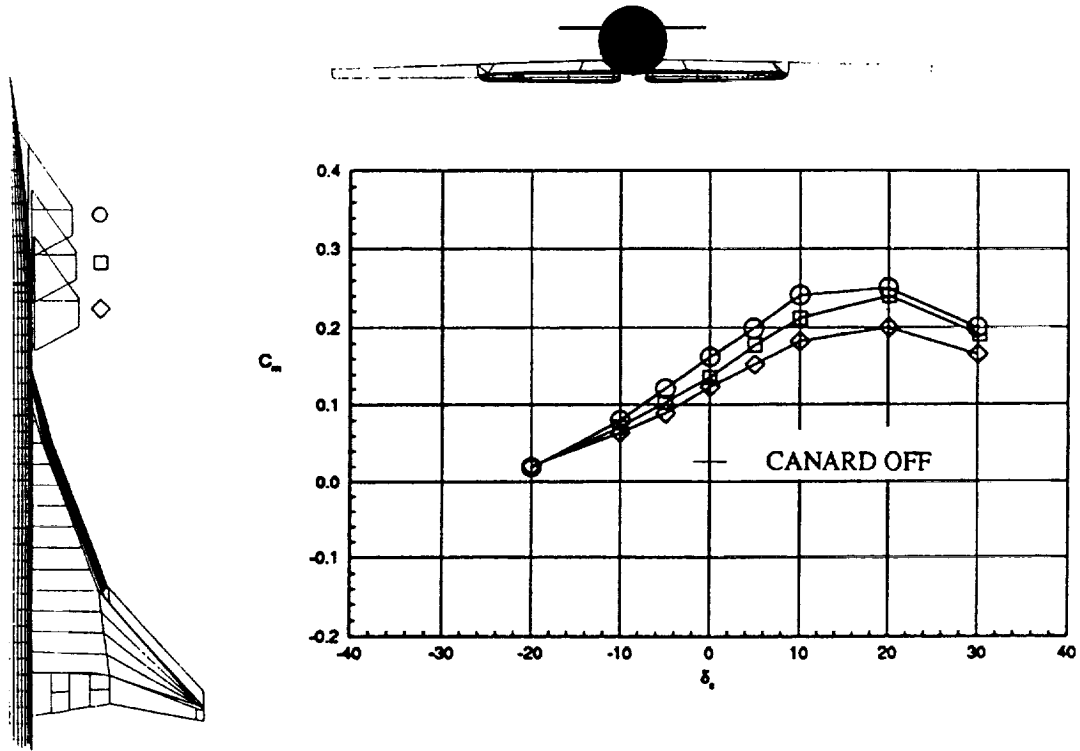
The magnitude of control power for each canard location is show for a range of canard incidence angles. Clearly, the more forward position provided significant improvements.

Aerodynamic Effects of Canard Height Placement

Baseline Canard, Forward Position, $\delta_c=0^o$, Flaps at $30^o/10^o$, q=25 psf

○ CANARD OFF

UNTRIMMED

The overall pitch up of the model is reduced by lowering the canard height on the fore-body. However, doing so adversely effects the untrimmed L/D.

Aerodynamic Effects of Canard Height Placement

Baseline Canard, Middle Position, $\delta_c=0^o$, Flaps at $30^o/10^o$, q=25 psf

○   CANARD OFF

UNTRIMMED

Aerodynamic Effects of Canard Height Placement

Baseline Canard, Aft Position, $\delta_c=0°$, Flaps at $30°/10°$, q=25 psf
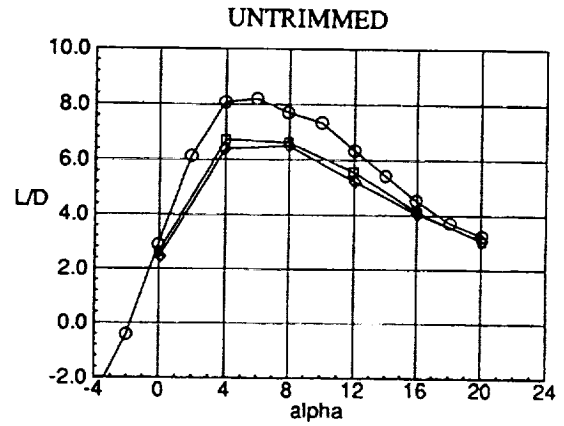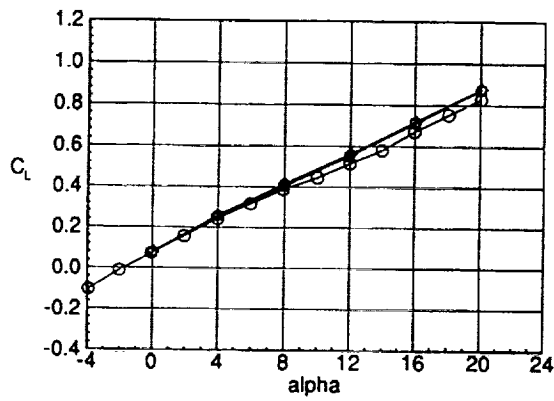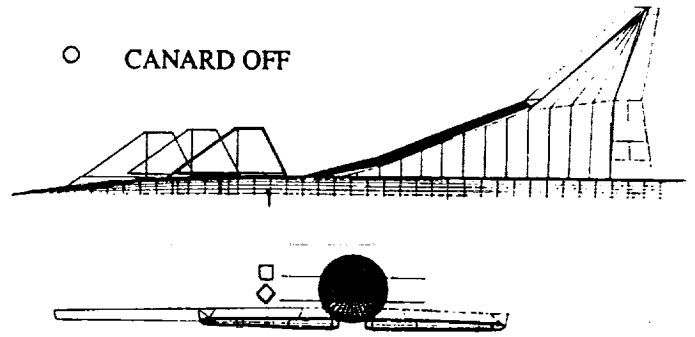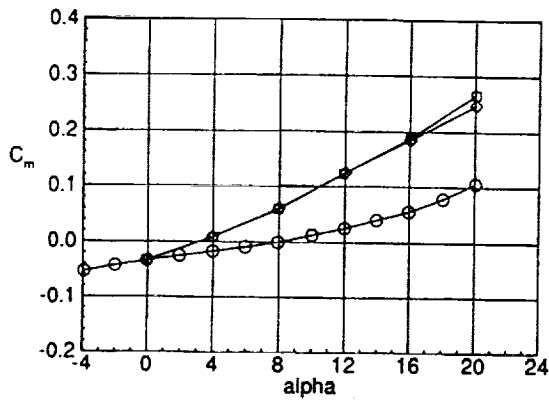
○ CANARD OFF

UNTRIMMED

Aerodynamic Effects of Canard Surface Area

Forward Position, Height = upper, $\delta_c=0°$, Flaps at $30°/10°$, q=25 psf
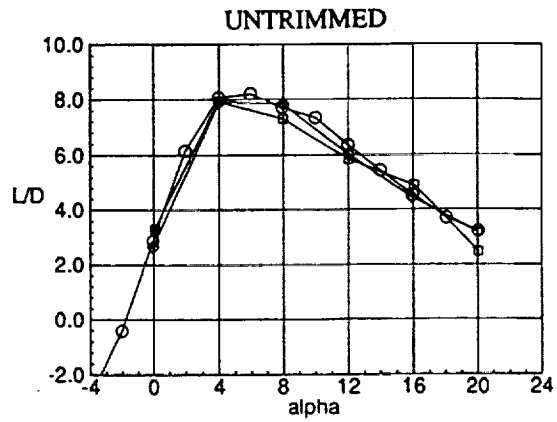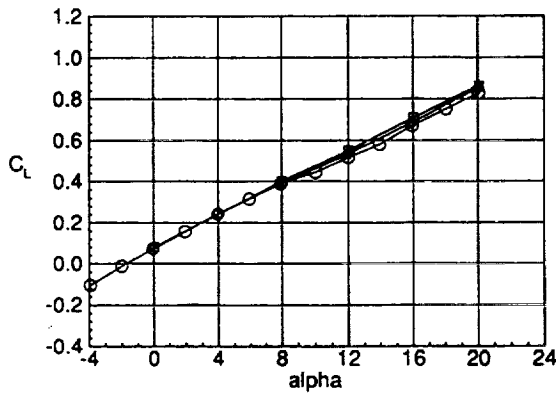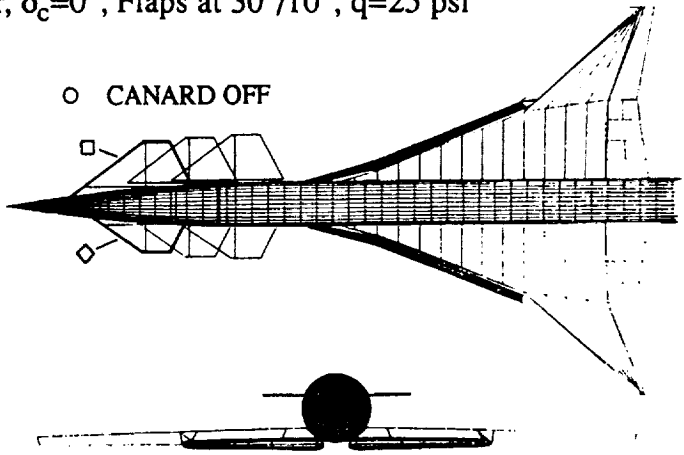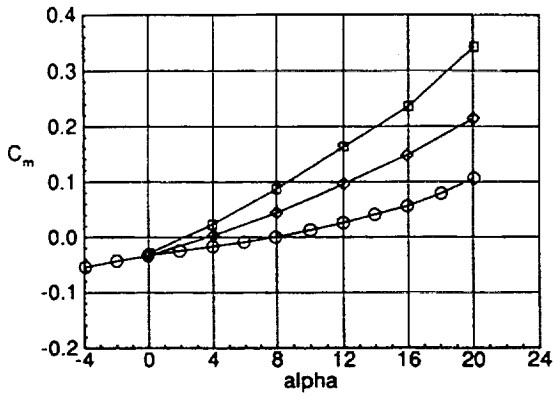
Halving the canard surface area had the effect of halving the overall model pitch up with little influence on lift. The untrimmed L/D, however, reflects an improvement.

Control Power Effects of Canard Surface Area

Forward Position, Height = upper, $\alpha=12^{\circ}$, Flaps at $30^{\circ}/10^{\circ}$, q=25 psf
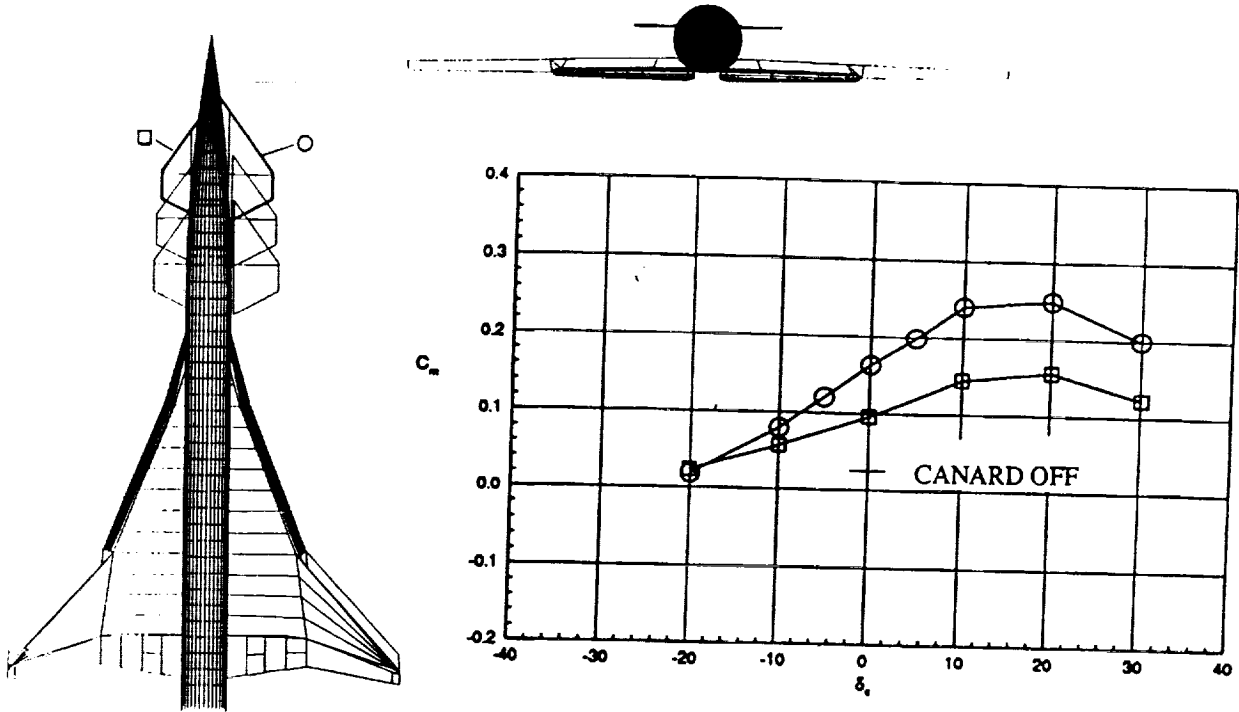
Control power seems to be linearly related to the canard surface area.

Control Power Effects of Canard Surface Area

Forward Position, Height = lower, α=12°, Flaps at 30°/10°, q=25 psf
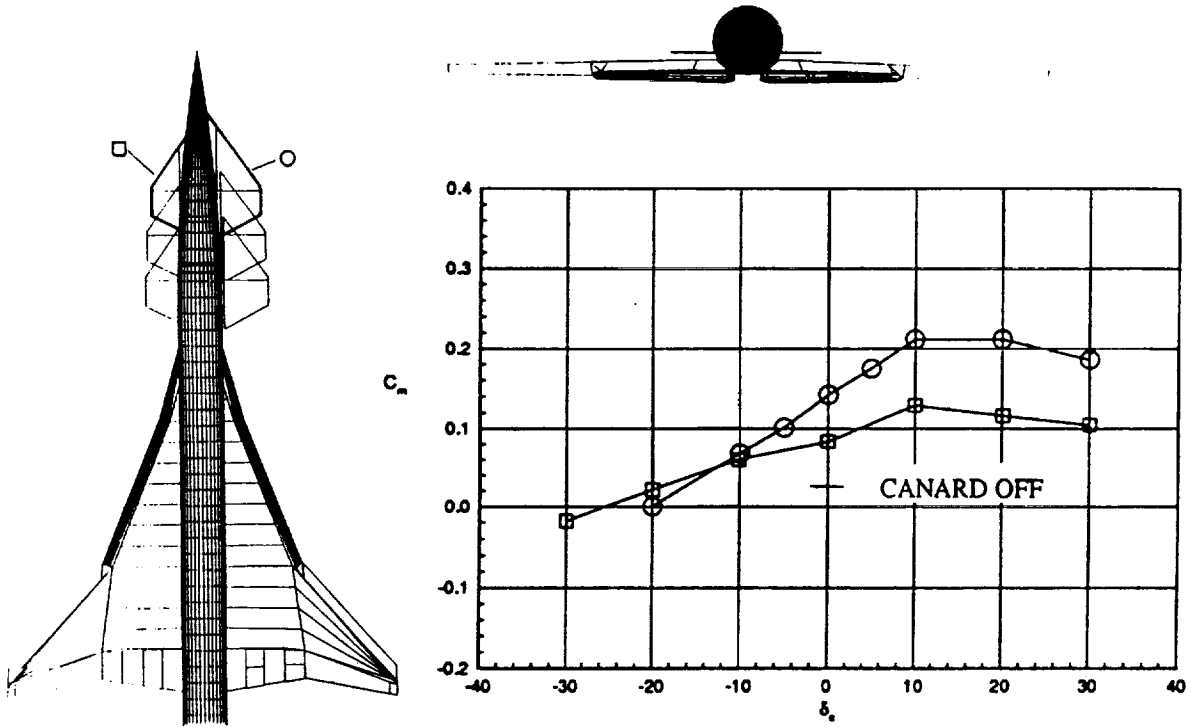
Although the linearity of canard surface area to control power is preserved for the lower height position, the overall magnitude for a given deflection angle is reduced.

Aerodynamic Effects of Canard Aspect Ratio

Forward Position, Height = upper, $\delta_c=0°$, Flaps at $30°/10°$, q=25 psf

O   CANARD OFF
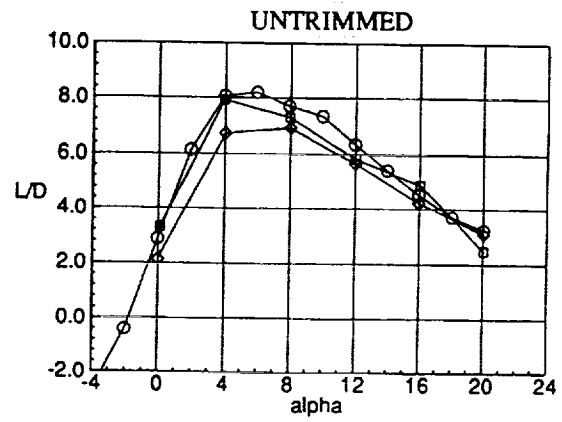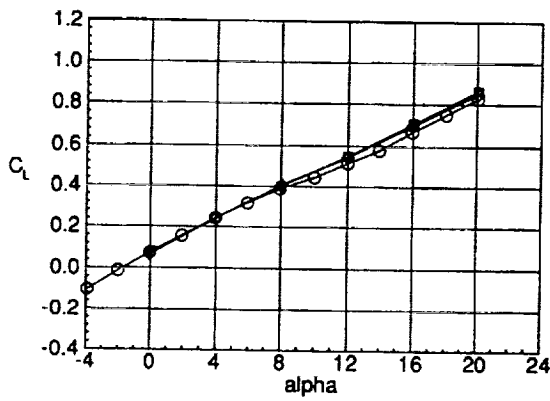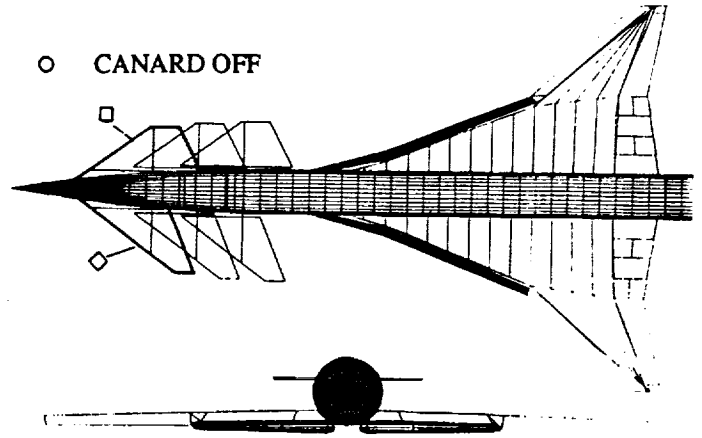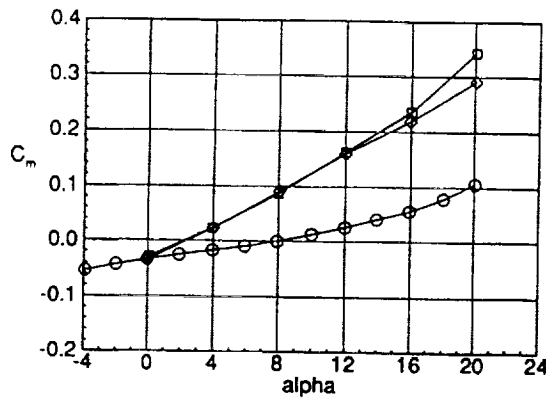
UNTRIMMED

The change in aspect ratio has a direct effect on model pitch at higher angles of attack. The effects on lift are relatively small. Whereas, the effects on untrimmed L/D are significant.

Control Power Effects of Canard Aspect Ratio

Forward Position, Height = upper, $\alpha=12^{o}$, Flaps at $30^{o}/10^{o}$, q=25 psf
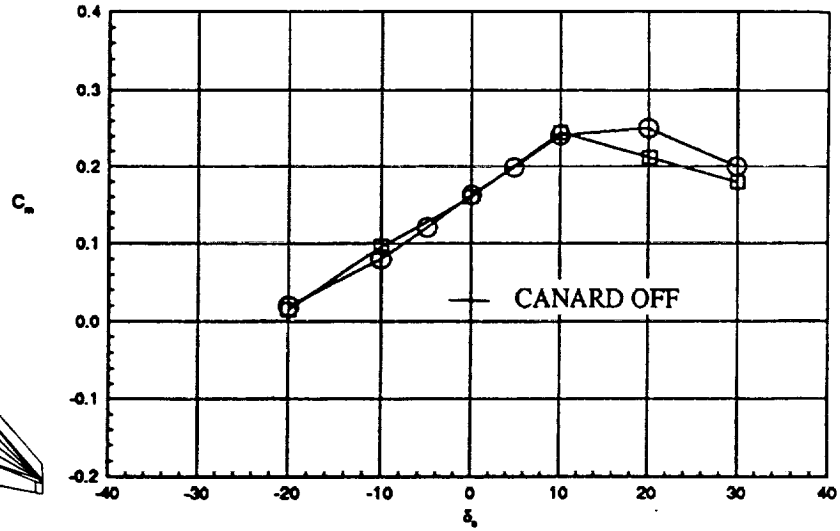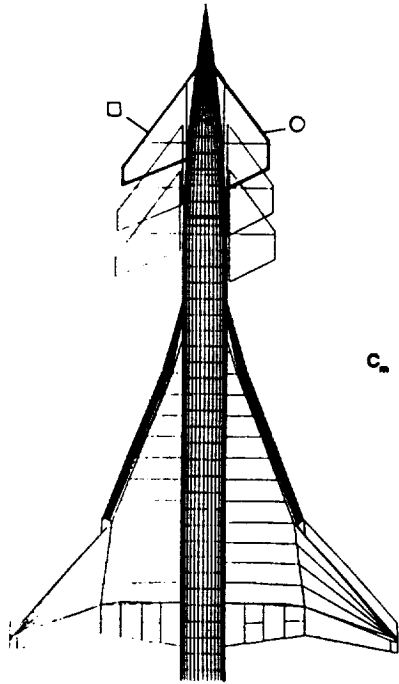
No significant effects on control power due to canard aspect ratio are observed over the linear range. The are some effects over the canard stall range.

Directional Control Effects of Longitudinal Chine Placement

Asymmetric Chines = right side only, $\beta=0°$, Flaps at $30°/10°$, q=20 psf

SYMBOL	X, in
○	--
□	5
◇	7
△	9
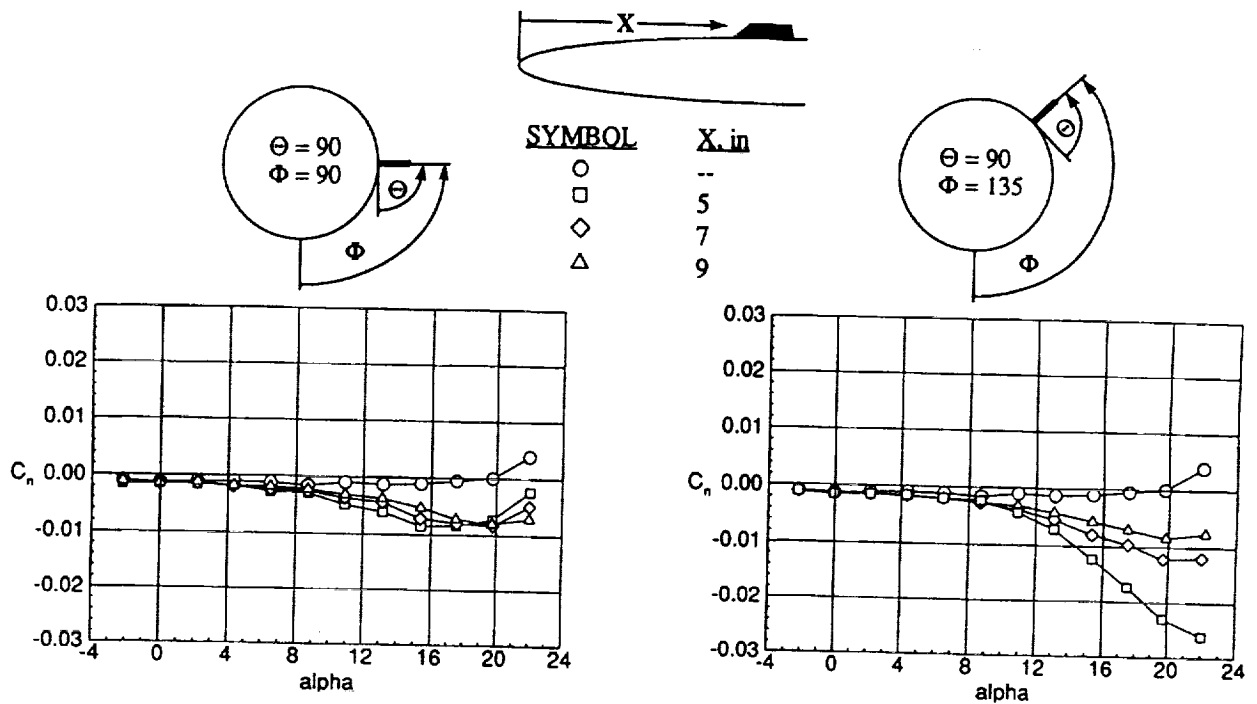
Moving an asymmetric chine forward on the forebody increases the directional control. Increasing the azimuthal angle further enhances these effects.

Directional Control Effects of Chine Incidence

Asymmetric Chines = right side only, β=0°, Flaps at 30°/10°, q=20 psf
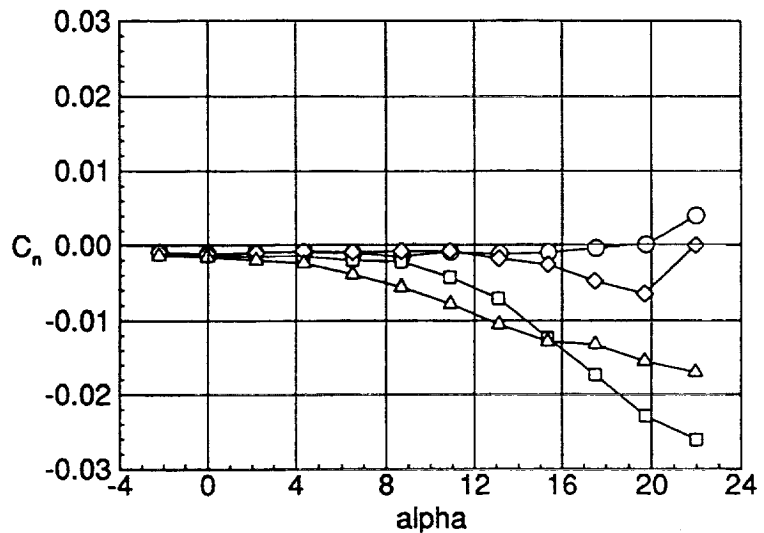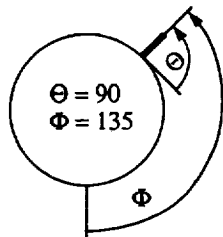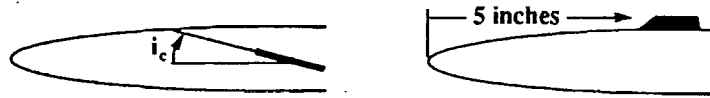
Increasing the relative chine incidence angle further increases directional control. At high angles of attack, the undeflected chine provides greater control. This would indicate a changing local forebody flowfield, and thus warrant a schedule for chine incidence as a function of angle of attack to supplement the vertical tail.

Directional Control Effects of Chine Dihedral

Asymmetric Chines = right side only, $\beta=0°$, Flaps at $30°/10°$, q=20 psf
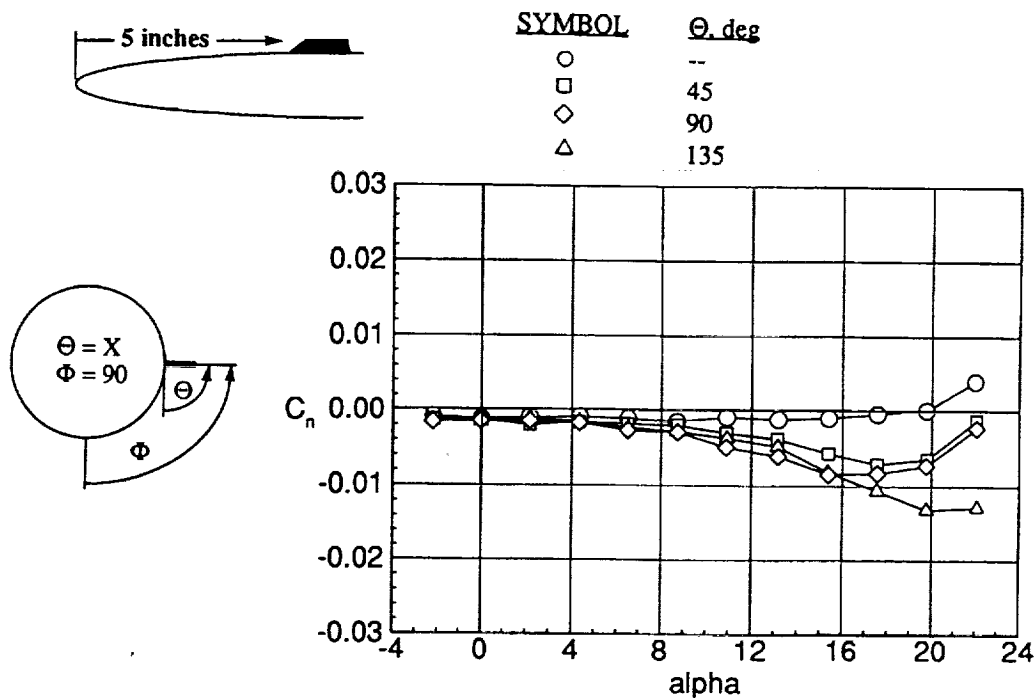
As with asymmetric chine incidence angle, the effects of chine dihedral vary with angle of attack and would benefit from a deflection schedule.

Potential Benefits from Wing-Mounted Upper Surface Fins
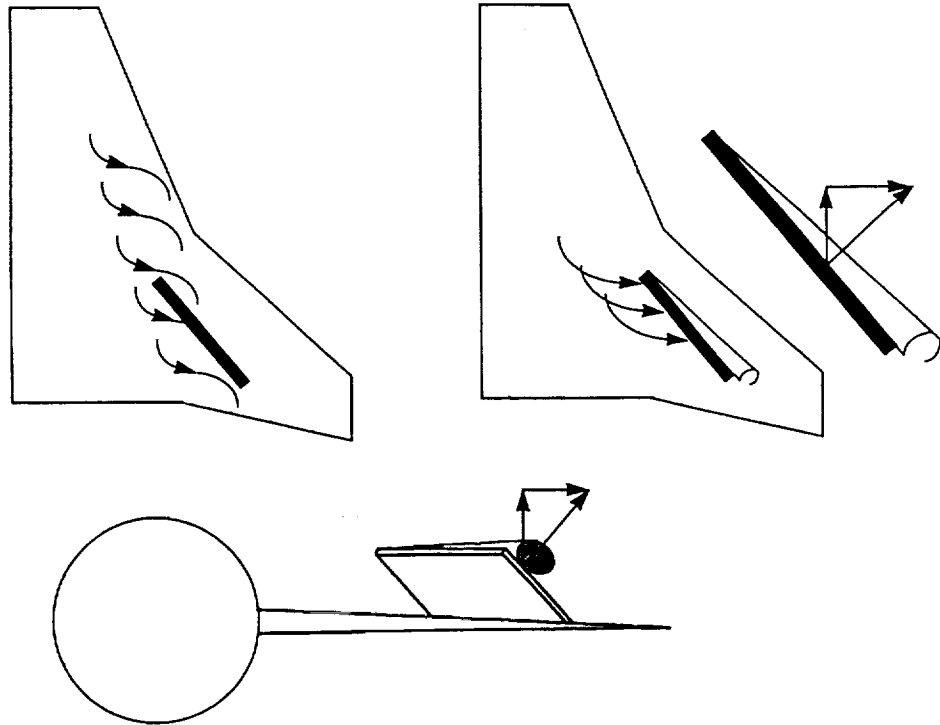
Potential aerodynamic improvements exist by properly aligning wing mounted upper surface fins relative to the local vortex induced spanwise flow. However, proper fin rotation and cant are essential to gain the benefits of increased lift and cleaner flow over the aileron.

71/50 HSR Model Showing Fin Concept
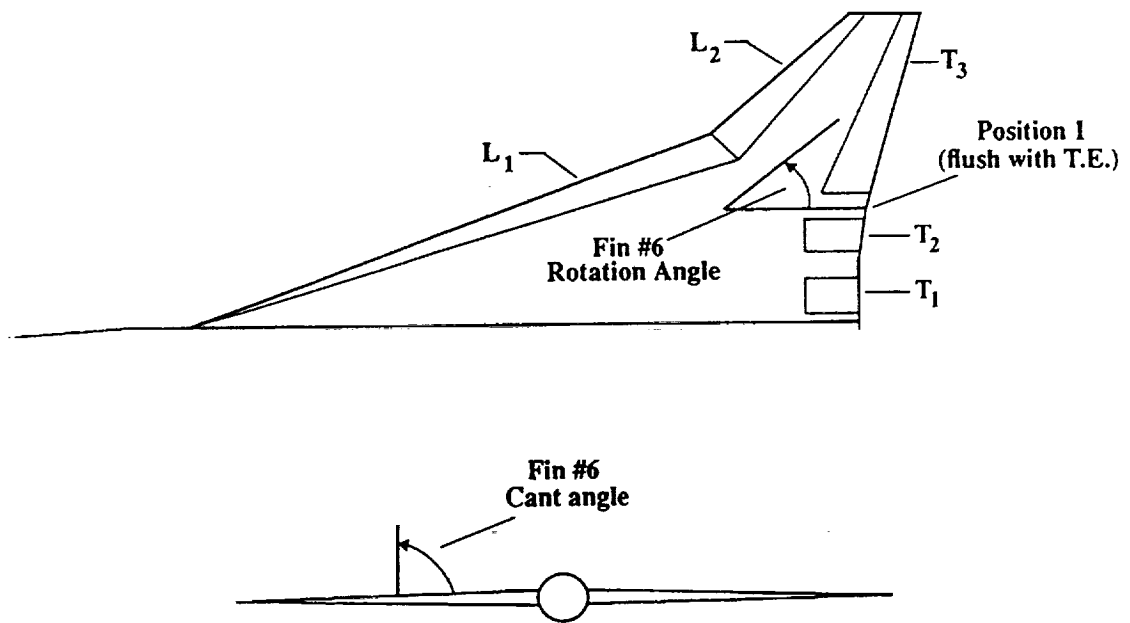
The concept of fin rotating and canting were tested on the HSR 71/50 model at the 14- by 22-Foot Subsonic Tunnel.

L/D Effects of Wing Fin Rotation with Cant at 90°

Fin L.E. Sweep=65, Fin Aspect Ratio=0.5, Flaps at 26/10/13, q=70 psf

Configuration

o	$\beta_F = 0°$, $\phi_F = 90°$
□	$\beta_F = 10°$, $\phi_F = 90°$
◇	$\beta_F = 20°$, $\phi_F = 90°$
△	$\beta_F = 30°$, $\phi_F = 90°$
▲	$\beta_F = 40°$, $\phi_F = 90°$
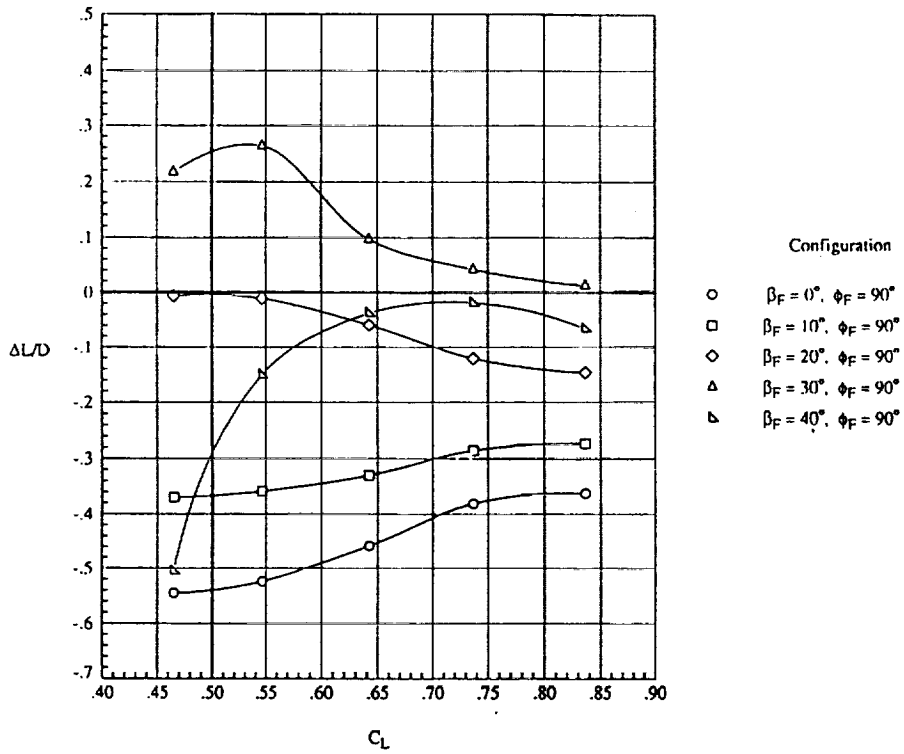
There exists a precise angle of fin rotation for each angle of attack due to the changing location of the vortex trajectory.

L/D Effects of Wing Fin Canting with Rotation at 30°
Fin L.E. Sweep=65, Fin Aspect Ratio=0.5, Flaps at 26/10/13, q=70 psf

Configuration

○ $\beta_F = 30°$, $\phi_F = 90°$

□ $\beta_F = 30°$, $\phi_F = 75°$

◇ $\beta_F = 30°$, $\phi_F = 60°$
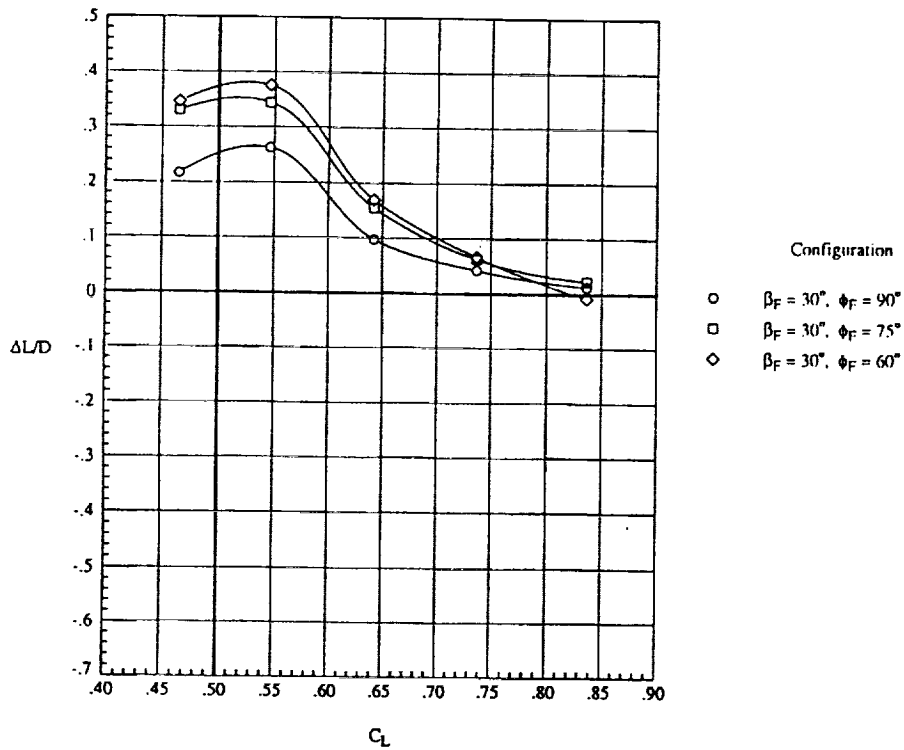
Significant improvements in L/D can be achieved by properly canting the rotated fin.

Recommendations

The placement of canards on the forebody must take into account not only the local airflow around the forebody, but the resulting impact of the canard wake interaction and its ability to alter the local wing upwash field as it articulates through its relative deflections.

The use of asymmetric chine deflections provide a powerful tool for increased directional control. However, the relative placement of the chine is very sensitive to the local forebody flow; thus, great care must be given to its location.

Methods such as the optimally placed wing mounted fins may be desirable to favorably utilize the local spanwise flow to increase L/D, and by the nature of their placement, decrease the spanwise flow over the aileron surfaces, thus allowing greater roll authority and the possible use of split ailerons for increased yaw control.

The placement of canards, chines, and wing fins must take into account the pattern and the dynamics of the local flow structures, not necessarily the global free stream characteristics. By following this thought process, significant aerodynamic improvements in high lift and control are possible.

THIS PAGE IS INTENTIONALLY LEFT BLANK

Status of NASA #442 Test Results

6% Ref. H Upflow and Interference Test in the LaRC 14'x22'

Robert C. Griffiths
Boeing Commercial Aircraft Group

High Speed Research Program
Aerodynamic Performance Technology Workshop

February 26, 1997

Status of NASA #442 Test Results

Status of NASA Test # 442, an upflow and interference (U&I) test
conducted in the Langley 14'x22' low speed wind tunnel,
November 5 - 27, 1996.

WBS: 4.3.2.2 High Lift System Concept Design

Other information:

Model used was the 6% Ref. H.

Total of 318 runs.

Limited titanium dioxide flow visualization.

Outline

- Purpose / objectives

- Importance of upflow & interference (U&I) to HSR

- Test background

- U&I short course

- Data - preliminary results and anomalies

- Summary & recommendations

Purpose of Test

- Determine upflow and support interference in the 14'x22' using the 6% Ref. H.

- Comparison to computational data (panel codes).

- Satisfy contract deliverable.

Purpose of Test

The purpose of this Test #442 was to test Ref. H model configurations in such a manner that 14'x22' upflow and post mount support interference could be determined.

Comparisons of experimentally derived interference data will be compared to computationally calculated support interference.

The results of this test will support an HSR contract deliverable.

Importance of Upflow

$0.1°$ positive upflow $\approx .10$ drag ct $\approx$

+6000 lbs. MTOW at Stage 3 - 3dB

<u>OR</u>

+9800 lbs. MTOW at Stage 3 - 5dB

Importance of Upflow

If the wind tunnel proves to have upflow, the re-corrected data will result
in performance degradation apparent in drag at a constant lift value.
This increased drag will result in an increase in MTOW required to meet
the stated noise objectives for the TCA model.

Correcting for Upflow

Or, What Happens to the Data

If upflow is positive:

- Lift decreases.

- Drag increases.

- $(L/D)_{corr}$ decreases.

Expected Impact of Post Support Interference

Based on A502 panel code, effect of post will be to:

- decrease CL by ≈ 0.008 (3%)

- decrease CD by ≈ 0.0007 (5%)

- increase CM by ≈ 0.0002 (3%)

at 10 degrees alpha.
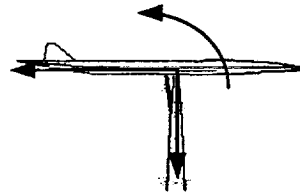
How to Calculate Upflow

- Generally, 2 methods are used:

    - differencing upright and inverted lift curves, and

    - "rotating" upright and inverted drag polars.

- Upflow determined by one method can be checked by the other.
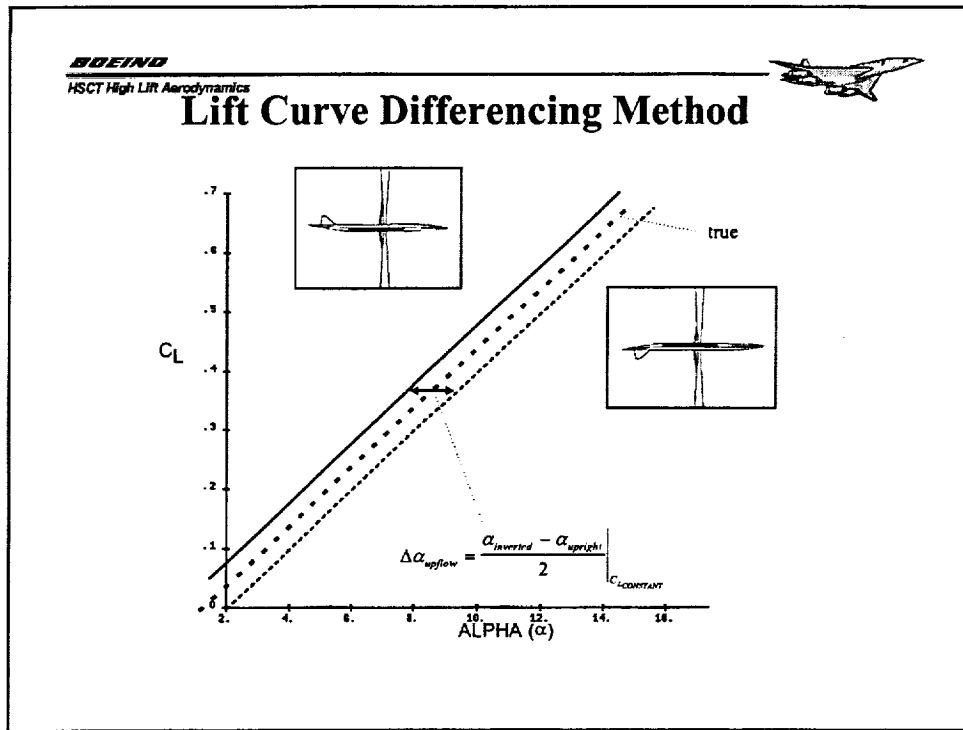
Lift Curve Differencing Method

The lift curve differencing method involves subtracting the (inverted + image) lift curve from the (upright + image) lift curve at a constant CL. A positive resultant means positive upflow. The true lift curve lies midway between the upright and inverted runs.

$$\Delta\alpha_{upflow} = \left.\frac{\alpha_{inverted} - \alpha_{upright}}{2}\right|_{C_{L_{CONSTANT}}}$$

An image is required for both the upright and inverted runs to ensure equal support interference; want to avoid upflow measurements skewed by support induced local upflow.

Drag Polar Rotation
Illustrative only. Upflow is shown.

$$\Delta\alpha_{upflow} = \sin^{-1}\left(\frac{\Delta C_D}{2C_L}\right)$$
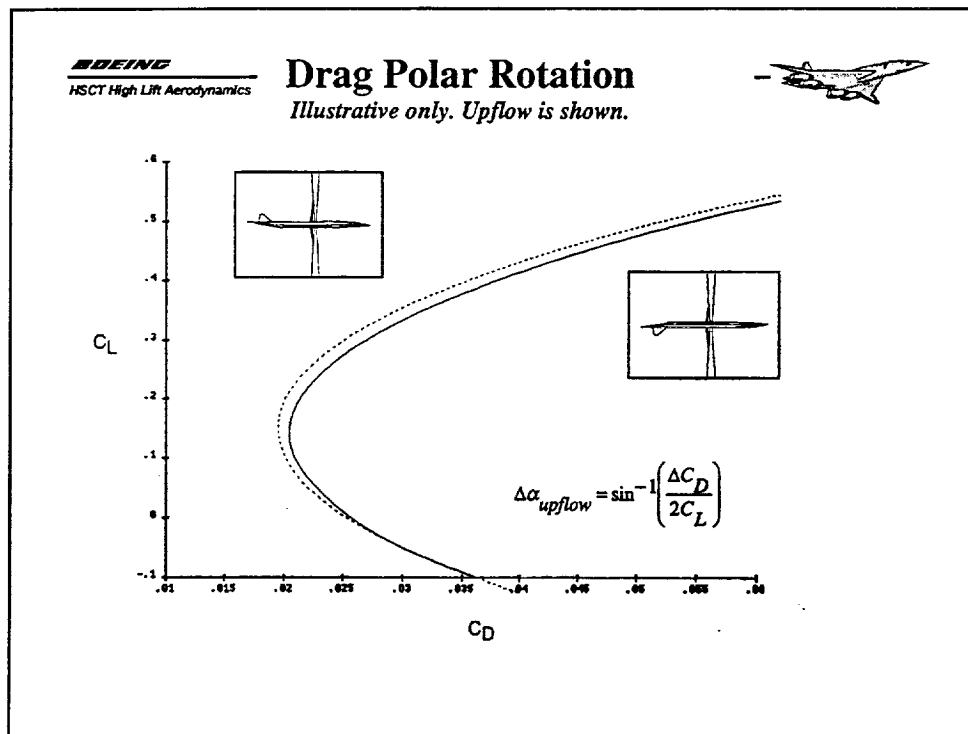
Drag Polar Rotation

When there is upflow (or downflow) in the tunnel, the model balance is at a greater (or lesser) angle than thought, resulting in a component of lift adding to (or subtracting from) the component of drag.

Drag polar rotation occurs when *the rate of drag increase* with lift is greater for one of the (upright or inverted, with image) model configurations.

$$\Delta\alpha_{upflow} = \sin^{-1}\left[\frac{d\left(\frac{\Delta C_D}{2}\right)}{dC_L}\right]$$

$$\Delta C_D = C_{D_{inverted+image}} - C_{D_{upright+image}}$$

2417

Correcting for Upflow

Or, The Effect on Lift and Drag When Upflow Corrected

If upflow is present, the lift resolved (using balance normal and axial force components) at the indicated angle of attack is higher than the true lift, and the indicated drag is lower than true drag.

If downflow is present, the lift resolved at the indicated angle of attack is lower than the true lift, and the indicated drag is higher than true drag.
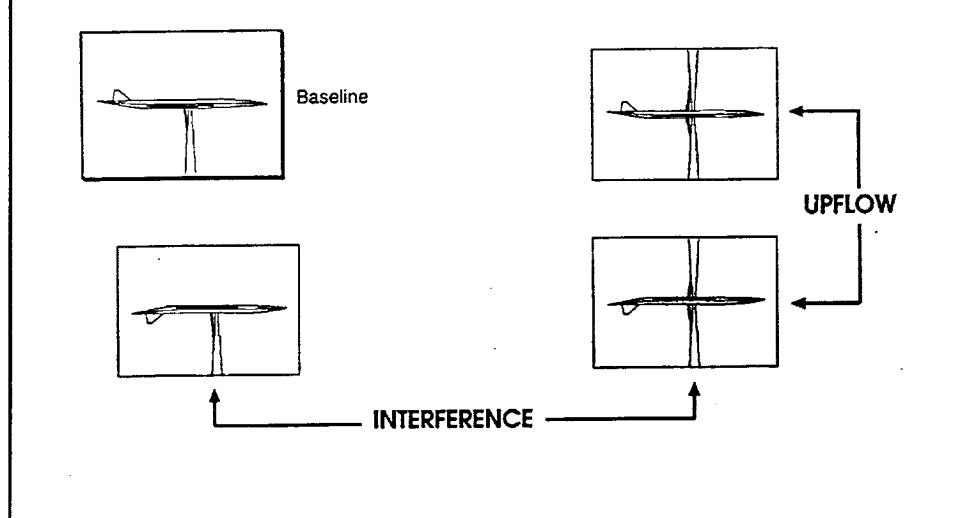
Test Setup

The method chosen for determining tunnel upflow was to fly the model upright and inverted, with an image post. The image post is required to reduce local upflow asymmetries which may be induced by the mounting post alone.

The interference increment is determined by flying the model in the inverted position, with and without the image post. Flying in this manner will provide the effect of the post support on the lower surface of the model.

The baseline upright model would be the configuration against which to apply the upflow and interference increments.

U&I free data = Upright data + upflow + interference

The Model
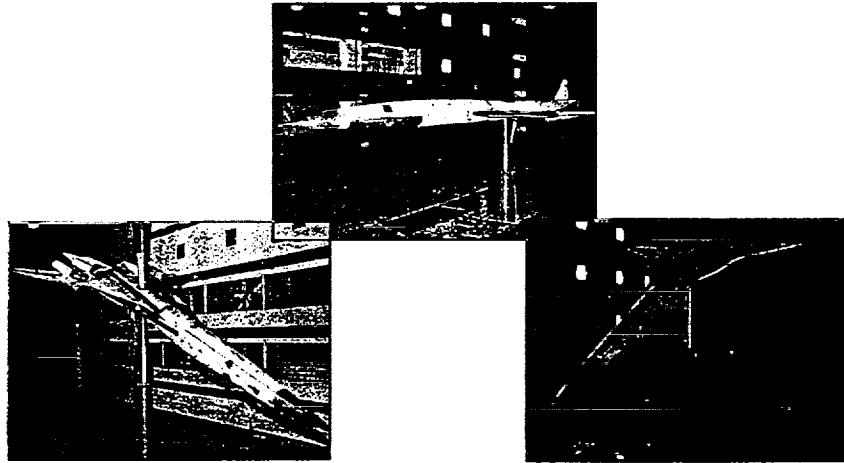
The Model

The model flown was the 6% Ref. H. Three of the configurations necessary for upflow and interference testing are shown here; the upright, the inverted, and the inverted with image post.

Image Post
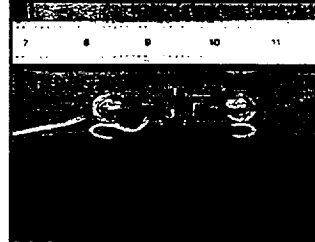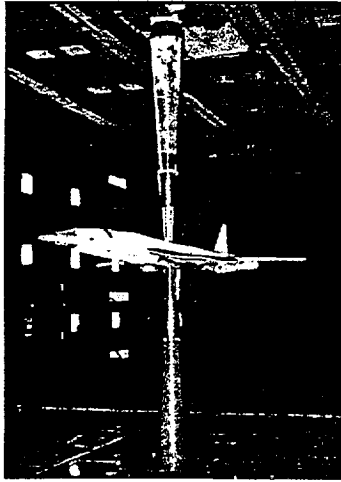
Image Post

The image post was designed to have the identical exterior shape as the main structural support post.

The image post contacted the model, but did not penetrate the fuselage.

The upper portion of the image post was hard-mounted to the 14'x22' ceiling, while the lower portion of the image telescoped as the model pitched.

As the image was metric, a balance was placed at the image/model interface to directly measure the normal force load. There was assumed to be no axial load imparted by the image post.

Representative Test Data = Upflow

The data indicates that upflow is present in the tunnel by analyzing the lift curves of the upright + image and the inverted + image runs. At a given indicated alpha, the upright run has a higher indicated lift than the inverted run; therefore, the upright model can fly at a lower indicated alpha than the inverted model while matching lift. Positive upflow provides the additional, unseen lift in the form of an alpha increase.

Representative Test Data = Downflow

At a given C , the representative upright and inverted (with image) data shows tunnel downflow. The data shown has all standard corrections except upflow and interference. For a given C , the upright run shows a higher C than the inverted run, indicative of tunnel downflow. In addition, the drag increases with lift more for the upright run than the inverted run; also indicating downflow.

Interference Increments

Interference calculations depend on differencing forces and coefficients measured with the inverted model configuration and the inverted + image post model configuration.
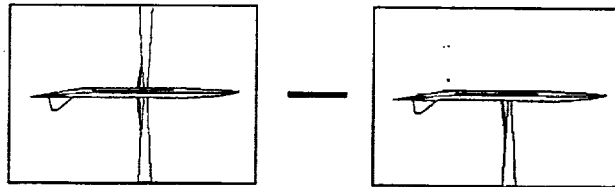
Interference Increments

Assumption made before analyzing interference effects:

Although there appears to be a bias in the final data between the upright and inverted runs, the upright and inverted runs by themselves repeated well (no bias apparent *within* either the upright or inverted runs).

Interference Increment - Lift

(Inverted + Image) - Inverted increment.
Shows that the image post effect is to reduce lift below 15 and above 17.
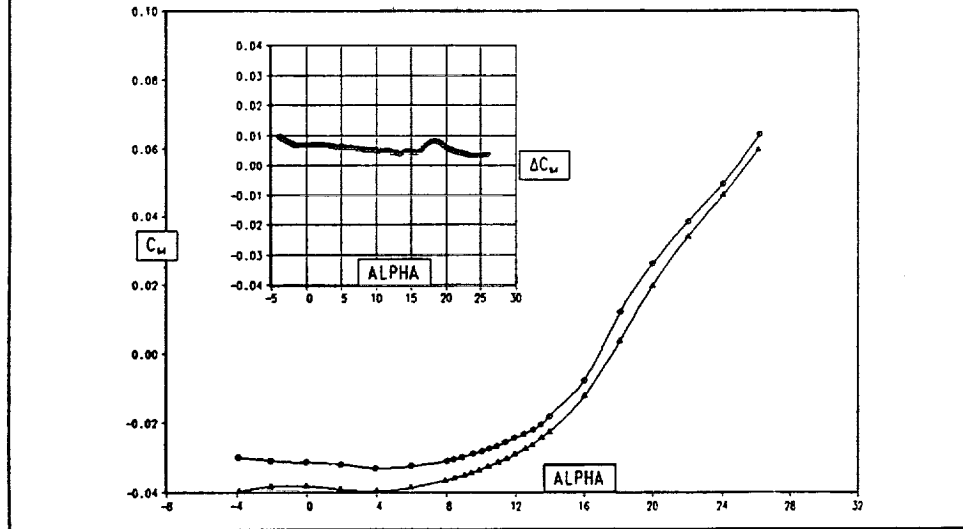
Interference Increment - Drag

(Inverted + Image) - Inverted increment.

Shows that the image post effect is to reduce drag below 2, with a slight local increase in drag 16.

Interference Increment - Pitching Moment

(Inverted + Image) - Inverted increment.

Shows that the image post effect is a decreasing trend of pitching moment increase with alpha.

Preliminary Experimental / A502 Comparison

Force Coefficient:	Test #442	A502
C_L	add 0.012 ...	add 0.008 ...
C_D	add 0.0020 ...	add 0.0007 ...
C_M	add -0.005 ...	add -0.0006 ...
	...to / from data.	

Summary

- Upflow? Downflow?

- Assume interference increments OK.

- Interference increments:
    - agree with A502 panel code in direction.
    - lift increments compare favorably.
    - drag and pitching moment less favorable.

- Investigate alternative methods to determine upflow.

- A NASA-owned symmetric model(s) would be desirable.

- Additional work required to understand data.

This page intentionally left blank.

Application of a 3-D Panel Method to the Prediction of Wind Tunnel Wall and Support Interference

by
Ryan C. Polito, Arthur G. Powell, and
Roger W. Clark
McDonnell Douglas Corporation
Long Beach CA

Outline

- Objective
- 3-D Panel Method - DACVINE
- Tunnel Wall Modeling:
  - Effect of walls (DACVINE Vs 14'x22' data)
  - Effect of model location (DACVINE)
- Support Strut Effects:
  - DACVINE (With/without strut)
  - 14'x22' data (inverted with/without image post)

This paper addresses the computation of wind tunnel wall and support effects using a panel method. The panel method used is the McDonnell Douglas 3-D Panel method, and the results obtained include a preliminary comparison with data from the 14'x22' LaRC Wind Tunnel test of the 6% Ref H High-Lift model.

Since the corrected data from this test has only recently been released, the comparison of the computational results is still in progress.

The paper presents an outline of the panel method used, and is followed by a comparison of the computed effects of the wind tunnel walls, compared with the Heyson's and blockage corrections applied to the tunnel data. This is followed by an evaluation of the computed effects of the model support post on the computed lift, drag, and pitching moment.

Objective

- Evaluate prediction of wind tunnel wall and support effects using a 3-D panel method
- Define method to be used for wind tunnel support interferencecorrection for future high-lift tests

The objective of this study is to evaluate the prediction of wind tunnel wall and support effects using a 3-D panel method.

The results presented here are based on the 6% Ref H model installed in the NASA LaRC 14'x22' wind tunnel. However, the modeling developed will be used for the correction of data to be obtained for the TCA configuration in both the LaRC 14'x22' tunnel as well as in the ARC 12' Pressure Tunnel.

Since the data from the 6% Ref H test has only recently been released, this effort is still in progress. The results presented here are therefore regarded as preliminary.

DACVINE 3-D Panel Method Features

- Higher-Order Surface Fitting:
  - Parametric cubic patches
- Higher-Order Singularity Distribution:
  - Source distribution - linearly varying
  - Vorticity distribution - parabolic chordwise, linear spanwise

The panel method used is a higher-order panel method which uses surface source singularities to satisfy the normal velocity boundary condition, combined with a dipole distribution on the lifting surface to satisfy the Kutta condition.

The method includes a strip theory boundary layer model, and several compressibility correction options. However, the results presented here are all inviscid, incompressible solutions.

DACVINE 3-D Panel Method Features (continued)

- Boundary Conditions:
  - Zero Normal Velocity (linear)
  - Kutta Condition - Equal pressures (nonlinear)
- Iterative Matrix Solver:
  - Block Gauss-Siedel
  - Up to 20,000 panels

The normal velocity boundary condition is applied at the control point of each panel, while an equal pressure Kutta condition is applied at the trailing edge of each lifting strip.

An iterative matrix solver is used which enables the method to use large panel numbers for modeling of complex geometries.
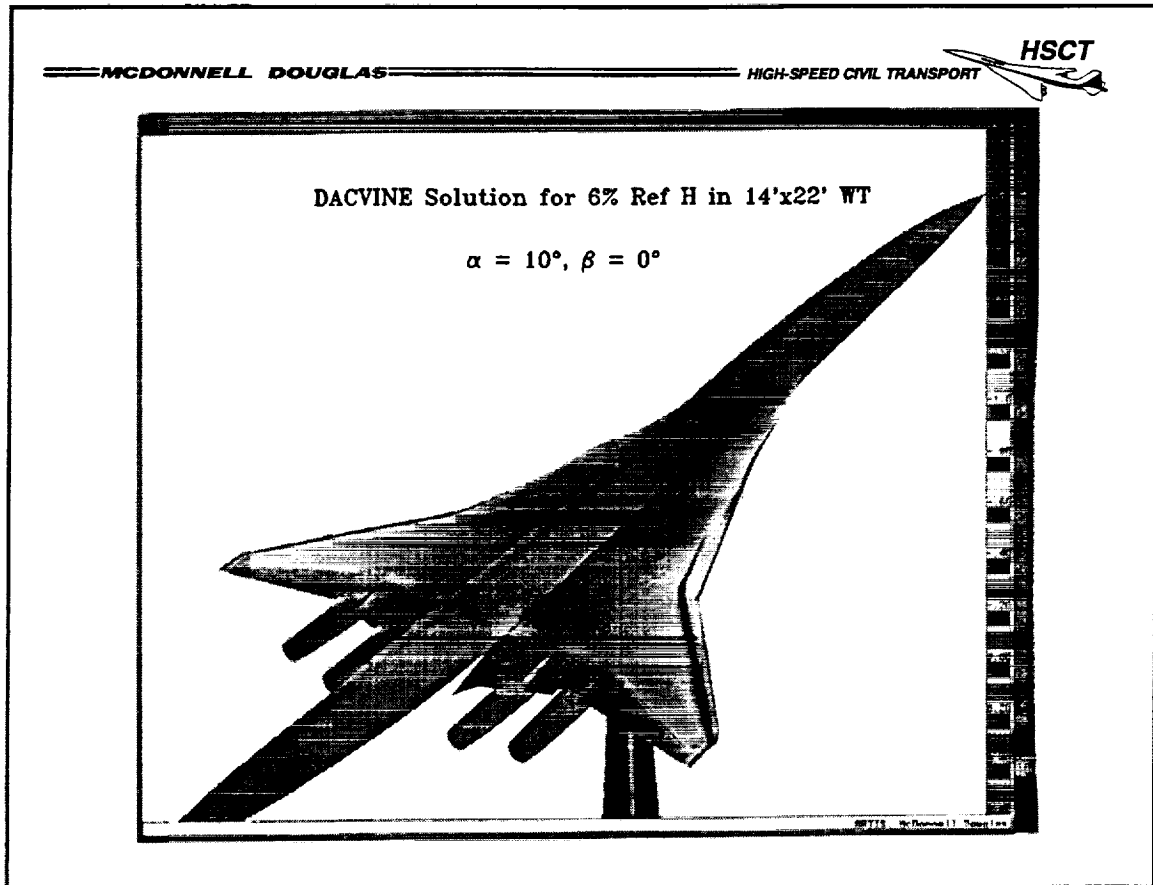
DACVINE Solution for 6% Ref H in 14'x22' WT

$\alpha = 10°, \beta = 0°$

This figure shows the 6% Ref H model located in the 14'x22' wind tunnel. The configuration is the 30° /10° high-lift configuration.

DACVINE Solution for 6% Ref H in 14'x22' WT

$\alpha = 10°, \beta = 0°$
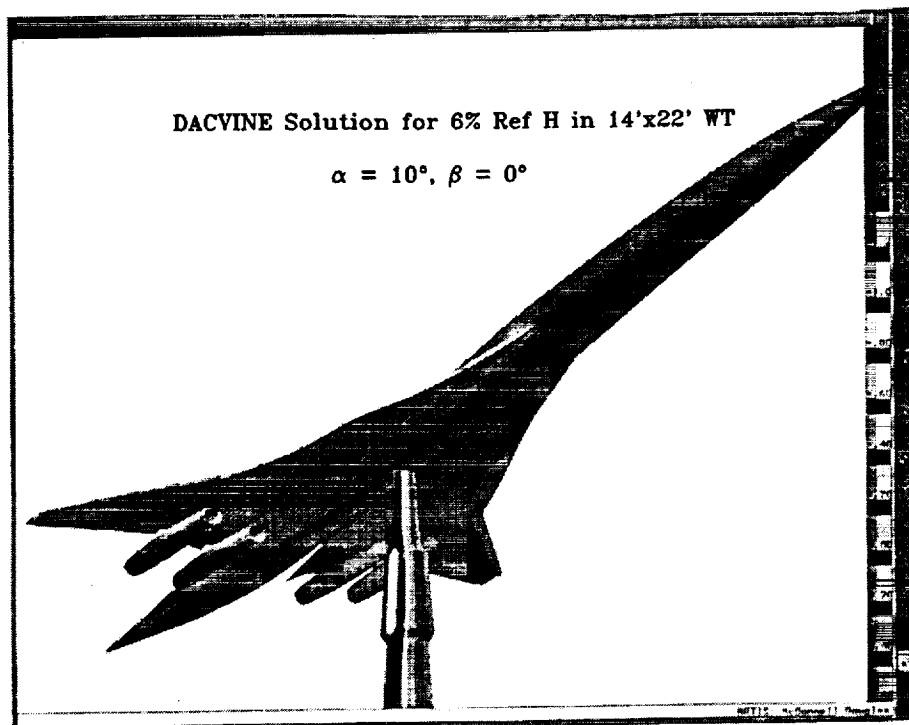
This figure shows the 6% Ref H model located in the 14'x22' wind tunnel. The configuration is the 30° /10° high-lift configuration.

Effect of Tunnel Walls

- DACVINE model - with/without walls
- 14'x22' data - corrected lift/drag/alpha compared to uncorrected
  - No Heyson's correction, no blockage correction
- Effect on lift well predicted by DACVINE
- Effect on drag reasonably well predicted by DACVINE

The following figures present a comparison of the effects of the wind tunnel walls as computed using the inviscid panel code, DACVINE with the classical corrections applied to the wind tunnel data.

Computed Effect of Wind Tunnel Walls: 30°/10° Configuration
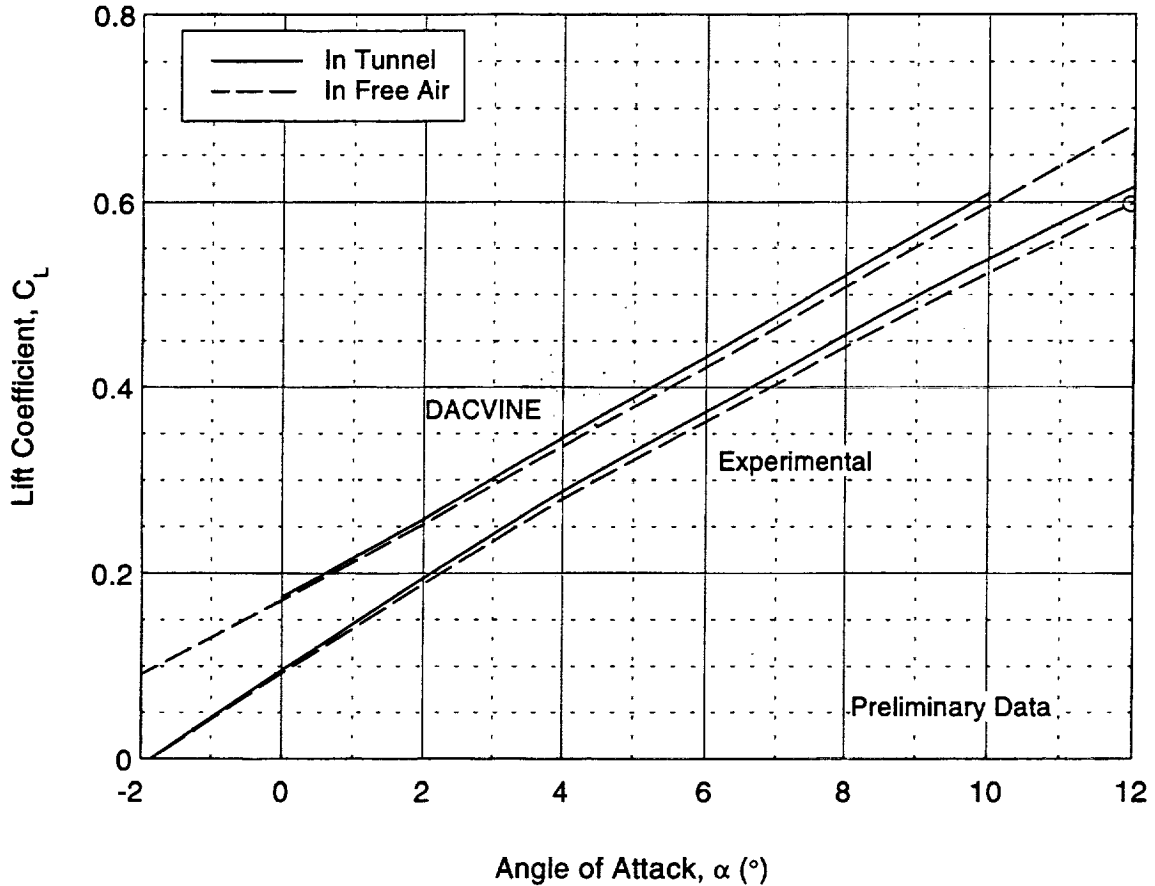
This figure shows the computed and experimental lift for the 30°/10° configuration with and without the tunnel wall effects. The free air computations from DACVINE are simply obtained by modeling the isolated model geometry. The test data was corrected to free air using Heyson's classical corrections to C_L and α for the effect of the wall, and model and wake blockages.

Since the DACVINE results are for inviscid, attached flow with no viscous effects, the computed C_L values are higher than the corresponding experimental values. In order to match the lift curves more accurately, some modeling of the viscous effects particularly on the deflected flaps, would have to be included. Since we are interested primarily in the increments due to the tunnel wall and model support strut, no attempt to include such viscous effects is included here.
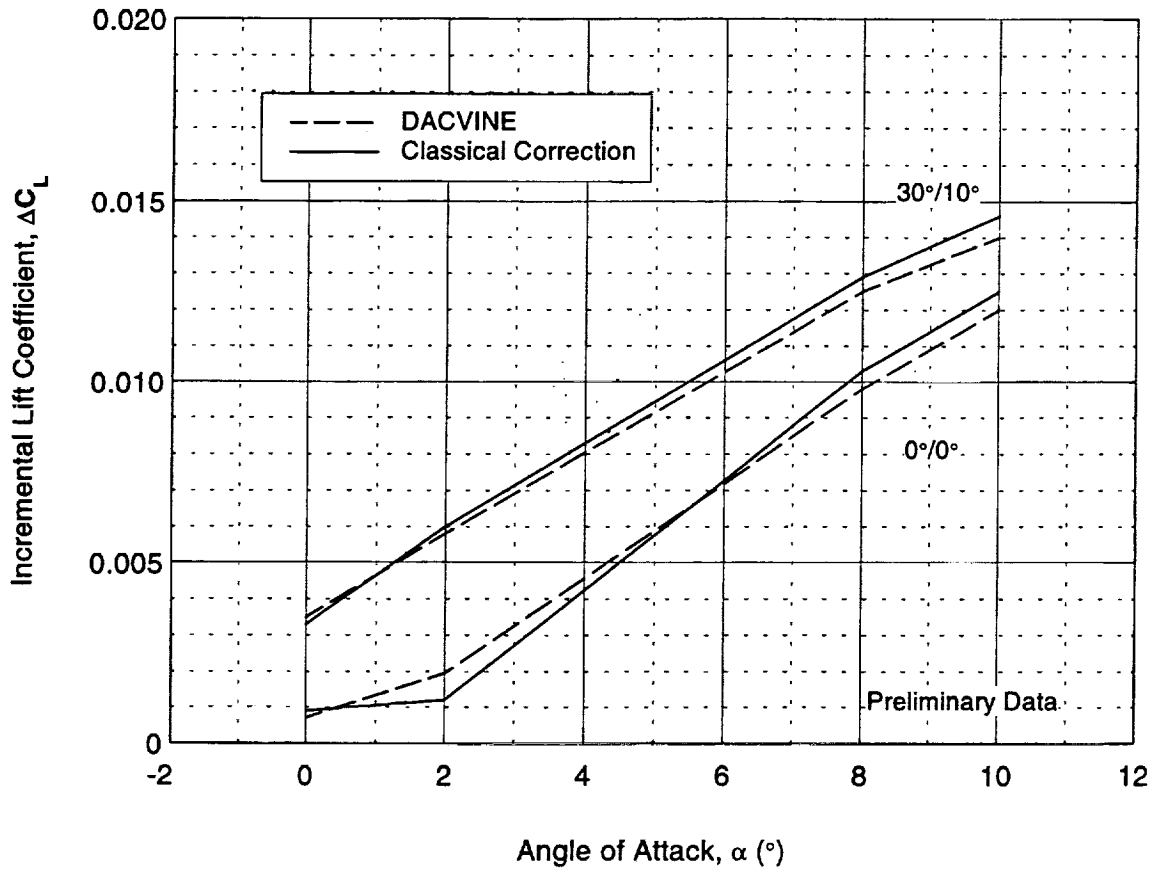
Computed Effect of Wind Tunnel Walls: 0°/0° Configuration

Angle of Attack, α (°)
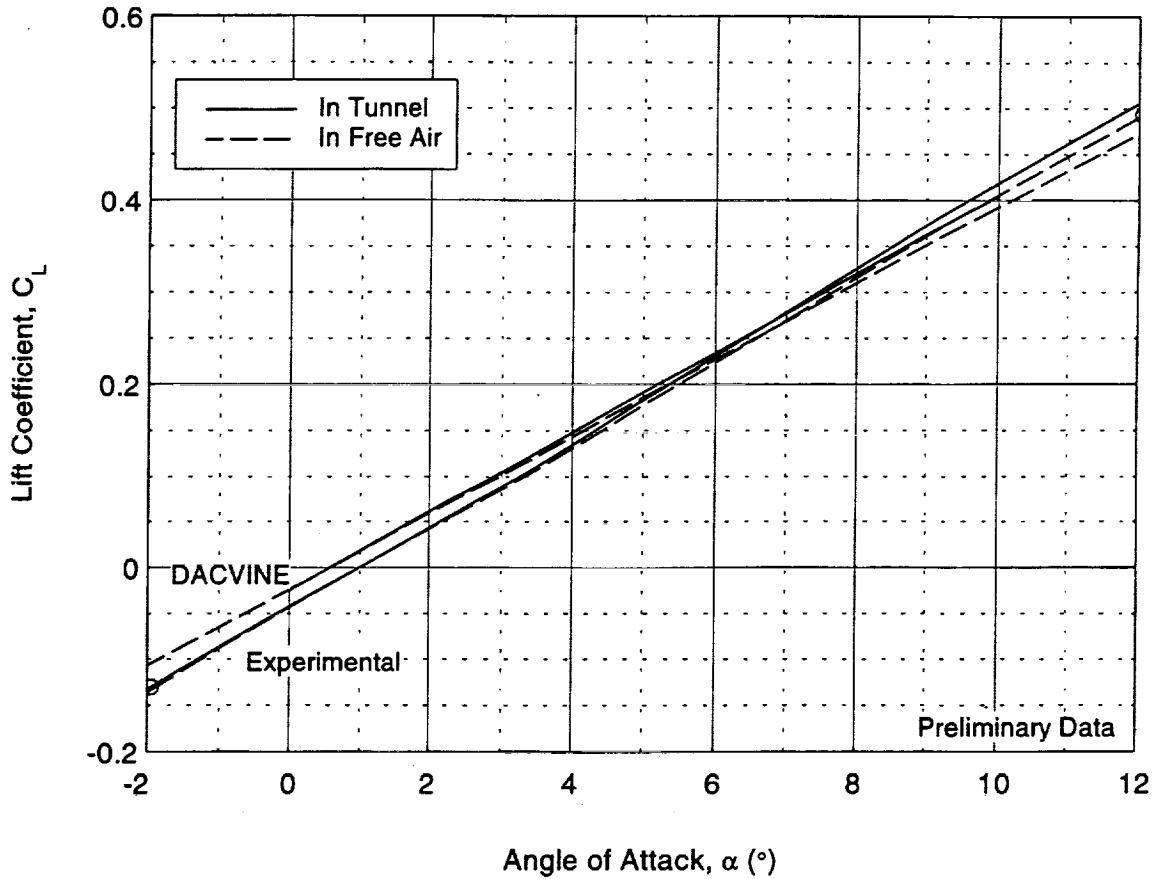
This figure shows the computed and experimental lift for the baseline 0°/0° configuration with and without the tunnel wall effects. The free air computations from DACVINE are simply obtained by modeling the isolated model geometry. This experimental wall effect is obtained by comparing the uncorrected C_L (plotted Vs. uncorrected angle of attack) with the Heyson's corrected C_L plotted Vs. the angle of attack corrected for model and wake blockage.

Computed Effect of Wind Tunnel Walls

This figure shows a comparison of the DACVINE-computed and experimental (classical) C_L correction increments for the 30°/10° and 0°/0° configurations. It can be seen that there is a close correlation between the predicted potential flow lift increments and the classical corrections for wind tunnel wall effects.

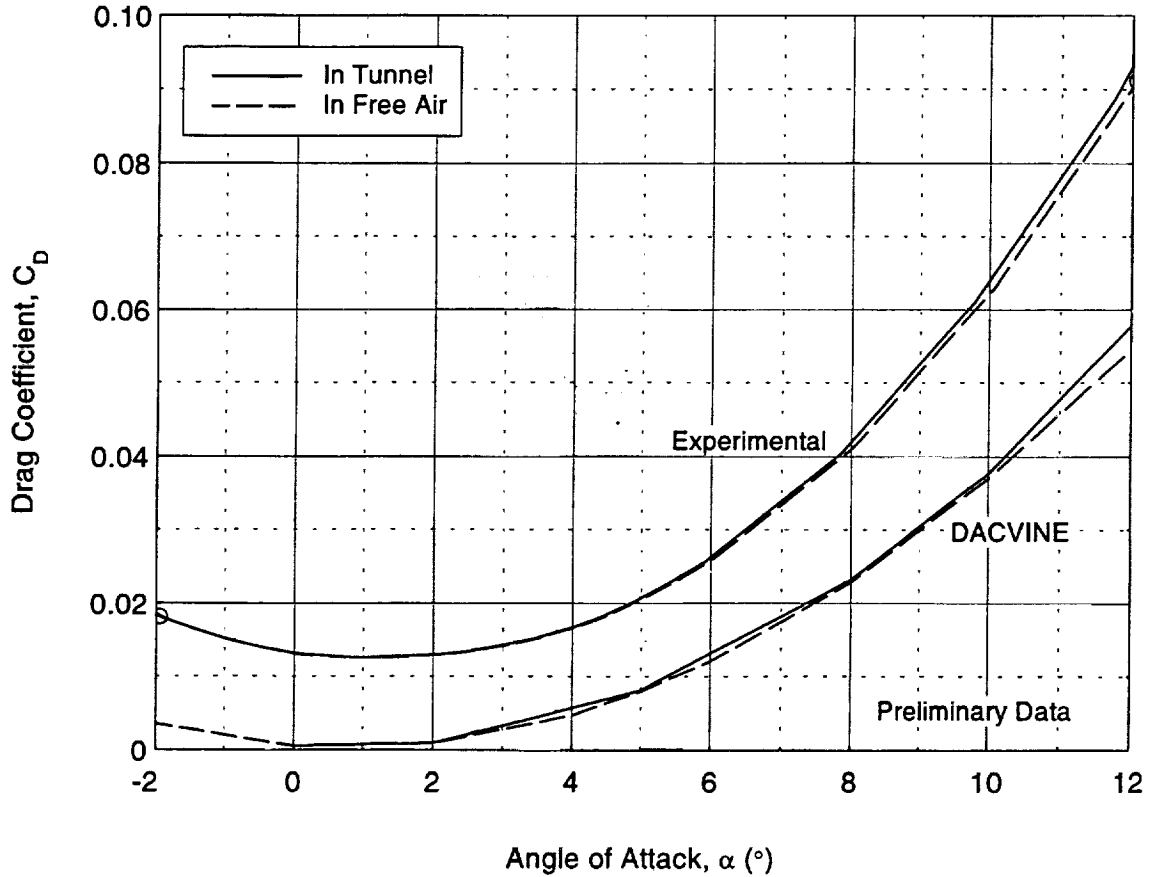## Effect of Wind Tunnel Walls: 30°/10° Configuration
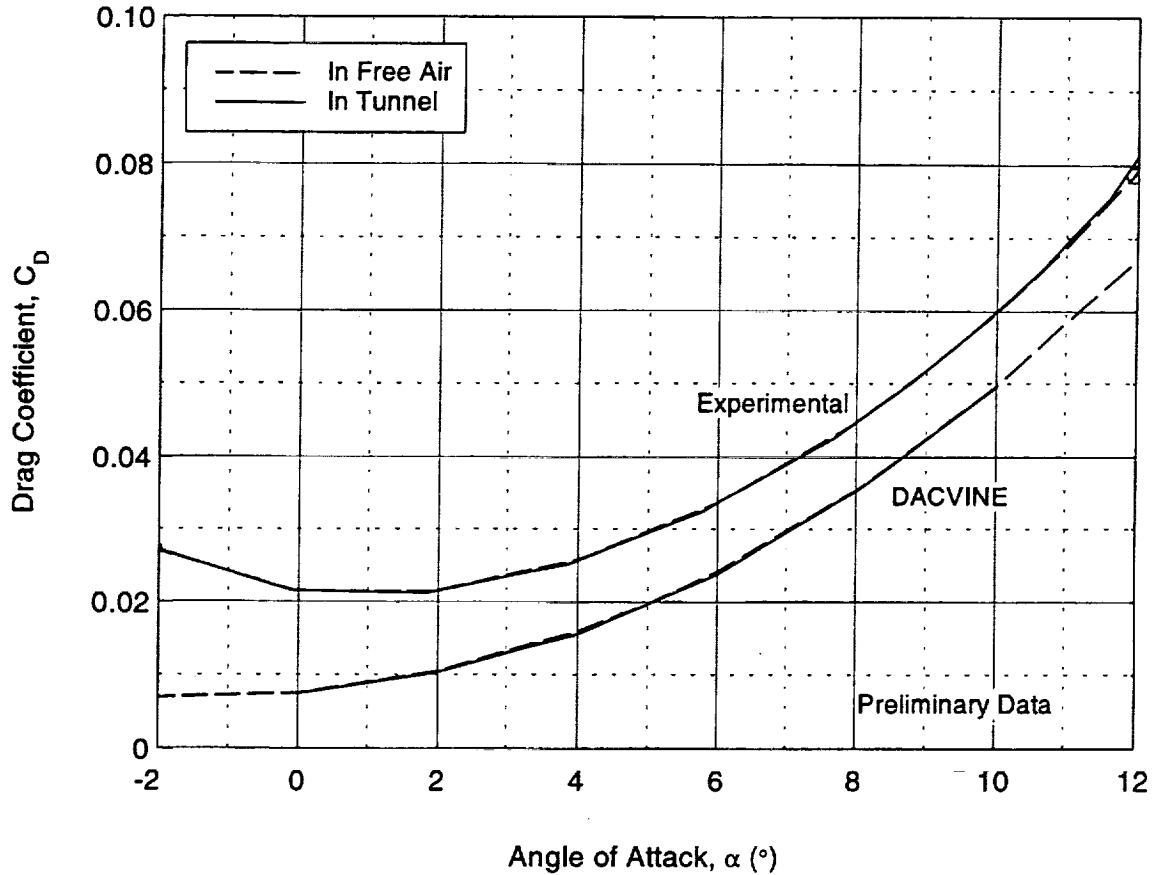
This figure shows the computed and experimental drag for the 30°/10° configuration with and without the tunnel wall effects. The free air computations from DACVINE are simply obtained by modeling the isolated model geometry. This experimental wall effect is obtained by comparing the uncorrected forces (plotted Vs. uncorrected angle of attack) with the Heyson's corrected forces plotted Vs. the angle of attack corrected for model and wake blockage.

As noted in a previous slide, we have not included any viscous effects in the computed results. The computed drag therefore represents only the induced drag term with no accounting for the skin friction and profile drag terms. The C_D increment in either case is negligible.

Computed Effect of Wind Tunnel Walls: 0°/0° Configuration

Angle of Attack, α (°)

This figure shows the computed and experimental drag for the 0°/0° configuration with and without the tunnel wall effects. The free air computations from DACVINE are simply obtained by modeling the isolated model geometry. This experimental wall effect is obtained by comparing the uncorrected forces (plotted Vs. uncorrected angle of attack) with the Heyson's corrected forces plotted Vs. the angle of attack corrected for model and wake blockage.

As noted in a previous slide, we have not included any viscous effects in the computed results. The computed drag therefore represents only the induced drag term with no accounting for the skin friction and profile drag terms.

Computed Effect of Wind Tunnel Walls
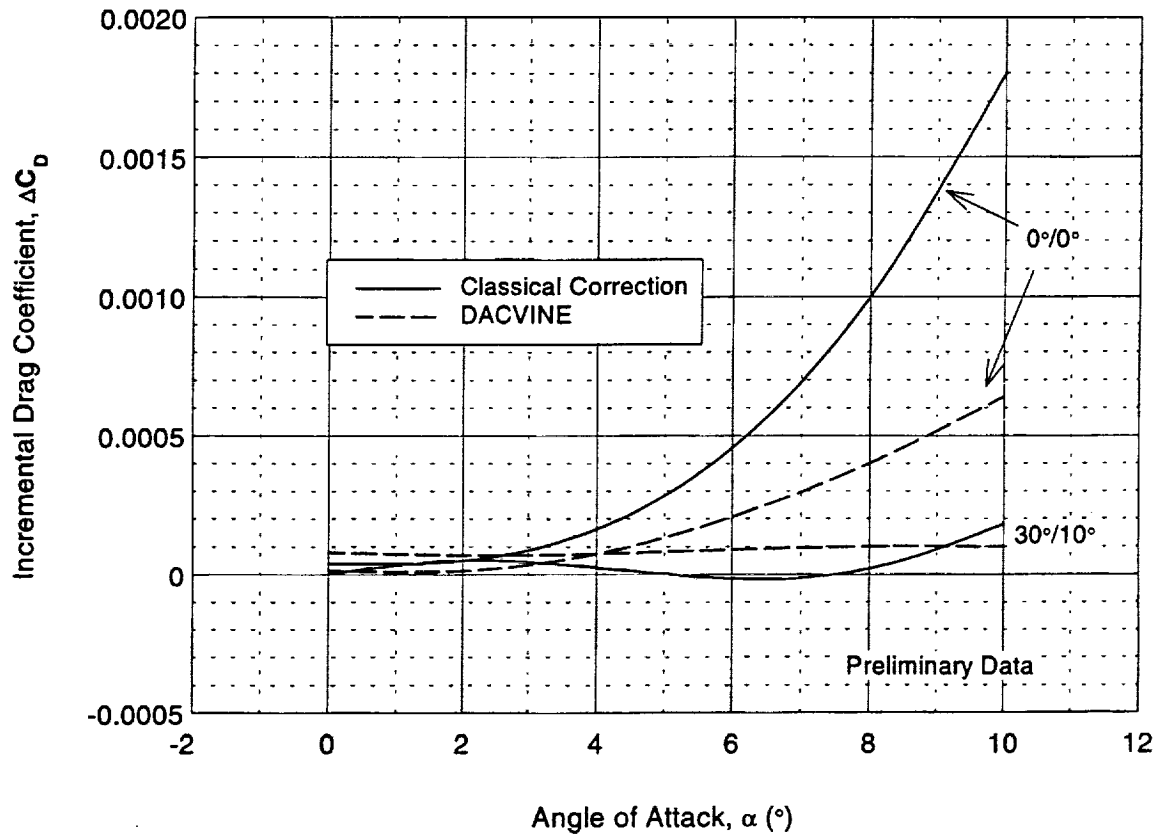
The figure presents a comparison of the drag increments from the DACVINE and the classical corrections due to the wind tunel walls. At the lower angles of attack, the drag increments agree closely.

At the higher angles the classical correction is larger than the DACVINE-computed induced drag increment. This is believed to be due to the inclusion of the wake blockage correction which is included in the classical tunnel corrections, but absent in the DACVINE modeling.

Effect of Model Location in Wind Tunnel

Computed Delta Cl Due to Tunnel Walls
30°/10° Flaps, Alpha=10°
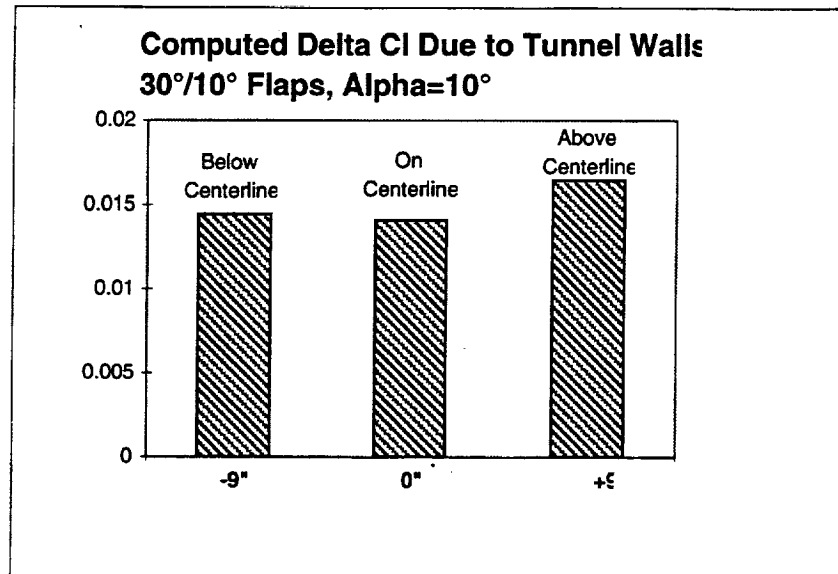
The computed DACVINE results presented here have the model geometry installed along the tunnel centerline. In the 6% Ref H tests, the model is actually installed at 9" below the tunnel centerline. The inverted model runs therefore correspond to a model location at 9" above the centerline.

In order to evaluate the effects of this off-center location, a limited number of DACVINE runs were completed with the model located above and below the centerline. The runs were made for the 30°/10° configuration at 10° angle of attack.

The results presented here indicate that there is only a small variation in the lift associated with moving the model off the centerline. As the model is moved above the centerline there is a larger increase noted, presumably due to the interaction between the upper surface flow and the tunnel ceiling.

Computed Vs Measured Model Support Effects (preliminary)

- DACVINE in Tunnel, with and without support strut
  - Inviscid model - (no wake behind post)
  - No pitch link
- 14'x22' Inverted with and without Image post
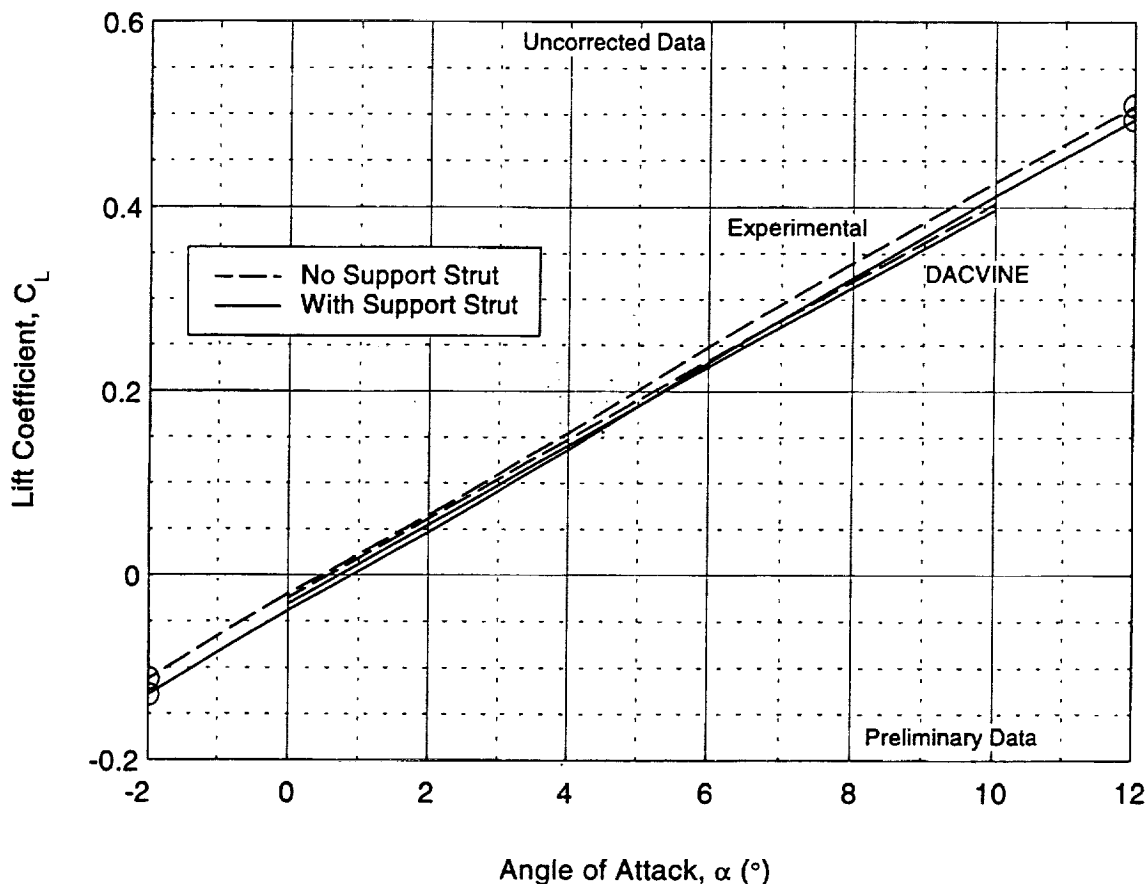- 30°/10° Flaps and 0°/0° configurations

The following pages present a comparison of the computed and experimental effects of the support strut on the lift, drag, and pitching moment. The DACVINE model was run in the presence of the tunnel walls, and the code has been run with the main strut as well as with the image post. The pitch link was not modeled since it is assumed to be embedded within the viscous wake behind the main strut. The results presented here do not include any modeling of the effects of this viscous wake. An evaluation of the effects of the strut wake is still in progress.

The computations have been performed for both the 0°/0° and the 30°/10° flap configurations.

It will be seen from the results presented here that the increments due to the support strut are all underpredicted here. The reasons for this disagreement are still being evaluated, and will be discussed in more detail later.

Effect of Support Strut: 0°/0° Configuration

The following figures compare the effects on lift, drag, and pitching moment of the support strut computed in DACVINE with that measured in the 14'x22' tunnel for the baseline (0°/0° flaps) and high-lift (30°/10° flap) wing/body/nacelle configurations. Comparisons of the absolute values of the forces will be presented first, followed by a comparison of the DACVINE-computed and classical correction increments.

The DACVINE results are computed with the model installed in the tunnel with and without the support strut. The experimental runs compared here are for the model inverted, with and without the image post. Since the computed results include the effects, of the wind tunnel walls, the experimental data used for comparison is uncorrected for tunnel wall and blockage effects where that data was available. Although the image post was not included in these DACVINE results, the differences due to the effect of the main post are not expected to be significantly different.

This figure shows the lift for the baseline configuration. The basic lift levels are reasonably well predicted.

Effect of Support Strut: 30°/10° Configuration
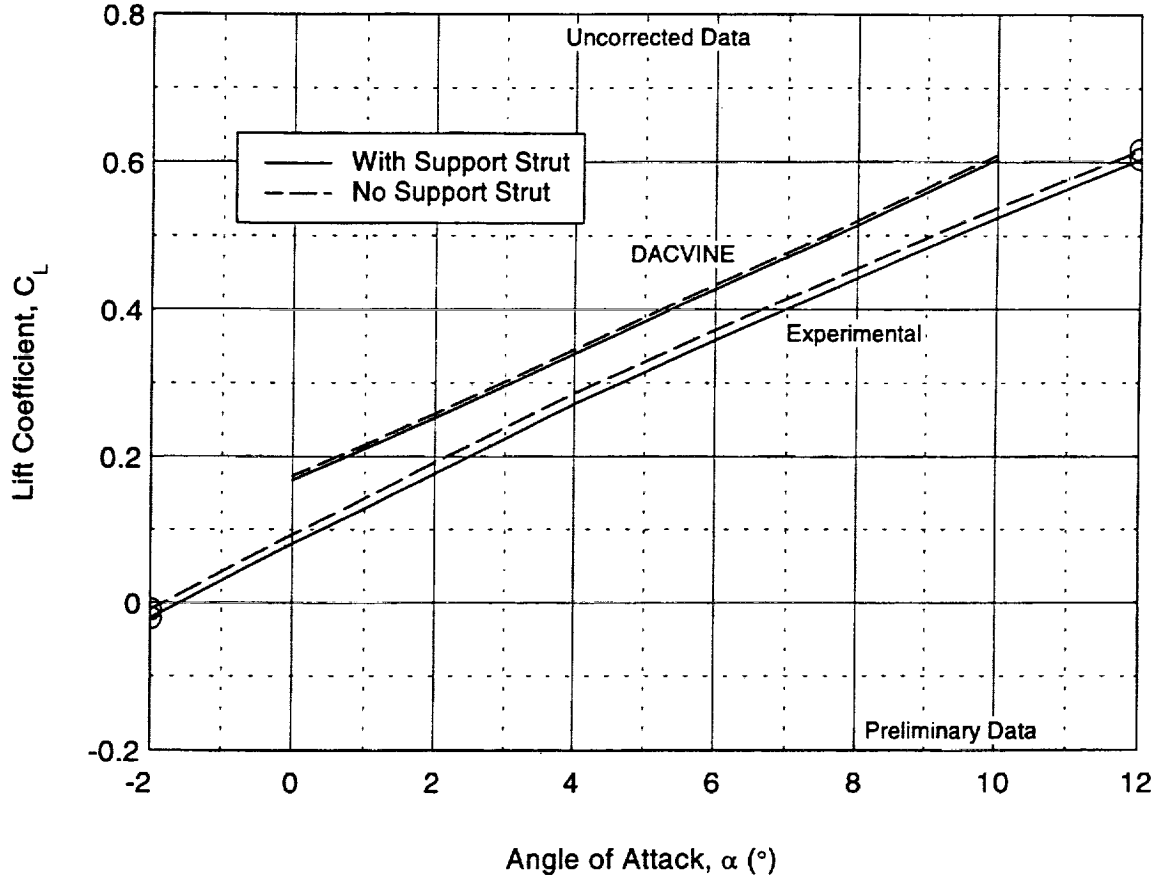
This figure shows the lift for the high-lift (30°/10° flap) configuration. The lift levels for this configuration are overpredicted by DACVINE as might be expected from an inviscid calculation in which no flow separation occurs. The boundary layer thickening over the upper surface of the flaps would be expected to cause a reduction in flap effectiveness when compared to the inviscid calculation. However, since we are interested mainly in the increments due to the support strut, no attempt has been made here to account for this effect. The support strut effect is similar to that of the baseline (0°/0° flaps) configuration.
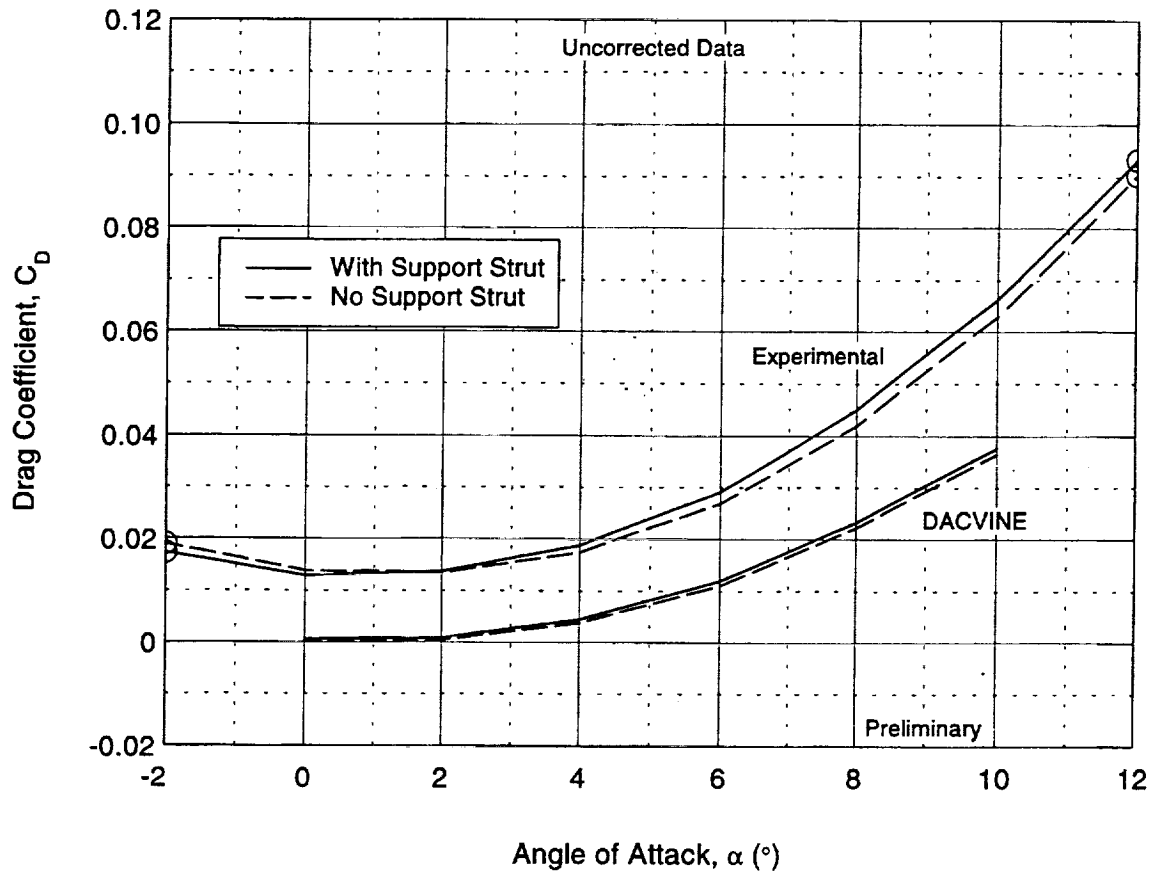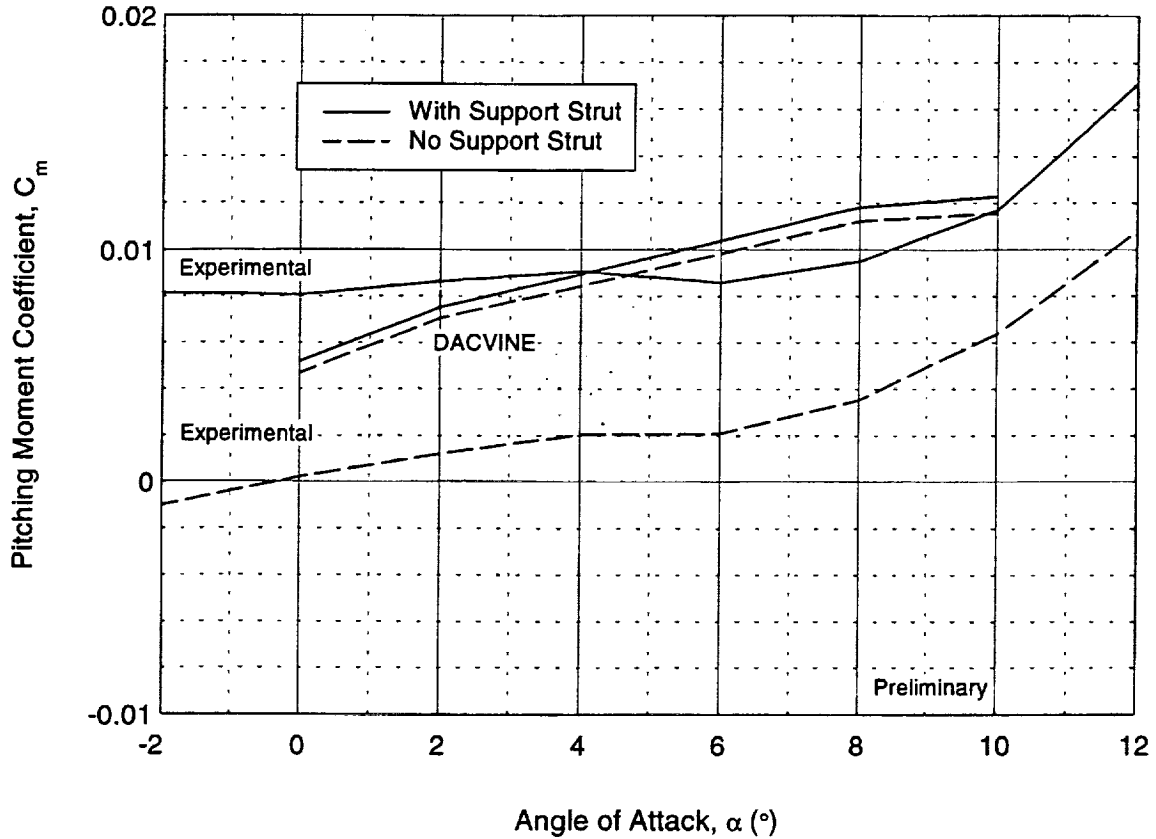
Effect of Support Strut: 0°/0° Configuration

This figure shows the computed and experimental drag, plotted against angle of attack for the baseline baseline (0°/0° flaps) configuration. As noted earlier, the computed results are inviscid, and so the drag computed is only the induced drag with no skin friction or profile drag effects. Also, since the DACVINE results are computed for attached potential flow, the increase in drag at the higher angles of attack due to the vortex separation is also not predicted.

Effect of Support Strut: 30°/10° Configuration
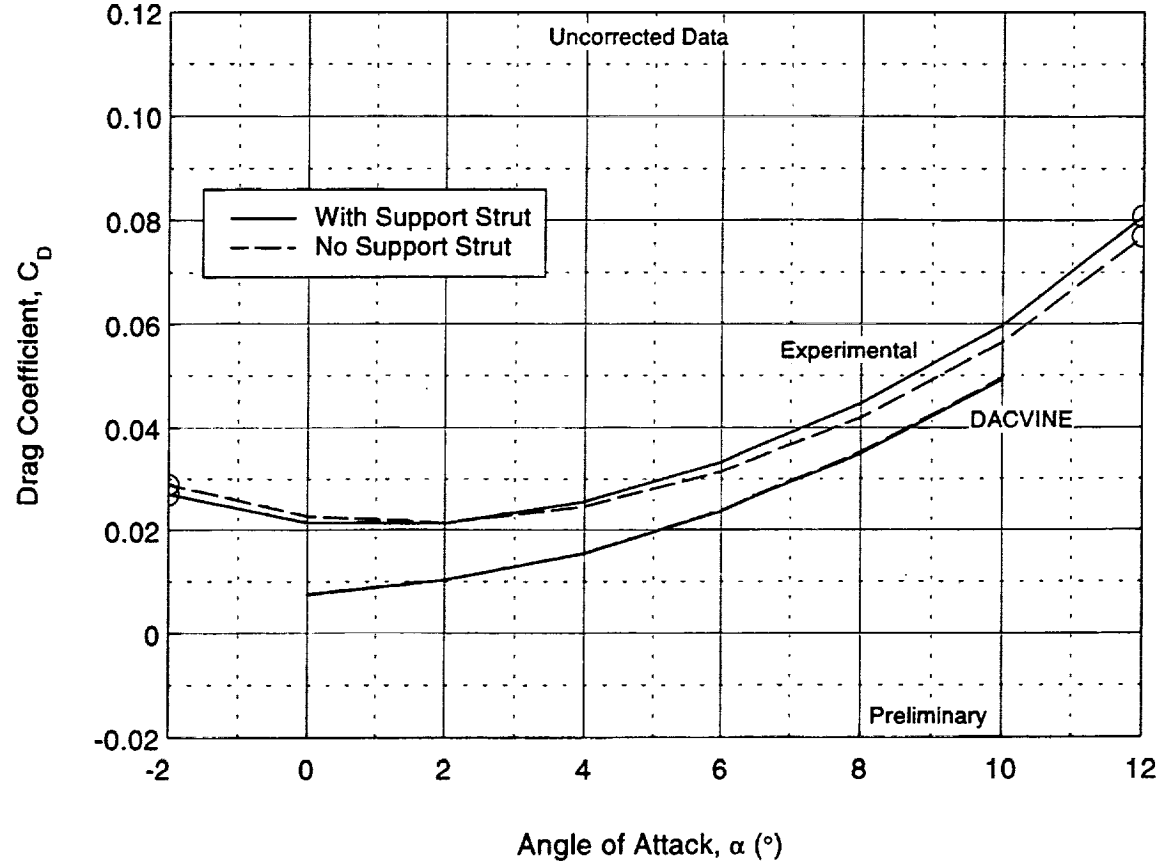
This figure shows the computed and experimental drag, plotted against angle of attack for the high-lift baseline (30°/10° flaps) configuration. For this case, the DACVINE-predicted drag increment for the support strut is negligbly small.
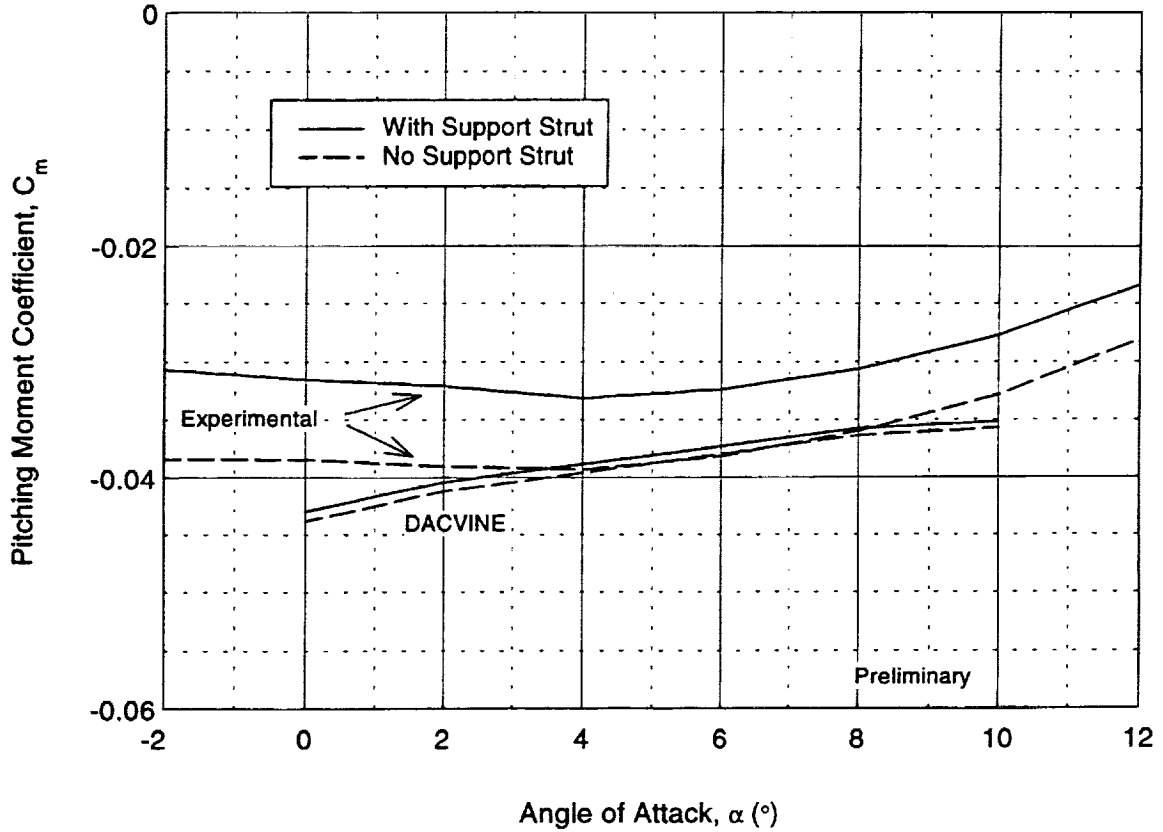
Effect of Support Strut: 0°/0° Configuration

This figure shows the DACVINE-computed and experimental pitching moment for the baseline baseline (0°/0° flaps) configuration. It can clearly seen that the moment increments due to the strut are significantly underpredicted by DACVINE.

Effect of Support Strut: 30°/10° Configuration

This figure shows the computed and experimental pitching moment for the high-lift configuration. It can clearly be seen that the moment coefficient increments due to the strut are significantly underpredicted by DACVINE.
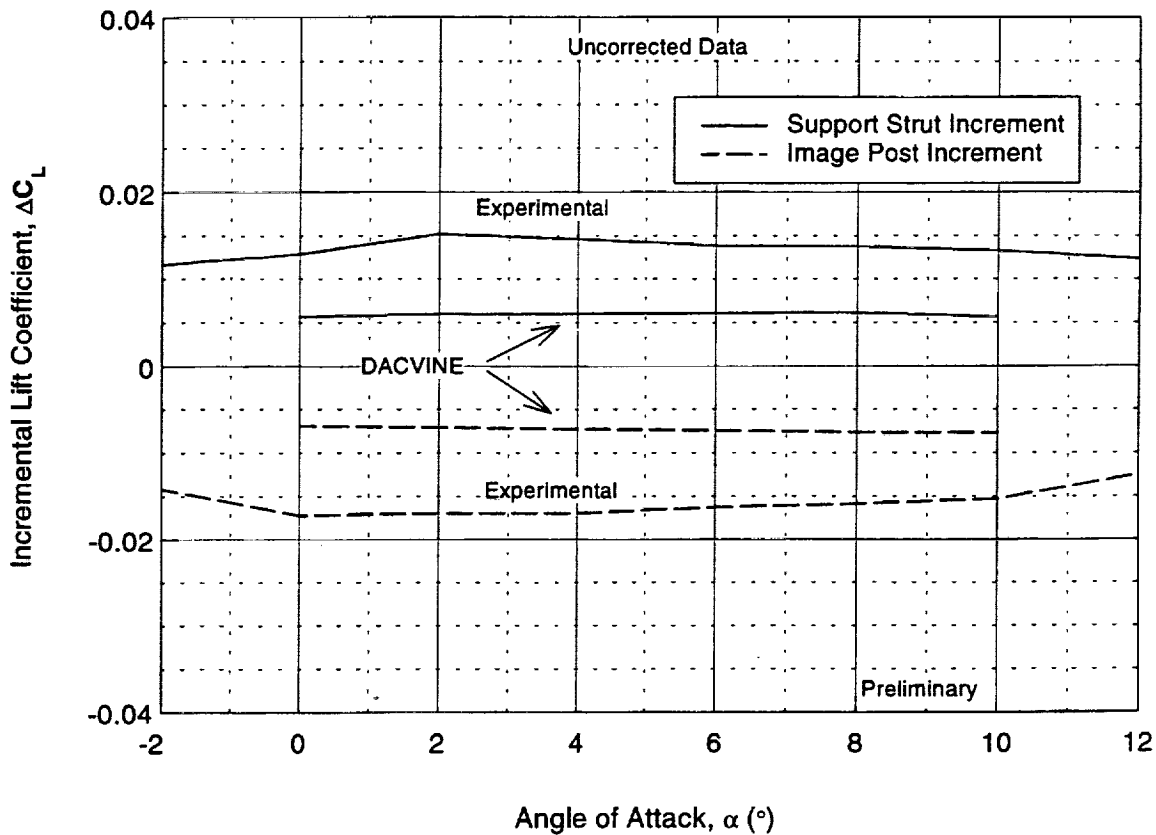
Effect of Support Strut: 0°/0° Configuration
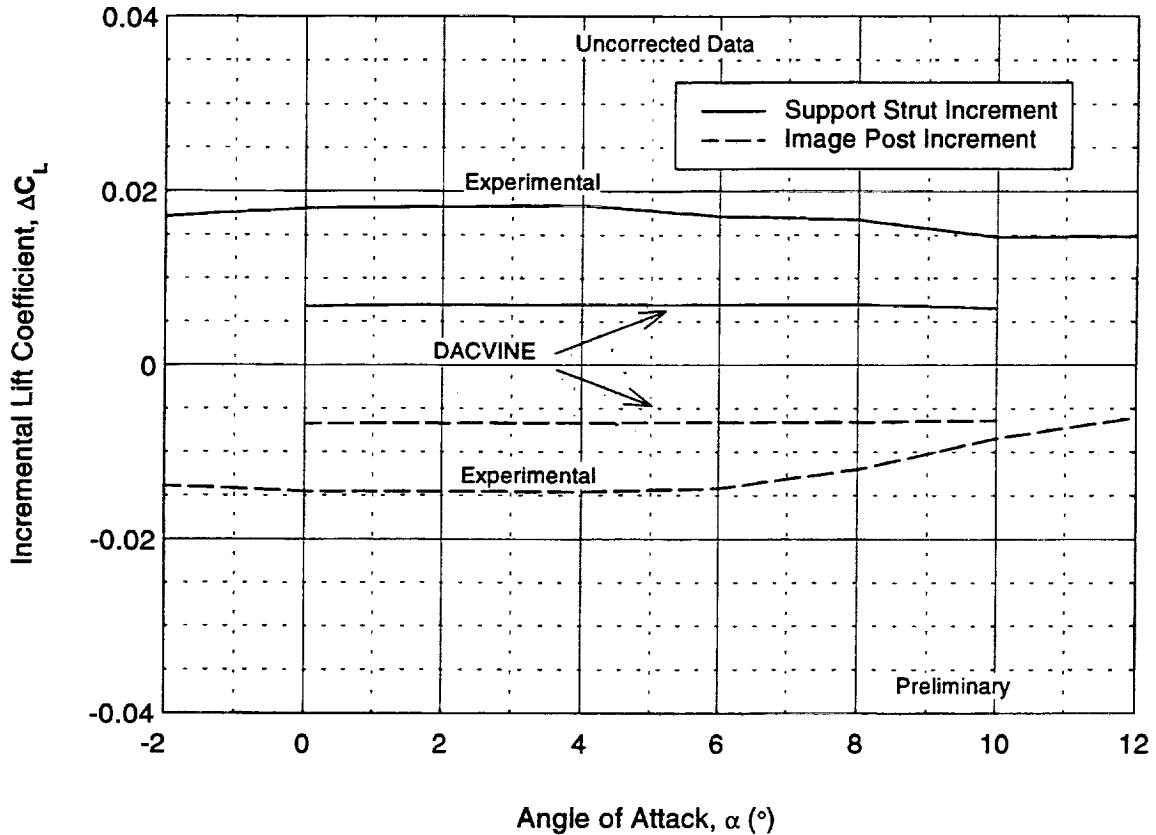
The following six figures show comparisons of DACVINE-predicted and measured support post increments in the lift, drag, and pitching moment. While the absolute force coefficient plots presented previously are focused on the effects of the main support strut, the force coefficient increments presented in these plots also show the effects of the image post, by comparing the upright model installation with and without the image post. It can be seen that the effects of this image post are very close to those of the support strut, both computationally and experimentally, although the sign of the increment is reversed.

This figure compares the DACVINE-computed and measured lift coefficient increments for the baseline baseline (0°/0° flaps) configuration.
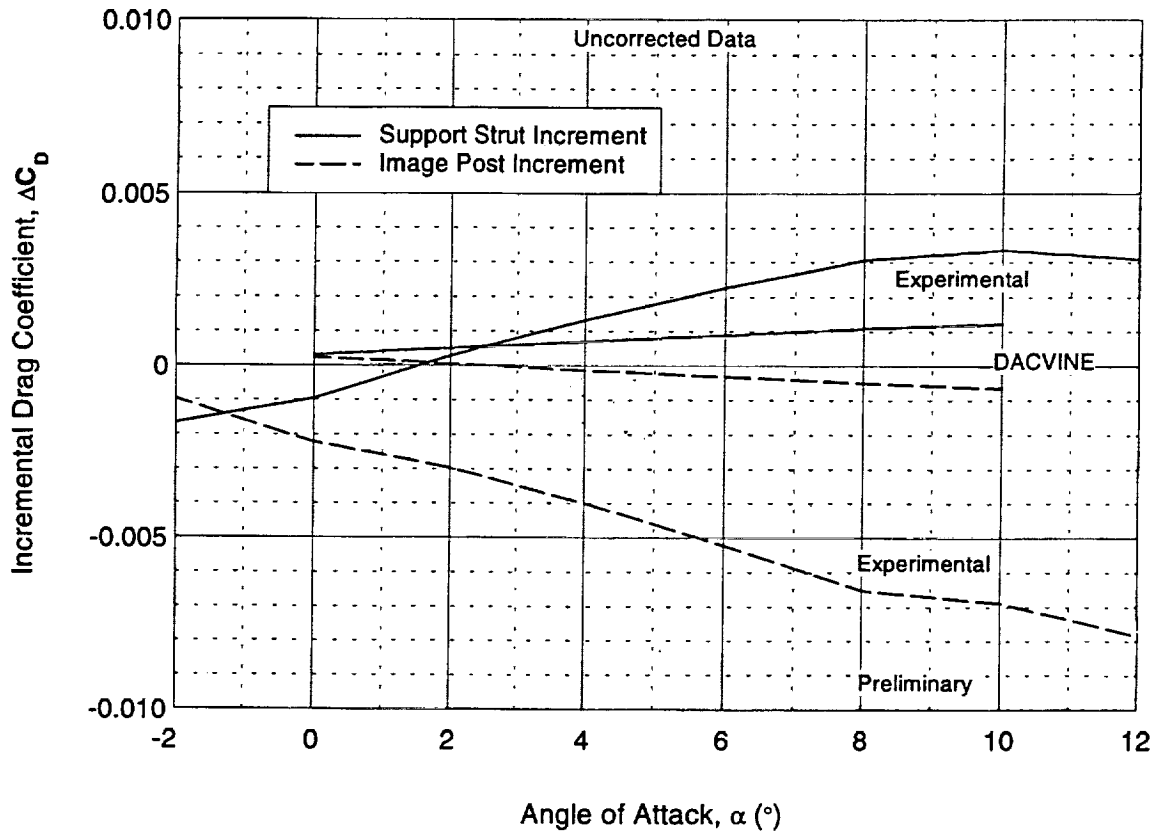
Effect of Support Strut: 30°/10° Configuration

This figure compares the DACVINE-computed and measured strut and post lift increments for the high-lift (30°/10° flaps) configuration.
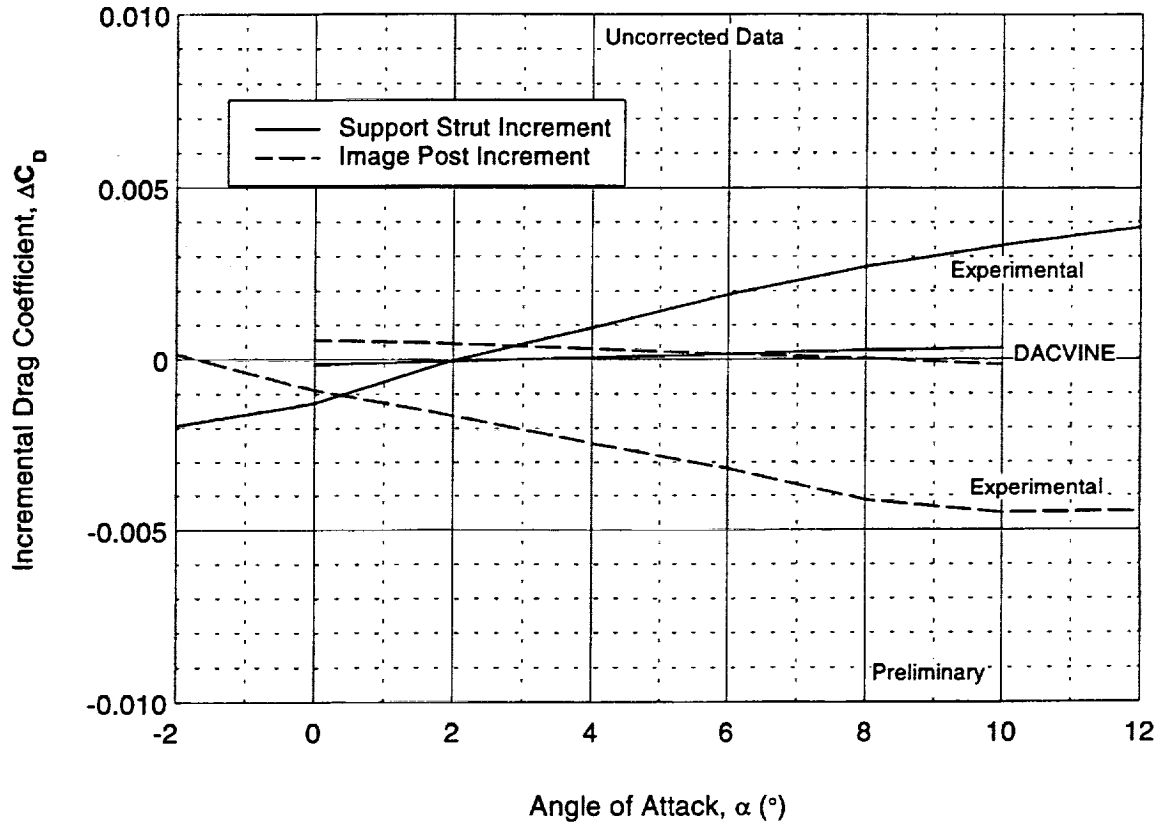
Effect of Support Strut: 0°/0° Configuration

This figure compares the DACVINE-computed and measured strut and post drag increments for the baseline (0°/0° flaps) configuration.
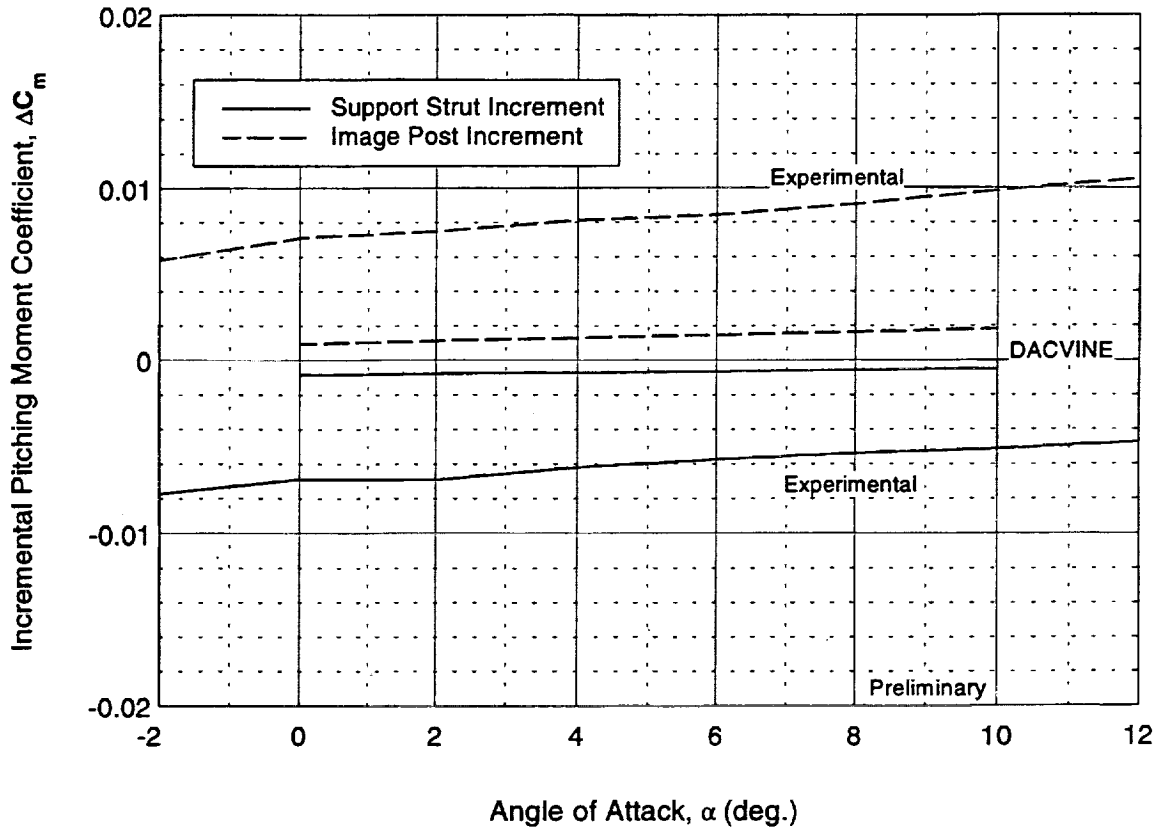
Effect of Support Strut: 30°/10° Configuration

This figure compares the DACVINE-computed and measured strut and post drag increments for the high-lift (30°/10° flaps) configuration.
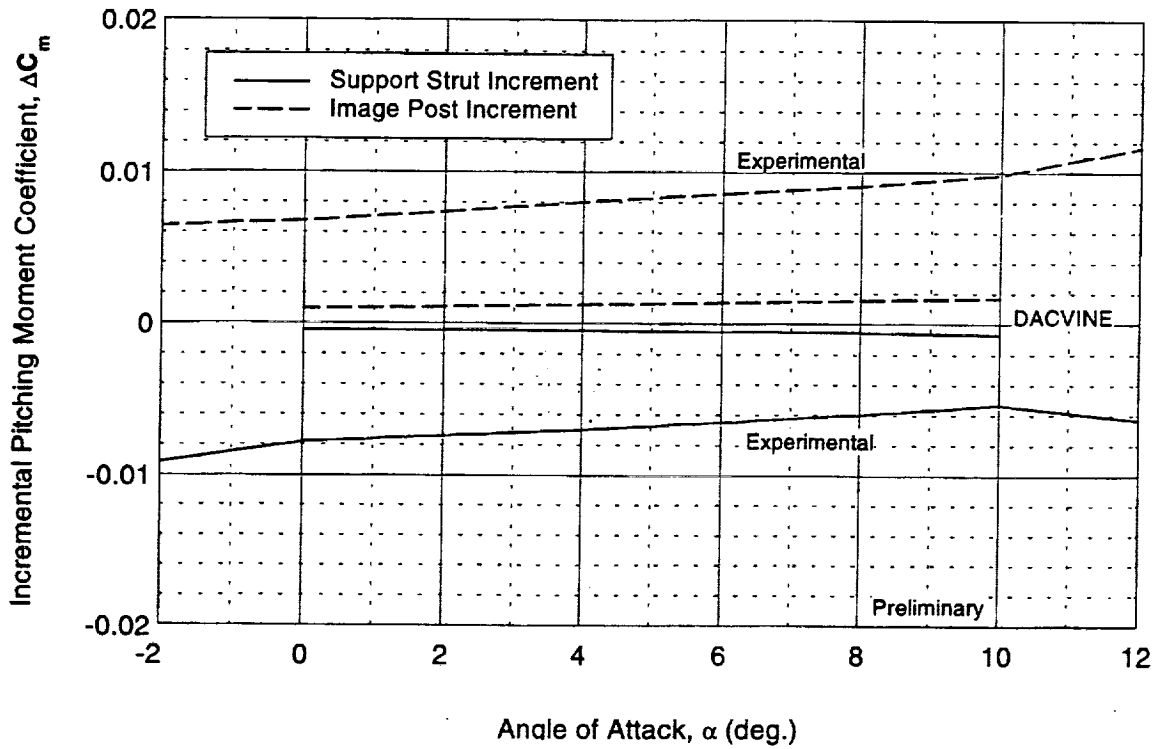
Effect of Support Strut: 30°/10° Configuration

Angle of Attack, α (deg.)

This figure compares the DACVINE-computed and measured strut and post pitching moment increments for the high-lift (30°/10° flaps) configuration.

Effect of Support Strut: 0°/0° Configuration

This figure compares the DACVINE-computed and measured strut and post pitching moment increments for the baseline (0°/0° flaps) configuration.

Summary

- DACVINE and classical wall prediction methods agree closely for 14'x22' tunnel for both lift and drag
- Only small correction would be required for off-centerline location
- Strut effects under predicted for lift, drag and pitching moment - currently under investigation

The computed tunnel wall effects computed by DACVINE agree closely with the classical wall corrections for lift and drag.

The DACVINE model shows that there is only a small sensitivity to the off-center model location which has been used in the 14'x22' tunnel for all of the post-mounted Ref H tests.

The effects of the support strut on lift, drag, and pitching moment are all underpredicted by DACVINE. The reasons for this disagreement are still under investigation, but it is believed to be due to the absence of any modeling of the viscous wake behind the support or image posts.

Work is currently in progress to modify the panel method geometry to include an empiical modeling of the viscous wake.

REPORT DOCUMENTATION PAGE

1. AGENCY USE ONLY (Leave blank)	2. REPORT DATE December 1999	3. REPORT TYPE AND DATES COVERED Conference Publication

4. TITLE AND SUBTITLE
1997 NASA High-Speed Research Program Aerodynamic Performance Workshop
Volume II—High Lift

5. FUNDING NUMBERS
WU 537-07

6. AUTHOR(S)
Daniel G. Baize, Editor

7. PERFORMING ORGANIZATION NAME(S) AND ADDRESS(ES)

NASA Langley Research Center
Hampton, VA 23681-2199

8. PERFORMING ORGANIZATION REPORT NUMBER

L-17916D

9. SPONSORING/MONITORING AGENCY NAME(S) AND ADDRESS(ES)

National Aeronautics and Space Administration
Washington, DC 20546-0001

10. SPONSORING/MONITORING AGENCY REPORT NUMBER

NASA/CP-1999-209691/VOL2

11. SUPPLEMENTARY NOTES

12a. DISTRIBUTION/AVAILABILITY STATEMENT

Unclassified–Unlimited
Subject Category 02   Distribution: Nonstandard
Availability: NASA CASI (301) 621-0390

12b. DISTRIBUTION CODE

13. ABSTRACT (Maximum 200 words)
The High-Speed Research Program and NASA Langley Research Center sponsored the NASA High-Speed Research Program Aerodynamic Performance Workshop on February 25–28, 1997. The workshop was designed to bring together NASA and industry High-Speed Civil Transport (HSCT) Aerodynamic Performance technology development participants in areas of Configuration Aerodynamics (transonic and supersonic cruise drag prediction and minimization), High-Lift, Flight Controls, Supersonic Laminar Flow Control, and Sonic Boom Prediction. The workshop objectives were to (1) report the progress and status of HSCT aerodynamic performance technology development; (2) disseminate this technology within the appropriate technical communities; and (3) promote synergy among the scientist and engineers working HSCT aerodynamics. In particular, single- and multi-point optimized HSCT configurations, HSCT high-lift system performance predictions, and HSCT Motion Simulator results were presented along with executives summaries for all the Aerodynamic Performance technology areas.

14. SUBJECT TERMS
High-Speed Research; High-Speed Civil Transport

15. NUMBER OF PAGES
794

16. PRICE CODE
A99

17. SECURITY CLASSIFICATION OF REPORT Unclassified	18. SECURITY CLASSIFICATION OF THIS PAGE Unclassified	19. SECURITY CLASSIFICATION OF ABSTRACT Unclassified	20. LIMITATION OF ABSTRACT UL